



UNIVERSIDAD
AUTÓNOMA DE
QUERÉTARO

CONIIN

LOOKING FOR SOLUTIONS WITH APPLIED ENGINEERING



FACULTAD DE INGENIERÍA

CONIIN

LOOKING FOR SOLUTIONS WITH APPLIED ENGINEERING



CONCYTEQ



CONACYT
Consejo Nacional de Ciencia y Tecnología



UNIVERSIDAD
AUTÓNOMA DE
QUERÉTARO

CONIIN

LOOKING FOR SOLUTIONS WITH APPLIED ENGINEERING

Directorio

Dr. Gilberto Herrera Ruiz
Rector

Dr. Irineo Torres Pacheco
Secretario Académico

Dra. María Guadalupe Flavia Loarca Piña
Directora de Investigación y Posgrado

Dr. Aurelio Domínguez González
Director de la Facultad de Ingeniería

MDM Carmen Sosa Garza
Secretaria Académica de la Facultad de Ingeniería

CP Guadalupe del Carmen Molinero González
Secretaría Administrativa de la Facultad de Ingeniería

Dr. Manuel Toledano Ayala
Jefe de Investigación y Posgrado de la Facultad de Ingeniería

Dra. Karen Esquivel Escalante
Director de la Publicación

Dr. Eduardo Arturo Elizalde Peña
Sub director de la Publicación

Consejo Editorial

Dr. Aurelio Domínguez González

Dra. Karen Esquivel Escalante

Dr. Eduardo Arturo Elizalde Peña

Dr. Carlos Guzmán Martínez

CONIIN: Looking for solutions with applied engineering, es una publicación anual de la Facultad de Ingeniería de la Universidad Autónoma de Querétaro, con arbitraje interno y externo (revista publicada desde el año 2016)

CONIIN: Looking for solutions with applied engineering, año 1, No. 1, (2016), es una publicación anual publicada por la Universidad Autónoma de Querétaro, por medio de la Facultad de Ingeniería, con domicilio en el Edificio A de la Facultad de Ingeniería, Cerro de las Campanas S/N, Col. Las campanas, C.P. 76010.

Editores Responsables:

Karen Esquivel Escalante, Eduardo A. Elizalde Peña y Carlos Guzmán Martínez.

Reserva de derechos al título exclusivo: en trámite

ISSN: en trámite

Certificado de Licitud y contenido otorgado por la Comisión calificadoradora de Publicaciones y Revistas Ilustradas de la Secretaría de Gobernación (en trámite).

Se distribuye actualmente mediante descarga electrónica.

Informes y correspondencia: Edificio A, Facultad de Ingeniería, Universidad Autónoma de Querétaro, Cerro de las Campanas s/n, Col. Las Campanas, C.P. 76010, Querétaro-México. Tel: +52 (442) 192 1200 ext. 6016 y 65401.

GENERAL INDEX

	Pages
General index	i
Detecting the deficit of phosphorus and potassium in lettuce crops based on leaf area measured with digital images at different stages of growth.	1
CONIIN 2015 Initial testing of plain bushings as auxiliary bearings.	6
Electrical applications of infrared thermography: A review.	11
Thermal insulation design of housing. Numerical-experimental procedure.	15
Methodology for automatic detection of trees and shrubs in aerial pictures from UAS.	24
Measurement of agglomerates shape using three-dimensional reconstruction.	30
Characterization of inner product spaces.	36
Line transversals to very disjoint translates of convex bodies.	39
USA-Mexico border issues: trucks flow.	43
High performance of a microfluidic biofuel cell alcohol dehydrogenase/laccase for ethanol.	47
Microwave assisted sol-gel synthesis and characterization of M-TiO ₂ (M=Pt, Au) photocatalysts.	51
Synthesis and characterization of AlGaSb ternary compounds.	54
Synthesis and characterization of SBA-15 functionalized with amine -NH ₂ by conventional, microwave and ultrasound methods.	59
Biofuels of microalgae: A review of culture parameters that condition the lipidic productivity and importance to incorporation of natural settings.	65
Evaluation of 3D electrode in a membraneless microdevice for energy conversion.	73

Synthesis of hydroxyapatite nanostructures by microwave assisted hydrothermal method.	76
Synthesis, and functionalization of silica nanoparticles with quercetin, a physicochemical characterization of novel nano-antioxidants.	80
Wastewater treatment by fixed biomass, using PET bottles within a biological aerobic reactor.	86
Hysteresis cycles and its behavior in expansive soil-water retention curve.	90
Flow modelling in unsaturated soils.	98
Study degradation process by cracking in simple concrete through acoustic emission technique and correlation parameters.	104
Application of CCHE2D model to Mexican rivers.	111
Chilled mirror hygrometer for suction measurement on clays from Queretaro valley.	117
Experimental studies on reduction of soil expansion by using reinforced perforations.	124
Regionalization of the Dvorak technique; case study hurricanes Ingrid and Manuel (13-16 th September 2013).	129
Spatial analysis in realtime of the rainfall season in Queretaro's urban area.	135
Mechanical design and development of a haptic device.	139
Root mean square voltage tracking using analytic signals.	144
Nitrate evaluation on lettuce (<i>Lactuca sativa L.</i>) under organic and chemical fertilization in greenhouse conditions.	150
A finite element model to assess flexible pavement – vehicle interaction.	155
Development of an Intra-Ruminal monitoring system in realtime of physiological variables.	163
Minimum-latency pipeline embedded processor on FPGA.	169

FPGA-based online estimation of the fundamental frequency (period) in civil structures using a RDT-FFT approach.	175
CONIIN 2015: Automation of optoelectronic experiment of the Production of light, Interference, and quantum entanglement with orbital angular momentum for applications in optical communications.	181
Enhancement of the photoactivity RuO ₂ doped nanoparticles TiO ₂ supported on disordered mesoporous silica as photocatalysts for methylene blue photodegradation.	191
Image generation method for geographic information systems with PHP & MySQL.	197
Modification with lime and its effect on hydraulic conductivity of expansive soils.	202
BLDC Motor drive based on current shaping cell converter.	209
Influence of preactivation of type "F" fly ash on the compressive strength of mortars with short curing periods.	214
Optimization of gearbox dynamic by a continuous genetic algorithm.	219
Determination of the moisture active zone in expansive soils of Jurica, Querétaro, obtained by numerical solution of the diffusion equation.	226
Expansion analysis in high compressibility unsaturated clay.	234
Some geometrical properties of noncircular gears.	239
Implementation of an automatized photoluminescence system using LabView.	243
Comparative study of methods for segmentation of thermographic images of the soles of the feet in patients with diabetes.	247
Vibration analysis of ABB IRB 140 industrial manipulator using moving average filter and FIR filter.	252
Supported gold catalyst in Al ₂ O ₃ -TiO ₂ for oxidation of carbon monoxide.	257

A speed performance comparative of field oriented control and scalar control for induction motors.	263
Productivity appraisal of Lettuce (<i>Lactuca sativa</i> var. <i>Vulcan</i>) and Nile Tilapia (<i>Oreochromis niloticus</i> var. <i>Spring</i>) of three aquaponic systems under greenhouse conditions.	270
Implementation of high resolution unipolar PWM inverter using xilinx system generator.	278

Detecting the deficit of phosphorus and potassium in lettuce crops based on leaf area measured with digital images at different stages of growth

Avisaí Sánchez-Alegría ^{#1}, Madaín Pérez-Patricio ^{#2}, Jorge Luis Camas-Anzueto ^{#3}, Federico Gutiérrez-Miceli ^{#4}, Abiel Aguilar-González ^{#5}, Geovanny Robles-Escobar ^{#6}

*# Instituto Tecnológico de Tuxtla Gutiérrez
Carretera panamericana km 1080, Chiapas México*

¹avisai_2300@hotmail.com

²madperez@hotmail.com

³jcamas@ittg.edu.mx

⁴fgmiceli@gmail.com

⁵abiel_ag@hotmail.com

⁶iqgjre@gmail.com

Abstract— Nutritional state of vegetable foods, is a more studied parameter to defined quality them. A way to predict the deficit of phosphorus and potassium in hydroponic lettuce crops is presented. The method is based on the leaf area sizes at different stages of growth, measured with digital images. For acquisition, the camera was placed perpendicularly to the lettuce leaf, considering technical data of sensor and the known distance between this and the leaf, the area represented by each pixel of the image and the area occupied by the leaf is computed. Nutrient types was related with leaf area size, ANOVA table determined that phosphorus and potassium are the nutrients statistically related to plant growth.

Keywords— *Lettuce-crops; Phosphorus; Potassium; Area-measured; Image processing.*

I. INTRODUCTION

Vegetables are the main source of food for human consumption. If eaten raw, we receive bio-photons which are the smallest physical units of light and are used by all biological organisms in the human body. In big cities is difficult to get fresh vegetables of the day due to lack of land for harvest, therefore, have to be transported from distant places. Lose time since place of production to the place of consumption implies deterioration of some nutritional properties.

Hydroponic is an alternative for production of vegetable food without extension of land. This is a technique of soilless culture, the roots receive nutrients from a balanced nutrient solution dissolved in water with all the chemical elements required for the development of plants and growing on inert medium called substrate.

Chemical elements contained in nutrient solution applied in hydroponics crops, are divided into two groups: macronutrients (nitrogen (N), phosphorus (P) and potassium (K)) which are essential for the development and survival of the plant because compensate some deficiencies. The second group are the micronutrients that ensure production quality and avoid absorption of fruits, flowers or stems turgor.

To plants assimilate nutrients, these are applied in compounds called salts [1]. Contributing salts N, P, K are:

calcium nitrate, monopotassium phosphate and potassium nitrate respectively.

The health monitoring in hydroponic culture has led to develop methods that aim to predict the missing nutrient based on the physical characteristics of the plant. Features like size, thickness and color are those studied more.

In the literature there are different methods to monitoring vegetable health, some destructive, others difficult to implement. Most methods focus on nitrogen analysis in [2] the authors do a review of techniques used for nitrogen analysis, the majority studies is based on the spectral behavior of the leaves, and they use scanners or spectrophotometers to measure absorption, reflection and transmission.

In recent years, methods low-cost have been developed that utilize digital images. In [3], the author emphasizes that they are fast and easy to acquire images during different growth stages, allowing evaluate plant dynamics, including the files are easy to save, to be used in future comparisons.

Research based on digital images, have focused on analysis of color. Authors [4, 5] the analysis for the 3 macronutrients is presented, they use hyperspectral images. It is common for hyperspectral images are captured with satellite sensors, which presents a disadvantage because of the high cost and complication in processing.

RGB images (Red, Green, Blue) belonging to the visible spectrum, have been used for estimating the nitrogen content [7] or chlorophyll [8, 9]. The authors take the color green leaf and relate with nitrogen and chlorophyll content. Both elements are closely related because chlorophyll is a product of nitrogen.

The paper [10] presents a method based on computer vision for estimating the crop coefficient (Kc) of lettuce crops from the percentage of ground cover (PGC) extracted from digital photographs. In contrast to other methods, plant height (h) is estimated first; then, the term PGC/h is correlated with Kc. This allows determined crop water requirements from variables that are directly related to evapotranspiration. The method was successfully applied to and validated using a commercial crop of lettuce (*Lactuca sativa* L.) located in the southeast of Spain.

This paper presents a way to predict the deficit of phosphorus and potassium in lettuce crops based on leaf area at different stages of growth measured with digital images. The camera was placed perpendicularly to the leaf of lettuce. Considering technical data of sensor and the known distance between this and the leaf, the area represented by each pixel of the image and the area occupied by the leaf is computed. Finally, nutriment types was related with leaf area size, ANOVA table determined that phosphorus and potassium are the nutrients statistically related to plant growth.

II. EXPERIMENTAL AND METHOD SETUP

A. Growing hydroponic lettuce

A crop of lettuce (*Lactuca sativa* L.) was performed. To prevent plagues or excess water due to rains, the planting was conducted in the greenhouse of the Instituto Tecnológico de Tuxtla Gutiérrez. Substrate hydroponic system was applied. A substrate of peat moss and perlite, plastic bags of 35 x 35 cm, where used, finally, nutrient solution manually applied.

To analyze the effect of the macronutrients, the nutrient solution was prepared based on a factorial experimental design with three macronutrients as factors (N, P, K) and three content levels (0, 50%, 100%) for each factor, the design gives a total of 27 experimental units. Table 1 shows the amount of salts to prepare 5 liters of solution for each experimental unit.

TABLE 1. AMOUNT OF SALTS IN EACH EXPERIMENTAL UNIT

Experimental unit	Calcium nitrate	Monopotassium phosphate	Potassium nitrate
1	0	0	0
2	0	0	0.24405
3	0	0	0.4881
4	0	0.27655	0
5	0	0.27655	0.24405
6	0	0.27655	0.4881
7	0	0.5531	0
8	0	0.5531	0.24405
9	0	0.5531	0.4881
10	2.040525	0	0
11	2.040525	0	0.24405
12	2.040525	0	0.4881
13	2.040525	0.27655	0
14	2.040525	0.27655	0.24405
15	2.040525	0.27655	0.4881
16	2.040525	0.5531	0
17	2.040525	0.5531	0.24405
18	2.040525	0.5531	0.4881
19	4.08105	0	0
20	4.08105	0	0.24405
21	4.08105	0	0.4881
22	4.08105	0.27655	0
23	4.08105	0.27655	0.24405
24	4.08105	0.27655	0.4881
25	4.08105	0.5531	0
26	4.08105	0.5531	0.24405
27	4.08105	0.5531	0.4881

For each experimental unit, 3 samples were planted giving a total of 81 plants. Between sowing and germination the irrigation was water pure. With emergence of true leaves 450 ml of solution was applied every other day until harvest.

B. Image acquisition

DBK 31AU03 camera manufactured by the company "Imaging Source" was used for image acquisition, this has a SONY ICX204 sensor with dimensions of 5.8 x 4.92 mm, focal distance of 8 mm and resolution 1024 x 768. To calculate angles opening (A) of sensor, replace the values of the dimensions (d) and focal length (f) in Equation 1. The greater opening angle is 39.85 ° and the lower angle of 34.18°.

$$A=2\tan^{-1}(d/2f) \tag{1}$$

The (x) distance between the visual field (surface where the leaf is placed) and the camera is 250 mm, as show figure 1. This parameter is used in equation 2 to find the size of the visual field (L). The largest and smallest visual field lengths are equivalent to 181.24 and 153.72 respectively, this gives a capture area of 27860.2128 mm². Considering the camera resolution as 1024x768, this mean we have a total of 786,432 pixels, and the Rule of Three indicates that each mm² of area is equal to 28.23 image pixels.

$$L=2x \tan (A/2) \tag{2}$$

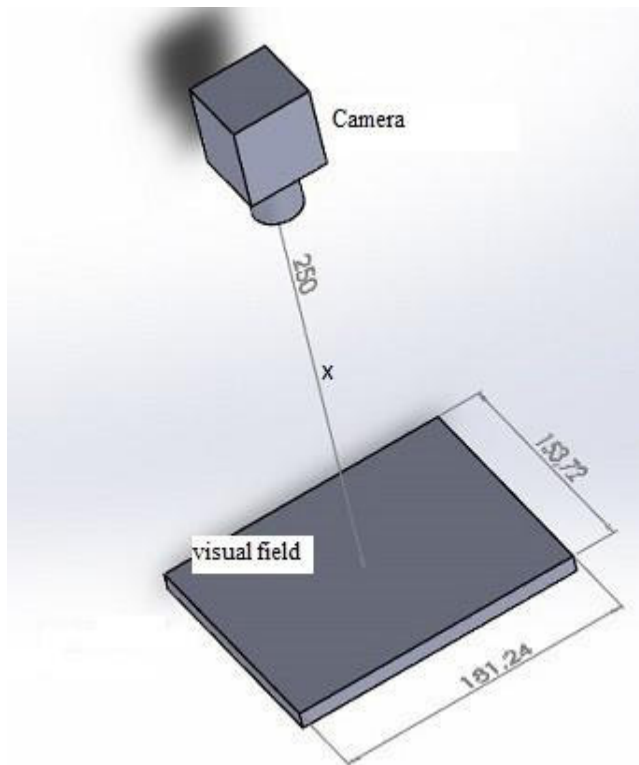


Fig. 1. System for Image acquisition

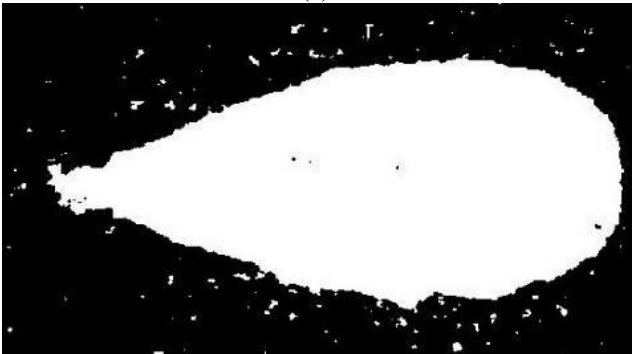
C. Image processing

Is necessary to apply a segmentation process for separating leaf from the background image. Hue (H) for RGB image of Figure 2a was calculated with equation 3, based on the histogram, optimal thresholds (0.15 <T <0.5) were computed for the binarization. The result of this process is presented in Figure 2b, due to white points are detected in areas outside the leaf, opening and closing morphological operations were applied, the end result is shown in Figure 2c where the part occupied by the leaf is white and the background is black.

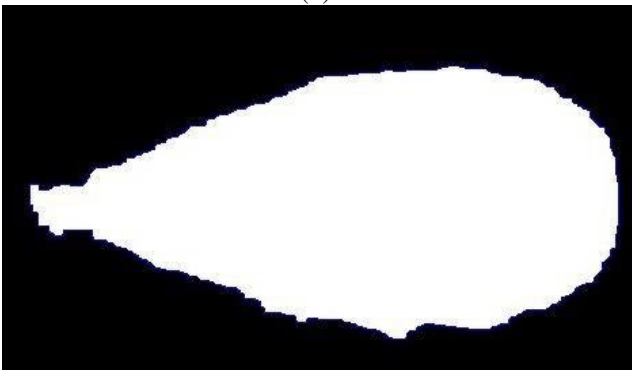
$$H = \cos^{-1} \left\{ \frac{\frac{1}{2}[(R - G) + (R - B)]}{[(R - G)^2 + (R - B)(G - B)]^{\frac{1}{2}}} \right\} \quad (3)$$



(a)



(b)



(c)

Fig. 2. Image processing

The white pixels the binaries image, are the necessary data for image processing, however, black cover a good part as shown figure 2c. The binaries image was cut, leaving the edges defined on the first white pixel of each of the four sides as shown in Figure 3. The cut served to reduce the weight of the image, save space on the storage disk and speed up the processing.

In programming software (Matlab 2013a) a count of white pixels contained in the cropped image of Figure 3, was did. According to calculations each mm² covers 28.23 pixels. The result of white pixels counting was divided by 28.23 and the area occupying lettuce leaf that is the resulting quotient.

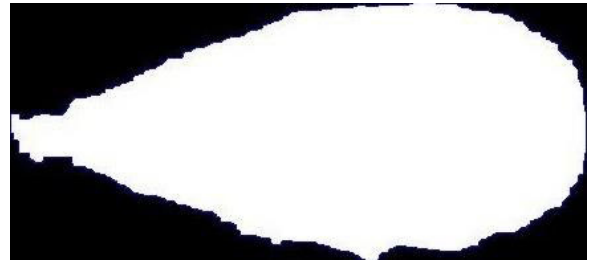


Fig. 3. Cropped image

The areas of the experimental units for 20, 30, 40 and 50 days after planting are presented in table 2. To making the acquisition, the 5 leaves most developed between the 3 plants from each experimental unit was selected. The result shown is the average of 5 measurements.

TABLE 2. ÁREA OF LEAVES IN DIFFERENT STAGES GROWTH

Experimental unit	20 days mm ²	30 days mm ²	40 days mm ²	50 days mm ²
1	1589.2	2052	2573.1	2734.3
2	2572.3	2771	3174.5	3504.4
3	2606.5	2862	3174	3303.3
4	2239.3	2685.9	2794.8	3847.1
5	2989.4	3105.2	4054.5	5593
6	4365	4500.3	4835.9	5161.7
7	2240.1	3471.2	4382.9	5175.1
8	2801.5	3420.7	3759.7	4511.4
9	3135.2	3523.7	4567.5	5625.1
10	2239.4	2548.2	2838.4	2917.9
11	1110	1895.4	2100	2200
12	1320.5	1927.3	2426.6	2640
13	2677.2	3082.6	4156.5	5449.3
14	3395.2	4540	5809.8	6585.7
15	3914.2	4997.7	5870	6974
16	3841.4	4457.2	4821.1	5908
17	3596.2	3939	4511.1	5391.3
18	2967.6	3521.9	4989.4	5847.7
19	2517.3	2614.6	2820.2	3307.3
20	2068.9	2516.3	3846.3	4669.4
21	2379.6	3378.9	4019.5	5489.7
22	2263.6	2849.6	3817.6	4091
23	4110.7	4659.9	5001.9	6369
24	3496.1	3912.2	4689.5	5395.2
25	2872.3	3771	4253.2	5433.4
26	3558.9	4201.9	5032	5802.6
27	2612.4	3577.8	4713.1	5767.7

III. RESULTS

A multifactorial analysis of variance was applied, as factors, the salts presented in Table 1 and the dependent variable the leaf areas of Table 2. We have four stages of growth and four ANOVA tables. Table 3 summarized percentage relationship between nutrients and leaf area for each growth stage. By analysis them, an increases the relationship between nutrients and leaf area is observed. Nitrogen ratio does not become significant until the plant reaches maturity. On the other hand, phosphorus and potassium are statistically related to the development of plants.

TABLE 3. PERCENTAGE RELATIONSHIP BETWEEN NUTRIENT SALTS AND LEAF AREA

	Calcium nitrate	Monopotassium phosphate	Potassium nitrate
20 days	27.63	99.97	93.6
30 days	67.84	99.94	88.52
40 days	94.73	99.99	98.62
50 days	98.21	100	98.96

According to the results and [11, 12] authors, it is known that nitrogen does not significantly affect in crop leaf area. Table 4 is based on P and K, it decomposes the variations of the areas and because we had select the sum of squares, the contribution of each factor is measured by removing the effects of the other factors.

To detect the presence or absence of phosphorus or potassium, is necessary to know the age of the plant, measure the area of them and compare against the values in Table 4. The lower limits represent the minimum area that must have a leaf for to be considered within the range, and the upper limit is the maximum. The mean column is the average of the measurements of leaf area. If a crop is 30 days old, and its area is less than 3447.07 mm², do not have enough phosphorus to develop, and to determines that this same leaf has necessary potassium, its area must be greater or equal to 4234.24 mm²

Phosphorus and potassium affect crop growth, but only if are completely absent, as shown in table 4. The proposed method is useful only to predict the absence or presence of phosphorus and potassium.

TABLE 4. MEDIAS OF AREAS CALCULATED PER SQUARE MINIMUM IN EACH GROWTH STAGE

Age	Salts names	Salts amount	Cases	Mean	Lower limit	Upper limit
20 days	Monopotassium phosphate	0	9	2044.86	1746.4	2343.31
		0.27655	9	3272.3	2973.84	3570.76
		0.5531	9	3069.51	2771.05	3367.97
	Potassium nitrate	0	9	2497.76	2199.3	2796.21
		0.24405	9	2911.46	2613.0	3209.91
		0.4881	9	2977.46	2679.0	3275.91
30 days	Monopotassium phosphate	0	9	2507.3	2139.54	2875.06
		0.27655	9	3814.82	3447.07	4182.58
		0.5531	9	3764.93	3397.18	4132.69
	Potassium nitrate	0	9	3059.14	2691.39	3426.9
		0.24405	9	3449.93	3082.18	3817.69
		0.4881	9	3577.98	3210.22	3945.73
40 days	Monopotassium phosphate	0	9	2996.96	2672.25	3321.66
		0.27655	9	4558.94	4234.24	4883.65
		0.5531	9	4558.89	4234.18	4883.59
	Potassium nitrate	0	9	3606.42	3281.72	3931.13
		0.24405	9	4143.31	3818.61	4468.02
		0.4881	9	4365.06	4040.35	4689.76
50 days	Monopotassium phosphate	0	9	3418.48	3079.4	3757.56
		0.27655	9	5496.22	5157.14	5835.3
		0.5531	9	5495.81	5156.73	5834.89
	Potassium nitrate	0	9	4318.16	3979.07	4657.24
		0.24405	9	4958.53	4619.45	5297.61
		0.4881	9	5133.82	4794.74	5472.9

CONCLUSIONS

The leaf size is affected by the three macronutrients, however, nitrogen do not significantly affect until the plant has reached maturity. Is understood that nitrogen has other functions such as development of chlorophyll. Phosphorus is the most important in the size of the leaves because it is the only that affects with a close relationship to 100%, potassium also has high correlations, but not more than phosphorus.

Applying the proposed method, is possible detect the deficit of phosphorus and potassium by analysis of leaf area. Furthermore, we demonstrated that leaf area is similar for two levels of content, this phenomenon occurs in all stages of growth, and for both macronutrients.

REFERENCES

- [1] D.M. Yeh, L. Lina, C.J. Wright, S. Jacobs and C. P. Bean, "Effects of mineral nutrient deficiencies on leaf development, visual symptoms and shoot-root ratio of *Spathiphyllum*", *Scientia Horticulturae*, 2000, vol. 86 pp. 223-233.
- [2] Rafael F. Muñoz-Huerta 1, Ramon G. Guevara-Gonzalez, Luis M. Contreras-Medina, Irineo Torres-Pacheco, Juan Prado-Olivarez and Rosalia V. Ocampo-Velazquez, "A Review of Methods for Sensing the Nitrogen Status in Plants: Advantages, Disadvantages and Recent Advances", *Sensors*, 2013, vol.13, pp. 10823-10843.
- [3] Xiaoming Yao, Wencai Du, Siling Feng, Jun Zou. "Image-based Plant Nutrient Status Analysis: An Overview," *Intelligent Computing and Intelligent Systems (ICIS)*, 2010 IEEE International Conference on, IEEE,2010, pp. 450-464.
- [4] Xiaolei Zhang, Fei Liu, Yong He, Xiangyang Gong, "Detecting macronutrients content and distribution in oilseed rape leaves based on hyperspectral imaging", *biosystems engineering*, 2013, vol. 115, pp. 56-65.
- [5] R.O. Pacumbaba Jr., C.A. Beyl, "Changes in hyperspectral reflectance signatures of lettuce leaves in response to macronutrient deficiencies," *Advances in Space Research*, 2011, vol. 48, pp. 32-42.
- [6] Marian Wiwart, Gabriel Fordonski, Krystyna uk-Golaszewska, Elzbieta Suchowilska, "Early diagnostics of macronutrient deficiencies in three legume species by color image analysis", *computers and electronics in agriculture*, 2009, vol. 65, pp. 125-132.
- [7] Lili Ma., Junlong Fang, Yuehua Chen, Shuipeng Gong, "Color Analysis of Leaf Images of Deficiencies and Excess Nitrogen Content in Soybean Leaves", *International conference on E-product and service*, 2010.
- [8] Wang Juan, Wei Changzhou, Guo Jinqiang, Lei Yongwen, "A method based on Digital Image Analysis for Estimating Crop Canopy Parameters," *International Conference on Computer Distributed Control and Intelligent Environmental Monitoring*, 2011.
- [9] V. K. Tewari, Ashok Kumar Arudra, Satya Prakash Kumar, Vishal Pandey, Narendra Singh Chandel, "Estimation of plant nitrogen content using digital image processing", *Agric Eng Int: CIGR Journal*, 2013, vol. 15, pp. 78-86.
- [10] Daniel G. Fernández-Pacheco, David Escarabajal-Henarejos, Antonio Ruiz-Canales, Julián Conesa, Jose M. Molina-Martínez, "A digital image-processing-based method for determining the crop coefficient of lettuce crops in the southeast of Spain", *biosystems engineering*, 2014, vol. 117, 23-34.
- [11] Cordon Gabriela Beatriz, "Métodos ópticos no destructivos para el monitoreo de salud vegetal" *Universidad de buenos aires*, 2009.
- [12] Yuan Wang, Dejian Wang, Peihua Shi and Kenji Omasa, "Estimating rice chlorophyll content and leaf nitrogen concentration with a digital still color camera under natural light" *Plant methods*, 2014, 10:36.

CONIIN 2015 Initial testing of plain bushings as auxiliary bearings

Victor Solorzano ^{#1}, Oscar De Santiago ^{*2}, Juan Carlos Jauregui ^{#3}

^{#1} *Especialistas en Turbopartes*
Querétaro, Qro., México.

¹ victor.solorzano@etu.mx

^{*2} *Centro de Tecnología Avanzada (CIATEQ)*
Querétaro, Qro., México.

^{*2} oscar.desantiago@ciateq.mx

^{#3} *Universidad Autónoma de Querétaro*
Querétaro, Qro., México

^{#3} jc.jauregui@uaq.mx

Abstract— Recent challenges in turbocompressor design include applications in subsea installations as well as remote operation in unmanned floating platforms. These applications benefit from oil-free operation which solves technical hurdles while being environmentally friendly. The most mature oil-free rotor support technology today is the magnetic bearing which is being used by several manufacturers as their standard solution to these advanced applications. These systems require auxiliary bearings to contain the rotor in case of a power failure to the magnetic bearings or a transient event. In general, there exists the need to develop commercial solutions for auxiliary bearings to extend its life, in particular regarding cumulative damage associated to drop events.

This paper presents initial experiments in a configurable test rig that can accommodate different rotor sizes, up to 1200 mm in bearing span, and 711 mm diameter wheels. Initial experiments on bushings as auxiliary bearings are shown for a 5-impeller, 57.8 kg, subcritical compressor rotor without drop events to study the baseline dynamic behavior of plain bushings (with inner clearance) on soft supports (o-rings). These experiments are presented to illustrate non-linear vibration regimes present during rotor-stator interaction with a highly unbalanced rotor. Results are promising and resemble similar phenomena than the reported in rotor drop tests although further testing is recommended.

Keywords—auxiliary bearings; dry friction; rubbing

I. INTRODUCTION

Auxiliary bearings have to support the static and the high dynamic loads generated during an event of magnetic bearing levitation loss. Generally, auxiliary bearings are of the ball bearing type and they have a flexible support, which can absorb part of the impact, in order to reduce the dynamic force on the bearings. Another important challenge is to maintain the system integrity during this period; this is that the system can operate on the auxiliary bearing, or at least that these bearings allow to stop the rotor without damaging the system [1].

^{*2} Currently at ETU - Turbo i+D

In a rotor drop event when the rotor is rotating at high speed, a series of impacts takes place on the auxiliary bearings. This state of operation can be destructive for the machinery if a chaotic dynamic response is developed. By design, the main element to suffer damage is the auxiliary bearing and its wear sleeve. Recently the oil industry has shown the need for auxiliary bearings that allows the operation even after a drop of the rotor. Furthermore, it's desirable that the system could be capable of operating on the auxiliary bearings for long periods of time if the magnetic bearings fail to regain normal operation. This is true for remotely installed equipment that is of difficult access (for example in subsea applications).

Currently there is theoretical and experimental research focused on rotor drop event [2, 3 among others]. However there is still the need for a better understanding on the auxiliary bearing fundamental behavior (without rotor drop). There is some research on rotor-stator rubbing phenomena; however it has been focused on non-support components (as interstage seals) [4-8] and never with a rotor mounted with clearance in its support elements.

In the past De Santiago and Huerta [9] develops a parametric study on rotor drop events using an existent rotordynamic simulation tool for rotor-stator rubbing. The rubbing model consists of a stator with predefined friction coefficient in a flexible support (with predetermined stiffness and damping) mounted with clearance with the rotor. In order to validate the model used in [9] a plain bushing flexibly mounted is proposed. These initial tests also intends to be a starting point to model more complicated arrangements (such as rolling bearings with or without cage, etc.).

Following the hypothesis that the main instability source is radial clearance and unbalance (not initial impact caused by rotor drop) this work experiments with a rotor mounted in dry bushings with radial clearance and an elastomeric damper (in a typical arrangement for auxiliary bearings).

II. TEST RIG DESCRIPTION

Figure 1 shows the test rig assembly described in detail in [10], and which is intended to study advanced supports in turbomachinery at real scale. An electric motor drives an intermediate shaft through a multiplying belt and pulley arrangement (ratio of 1:2.63). The intermediate shaft connects to the main testing rotor through a gear-type coupling. The rig allows for different rotor configurations and bearing spans. The current experimental rotor is a 5-stage, 57 kg (without coupling and magnetic bearing sleeves) centrifugal compressor rotor with a balance drum. This is a rigid rotor well above maximum running speed (first free-free mode is at 15,700 cpm as predicted with a model calibrated by free-free impact tests [11]).

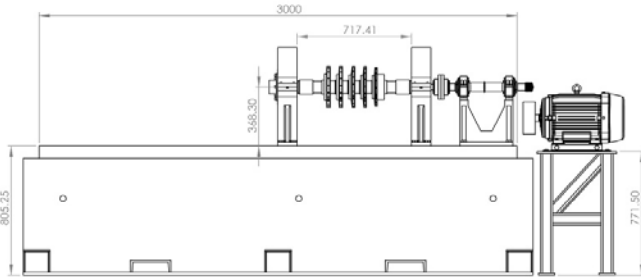


Figure 1. Lateral view of advanced bearing test rig (mm).

The rig motor can drive the test rotor up to 10,000 rpm. For the current experiments, intermediate shaft bearings limit the rig to a top speed of 9,000 rpm. The test rotor has wear-out bearing sleeves of 69.89 mm (2.75 in) in diameter.

Figure 2 shows the rotor configuration and main dimensions. Prior to the experiments, the rotor is balanced in-situ. It is important to note that the rotor does not have an axial constraint during the experiments other than the gear coupling, because the tests focus on the performance of the radial bearings. This is an important feature that highlights the need for considering system integration, as it is shown in [12] for gas bearings tests.

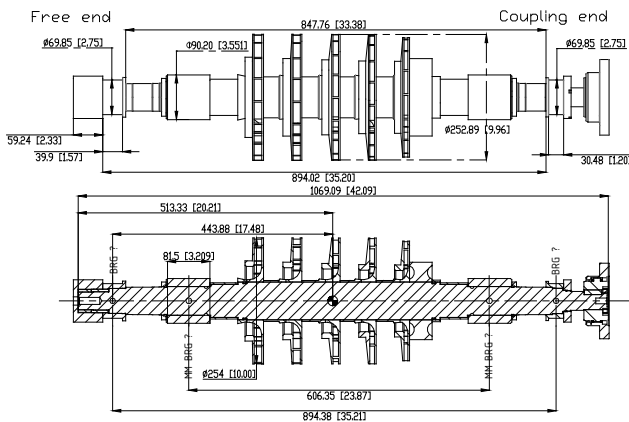


Figure 2. Test rotor configuration (dimensions in mm [in.]).

An instrumentation system monitors and records rotor vibration and operating personnel registers bearing temperature manually. Main instrumentation consists of eddy-current probes for rotor displacement measurements in two planes, inboard of the bushings plus an axial vibration probe. Piezoelectric accelerometers measure main rotor and intermediate shaft pedestal acceleration as well as motor vibration in the horizontal direction. A 24-channel data acquisition system specialized for rotating machinery in parallel with an 8-channel generic DAQ system perform data acquisition, signal processing and storage for data post-processing.

III. DESCRIPTION OF EXPERIMENTS

Previously [9] a rotor-stator rubbing model is employed for rotor drop modelling. Model consist of a stator (one piece without mobile parts) with a predefined friction coefficient and radial clearance mounted on a flexible support with predefined stiffness and damping that are speed independent. In order to provide valid experimental data for comparison with the model, the experiments use dry brass bushings mounted on a flexible support (o-ring damper) (test are developed without rotor drop) and with radial clearance. During test the rotor will rub without lubrication over the bushing causing damage, residues accumulation and heat generation, these results are expected in advance, although it is not desired, it cannot be avoided in the current test arrangement.

Three individual tests are planned although premature bushing damage (damage was expected) prevents the test schedule to be completed. For the experiment, the rotor is accelerated with constant acceleration (the same for all tests) up to 5,400 rpm, it is maintained at full speed for 30 seconds at least and then is decelerated with a characteristic ramp for each test.

High unbalance levels present in the rotor prevented a higher test speed for safety reasons although; results are valuable since unbalance constitute one of the main variables determining the rotor vibration regime. A high unbalance level will increase the normal force in the rotor-stator contact, in consequence it will increase friction force and this could lead to potentially destructive backward whirl.

First test deceleration is achieved by turning off the motor and thus it corresponds to the deceleration rate characteristic of the system friction losses (namely a “natural” deceleration rate). Second deceleration rate was planned (seizure occurred before deceleration stage) to be faster than natural deceleration and the third deceleration slower than natural deceleration. Third test was planned to be slower than natural deceleration, although the second test failure prevented following the test schedule.

Figure 3 shows speed vs time for first and second bushing tests. Acceleration ramp is identical for both tests, although during second test heat and residues accumulation caused a seizure (described later).

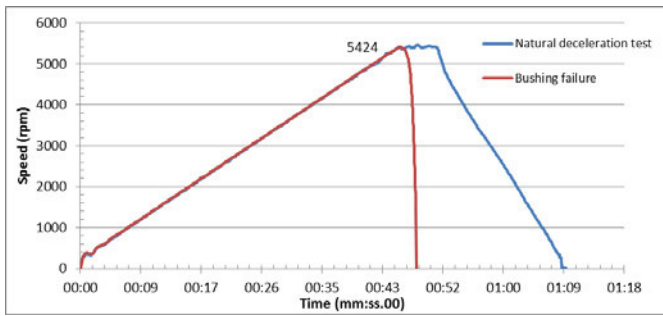


Figure 3. Speed vs time.

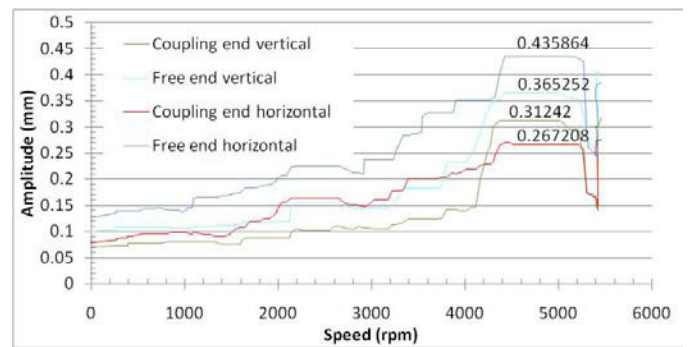


Figure 5. Bode plot for overall vibration during coast down for the first test with natural deceleration

A. First test with natural deceleration

Figure 4 shows total vibration vs time for the complete first (natural deceleration) test during run-up. At 4,000 rpm (66.6 Hz) a series of jumps starts with a caothical behavior. It is worth to notice that jumps take place in both rotor ends and directions simultaneously.

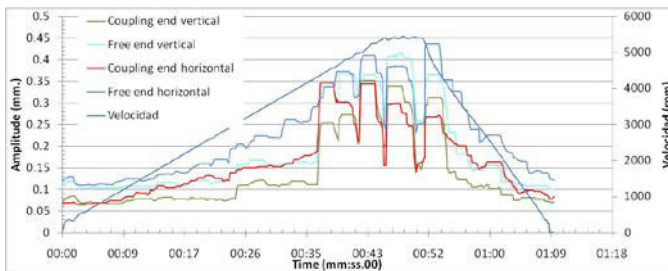


Figure 4. Vibration trend for overall vibration for the first test with natural deceleration (amplitude vs time)

Figure 5 shows a coast down Bode Plot for overall rotor vibration during natural deceleration experiment. Coast down data is presented in order to disregard torque present during acceleration stage. A jump phenomena is present at 4,300 rpm (71.6 Hz) in vertical direction, this jump is similar to the one described in [10] for rolling bearings. Jump phenomena could be caused by dry friction present in the experiment that might potentially provoke a partial backward whirl or even a full backward whirl however it would appear at frequencies above current tests bandwidth. The most severe jump takes place in the coupling end causing an amplitude decrease from 0.312 mm p-p (0.0123 in) to 0.139 mm p-p (0.055 in), corresponding to a 55% decrease in amplitude. Free end vertical jump is less severe causing an amplitude decrease from 0.365 mm p-p (0.014 in) to 0.231 mm p-p (0.0091 in), corresponding to a 36% decrease in amplitude. In the horizontal direction a series of small jumps takes place during deceleration with the most severe jump at the same speed of the vertical jump.

Figure 6 shows vibration amplitude vs time for the same samples as Figure 5. Figure 6 shows a sudden amplitude decrease at constant speed (close to 5,420 rpm) for all proximity probes. Also it shows a sudden vibration increase about 0.25 seconds after motor turning off. Vibration change after motor turn off could be caused by speed change or to motor torque suppression. The last abrupt vibration change takes place about 2.5 seconds after motor turning off with the rotor at 4,300 rpm (corresponding to the jump visible in Fig 4).

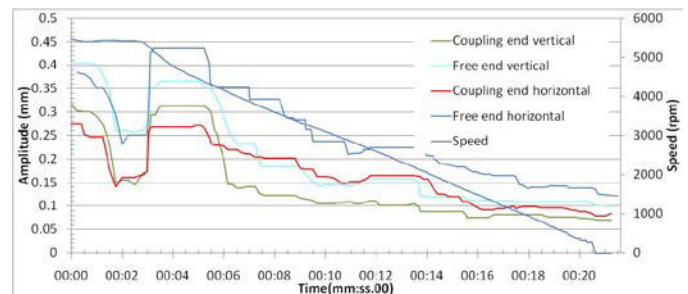


Figure 6. Vibration trend for overall vibration during coast down for the first test with natural deceleration (amplitude vs time).

Figure 7 shows temperatures registered manually with an infrared thermometer, there is a greater temperature increase in the coupling end bearing influencing the seizure during the second test.

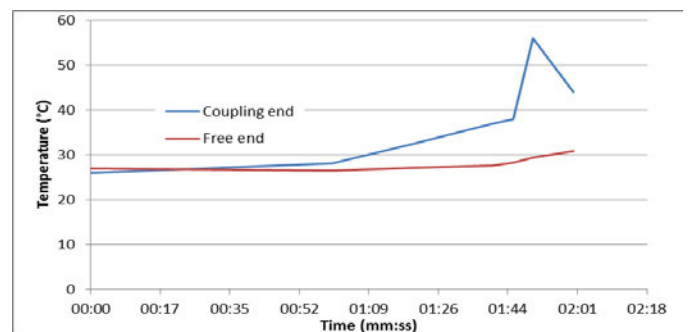


Figure 7. Bushing temperature during first test.

B. Second test and bushing failure

During the second test a seizure caused the rotor to stop abruptly and triggered the motor current protection. Figure 8 shows a speed plot for the second bushing test. Bushing heat, rotor thermal expansion (caused by dry friction) and residues accumulation caused the rotor to stick rigidly with the bushing in the phenomenon known as seizure. Rotor deceleration from 5,368 rpm to 0 rpm took place in 1.8 seconds.

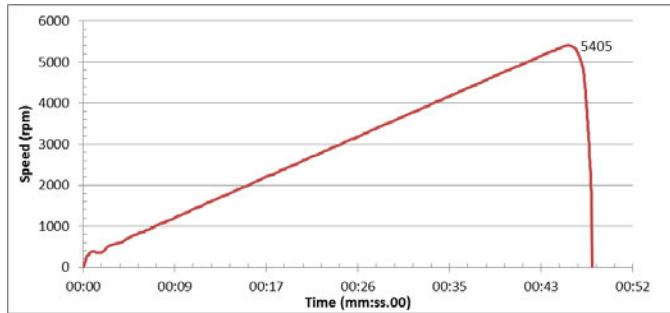


Figure 8: Bushing temperature during second test.

Coast down was so abrupt that there is insufficient data for a Bode Plot, Figure 9 shows vibration measurements during rotor run up. The jump phenomenon is visible in both rotor ends and directions; the larger jump took place in rotor free end (0.325 mm, 0.0128 in).

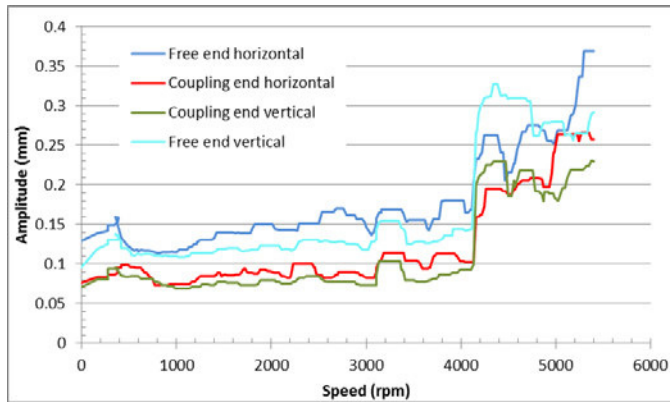


Figure 9. Bode plot for overall vibration during run up for the second bushing test.

Figure 10 shows damage on the o-rings caused by the seizure. Braking torque during seizure is transmitted through bushing to the o-rings and auxiliary bearings housing.

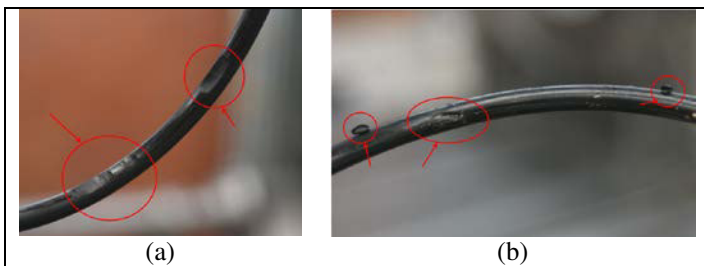


Figure 10. Damaged coupling end o-rings.

Figure 11 shows coupling end bushing damage. Note that damage occurred at both sides of the blue diagonal at about 45° from the vertical (in the direction of rotation). Figure 12 shows a drawing with the direction of rotation and main contact angle.

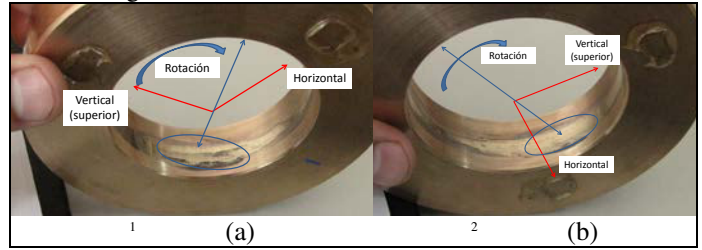


Figure 11. Bushing damage

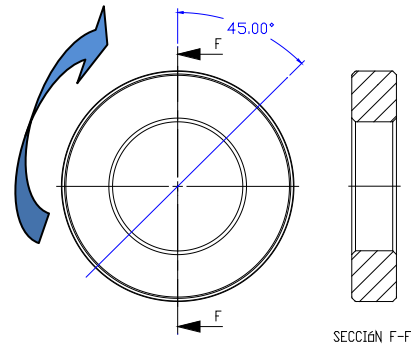


Figure 12. Main contact angle.

Figure 13 shows temperature registered manually during bushing second test. Note that the second test started with bushing with a higher temperature than the first test with natural deceleration. Initial temperature and residues accumulation are the main causes for seizure.

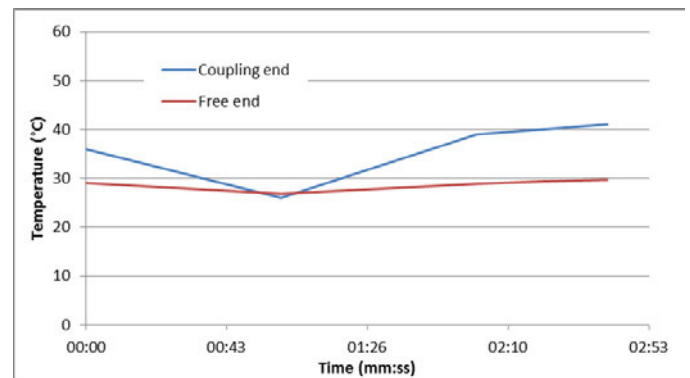


Figure 13. Bushing temperature during second test.

IV. PRELIMINARY CONCLUSIONS

Experiments show chaotical behavior and vibration amplitude jumps that have been observed during auxiliary bearings drop down tests. Lack of data impedes to characterize the orbit during jump with dry bushings although jump severity and its characteristic direction could be caused by impacts or by a partial backward whirl. Backward whirl is among the most

dangerous phenomenon possible during a rotor drop and if confirmed without rotor drop nor an external excitatory force could improve its prediction and thus prevent real systems to fall in dangerous design parameters.

Results are promising although, in order to make a complete comparison with the model described in [9], more tests are recommended with an extensive instrumentation revision. Instrumentation should include at least capability of synchronous waveform, asynchronous waveform, speed reference, and automatic temperature acquisition.

ACKNOWLEDGMENT

The authors thank the following persons for their help in preparing the test bearings, test apparatus and conducting the experiments: Mr. Conín Arcega, Mr. Edmundo Rodríguez, Mr. Vicente Rangel and Dr. Ruben Perez. Thanks also to CIATEQ for providing a grant for this project.

REFERENCES

- [1] E. N. Cuesta, N. I. Montburn, V. Rastelli, and S. E. Diaz, 2005, "Simple model for a magnetic bearing system on the auxiliary bearing", ASME Paper GT2005-69013. J. Clerk Maxwell, A Treatise on Electricity and Magnetism, 3rd ed., vol. 2. Oxford: Clarendon, 1892, pp.68–73.
- [2] L. Hawkins, A. Filatov, S. Imani, and D. Prosser, 2006, "Test results and analytical predictions for rotor drop testing of an AMB Expander/Generator," ASME Paper GT2006-9028.
- [3] A. Masala, G. Vannini, D. Ransom, J. Moore, and L. Baudelockque, 2011, "Numerical simulation and full scale landing test of a 12.5 MW vertical motorcompressor levitated by active magnetic bearings," ASME Paper GT2011-46411.
- [4] J. C. Wilkes, D. Childs, B. J. Dyck, and S. G. Phillips, 2010, "The Numerical And Experimental Characteristics Of Multimode Dry-Friction Whip And Whirl," Journal of Eng. For Gas Turbines and Power, May, Vol. 132, pp. 052503-1 – 052503-9.
- [5] T. Yamamoto, (1954), "On the critical speeds of a shaft," Memoirs of the faculty of engineering, Nagoya Univ., Vol. 6, No. 2, pp. 755.
- [6] H. Black, 1968, "Interaction of a whirling rotor with a vibrating stator across a clearance annulus," Journal of Mechanical Engineering Science, Vol. 10, pp. 1-12.
- [7] D. Childs, and A. Bhattacharya, 2007, "Prediction of Dry-Friction Whirl and Whip Between a Rotor and a Stator," Journal of Vibration and Acoustics, Vol. 129, pp. 355-262.
- [8] D. E. Bently, P. Goldman, and J. Yu, 2002, "Full annular rub in mechanical seals, Part II: Analytical Study," International Journal of Rotating Machinery, Vol. 8, Issue 5, pp. 329-336.
- [9] O. De Santiago and L. Huerta, 2011, "Análisis de caída de rotores sobre cojinetes auxiliares en máquinas con cojinetes magnéticos," XII Congreso y exposición latinoamericana de turbomaquinaria, 21-25 febrero, Querétaro, Qro.
- [10] O. De Santiago, V. Solórzano, and S. E. Diaz, 2012, "Full-Size Rotordynamic Test Rig For Magnetic And Auxiliary Bearing Testing And Initial Results", ASME Paper GT2012-69338, Presented at the 2012 IGTI conference, Copenhagen, Denmark, June.
- [11] S. E. Díaz, O. De Santiago, V. Solórzano, 2012, "Rotordynamic modeling of centrifugal compressor rotors for use with active magnetic bearings," Paper No. CELT-019-2012, XIII Latin American Turbomachinery Congress and Exposition, Queretaro, Mexico, March.
- [12] O. De Santiago and V. Solórzano, 2013, "Experiments with scaled foil bearings in a test compressor rotor" ASME Paper GT2013-94087, Presented at the 2013 IGTI conference, San Antonio, Texas, June.

Electrical applications of infrared thermography: A review

M. Á. Herrera Arellano ^{*1}, L. A. Morales Hernández ^{*2}

División de Posgrado, Facultad de Ingeniería Universidad Autónoma de Querétaro.
Cerro de las Campanas S/N, Las Campanas, 76010 Santiago de Querétaro, México.

¹ ing.ma.herrera@hotmail.com

² luis.morales@uaq.mx

Abstract—Temperature is an important indicator of the electrical equipment condition. We can make an accurate fault diagnosis by using the temperature profile of the electrical equipment surface. Infrared thermography (IRT) has gained more attention and become an interesting method in electrical fault diagnosis because of the advantages it provides. This paper is a review of the application of IRT for diagnosing faults in electrical equipment; furthermore we have included theoretical background, monitoring techniques, the fault classifications and fault diagnosis in electrical engineering fields.

Keywords—Infrared thermography, Electrical equipment, Fault detection, Fault diagnosis.

I. INTRODUCTION

Due to increasing demands for efficiency and product quality and progressing integration of automatic control systems in high cost and safety critical processes, the field of monitoring, fault detection and fault diagnosis play an important role.

The analysis to get fault diagnosis is a systematic process that determines the origin of the failure and uses this information to make the proper handling of electrical equipment. This process consist of four basics steps: monitoring, fault detection, fault diagnosis, fault management [1, 2]. This process is displayed on the figure I.1.

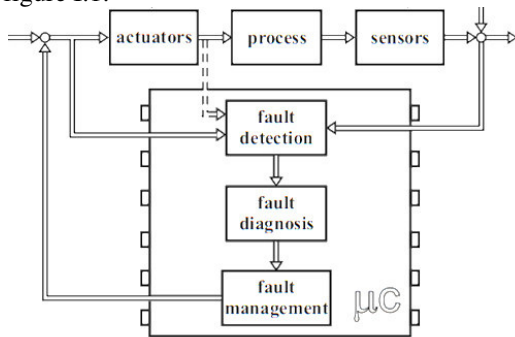


Fig. I.1 Process of fault diagnosis [1].

The equipment which is referred to as electrical equipment in this work consist of switches, circuit breakers, bus bar connections, cables, wires and fuses in the main switch and distribution boards of the buildings, transformers [3, 4]. Generally, faults of electrical systems show overheating of conductor contacts and connectors, loose connection and breakdown of insulation, etc. before they cause a catastrophic failure or serious damage [5].

Temperature is an indicator of the condition of electrical equipment.

There are two ways to measure the thermal condition of electrical equipment. The first is known as quantitative, which is to take the exact temperature of the equipments. The second type is qualitative, which takes the relative temperature values of a hotspot with respect to other parts of the equipment under similar conditions. Some applications do not require to obtain exact surface temperatures. It is sufficient to acquire thermal signatures, which are characteristic patterns of relative temperatures of the equipment. This method of qualitative visual inspection is expedient for collecting a large number of detailed data and conveying them into a way that can be easily interpreted [9].

The use of infrared thermography (IRT) in monitoring is to gain importance in many industrial fields. IRT is one of the popular non-destructive testing and condition monitoring tools which is generally used to investigate the invisible thermal abnormalities on the surface of the materials in various applications such as military, industrial, electrical, structure and medical fields [5, 6, 7, 8].

A. Definitions

The infrared (IR) radiation that typically falls between wavelengths of 2-15 μm that is between the visible and microwave parts of the electromagnetic spectrum. Near IR waves (0.7-25 μm) are close to visible light but with a wavelength that is longer than visible and shorter than microwaves and with a frequency that is lower than visible and higher than microwaves. Far IR waves (25-1000 μm) are closer to the microwave region.

All objects radiate energy that is transported in the form of electromagnetic waves, which travel at speed of light. The amount of energy leaving a surface as radiant heat is proportional to its emissivity and the fourth power of its absolute temperature given by:

$$q^n = \epsilon T^4 \quad (1)$$

Where q^2 is the hemispherical total emissive power (radiated energy per unit area, W/m^2), σ the Stefan-Boltzmann constant ($5.67051 \times 10^{-8} \text{ W}/\text{m}^2 \cdot \text{K}$), ϵ is the total hemispherical emissivity of the surface ($0 < \epsilon < 1$) and T is the surface absolute temperature (K). Any object with a temperature other than

absolute zero radiates within a range of wavelengths from 0 to ∞ .

All objects with temperature above absolute zero emit electromagnetic radiation, which is known as infrared radiation or thermal radiation. Table 1 shows the emissivity of different materials that are used for electrical equipment [8].

Table 1 Emissivity of some materials

Materials	Temperature (K)	Emissivity
Aluminum (heavily weathered)	290	0.83–0.94
Brass (polished)	301	0.03
Copper (oxidized)	311	0.87
Cast iron (heavy oxidation)	377	0.95
Nickel (polished)	298	0.05
Tempered iron (polished)	313–523	0.28

An IR thermal camera is a device that makes an image of thermal patterns and is calibrated to measure the emissive power of surfaces in an area at various temperature ranges. They use a lens to focus the emitted IR radiation on to a detector and the electrical response signal is converted into visual display (digital picture) in which the different colors correspond to various temperature levels of the surface (target) on which it is focused. Available software can then be used to analyze the thermographic images and even quantify these differences [9]. Thermography is non-contact type technique which provides a fast, reliable and accurate temperature profile of any material surface. Several standards for measurement of the temperature by using IR are found such as Electrical Testing Association (NETA) [10], National Fire Protection Association (NFPA) e NFPA 70-B [11] and International American Society for Testing & Materials (ASTM) [12], etc.

II. MONITORING

Monitoring is to measure variables to check with regard to tolerances, and alarms that are generated by the operator. After an alarm is triggered the operator then has to take the appropriate counteractions [1].

In recent years, many temperature monitoring techniques have been implemented. These techniques find their application based on the measurable temperature range, sensitivity and easy application [3]. One of the main advantages of IRT based-condition monitoring technique is that it requires minimal instrumentations.

The essential requirements for measurement in electrical devices are an IR thermal camera, a tripod or camera stand and a video output unit for displaying the acquired infrared thermal images, inspections can be done without shutting down the system operation [10, 13].

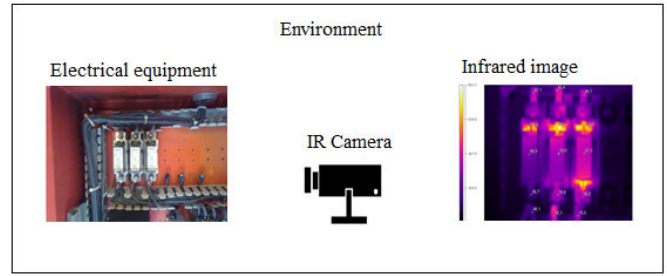


Fig. II.1 Schematic of a typical experimental for monitoring using thermography.

To make an accurate measurement, it is necessary to consider some parameters that are the relative humidity, the reflected temperature, the distance between the object and the camera, the ambient temperature, the emissivity of the object. According to [14] the correct and incorrect parameters to make an accurate measurement are mention in table 2.

Table 2 Parameter to consider for measurement

Parameters	Humidity [%]	Reflected temperature [°C]	Ambient temperature [°C]	Distance [m]
Correct parameters	50	24.6	24.6	0.5
Incorrect parameters	95	34.6	34.6	10.0

a) *Distance*: distance from the thermo viewer and the object being examined also called target distance.

b) *Ambient temperature*: The unit will not perform in terms of the ac-curacy and repeatability if used outside the stated oper-ating temperature range.

c) *Relative humidity*: is defined as the ratio, expressed as a percent, of the amount of water vapor actually present in a sample of air to the greatest amount of water vapor possible at the same temperature [15].

Another measurement work mentions the parameters to consider which are the distance between the target electrical installations and IR thermal camera is between 0.5 m and 1.0 m. The ambient temperature was between 30 and 33°C during inspection [4].

One of the most relevant aspects is the camera for the measurements. Several parameters must be considered before choosing an IR thermal camera as the ability of producing a sharp and accurate thermal image which largely depends on these performance parameters. A few important parameters are mention below: spectral range, spatial resolution, temperature resolution. A detailed study of these performance parameters of thermal imaging systems are reported by Venkataraman and Raj [10].

Usually, applying infrared thermography technology, the electrical thermal defect and level of defect are identified by monitoring its Delta T (ΔT) criteria. The Delta T criteria of a component is defined as an increase in the temperature value above the temperature of a reference value, which is typically the ambient temperature, temperature of a similar component

under the same condition or the maximum allowable temperature of the component [4].

Moreover in recent years the development of intelligent diagnostic system using fuzzy logic, expert system and neural networks are potentially powerful, robust and adaptive mathematical model for pattern recognition and classification. The four input parameters of neuronal networks were used which are absolute maximum temperature, relative maximum temperature, mean temperature difference compared to the other regions of the image and histogram distance to other regions of the image [2, 4, 16].

Sometimes thermographers prefer to classify thermal condition based on their own inspection experiences instead of using the available standards.

III. FAULT DETECTION

The main purpose is to find out if there is an incipient fault appearing in the machine so that the alarm can be activated and further analysis can be exerted.

There are two deferent methods for fault detection, named model-referenced method and feature extraction. The former detects faults by comparing the results of measurements with predictions of models that may be mathematical simulation models or artificial intelligence based. For most feature extraction methods, frequency and time-domain signal processing technologies will be used to obtain ‘signatures’ which can represent normal and faulty performance [2].

The internal faults of the electrical equipment can be divided into loose connection or contact of internal conductors and poor insulation and other faults [11].

Corrosion, loose connection, damaged contacts, worn out wires, over loading or load imbalance are the major types of faults in electrical components that causes abnormal rise of temperature which can be easily monitored by IRT[10].

A. Defect in circuit breaker

A circuit breaker (CB) always senses the heat produced by the current. If it finds the abnormality of heat, instantly opens the circuit automatically and protects the electrical equipment from damage. Thermographic inspection has the advantages to find the abnormalities by analyzing the surface temperature variation of circuit breaker and can prevent these abnormalities earlier [4].

B. Fuse connection

Fuses are used to protect the system against overloading condition. Overloading condition in a system can increase the fuse connection heating and moreover, the fuse clips can be overheated due to the loose and dirty connections [4]. Overload condition usually shows a uniformed heat pattern that appears through the entire circuit. Total heat generated from the equipments depends on the load and the ambient operating temperature of the equipment [13].

C. Defect in contact

Electrical connection switches, breakers and other reclosing devices operate with contacts. If these contacts become loose,

oxidized, and dirty or anyhow increase in resistance, then the fault can be occurred in the contacts [4].

D. Insulation problem

Insulation failure can cause short circuit current between two conductors. Overcurrent generates overheating and allows the circuit breaker or fuse to open. Poor insulation can also cause overheating [4].

E. Utility connection box break elbows

In residential areas, many underground connection and switching locations are in utility box enclosures. Normally, break elbows provide a point of disconnection and if these break elbow connections are not installed properly or connection resistance increases, then faults can occur [4].

F. Surge arrestors problem

Problems with surge protection and lightning arrestors leaking to ground and current tracking over insulators can also be detected using thermography. However, such problems require the capture of subtle temperature differences which are often too difficult to be monitored [4].

On Jadin et al 2014 [4] they had evaluated the usage of radial basis kernel function (RBF), support vector machine (SVM) and multilayer perceptron neural network classifiers. Using a wrapper model approach for feature selection, the classification performances for various input features are examined after finding the optimal configuration and parameters of the classifiers. From the experimental result, the most suitable input features are the combination of maximum temperature, average region’s temperature and temperature difference between the target and reference region. However, choosing the type of classifier between SVM and MLP neural network has no significant effect upon the classification accuracy.

To develop a robust and reliable system, a new Recursively Constructed Fuzzy System (RCFS) is introduced in this study to classify the conditions of hotspots in components. The proposed system employs Automatic Feature Extraction (AFE) and a novel intelligent classification system. The gray scale images of infrared thermal images of components are segmented by using a manual thresholding technique [17].

IV. FAULT DIAGNOSIS

The task of fault diagnosis consists in determining the type, size and location of the possible fault, as well as its time of detection [1].

Manual and Automatic Feature Extraction (AFE) methods are currently employed for the intelligent classification of the thermal conditions of electrical equipment on the basis of thermography. Almeida et al. 2009 [15] proposed an intelligent fault diagnosis system based on thermography for lightning arrestors by using 2 types of variables as inputs of a neuro-fuzzy network.

Several articles about the application of artificial neural networks (ANN) for electrical fault diagnosis system using infrared thermography have been proposed in the past few

years. In these articles, different features were used as inputs of ANN. Almeida et al used a neuro-fuzzy approach for fault diagnosis of lighting arrester while the inputs of the ANN were thermographic and identification variables.

V. CONCLUSIONS

Infrared thermography has become a very useful tool for temperature monitoring of objects or processes in a non-invasive way. This technique is helping to diagnosis faults in electrical equipment. It provides pertinent information about the state of the equipment. In order to obtain better results on the faults diagnosis is necessary to make an accurate measurement this is the base of the diagnosis process. Once we get to the diagnostic then we can make the fault management. For future works, the diagnosis based on IR thermography is a practical and useful tool in industry's fields. So it is recommended for further information to explore this topic in depth.

This review would also help understand the thermography technique and start to use it for various condition monitoring applications, detecting faults.

Acknowledgements

The authors are very grateful to acknowledge Universidad Autónoma de Querétaro for encouragements and facilities and the first autor to "Consejo Nacional de Ciencia y Tecnología" (CONACYT) for providing the support for this investigation. Also like to thank M.E.S. Gavina Quintanar Martínez Language Services department of the School of Engineering campus San Juan del Río, University of Querétaro, México for provide the English language editing of this paper.

References

[1] R. Isermann. *Fault-Diagnosis Systems: An Introduction from Fault Detection To Fault Tolerance*. Germany: Springer, 2006.

[2] Y. Han & Y. H. Song. *Condition Monitoring Techniques for Electrical Equipment-A Literature Survey*. IEEE Transactions on Power Delivery, 18 (2003), 4-12.

[3] M. Shawal, S. Taib & K. Hawari. *Feature extraction and classification for detecting the thermal faults in electrical installations*. Measurement, 57(2014), 15-24.

[4] A. Huda & S. Taib. *Application of infrared thermography for predictive/preventive maintenance of thermal defect in electrical equipment*. Applied Thermal Engineering, 61(2013), 220-227.

[5] C. Balaras, A. Argiriou, *Infrared thermography for building diagnostics*, Energy Build. 34 (2002) 171–183.

[6] B. Lahiri, S. Bagavathiappan, T. Jayakumar & J. Philip, *Medical applications of infrared thermography: A review*, Infrared Physics & Technology, 55 (2012) 221–235.

[7] A. Huda, S. Taib, K. Ghazali & M. Jadin. *A new thermographic NDT for condition monitoring of electrical components using ANN with confidence level analysis*. ISA Transactions, 53(2014), 717-724.

[8] S. Bagavathiappan, B. Lahiri, T. Saravanan, J. Philip & T. Jayakumar, *Infrared thermography for condition monitoring a review*, Infrared Physics & Technology. 60 (2013) 35–55.

[9] L. Eads, R. Epperly & J. Snell, *Thermography*, ASHRAE Journal 42 (2000) 51-55.

[10] Standard for Infrared Inspection of Electrical Systems & Rotating Equipment, Infraspection Institute, 2008, 2011. <http://www.armcoinspections.com/files/ir/Electrical%20Rotating%20Std.pdf> (accessed 10.02.2015).

[11] NFPA, NFPA 70B: *Recommended Practice for Electrical Equipment Maintenance*, National Fire Protection Association, Quincy, Massachusetts, 2006.

[12] ASTM, ASTM E 1934: *Standard Guide for Examining Electrical and Mechanical Equipment with Infrared Thermography*, ASTM International, West Conshohocken, Pennsylvania, 2005.

[13] M. Shawal & S. Taib. *Recent progress in diagnosing the reliability of electrical equipment by using infrared thermography*. Infrared Physics & Technology, 55 (2012), 236-245.

[14] M. Barański & A. Polak. *Thermographic diagnostic of Electrical Machines*. XIX International Conference on Electrical Machines, (2010).

[15] C. Almeida, A. Braga, S. Nascimento, V. Paiva, H. Martins, R. Torres, and W. Caminhas. *Intelligent Thermographic Diagnostic Applied to Surge Arresters: A New Approach*. IEEE TRANSACTIONS ON POWER DELIVERY, 24(2009), 751-755.

[16] A. Huda and S. Taib. *Suitable features selection for monitoring thermal condition of electrical equipment using infrared thermography*. Infrared Physics & Technology, 61(2013), 184-191.

[17] M. Ahmeda, A.Huda and N. Ashidi. *Recursive construction of output-context fuzzy systems for the condition monitoring of electrical hotspots based on infrared thermography*. Engineering Applications of Artificial Intelligence, 39 (2015), 120-131.

Thermal Insulation Design of Housing. Numerical-Experimental Procedure.

J. M. González-Castañeda¹, J. Horta-Rangel², J. B. Hernández-Zaragoza³, J. R. Galaviz-González⁴,
B. Quitero-Mendoza⁵, I. G. Arreola-Ruiz⁶

*División de Investigación y Posgrado, Facultad de Ingeniería, Universidad Autónoma de Querétaro.
Centro Universitario, Cerro de las Campanas, 76160, Santiago de Querétaro, Querétaro, México.*

¹ jumartingo@msn.com

² horta@uaq.mx

³ bosco@uaq.mx

⁴ btoviz@hotmail.com

⁵ bqm_301293@hotmail.com

⁶ itzel.arreola.ruiz@gmail.com

Abstract— In order to meet the demands of increased energy efficiency, thermal insulation of housing plays an important role. The thermal behavior of a housing is related with the thermophysical properties of building materials and are sensitive to thermal effects that largely define temperature ranges within the housing, so it is important to involve variations in temperature to thereby establish the thermal conditions of the interior spaces for thermal comfort conditions. In this paper the behavior of the thermal insulation of a house is studied by means of a proposed design procedure of structured envelopes of housing which permit the identification of appropriate building materials that ensure thermal comfort within the housing. Based on experimental prototype dwelling where temperatures were recorded in environments both external and within housing, validation of a volumetric thermal transient model was performed through the program ANSYS modeling. For this purpose were designed programming codes in APDL language inside Ansys environment, creating friendly interacting windows to register data record of weather conditions as well types of component materials of the house. Geometric conditions, materials of housing envelopes as well external temperatures were simulated. Of great interest was the simulation of different arrangements of thermal insulation materials registering their behavior and influence on energy efficiency and comfort inside housing.

Keywords— *computer modeling; envelope design; thermal analysis; finite element method; thermal comfort*

I. INTRODUCTION

The growing concern for energetic efficiency of housing in Mexico, has prompted the development of several Mexican official standards for energy as the NOM-ENER [1]. Normalization for energetic efficiency in buildings represents an effort to improve the thermal design of these, and achieve comfort of its inhabitants with lower energy consumption [2].

Currently over 90% of the energy consumed in Mexico, originated in burning fuel that produces large amounts of CO₂. Therefore, the energy can be saved in homes and buildings,

this help us to reduce energy demand and emissions of air pollutants [3]. A proper thermal insulation of houses contributes to reduced energy demand for heating and cooling, reducing environmental impact and generates a better quality of life of the population. Thermal isolation increases the life of the building and represents a gain as the quality and equity of the construction is appreciated.

The NOM-020-ENER-2011 standard, defines the envelope of a home, as the set of elements that limit or make your interior space, such as roofs, walls, doors, floors and lower surfaces. While the term "structured element" refers to the combination of various materials to form an array that presents constructive solutions of thermal insulation and may form part or all of the elements of the envelope [4].

The architectural designs, construction techniques, materials currently used, referring to housing low-and middle-income leading to increasingly smaller spaces, inferior materials, producing negative circumstances in the inhabitants of the houses. For this reason, the interest of the parameter identification, and materials that improve the energetic efficiency of housing.

The housing construction techniques, materials used, an appropriate architectural design that considers an efficient orientation, and others, are aspects that influence the comfort of a home. The NOM-020-ENER (Energy Efficiency in buildings) establishes general criteria for assessing the overall thermal efficiency of a home, based on an energy budget. This determines heat gains, which is not a parameter that allows a comprehensive solution that includes all locations in the Mexican republic and the different designations of each in any season, whereas in other countries if it is considered.

This paper considers the application of thermal analysis procedures for different types of materials used on a daily basis in construction in Queretaro. These are applicable in medium and popular housing, while reviewing viable, affordable options for use and applicability, due to some architectural

solutions increase the cost of housing and its use is often restricted to this type of houses.

The procedure involves a volumetric thermal analysis, which identifies the temperature distribution inside the house. It is useful information to calculate the heat gain into it and interpret their behavior. This analysis was performed using finite element equations for determining the volumetric temperature distribution inside the house, where the basic unknown in heat transfer is the temperature [5]. Within these equations takes into account the thermal diffusivity constants involving thermal conductivity, density and specific heat of the elements of the enveloping house.

The use of thermal insulation is one of the most effective ways of energy conservation in construction. Therefore, the selection of a suitable insulation material and determination of optimal insulation thickness are particularly crucial [6].

Standards on energy in housing propose using average temperatures of the town for summer time, without specifying criteria for cold weather of winter and particularly in the Queretaro region, where some locations exceed 10 °C, so the heat loss in homes at this time is critical and the use of heating is inevitable for comfort inside the house.

In Mexico the thermal conditioning of buildings greatly affects the electrical system peak demand, being greater impact in the northern and coastal areas of the country where it is more common to use cooling equipment instead of heating. In this sense there are rules to optimize the design from the standpoint of the thermal behavior of the envelope, among other benefits obtained as the energy saving and the decrease of the capacity of cooling equipment.

The Mexican NMX-C-460-ONNCCE-2009 incorporates information that helps reduce energy use in homes by way of conditioning. It provides for the different climatic zones of the country and the immediate purpose of insulation, the features to be met by building elements constituting the shell of the building: roof, walls and floor, by determining the values of the total thermal resistance ("R" value). So, establishes minimum values, to save energy and achieve habitability. These values associated thermal properties of the component materials of the envelopes. This research focuses on the study of the city of Queretaro, which is located in the thermal zone 3A [7].

In particular, the norm establishes, a minimum values of total thermal resistance of an element of the envelope: for walls, $R=1.0 \text{ m}^2\text{K/W}$, while roofing $R=1.40 \text{ m}^2\text{K/W}$.

II. THERMAL PHENOMENOLOGY

Thermal analysis involves the effects of conduction, convection and radiation.

A. Conduction

The rate of heat conduction or flow Q_{cond} by a layer of constant thickness Δx is proportional to the temperature difference ΔT in the layer and the normal area A to the direction of heat transfer, while it is inversely proportional to the thickness of the layer. Therefore,

$$Q_{cond} = \lambda A (\Delta T / \Delta x) \quad (1)$$

where the constant of proportionality λ is the thermal conductivity of the material passing through the flow of heat and which is a measure of the material's ability to conduct heat, its units are $\text{W/m}^\circ\text{C}$ according to International System of Units. Materials having low thermal conductivity are called insulating [8].

B. Convection

The rate of heat transfer by convection is determined from Newton's law of cooling, expressed as:

$$Q_{conv} = h A (T_s - T_f) \quad (2)$$

where h is the local heat transfer coefficient by convection or thermal convection coefficient (film coefficient), A is the surface area in which heat transfer takes place, T_s the temperature of the surface and T_f is the temperature of fluid away from the surface. (On the surface, the fluid temperature is equal to the surface solid temperature).

The heat transfer coefficient by convection h , is experimentally determined parameter whose value depends on all variables that affect the convection, as the geometry of the surface, the nature of the fluid motion, fluid properties and volumetric fluid velocity. Representative values of h , in $\text{W/m}^2\text{C}$, are in the range of between 5 and 25 for the free convection in air [9]. However, Szokolay [10] proposes to assess convection coefficients of houses according to the outside air velocity, as follows:

$$h_e = 5.8 + 4.1v \quad ; \quad h_i = h_e / 3 \quad (3)$$

where h_e is the coefficient of convection outside, h_i is the internal convection coefficient and v is the air velocity.

C. Radiation

Radiation for this work focuses on the energy emitted by the sun in the form of electromagnetic waves (or photons) and is received in significant gains heat by different elements enclosures houses. This type of heat transfer is the fastest and is a phenomenon that affects more to the transparent parts (windows, domes, etc.) of housing.

D. Thermal resistance and overall heat transfer coefficient

The Mexican Standard NOM-020-ENER-2011 proposes to calculate the total thermal resistance of a wall or ceiling with homogeneous layers, using the simplified method, which is the sum of the partial thermal resistances of each layer, such as:

$$R_T = (1/h_i) + (1/h_e) + (L_1 / \lambda_1) + (L_2 / \lambda_2) + \dots + (L_n / \lambda_n) \quad (4)$$

where R_T is the total thermal resistance (insulation) of a portion of the envelope of the housing, surface to surface, in $\text{m}^2\text{C/W}$; h_i is the inner surface conductance (film coefficient) in $\text{W/m}^2\text{C}$, according to standard wallboard its value is 8.1; h_e

is the outer surface conductance value as the standard is $13 \text{ W/m}^2\text{C}$; n is the number of layers forming the envelope portion; L is the thickness of each of the materials making up the portion of the envelope, in m. and λ is the thermal conductivity of each of the materials making up the portion of the envelope of the housing, in $\text{W/m}^2\text{C}$ [4].

Therefore, to determine the overall heat transfer coefficient is necessary to know the thicknesses and thermal conductivities of each of the materials forming the envelope portion (heat transfer coefficient) is computed using the following equation:

$$K = 1 / R_T \quad (5)$$

where K is the heat flux passing through 1 m^2 of a portion of the envelope with thickness of 1 m . for one hour between the two faces when there is a difference of $1 \text{ }^\circ\text{C}$, its units are $\text{W/m}^2\text{C}$ [7].

E. Thermal retardation and thermal comfort threshold

Thermal delay (δ), sometimes called lag, refers to the time it takes to move the heat (the temperature outside to inside) through an element of the envelope (wall or ceiling). In other words, is the time elapsed between the time when the maximum temperatures appear in each of the surfaces (interior and exterior) of the element. The greater the thickness and thermal capacity, and lower the conductivity, the longer require the heat energy to get through it. Furthermore the larger the offset value, the better the thermal behavior of the envelope. Furthermore, the thermal buffer, measures the reduction of cyclic temperature of a surface (typically the inside) with respect to the cyclical temperature of the opposite surface.

In Fig. 1 it can display this phenomenon by two curves representing the temperature oscillation daily on each surface [11]. Another important concept is the thermal comfort threshold, which are temperatures between 21°C (70°F) and 26°C (79°F) and humidity of between 30 and 60 percent, in which the human body is in harmony and balance with the environment, and take comfort in the home, requiring less use of heating and air conditioning, with the consequent economic savings [12].

Since the model of volumetric character study, finite element used is a SOLID70 under the ANSYS nomenclature, is a proper solid to study 3-D transient thermal problems, and offers 8 appropriate nodes for potential problems. It has the characteristic to degrade solids to 4-node triangular pyramid type which makes it possible for meshing complex geometry. The data required for its implementation are the thermal properties of the materials in each envelope of houses, so it is necessary to construct the model based on the different materials used in house, or if you can insert the mass transport velocities [13].

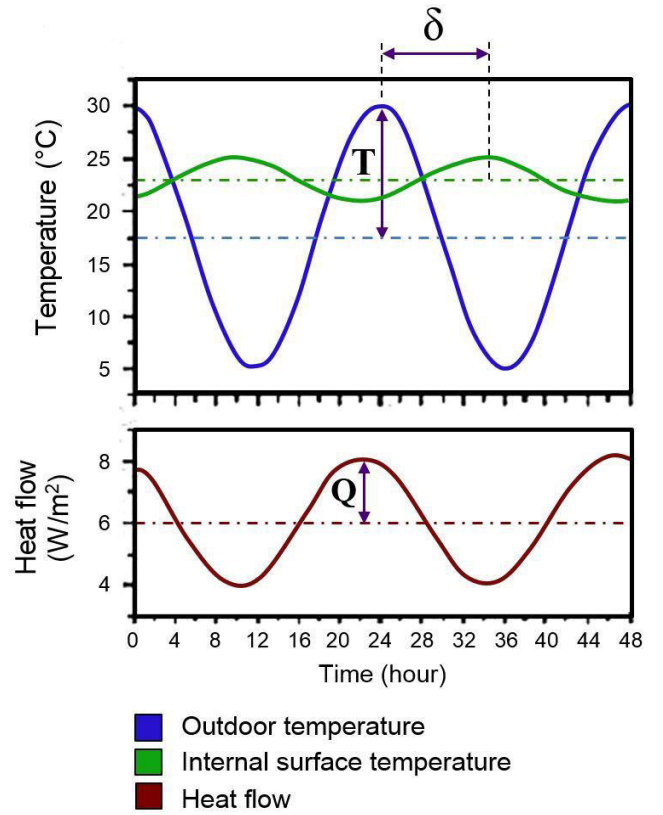


Fig. 1. Graphical representation of the heat flow amplitude, the amplitude of the external temperature and the offset or delay δ (hours) [11].

The general equation governing the thermal behavior of 3-D transient phenomenon in terms of the discrete model used is as follows:

$$\begin{aligned} & \rho \int c [N][N]^T dv \{\dot{T}\} + \rho \int c [N]\{V\}^T [B] dv \{T\} + \\ & \int [B]^T [D][B] dv \{T\} = \int [N] q^* d\Gamma_1 + \int \{T_B\} h_f [N] d\Gamma_2 - \\ & \int h_f [N][N]^T \{T_e\} d\Gamma_2 + \int q' [N] dv + \{T\}_n \end{aligned} \quad (6)$$

where ρ the density of the corresponding material, variable for each envelope, c the specific heat, $[N]$ the matrix of shape functions of the finite element $[B]$ the matrix of derivatives of shape functions, $\{V\}$ the velocity vector, $\{T\}$ temperature vector, h_f the convection coefficient, $\{T_B\}$ and $\{T_e\}$ temperatures corresponding to the heading of convection, q^* y q' associating the type of heat flow and finally $\{T\}_n$ refers to temperatures nodal.

The general model presented here is reduced to considering zero, the advective term, also does not consider heat generation by a source inside the housing. Thus, the resulting model is analogous to the case of potential phenomenology, as suction in unsaturated soils. For the assessment of the convection coefficient as already mentioned, is part of the equation proposed by which Szokolay to assume a low speed in the vicinity of the walls. Environmental temperature measured in situ is the other parameter required in this process.

III. METHODOLOGY

It describes the procedure for each of the two phases both theoretical and experimental development comprising the thermal study described of housing.

In addition to the indicated phases, the validation of the obtained results (experimental against analytical) is very important. Likewise, treatment established to review options for thermal insulation such as the introduction of insulating materials in walls that improve energy response.

A. Theoretical Phase

The theoretical phase (Fig. 2) requires the material data and the geometry of the housing including dividing walls and various areas thereof, so that the availability of an actual context of the housing itself. The process described below, begins with data entry by mean of windows created in order to propose a user-friendly tool, plus requested external temperatures at which the housing is subject.

B. Experimental Phase

This phase as shown on Fig. 3, consists on register the temperature measurements at different points of the house to evaluate the numerical experimental phase and to introduce the general boundary data for the thermal analysis of housing under a transient thermal model.

In Fig. 4 the sensors used to measure temperature inside and outside the home are shown.

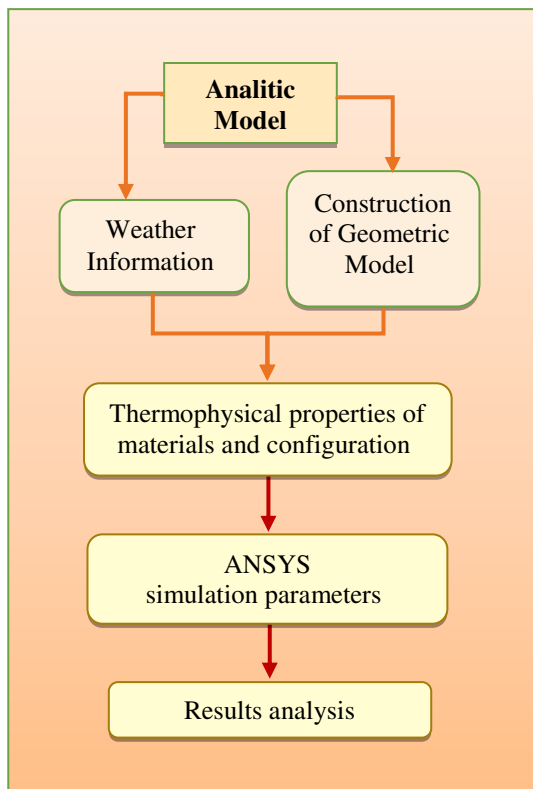


Fig. 2. Analytical phase of thermal study.

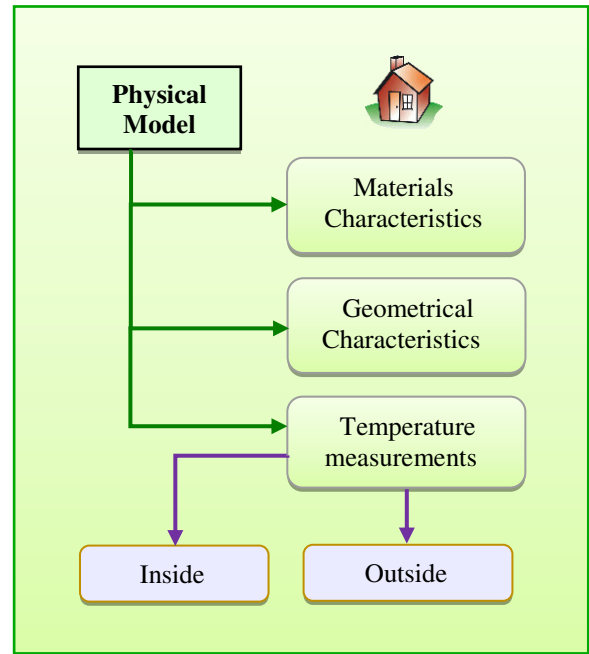


Fig. 3. Experimental phase of the study.



Fig. 4. Data Logger Watchdog 1000 Series and external temperature sensor for experimental measurements.

C. Layers compound of the envelopes.

The concrete slab foundation of housing was analyzed with the materials shown in Fig. 5.

The exterior walls of the house, were studied according to the materials shown in Fig. 6.

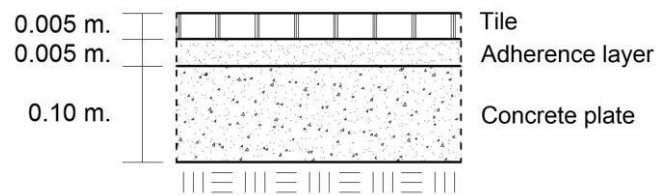


Fig. 5. Slab foundation of analyzed housing.

In turn the inner walls were analyzed as shown in Fig. 7.

In Fig. 8, the thicknesses and materials that were considered for the structured element of roof slab of the computational model is shown.

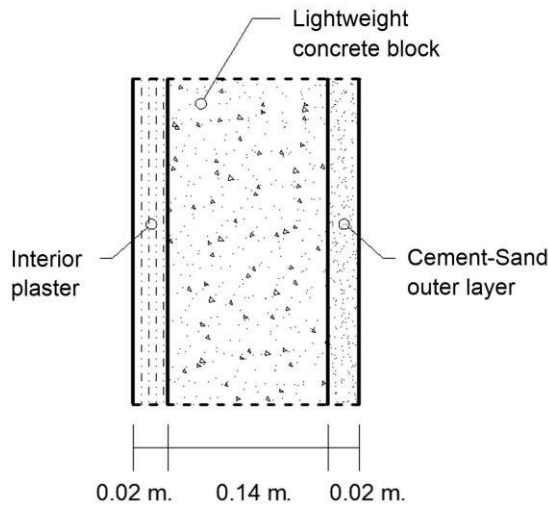


Fig. 6. Exterior walls of housing.

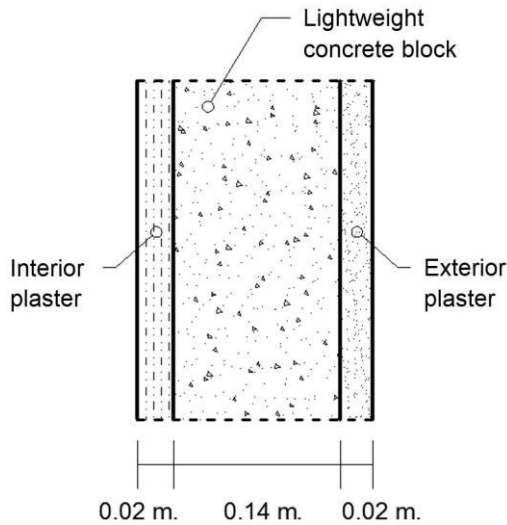


Fig. 7. Inner walls of housing.

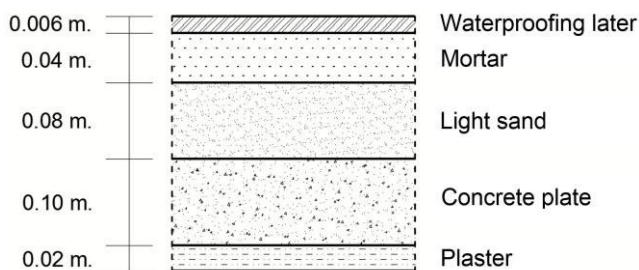


Fig. 8. Solid roof slab.

Were considered the wooden doors, with a thickness of 4 cm, in normal glass windows 3 mm thick were used, although if required can be easily modified in an interactive change.

The computational model developed displays windows to assign the value of the different variables involved in the analysis. As an example a window that displays the program during analyzes. The first window corresponds to the geometric characteristics (Fig. 9), there external actions of the house study as well as the dimensions of the shell structured elements are indicated.

In other display window (Fig. 10), layers and materials constituting the housing envelope are inserted.

A screenshot of a software window titled "Multi-Prompt for Variables". The window contains a list of variables for house geometry with input fields for their values in meters. The variables and their values are:

"INDICATE THE DIMENSIONS IN METERS"	
TOTAL EXTERNAL LENGTH HOUSE (M) LH	8
TOTAL EXTERNAL WIDTH HOUSE (M) WH	10
INTERIOR HEIGHT HOUSE (M) HLH	2.6
TOTAL THICKNESS WALL (M) THWALL	0.2
TOTAL THICKNESS ROOF (M) THROOF	0.2
TOTAL THICKNESS FOUNDATION (M) THFOUN	0.2

Fig. 9. Window overall geometry of the house and its envelopes.

A screenshot of a software window titled "Multi-Prompt for Variables". The window displays construction characteristics for the outer wall, with a list of materials and their corresponding layer counts. The variables and their values are:

CONSTRUCTION CHARACTERISTICS OF HOUSING "INDICATE THE LAYERS OF THE OUTER WALL" NO = 0 SI = 1	
BRICK WALL1	0
LIGHTWEIGHT CONCRETE BLOCK WALL2	1
HOLLOW CONCRETE BLOCK WALL3	0
CEMENT-SAND OUTER LAYER WALL4	1
INTERIOR PLASTER WALL5	1
EXPANDED POLYSTYRENE LAYER 1 INCH WALL6	0
GLASS WOOL LAYER OF 1 INCH WALL7	0

Fig. 10. Window of materials for the outer wall.

For the approach of the transient problem we proceeded to record experimental data for 5 months (from January 13 to June 12, 2014), identifying the temperatures both the exterior and the interior, at various points in the housing as shown in Fig. 11.

Fig. 12 shows the volumetric structure of the house of study. Has removed the ceiling to view it, its different spaces generated inside are observed.

Fig. 13 shows the temperature measurements recorded from the external environment by the sensor Sun "Text sun" during a representative hot season (April 11 to May 10, 2014), these data were entered into the tabular temperature program at intervals of 3 hours for a total of 240 data and was allocated to program a maximum analysis time 720 hours (30 days).

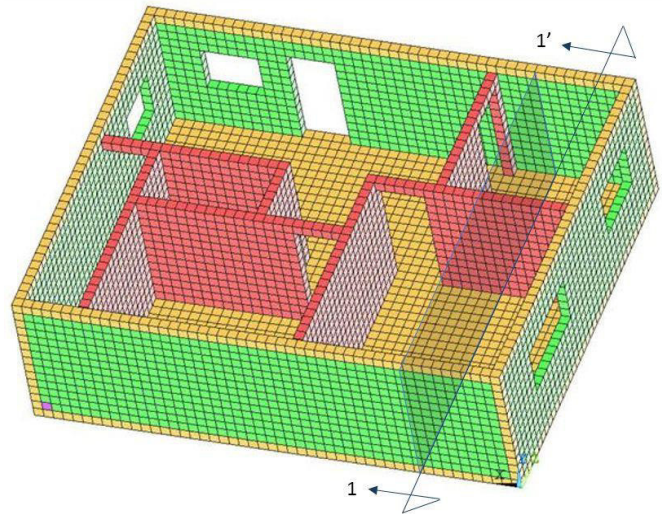


Fig. 12. 3D Interior model of housing in study.

Considering the initial conditions for the model, it was assumed an internal temperature of 25 °C, the external wind speed was considered quiet with a speed of 2 m/s (7.2 km/h), the ratio of Szokolay for this wind speed, the convection coefficient assigned to the outer areas of the model was 14.0 W/m²K, while the inner convection coefficient was 4.66 W/m²K.

IV. RESULTS

Fig. 14 shows one of the results of the computational model that relates the temperatures in section 1-1 'shown in Fig. 12. In this case a temperatures ranges between 21 °C and 28 °C. The effect of convection by the lower boundary temperature tends to increase in that area. Importantly display capabilities of different outcomes, but especially here focuses on basic form to show the temperatures measured.

The volumetric thermal solution is sometimes difficult to appreciate the different layers or blocks of discrete model, because the interior volume has also been discretized with volumetric finite element thermal associating their particular properties.

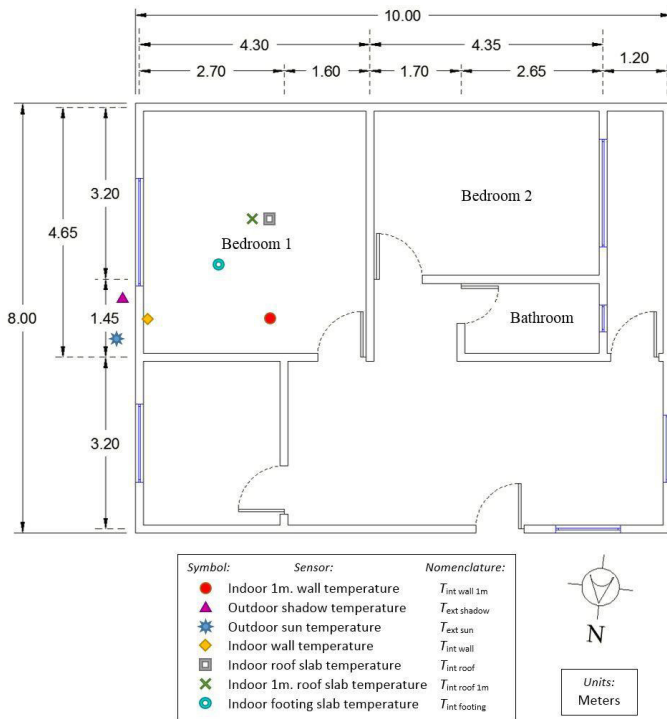


Fig. 11. Location of the sensors inside and outside the home.

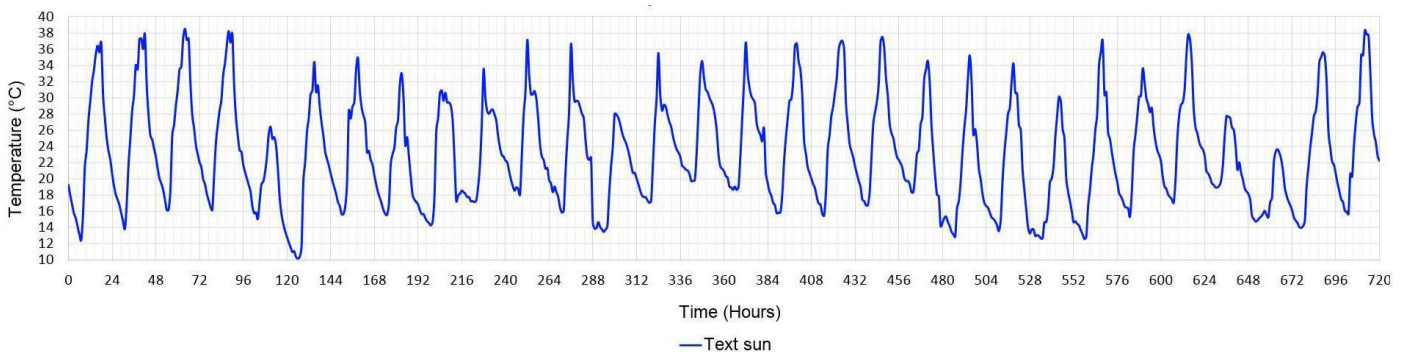


Fig. 13. Temperature behavior over time, "Outdoor sun temperature sensor".

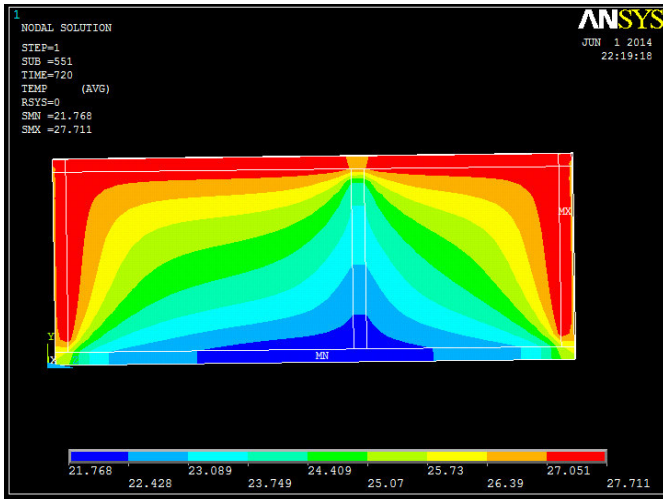


Fig. 14. Volumetric thermal behavior on housing in study accordance with the 1-1 section.

V. COMPUTATIONAL MODEL VALIDATION

To validate the computational model, the curve of temperature recorded with the "Tint wall 1m sensor" inside of housing was compared with that obtained by the program on the node where this temperature sensor was placed.

Fig. 15 shows in red the temperature curve recorded by the "Tint wall 1m sensor" and in blue curve simulation by ANSYS presented as a solution.

For comparison of the results, it was found that the model was properly calibrated and reliable for the use of other materials in the enveloping housing, because maximum temperature difference 0.8°C between the curves presented. According to statistical analysis a percentage of 94.3% of accuracy of calculated in the program against experimentally measured was obtained.

It was also noted in this figure that the beginning of the convergence process of the program was around the time 48 hours (2 days).

VI. INFLUENCE OF THERMAL INSULATION MATERIALS. CASE: EXPANDED POLYSTYRENE.

At this stage, the influence of expanded polystyrene (EPS) is revised as thermal insulation material in the envelope of the

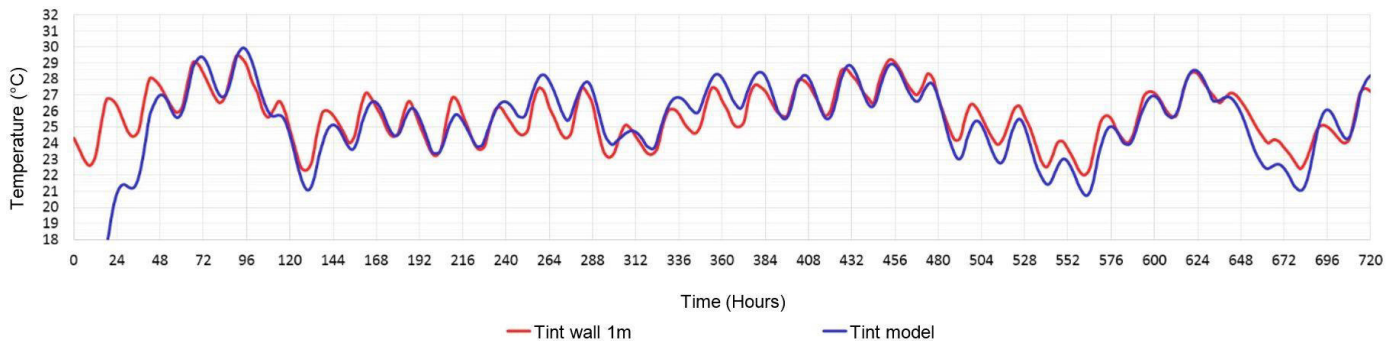


Fig. 15. Graph of validation of computational model.

house, studying the thermal behavior within the housing study. This study is under a computational context.

It proceeded to consider the exterior walls a layer of EPS. Firstly determining a thickness of 1" was sufficient to meet the requirements of thermal insulation according to the NMX-C-460-ONNCCE regulations.

In the simulation its influence was observed into the house at the same point in the first analysis. This allowed faithfully establish a comparative aspect. Fig. 16 shows the envelope materials of the wall. The inclusion of polystyrene was applied to the envelope of the outer wall and the value of thermal resistance "R" under rule which proved to $1.247\text{ m}^2\text{K/W}$ so that the thickness of 1 inch was appropriate because it is greater than $1.0\text{ m}^2\text{K/W}$ as set out in the NMX-C-460-ONNCCE standard.

Fig. 17 shows the relationship between the density of the EPS versus thermal conductivity. With the intrusion of EPS of 1 inch, in the wall components, housing showed better thermal behavior: the wave amplitude was reduced from 144 to 360 hours, generating comfort temperatures inside of house. Furthermore, a gap of four hours with respect to the maximum temperature inside ($T_{\text{int wall 1m}}$) of the actual housing without EPS, a thermal delay for 8 hours, from the heat temperature to the outside ($T_{\text{ext sun}}$).

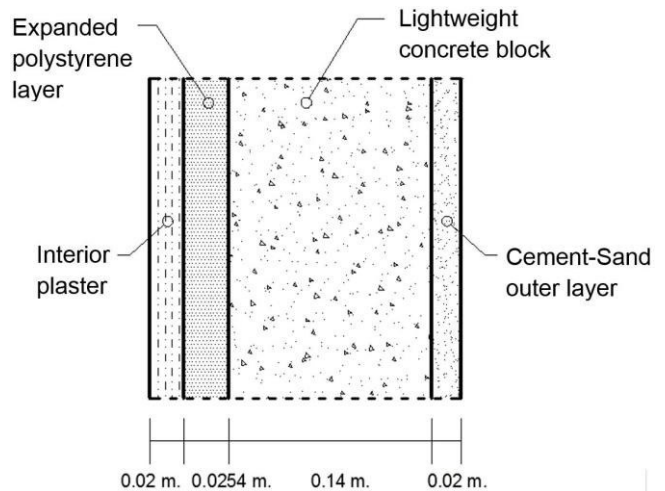


Fig. 16. External wall with expanded polystyrene used on modeling.

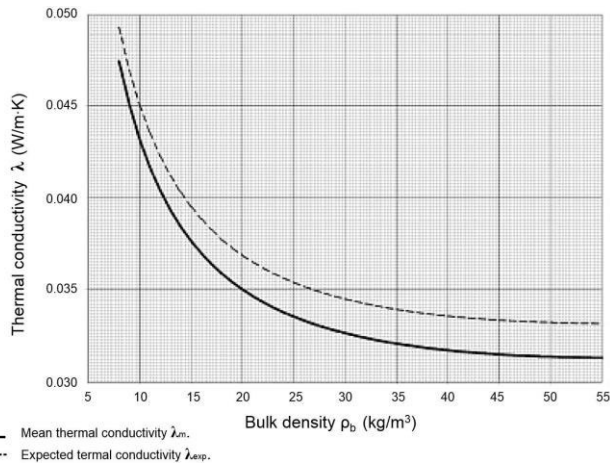


Fig. 17. Thermal conductivity versus. Bulk density of expanded polystyrene [14].

Fig. 18 shows the comparison of the results of the temperatures inside the "Tint wall 1m sensor" with those obtained by the computational model in exterior walls using expanded polystyrene (EPS). Also was done with glass wool (GW). The dotted lines correspond to the threshold of thermal comfort inside of housing.

It should be noted that the study raises at all times that the behavior inside the housing is defined by the materials, internal structure of component, etc. as well as outside temperatures. Therefore, experimentally registered temperatures have served only to confirm and validate the computational model. Hence the importance of monitoring proposed as enough just to set the external environmental conditions of housing.

VII. CONCLUSIONS

According to the analysis of element designs structured insulation materials using EPS, it was observed that the material properties lessen the impact of environmental conditions are within a home. This is demonstrated through computational modeling, and that changing the properties of

the walls of the housing type, for thermal insulation solutions, an increase in time was obtained for the material stop passing the heat inside, i.e., a greater thermal lag was taken, which showed curves of phase temperatures and different amplitudes ridges, resulting into more stable temperatures.

Using EPS on the outer walls of the model, there was a decrease of heat within 1.2 °C, this in most of the days of the month analyzed, compared to the walls without EPS.

The use of EPS produced a thermal delay in the phase heat wave 8 hours, that with respect to the maximum temperature of the various days of the studied month (April 11 to May 10) by the temperature sensor (Tint wall 1m) into the actual housing.

It was found that the EPS has a better thermal behavior of some other insulation materials such as glass wool (GW) having a lower thermal conductivity on the latter.

Additionally, the thermal resistance proved to be a useful tool to compare different insulation materials with different thickness and different thermal conductivity parameter because the higher the value of thermal resistance "R value" is best behavior as thermal insulation, offering more resistance without letting the heat into the house through the envelopes as walls or ceilings, keeping it with adequate comfort (above 21 °C and below 26 °C), especially in critical times of the year.

On the other hand, the transient and spatial modeling in ANSYS, was used successfully to simulate the thermal behavior of experimental prototype proposed in this methodology, allowing know the different temperature distributions within the house and observe those critical comfort points in the interior.

Finally, computational modeling has the advantage of being able to study the thermal behavior of a house in a versatile way, since you can vary the properties of the materials, dimensions and thermal characteristics thereof. This is difficult to perform in a full-scale prototype, and would be required to build as many as variants want to analyze.

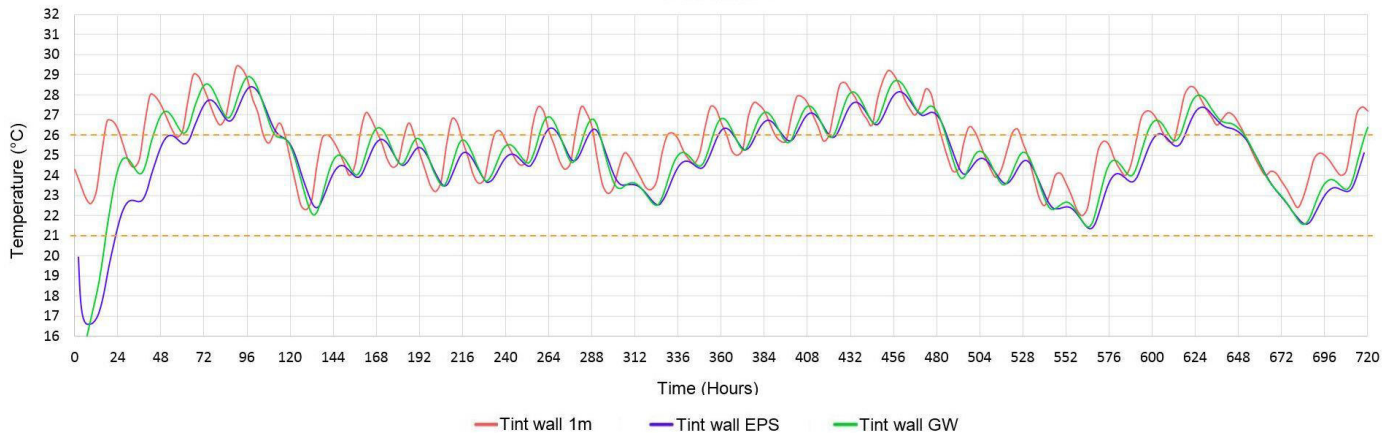


Fig. 18. Comparative temperature values inside the house using thermal insulation materials.

The aim of the study was the development of a computational tool based on the program developed in APDL language that allows a friendly way (not discussed here in detail) to solve a major problem that affects thermal comfort at home. It is true that the use of additional materials such as polystyrene or various fibers affect better thermal insulation of housing in general, however, this tool allows the study of different materials in a fast and simple way.

It should not be forgotten that the thermal conductivities of the envelopes have been built here, based on a model of one-dimensional conductivity, however, its influence on the volume set and the final behavior is the problem raised here, i.e., not regard the wall or roof element in isolation.

ACKNOWLEDGEMENTS

This study was conducted with the support of resources from the Research Project FOFI-UAQ; Fund: 1299; Nue: 4131; Program: 20501155 09.06.02.

REFERENCES

- [1] D. Griego, M. Krarti and A. Hernández-Guerrero, "Optimization of energy efficiency and thermal comfort measures for residential buildings in Salamanca, Mexico", *Energy and Buildings*, 2012, 54 pp. 540–549.
- [2] Programa Nacional para el Aprovechamiento Sustentable de la Energía, Comisión Nacional para el Uso Eficiente de la Energía, CONUEE, 2012.
- [3] J. Rojas, G. Huelsz, R. Tovar, G. Barrios, A. Lira-Oliver y A. Castillo, "Energía y confort en edificaciones". Centro de Investigación en Energía, UNAM, Volumen 11 Número 10, 2010, ISSN: 1067-6079.
- [4] Norma Oficial Mexicana, NOM-020-ENER, "Eficiencia energética en edificaciones", *Envolvente de edificios para uso habitacional*, 2011.
- [5] S. Rao, *The Finite Element Method in Engineering*, Fifth Edition, University of Miami, Coral Gables, Florida, USA, 2011, Elsevier Inc.
- [6] J. Yu, C. Yang, L. Tian and D. Liao, "A study on optimum insulation thicknesses of external walls in hot summer and cold winter", *Applied Energy*, Volume 86, Issue 11, 2009, p. 2520–2529.
- [7] Norma Mexicana, NMX-C-460-ONNCCE, Valor "R" para las envolventes de vivienda por zona térmica para la república Mexicana, Organismo Nacional de Normalización y Certificación de la Construcción y Edificación, S. C. 2009.
- [8] J. A. Manrique, *Termodinámica*, Tercera edición, Editorial Oxford University Press, México, 2005.
- [9] Y. A. Çengel y M. A. Boles, *Termodinámica*, Sexta edición, Editorial McGraw-Hill, México, 2009.
- [10] S. V. Szokolay, *Thermal Design of Buildings - RAIA*, Canberra, 1996.
- [11] C. Ruivo, P. Ferreira and D. Vaz, "On the error of calculation of heat gains through walls by methods using constant decrement factor and time lags values", *Energy Buildings*, 2013, 60 p. 252-261.
- [12] A. F. Emery, "Human comfort and health requirements", Chapter 1, *HVAC Engineering, Mechanical Engineering Design*. University of Washington Seattle, WA, 2008.
- [13] ANSYS Inc. Software, Version 14.0 (Systems analysis), Pittsburgh, USA, 2011.
- [14] Guía técnica para la rehabilitación de la envolvente térmica de los edificios. Soluciones con aislamiento de poliestireno expandido (EPS). Instituto para la Diversificación y Ahorro de la Energía, IDAE, 2007.

Methodology for automatic detection of trees and shrubs in aerial pictures from UAS

Garduño-Ramón M. A. ^{#1}, Sánchez-Gómez J. I. ^{*2}, Morales Hernández L. A. ^{#3},
Benítez-Rangel J. P. ^{#4}, Osornio-Rios R. A. ^{#5}

^{#1,2,3,4,5} *Facultad de Ingeniería, Campus San Juan del Río, Universidad Autónoma de Querétaro*
Av. Río Moctezuma 249, CP 76808, San Juan del Río, Querétaro

¹ mgarduno01@alumnos.uaq.mx

² jesus.sangomez@gmail.com

³ luis_morah@yahoo.com

Abstract—Unmanned aerial systems (UAS) provide an invaluable tool for academic and scientific research. Drone devices are even capable of flight autonomously through a specified route. Most of the UAS systems have an image acquisition device which allows them to record areas of interest during its flights and give the user a new point of view from the heights of some phenomenon in particular. RGB space color is the scheme most popular in transmission, representation and storage of images, but the high number of possible combination of colors (16,777,216) make it not adequate to identify dominant colors in certain regions of interest. HSV color space offers a simplified way to approach this problem in which color is mainly modified by just one single channel, specifically the hue channel (H), which range is from 0 to 360 degrees. In this paper, a methodology that uses aerial images from the Universidad Autónoma de Querétaro campus San Juan del Río acquired using a UAS drone device to automatically detect trees and shrubs is presented and tested. This methodology uses transformations of color space to detect the range of hue in which trees and shrubs are in images, and use this information as discriminant to make the automatic detection.

Keywords—UAS; image processing; trees detection; shrubs detection; color spaces

I. INTRODUCTION

UAS (Unmanned Aerial Systems) have become very popular in part because some of them are now accessible to the people mostly as hobby devices. However, there is still a thick line between those used for fun and those used in research, commercial and military applications [1]. The drone concept, indiscriminate applied to all devices that have multiple rotors, is a term only reserved for those UAS devices that can accomplish an autonomous flight. UAS systems have been used in a wide range of applications since military [2], to civil [3] and electromechanical engineering [4], architecture [5], and even in emergency situations [6], because the most of the time they incorporate high quality images acquisition devices which allow to make advanced analysis. This allows to apply image processing techniques to do, for example, segmentation of areas or regions of interest remotely [7]. In this paper, a methodology that uses aerial images from the Universidad Autónoma de Querétaro (UAQ) campus San Juan del Río (SJR) acquired using a UAS drone device to automatically

detect trees and shrubs is presented and tested. This automatic detection is first realized identifying the main range hue value of the regions of interest using color transformations from RGB to HSV spaces [8]. Then the color of those pixels whose hue values are inside the interest range is changed and then transformed again to RGB color space to show the results.

II. BASIC CONCEPTS

A. UAS

The term UAS (Unmanned Aerial System) defined by the U.S.'s Federal Aviation Administration covers a wide array of aircraft, from drones to average hobby radio-controlled airplanes [9]. A multicopter uses multiple propellers (rather than a single rotor blade such as on a traditional helicopter) to provide lift. Also, there is no tail rotor (used to provide yaw control and counter the torque put out by driving the main rotor on a helicopter). Multicopters come in many configurations. There are bi-copters (two rotors), tri-copters, quadcopters, and so on. The Fig. 1 shows an example of a quadcopter as well as two configurations of hexacopters (six rotors). Most multicopters are piloted in the line of sight (LOS), just as any radio-controlled airplane. This variety is not considered a drone. Technically, a drone both flies outside LOS and has the capability of autonomous flight (autopilot).

Fig. 1. Example of UAS multicopters.

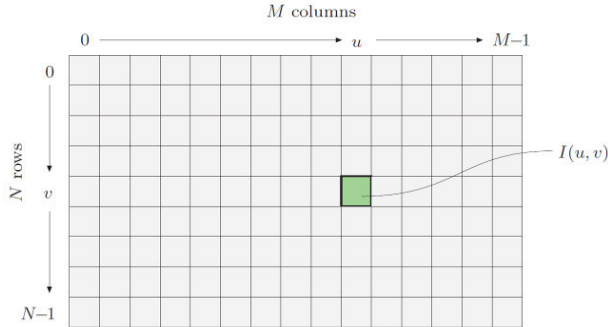


B. Digital image

A digital image I (Fig. 2) is a two-dimensional function of integer coordinates $N \times N$ that maps to a range of possible image (pixel) values P , Ec. 1.

$$I(u,v) \in P \text{ and } u,v \in N \quad (1)$$

Fig. 2. Digital image. (The size of an image is determined directly from the width M (number of columns) and the height N (number of rows) of the image I . In digital images processing, it is common to use a coordinate system where the origin ($u=0, v=0$) lies in the upper left corner.)



C. RGB color space

This is the color scheme most widely used in transmission, representation and storage of color images on both analog devices such as television sets and digital devices as computers and digital cameras [10]. The RGB space color encodes colors as combinations of the primary colors red (R), green (G) and blue (B). RGB is an additive color system and can be visualized as a three-dimensional unit cube in which the three primary colors form the coordinate axis (Fig. 3). The RGB values are positive and lie in the range $[0, C_{max}]$; for most digital images, $C_{max}=255$. Every possible color C_i corresponds to a point within RGB color cube of the form shown in Ec. (2).

$$C_i = (R_i, G_i, B_i) \quad (2)$$

Where $0 \leq R_i, G_i, B_i \leq C_{max}$. RGB values are often normalized to the interval $[0, 1]$ so that the resulting color space forms a unit cube. The point $S = (0, 0, 0)$ corresponds to the color black, $W = (1, 1, 1)$ corresponds to the color white, and the points lying on the diagonal between S and W , are shades of gray created from equal color components $R = G = B$.

D. HSV color space

In the HSV color space, colors are specified by the components hue, saturation, and value. The HSV color space is traditionally shown as an upside-down (Fig. 4), six-sided pyramid, where the vertical axis represents the V (brightness) value, the horizontal distance from the axis the S (saturation) value, and the angle the H (hue) value. The black points at the

tip of the pyramid and the white point lies in the center of the base. The three primary colors red, green and blue and the pairwise mixed colors yellow, cyan and magenta are the corner points of the base. Even this system is often portrayed in this intuitive graphical way, mathematically HSV space represent, actually, a cylinder [10], Fig 5.

Fig. 3. Representation of the RGB color space as three-dimensional unit cube. (The primary colors red (R), green (G), and blue (B), form the coordinate system. The "pure" red color (R), green (G), blue (B), cyan (C) magenta (M) and yellow (Y) lie on the vertices of the color cube.)

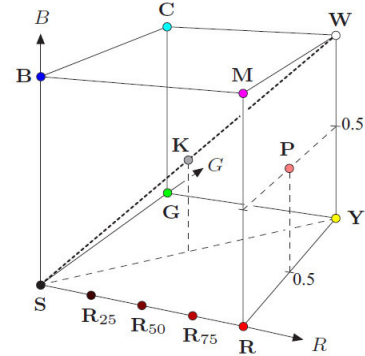
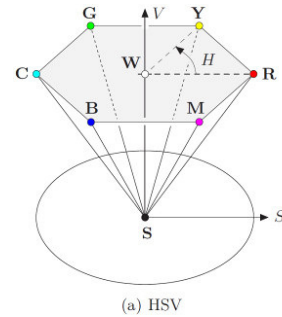


Fig. 4. HSV traditional representation. (The brightness V (or L) is represented by the vertical dimension, the color saturation S by the radius from the pyramid's axis, and the hue H by the angle.)



(a) HSV

E. RGB to HSV

To convert from RGB to HSV color space we first need to find the saturation of the RGB color components $R, G, B \in [0, C_{max}]$, with C_{max} being the maximum component value (typically 255), as

$$S_{HSV} = C_{mg} / C_{high}, \text{ for } C_{high} > 0$$

$$S_{HSV} = 0, \text{ otherwise} \quad (3)$$

and then the luminance (value)

$$V_{HSV} = C_{high} / C_{max} \quad (4)$$

with C_{high} , C_{low} , and C_{mg} defined as

$$C_{high} = \max(R, G, B)$$

$$C_{low} = \min(R, G, B) \quad (5)$$

$$C_{mg} = C_{high} - C_{low}$$

Finally we need to specify the hue value H_{HSV} . When all three RGB color components have the same value ($R = G = B$), then that pixel is achromatic. In this particular case hue value is not defined. To compute H_{HSV} when C_{mg} , it is necessary first to normalize each component using

$$R' = (C_{high} - R) / C_{mg}$$

$$G' = (C_{high} - G) / C_{mg} \quad (6)$$

$$B' = (C_{high} - B) / C_{mg}$$

Then, depending on which of the three original color component had the maximal value, is possible to compute a preliminary hue H' as

$$H' = B' - G' \text{ if } R = C_{high}$$

$$H' = R' - B' + 2 \text{ if } G = C_{high} \quad (7)$$

$$H' = G' - R' + 4 \text{ if } B = C_{high}$$

Since the resulting value for H' lies on the interval $[-1 \dots 5]$, is possible to obtain the final hue value by normalizing to the interval $[0, 1]$ as

$$H_{HSV} = 1 / 6 * (H' + 6) \text{ for } H' < 0$$

$$H_{HSV} = 1 / 6 * H' \text{ otherwise} \quad (8)$$

The three components will lie within interval $[0, 1]$. The hue value H_{HSV} can be computed in another angle interval, for example in the 0° to 360° interval using

$$H^\circ_{HSV} = H_{HSV} * 360 \quad (9)$$

F. HSV to RGB

To convert an HSV tuple (H_{HSV} , S_{HSV} , V_{HSV}), where H_{HSV} , S_{HSV} and $V_{HSV} \in [0, 1]$, into corresponding (R, G, B) color values, the appropriate color sector

$$H' = (6 * H_{HSV}) \% 6 \quad (10)$$

($0 \leq H' < 6$) is determined first, follow by computing the intermediate values

$$c_1 = H'$$

$$c_2 = H' - c_1$$

$$x = (1 - S_{HSV}) * v \quad (11)$$

$$y = (1 - (S_{HSV} * c_2)) * V_{HSV}$$

$$z = (1 - (S_{HSV} * (1 - c_2))) * V_{HSV}$$

Depending on the value of c_1 , the normalized RGB values R' , G' , $B' \in [0, 1]$ are then computed from $v = V_{HSV}$, x , y , and z as follows

$$(R', G', B') = (v, z, x) \text{ if } c_1 = 0$$

$$(R', G', B') = (y, v, x) \text{ if } c_1 = 1$$

$$(R', G', B') = (x, v, z) \text{ if } c_1 = 2 \quad (12)$$

$$(R', G', B') = (x, y, w) \text{ if } c_1 = 3$$

$$(R', G', B') = (z, x, w) \text{ if } c_1 = 4$$

$$(R', G', B') = (v, x, y) \text{ if } c_1 = 5$$

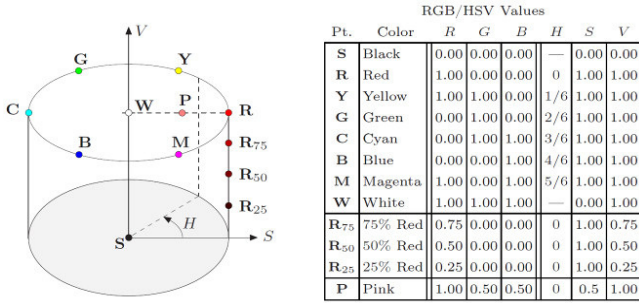
The scaling of the RGB components to whole numbers in range $[0, N-1]$ (typically $N = 256$) is carried out as follows

$$R = \min(\text{round}(N * R'), N-1)$$

$$G = \min(\text{round}(N * G'), N-1) \quad (13)$$

$$B = \min(\text{round}(N * B'), N-1)$$

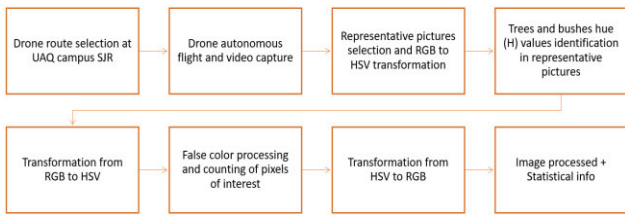
Fig. 5. HSV cylindrical representation. (The brightness V (or L) is represented by the vertical dimension, the color saturation S by the radius from the pyramid's axis, and the hue H by the angle.)



III. METHODOLOGY

The proposed methodology for this paper is shown in the Fig. 6.

Fig. 6. Methodology.



The first step consists in determinate a flight route through the Universidad Autonoma de Queretaro campus San Juan del Rio using the Google Maps tool and the GPS control drone station (Figs. 7 and 8). It is important to consider the height of the different elements in the environment as trees, buildings and communication antennas in order to avoid possible collisions during the independent drone flight.

With the route selected is time for the UAS to flight. During the route the independent gimbal control of the camera allows to rotate it and take pictures or videos of the interest areas. Images and videos are stored in the Canon Mark III SD memory card.

Fig. 7. Route for drone flying no. 1.



Fig. 8. Route for drone flying no.2



Once in land (Fig. 9), the memory card is removed and the processing stage begins. From the video saved, some significant frames are taken and treated as images and from those, green areas that belong to trees or shrubs are analyzed. These small but representative areas are transformed to HSV color space, and from its hue values, minimum and maximum are registered as color predominant range for these elements. The next step consist in take the complete images or frames, transform it to HSV color space and look for which pixels are into this color predominant range. For those inside this color predominant range the hue value is changed to another one not present in the original frame. During this process the number of pixels of interest can be stored in an array to use it as statistical information.

Fig. 9. UAS landing.



Finally, the images are transformed again from HSV to RGB color space to show the results.

IV. EXPERIMENTS AND RESULTS

In order to test the proposed methodology a series of images taken from two sequences of video from an autonomous UAS flight around the UAQ campus SJR are analyzed (Figs. 10, 11, 12 and 13). Both flights were realized in January 29th of 2015 during the afternoon (Figs. 7 and 8). The heights of the flights were around 35 to 45 meters.

Fig. 10. Test image 1 (*Back of the Library of the Universidad Autonoma de Querétaro campus San Juan del Río*)



Fig. 11. Test image 2 (*Faculty of Law and Faculty of Nursing.*)



Fig. 12. Test image 3 (*Faculty of Engineering.*)



Fig. 13. Test image 4 (*Faculty of Accounting and Administration.*)



The next step is to select at least one area in all this images where there are trees or shrubs. The Table 1 shows the areas selected from each image denoted by 2 coordinates (x1, y1) and (x2, y2) in pixels. This selected areas are transformed to HSV color space and then the minimum and maximum value of hue (H) are calculated. From this values is possible to calculate the mean so is possible to set the hue range for trees and shrubs from 145 to 200.

TABLE I. TREES AND SHRUBS AREAS + H VALUES

Image	Areas and H ranges for color change ^a		
	Trees and shrubs areas of interest	H min	H max
1	(849, 321) and (883, 348)	152	202
2	(386, 838) and (528, 916)	150	220
3	(646, 649) and (729, 728)	156	190
4	(987, 300) and (1026, 403)	120	194

^a. Trees and shrubs areas in pixels taken from their respective image, hue values are in degrees.

With the range selected finally is possible to change the full images to HSV color space, then using a programming conditional verify if a pixel belongs or not inside this range. If the pixel hue value is inside this range then its hue values is changed to a 0 value. After that the image is changed again, now from HSV to RGB color space. The result of this process is shown in Figs 14, 15, 16 and 17.

Fig. 14. Test image 1 after false color processing.



Fig. 15. Test image 2 after false color processing.



Fig. 16. Test image 3 after false color processing.



Fig. 17. Test image 4 after false color processing.



Fig. 14 shows how almost all of the visible trees are in a purple color. Some grass also got the new color but is not consistent and is not very well segmented. Some buildings around the campus also got the new color. For this image 358,074 pixels were changed to purple. Fig. 15 and 16 presents similar results, also some grass also is segmented. This paper can help to segment green and dry grass areas. For this two images 364,170 and 759,406 pixels were changed. For the last image, Fig. 17, which is the picture taken from higher, a full line of shrubs around the building is well segmented, and is the only image where all trees are now in purple. The grass presents the same bad segmentation. For this last image 464,098 were changed.

V. CONCLUSIONS

In this paper a methodology that allows to automatically detect trees and shrubs from UAS pictures using image processing and color spaces is presented and tested. Trees and shrubs were easily detected once the range of the dominant hue was calculated. Also, it was possible to detect some areas with grass, but only those where green color it was similar to those

present in trees and bushes. Actually, this methodology could be applied to detect dry and green grass areas in order to analyze damaged areas or places where is necessary to put attention in the grass or even other vegetation growth. Another possible application could be take the UAS device to a considerable high, take a perpendicular picture of an area of interest and, with the terrain area known, estimate the percentage of green areas in different seasons of the year. UAS devices provide an invaluable tool as auxiliary in the development of academic and scientific research. The ease of use and the autonomous capabilities allow planning trajectories almost from the office and then, taking the drone to the field, flight and registering all the elements of consideration using the camera on board. Finally, this methodology is intended to be directly implemented on the UAS system using a very small PC, like a Raspberry Pi, to implement the image algorithm, so the integrated system automatically deliver the images with the areas of interest enhanced.

ACKNOWLEDGMENT

The authors would like to thank CONACYT for the support with the project number 221608. Garduño-Ramón would like to thank CONACYT for the funding of this research in the form of the PhD scholarship no. 487601/278034.

REFERENCES

- [1] K. P. Valavanis and G. J. Vachtsevanos, *Handbook of Unmanned Aerial Vehicles*, Springer Reference
- [2] L. C. Warrior, *Drones and Targeted Killing: Costs, Accountability, and U.S. Civil-Military Relations*, *Orbis*, Volume 59, Issue 1, 2015, Pages 95–110.
- [3] P. Rodriguez-Gonzalvez et al., *Image-based modeling of built environment from an unmanned aerial system*, *Automation in Construction* 48 (2014) 44–52.
- [4] M. Gerke and P. Seibold, *Visual inspection of power lines by U.A.S.*, *Electrical and Power Engineering (EPE)*, 2014 International Conference and Exposition on, 16-18 Oct. 2014, pp 1077 – 1082, DOI: 10.1109/ICEPE.2014.6970074.
- [5] I. Jazayeri, A. Rajabifard, and M. Kalantri, *A geometric and semantic evaluation of 3D data sourcing methods for land and property information*, *Land Use Policy*, Volume 36, January 2014, Pages 219–230.
- [6] Z. Xu et al., *Development of an UAS for post-earthquake disaster surveying and its application in Ms 7.0 Lushan Earthquake, Sichuan, China*, *Computers & Geosciences* 68(2014)22–30.
- [7] I. Colomia and P. Molilna, *Unmanned aerial systems for photogrammetry and remote sensing: A review*, *ISPRS Journal of Photogrammetry and Remote Sensing* 92 (2014) 79–97.
- [8] J. J. Baez-Rojas, and M. A. Alonso Pérez, *Uso del sistema HSI para asignar falso color a objetos en imágenes digitales*, *REVISTA MEXICANA DE FÍSICA E* 54 (2) 186–192.
- [9] T. Audronis, *Building Multicopter Video Drones*, Packt Publishing, August 2014.
- [10] W. Burguer and M. J. Burge, *Principles of Digital Image Processing - Fundamental Techniques*, Springer-Verlag London Limited 2009, DOI 10.1007/978-1-84800-191-6

Measurement of Agglomerates Shape Using Three-Dimensional Reconstruction

J. P. Zavala De Paz^{#1}, César Isaza^{#2}, E. K. Anaya Rivera^{#3}, F. Castillo Velásquez^{#4}

[#]Universidad Politécnica de Querétaro, Carretera Estatal 420 S/N, El Marqués, Querétaro, México. C.P. 76240

¹ jonny.zavala@upq.edu.mx, jopazavala@hotmail.com

² cesar.isaza@upq.mx

³ karina.anaya@upq.mx

⁴ francisco.castillo@upq.edu.mx

Abstract—The agglomeration of particles is a process that modifies the physical properties of a product originally manufactured as a powder. During milk powder agglomeration of fluidized bed, resulting agglomerates are sufficiently porous to improve the solubility of the final product but, at the same time, their rigidity decreases and agglomerates can be destroyed during packing. The porosity and rigidity properties depend on both the volume and shape characteristics of the agglomerates. This paper presents a three-dimensional reconstruction technique based on a laser displacement sensor (LDS) applied to characterize milk agglomerates. This technique allows three-dimensional scanning to estimate particle volume and extract shape parameters such as: sphericity, elongation and flatness ratio, shape factor and aspect ratio. This technique was implemented using a mechatronic device with two degrees of freedom. The device is composed of an angular positioning system to rotate the agglomerate and a linear positioning system to displace the LDS. Experimental result allows agglomerates classification according to shape parameters.

Keywords— *agglomerated particles; laser displacement sensor; shape parameters; three-dimensional reconstruction*

I. INTRODUCTION

In the food industry the agglomeration process of powders increases the particle size as well as its porosity and then modifies end-user properties such as wettability, sinkability, dispersibility and solubility. The main application of agglomeration is to produce instant products (e. g. instant coffee, milk powder, cocoa beverages, etc.) that acquire the ability for dispersing or rapidly dissolving in liquids (water, milk, etc.) [1].

Furthermore, many of the physical and structural properties of agglomerates such as density, surface properties, size and shape, influence the particles rigidity and then modify their behavior during handling [2,3]. The measurement of these physical properties is important since they affect the behavior of powder particles during storage, packing and processing.

The size parameter (usually associated to diameter, surface area or volume) describes the geometry of the object regardless of its form [4]. The shape parameter characterizes the object regardless of the size. Currently, the measurement of the shape parameters of agglomerates is performed from 2D data, usually from microscope images. One of the shape parameters

frequently used in the characterization of objects is the sphericity. However, there are no works to report measurements of sphericity in the characterization of agglomerates of milk powder from 3D data.

There are different methods for characterization of agglomerated particles. In [5] the shape of agglomerates is computed from 2D microscope images by finding the circle that best fits the estimated area on each image, assuming that particles have a circular shape. A highly accurate technique is the use of confocal microscopy [6] that creates sharp images of a specimen, normally blurred with conventional microscopes; however, stimulating fluorescence from dyes that should be applied to the specimen, can modify the agglomerates properties. Another method to characterize agglomerate is the use of mercury porosimetry applying various pressure levels to the sample. This technique is not suitable to characterize agglomerates, normally fragile, that are broken during the measurement [7].

The work presented in [8] computes the porosity of fragile agglomerates from only three images acquired with a CCD camera. The work described in [9,10] present a method based on silhouettes extraction of multiple views to estimate the volume of the envelope of milk powder agglomerates; agglomerates concavities are not considered. The works in [11-13] developed methods to estimate the shape of particles using 2D shape parameters from image analysis techniques.

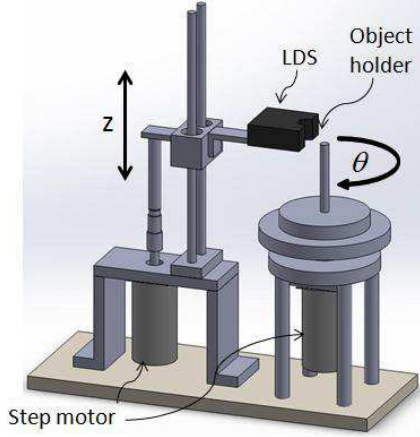
The aim of this paper is to propose a methodology to characterize the shape of agglomerated particles of milk powder using 3D parameters. This methodology is based on a laser displacement sensor that allows a three-dimensional reconstruction of the agglomerated particles. This approach can be extended to measure other particle systems. The shape of the agglomerates was analyzed using the following form factors: elongation, flatness, aspect ratio and sphericity. Also, the particle volume is determined since it is used as a basic parameter to determine the particle sphericity.

II. 3D RECONSTRUCTION SYSTEM

A. Positioning System

The positioning system is shown in Fig. 1. The agglomerate is placed on the object holder that rotates, driven by a stepper motor, at $\Delta\theta$ degrees increments controlled by a PIC-STEP control board. The laser displacement sensor (LDS) is rigidly mounted on a linear positioning system that moves along z-axis at Δz increments ($\Delta z = 30\mu\text{m}$).

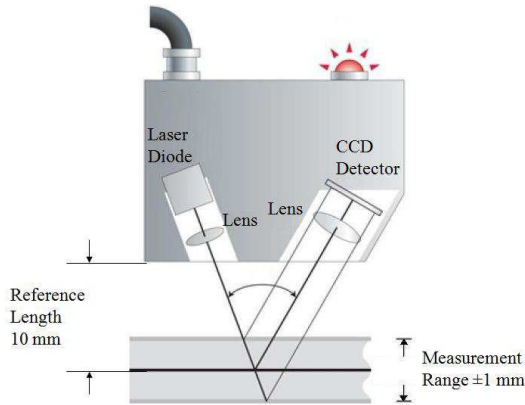
Fig. 1. 3D reconstruction system.



B. LDS Description

The LDS used works on optical triangulation principle. A laser diode (wavelength 650 nm) is the light source, projecting a spot onto the surface to be measured. The LDS is mounted on the linear positioning system. The LDS controller estimates the distance between its emitter and the target (agglomerate surface). Fig. 2 shows the laser triangulation principle.

Fig. 2. Laser triangulation principle.



The measurement technique is based on the LDS model LK-G10 from KEYENCE. TABLE 1 shows the technical specifications of the sensor.

TABLE I. TECHNICAL SPECIFICATIONS OF LDS

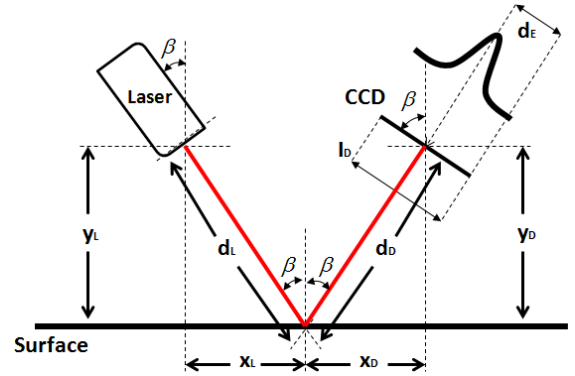
Reference length	10mm
Measuring range	$\pm 1\text{mm}$
Kind of laser	Laser diode
Spot diameter	$20\mu\text{m}$
Resolution	$0.01\mu\text{m}$

C. Principle of Distance Estimation

Fig. 3 illustrates the sensor principle to estimate the distance to target where:

- d_L : Distance to laser,
- d_D : Distance to detector,
- β : Angle of incidence,
- d_E : Speculate distance,
- I_D : Intensity on detector,
- x_L : x-axis component of incident laser beam,
- y_L : y-axis component of incident laser beam,
- x_D : x-axis component of reflected laser beam,
- y_D : y-axis component of reflected laser beam,

Fig. 3. Measurement principle of distance.



By geometry, we obtain the following equations for the distance to the laser and the angle of incidence:

$$d_L = \sqrt{x_L^2 + y_L^2} \quad (1)$$

$$\beta = \arctan\left(\frac{x_L}{y_L}\right) \quad (2)$$

and the distance to the CCD:

$$d_D = \sqrt{x_D^2 + y_D^2} \quad (3)$$

$$\beta = \arctan\left(\frac{x_D}{y_D}\right) \quad (4)$$

According to the law of reflection, the reflected beam has the same angle that the incident, so we have:

$$\frac{x_L}{y_L} = \frac{x_D}{y_D}. \quad (5)$$

The normal density function (Gaussian curve), in Fig. 3, represents the laser beam intensity detected by the CCD and corresponds to the distance to the specular (d'_E) from the laser to the object surface. This distance is defined by:

$$f(x - \mu) = \frac{1}{\sigma\sqrt{2\pi}} e^{-\frac{1}{2}\left(\frac{x-\mu}{\sigma}\right)^2}, \quad (6)$$

where σ is the standard deviation and μ is the average intensity obtained by the CCD detector.

Fig. 4 shows how a variation (Δy) in the distance to the object's surface (displacement) produces a change in the mean of the Gaussian curve.

Fig. 4. Measuring displacement of object's surface.

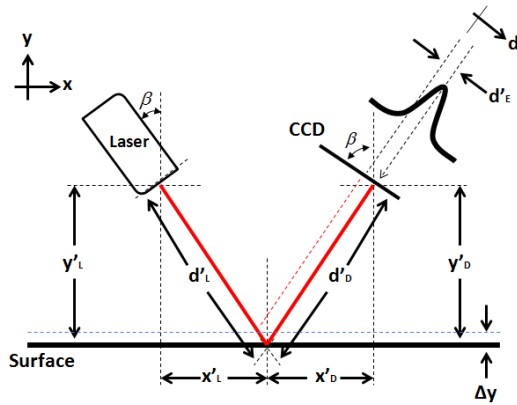


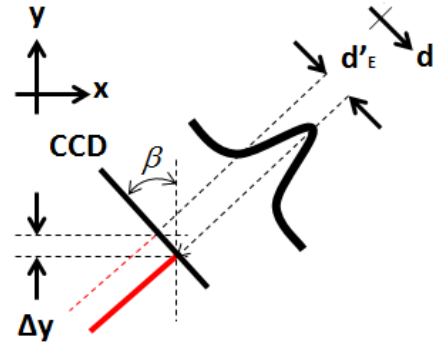
Fig. 5 shows the relationship between the displacement of the Gaussian curve d'_E and the displacement Δy is given by:

$$\Delta y = -d'_E \cos(\beta) \quad (7)$$

Since the measuring range of CCD is limited, the maximal variation Δy is given by:

$$\Delta y_{Max} = \frac{I_D}{2} \cos(\beta). \quad (8)$$

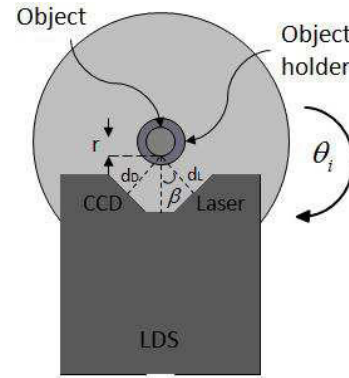
Fig. 5. Relationship between distance to specular and Δy .



D. Estimation of 3D Coordinates

The purpose of distance measurement by laser triangulation is to calculate the radius (r), which is the distance from the center of the object holder to the point where the laser beam strikes the object, see Fig. 6.

Fig. 6. Laser triangulation measurement.



The object is mounted on the object holder. Fig. 6 shows a circle shaped object, the laser beam is projected onto the object surface and reflected towards the CCD. The angular positioning system rotates using a constant increment ($\Delta\alpha = 0.9^\circ$) which is calculated by dividing 360° by the number N of steps of the motor ($N=400$). The 3D coordinates of each point of the object surface, $D_i=(x_{d_i}, y_{d_i}, z_{d_i})$, are obtained from $r_i, i=1,2,3,\dots,N$ and β_i as follows:

$$\begin{bmatrix} x_{d_i} \\ y_{d_i} \\ z_{d_i} \end{bmatrix} = \begin{bmatrix} \cos \beta_i & 0 & 0 \\ 0 & \sin \beta_i & 0 \\ 0 & 0 & 1 \end{bmatrix} \begin{bmatrix} r_i \\ r_i \\ z_i \end{bmatrix} \quad (9)$$

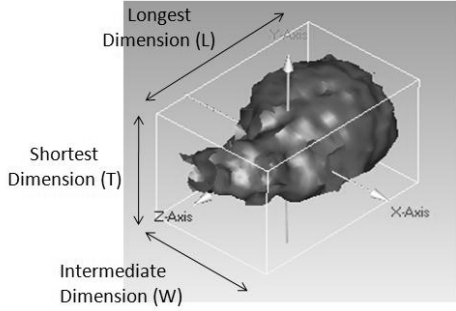
Where $\beta_i = \beta_{i-1} + \Delta\alpha$. The value of z_i is also a constant defined by the increments of the micrometer.

E. Shape Parameters

The spheres and cubes are the only objects whose size can be given for only a number (diameter or length). Food powder

particles are irregularly shaped particles and their characterization requires several parameters of size and shape [11]. The shape parameters used in this work are based on the three representative lengths: L (longest dimension), W (intermediate dimension) and T (shortest dimension) [14], see Fig. 7. These lengths are equivalent to the lengths of the sides of a solid rectangle of a particle boundary, as shown in Fig. 7.

Fig. 7. Main dimensions of an irregular particle.



The elongation ratio (ER) is defined in as:

$$ER = \frac{W}{L}. \quad (10)$$

For circular objects ER is equal to 1. The more elongated shape, the greater is its elongation factor [11].

The flatness ratio (FR) and the aspect ratio (AR) are as:

$$FR = \frac{T}{W}, \quad (11)$$

$$AR = \frac{L}{W}, \quad (12)$$

respectively.

The shape factor (SF) has been used to describe the irregularity of the surface and is defined as:

$$SF = \frac{T}{\sqrt{WL}}. \quad (13)$$

From 3D coordinates of the object surface, obtained from the LDS, one can estimate the particle sphericity (Sp). The sphericity value varies from 0 to 1, where a value of 1 indicates a perfect sphere [14]. The sphericity is defined by:

$$Sp = \frac{d_n}{L}. \quad (14)$$

Nominal diameter d_n and nominal surface s_n are computed as:

$$d_n = \left(\frac{6V}{\pi} \right)^{\frac{1}{3}}, \quad (15)$$

$$s_n = (36\pi V^2)^{\frac{1}{3}}, \quad (16)$$

respectively.

The volume V and lengths L , W and T of the agglomerated particles may be obtained from the 3D coordinates estimated by the LDS.

III. PARAMETER EXTRACTION FROM AGGLOMERATES

A. Test Agglomerates

To carry out the experimental part of this work, 10 samples of milk powder agglomerates were obtained using the fluidized bed technique, see Fig. 8. The particles were divided into three size fractions by sieving: up to 630 μm for size A, up to 1250 μm for size B and from 630 to 1250 μm for size C. Prior to analysis, the agglomerates were stored for one week in a desiccator with silica gel for drying.

For weighing of the individual agglomerates, a laboratory precision balance (AX205 Delta Range, Mettler Toledo, France) was used. This balance has a precision of 0.01 mg with a weighing error that might be up to 0.005 mg. It was therefore not sufficient for individual agglomerates in the small size fraction (inferior to 630 μm). For this reason, only agglomerates larger than 630 μm were considered for the measurement of shape using 3D reconstruction method.

Fig. 8. a) Agglomerates samples, b) Zoomed view of one agglomerate.



B. Shape Parameters Estimation

The experiment was conducted at an ambient temperature of 24° C. The agglomerate was mounted on object holder, as shown in Fig. 9. Ten repeated measurements were performed. The LDS was placed at a distance of 10 mm to the center of the object holder.

Fig. 9. Agglomerate mounted on the positioning system for scanning.

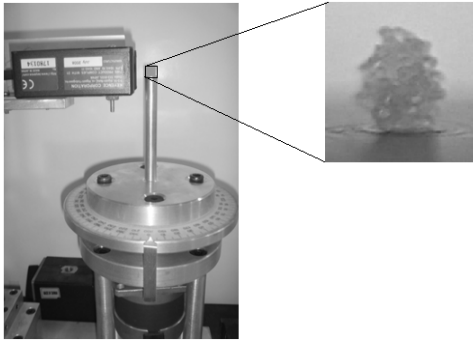


Fig. 10 shows real images of two of ten agglomerates used in this experiment, the obtained cloud of 3D points, and a textured representation of the agglomerate.

Fig. 10. a) Real agglomerate, b) cloud of 3D points, c) textured object.

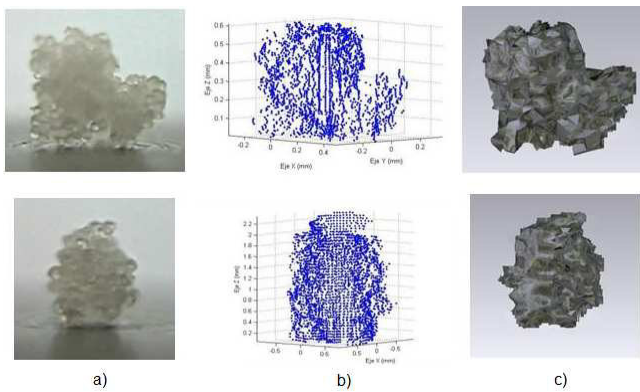


TABLE II. SHAPE PARAMETERS COMPUTED FOR TEN AGGLOMERATES

V (mm ³)	S _n (mm ²)	ER	FR	AR	SF	S _p
0.1823	1.0582	0.7467	0.8734	1.3391	0.7548	0.6797
2.1714	8.1092	0.6546	0.9303	1.5274	0.7528	0.6405
1.934	7.506	0.7361	0.9441	1.3583	0.811	0.6569
1.345	5.8924	0.7445	0.8883	1.3431	0.7665	0.6325
0.189	1.5926	0.8098	0.8524	1.2348	0.7671	0.8441
1.221	5.5245	0.7272	0.9499	1.375	0.81	0.7305
1.676	6.8233	0.8036	0.7015	1.2443	0.6289	0.626
0.987	4.7939	0.7372	0.806	1.3563	0.6921	0.6594
2.056	7.8192	0.8256	0.7365	1.2112	0.6692	0.6538
1.578	6.5547	0.7618	0.5658	1.3125	0.6482	0.6076

Agglomerated particles were scanned using the three dimensional reconstruction technique based on LDS as shown in Fig. 9. Based on the representative three lengths: L , W and T , were determined to describe the shape parameters presented in TABLE 2. It is evident that the agglomerates are near to spherical. The agglomerates are the extreme case, in which variations of volume, surface area, ER , FR , AR and SF depends on the form of agglomerates due to irregular shape.

IV. CONCLUSIONS

This paper presents an experimental validation of a 3D reconstruction technique of milk powder agglomerates based on a laser displacement sensor. This technique allows the estimation of the particles volume (V) and surface (S_n) as well as some size lengths (L , W , T) to determine some shape parameters (ER , FR , AR , SF , S_p). Since we have a 3D cloud of points, a textured representation of the agglomerate is also available.

As expected, the reconstructed object has errors associated with the discretization of the data. Those errors are less than 1% considering only scanning along z-axis. The experimental results demonstrate the feasibility of this technique to estimate the shape parameters of agglomerate small particles that can be generalized for other kind of objects. A better accuracy is possible simply by increasing the number of points per turn (on the angular positioning system), for example by using a DC servomotor instead of a step motor. In the same way, accuracy can be improved by reducing the increments in the z-axis using a DC servomotor to move the LSD. Perspectives for our work mainly are that the method presented could be used in combination with more complex morphological analyses [15] or to validate other optical particle characterization methods [16].

REFERENCES

- [1] Schubert, H. (1987). Food particle technology: Part I. Properties of particles and particulate food systems. *Journal Food Engineering*, 6(1), 1-32.
- [2] Mekki, B.K., Pons, M.N., Falk, V., Vivier, H. (2002). Recherche de relations entre la coulabilité et la morphologie des poudres, Groupe «solides divisés» de la SFGP.
- [3] Tanguy, P.A., Thibault, F., Dubois, C., Ait-Kadi, A. (1999). Mixing hydrodynamics in a double planetary mixer. *Chemical Engineering Research and Design*, 77(4), 318-324.
- [4] Valdek, M., Helmo, K., Priit, K., Michal, B. (2001). Characterization of Powder Particle Morphology. *Proc. Estonian Acad. Sci. Eng.*, 7(1), 22-34.
- [5] Turchiuli, C., Eloualia, Z., El-Mansouri, N., Dumoulin, E. (2005). Fluidised bed agglomeration: Agglomerates shape and end-user properties. *Powder Technology*, 157(1-3), 168-175.
- [6] Pawley, J.B. (2006). *Handbook of Biological Confocal Microscopy*, 3rd ed. Springer, Berlin.
- [7] Emeruwa, E., Jarrige, J., Mexmain, J., Bernardin M. (1991). Application of mercury porosimetry to powder (UO₂) analysis. *Journal of Nuclear Materials*, 184(1), 53-58.
- [8] Hogeckamp, S., Pohl, M. (2003). Porosity measurement of fragile agglomerates. *Powder Technology*. 130, 385-392.
- [9] Turchiuli, C., Castillo, C.E. (2009). Agglomerates structure characterization using 3D-image reconstruction. *Particle and Particle Systems Characterization*, 26, 25-33.

- [10] Castillo, C.E., Turchiuli, C. (2008). Volume estimation of small particles using three-dimensional reconstruction from multiple views. *ICISP '08 Proc. of the 3rd International Conference on Image and Signal Processing*, 218-225.
- [11] Saad, M., Sadoudi, A., Rondet, E., Cuq, B. (2011). Morphological characterization of wheat powders, How to characterize the shape of particles?. *Journal Food Engineering*, 102, 293-301.
- [12] Alander, E.M., Uusi-Penttilä, M.S., Rasmuson, A.C. (2003). Characterization of paracetamol agglomerates by image analysis and strength measurement. *Powder Technology*, 130, 298-306.
- [13] Realpe, A., Velázquez, C. (2006). Pattern recognition for characterization of pharmaceutical powders. *Powder Technology*, 169, 108-113. Yuichi, H., Takashi, O. (2005). Evaluation of gravel sphericity and roundness based on surface-area measurement with a laser scanner. *Computers and Geosciences*, 31, 735-741.
- [14] Wozniak, M., Onofri, F.R.A., Barbosa, S., Yon, J., Mroczka, J. (2012), Comparison of methods to derive morphological parameters of multi-fractal samples of particle aggregates from TEM images. *Journal of Aerosol Science*, 47, 12-26.
- [15] Mroczka, J., Wozniak, M., Onofri, F.R.A. (2012), Algorithms and methods for analysis of the optical structure factor of fractal aggregates. *Metrology and Measurement Systems*, XIX (3), 459-470.

Characterization of Inner Product Spaces

Jesús Jerónimo Castro ^{#1}, Marco Antonio Rojas Tapia ^{#2}

[#] Facultad de Ingeniería, Universidad Autónoma de Querétaro.
Cerro de las campanas s/n, C. P. 76010; Querétaro, Qro. México.

¹ *jesusjero@hotmail.com*

² *milo_marco013@hotmail.com*

Abstract— The purpose of this work is to prove that the following property is only true in inner product spaces: there exists a positive number λ such that for every K -equilateral triangle (quadrilateral) inscribed in the unit circle S it holds that its sides touches λS at its midpoints. We also review a characterization of inner product spaces in terms of the closest points of chords of the unit circle.

Keywords—inner product spaces; Birkoff orthogonality; Minkowski plane

I. INTRODUCTION

Consider the unit circle centered at the origin (O) in the Euclidean plane and denote it as B . Many of the properties of it are known by anyone who has taken a course of Euclidean Geometry.

For instance, given a pair of unit vectors, which are orthogonal, we have that the point of the segment ending in x and y which is closest to the origin is precisely its middle point. Denote $[x, y]$ as the segment ending in x and y . With this notation the above mentioned property is expressed as: the point of $[x, y]$ which is closest to the origin is the point $m = \frac{x+y}{2}$. Notice also that the segment $[O, m]$ is orthogonal to segment $[x, y]$.

Also, if we inscribe regular polygons in the unit circle, we can find a dilation of the circle such that the sides of the polygon are tangent to the dilated circle and also the point of tangency is the midpoint in each side of the polygons.

Suppose now we want to define a new way to measure distance on the plane and that our unit ball will be a convex set K which has a center of symmetry. We ask ourselves: What properties about the Euclidean ball still fulfilled for the new unit ball K ? In the case that some property is not fulfilled, it will be that this is a characteristic property of the Euclidean plane? In other words, does this property characterizes inner product spaces?

The purpose of this work is to show that the mentioned properties are characteristics of inner product spaces, in other words, only fulfill if K is a circle or an ellipse.

II. DEFINITIONS AND BASIC NOTATION

From now on, we will refer to a 2-dimensional normed space as Minkowski Plane. The definition is as follows:

Definition. A Minkowski plane with unit ball K is a 2-dimensional vector space provided with a norm $\|\cdot\|_K$.

The norm $\|\cdot\|_K$ is defined as follows: given a point $x \in \mathbb{R}^2$ its Minkowski norm is:

$$\|x\|_K = \inf\{\lambda > 0 : x \in \lambda K\}.$$

Intuitively, the geometric meaning of the Minkowski norm of a given point $x \in \mathbb{R}^2$ is as follows: if y is the point where the ray Ox intersects the boundary of K , then

$$\|x\|_K = \frac{\|x\|}{\|y\|}$$

where $\|w\|$ denote the Euclidean norm of w .

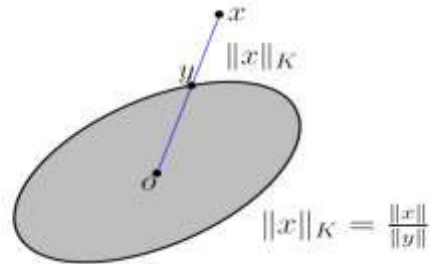


Fig.1. Geometric meaning of the Minkowski norm.

Many of the notions in Euclidean geometry can be extended to Minkowski planes, however, in the case of vectorial orthogonality, exist a lot of definitions. In this work, we will be mainly concerned with Birkhoff and James orthogonality.

Definition. A vector $x \in (\mathbb{R}^2, \|\cdot\|_K)$ is orthogonal to vector $y \in (\mathbb{R}^2, \|\cdot\|_K)$, in the sense of Birkhoff, if

$$\|x\|_K \leq \|x + \lambda y\|_K,$$

for every real number λ , and denote it as $x \perp_B y$ or x is B-orthogonal to y .

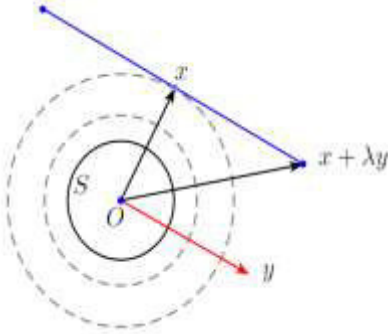


Fig.2. Geometric meaning of Birkhoff orthogonality.

Notice that Birkhoff orthogonality generally is not symmetrical, in other words, if a vector x is B-orthogonal to y , then is not necessary that y is B-orthogonal to x . However, if Birkhoff orthogonality is symmetrical then the form of the unit ball K is known as *Radon body* (see [10]). Many properties of geometric figures that deal with vectorial orthogonality are not true in general on Minkowski planes; indeed, they are characteristics of inner product spaces.

Another orthogonality is the following.

Definition. It is said that x is orthogonal to y in the sense of James if $\|x + y\|_K = \|x - y\|_K$ and denote it as $x \perp_J y$. Unlike the previous orthogonality, this one is symmetrical, in other words, if $x \perp_J y$ then $y \perp_J x$. This orthogonality geometrically tells us that the two diagonals of every parallelogram have equal length.

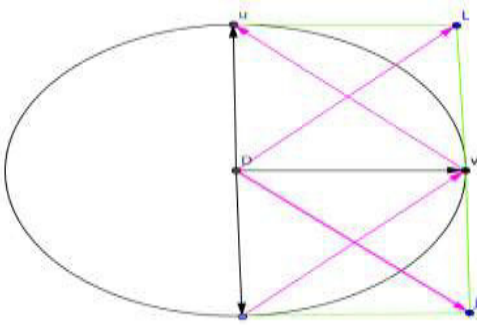


Fig.3. Geometrical meaning of James orthogonality

III. BARONTI-CASINI THEOREM

In what follows we will denote the Minkowski unit circle by S , in other words, S is the boundary of K .

The next theorem, proved by M. Baronti and E. Casini in [2] establishes a criteria to know when a Minkowski plane is Euclidean, in other words, when the unit ball K is an ellipse.

Theorem 1. If for any $x, y \in S$, with $x \perp_B y$, it holds that

$$k(x, y) = \inf \left\{ \|tx + (1 - t)y\|_K : t \in [0, 1] \right\} = \frac{\|x + y\|_K}{2},$$

then K is an ellipse.

Proof. Consider $x, y \in S$, with $x \perp_B y$, then by hypothesis

$$k(x, y) = \frac{\|x + y\|_K}{2}.$$

Define the function $g: \mathbb{R} \rightarrow \mathbb{R}$ as

$$g(t) = \|tx + (1 - t)y\|_K.$$

We have that $g(\frac{1}{2}) \leq g(t)$, $\forall t \in [0, 1]$.

Then

$$\begin{aligned} \frac{\|x + y\|_K}{2} &\leq \left\| y + t(x - y) + \frac{x + y}{2} - \frac{x + y}{2} \right\|_K \\ &= \left\| \frac{x + y}{2} + \frac{2t - 1}{2}(x - y) \right\|_K. \end{aligned}$$

In other words,

$$\frac{\|x + y\|_K}{2} \leq \left\| \frac{x + y}{2} + \lambda(x - y) \right\|_K, \quad \forall \lambda \in \mathbb{R}.$$

This is equivalent to say that $x + y \perp_B x - y$ in the sense of Birkhoff. Therefore, for every $x, y \in S$, with $x \perp_B y$ it holds that $x + y \perp_B x - y$, which is known that characterizes the 2-dimensional inner product spaces (see [1]). \square

IV. POLYGONS INSCRIBED IN THE UNIT BALL

Suppose now that for a fixed natural number n and a centrally symmetric convex body K with center at the origin we have the following: there is a homothetic copy of K , to say K' , with center of homothety at the origin, such that the sides of every equilateral n -gon inscribed in K are tangent to K' precisely at their midpoints. Is this property characteristic of inner product spaces, or there exist any convex body K , besides the ellipse, with this property?

In this section we will analyze the cases $n=3$ and $n=4$.

Definition. A K -equilateral n -gon is a polygon with n vertices such that all its sides have equal Minkowski lengths.

With respect to the case $n=3$, we shall prove that the unit circle S is an ellipse. We easily derive this result from a theorem due to C. Benitez, and D.Yañez [3]:

Theorem 2 (Benitez-Yañez). Let S be the unit circle of a Minkowski plane such that every chord of S that supports $\frac{1}{2}S$ touches $\frac{1}{2}S$ at its middle point. Then S is an ellipse.

The statement for K -equilateral triangles is as follows.

Theorem 3. Suppose there is a number $0 < \lambda < 1$ such that every K -equilateral triangle inscribed in S touches λS at its middle points. Then S must be an ellipse.

Proof. Let Δabc be a K -equilateral triangle inscribed in S and let m, n , and p , be the midpoints of the sides as shown in Fig. 4.

By hypothesis, the triangle Δmnp is inscribed in λS and from elementary geometry we know that Δmnp and Δabc are similar with a similarity ratio equal to 1:2. Consider now, the triangle $\Delta a'b'c'$ which is symmetric to Δabc with respect to O . Clearly, $\Delta a'b'c'$ is congruent to Δabc , hence $b'c' = bc$, and so

$mp = \frac{1}{2} b'c' = \frac{1}{2} bc$. It follows that $\lambda = \frac{1}{2}$.

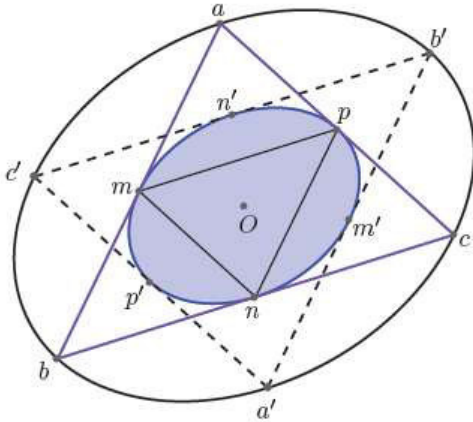


Fig. 4. λ must be equal to $\frac{1}{2}$.

We have that every chord of S and tangent to $\frac{1}{2}S$, touches $\frac{1}{2}S$ at its midpoint, therefore, by Theorem 2 we have that S is an ellipse. \square

Finally, for the case of K -equilateral inscribed quadrilaterals we have the following.

Theorem 4. Suppose there is a number $0 < \lambda < 1$ such that every K -equilateral quadrilateral inscribed in S touches λS at its middle points. Then S must be an ellipse.

Proof. It is easy to see that every inscribed K -equilateral quadrilateral is a parallelogram whose opposite vertices are diametrically opposite, with respect to the unit circle S . Let $x, y, -x$, and $-y$, be the vertices of one such quadrilateral (see Fig. 5). We have that $\|x - y\|_K = \|x + y\|_K$, which means that $x \perp y$.

Now, since $\frac{x+y}{2}$ is Birkhoff orthogonal to $x - y$, we have that

$$x + y \perp_B x - y.$$

As we mentioned before, this property is characteristic of inner product spaces, and so S is an ellipse. \square

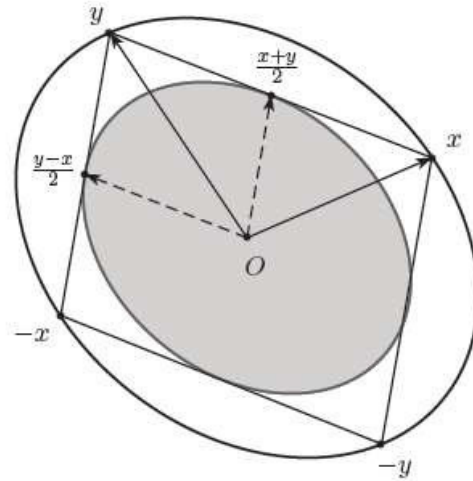


Fig. 5. $x + y$ is Birkhoff orthogonal to $x - y$.

REFERENCES

- [1] D. Amir, Characterizations of Inner Product Spaces, Birkhäuser, Basel, (1986).
- [2] M. Baronti, and E. Casini. Characterizations of inner product spaces by orthogonal vectors, J. Funct. SpacesAppl. 4 (2006), 1–6.
- [3] C. Benitez, and D.Yañez. Middle points, medians and inner products, Proceedings Amer. Math. Soc. 135, (2007), 1725-1734.
- [4] G. Birkhoff, Orthogonality in linear metric spaces, DukeMath. J. 1 (1935), 169-172.
- [5] J.R. Holub, Rotundity, orthogonality, and characterizations of inner product spaces, Bull. Amer. Math. Soc.81 (1975), 1087-1089.
- [6] R. C. James, Orthogonality in normed linear spaces, DukeMath. J. 12(1945), 291–301.
- [7] O.P. Kapoor and J. Prasad, Orthogonality and Characterizations of inner product spaces, Bull. Austral. Math. 19 (1978), 403-416.
- [8] O.N. Kosukhin, A Geometric Criterion for the Hilbert Property of a Banach space, Moscow Univ. Math. Bull.63(2008),205–207.
- [9] D. S. Marinescu, A characterization of the inner product spaces involving trigonometry, Ann. Funct. Anal. 4 (2013), 109-113.
- [10] Mahlon M. Day, On criteria of Kasahara and Blumenthal for inner product spaces, Proc.Amer. Math. Soc.10 (1959), 92-100.
- [11] A.C. Thompson, Minkowski Geometry, Cambridge University Press, (1996).
- [12] S. Wu, Geometry of Minkowski Planes and Spaces. Tesis doctoral.

Line transversals to very disjoint translates of convex bodies

Jerónimo-Castro Jesús ^{#1}

[#] *Facultad de Ingeniería, Universidad Autónoma de Querétaro, Centro Universitario
Cerro de las Campanas s/n, C. P. 76010; Santiago de Querétaro; Qro., México.*

¹ *jesusjero@hotmail.com*

Abstract—In this short paper we study the existence of line transversals to families of translates of convex bodies. For general convex bodies we prove the following: for every 2-disjoint family of translates of a convex body, in the plane, we have that there exists a common line transversal to all members provided that every three translates have a line transversal. For the special case of a family of translates of a circle or a square we have better bounds for the necessary disjointness.

Keywords—line transversals; families of translates; unit circle; unit square.

I. INTRODUCTION

Let P be a finite set of points in the plane such that every three of them are on the same line. It is quite easy to see that indeed all the points of P are aligned. However, if we replace the points by convex figures the analogue statement is not longer true, that is, if P is a finite family of convex figures such that any three of them have a line transversal (a line intersecting simultaneously the three figures) then is not necessarily true that there is a line intersecting all the members of P . Even if we restrict ourselves to consider only families of translates of a disc with the property that any three of them have a line transversal, the existence of a common line transversal to all the disks is not clear. In the following figure (Fig. 1) we have four congruent circles with the property that any three of them have a common tangent line, however, there is not a line intersecting the four disks at the same time.

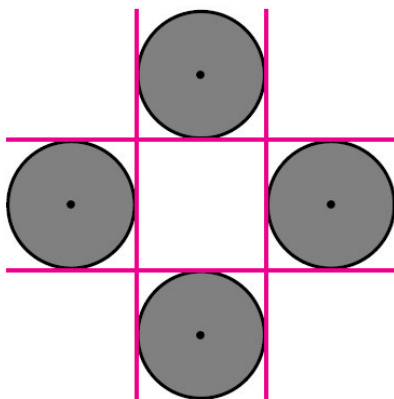


Fig. 1. Four disks without a common line transversal and such that every three have a common tangent line.

However, if the members of P are sufficiently far away from each other, we expect they behave as points with respect to collinearity. This is indeed true, as we will see soon, but we first need to introduce some notation.

Let K be a centrally symmetric convex set centered at the origin and let $F = \{x_1 + K, x_2 + K, \dots, x_n + K\}$ be a finite family of translates of K by the vectors x_1, x_2, \dots, x_n . We say that F is λ -disjoint if for every pair $i, j \in \{1, 2, \dots, n\}$ we have that the homothetic copies of K , $x_i + \lambda K$ and $x_j + \lambda K$, are disjoint. With this notation, two convex sets are 1-disjoint if they are disjoint.

We also say that F has a line transversal if there is a line intersecting simultaneously to all the members of F , and write $F \in T$. Also, we will say that $F \in T(k)$ if every k -membered subfamily of F has a line transversal or, in other words, has the property T .

As was discovered by H. Hadwiger in 1960 (see [3]), a 2-disjoint finite family of translates of the unit disc B with the $T(3)$ property have a line transversal. Later, in 1964, B. Grünbaum (see [2]) proved a stronger result: any $\sqrt{2}$ -disjoint finite family of translates of B with the $T(3)$ property has a line transversal. For a general convex body K it is known that 2-disjointness is sufficient to ensure the existence of a line transversal (see [2]). With respect to the property $T(4)$ the following is known: any $\frac{2\sqrt{2}}{\sqrt{3}}$ -disjoint finite family of translates of a convex body K has a line transversal (see [5]), and any $\frac{2}{\sqrt{3}}$ -disjoint finite family of translates of B has a line transversal (see [1]).

The main purpose of this paper is to give another proof that any $\sqrt{2}$ -disjoint finite family of translates of the unit disc with the $T(3)$ property has a line transversal. We also prove that any 3/2-disjoint finite family of translates of a square with the $T(4)$ property has a line transversal.

II. COVERING POINTS BY STRIPS

Before giving the proofs of the mentioned results, we shall see how the problem about line transversals to translates of a convex body can be transformed into a problem about minimum strips covering a finite set of points. For the disc we have the following: three unit discs have a line transversal if and only if the triangle with vertices at the centers of the circles has an altitude of length at most 2 (see Fig. 2).

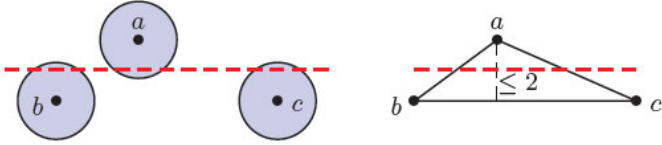


Fig. 2. Three discs with a common line transversal.

Equivalently, if three discs have a line transversal (as shown in Fig. 2) then there is a parallel strip of width 2 covering the centers, this strip is precisely the region between the line bc and its parallel through a .

For convex sets different of the disc we need to introduce the notion of relative width. Given a centrally symmetric convex set K , we define the relative width (or K -width) of a compact set X in direction $u \in \mathbb{S}^1$ as $w_{rel}(X, u) = \frac{w_u(X)}{w_u(\frac{1}{2}K)}$, where $w_u(X)$ denotes the Euclidean width in direction u , that is, the distance between the two lines supporting X in a direction parallel to u .

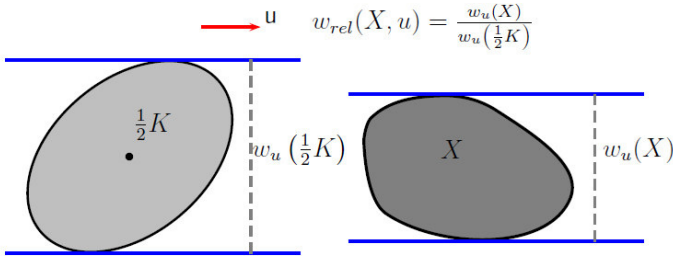


Fig. 3. The relative width.

It is not difficult to see that if three translates $K + b$, $K + a$, and $K + c$ have a common line transversal ℓ intersecting them in that order, then the line ℓ' parallel to bc and equidistant from the points a , b , c , also intersects the translates in the same order. To see this we proceed as follows: start to shrink (continuously and uniformly) the translates until they have no longer a line transversal intersecting them in that order. Consider the last moment they still having a transversal in the given order, then the transversal is tangent to each one of the shrunk translates $\alpha K + b$, $\alpha K + a$, and $\alpha K + c$ (see Fig. 4 and Fig. 5).

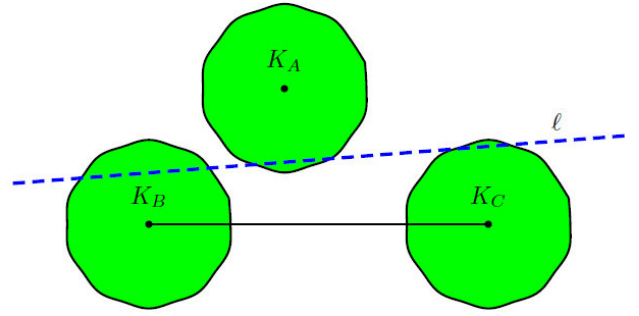


Fig. 4. Three translates of K with a common line transversal.

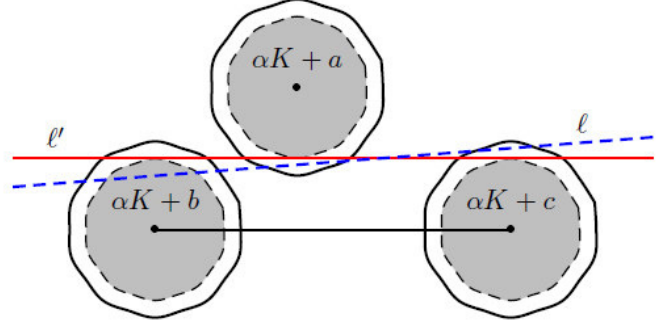


Fig. 5. There is a line transversal parallel to one side of the triangle of centers.

Again, we have that if three translates of a convex body K have a line transversal then there is a parallel strip, with K -width equal to 2 and covering the three centers. This strip is the region between two lines parallel to one side of the triangle of centers.

III. SUPER DISJOINT FAMILIES OF TRANSLATES OF THE DISC

Given any three non collinear points x , y , and z , we denote the distance of the segment xy as $|x, y|$, and the distance from x to the line yz as $|x, yz|$.

Theorem 1. Let F be a $\sqrt{2}$ -disjoint finite family of translates of the unit disc B with the $T(3)$ property. Then F has a line transversal.

Proof. We will first prove that any four translates of B have a line transversal. Consider an arbitrary subfamily $\{a + B, b + B, c + B, d + B\} \subseteq F$ and suppose that among the triangles with vertices in the set $\{a, b, c, d\}$, the triangle Δabc is the one with largest area. We then have that d must be contained in the triangle $\Delta a'b'c'$ homothetic to Δabc with ratio -2 and center of homothety at the centroid of Δabc (see Fig. 6). Without loss of generality we may assume that the altitude from a to bc has length at most 2. Here we distinguish two cases:

1. $d \in \text{conv}\{c', b, c, b'\}$. This case is trivial since the strip of width at most 2 bounded by the line $c'b'$ and the line bc covers the set $\{a, b, c, d\}$, which implies that $\{a + B, b + B, c + B, d + B\}$ has a common line transversal.

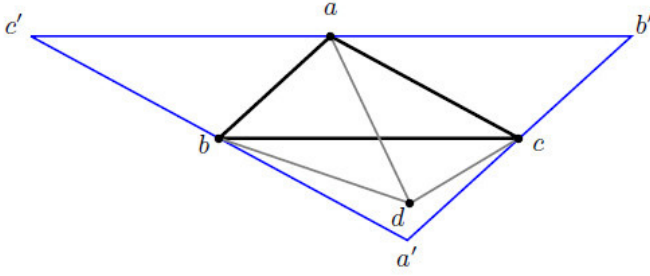


Fig. 6. The set of centers must be contained in the triangle $\Delta a'b'c'$.

2. $d \in \text{conv}\{b, a', c\}$. Since $|a, b|, |a, c|, |b, c| > 2\sqrt{2}$, and $|a, bc| \leq 2$ we have that $\angle bac > 90^\circ$. Now, since the triples $\{a, b, d\}$ and $\{a, c, d\}$ also have the $T(3)$ property, $\angle abd, \angle acd < 90^\circ$, $|b, d|, |a, d|, |c, d| > 2\sqrt{2}$, and at least one of the angles $\angle adb$ or $\angle adc$ is smaller than 90° , we have that either $\angle bad$ or $\angle dac$ is bigger than 90° . Assume, W.L.G., that $\angle dac > 90^\circ$, then in the triangle Δadc we have that $|a, dc| \leq 2$. Hence, the strip bounded by the line dc and its parallel through a has width less than 2 and contains also the point b .

Now, since the set $\{a, b, c, d\}$ is arbitrary we have that F has the property $T(4)$. Among all the quadrilaterals with vertices at the centers of the circles in F , we consider one such that its width is the minimal. Suppose such a quadrilateral is $abcd$ and the width is obtained by the distance between the line bc and its parallel through a . It is known that the projection of a over the line bc is in the interior of the segment bc (see for instance [4]), and moreover, we may apply a rescaling and suppose that the distance from a to bc is exactly equal to 2. Since all the sides in triangle Δabc are larger than $2\sqrt{2}$ and the altitude from a to bc is 2, we have that the other two altitudes of Δabc are larger than 2. It follows that the unique line transversal to $a + B$, $b + B$, and $c + B$ is the line ℓ parallel to bc through the midpoint of the altitude from a to bc . We have proved that any four translates of B have a line transversal, then if we consider any fourth translate $x + B$ from F , it must be intersected by ℓ . \square

IV. FAMILIES OF TRANSLATES OF A SQUARE

In this section we will consider families of translates of a unit square (with side of length 1) with the $T(4)$ property. We have the following result.

Theorem 2. Let F be a $\frac{3}{2}$ -disjoint finite family of translates of the unit square with the $T(4)$ property. Then F has a line transversal.

Proof. We denote the minimum of the K -widths of the quadrilaterals, with vertices in the set of centers, by $\lambda \leq 2$. If $\lambda < 2$ then replace every translate by a concentric homothetic copy of K with coefficient $\lambda/2$. Clearly, if the new family of

translates has the $T(4)$ property then the original family also has the $T(4)$ property. Hence it is enough to prove the theorem for such “tight” families in which exists a 4-tuple of translates such that the four centers are just covered by a parallel strip of K -width 2. In this case there are three translates among the four which have a common tangent line, say A , B , and C (intersected by the tangent line in this order), and such that A and C are separated from B , otherwise the 4-tuple of translates is not tight.

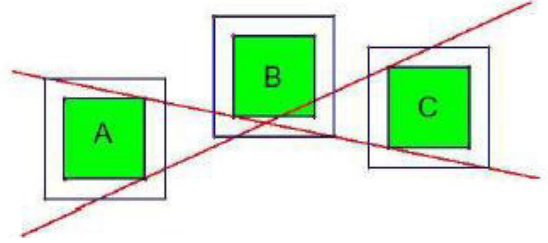


Fig. 7. If A and C are not separated from B then the 4-tuple of translates is not tight.

There are essentially two configurations for the three translates with respect to the tangent line, as shown in Fig.8:

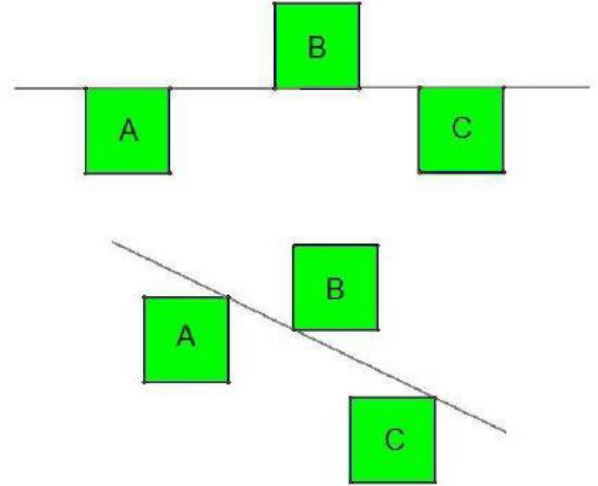


Fig. 8. The two possible configurations.

For the case when the tangent line is parallel to a side of the square is easy to see that there is not another line tangent to A , B , and C . For the case when the tangent line touches A , B , and C at a vertex we proceed as follows: we introduce a Cartesian system of coordinates such that the origin is at the point Y , as shown in Fig. 9. The line through Y , Q , and T is the x -axis and the line through P and S is the y -axis. Set $Y = (0, 0)$, and $P = (0, p)$ for a positive number p , then $S = (0, -1 + p)$. Since A and B are $\frac{3}{2}$ -disjoint then the distance between Y and Q is at least $\frac{1}{2}$. Suppose $Q = (\frac{1}{2}, 0)$, and $T = (\frac{3}{2}, 0)$. If $X = (x_0, y_0)$ is the intersection between the lines PQ and ST , we have that

$$y_0 = -2px_0 + p = \frac{2(1-p)x_0}{3} + p - 1,$$

then $x_0 = \frac{3}{2+4p}$ which implies that $y_0 = \frac{2p(p-1)}{2p+1}$.

Let ℓ be the line tangent to A , B , and C and suppose they share another common tangent m through the points S and T , then C is the reflected image of B about the point X . If $y_0 \leq \frac{1}{4}$ then the homothetic copies of B and C , concentric with them and by the factor $\frac{3}{2}$, are not disjoint. Solving the corresponding inequality we have that $y_0 \leq \frac{1}{4}$ if $p \in \left[\frac{5-\sqrt{33}}{8}, \frac{5+\sqrt{33}}{8}\right]$, that is, if the line TQ intersects the segment PS . Since the angles $\angle XQT$ and $\angle XTQ$ are decreasing if we increase the distance between Y and Q , we have that if the line TQ intersects the segment PS then the translate C cannot touch m , otherwise B and C would not be $\frac{3}{2}$ -disjoint.

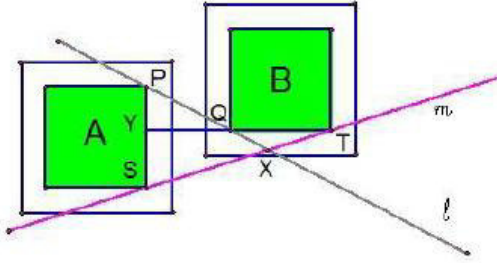


Fig. 9. The point X is contained in the copy homothetic to B by the factor $3/2$.

Now, if the line TQ does not intersect the segment PS then it is easy to see that no any other common tangent line to A and B can intersect to C . We have proved that A , B , and C have a

unique common tangent line ℓ , and because every four translates of the square have a common transversal line, we conclude that ℓ intersects all the members of F . \square

V. FINAL COMMENTS

We suspect that the factor $3/2$ in Theorem 2 could be reduced, however, we were not able to improve it with the technique used in this work. It would be very interesting to find the minimum factor possible for families of translates of the square. We hope to be successful in this task in a near future.

ACKNOWLEDGMENT

We thank to Aladar Heppes by the interesting and fruitful talks about line transversals.

REFERENCES

- [1] K. Bezdek, T. Bisztriczky, B. CsikVos, and A. Heppes, "On the transversal Helly numbers of disjoint and overlapping disks," Arch. Math. 87, pp. 86-96, 2006.
- [2] B. Grünbaum, "Common transversals for families of sets," J. London Math. Soc. 35, pp. 408-416, 1960.
- [3] H. Hadwiger, "Kombinatorische Geometrie in der Ebene," Monographies de l'Enseignement Mathématique, No. 2., Institut de Mathématiques, Université, Genève, 1960.
- [4] A. Heppes, "Transversals in superdisjoint $T(3)$ -families of translates," Discrete Comput. Geom. 45, pp. 321-328, 2011.
- [5] A. Heppes, and J. Jerónimo-Castro, " $T(4)$ -families of φ -disjoint ovals," submitted,

USA-Mexico border issues: trucks flow

María Guadalupe Barrón-Evaristo^{#1}, Eric Moreno-Quintero^{*2}

[#] *Facultad de Ingeniería, Universidad Autónoma de Querétaro
Centro Universitario, Cerro de las Campanas s/n C.P. 76010, Santiago de Querétaro, Qro., México*

¹ gbaevaristo@gmail.com

^{*} *Instituto Mexicano del Transporte.
Carretera Querétaro- Galindo km 12, C.P. 76703, Sanfandila, Pedro Escobedo, Qro., México*

² emoreno@imt.mx

Abstract— This paper explores the problems that truck transport faces up at the USA-Mexico border. The economic impact and factors involved in the international competitiveness are analyzed using some operations research methods. As a specific focus, a methodology to deal with the problem is developed on the basis of simulation techniques.

Keywords— USA-Mexico border, trucks, international transport, optimization, simulation.

I. INTRODUCTION

“The U.S.-Mexico border region is one of the busiest trade centers in the world and a strategic economic asset for both Mexico and the United States.” [1]

The purpose of this paper is to make a review of the process of trucks' entries and exits at the Mexico-US border. This paper is organized in three parts; the first one is an introduction, it talks about border issues, then, a review on the usual methodology to assess the economic impact generated by the problems when crossing the border, and the last one is about adequate software to model the transborder flows and some techniques from operations research.

Trade between Mexico and United States is an important economic activity, since this country is our main commercial associate. Border ports are key elements for trading, in these ports cross large volumes of merchandise imports and exports. The huge amount of merchandises that cross there share space with dozens of people, cars, buses, trucks and other vehicles that cross the north border every day producing traffic jam and inefficiencies, so involving economic cost and long waiting times that affect users and competitiveness of the national economy..

The Border Legislative Conference states that to keep economic growth, the USA-Mexico transborder trade should be more efficient in transit and best prepared to face with security issues; and it should reduce the waiting times and commerce costs with Mexico. It also states that the border region economic development is essential to maintain the competitive advantage for both U.S.A and Mexico economies, and also notes that the cost, the slow traffic and the inefficiency will force consumers to look for other more competitive markets.

In [2] is pointed out the necessity to make improvements to the process and the infrastructure with the objective to get a strategic access to the Northern America markets and around the world, and recover the competitive dynamism. Besides, significant improvements in the entry ports and the commercial process flow are suggested.

II. ECONOMIC IMPACT

There are some investigations related to this topic, most of them are focused on the economic impact produced by waiting times when crossing the border.

In [3] the authors analyzed difficulties and chances when exporting wooden products from Virginia to Mexico and Dominican Republic. Smith states that in wooden products, Mexican hardwood lumber manufacturers are less competitive in these markets in large part because of inefficiencies in the distribution system. The authors claim that USA-Mexico border makes Mexico a strategic mate in the economic American growth but states that Mexico has inefficient transportation services. Some problems related to transportation involve the availability of trucks, the high costs of transportation, delays in delivering the products, and the lack of experience in handling of shippings.

In [4], Pesut claims the transport importance as a competitiveness indicator. Besides the necessity of a new methodology showing the technological, commercial and regulatory changes.

In [5], Song and Na focused on International transport logistics in Asia, they claim that in order to get a better development in international transport is necessary a low cost in transporting merchandise and efficient and reliable delivery times.

The Principal Component Analysis methodology and the Factorial Correspondence Analysis are used in [6] to evaluate the International transport competitiveness of 29 countries among them Mexico and USA. The authors claim this methodology has been used by The Global Competitiveness Report of the World Economic Forum and by IMD World Competitiveness Yearbook, to calculate the competitiveness index.

The Factorial Correspondence Analysis was developed by the french Benzacri in 1987 [6], by considering all variables in a simultaneous way, this method has four stages:

- Test of reliability (it shows the validity of the variables).
- Calculation of a matrix to express the joint change of the variables (it uses the process of standardization of varimax, to determine the number of factors).
- Estimation of the graphical scores (it shows the interrelation of the cases with the variables).
- Determination of the competitiveness index. Methods of statistical regression are used.

With this method [6] got as a result for road transportation, the following factors:

- Factor 1. Cost and distance. Export distances (km), Export costs (USD), Import distances (km).
- Factor 2. Execution period. Term of execution exportation (days), term of execution import (days).
- Factor 3. Quality of the transport. Commerce of goods (% of the GDP), quality of the port infrastructure, quality of activities related to the transport.
- Factor 4. Competitiveness. Goods moved by road (million ton-km).
- Factor 5. Considers only the rail transport.
- Factor 6. Indexes for transportation services (export services, balance of payments and imports services).

In this analysis Mexico is located in 26th place with a competitiveness index of 3.1 in international transport.

III. METHODOLOGIES AND OPERATION RESEARCH

In 2004, the Mexican Institute of Transport participated in the implementation of a platform to simulate the operation of border ports [7]. This platform, is called SIM_Fronteras, had a high cost and a dependence of the technology supplier which has limited the update of operational changes in development ports.

In [8] the authors used the software Global Trade Analysis Project (GTAP) and IMPLAN to analyze the economic Impact of waiting times on border crossings of USA (USA-Mexico and USA –Canada). The used variables were: wait times average, average number of inspections and the average time for inspection. The scheme in Fig. 1 [8] shows the used methodology.

Also, the author makes use the simulation to validate its results. It concludes that a more sophisticated statistical analysis is necessary to quantify the advantages and disadvantages on the border of the USA.

In [9] the focus is on the road infrastructure and its impact on accessibility and industrial productivity on the USA–Mexico border. It uses three models of the network of transport, the first model is about accessibility based on the infrastructure for ground transportation, the second model is about the national road network in Mexico to estimate the optimal routes that minimize the time, and in the third one develops the methodology to analyze the advantages of the infrastructure of highways in Mexico. It conclude in that the investment in infrastructure has the potential to improve the international accessibility, and that the elimination of thebottleneck will occur across improvements in the frontier ways, avoiding high economic costs. In addition to the simplification of the inspection process between both countries.

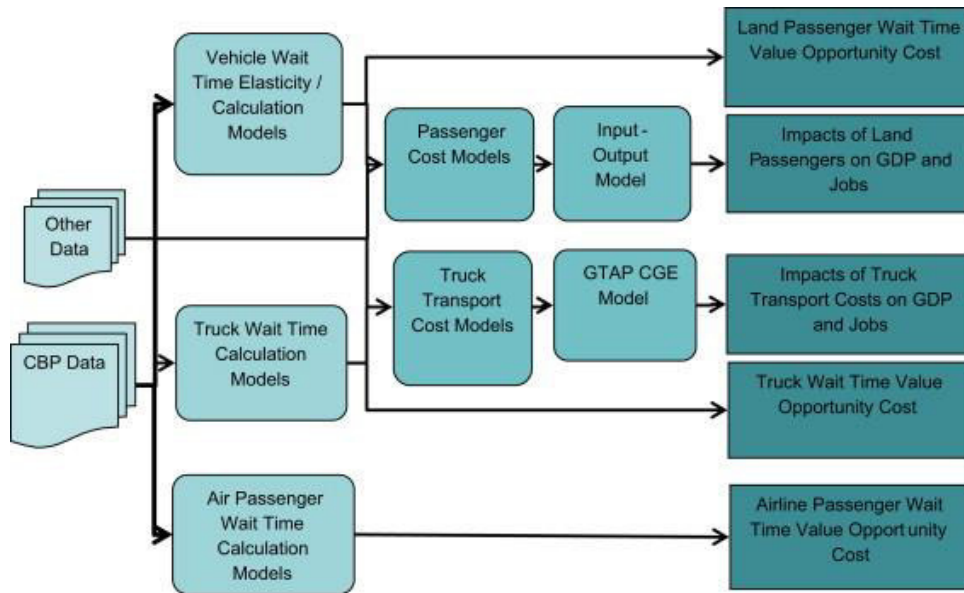


Fig. 1. Schematic of the Methodology.

In [10] the authors design a chain of intermodal transport for In [10] the authors show a design of a chain of intermodal transport with optimal cost and delivery time of products imported from the United States, for the particular case of a company of car parts that operates in the Toluca industrial area in the state of Mexico. An optimization bi-criterion programming model with mixed integer variables and Lagrangean relaxation is used. This paper makes a literature review, describing some methods as discrete simulation, stochastic dynamic programming, Integer Linear Programming, design of an intermodal network transport, some special algorithms and a graphical interactive software for the analysis of the frontier crossings.

In [11] proposes a system dynamics model to describe entry and exit transport flows at USA-Mexico border. With this model it is analyzed the automotive supply chain. It focus in the uncertainty caused by delays and disruptions at border. It proposes two equations that explain the system Mexican and the USA subsystem. The methodology used is summed up in the following diagram Fig. 2 [11]:

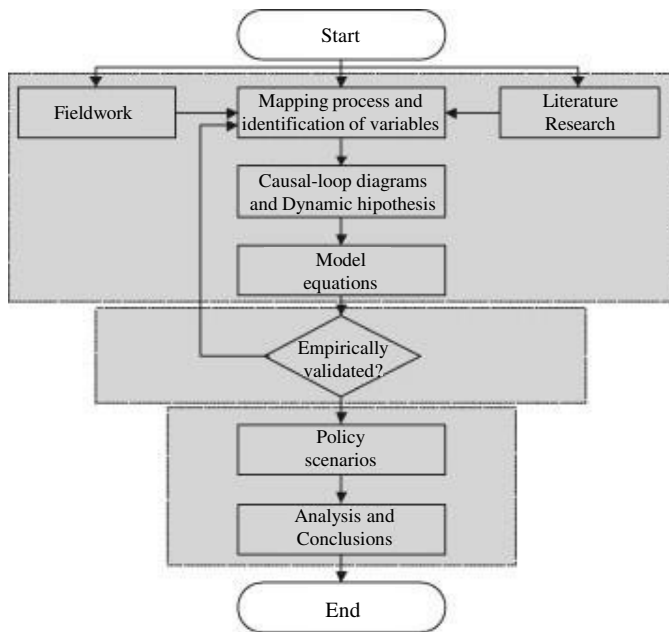


Fig. 2. Flowchart of the proposed methodology.

The models mentioned above propose workable solutions validated with the use of simulation.

IV. CONCLUSION

There are much research on border USA-Mexico issues, which identify the cost and time as main variables in the merchandise transfer. Most of the studies are focused on the United States problems, so there is a broad field to work on the difficulties and deficiencies in Mexican transborder ports.

This paper is the antecedent of a simulation and optimization model on truck flows in border ports with the objective to assess improvements in the Mexico management policies. The variables to consider are:

- Percentage share of the flows by type as motorcars, buses, trucks and others (motorcycles, pickups, passengers' vans, etc.)
- Average estimations in the process of arrivals of vehicles.
- Estimation of crossing times for transport types.
- Average size of queues.
- Maximum size of queues.
- Average stay time in queueing.
- Number of vehicles with zero waiting time in queueing.

The diagram below shows the methodology to follow Fig. 3:

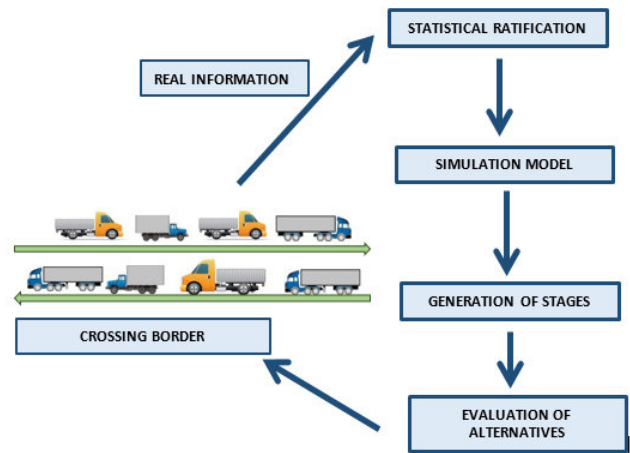


Fig. 3. Proposed methodology.

Typical data on truck crossing as those moving on the International Commerce Bridge in Nuevo Laredo, Mexico is considered. Fig. 4 shows an example of this data for the period June 9-22, 2014 where the typical weekly distribution of labour days and weekend days is easily observed.

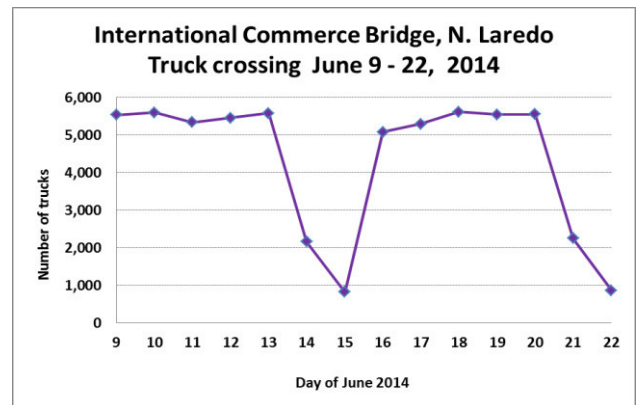


Fig. 4. Truck crossing data from International Commerce Bridge, Nuevo Laredo, Mexico. (Source, Mexican Secretariat of Transport).

ACKNOWLEDGMENT

This work was supported by the National Council for Science and Technology, CONACYT.

REFERENCES

- [1] (2014) The Border Legislative Conference website.[Online]. Available: <http://www.borderlegislators.org/>
- [2] F. Contreras, F. García, and O. Rosales, "El crecimiento económico de Nuevo Laredo como eje del desarrollo de la frontera norte de México (tercera y última parte)", *CienciaUAT*, vol. 2, no 4, pp 51-55, 2014.
- [3] R. Smith, C. Miller, and O. Parhizka, "Improving the international competitiveness of the forest products industry through proved transportation methods", Virginia: USA, Virginia Tech, Center of Forest Products Marketing and Management. Department of Wood Science and Forest Products, Prepared for the US Department of Agriculture, Federal-State Marketing Improvement Program, pp 129, 2008.
- [4] M. Pesut, "Global supply chains, transport and competitiveness", Proceedings of the Joint Trade and Transport Conference on the Impact of Globalization on Transport, Logistics and Trade: The UNECE Work, February 2009.
- [5] J. Song, and H. Na, "A study on the intercontinental transportation competitiveness enhancement plan between Northeast Asia and Europe using the Trans-Siberian railway" *IACSIT International Journal of Engineering and Technology*, vol. 4, no 2, pp 208-212, 2012.
- [6] A. Zamora, I. América, O. Pedraza, "El transporte internacional como factor de competitividad en el comercio exterior", *Journal of Economics, Finance and Administrative Science*, vol. 18, no. 35, pp 108-118, 2013.
- [7] A. Herrera, A. Moreno, J. Martínez, and J. Acha, "Modelo conceptual de un puerto fronterizo y plataforma para simular su operación", *Instituto Mexicano del transporte*, Publicación Técnica no. 408, 2014.
- [8] B. Roberts, A. Rose, N. Heatwole, D. Wei, M. Avetisyan, O. Chan, and I. Maya, "The impact on the US economy of changes in wait times at ports of entry", *Transport Policy*, vol. 35, pp 162-175, 2014.
- [9] R. Duran, "Infrastructure policy in the USA–Mexico border: Evaluation and policy perspectives", *Research in Transportation Economics*, vol. 46, pp 70-102, 2014.
- [10] C. Argueta, M. López, M. Arrollo, and J. Iniestra, "Un enfoque multicriterio para el diseño de una red para el transporte de embarques internacionales", *Contaduría y Administración*, vol. 59, no 4, pp 193-221, 2014.
- [11] M. Cedillo, C. Sánchez, S. Vadali, J. Villa, and M. Menezes, "Supply chain dynamics and the "cross-border effect": The US–Mexican border's case" *Computers & Industrial Engineering*, vol. 72, pp 261-273, 2014.

High performance of a microfluidic biofuel cell alcohol dehydrogenase/laccase for ethanol.

J. Galindo-de-la-Rosa,¹ N. Talamantes-Morales,¹ N. Arjona,² E. Ortiz-Ortega,¹ Ricardo A. Escalona-Villalpando,³

J. Ledesma-García,¹ L.G. Arriaga,⁴ and M. Guerra-Balcázar.^{1*}

¹*Facultad de Ingeniería, División de Investigación y Posgrado, Universidad Autónoma de Querétaro, Centro Universitario Cerro de las Campanas, Querétaro, Qro., C.P. 76010, México.*

²*Centro de Investigación y Desarrollo Tecnológico en Electroquímica, Unidad Tijuana, Tijuana, B.C., C.P. 22444, México*

³*Facultad de Química, Universidad Autónoma de Querétaro, Centro Universitario Cerro de las Campanas, Querétaro, Qro., C.P. 76010, México.*

⁴*Centro de Investigación y Desarrollo Tecnológico en Electroquímica, Pedro Escobedo, Qro., C.P. 76703, México.*

*E-mail: minbalca@yahoo.com.mx, Phone: +52 (442) 1921200 ext. 65421, Fax: +52 (442) 1921200 ext. 6007

Abstract—Use of biocatalysts such as enzymes for the conversion energy is an alternative to the design of more efficient, biocompatible and stable biofuel cells. In this paper the enzyme alcohol dehydrogenase was used in a bioanode array immobilized through a covalent binding and laccase by adsorption immobilized and tested for the first time in a hybrid membraneless microfluidic fuel cell showing a voltage of 0.94 V and a power density of 1.2 mW cm⁻². The stability was tested by chronoamperometry which showed high capability to provide a constant current density.

Keywords: Biofuel cell, alcohol dehydrogenase, laccase, ethanol.

I. INTRODUCTION

Biofuel cells are devices for the production of electrical energy, inspired in chemical reactions by biological catalysts. [1] Currently the use of enzymatic biofuel this being an area of opportunity as, presents major advantages over commonly used inorganic electrocatalysts, derived enzymes have excellent properties relating to their activity, selectivity and specificity towards molecules or a fuel. Selection of enzymes for manufacturing the bioelectrode is based on the choice of substrate used to generate power.[2] From this perspective, the substrates of alcohol, primarily methanol and ethanol have received increasing attention for the development of cells of chemical fuel. The advantages of using alcohols as fuels and their aqueous solubility are widely available, since these compounds can be easily produced. [3]

Ethanol -among alcohols used as fuels- has been recognized as the most promising alcohol to be used in energy conversion area since it is less toxic and it has many unique physicochemical properties including high energy density (8.0 kWh⁻¹ kg⁻¹)[4,5]. Ethanol fuel cells have been of interest due

to the generation of sustainable energy that can be used for different applications [6, 7]. It also offers an attractive alternative fuel because it can be produced in large quantities from agricultural products, the main renewable biofuel from biomass fermentation [8].

However the ethanol cells currently reported are not stable and have a very low yield particularly enzymatic microfuel cells. Enzymes can catalyze reactions in different states, as individual molecules in solution and that immobilized on surface [9]. Using the method of immobilization by covalent binding provides an ideal environment for increased transport of ions and serves for design of most stable biofuel cells [10].

This paper presents the results obtained using electrodes with alcohol dehydrogenase immobilized by covalent union to the anode and laccase immobilized by adsorption to the cathode for microfluidic biofuel cell.

II. EXPERIMENTAL

A. Reagents

Methylene blue, alcohol dehydrogenase (EC 1.1.1.1 initial activity ≥ 300 units/mg protein from *Saccharomyces cerevisiae*), β -nicotinamideadenine dinucleotide sodium salt (NAD⁺) and tetrabutylammonium bromide (TBAB), laccase enzyme from *Trametes versicolor* (15 U/mg), glutaraldehyde solution 50%, sodium phosphate dibasic dihydrate (Na₂HPO₄·2H₂O), sodium phosphate monobasic monohydrate (NaH₂PO₄·H₂O), Nafion[®] (5% diluted in water), potassium hydroxide (88.7%.) were purchased from Sigma-Aldrich. The phosphate buffer was prepared with Na₂HPO₄·2H₂O and

$\text{NaH}_2\text{PO}_4 \cdot \text{H}_2\text{O}$ (pH 8.86, 0.1 M). Acetate buffer solution was prepared by using $\text{C}_2\text{H}_3\text{NaO}_2$ and $\text{C}_2\text{H}_4\text{O}_2$ (pH 5.0, 1M) from Sigma-Aldrich.

B. Anode preparation.

The bioanode consist in a 2.5×30 mm Toray porous paper electrode, placing 100 μL of 5:100 v/v% Nafion-water covering the total electrode area and dried with hot air. These electrodes were employed for methylene blue electro-polymerization through a Biologic VSP Potentiostat/Galvanostat by using cyclic voltammetry from -1 to 1 V vs. SCE for 15 cycles at 0.05 V s^{-1} scan rate. The electrolytic bath was composed by 0.05 M methylene. At the same time, an ink with the following components was prepared: for each mg of enzyme were added 5 μL of Nafion, 10 μL glutaraldehyde, 1000 μL of deionized water, 10 mg of NAD and 20 mg of TBAB. The ink was then sonicated for 20min and mixed by vortex for other 15min; 100 μL of this ink were taken and deposited on the electro-polymerized Toray electrodes and dried.

C. Cathode preparation.

The laccase biocathode was prepared using carbon nanofoam (2×0.3 cm, Marketech[®]) instead Toray as electrode. Carbon nanofoam was immersed for one hour in a solution composed by laccase (5 mg mL^{-1}), 0.1 M acetate buffer pH 5 and 1 v/v% glutaraldehyde. After that, nanofoam electrodes were added a dispersion of multi wall carbon nanotubes (2 mg mL^{-1}) in a ratio 1:1 v/v and allowed to dry at room temperature for 2 h before being used. The abiotic cathode was prepared using commercial Pd/C (20% E-TEK) as catalyst and carbon nanofoam as electrode. In this manner, 120 μL isopropyl alcohol and 14 μL Nafion were added per milligram of catalyst and mixed for 30 minutes. The catalytic ink was deposited on the carbon nanofoam through the spray technique until the electrode weight increase 1 mg.

D. Biofuel cell evaluation.

The details of fabrication procedure and dimensions of the microfluidic device have been previously reported [11]. Briefly, Poly-(methyl methacrylate) plates used as supporting plates were designed and patterned employing a CNC machining. A home-made Silastic elastomer film (Dow Corning, 200 μm) was used as gasketing and as channel structure. The hybrid microfluidic fuel cell performance tests were carried out injecting fuel (0.1 M ethanol) and a combination of dissolved oxygen (4 U. P. D., Praxair) and oxygen from air as oxidants within two aqueous streams that contain the phosphate buffer (pH 8.86) in the anodic side and acetate buffer (pH 5) in the cathodic side as supporting electrolytes (Figure.1). The flow rates were of 50 $\mu\text{L min}^{-1}$ in both streams.

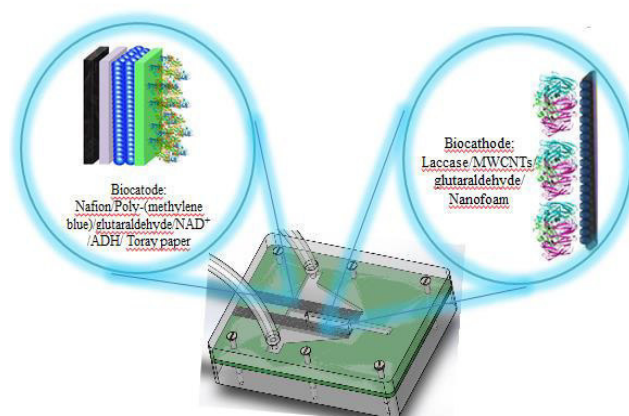


Figure. 1. Biofuel cell alcohol dehydrogenase/laccase.

III. RESULTS AND DISCUSSION

A. Electrochemical characterization.

The electrochemical response of anode array in phosphate buffer (pH=8.86) with and without ethanol at several concentrations is showed in Figure 1a. Without ethanol, the control voltammogram (dark gray line) showed no significant response of the electrode to the solution. Peaks of a redox reaction emerged with the presence of ethanol (Figure. 2) and where located at -0.7 and -0.74 V vs. Hg/HgSO_4 , these peaks correspond to NAD^+/NADH redox couple. The increase of ethanol concentration resulted in an increase of the current density of the NAD^+/NADH reactions due to a higher oxidation of the substrate by the enzyme which is reflected in a higher reduction of NAD^+ to NADH [12]; at 100 mM ethanol, ADH enzyme showed the highest current density as consequence of its good biocatalytic activity.

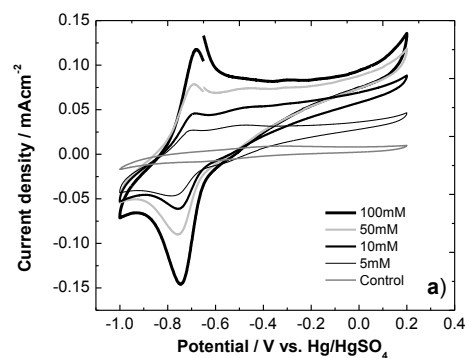


Figure. 2. Bioanode electrochemical evaluation at different concentrations of ethanol.

The results obtained for the microfluidic biofuel shown in Figure 3. For the case of biofuel MFC cell (laccase-based cathode) showed a voltage of 0.94 V and a current density of 3.06 mA cm⁻².

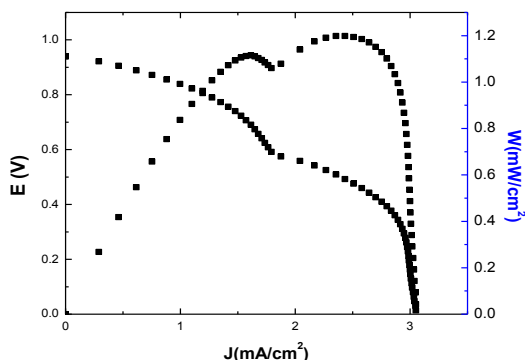


Figure 3. Polarization curve of the biofuel cell alcohol dehydrogenase/laccase.

Compared to the biofuel cell using the enzyme alcohol dehydrogenase in the anode currently reported (table 1) shows that there is an increase in the power generated by the cell of this work.

TABLE I. BIOFUEL CELL USING ALCOHOL DEHYDROGENASE AS ANODE FOR THE OXIDATION OF ETHANOL

Anode (anolyte)	Cathode (catholyte)	OCV (V)	μWcm^{-2}	Fuel Cell type	Reference
QH-ADH + glutaraldehyde + glassy carbon (EtOH .025M in acetate solution pH=6.0)	AOx-MP8 (EtOH .025M in hydrogen peroxide)	0.24	1.5	PEM	[13]
C cloth + poly-MG + CHIT + MWCNTs + ADH + NAD ⁺ (EtOH 0.475M in PBS pH=7.4)	Laccase onto carbon black XC-72 (gas diffusion electrode)	0.618	20	PEM	[3]
ADH+carbon KS6+NAD ⁺ +VK3+acetone+PEI (EtOH 160 μL in PBS pH 9)	Laccase+ABTS+ Super P@+Nafion (PBS at pH 5 saturated with O ₂)	0.6	90	MFC	[14]
Toray paper + poly-MB + Nafion+glutaraldehyde + ADH + NAD ⁺ (EtOH 0.1M in PBS pH=8.86)	Laccase+MWCT ₅ + glutaraldehyde (acetate buffer at pH 5 saturated with O ₂)	0.94	1200	MFC	This work

TBAB:tetrabutylammonium bromide; poly-MG: poly-methylene green; Poly-MB: poly-methylene ble;MWCT₅:carbonnanotubes; QH:quino-hemoprotein; CHIT: chitosan; VK3: 2-methyl-1,4-naphthoquinone; PEI:polyethylenimine;ABTS: diammonium salt; MFC: microfluidic fuel cell.

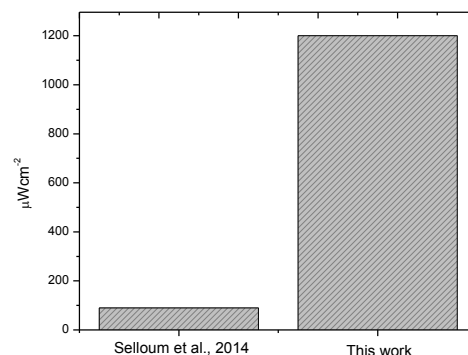


Figure 4.Comparison microfluidic biofuel cell.

The figure 4 shows the comparison of the power generated between the single microfluidic biofuel cell that uses the alcohol dehydrogenase and laccase enzymes reported to date and the biofuel cell developed in this work which presents a higher performance.

The stability tests of the microfluidic biofuel cell are shown in Figure 5 to Chronoamperometric test was performed in order to determine the capability to supply a constant current density over time; from this figure it was observed that the system can provide a current density of 3.6 mA cm⁻² over 12000 seconds time in which the experiment was carried out.

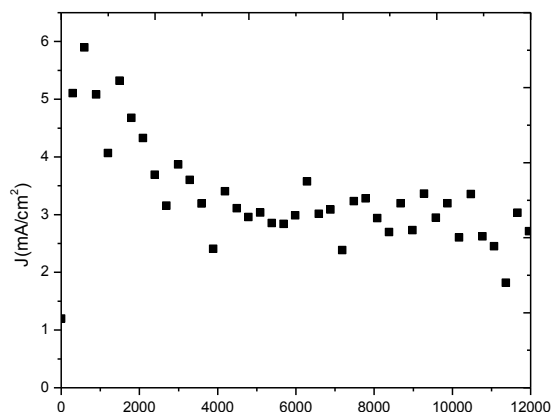


Figure 5. Chronoamperometric test for biofuel cell alcohol dehydrogenase/laccase.

IV. CONCLUSIONS

A microfluidic biofuel cell were constructed using two and three-dimensional electrodes and the flow-through electrode concept in order to increase the bio-electrocatalytic activity of alcohol dehydrogenase enzyme-based anodes. On the other hand, a covalent binding immobilization method based on Nafion, poly-(methylene blue), glutaraldehyde and NAD⁺ was used in order to enhance the durability of the biofuel cell. As result, were achieved the highest cell voltage (0.94 V) and cell performance (1.2 mW cm⁻²) to date reported. Furthermore, this device showed superior performance in terms of activity and .

ACKNOWLEDGMENT

The authors gratefully acknowledge for financial support through SEP-CONACYT-2012-01-179921

REFERENCES

- [1] P. Lamberg, S. Shleev, R. Ludwig, T. Arnebrant, T. Ruzgas. Performance of enzymatic fuel cell in cell culture. *Biosensors and Bioelectronics*, 55, 168-173, 2014.
- [2] Shelley D. Minteer, Bor Yann Liaw, Michael J. Cooney. Enzyme-based biofuel cells. *Current Opinion in Biotechnology* 18:1-7, 2007.
- [3] R.A. Rincon, C. Lau, H.R. Luckarift, K.E. Garcia, E. Adkins, G.R. Johnson, P. Atanassov. Enzymatic fuel cells: Integrating flow-trough anode and air-breathing cathode into a membrane-less biofuel cell design. *Biosens. Bioelectron.*, 27, 132-136, 2011.
- [4] R. Carrera-Cerritos, R. Fuentes-Ramírez, F.M. Cuevas-Muñiz, J. Ledesma-García, L.G. Arriaga. *Journal of Power Sources* 269, 370-378, 2014.
- [5] J.P. Pereira, D.S. Falcão, V.B. Oliveira, A.M.F.R. Pinto. *Journal of Power Sources* 256, 14-19, 2014.
- [6] Afilton de Souza Gomes, José Carlos Dutra Filho. *International Journal of Hydrogen Energy* 37, 6246-6252, 2012.
- [7] David M. Mackie, Sanchao Liu, Marcus Benyamin, Rahul Ganguli, James J. Sumner. *Journal of Power Sources* 232, 34-41, 2013.
- [8] Ermete Antolini. *Journal of Power Sources* 170, 1-12, 2007.
- [9] Sabina Topcagic, Shelley D. Minteer. *Electrochimica Acta* 51, 2168-2172, 2006.
- [10] Akers Nick L., Moore Christine M., Minteer Shelley D.. *Electrochimica Acta* 50, 2521-2525, 2005.
- [11] E. Ortiz-Ortega, M.-A. Goulet, J.W. Lee, M. Guerra-Balcázar, N. Arjona, E. Kjeang, J. Ledesma-García, L.G. Arriaga, *Lab Chip*, 14, 4596-4598, 2014.
- [12] S.D. Minteer, B.-Y. Liaw, M.J. Cooney, *Curr. Opin. Biotech.*, 18, 228-234, 2007.
- [13] Arunas Ramanavicius, Asta Kausaite, Almira Ramanaviciene. *Biosensors and Bioelectronics* 24, 761-766, 2008.
- [14] D. Selloum, S. Tingry, V. Techer, Renaud, C. Innocent, Zouaoui. *Journal of Power Sources* 269, 834-840, 2014.

Microwave assisted sol-gel synthesis and characterization of M-TiO₂ (M=Pt, Au) photocatalysts

R. Hernández^{1†}, S.M. Durón - Torres¹, K. Esquivel², C. Guzmán^{1,2‡}.

¹ UACQ – UAZ, CU Siglo XXI Edificio 6, Km 6 Carr. Zac – Gdl, La Escondida Zacatecas, Zac, C.P. 96160, México.

² Facultad de Ingeniería, Universidad Autónoma de Querétaro, Cerro de las Campanas, C.P. 76000, Santiago de Querétaro, Qro., México.

† rafita_bot@hotmail.com

‡ cgm1909@hotmail.com

Abstract—Pt-TiO₂ and Au-TiO₂ photocatalysts have been synthesized by a microwave assisted sol-gel method and characterized by means of X-ray diffraction techniques (XRD) and UV-vis diffuse reflectance spectroscopy. Particle sizes have been determined by means of Scherrer equation. Depending on the weight percentage of dopant, some changes in the band gap energy can be observed.

Keywords—Titanium dioxide, photocatalysis, Pt-TiO₂, Au-TiO₂, X-ray diffraction.

I. INTRODUCTION

Titanium dioxide (TiO₂) has been widely used and investigated due to the stability of its chemical structure, biocompatibility and its physic, optic and electric properties. Its photocatalytic properties have been utilized in many environmental application to remove pollutants in water and air. The main feature of the photocatalytic process is that it breaks the complex organic molecules into simple molecules such as carbon dioxide and water, this process has been used for a variety of applications such as decomposition of organic pollutants [1].

TiO₂ exists as three different polymorphs: anatase, rutile and brookite. The most stable form of TiO₂ is rutile. Anatase form has a crystalline structure corresponding to a tetragonal system and is used mostly in photocatalytic applications due to its photocatalytic activity under UV radiation. Rutile form of TiO₂ has a tetragonal structure and brookite an ortorombic structure [2].

Typically, titanium dioxide is an n-type semiconductor. The energy gap is 3.2 eV for anatase, 3.0 eV for rutile and 3.2 eV for brookite. Generally, anatase form of TiO₂ is desired owing to its higher photoactivity, high superficial area and low toxicity. Due to its high photoinduced reduction, anatase form is a better photocatalytic material for degradation of organic pollutants in both water and air [3].

The application of TiO₂ is limited due to its low photoactivity under visible light. Therefore, attempts to extend

its photoactivity to the visible region have been made by substitution of Ti⁴⁺ on the crystalline structure for metallic ions such as Fe, Ni, Co, Ag, Au, Pt, etc [4]–[8].

Sol-gel synthesis technique has been widely used for catalysts development, such as TiO₂ nanopouders. In comparison to traditional techniques, it offers many advantages. For instance, in supported metals catalysis, the active metal and support can be prepared in a single step. This allows an economy in the catalyst preparation [9].

In the present paper, we report the synthesis and characterization of Pt-TiO₂ and Au-TiO₂ catalyst prepared by the microwave assisted sol-gel technique.

II. EXPERIMENTAL

The synthesis of the TiO₂ catalyst was carried out by dissolving the titanium precursor (titanium isopropoxide) in an organic solvent (isopropanol, 99.9%), the titanium solution was magnetically stirred for 20 min under nitrogen atmosphere. The hydrolysis process was then performed by adding water into the precursor/solvent solution and was magnetically stirred for 1 h in a dark box. For the Pt-modified TiO₂ samples, the platinum precursor was H₂Pt(NO₂)₂SO₄, and for the Au-modified TiO₂ samples, the precursor was NaAuCl₄•2H₂O. These precursors were added by dissolving them into the water used for the hydrolysis process in different weight percentage (0.01, 0.05, 0.1, 0.5, 1, and 5 wt. %). The obtained sol was transferred into teflon vessels and placed on a microwave reaction system. The heating procedures were carried for 30 min at 220 °C. The obtained product was filtered and dried at room temperature for 12 h. A calcination process was carried out at 450 °C for 3 h to promote the anatase form of TiO₂.

III. PHOTOCATALYST CHARACTERIZATION

Elemental analysis was performed by Energy Dispersive X-ray Spectroscopy (EDS) (EDS Oxford Inca X-Sight coupled to a MT 1000, Hitachi). Particle size was determined using Scherrer equation [10]. Bandgap energy (E_{bg}) values

were determined from diffuse reflectance measurements (Cary 5000 UV-Vis-NIR Varian spectrophotometer) by applying Kubelka-Munk [11] function and Tauc's graphics.

IV. RESULTS AND DISCUSSION

A. X-ray diffraction (XRD)

X-ray diffractions patterns were recorded to study the formation of TiO_2 crystalline species. The diffraction peaks detected after the calcination process indicates the presence of the crystalline anatase phase and no presence of rutile phase was observed. For the Pt- TiO_2 samples (Fig 1(a)), the peaks detected in 2θ (39.4° , 45.9° , 67°) indicates the presence of particles of metallic platinum. For the Au- TiO_2 samples (Fig 1(b)), the peaks detected in 2θ (38° , 44.2° , 64.4° , 77.2°) indicates the presence of particles of metallic gold. As can be seen from the XRD patterns crystallinity of the photocatalyst decreased on platinum and gold doping.

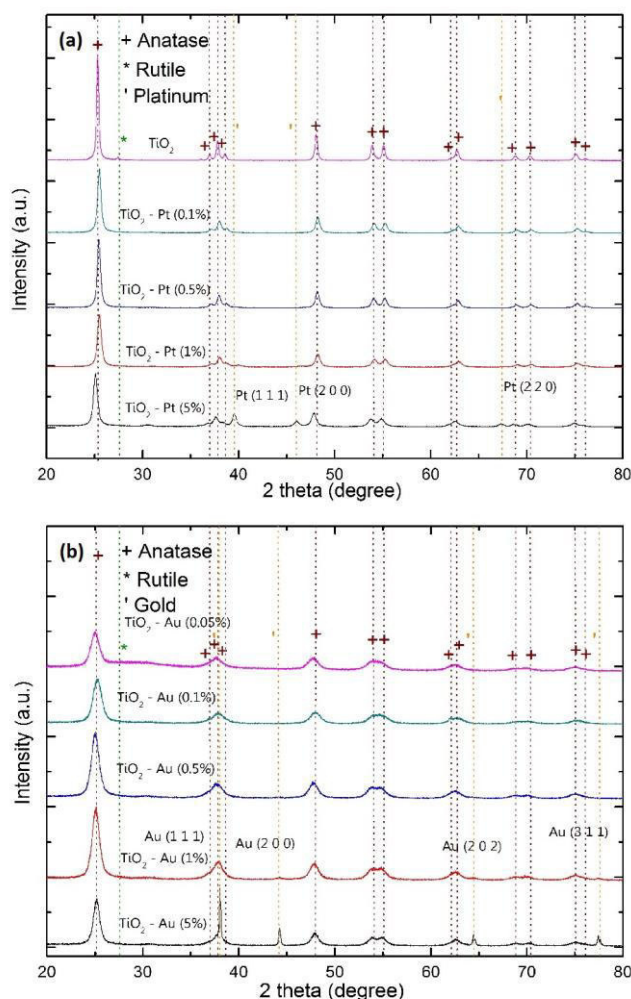


Fig. 1. XRD diffraction patterns of synthesized TiO_2 , (a) Pt- TiO_2 , (b) Au- TiO_2 .

TABLE I. CRYSTALLITE SIZES

Photocatalyst	Crystallite sizes (nm)	Crystallite sizes (nm)	Photocatalyst
$\text{TiO}_2 - \text{Au}$ (5%)	4.74	3.71	$\text{TiO}_2 - \text{Pt}$ (5%)
$\text{TiO}_2 - \text{Au}$ (1%)	4.10	11.2	$\text{TiO}_2 - \text{Pt}$ (1%)
$\text{TiO}_2 - \text{Au}$ (0.5%)	3.97	10.8	$\text{TiO}_2 - \text{Pt}$ (0.5%)
$\text{TiO}_2 - \text{Au}$ (0.1%)	3.59	10.7	$\text{TiO}_2 - \text{Pt}$ (0.1%)
$\text{TiO}_2 - \text{Au}$ (0.05%)	3.17	-	-

The crystallite sizes were calculated by the Scherrer equation and are compiled in Table 1. The Au-loaded samples have a crystal size between 4.74 nm for 5 wt. % of gold and 3.17 nm for 0.05 wt. % of gold. The Pt-loaded samples have sizes between 3.17 nm and 10.7 nm for 5 wt. % and 0.1 wt. % of platinum respectively.

B. Band gap measurements

UV-Vis DSR technique was used to study the influence of metal load and type. The Tauc's graphics showed in Fig. 2 and Fig. 3 for Pt- TiO_2 and Au- TiO_2 respectively are utilized to estimate the band gap energies by means of Kubelka-Munk method.

The band gap energies estimated are listed in Table 2. The band gap decreases according to the metal load; it shows that at higher metal load (5%) the band gap changes from 3.2 eV (pure TiO_2) to 2.98 eV and 3.04 eV for the samples loaded with gold and platinum respectively.

For the Pt- TiO_2 sample, the band gap varies from 3.04 eV (5 wt. %) to 3.2 eV (0.1 wt. %), the same behavior is found on the Au loaded samples, with a band gap energy variation from 2.98 eV (5 wt. %) to 3.21 eV (0.01 wt. %). It is interesting to note that the band gap energies increase on metal doping for both platinum and gold.

TABLE II. BAND GAP ENERGIES

Photocatalyst	Band gap (eV)	Band gap (eV)	Photocatalyst
$\text{TiO}_2 - \text{Au}$ (5%)	2.98	2.87	$\text{TiO}_2 - \text{Pt}$ (5%)
$\text{TiO}_2 - \text{Au}$ (1%)	3.05	3.09	$\text{TiO}_2 - \text{Pt}$ (1%)
$\text{TiO}_2 - \text{Au}$ (0.5%)	3.23	3.05	$\text{TiO}_2 - \text{Pt}$ (0.5%)
$\text{TiO}_2 - \text{Au}$ (0.1%)	3.24	3.15	$\text{TiO}_2 - \text{Pt}$ (0.1%)
$\text{TiO}_2 - \text{Au}$ (0.05%)	3.19	-	-

V. CONCLUSIONS

Microwave-assisted synthesis methodology can be applied for the preparation of TiO₂-base photocatalysts and modify its properties using a dopant metal such as Au and Pt. With this metals is possible to observe a change in the band gap energy which can be related to the metal load in the photocatalyst.

ACKNOWLEDGMENT

The authors thank to the CONACyT for the masters scholarship, and to the Zacatecas University.

REFERENCES

- [1] D. P. Macwan, P. N. Dave, and S. Chaturvedi, "A review on nano-TiO₂ sol-gel type syntheses and its applications," *J. Mater. Sci.*, vol. 46, no. 11, pp. 3669–3686, Jun. 2011.
- [2] M. Pelaez, N. T. Nolan, S. C. Pillai, M. K. Seery, P. Falaras, A. G. Kontos, P. S. M. Dunlop, J. W. J. Hamilton, J. A. Byrne, K. O'Shea, M. H. Entezari, and D. D. Dionysiou, "A review on the visible light active titanium dioxide photocatalysts for environmental applications," *Appl. Catal. B Environ.*, vol. 125, pp. 331–349, agosto 2012.
- [3] K. Esquivel, R. Nava, A. Zamudio-Méndez, M. V. González, O. E. Jaime-Acuña, L. Escobar-Alarcón, J. M. Peralta-Hernández, B. Pawelec, and J. L. G. Fierro, "Microwave-assisted synthesis of (S)Fe/TiO₂ systems: Effects of synthesis conditions and dopant concentration on photoactivity," *Appl. Catal. B Environ.*, vol. 140–141, pp. 213–224, agosto 2013.
- [4] Alamgir, W. Khan, S. Ahmad, M. Mehedi Hassan, and A. H. Naqvi, "Structural phase analysis, band gap tuning and fluorescence properties of Co doped TiO₂ nanoparticles," *Opt. Mater.*, vol. 38, pp. 278–285, diciembre 2014.
- [5] Y. Kobayashi, Y. Ishii, H. Yamane, K. Watanabe, H. Koda, H. Kunigami, and H. Kunigami, "Fabrication of TiO₂/Pt core-shell particles by electroless metal plating," *Colloids Surf. Physicochem. Eng. Asp.*, vol. 448, pp. 88–92, abril 2014.
- [6] X. F. Lei, X. X. Xue, and H. Yang, "Preparation and characterization of Ag-doped TiO₂ nanomaterials and their photocatalytic reduction of Cr(VI) under visible light," *Appl. Surf. Sci.*, vol. 321, pp. 396–403, diciembre 2014.
- [7] Q. Liu, D. Ding, C. Ning, and X. Wang, "Black Ni-doped TiO₂ photoanodes for high-efficiency photoelectrochemical water-splitting," *Int. J. Hydrog. Energy*, vol. 40, no. 5, pp. 2107–2114, Feb. 2015.
- [8] H. Park, Y. Park, W. Kim, and W. Choi, "Surface modification of TiO₂ photocatalyst for environmental applications," *J. Photochem. Photobiol. C Photochem. Rev.*, vol. 15, pp. 1–20, Jun. 2013.
- [9] E. Sánchez, T. López, R. Gómez, Bokhimi, A. Morales, and O. Novaro, "Synthesis and Characterization of Sol-Gel Pt/TiO₂Catalyst," *J. Solid State Chem.*, vol. 122, no. 2, pp. 309–314, Mar. 1996.
- [10] A. L. Patterson, "The Scherrer Formula for X-Ray Particle Size Determination," *Phys. Rev.*, vol. 56, no. 10, pp. 978–982, Nov. 1939.
- [11] A. Escobedo Morales, E. Sánchez Mora, and U. Pal, "Use of diffuse reflectance spectroscopy for optical characterization of un-supported nanostructures," *Rev. Mex. Fis. Suppl.*, vol. 53, no. 5, pp. 18–22, Jan. 2007.

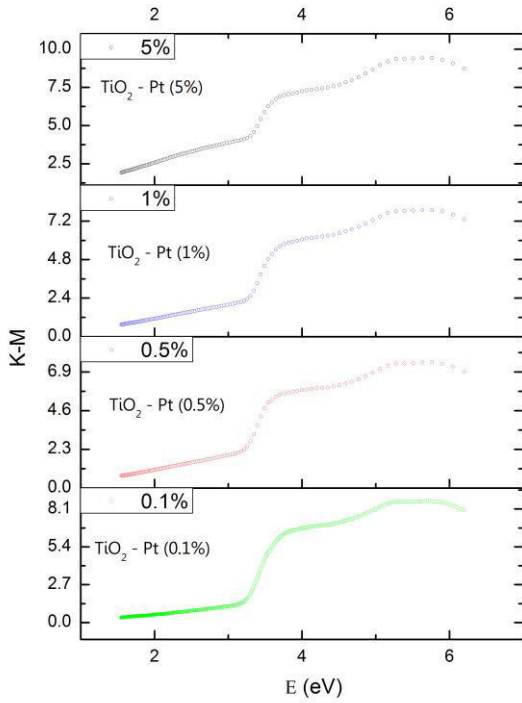


Fig. 2. Tauc's graphics for Pt-TiO₂.

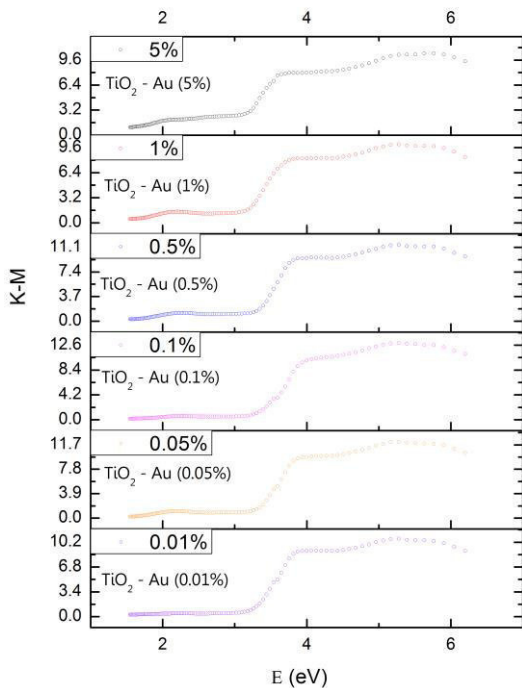


Fig. 3. Tauc's graphics for Au-TiO₂.

Synthesis and characterization of AlGaSb ternary compounds

A. Méndez-López^{*1}, Y.J. Acosta-Silva², A.E. Sanchez-Robles³, A.D Linares-Ojeda³, R. Hernandez-Tovar³

¹ *Sección de Electrónica del Estado Solido (SEES), Depto. de Ingeniería Eléctrica, Centro de Investigación y de Estudios Avanzados del Instituto Politécnico Nacional, Avenue IPN No. 2508, 07360 Mexico City, DF, Mexico.*

¹ amendez@cinvestav.mx

² *Depto. de Física, Centro de Investigación y de Estudios Avanzados del Instituto Politécnico Nacional, Avenue IPN No. 2508, 07360 Mexico City, DF, Mexico.*

² yuliacoss@gmail.com

³ *Ingeniería Telemática, Unidad Profesional Interdisciplinaria en Ingeniería y Tecnologías Avanzadas del Instituto Politécnico Nacional, Avenue IPN No. 2580, 07360 Mexico City, DF, Mexico.*

Abstract— A lattice-matched $\text{Al}_x\text{Ga}_{1-x}\text{Sb}$ ternary solid solutions were grown to the GaSb (001) substrate with composition in the range $0.05 \leq x \leq 0.2$ by liquid phase epitaxy. High resolution X-ray diffraction and Raman scattering techniques were applied to characterize $\text{Al}_x\text{Ga}_{1-x}\text{Sb}$ alloys. The out of plane lattice parameter as a function of Aluminum content is higher than the corresponding bulk lattice parameter of $\text{Al}_x\text{Ga}_{1-x}\text{Sb}$ layers obtained with Vegard's law. These results show that some of the layers are more strained than others. Two peaks are observed in their Raman spectra over this composition range. The assignment of the observed modes to GaSb-like modes is discussed.

Keywords—AlGaSb; GaSb; Thin Film; Liquid phase epitaxy; Ternary compounds;

I. INTRODUCTION

Recently, the $\text{Al}_x\text{Ga}_{1-x}\text{Sb}$ alloy has attracted much interest as a constituent of the InAs-(Ga,Al)Sb system for its possible applications in bandstructure engineering. It is known that in the type II InAs-GaSb heterostructure the top of the GaSb valence band lies higher in energy than the bottom of the InAs conduction band, giving rise to the coexistence of electrons and holes separated at the interfaces [1]. The bandgap of the $\text{Al}_x\text{Ga}_{1-x}\text{Sb}$ alloy increases with the Al composition, allowing the band offset of InAs-(Ga,Al)Sb heterostructures to be engineered by changing the substitutional species composition. In fact, a strong decrease of hole concentration with increasing Al composition, reaching zero at about $x \sim 0.3$, has been reported [2], which demonstrates the crossing of the valence band edge of $\text{Al}_x\text{Ga}_{1-x}\text{Sb}$ and the conduction band edge of InAs at that alloy composition.

Some years ago the research of several III-V semiconductor alloys is associated with the wavelength of the optical fiber loss minima (0.8 μm). In particular, gallium antimonide (GaSb) is interesting as a potential substrate material for devices in the band-gap range of 0.3-1.58 eV [3] and its related compounds are of interest as low band gap materials with applications in devices operating in the infrared range. For this reason, it is

necessary to improve the quality of GaSb and its alloys and to get a deep knowledge of their physical properties [4]. $\text{Al}_x\text{Ga}_{1-x}\text{Sb}$ is also used in the field of optical communications as a constituent of (Ga, Al)Sb-GaSb based lasers operating in the region of minimal absorption and dispersion in optical fibers. Tsang and Olsson [5] reported 1.78 μm wavelength $\text{Al}_{0.2}\text{Ga}_{0.8}\text{Sb}/\text{GaSb}$ double-heterostructure lasers, and Ohmori et al. [6] reported room-temperature lasing operation of an $\text{Al}_{0.2}\text{Ga}_{0.8}\text{Sb}/\text{GaSb}$ multi-quantum-well laser at 1.646 μm .

In this paper presents the structural characterization was made by HRXRD and Raman scattering study of the $\text{Al}_x\text{Ga}_{1-x}\text{Sb}$ alloys for $0.05 < x < 0.2$ grown by liquid phase epitaxy (LPE) technique. High resolution X-Ray diffraction (HRXRD) is applied in the investigation of epitaxial structures of semiconductors. The lattice parameters of semiconductor alloys gradually change with the chemical composition giving rise to an increase of strain until mismatch dislocations appear lead to the relaxation of the thin film. A two-mode behavior was found for this alloy composition, and TO-LO splitting of both GaSb-like and AlSb-like modes could not be resolved in the high-resolution first-order Raman spectra. Although the TO-LO splitting of AlSb-like modes was not well-resolved at room temperature. One also report second-order Raman spectra that show structures associated with GaSb-like modes, AlSb-like modes, and combinations of both.

II. EXPERIMENTAL

First, the mirror-like surface epilayers of lattice matched $\text{Al}_x\text{Ga}_{1-x}\text{Sb}$ ternary solid solutions with $0.05 \leq x \leq 0.2$ were grown by liquid phase epitaxy on (001) oriented GaSb substrates. The $\text{Al}_x\text{Ga}_{1-x}\text{Sb}/\text{GaSb}$ heterostructure studied in this work was grown by LPE at 400 °C, using a sliding boat system under hydrogen stream in horizontal furnace and in its variant of super cooling technique [6]. The melt was made using 6N polycrystalline GaSb undoped, 6N aluminum (Al) and 7N gallium (Ga). The melt was homogenized at 560°C during 30 min. The used substrates were Te doped n-type (100) GaSb wafers with a carrier concentration of about $5 \times 10^{17} \text{ cm}^{-3}$ at 300K. Before charging the components into the furnace, the substrates were etched with $\text{HF}:\text{H}_2\text{O}_2:(\text{citric acid}):\text{H}_2\text{O}$ solution. The layers were grown using the super-cooling technique. The lattice mismatch orthogonal to the surface

between epitaxial layers and substrate was determined by HRXRD measurements in a Bruker D8 Discover diffractometer, parallel beam geometry and monochromator of gobe mirror, CuK α radiation = 1.5406 Å, in the range of 20° <2 θ <80°, by step of 0.02°. The HRXRD data were refinement using the programs POWDERX and DICVOL04 to determine the crystal system, the parameters of unit cell, parallel (a) and perpendicular (a_{\perp}) and the atomic fraction x corresponding. Raman scattering experiments were performed at room temperature using the 6328 Å line of a He-Ne laser at normal incidence for excitation. The light was focused to a diameter of 6 μ m at the sample using a 50x (numerical aperture 0.9) microscope objective. The nominal laser power used in these measurements was 20 mW. Care was taken to avoid the heating of the sample inadvertently to the point of changing its Raman spectrum. Scattered light was analyzed using a micro-Raman system (Lambdam model of Dilor), a holographic notch filter made by Kaiser Optical System, Inc. (model superNotch-Plus), a 256x10²⁴-pixel CCD used as detector cooled to 140 K using liquid nitrogen, two interchangeable gratings (600 and 1800 g/mm). Typical spectrum acquisition time was limited to 60 s to minimize the sample heating effects discussed above. Absolute spectral feature position calibration to better than 0.5 cm⁻¹ was performed using the observed position of Si which is shifted by 521.2 cm⁻¹ from the excitation line.

III. RESULT AND DISCUSSION

Fig. 1 shows the Al_xGa_{1-x}Sb diffraction peak of the symmetrical reflection (115) plane, the diffraction peaks of the alloy are as narrow as the substrate peak, indicative of good crystalline and homogenous composition of the layer [7]. It is known that the crystalline quality of semiconductor compounds obtained by the LPE technique is dependent on the grown temperature. Figure shows the Al_xGa_{1-x}Sb diffraction peak of the symmetrical reflection (004) plane is clearly separated from the (004) GaSb diffraction peak. The samples with aluminum fractions 5, 10, 15 and 20 percent are presented in Figs. AY1, AY2, AY3 and AY4, respectively (see Table I). A measure for the crystalline quality of the layer is the perpendicular lattice mismatch. To determinate the alloy bulk lattice constant, it is necessary to know a_{\perp} and a_{\parallel} , these values were obtained using different reflections, [(115) and (-1-15)] and the Macrander's formulas [8]:

$$a_{\perp} = a_s \frac{\sin \theta_B}{\sin (\theta_B + \Delta\theta)} \frac{\cos \tau_s}{\cos (\tau_s + \Delta\tau)} \quad (1)$$

$$a_{\parallel} = a_s \frac{\sin \theta_B}{\sin (\theta_B + \Delta\theta)} \frac{\sin \tau_s}{\sin (\tau_s + \Delta\tau)} \quad (2)$$

where a_s is the substrate lattice constant, θ_B is Bragg angle for (115) direction, τ_s is the angle between (115) plane and the

surface plane of the sample, $\Delta\theta$ and $\Delta\tau$, which are obtained with the following equations [8]:

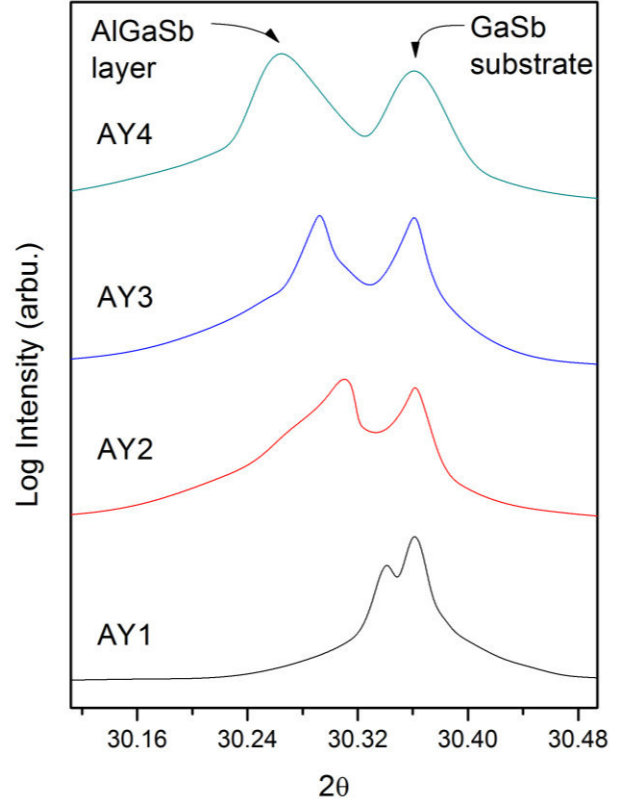


Figure 1 X-ray rocking curves of Al_xGa_{1-x}Sb layers grown on (001) GaSb substrates.

$$\Delta\theta = \frac{\Delta\omega^+ + \Delta\omega^-}{2} \quad (3)$$

$$\Delta\tau = \frac{\Delta\omega^+ - \Delta\omega^-}{2} \quad (4)$$

$\Delta\omega^+$ is the difference between the peak and the layer peaks in (-1-15) direction, $\Delta\omega^-$ is the difference between substrate and the layer peaks in (115) direction. It has found that the bulk lattice constant of the alloy a_0 is related with orthogonal and parallel lattice constant of the grown films. A measure for the crystalline quality of the layer is the perpendicular lattice mismatch and it can be obtained using the expression [9].

TABLE I. SUMMARY OF THE ALGASB SAMPLES STUDIED, AND THE AL MOLAR FRACTION ADDED TO EACH ONE TO THE MELT SOLUTION.

Sample	Added Al molar fraction
AY1	5 %
AY2	10 %
AY3	15 %
AY4	20 %

$$\frac{\Delta a}{a} = \frac{a_{\perp} - a_o}{a_o} \quad (5)$$

Figure 1 shows the HRXRD measurements of $\text{Al}_x\text{Ga}_{1-x}\text{Sb}$ alloys on GaSb substrates. The diffraction peaks of the alloy are as narrow as the substrate peak, indicative of good crystalline quality and homogenous composition of the layer as Kagawa and Motosugi [10] and Joullié [11] in their work stated when the lattice mismatch is about the value of 10^{-4} the interface can be considered well matched and the crystalline quality of the layer is similar to that of the substrate. The values of the lattice mismatch obtained from the samples are around 10^{-4} , see table II. And it indicates that the samples are well matched and consequently, they should have a good crystalline quality. Table II shows lattice constants obtained from equations (1) to (4), and the estimated aluminum fraction molar (Figure 2).

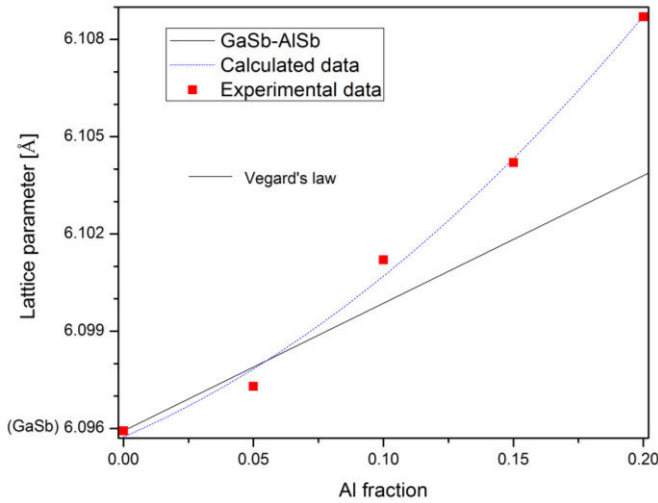


Figure 2 $\text{Al}_x\text{Ga}_{1-x}\text{Sb}$ lattice parameter versus content of the layer.

The solid phase composition was obtained by simulation of the experimental data from the rocking curves. The values of the Al concentration appear in Table II; it is observed that this one varies lightly from proposed concentration. To the Al molar fraction of 0.2, the diffraction peak shows a broadening in the FWHM characteristic which may be related to stages of phase separation of the $\text{Al}_x\text{Ga}_{1-x}\text{Sb}$ meta-stable alloy to GaSb and AlSb rich regions [12]. In this case, broadening of the spectra is related to imperfections in the structure of the alloys such as complex gallium vacancies-gallium on antimony site ($V_{\text{Ga}}\text{GaSb}$) [13].

TABLE II. RESULT OF THE ANALYSIS BY HRXRD OF THE SAMPLES.

Sample	a_{\perp} (Å)	a_{\parallel} (Å)	a_o (Å)	$\frac{\Delta a}{a}$ ($\times 10^{-4}$)	x_{exp}
AY1	6.0994	6.0950	6.0973	3.44	0.0463
AY2	6.1055	6.0967	6.1012	7.05	0.1154
AY3	6.1097	6.0984	6.1042	9.01	0.1552
AY4	6.1134	6.1037	6.1087	7.69	0.2253

Figure 3 shows Raman scattering results of $\text{Al}_x\text{Ga}_{1-x}\text{Sb}$ alloys grown on (100) n-GaSb with different concentrations of Al in the growth melt. In the Raman spectra are present mainly five bands at about 138, 235, 271, 320 and 438 cm^{-1} labeled as A, B, C, D and E, respectively. As can be seen in Fig. 2, the bands that depend strongly on the aluminum concentration are B, C, D and E. As has been reported the bands named by B and D can be associated to the GaSb and AlSb vibrational modes [14], respectively. A standard fitting procedure suggests these associations.

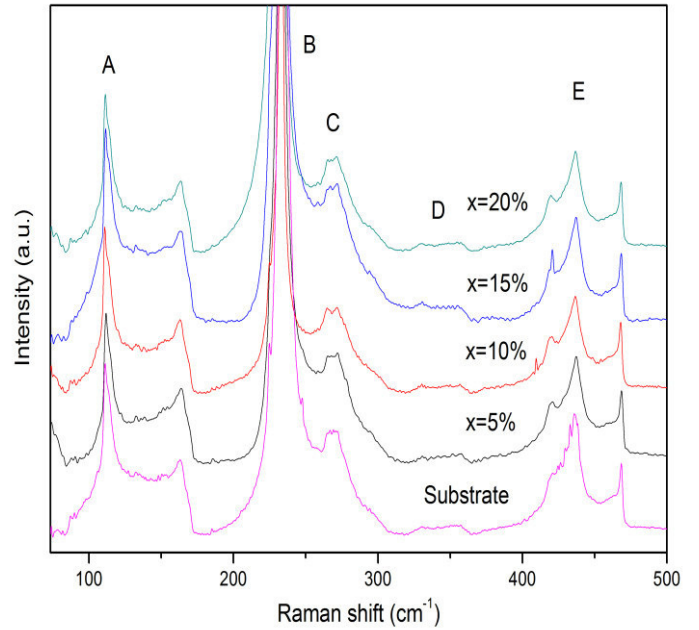


Figure 3 Raman spectra of the ternary alloys grown on (1 0 0) n-type GaSb with different aluminium molar fractions.

In this kind of alloys, generally, one should expect two modes (AlSb-like and GaSb-like) in the First order Raman scattering of the ternary $\text{Al}_x\text{Ga}_{1-x}\text{Sb}$ [14]. Taking into account that phonons are active in the first order Raman process in back scattering on the (001) face, one may assign our bands to the GaSb-like (221 cm^{-1}) TO, GaSb-like (230 cm^{-1}) LO, AlSb-like (315 cm^{-1}) TO and AlSb-like (321 cm^{-1}) LO [14] modes, respectively. From the least-squares fits one also obtained an estimation of the widths of the overlapping TO and LO peaks, which were found to be (11 and 3 cm^{-1}) and (8 and 5 cm^{-1}), for GaSb-like and AlSb-like modes, respectively. The Raman shift of these vibrational modes in the alloy is modified with respect to its bulk values due to the effect of the internal stress originated on the difference in lattice constant between GaSb and AlGaSb. The low frequency asymmetry of the GaSb-like mode is then obviously due to the contribution of the scattering process of phonon with non-zero q-vectors that become active due to the alloying disorder process [15,16]. The GaSb-like TO mode is forbidden for the (100) orientation of the substrate, and becomes active by the breakdown of the selection rules in the backscattering configuration [17] and as its intensity is very small one assumes that its presence possibly is due to crystalline

quality of the quaternary alloy layers is slightly imperfect, but as the Raman spectra are result of averaging at least on 20 different points on the sample the homogeneity of the samples is quite good. This breakdown is attributed to structural defects in the alloy originated from compositional fluctuations and by elastic scattering and by the ionized doping impurities [18]. The twomodes behavior of $\text{Al}_x\text{Ga}_{1-x}\text{Sb}$ is consistent with the fact that the two necessary requirement for such behavior are satisfied. First, the frequency of the LO mode in pure GaSb at 233 cm^{-1} [19] allows the existence of a GaSb:Al local mode, which was experimentally observed at 317 cm^{-1} by infrared absorption measurements [20] and theoretical calculated at 318 cm^{-1} [21]. Second, the gap which exists between acoustic and optical branches of AlSb between 132 and 297 cm^{-1} [22] allows the existence of an AlSb:Ga gap mode, reported by Talwar and Agrawal [23] to occur at $\sim 212\text{ cm}^{-1}$. As x increases, GaSb-like first-order mode lightly redshifts while AlSb-like blueshifts.

Figure 4 shows PL spectra at various values of x (aluminum) from the GaSb/ $\text{Al}_x\text{Ga}_{1-x}\text{Sb}$. As shown in Fig. 4 (left side), only one peak corresponding to GaSb transition is observed around 760 meV to 30 K , in all cases. Addition, in Fig. 4 (right side), another peak is observed at the high energy from $x=5\%$ to 20% . Figure 5 shows the PL bandgap of the sample plotted against atomic fraction from x 30 K and 300 K . The sample shows two remarkable similitude regimes which obey line aluminum dependence. This behavior corresponds to good growth and aluminum coupling in GaSb.

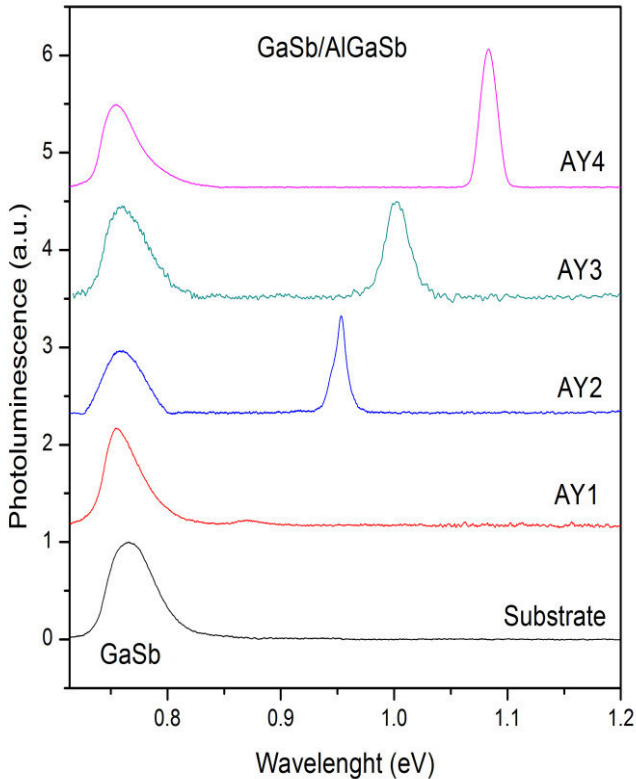


Figure 4 Excitation power dependence of PL spectrum from a GaSb and $\text{Al}_x\text{Ga}_{1-x}\text{Sb}$ at 30 K temperature.

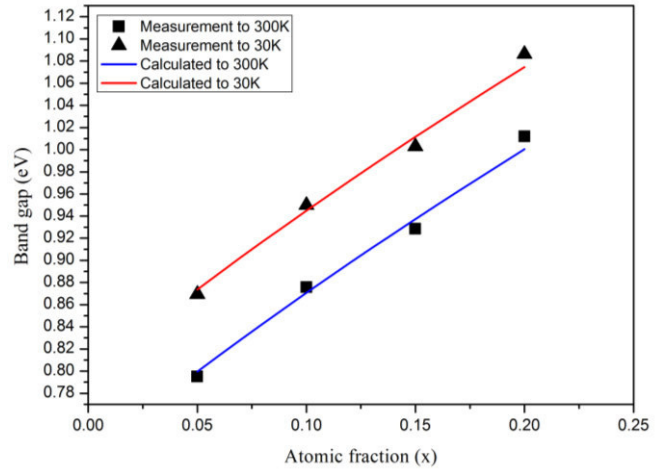


Figure 5 PL spectra at various temperatures from 30 and 300 K with comparison of calculated values.

IV. CONCLUSIONS

$\text{Al}_x\text{Ga}_{1-x}\text{Sb}$ epitaxial layers were grown at several Al contents by using the liquid phase epitaxy method at $400\text{ }^\circ\text{C}$ on (001) GaSb substrates with x ranging between 0.05 and 0.2 . The lattice parameters of the samples have been obtained from the mismatch components measured by HRXRD under the assumption that the epilayers elastic deformation follows the first-order elasticity theory. From the comparison between the results obtained by the different experimental techniques, it has been possible to show that the lattice parameter of the layer increases nonlinearly with the Al content: Vegard's law is not obeyed. High-resolution first-order Raman spectra of the $\text{Al}_x\text{Ga}_{1-x}\text{Sb}$ alloy were recorded at room temperature. The spectra displayed two-mode behaviour and TO-LO splitting even for the AlSb-like modes despite the low Al content of the alloy. The values of TO-LO splitting of GaSb-like and AlSb-like modes suggest the occurrence of charge transfer from the less ionic Ga-Sb bond to the more ionic Al-Sb bond. The large width of the AlSb-like LO peak in relation to its GaSb-like counterpart reflects the short-range order of the AlSb sublattice. Conversely, the quite narrow GaSb-like peak indicates a high degree of structural order in the GaSb sublattice, according with previous reports of long-range order in other III-V alloys. Photoluminescence measurements showed good scattering of the band gap with the incorporation of Aluminum in compound GaSb binary. Similar results we observed in the measurement at 300 K and also we showed the theoretical calculated measurement.

REFERENCES

- [1] H. Munekata, E.E. Mendez, Y. Iye, L. Esaki, "Densities and mobilities of coexisting electrons and holes in GaSb/InAs/GaSb quantum wells" Surf. Sci. vol. 174, pp. 449-453, 1986.
- [2] H. Munekata, L. Esaki, L.L. Chang, "Carrier densities in InAs-Ga(Al)Sb(As) quantum wells", J. Vac. Sci. Technol. B vol. 5 pp. 809-810, 1987.

- [3] P.S. Dutta, B. Méndez, J. Piqueras, E. Dieguez, H.L. Bhat. "Nature of compensating luminescence centers in Te - diffused and - doped GaSb", *J. Appl. Phys.* vol. 80, pp. 1112-1115, 1996.
- [4] M.F. Chioncel, C. Díaz-Guerra, J. Piqueras. *Semicond.* "Luminescence from indented Te-doped GaSb crystals", *Sci. and Technol.* 19, pp. 490-493, 2004.
- [5] W. T. Tsang, N. A. Olsson. "Preparation of 1.78 - μ m wavelength Al_{0.2}Ga_{0.8}Sb/GaSb double - heterostructure lasers by molecular beam epitaxy", *Appl. Phys. Lett.* vol. 43 pp. 8-10, 1983.
- [6] Y. Ohmori, S. Tarucha, Y. Horikoshi, H. Okamoto. "Room Temperature Operation of Al_{0.17}Ga_{0.83}Sb/GaSb Multi-Quantum Well Lasers Grown by Molecular Beam Epitaxy", *Jpn. J. Appl. Phys.* vol. 23 pp. L94-L96, 1984.
- [7] J.L. Lazzari, J.L. Leclercq, P. Grunberg, A. Joullié, B. Lambert, D. Barbusse, R. Fourcade, "Liquid phase epitaxial growth of AlGaAsSb on GaSb", *J. Cryst. Growth*, vol. 123, pp. 465-478, 1992.
- [8] A.T. Macrander, G.P. Schwartz, G.J. Gualtieri. "X - ray and Raman characterization of AlSb/GaSb strained layer superlattices and quasiperiodic Fibonacci lattices", *J. Appl. Phys.* vol. 64, pp. 6733-6745, 1988.
- [9] D.I. Westwood, D.A. Woolf. "Residual strain measurements in thick In_xGa_{1-x}As layers grown on GaAs (100) by molecular beam epitaxy", *J. Appl. Phys.* vol. 73, pp. 1187-1192, 1993.
- [10] T. Kagawa, G. Motosugi. "AlGaAsSb Photodiodes Lattice-Matched to GaSb", *Jpn. J. Appl. Phys.* vol. 18, pp. 1001-1002, 1979.
- [11] A. Joullié, F. Jia Hua, F. Karouta, H. Mani, "LPE growth of GaInAsSb/GaSb system: The importance of the sign of the lattice mismatch", *J. Cryst. Growth* vol. 75, pp. 309-318, 1986.
- [12] Y.J. Van der Meulen, "Growth properties of GaSb: The structure of the residual acceptor centres", *J. Phys. Chem. Solids* vol. 28, pp. 25-32, 1967.
- [13] C.A. Wang, H.K. Choi, D.C. Okley, G.W. Charache, "Recent progress in GaInAsSb thermophotovoltaics grown by organometallic vapor-phase epitaxy", *J. Cryst. Growth* vol. 195, pp. 346-355, 1998.
- [14] R. Cuscó, L. Artús, K.W. Benz. "First- and second-order Raman scattering of the Al_xGa_{1-x}Sb alloy for x=0.14", *J. Phys: Condens. Matter* vol 7, pp. 7069-7076, 1995.
- [15] T.C. McGlenn, T.N. Krabach, M.V. Klein, G. Bajor, J.E. Greene, B. Kramer, S.A. Barnett, A. Lastras, S. Gorbatkin. "Raman scattering and optical-absorption studies of the metastable alloy system GaAs_xSb_{1-x}", *Phys. Rev. B*, vol. 33, pp. 8396-8401, 1986.
- [16] D.H. Jaw, Y.T. Cherng, G.B. Stringfellow, "Long-wavelength lattice dynamics of GaInAsSb quaternary alloys" *J. Appl. Phys.* vol. 66, pp. 1965-1969, 1989.
- [17] R. Loudon, "The Raman effect in crystals", *Adv. Phys.* vol. 13, pp. 423-468, 1964.
- [18] D. Olego, M. Cardona, "Raman scattering by coupled LO-phonon-plasmon modes and forbidden TO-phonon Raman scattering in heavily doped p-type GaAs", *Phys. Rev. B.* vol. 24, pp. 7217-7232, 1981.
- [19] K. Aoki, E. Anatassakis, M. Cardona, "Dependence of Raman frequencies and scattering intensities on pressure in GaSb, InAs, and Insb semiconductors", *Phys. Rev. B*, vol. 30, pp. 681-687, 1984.
- [20] W. Hayes, "Localized vibrations of phosphorous and aluminum impurities in GaSb", *Phys. Rev. Lett.* vol. 13, pp. 275-277, 1964.
- [21] G. Lukovsky, M. H. Brodsky, E. Burstein, "Extension of a Linear Diatomic-Chain Model for the Calculation of Local-Mode Frequencies in Real Crystals", *Phys. Rev. B*, vol. 2, 3295-3302, 1970.
- [22] W.J. Turner, W.E. Reese, "Infrared Lattice Bands in AlSb", *Phys. Rev. B*, vol. 127, pp. 126-131, 1962.
- [23] D.N. Talwa, B.K. Agrawal, "Local-mode frequencies due to isoelectronic impurities in zinc-blende-type crystals", *Phys. Rev. B*, vol. 9, pp. 2539-2543, 1974.

Synthesis and Characterization of SBA-15 Functionalized with Amine -NH₂ by Conventional, Microwave and Ultrasound Methods

V. Hernandez-Morales ^{#1}, R. Nava ^{§2}, Eric M. Rivera-Muñoz ^{#3}

[#] *Centro de Física Aplicada y Tecnología Avanzada, Universidad Nacional Autónoma de México, A.P. 1-1010, Querétaro, Qro C.P. 76000, México.*

¹ vero_hm@hotmail.com

³ emrivera@fata.unam.mx

[§] *División de Investigación y Posgrado, Facultad de Ingeniería, Universidad Autónoma de Querétaro, Centro Universitario, 76000 Querétaro, Qro., México.*

² rufino@uaq.mx

Abstract— The SBA15-0.3NH₂ were prepared by grafting of synthesized SBA-15 substrate with 3-aminopropyltriethoxysilane (APTES) by conventional, microwave and ultrasound methods. The sorbents were prepared using tetraethyl orthosilicate (TEOS)/APTES molar ratio of 3.3 because of its high adsorption capacity for Pb (II) ions than pure SBA-15. All sorbents were characterized by N₂ adsorption– desorption isotherms, Fourier transform infrared (FT-IR) spectroscopy and thermogravimetric analysis (TGA–DTG). The characterization of sorbents after Pb(II) adsorption was performed by UV–vis technique. The use of microwaves and ultrasound for functionalization of the amino group on the SBA-15 lead to a greater success than in the case of conventional method, showing higher number of groups grafted onto the substrate, therefore the adsorption of Pb (II) was higher than that presented by the substrate obtained by the conventional method.

Keywords— SBA15-0.3NH₂; functionalization; microwave; ultrasound.

I. INTRODUCTION

Adsorption and recovery of heavy metal ions has become an important issue in the environmental and industrial fields [1-4].

The discovery of mesoporous molecular sieves has stimulated a renewed interest in developing adsorbents [5-8]. The discovery of hexagonally ordered mesoporous silicas [9] has stimulated a renewed interest in adsorbents and catalysts design because of their unique large surface area and well-defined pore size and shape. The addition of organic groups, by grafting of organosiloxane precursors onto the surface of the pores result in functional mesoporous hybrid materials [10-14].

In 1998, Zhao et al. (1998) developed SBA-15 mesostructured silica, which consist of parallel cylindrical pores with axes arranged in a hexagonal unit cell, exhibiting thicker pore walls (between 3.1- 6.4 nm) which provide high

hydrothermal stability [15]. Successful surface modification is often an integrated and crucial part of the material processing and is the basis for the functionality of the material. These functional groups provide further accessibility for anchoring other substrates (or complexes), such as biomolecules or metal ions, into the pore channels of the carrier material. Commonly applied methods for the introduction of functional groups onto the silica surface is the ex-situ by Conventional Method (CV), however, in recent years, microwave irradiation method (MW) has received considerable attention as a new promising method for the preparation of nanomaterials with controlled shape and size [16-19].

The main advantage of microwave irradiation is that it offers a simple, rapid, and economical strategy of heating. Compared with conventional heating, microwave heating has advantages for chemical synthesis, for example, the microwave energy is introduced without direct contact between the energy source and the reacting chemicals and this process can lead to much higher heating rates and in certain way it can realize selective heating, also other advantages are the reduction of reaction time by orders of magnitude, higher uniformity in the product and better properties when compared to conventional heating methods [20-28].

In the same way the method assisted by ultrasound (US) provides savings in time and energy in the functionalization of mesoporous silicas (hybrid mesoporus) [29].

Considering the properties of both SBA-15 mesoporous material and amino groups, the aim of the study was to deal with the Synthesis and Characterization of functionalized SBA-15 with -NH₂ by Conventional, Microwave and Ultrasound Methods to obtain an effective method of functionalization in the adsorbents, whit subsequent application of adsorption of lead (II) in aqueous solutions. The evidences for physicochemical characteristics of amino-functionalized SBA-15, obtained from FTIR spectra, X-ray

diffraction (XRD), N₂ adsorption-desorption isotherms, and thermogravimetric analysis (TGA-DTG) are presented.

II. EXPERIMENTAL

A. Preparation of the SBA-15 support

Siliceous SBA-15 mesoporous material was synthesized according to the procedure described by Flodström and Alfredsson [30]. The Pluronic triblock copolymer (BASF, EO₂₀-PO₇₀-EO₂₀, P123) was used as the structure-directing agent and tetraethyl orthosilicate (TEOS, 98%, Aldrich) as a source of silica. In a typical synthesis, the triblock copolymer was dissolved in a mixture of deionized water (High Purity, specific conductance of 0.2 μOhm⁻¹ cm⁻¹) and 4 M hydrochloric acid solution (pH = 0.6) in a Teflon bottle while the solution was heated at 75 °C for 4 h. After this, the required amount of silica precursor (TEOS/P123 molar ratio of 58) was added dropwise to the solution under vigorous stirring at 35 °C for 1 min and kept under slow stirring for 24 h. The synthesis gel was subsequently transferred into polypropylene containers and kept at 85 °C for another 24 h under static conditions. The final product was filtered, washed thoroughly with distilled water, and thereafter dried in air at 100 °C for 12 h. The polymer was removed by calcination in air at 500 °C for 6 h.

B. Preparation of amine-functionalized SBA-15

The amino-containing SBA-15 mesoporous substrates were synthesized using, as source of amino groups, 3-aminopropyltriethoxysilane/APTES, 99%; Aldrich in ethanol (absolute, Sigma-Aldrich). Each organic-inorganic hybrid material was prepared in unequal concentration solutions of TEOS:APTES to obtain the molar composition 1:0.3 [31].

C. Preparation of amine-functionalized SBA-15 by Conventional Method (CV)

1 g of SBA-15 was dispersed into APTES-ethanol solution at room temperature in an inert atmosphere for 30 min. Then, deionized water was slowly added and the liquid suspension was stirred for 30 min. Finally, the solids were dried at room temperature and then at 110 °C for 18 h.

D. Preparation of amine-functionalized SBA-15 Microwave Assisted (MW)

1 g of SBA-15 was dispersed into APTES-ethanol solution at room temperature in an inert atmosphere for 5 min, then, deionized water was added, the solution was placed within the rotor and placed in the microwave apparatus with the following conditions: temperature of 110 °C and 2.59 bar of pressure for 2 h. Finally, the solid was dried at room temperature and then at 110 °C for 18 h.

E. Preparation of amine-functionalized SBA-15 Ultrasonic Assisted (US)

1 g of SBA-15 was dispersed into APTES-ethanol solution at room temperature in an inert atmosphere for 5 min, then deionized water was added, an ultrasound, Hielscher model UP50H, equipment was used. The ultrasound tube was introduced in the sample for different times (1, 2 y 3 min), then the solids were dried at room temperature and then at 110 °C for 18 h.

F. Characterization methods

N₂ adsorption-desorption isotherms. The textural properties of the mesoporous matrices were determined from the nitrogen adsorption isotherms recorded at 77 K with a Micromeritics TriStar 3000 apparatus. The samples were previously degassed at 200 °C for 24 h under a vacuum (10⁻⁴ mbar) to ensure a clean, dry surface, free of any loosely bound adsorbed species. The specific areas of the samples were calculated according to standard BET procedure using nitrogen adsorption data collected in the relative equilibrium pressure interval of 0.03 < P/P₀ < 0.3. Pore size distributions were calculated from the adsorption and desorption branches of the corresponding nitrogen isotherm using the BJH method. The total pore volume (V_{total}) was estimated from the amount of nitrogen adsorbed at a relative pressure of 0.99.

Fourier transform-IR (FT-IR) spectra of the mesoporous matrices SBA15-0.3NH₂(CV, US and MW) were recorded by means of a Bruker Vector 3.3 spectrophotometer using the KBr wafer technique in 400–1800 cm⁻¹ range.

Diffuse reflectance spectroscopy (DRS). The UV-vis diffuse reflectance spectra of the sorbents containing adsorbed lead were recorded at RT on an Ocean Optics Inc. spectrometer First in Photonics (Mini-DT 2).

Thermal gravimetric analysis (TGA-DTG). In order to evaluate the influence of temperature on the catalyst stability, the calcined adsorbents were studied by thermal gravimetric analysis. All TG/1st DTG/2nd DTG curves were obtained on a Model TGA 2950 high-resolution thermogravimetric analyzer V5.4a, on a temperature level from 25 to 600 °C with a warming speed of 5 °C/min under nitrogen flow.

III. RESULT AND DISCUSSION

A. Characterization of the adsorbents

The textural properties of the mesoporous SBA-15 adsorbent, before and after of the assisted functionalization (CV, MW, and US) with amino groups, were studied by N₂ adsorption-desorption Isotherms at 77 K and are shown in Fig. 1.

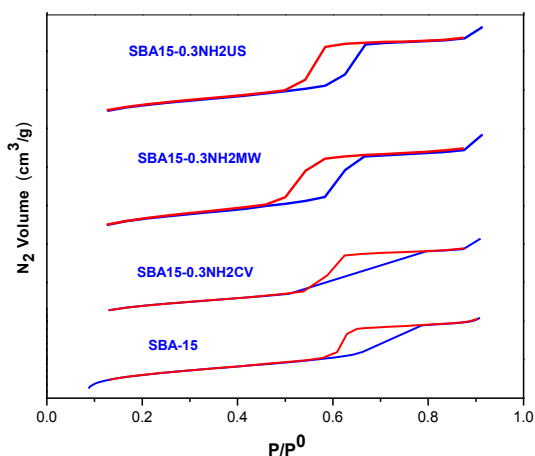


Fig. 1. N₂ adsorption-desorption isotherms of SBA-15 adsorbent before and after functionalization with amino groups.

All samples exhibit irreversible type IV adsorption-desorption isotherms with a H1-type hysteresis loop in the partial pressure range from 0.55 to 0.80, which is characteristic of materials with 6-8 nm pore diameter [32].

A well-defined step occurs approximately at $P/P_0 \approx 0.50 - 0.55$, which is associated with the filling of the mesopores due to capillary condensation. After modification of SBA-15 with amino groups, the amount of adsorbed nitrogen decreases and the inflection point of the step shifts from 0.7 to 0.50 for the sample SBA15-0.3NH₂MW/US and 0.8 to 0.55 value of relative pressure for SBA15-0.3NH₂CV. The pore size distributions of pure SBA15 and SBA15-0.3NH₂(CV, MW, and US) and sorbents, as calculated from the adsorption branch of N₂ isotherm by using the Barrett-Joyner-Halenda (BJH) model [33], are shown in both inlets of Fig. 2. It should be noted that both SBA15 and SBA15-0.3NH₂(CV, MW, and US) sorbents show a uniform, narrow pore size distributions centered at about 4 and 6 nm, confirming that the modification of the SBA-15 with 0.3 molar de APTES does not damage the hexagonal structure of this material.

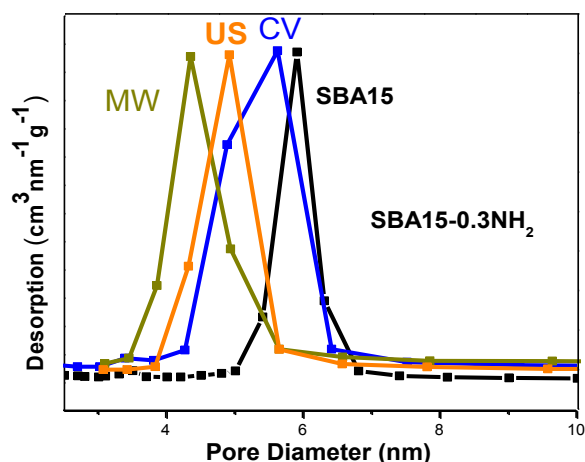


Fig. 2. Pore size distribution of SBA-15 adsorbent before and after assisted functionalization with amino groups.

Table 1 lists some textural properties of SBA-15 before and after grafting, which were calculated from nitrogen sorption studies by applying the BET equation for specific surface area [34] and the BJH formula for pore size distribution [33]. For the functionalized SBA-15 samples the BET surface and volume were standardized versus pure silica weights. As expected, the BET surface area and the mesoporous volume strongly decrease after grafting, according to the sequence SBA15 > SBA15-0.3NH₂ CV > SBA15-0.3NH₂ US > SBA15-0.3NH₂ MW, suggesting that the grafted species are located inside the mesoporous structure of the SBA-15 and, depending on the method of functionalization, the number of amino groups change decreasing the surface area and they are not only on its outer surface. For example, for the SBA15-0.3NH₂ CV sample and SBA15-0.3NH₂/(MW,US) the mesoporous volume decrease by 40% and 60%, respectively, with respect to the SBA15 material. Similar decrease suffers the average pore diameter. Due to the functionalization of -NH₂ groups, this result indicates the presence of amino groups, functionalization methods by microwave and ultrasound decreases the pore diameter and pore volume, indicating better functionalization which is reflected in greater amount of -NH₂ groups.

Fig. 3 shows the IR spectra of the samples SBA15-0.3NH₂ CV, SBA15-0.3NH₂ US, SBA15-0.3NH₂ MW and SBA15, where is observed a typical silica's spectrum (SiO₂). The bands at 811 and 1087 cm⁻¹ correspond to the symmetrical and anti-symmetric vibrations of the Si-O-Si bonds. The band located at 967 cm⁻¹ has been assigned to the torsion vibration of the Si-O-Si bond and the vibration of the silanol's group (Si-OH), respectively. Thus, the bands at 1087 and 811 cm⁻¹ are assigned to SBA-15 framework [32]. Additionally, all samples show a band located at 1635 cm⁻¹ which corresponds to free molecular H₂O. Finally, in the spectra of SBA15/(CV, US, MW), the characteristics bands that correspond to vibrations of the N-H bonds (1558, 950 cm⁻¹), and of the C-N bonds (1650 cm⁻¹) of methylene groups can be observed.

These results confirm the successful functionalization of SBA-15 with aminopropyl groups and it can be seen that the US and MW methods improve the functionalization with NH₂, the vibrations of the amino group are well defined.

Table. 1. Textural properties of calcined SBA-15 before and after of assisted functionalization with NH₂ groups.

Sample for method	Surface Area (m ² /g)	Diameter de poro (nm)	Pore Volume (cm ³ /g)
MW	220.12	4.30	0.39
US	247.83	4.90	0.42
CV	475.00	5.80	0.67
SBA-15	933.00	6.50	1

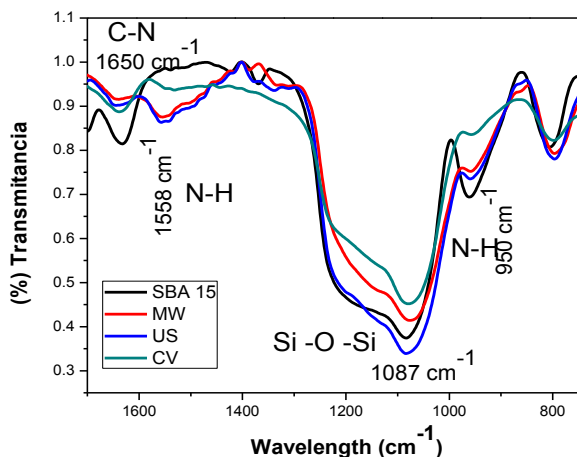


Fig.3 FTIR spectra of SBA-15 and SBA15-0.3NH₂/Conventional (CV), microwave (MW) and ultrasound (US) methods.

The thermal analysis TGA and DTG curves of the pure SBA-15 silica sample, SBA15-0.3NH₂/(CV, MW, and US) samples are shown in Fig. 4a and 4b. The TGA curves of the samples indicate a significant weight loss, which starts immediately with the increase of the temperature. Compared with 9.1% weigh loss of the SBA15 sorbent recoded during heating from the room temperature to 600 °C, the SBA15-0.3NH₂/(CV, MW, and US) samples exhibit weigh losses of 10%. The TG curves of the SBA15-0.3NH₂/(CV, MW, and US) samples (Fig. 4a) show the presence of the inflection points at 50 and 255 °C already observed in the pure SBA-15 silica sample. Those inflection points correspond to dehydration and to the dehydroxylation of the SBA-15 silica material, respectively [35]. Additionally, the samples grafted with amino groups show the inflection points at approximately 298 °C and 320 °C (Fig. 4b), which are related to the decomposition of the amino and ethylene groups. Thus, the results of the thermogravimetric analysis confirm the presence of the functional groups on the SBA-15 surface. Those groups have high thermal stability (above 250 °C), suggesting that the SBA-15 silica sample has a stabilizing effect on the temperature of decomposition of the surface species.

Fig. 5. Shows the UV-vis adsorption spectra showing the spectral change upon lead adsorption on SBA15-0.3NH₂/(CV,US and MW) of 200 ppm Pb(II) ions solutions. As can be observed in this figure, a larger Pb(II) adsorption on SBA15-0.3NH₂/(CV,US and MW) occurs when the water solution contain a larger Pb(II) ion concentration. The room-temperature electronic absorption spectra of all sorbents show two bands: an intense absorption band in 210 nm and a less intense in 310 nm (Fig. 5) [36]. These transitions contain both ligand-to-metal charge transfer (N 2p → Pb 6sp) and intraatomic (Pb 6s² → Pb 6sp) character (for Pb in O_h: a_{1g}² → a_{1g}^{*} t_{1u}¹) [37-39]. These absorption bands can be used to gain qualitative information about the affinity of Pb²⁺ for the amine groups of the SBA15-0.3NH₂ with different methods of synthesis, however the US and MW methods show higher functionalization therefore greater adsorption of lead (II).

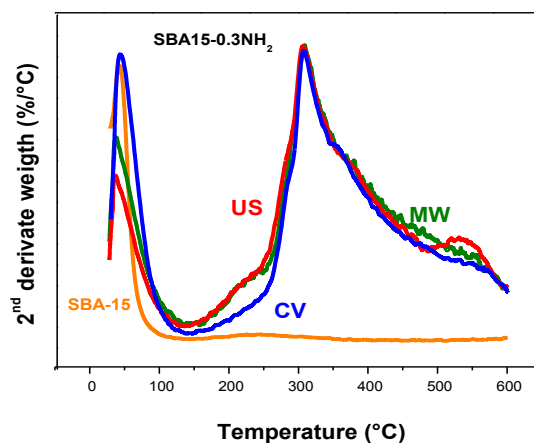
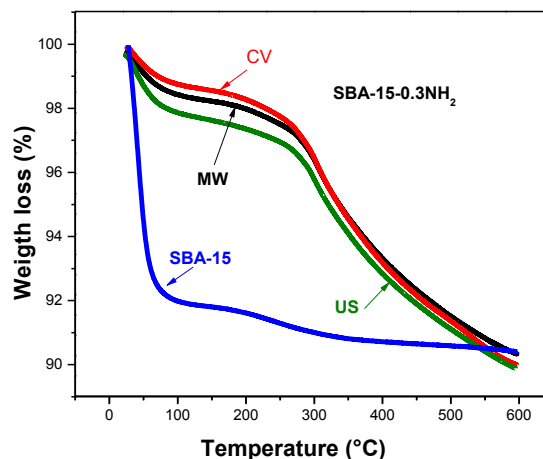


Fig. 4. TG (a) and DTG (b) curves of SBA15, SBA15-0.3NH₂/ Conventional (CV), microwave (MW) and ultrasound (US) methods.

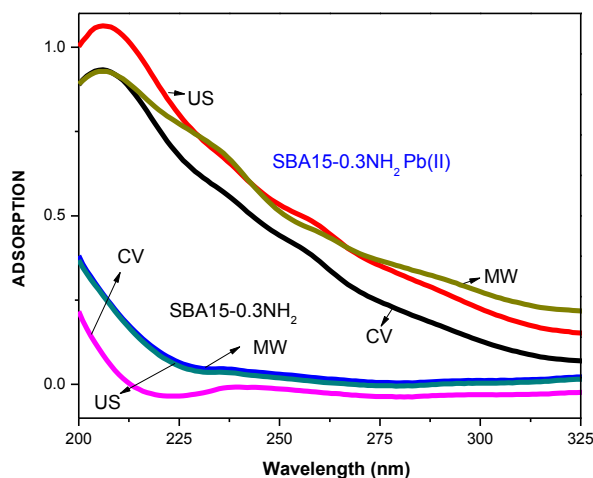


Fig. 5. UV-vis spectra showing the spectral change upon lead adsorption on SBA15-0.3NH₂/ Conventional (CV), microwave (MW) and ultrasound (US) methods. As adsorbent from 200 ppm Pb(II) ions solutions.

IV. CONCLUSION

In this study, the ability of modified mesoporous silica material SBA-15 with amino functional group (-NH₂) by Conventional, Microwave and Ultrasound Methods, to obtain an effective method of functionalization in the adsorbent, was investigated. It was found out that: (i) The three proposed methods for surface modification of mesoporous silica SBA-15 are feasible (supported by spectroscopic techniques results S_{BET}, FT-IR and TGA-DTG), however with the ultrasound method better functionalization, the bonds vibrations representative of the amino groups are more defined (FT-IR), this is attributed to a greater number of amino groups on the surface of the silica, which in turn represents a greater number of active sites for use as adsorbent lead (II), offering quick, easy and inexpensive method for modification. (ii) The abilities of the sorbents depend of the number of grafted amino groups. (iii) SBA15 functionalization with amino groups is efficient for the adsorption of Pb (II), in aqueous solutions (UV-vis), the functionalization by ultrasound method, adsorbed greater amount lead (II).

ACKNOWLEDGMENT

The authors would like to express their gratitude to CONACYT, CFATA-UNAM and Universidad Autónoma de Querétaro (UAQ) for their support for the realization of this work, and M.C. Riverino Flores (CINVESTAV-Queretaro) for technical assistance in FT-IR.

REFERENCES

- [1] T. Kang, Y. Park, and J. Yi, "Highly selective adsorption of Pt²⁺ and Pd²⁺ using thiol-functionalized mesoporous silica", *Ind. Eng. Chem. Res.* 43 (2004) 1478.
- [2] B. Lee, Y. Kim, H. Lee, J. Yi, "Synthesis of functionalized porous silicas via templating method as heavy metal ion adsorbents: the introduction of surface hydrophilicity onto the surface of adsorbents", *Micropor. Mesopor. Mater.* 50 (2001) 77.
- [3] H. Lee, J. Yi, "Removal of copper ions using functionalized mesoporous silica", *Sep. Sci. Technol.* 36 (2001) 2433.
- [4] A.K. Meena, G.K. Mishra, P.K. Rai, Ch. Rajagopal, P.N. Nagar, "Removal of heavy metal ions from aqueous solutions using carbon aerogel as an adsorbent", *J. Hazard. Mater.* 122 (2005) 161.
- [5] B. Lee, Y. Kim, H. Lee, J. Yi, "Synthesis of Functionalized Porous Silicas via Templating Method as Heavy Metal Ion Adsorbents: The Introduction of Surface Hydrophilicity onto the Surface of Adsorbents", *Microporous Mesoporous Mater.* 50 (2001) 77.
- [6] S. Dai, M.C. Burleigh, Y.H. Ju, H.J. Gao, J.S. Lin, S.J. Pennycook, C.E. Barnes, Z.L. Xue, "Hierarchically Imprinted Sorbents for the Separation of Metal Ions". *J. Am. Chem. Soc.* 122 (2000) 992.
- [7] M.C. Burleigh, S. Dai, E.W. Hagaman, L.S. Lin, "Imprinted Polysilsesquioxanes for the Enhanced Recognition of Metal Ions", *Chem. Mater.* 13 (2001) 2537.
- [8] Y.H. Ju, O.F. Webb, S. Dai, J.S. Lin, C.E. Barnes, "Synthesis and Characterization of Ordered Mesoporous Anion-Exchange Inorganic/Organic Hybrid Resins for Radionuclide Separation", *Ind. Eng. Chem. Res.* 39 (2000) 550.
- [9] C.T. Kresge, M.E. Leonowicz, W.J. Roth, J.C. Vartulli, J.S. Beck, "Ordered mesoporous molecular sieves synthesized by a liquid-crystal template mechanism", *Nature*, 359 (1992) 710.
- [10] A. Bibby, L. Mercier, "Mercury(II) ion adsorption behavior in thiol-functionalized mesoporous silica microspheres". *Chem. Mater.* 14 (2002.) 1591.
- [11] A. Walcarius, M. Etienne, J. Bessière, "Rate of Access to the Binding Sites in Organically Modified Silicates. 1. Amorphous Silica Gels Grafted with Amine or Thiol Groups", *Chem. Mater.* 14 (2002.) 2757.
- [12] H. Yoshitake, T. Yakoi, T. Tatsumi, "Adsorption behavior of arsenate at transition metal cations captured by amino-functionalized mesoporous silicas", *Chem. Mater.* 15 (2003) 1713.
- [13] L. Zhang, C. Yu, W. Zhao, H. Chen, L. Li, J. Shi, "Preparation of multi-amine-grafted mesoporous silicas and their application to heavy metal ions adsorption", *J. Non-Cryst. Solids* 44 (2007) 4055.
- [14] H. Yang, R. Xu, X. Xue, F. Li, G. Li, "Hybrid surfactant-templated mesoporous silica formed in ethanol and its application for heavy metal removal", *J. Hazard. Mater.* 152 (2008) 690.
- [15] D.Y. Zhao, Q.S. Huo, J.L. Feng, B.F. Chmelka, G.D. Stucky, "Onionic triblock and star diblock copolymer and oligomeric surfactant syntheses of highly ordered, hydrothermally stable, mesoporous silica structures", *J. Am. Chem. Soc.* 120 (1998) 6024.
- [16] A. Bonamartini-Corradi, F. Bondioli, B. Focher, A.M. Ferrari, C. Grippo, E. Mariani, C. Villa, "Conventional and Microwave-Hydrothermal Synthesis of TiO₂ Nanopowders", *J. Am. Ceram. Soc.* 88 (2005) 2639.
- [17] G. Li, Y. Ding, Y. Zhang, Z. Lu, H. Sun, R. Chen, "Microwave synthesis of BiPO₄ nanostructures and their morphology-dependent photocatalytic performances", *Journal of Colloid and Interface Science* 363 (2011) 497.
- [18] C.-H. Huang, Y.-T. Yang, R.-A. Doong, "Microwave-assisted hydrothermal synthesis of mesoporous anatase TiO₂ via sol-gel process for dye-sensitized solar cells", *Microporous and Mesoporous Materials*, 142 (2011) 473-480.
- [19] S. Cho, K.H. Lee, "Synthesis of crystalline TiO₂ nanostructure arrays by direct microwave irradiation on a metal substrate", *Journal of Crystal Growth*, 312 (2010) 1785.
- [20] Ou. Hsin-Hung, Lo. Shang-Lien, Liao. C.-H, N-Doped TiO₂ "Prepared from Microwave-Assisted Titanate Nanotubes (Na_xH_{2-x}Ti₃O₇): The Effect of Microwave Irradiation during TNT Synthesis on the Visible Light Photoactivity of N-Doped TiO₂", *J. Phys. Chem.*, 115 (2011) 4000-4007.
- [21] C.H. Huang, Y.T. Yang, R.A. Doong, "Microwave-assisted hydrothermal synthesis of mesoporous anatase TiO₂ via sol-gel process for dye-sensitized solar cells", *Microporous and Mesoporous Materials*, 142 (2011) 473-480.
- [22] N.F. Hamedani, A.R. Mahjoub, A.A. Khodadadi, Y. Mortazavi, "Microwave assisted fast synthesis of various ZnO morphologies for selective detection of CO, CH₄ and ethanol, *Sensors and Actuators*", *B: Chemical*, 156 (2011) 737-742.
- [23] L.H. Hoang, P. Van Hai, P. Van Hanh, N.H. Hai, X.-B. Chen, I.-S. Yang, "Microwave-assisted synthesis and characterization of Ti_{1-x}V_xO₂ (x=0.0-0.10) nanopowders", *Materials Letters*, 65 (2011) 3047-3050.
- [24] H.E. Wang, L.X. Zheng, Ch.P. Liu, Y.K. Liu, Ch.Y. Luan, H. Cheng, Y.Y. Li, L. Martinu, J.A. Zapien, I. Bello, "Rapid Microwave Synthesis of Porous TiO₂ Spheres and Their Applications in Dye-Sensitized Solar Cells", *J. Phys. Chem.*, 115 (2011) 10419-10425.
- [25] S. Horikoshi, Y. Minatodani, H. Sakai, M. Abe, N. Serpone, "Characteristics of microwaves on second generation nitrogen-doped TiO₂ nanoparticles and their effect on photoassisted processes", *Journal of Photochemistry and Photobiology A: Chemistry*, 217 (2011) 191-200.
- [26] Li Li, Xiaomei Qin, Guobing Wang, Limin Qi, Guoping Du, Z. Hu, "Synthesis of anatase TiO₂ nanowires by modifying TiO₂ nanoparticles using the microwave heating method", *Applied Surface Science* 257 (2011) 8006-8012.
- [27] P. Marcasuzaa, S. Reynaud, B. Grassl, H. Preudaomme, J. Desbriares, M. Trchova, O.F.X. Donard, "Microwave synthesis: An alternative approach to synthesize conducting end-capped polymers", *Polymer*, 52 (2011) 33-39.

- [28] Y. Shi, S. Wang, X. Ma, "Microwave preparation of Ti-containing mesoporous materials. Application as catalysts for transesterification", *Chemical Engineering Journal*, 166 (2011) 744-750.
- [29] Z. Shenmin, Z. Zhengyang, Z. Di, W. Honghua "Synthesis of mesoporous amorphous MnO₂ from SBA-15 via surface modification and ultrasonic waves", *Microporous and Mesoporous Materials*, 95 (2006) 257-264.
- [30] K. Flodström, V. Alfredsson. "Influence of the block length of triblock copolymers on the formation of mesoporous silica", *Micropor. Mesopor. Mater.* 59 (2003) 167.
- [31] V. Hernández-Morales, R. Nava, Y.J. Acosta-Silva, S.A. Macías-Sánchez, J.J. Pérez-Bueno, B. Pawelec. "Adsorption of lead (II) on SBA-15 mesoporous molecular sieve functionalized with -NH₂ groups", *Microporous and Mesoporous Materials* 160 (2012) 133-142.
- [32] Zhao, D. Y., Huo, Q. S., Feng, J. L., Chmelka, B. F., Stucky, G. D., 1998. "Onionic triblock and star diblock copolymer and oligomeric surfactant syntheses of highly ordered, hydrothermally stable, mesoporous silica structures", *J. Am. Chem. Soc.* 120 (1998) 6024-6036.
- [33] E.P. Barrett, L.G. Joyner, P.P. Halenda. "The determination of pore volume and area distributions in porous substances. I. computations from nitrogen isotherms", *J. Am. Chem. Soc.* 73 (1951) 373.r
- [34] S. Brunauer, P.H. Emmett, E. Teller. "Adsorption of gases in multimolecular layers". *J. Am. Chem. Soc.* 60 (1938) 309.
- [35] K.L. Josenák, L. Kuchta, P. Hudec, V.S. Fagnor, *J. Therm. Anal. Cal.* 55 (1999) 773.
- [36] M. Anbia, M. Lashgari, "Synthesis of amino-modified ordered mesoporous silica as a new nano sorbent for the removal of chlorophenols from aqueous media", *Chem. Eng. J.* 150 (2009) 555.
- [37] X. Gu, L.J. Evans. "Modelling the adsorption of Cd(II), Cu(II), Ni(II), Pb(II), and Zn(II) onto Fithian illite", *J. Colloid. Interf. Sci.* 307 (2007) 317.
- [38] D.K. Singh, D.P. Tiwari, D.N. Saksena, *Ind. J. Environment Health* 35 (1993) 169.
- [39] M. Uçurum, "A study of removal of Pb heavy metal ions from aqueous solution using lignite and a new cheap adsorbent (lignite washing plant tailings)", *Fuel* 88 (2009)1460.

Biofuels of microalgae: A review of culture parameters that condition the lipidic productivity and importance to incorporation of natural settings

Maritza L Soria Ornelas^{#1}, Marieke Vanthoor-Koopmans^{#2}

[#]*Maestría en ciencias de la energía. División de Investigación y Posgrado. Universidad Autónoma de Querétaro. Cerro de las Campanas s/n, Cp. 76010, Querétaro, Querétaro, México*

¹*ibq.mlso@gmail.com*

²*mariekekoopmans81@gmail.com*

Abstract— It is a fact that our continued energy dependence on fossil fuels is unsustainable in the future, due both to the depletion of world reserves as emissions of greenhouse gases associated with its use. Therefore, they have recently emerged strong research initiatives aimed at developing fuels produced from organic sources that are potentially an alternative to our current energy resources called biofuels.

The production of biofuels from microalgae have become relevant in the last decades, particularly the biodiesel from microalgal lipids, and despite of all the advantages that represent oil and other derivative products of microalgae, production remains an expensive technology due, among other things, to factors associated with the cultivation. So the focus should be maximum utilization of biomass from microalgae, minimize energy use and optimization of culture variables.

Numerous studies are available in the literature that have focused on the analysis of the culture conditions and stress under which the lipid could increase productivity. However, an approach that has not been given to investigations to maximize productivity in microalgae lipid is finding optimal conditions but under natural settings like sunlight conditions.

This study reviews the main growth parameters that affect the lipid productivity. Also the importance to consider synergistic effects or interactions of parameters for future investigations is discussed. The impact of integrated natural settings in the studies, e.g. natural daily light cycle is studied.

Keywords — *biofuel; microalgae; lipids; biodiesel; growth parameter; nitrogen starvation; effect of light; natural settings*

I. INTRODUCTION

Sustainability is a key principle in natural resource management, and it involves operational efficiency, minimization of environmental impact and socio-economic considerations; all of which are interdependent. It has become increasingly obvious that continued reliance on fossil fuel energy resources is unsustainable, owing to both depleting world reserves and the green house gas emissions associated with their use. Therefore, there are vigorous research initiatives aimed at developing alternative renewable and potentially carbon neutral solid, liquid and gaseous biofuels as alternative energy resources [1], [2].

Another problem with petroleum fuels is their uneven distribution in the world; for example, the Middle East has 63% of the global reserves and is the dominant supplier of petroleum [1]. Interestingly, the renewable energy resources are more evenly distributed than fossil or nuclear resources. Today's energy system is unsustainable because of equity issues as well as environmental, economic, and geopolitical concerns that will have implications far into the future. Hence, sustainable renewable energy sources such as biomass, hydro, wind, solar (both thermal and photovoltaic), geothermal, and marine energy sources will play an important role in the world's future energy supply.

Microalgae are considered one of the most promising feedstocks for biofuels. Microalgae contain several constituents, mainly including lipids, carbohydrates and proteins. Thus, microalgae have been investigated as a versatile biofuel feedstock for the production of biodiesel, bioethanol, biogas, bio-hydrogen and many other fuel types via thermochemical and biochemical methods. The production of flexible bioenergies from microalgae for sustainable development is theoretically viable and could be complemented with other resources to produce biofuel in a large-scale process as shown in [Fig. 1](#) [3].

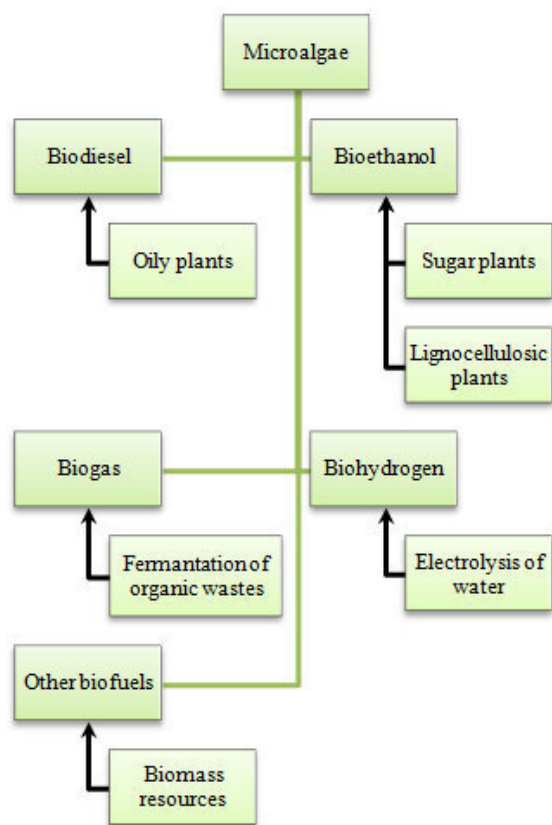
Worldwide, research and demonstration programs are being carried out to develop the technology needed to expand algal lipid production to a major industrial process [4], [5]. Although microalgae are not yet produced at large scale for bulk applications, recent advances present opportunities to develop this process in a sustainable and economical way within the next 10 to 15 years [5].

II. MICROALGAE AS A POTENTIAL SOURCE FOR THE PRODUCTION OF BIOFUELS

The whole algal biomass or algae extracts can be converted into different fuel forms like biogas, liquid and gaseous transportation fuels as kerosene, diesel, ethanol, jet fuel, and biohydrogen through the implementation of processing technologies such as anaerobic digestion, pyrolysis, gasification, catalytic cracking, enzymatic or chemical transesterification. For biodiesel production, lipids transesterification is needed, while starch hydrolysis and fermentation is used to produce bioethanol.[6], [7].

In the right conditions biofuels can reduce emissions and make a huge contribution to energy security. In terms of greenhouse gases emissions, the CO₂ emitted from burning biofuel is assumed to be zero, as the carbon was taken out of the atmosphere when the algae biomass grew. Therefore, biofuels from microalgae do not add new carbon to the atmosphere [7]. However, these processes are complex, technologically challenging and economically expensive [1], [5].

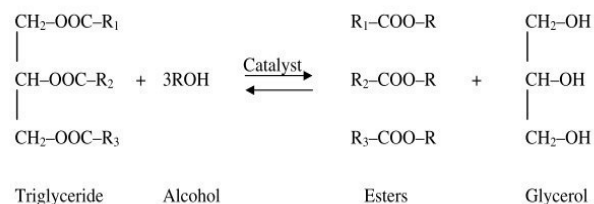
Fig. 1. Flexible biofuels production from microalgae for sustainable development [8]



A. Biodiesel: main biofuel derived by microalgae

Biodiesel has great potential; however, the high cost and limited supply of renewable oils prevent it from becoming a serious competitor for petroleum fuels. As petroleum fuel costs rise and supplies dwindle, biodiesel will become more attractive to both investors and consumers. For biodiesel to become the alternative fuel of choice, it requires an enormous quantity of cheap biomass. Using new and innovative techniques for cultivation, algae biodiesel production can achieve the price and scale of production needed to compete with, or even replace, petroleum [9].

Fig. 2. Transesterification of triglycerides with alcohol



Many species of algae accumulate large amounts of oils that to a large extent are made up of triacylglycerols (TAGs) consisting of three fatty acids bound to glycerol. The algal oil is converted into biodiesel through a transesterification process (Fig. 2). Oil extracted from the algae is mixed with alcohol and an acid or a base to produce the fatty acid methylesters that makes up the biodiesel [6].

Lipids can be classified as fatty acids, glycerolipids, glycerophospholipids, sphingolipids, sterol lipids, prenol lipids, saccharolipids and polyketides. They contain different biomolecules such as fats, waxes, sterols, fat-soluble vitamins, monoglycerides, diglycerides, triglycerides and phospholipids. The energy storage and signaling are the main biological functions of lipids molecules. Triacylglycerols (TAGs) are storage lipids for chemical energy that consists of three fatty acids bound to a glycerol backbone and it synthesizes to biological parts of plant species and microalgae [10].

The high proportion of saturated and monounsaturated fatty acids in lipid fraction of microalgae is considered optimal from a biodiesel quality standpoint, in that fuel polymerization during combustion would be substantially less than what would occur with polyunsaturated fatty acid-derived fuel [6].

B. Positive aspects of using algae as a feedstock

Microalgae are among the fastest-growing plants in the world and about 20%-80% of their weight could be oil [1], [11], [12]. Microalgae have very fast reproduction cycles, and therefore capable to allow multiple and continuous harvesting of biomass year round unlike oilseed crops. It has much faster growth-rates than terrestrial crops. The per unit area yield of oil from algae is estimated to be from 20,000 to 80,000 L per acre, per year; this is 7-31 times greater than the next best crop, palm oil [4].

Microalgal cultivation can occur on non-arable land, in brackish water thus reducing strain on resources required for the production of food crops whilst reducing other environmental effects. There is no need for use of chemicals such as herbicides or pesticides thus reducing costs and environmental impacts. In addition, these microorganisms require significantly less land, estimated 2% of the land required to produce the same amount of bio-diesel from oil bearing crops [4]. Growth of microalgae can effectively remove phosphates and nitrates from wastewater, thus making it an ideal substrate for the cultivation of microalgae for biofuels production whilst acting as a tertiary treatment for wastewater. Microalgae produce valuable by-products in the form of proteins, pigments, biopolymers and carbohydrates

such as docosahexanoic acid and carotenoids including antioxidant substances for commercial or pharmaceutical purpose [5], [11], [12]. Residual biomass post extraction offers methods for improving economics by using it as a fertilizer or for producing other high energy products. Microalgal biofuels are environmentally advantageous in that it is a carbon neutral fuel due to the photosynthetic fixation of atmospheric carbon dioxide. Microalgal growth actively utilizes 1.83 kg of CO₂ for every 1 kg dry biomass produced [11].

C. Challenges and opportunities for the use of microalgae

The technology for large scale production of microalgae already exists. Globally, current commercial production however is for high value products only such as pigments, antioxidants, amino acids and other additives to various industries e.g. the pharmaceutical. These ventures have established harvesting and processing methods but energy input is not of major concern due to the nature of the high value products [13]. The approach to large scale production of products such as lipids for biofuels production must however be approached differently in order to make the process feasible. The scale up of microalgal biomass production for biofuels must take into account various factors to aid in ensuring an economically feasible process. These include selection of cultivation method (open or closed system), the use of microalgae with a competitive advantage to avoid contamination, supply of nutrients and carbon dioxide and a viable source of water that has little to no environmental impact [4], [14]. In addition, nutrients should be obtained from a cheap source e.g. using urea as a source of nitrogen or wastewater as a complete medium.

Considering the process (fig. 3), microalgal biomass harvesting is one of the major steps in upstream processing and this stage at large scale poses major challenges. Harvesting of 25–33% of the reactor volume may be required daily for viable production of biodiesel [4].

The end results of many methods tend to be highly energy intensive and more complex [10], [15], [16]. Drying or dewatering of biomass is generally required as a pre-treatment prior to lipid extraction or use in various thermo-chemical conversion techniques. Moisture in the biomass will negatively interfere with the downstream processing and greatly influence the cost of product recovery [4], [13], [14].

Drying may be achieved by spray drying, drum drying, freeze-drying, solar drying, as well as various forms of oven drying. Microalgal lipid is generally extracted from biomass before conversion to biofuels. This may be achieved by mechanical methods such as cell homogenizers, bead mills, ultrasounds, autoclave, and spray drying or non-mechanical methods such as freezing, utilization of organic solvents, osmotic shock, acid and base as well as enzyme reactions [1]. The method of choice of lipid extraction will depend on the type of microalgal cells grown and the thickness of the cell walls impeding liberation of intracellular lipids [4], [13].

However, many of these mentioned methods are not feasible at large scale due to high energy input requirements. The most appropriate method of lipid extraction to date is the use of solvents and in a large scale process, it implies a huge amount of solvents and economic cost in process input.

Regarding growth step, there are important physicochemical parameters such as light intensity, pH, temperature, oxidation reduction potential (ORP), salinity, conductivity and nutrient composition inter alia which require rigorous optimization before scaling up can be considered [4]. When all these important variables affecting the microalgal strain of choice are known, it is desirable to design a suitable experimental run and generate and collate enough data for system testing and analysis.

More technological advances for production of biodiesel from microalgae are needed in order to be truly sustainable [15]. So should focus attention on the maximum exploitation of microalgae biomass and minimize energy use but now considering a new approach to the experimental work, incorporating natural conditions that allow maximizing the biotic resources that have available, and definitely would allow reducing operating costs, e.g. search of optimization of parameters of microalgae cultivation under natural daily light cycle.[1], [14].

III. GROWTH PARAMETERS TO ENHANCE THE LIPID PRODUCTIVITY

While many microalgae strains naturally have high lipid content (20–50% dry weight), it is possible to increase the concentration by modifying the growth determining factors such as the control of nitrogen level, light intensity, temperature, CO₂ concentration and harvesting procedure [1], [4], [17]–[19].

When microalgae are cultivated under sub- or supra-optimal conditions they react and change their metabolic pattern and strategies, in order to cope with the difficulties under the specific environmental conditions. This dynamic change on the metabolic strategy affects the biomass composition, fluctuating the relative content of the bio-mass compounds. When the environmental conditions are extreme and microalgae grow under stress, they synthesize and produce various secondary metabolites [11], [12], [18].

A serious concern about the cultivation of microalgae under stress conditions is the decrease of growth rates and consequently the decrease of the total production and productivity. However, this negative effect might be mitigated applying various techniques. One of the most suggested techniques is the cultivation of microalgae in multiple-stage process, in which in each stage optimum or appropriate conditions are applied. The most frequently suggested multiple-stage technique is the cultivation in two-stage systems, in which in the first stage optimum conditions are applied aiming the maximization of biomass production, while in the second stage, stress conditions are applied aiming the accumulation of the desired compound(s) [17], [19].

Nevertheless, the cultivation in multiple stages might consume more energy in comparison to the one-stage systems, especially in those systems, in which harvesting of biomass is essential for forwarding it to the next stage [18]

Change in cultural conditions may be used as a mechanism for the manipulation of metabolic pathways resulting in the redirection of cellular function to the production of desired products such as neutral lipids [11]. Optimization of growth and lipid yield is essential to the economic viability of production of biodiesel from microalgae. Lipid accumulation occurs naturally as a mechanism for energy storage during unfavorable conditions. The role of lipids in the growth of microalgae is as energy reserves and part of the structural components of the cell. Phospholipids and glycolipids are the primary components of cell wall structures and determine the fluidity of membranes under various conditions. This is achieved by being able to adapt quickly to changes in the environment by recycling of lipids and de novo synthesis [1]. Triacylglycerols (TAGs) are the primary storage components as energy reserves. The greater proportion of the lipids produced is TAGs which are produced as metabolic rate of microalgae slows [4]. Some microalgal species have high growth rates and the ability to produce high amounts of lipids under certain growth conditions. Lipid accumulation may be induced or effected by a variety of stress factors such as the removal or limitation of essential nutrients such as nitrogen as well as changes in inorganic carbon and light intensity [10], [13], [15]. Changes in cultural conditions may be used as a mechanism for the manipulation of metabolic pathways resulting in the redirection of cellular function to the production of desired products such as neutral lipid [4], [20].

Lipid accumulation generally has an antagonistic relationship to growth rate. Therefore it is important to determine the tradeoff between neutral lipid production and algal growth as part of the optimization for biodiesel production. E.g. nitrogen limitation has variable effects on different types of microalgae in terms of growth and cellular content. Amounts of lipid accumulation may be variable depending on the amount of nitrogen available [1], [17], [19], [20].

The temperature, in turn, greatly affects the lipid profile of microalgae, such that at low temperatures the unsaturation increases [17], [21]. In other hand, the degree of higher light intensities are other conditions which substantially favor the accumulation of triglycerides with high saturation profile where low intensities in turn promote the synthesis of highly unsaturated polar lipids structurally and functionally associated with membranes [14], [22], [23]. Salinity and pH are other

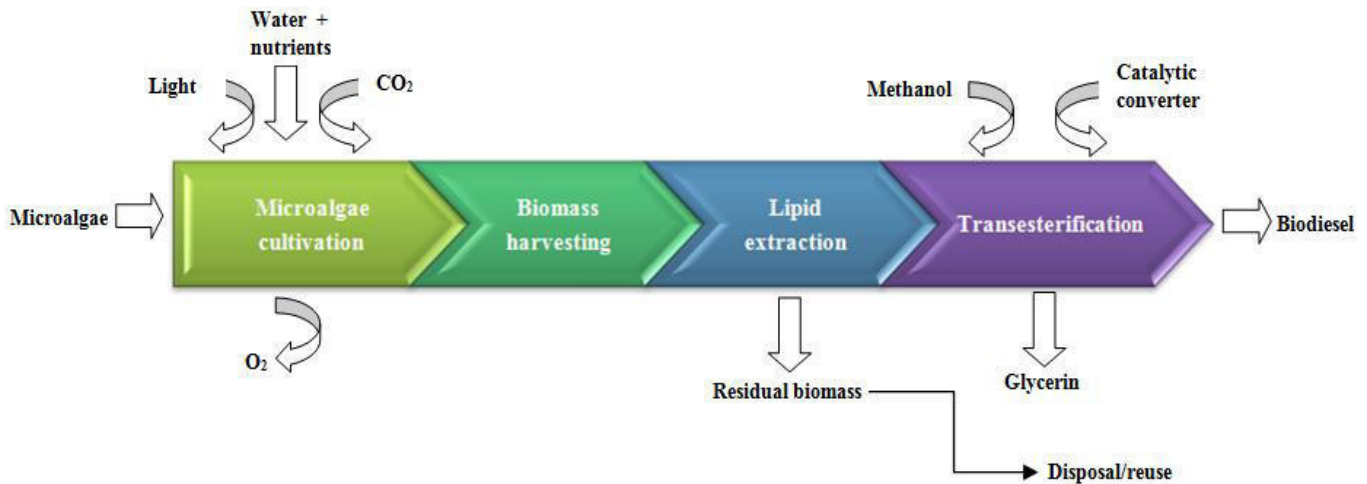
factors that modify lipid synthesis of various microalgae, however the type and amount of lipid produced also depends on the species and the amount of change of these variables [1], [4], [12].

A. Effect of light

Under natural growth conditions phototrophic algae absorb sunlight, and assimilate carbon dioxide from the air and nutrients from the aquatic habitats. Therefore, as far as possible, artificial production should attempt to replicate and enhance the optimum natural growth conditions. The use of natural conditions for commercial algae production has the advantage of using sunlight as a free natural resource. However, this may be limited by available sunlight due to diurnal cycles and the seasonal variations; thereby limiting the viability of commercial production to areas with high solar radiation [1], [22]. For outdoor algae production systems, light is generally the limiting factor. To address the limitations in natural growth conditions with sunlight, artificial means employing fluorescent lamps are almost exclusively used for the cultivation of phototrophic algae at pilot scale stages [23]. Artificial lighting allows for continuous production, but at significantly higher energy input. Frequently the electricity supply for artificial lighting is derived from fossil fuels thus negating the primary aim of developing a price-competitive fuel and increasing the systems carbon footprint [1].

The luminostat regime (harvesting system works by controlling the amount of light output from the reactor) has been proposed as a way to maximize light absorption and thus to increase the microalgae photosynthetic efficiency within photobioreactors (PBR) [24]. In this study, simulated outdoor light conditions were applied to a lab-scale PBR in order to evaluate the luminostat control under varying light conditions. The photon flux density leaving the reactor (PFD_{out}) was varied from 4 to 20 $\mu\text{mol photons m}^{-2}\text{s}^{-1}$ and the productivity and photosynthetic efficiency of *Chlorella sorokiniana* were assessed. Maximal volumetric productivity and biomass yield were found when PFD_{out} was maintained between 4 and 6 $\mu\text{mol photons m}^{-2}\text{s}^{-1}$. The reactor experiments were performed under nutrient replete conditions and light was the sole factor limiting growth. The daily light cycle on an east–west oriented vertical panel surface in June in Huelva (Spain, 37°15'0"North, 6°57'0" West) was simulated and applied to the PBR front side. The 14mm light-path panel PBR, with a working volume of 1.7 L was operated at the optimal growth temperature for *C. sorokiniana* of 37 ° C using a temperature-controlled water jacket [24].

Fig. 3. Stages of production of biodiesel from microalgae [19]



Under normal cultural growth conditions, e.g. with no nutrient stress, photosynthesis increases with an increase in light intensity until light saturation sets in, at which point the maximum growth rate will be attained. Photoinhibition and consequently decrease in microalgal growth rate is as a result of irradiance of the culture above the level of light saturation [3], [10], [16]. The outdoor production of microalgae therefore is also restricted by light limitation at the beginning, and end, of the day, and during the night period. Moreover, mutual shading of the cells at low sunlight levels or high biomass concentration will result in a dark zone inside the culture with negative rates of photosynthesis (respiration). This leads to a lower biomass productivity and lower overall photosynthetic efficiency [23], [25], [26].

Reference [25] developed the paper of studied the productivity of *Chlorella sorokiniana* in a short light-path (SLP) panel PBR under high irradiance. Under continuous illumination of $2,100 \mu\text{mol photons m}^{-2} \text{s}^{-1}$ with red light emitting diodes (LEDs) the effect of dilution rate on PBR productivity was studied. The light intensity used in this work is similar to the maximal irradiance on a horizontal surface at latitudes lower than 37° . During all chemostat experiments temperature was set at $37 \pm 1^\circ \text{C}$ and pH maintained at 6.7. The reactor was illuminated with a red LEDs panel composed by 128 red LEDs. The maximal productivity was $7.7 \text{gdw m}^{-2} \text{h}^{-1}$ (m^2 of illuminated PBR surface) and the photosynthetic efficiency was 1.0 g dw per mol photons. The conclusion was that this biomass yield on light energy is high but still lower than the theoretical maximal yield of 1.8 gdw mol photons which must be related to photosaturation and thermal dissipation of absorbed light energy.

There are very few studies under variation of stress parameters in culture that have been made during the daily cycle of light, almost all studies to maximize the productivity of lipids under stress use a fixed amount of light and different

photoperiods without considering the daily light cycle and these conditions are very difficult to reproduce and control in natural settings and large-scale cultures.

The advantage of performing the studies with fixed photoperiod conditions allows to find the effect of the parameters of cultivation and which has influence on the lipid productivity without having to face the problem of photoinhibition or photorespiration that usually occurs under high solar irradiance as occur when considered daily light cycle. But it is necessary to develop studies that consider natural setting and natural light in order to increase the feasibility of microalgas biodiesel production.

B. Effect of nitrogen depletion

Lipid accumulation in microalgae occurs when a nutrient is exhausted from the medium or becomes the growth limiting factor.

Nitrogen limitation or depletion is commonly used for the induction or increase of lipid content in microalgae and is regarded as the most effective method [18].

The nitrogen limitation which not only results in the accumulation of lipids, but also results in a gradual change of lipid composition from free fatty acids to triacylglycerol (TAG). TAGs are more useful for conversion to biodiesel. Cell proliferation is prevented but carbon is still assimilated by the cell and converted to TAG lipids that are stored within existing cells thereby increasing the concentration.

However, increasing lipid accumulation will not always result in increased lipid productivity as biomass productivity and lipid accumulation are not necessarily correlated. Lipid accumulation refers to increased concentration of lipids within the microalgae cells without consideration of the overall biomass production. Lipid productivity takes into account both the lipid concentration within cells and the biomass produced

by these cells and is therefore a more useful indicator of the potential costs of liquid biofuel production.

Research conducted to induce lipid synthesis small scale agree that under limiting nitrogen growth conditions is reduced, while there is great variation in lipid content and fatty acid profile [19].

In an experimental work were observed the effect of nitrogen concentration on the lipid accumulation showed that 22.5%, 20.0%, 18.5% and 15.9% of lipid contents were obtained at KNO_3 concentrations of 0.2, 1.0, 3.0 and 5.0 mM, respectively. It demonstrated that the lipid content decreased with the increase of nitrogen concentration KNO_3 consumption of *Chlorella vulgaris* (Feed gas, 1.0% CO_2 ; gas rate, 1.2 L/min; illumination, continuous; light intensity, $60 \mu\text{mol photons m}^{-2} \text{s}^{-1}$ temperature, 25°C) [20].

Chlorella sp. was evaluated for ability to yield high of biomass and lipid productivity under normal and various nutrient-deprived conditions (nitrogen, phosphate-potassium, iron, and all three combined). Under normal conditions, after 20 days of cultivation in Chu10 medium, yielded a biomass of $2.58 \pm 0.07 \text{ g/L}$, with lipid content of $312.16 \pm 2.38 \text{ mg/g}$. The organism was able to respond with different levels of lipid accumulation. Among the various post-harvest treatments, nitrogen deprivation yielded the highest lipid productivity of $53.96 \pm 0.63 \text{ mg/Ld}$, followed by the combined deprivation condition ($49.16 \pm 1.36 \text{ mg/L d}$). FAME profiles of the isolate were found to meet the requirements of international standards for biodiesel. The study leads to the conclusion that nitrogen starvation as post-harvest treatment would be suitable for gaining maximum biomass productivity, and lipid content of high quality fatty acids (conditions included white photo-fluorescence at a rate of $300 \mu\text{mol m}^{-2} \text{s}^{-1}$, with 12/12 h light/dark photoperiod, at 24°C) [14].

Reference [26] developed a research with the marine microalgae *Dunaliella tertiolecta* was used as a model organism and a profile of its nutritional requirements was determined. Inorganic phosphate (PO_4) and trace elements: cobalt (Co^{2+}), iron (Fe^{3+}), molybdenum (Mo^{2+}) and manganese (Mn^{2+}) were identified as required for algae optimum growth (The temperature of the culture was maintained at 23°C and pH was not controlled, algae cultures were set up in 650 mL culture flasks illuminated with one 12 inch, 8 watt fluorescent lamp and supplied with a feed of air/ CO_2 at 4%).

Cultures deprived of nitrogen, (as nitrate), iron, and to a lesser extent, cobalt, accumulated substantially more lipid than control cells by day 3. Cultures deprived of other nutrients did not accumulate high levels of lipid.

These studies confirm that nitrogen as the main regulator in the growth and accumulation of lipids.

Lipids accumulation under nitrogen starvation growth condition is the most studied culture condition. In overall, this kind of studies have been realized under one-factor-at-a-time (OFAT) design, i.e. other parameters like temperature, light and pH remained constants.

C. Effect of temperature

Temperature variations cause changes in growth rate, in the lipid content and composition of fatty acids in the cell, in addition to the effects are species specific [10], [17], [19].

In accordance with reference [17], variations of temperature and decrease in the concentration of nitrate in the medium continuous photon flux density of $70.0 \mu\text{mol m}^{-2} \text{s}^{-1}$) resulted in a significant change in cell composition (*Nannochloropsis oculata* and *Chlorella vulgaris*) favoring the accumulation of lipid components in both microalgae during the batch growths. A decrease in the growth temperature from 30 to 25°C led to an increase in the lipid content of *C. vulgaris* from 5.9 to 14.7%, while the rate of growth remained unchanged and, as a result, lipid productivity increased from 8 to $20 \text{ mgL}^{-1} \text{ day}^{-1}$. Even in *N. oculata*, there was an increase in the lipid component passing from 25°C (13.9%) to suboptimal temperature conditions (7.9% at 20°C and 14.9% at 15°C). However, also the growth rate was significantly affected by changes in temperature, thus leading a lipid productivity which was approximately the same for all three growth runs.

D. Effect of pH

The range of optimal pH for algae varies with species. The optimal level of growth for many freshwater microalgae is close to 8 and deviation from this level subsequently leads to reduction in biomass. Microalgae such as *Amphora sp.* and *Ankistrodesmus sp.* have been shown to grow uninhibited at pH 9 and 10 respectively [4], [27].

Reference [27] developed a work with variation of pH and two treatments (pH-regulation group and control group) were designed. The findings of the study prove that pH adjustment using acetic acid is efficient in cultivating *C. zofingiensis* in wastewater in winter for biodiesel production, the culture was exposed to sunlight in a daytime of December (light intensity of $835 \pm 450 \mu\text{mol m}^{-2} \text{s}^{-1}$), the range of average daily surrounding air temperature was from 6.0 to 17.2°C ; The results showed that higher biomass productivity of 66.94 mg/Ld with specific growth rate of 0.260 day^{-1} was achieved in the pH-regulation group. The lipid content was much higher when using acetic acid to regulate pH, and the relative lipid productivity reached 37.48 mg/L . The biodiesel yield in the pH-regulated group was 19.44% of dry weight, with 16–18 carbons as the most abundant composition for fatty acid methyl esters.

Finally, pH can also affect the lipid metabolism. Low pH stress in *Chlamydomonas sp.* increased the total lipid content compared with higher pH values [19]. However in *Chlorella spp.* alkaline pH resulted in TAGs accumulation [4], [19].

IV. FROM LABORATORY TO A LARGE-SCALE CULTIVATION

The move from laboratory to large-scale microalgae cultivation requires careful planning. It is imperative to do extensive pre-pilot demonstration trials and formulate a suitable trajectory for possible data extrapolation for large scale

experimental designs [4], [12], [22]. It is imperative to do a full optimization study at lab scale before considering scaling up. The volume at which large scale operations capacity must be established and the correct amount of seed culture for inoculation must be calculated [12], [27], [28].

All the details with regard to experimental design, data collation and parameter monitoring must be properly scheduled. At this point, the pilot scale experiments will enable the assessment of biomass and oil yields [4].

The one-factor-at-a-time approach for optimization experiments is frequently used for optimization studies despite being associated with drawbacks such as being time consuming and labour intensive and this strategy do not let to know the effect of interaction between factors. To date some workers have used the response surface methodology for optimization studies and this is reported to be fast and a large set of experiments can be done simultaneously [12], [28], [29].

Solar irradiance also varies throughout the year and outdoor cultivation clearly leads to a more complex operation process than during continuous cultivation based on artificial light [4], [24], [25].

Therefore, the accumulation of a specific compound can be triggered using more than one stress factors and the topic of the optimization of a desirable compound under stress conditions and natural settings is of particular significance and more research is needed.

V. FUTURE PROSPECTS AND CONCLUSION

Were reviewed separately each of the factors that have shown influence on lipid productivity, but these studies have been performed varying one-factor-at-a-time while other factors are fixed, this prevents understand the interactions that exist between factors and does not reveal its effect on the response variable. Moreover, the studies were performed under artificial light without considering what effect it would have if instead it simulates a day of daylight.

In terms of seeking to optimize the process is imperative to consider to be performed studies that seek to optimize variables culture but considering daylight conditions and other natural settings as the main criterion, it could not be done in otherwise since the energy to keep growing under a regime artificial light would not be profitable. Of course, this should have other considerations, for example the effect of photosaturation and an increase in culture temperature with high irradiance, effects of photorespiration and affectation on biomass productivity, the solar irradiance also varies throughout the year and outdoor cultivation, etc. All of these situations must be considered.

Certainly, research is needed to find strategies and solutions to each of these obstacles. We intend to develop a laboratory scale work where seeks to optimize the productivity of lipids in microalgae cultivation varying stress conditions and simulate a system of natural light into two different seasons of the year under natural photoperiod.

The goal is to obtain the information necessary to scale the process from laboratory to pilot plant process and after continue boosted the research to get a large-scale process.

Considering that other stages of the process represent a huge energy cost, any energy savings in this way that can be achieved in the cultivation is very relevant to achieve the profitability on the industrial scale production of biofuels from microalgae.

REFERENCES

- [1] L. Brennan and P. Owende, "Biofuels from microalgae-A review of technologies for production, processing, and extractions of biofuels and co-products," *Renew. Sustain. Energy Rev.*, vol. 14, pp. 557–577, 2010.
- [2] M. Vanthoor-koopmans, R. H. Wijffels, M. J. Barbosa, and M. H. M. Eppink, "Author 's personal copy Bioresource Technology Biorefinery of microalgae for food and fuel."
- [3] J. Liu, Y. Zhu, Y. Tao, Y. Zhang, A. Li, T. Li, M. Sang, and C. Zhang, "Freshwater microalgae harvested via flocculation induced by pH decrease.," *Biotechnol. Biofuels*, vol. 6, p. 98, 2013.
- [4] I. Rawat, R. Ranjith Kumar, T. Mutanda, and F. Bux, "Biodiesel from microalgae: A critical evaluation from laboratory to large scale production," *Appl. Energy*, vol. 103, pp. 444–467, 2013.
- [5] R. H. Wijffels and M. J. Barbosa, "An outlook on microalgal biofuels.," *Science*, vol. 329, pp. 796–799, 2010.
- [6] A. Demirbas and M. Fatih Demirbas, "Importance of algae oil as a source of biodiesel," *Energy Convers. Manag.*, vol. 52, no. 1, pp. 163–170, 2011.
- [7] S. P. Cuellar-Bermudez, J. S. Garcia-Perez, B. E. Rittmann, and R. Parra-Saldivar, "Photosynthetic bioenergy utilizing CO₂: an approach on flue gases utilization for third generation biofuels," *J. Clean. Prod.*, pp. 1–13, 2014.
- [8] L. D. Zhu, E. Hiltunen, E. Antila, J. J. Zhong, Z. H. Yuan, and Z. M. Wang, "Microalgal biofuels: Flexible bioenergies for sustainable development," *Renew. Sustain. Energy Rev.*, vol. 30, pp. 1035–1046, 2014.
- [9] A. Demirbas, "Progress and recent trends in biodiesel fuels," *Energy Convers. Manag.*, vol. 50, no. 1, pp. 14–34, 2009.
- [10] J. P. Maity, J. Bundschuh, C. Y. Chen, and P. Bhattacharya, "Microalgae for third generation biofuel production, mitigation of greenhouse gas emissions and wastewater treatment: Present and future perspectives - A mini review," *Energy*, 2014.
- [11] Y. Chisti, "Biodiesel from microalgae beats bioethanol," *Trends Biotechnol.*, vol. 26, pp. 126–131, 2008.
- [12] M. R. Bilal, V. Discart, D. Vandamme, I. Foubert, K. Muylaert, and I. F. J. Vankelecom, "Coupled cultivation and pre-harvesting of microalgae in a membrane photobioreactor (MPBR)," *Bioresour. Technol.*, vol. 155, pp. 410–417, 2014.
- [13] S. a. Choi, J. S. Lee, Y. K. Oh, M. J. Jeong, S. W. Kim, and J. Y. Park, "Lipid extraction from *Chlorella vulgaris* by molten-salt/ionic-liquid mixtures," *Algal Res.*, vol. 3, pp. 44–48, 2014.
- [14] R. Praveenkumar, K. Shameera, G. Mahalakshmi, M. A. Akbarsha, and N. Thajuddin, "Influence of nutrient deprivations on lipid

- accumulation in a dominant indigenous microalga *Chlorella* sp., BUM11008: Evaluation for biodiesel production,” *Biomass and Bioenergy*, vol. 37, pp. 60–66, 2012.
- [15] X. Gao, Y. Yu, and H. Wu, “Life cycle energy and carbon footprints of microalgal biodiesel production in western Australia: A comparison of byproducts utilization strategies,” *ACS Sustain. Chem. Eng.*, vol. 1, pp. 1371–1380, 2013.
- [16] L. B. Brentner, M. J. Eckelman, and J. B. Zimmerman, “Combinatorial life cycle assessment to inform process design of industrial production of algal biodiesel,” *Environ. Sci. Technol.*, vol. 45, pp. 7060–7067, 2011.
- [17] A. Converti, A. a. Casazza, E. Y. Ortiz, P. Perego, and M. Del Borghi, “Effect of temperature and nitrogen concentration on the growth and lipid content of *Nannochloropsis oculata* and *Chlorella vulgaris* for biodiesel production,” *Chem. Eng. Process. Process Intensif.*, vol. 48, pp. 1146–1151, 2009.
- [18] G. Markou and E. Nerantzis, “Microalgae for high-value compounds and biofuels production: A review with focus on cultivation under stress conditions,” *Biotechnol. Adv.*, vol. 31, no. 8, pp. 1532–1542, 2013.
- [19] M. Trinidad, A. Pe, A. D. E. Jes, N. E. Z. Rold, R. O. Ca, I. Villanueva, and E. Avanzados, “Producción de biodiesel a partir de microalgas: Biodiesel Production from Microalgae,” *Acta Biológica Colomb.*, vol. 18, pp. 43–68, 2013.
- [20] J. M. Lv, L. H. Cheng, X. H. Xu, L. Zhang, and H. L. Chen, “Enhanced lipid production of *Chlorella vulgaris* by adjustment of cultivation conditions,” *Bioresour. Technol.*, vol. 101, no. 17, pp. 6797–6804, 2010.
- [21] V. Bhola, R. Desikan, S. K. Santosh, K. Subburamu, E. Sanniyasi, and F. Bux, “Effects of parameters affecting biomass yield and thermal behaviour of *Chlorella vulgaris*,” *J. Biosci. Bioeng.*, vol. 111, no. 3, pp. 377–382, 2011.
- [22] N. T. Eriksen, “The technology of microalgal culturing,” *Biotechnol. Lett.*, vol. 30, pp. 1525–1536, 2008.
- [23] a. Muller-Feuga, R. Le Guedes, a. Herve, and P. Durand, “Comparison of artificial light photobioreactors and other production systems using *Porphyridium cruentum*,” *J. Appl. Phycol.*, vol. 10, pp. 83–90, 1998.
- [24] M. Cuaresma, M. Janssen, E. J. van den End, C. Vílchez, and R. H. Wijffels, “Luminostat operation: A tool to maximize microalgae photosynthetic efficiency in photobioreactors during the daily light cycle?,” *Bioresour. Technol.*, vol. 102, pp. 7871–7878, 2011.
- [25] M. Cuaresma, M. Janssen, C. Vílchez, and R. H. Wijffels, “Productivity of *Chlorella sorokiniana* in a short light-path (SLP) panel photobioreactor under high irradiance,” *Biotechnol. Bioeng.*, vol. 104, no. 2, pp. 352–359, 2009.
- [26] M. Chen, H. Tang, H. Ma, T. C. Holland, K. Y. S. Ng, and S. O. Salley, “Effect of nutrients on growth and lipid accumulation in the green algae *Dunaliella tertiolecta*,” *Bioresour. Technol.*, vol. 102, no. 2, pp. 1649–1655, 2011.
- [27] L. Zhu, E. Hiltunen, Q. Shu, W. Zhou, Z. Li, and Z. Wang, “Biodiesel production from algae cultivated in winter with artificial wastewater through pH regulation by acetic acid,” *Appl. Energy*, vol. 128, pp. 103–110, 2014.
- [28] J.-J. Chen, Y.-R. Li, and W.-L. Lai, “Application of experimental design methodology for optimization of biofuel production from microalgae,” *Biomass and Bioenergy*, vol. 64, pp. 11–19, 2014.
- [29] C. Y. Chen, K. L. Yeh, R. Aisyah, D. J. Lee, and J. S. Chang, “Cultivation, photobioreactor design and harvesting of microalgae for biodiesel production: A critical review,” *Bioresour. Technol.*, vol. 102, no. 1, pp. 71–81, 2011.

Evaluation of 3D electrode in a membraneless microdevice for energy conversion

C. Farias-Zuñiga¹, E. Ortiz-Ortega¹, Marco A. González¹, J. Galindo-de-la-Rosa¹, L.G. Arriaga², A.U. Chavez-Ramírez² and J. Ledesma-García.¹

¹*Facultad de Ingeniería, División de Investigación y Posgrado, Universidad Autónoma de Querétaro, Centro Universitario Cerro de las Campanas, Querétaro, Qro., C.P. 76010, México.*

²*Centro de Investigación y Desarrollo Tecnológico en Electroquímica, Pedro Escobedo, Qro., C.P. 76703, México.*

^{1*} janet.ledesma@uaq.mx _Tel: + (442)1921200 EXT 65411

Abstract— In fuel cells membraneless the use of three-dimensional microporous electrodes increases the geometric area, allowing increase the power density. Applications that can range from future biomedical applications to replacement of batteries are now achievable by the incorporation of electronic interfaces based on boosters.

Keywords: Fuel cell, microelectronic, electrodes.

I. INTRODUCTION

Recent increasing demands on small-scale power sources for portable electronics have significantly impeded the interest in miniaturized fuel cells. [1] The fuel cells, which defined as electrochemical devices that convert the chemical energy of a fuel into electrical energy. Among the different types of equipment that can meet this energy demand, we can find a microfluidic fuel cells, which are characterized by output power and reaction sites confined in a channel with measures in the range of 1-1000 μm without physical separation as a membrane. This multidisciplinary field lies at the interface of engineering, chemistry and biology and has a wide range of applications including drug discovery, biomedical analyses, genetics, proteomics, and energy conversion. [2].

Also within the extensive research on microfluidic cells can find use with different types of fuels such as glucose [2] [4], formic acid or glycerol, optimization at different concentrations of fuel [5] and its application [6], to which now intend to give them uses from diagnostic systems, measurement and medical treatment bioinstrumentation systems for organic fuels or purposes as future replacements for conventional batteries in the case of inorganic fuels taking into that a fuel cell produces electricity from an external source of fuel and oxygen as opposed to the limited storage capacity of energy possessed by a battery, giving at the microfuel cell a great advantage.

However, amount of energy produced is not enough for most electronic devices on the market today. For that reason DC / DC boosters are employed as electronic interfaces. Those devices were fabricated and tested for low power sources

such as microbial fuel cells in which the typical voltage of 0.3V obtained was increased to 3V obtained [7]. Another successfully work that have integrated booster with a battery was developed by Du in 2011 [8]. However, these studies have not integrated into a single component the producer of energy and its booster, so in this paper the idea of using fiberglass replacement of acrylic for the realization of cells it is proposed, with the advantage that the fiberglass is coated with a thin layer of copper where the booster circuit is constituted to thus be able to have a single device.

However the few works so far reported use these booster solutions coupled to a low power source, this work present the results of the evaluation of three-dimensional electrodes of Toray paper carbon microfibers tested in a membraneless microfuel cells, and its integration with a microelectronic interface.

II. EXPERIMENTAL

A. Design of microfuel cell

Fiberglass plates used as supporting plates were designed and patterned employing a computer numerical control (CNC) micromachining system. The cell design used in this study is inherited from reference [9]. 3D electrodes were made using commercial Toray paper carbon, the electrocatalysts were deposited onto 3D electrode surface by spray technique Pd/C (ETEK, 20 wt %) and Pt/C (ETEK, 20 wt %) as the anode and cathode electrocatalysts, respectively, with a base metal loading of 0.6 mg.

B. Fuel and Oxidant

Anolyte and catholyte were prepared using 0.5 M. H_2SO_4 as the electrolyte. The cathodic stream was bubbled with high purity oxygen before injected into the cell, where it was combined with oxygen from air in the air-breathing cathode (open window of 0.22 cm^2), and the anodic steam was mixed with formic acid (1.5 M) and bubbled with nitrogen for 15 min.

C. Construcción a voltage boost

The voltage booster used consists in an integrated TS 3310 model (Touchstone Semiconductors), with an array of resistors, capacitors and inductors, connected together through a series of tracks delineated by a microCNC system on one side of the fiberglass cell. As can be seen in Fig. 1.

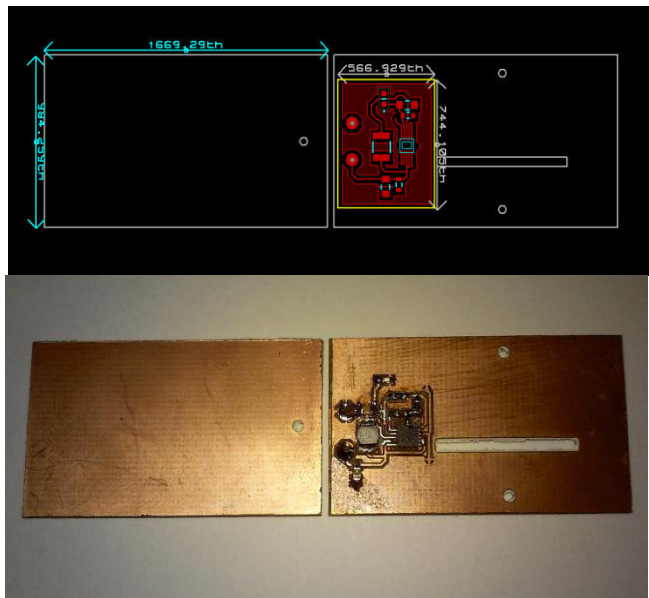


Fig. 1. - Design and construction of booster in fiberglass coated with copper.

III. RESULTS AND DISCUSSION

The performance evaluation of the cell was constructed as follows, you must first let it run until the open circuit potential (OCP). This stabilized, remaining at 0.9 V, once there we proceeded to give you three characterizations: density power, endurance and stability of the system. These characterizations were performed in the following order, first was made a measurement of resistance, then a discharge and finally an analysis of its stability.

A. Polarization curves

The power density characterization was performed by shocks to the micro fuel cell, shown in 3 different tests described below:

Test 1; when stabilize the OCP.

Test 2; after connecting the voltage booster circuit with a LED for 20 minutes.

Test 3; after the stability test with flow 450mV.

Finding the following results. test 1 (Fig. 2) shows a power density of 77 mW cm⁻², which is very good outcome bought with the results of similar cells [9], as shown in test 2, 20 minutes after the system show 73 mW cm⁻² due to this stabilization. Finally in test 3, a value of 75 mW cm⁻² was found, which compared with tests 1 and 2 are very similar. Showing the measurement of these parameters which is the power density of the microcell after being subjected to

different loading conditions and flow it is noteworthy that the tests are performed one after others, also be noted that the membraneless device using 3D electrodes whit integrated LED worked by 20 minutes, this way it demonstrated the device can operate continuously (Fig. 5).

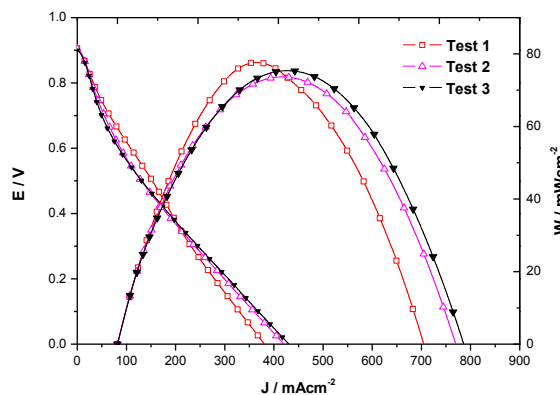


Fig. 2. -Polarization and power density curves after four testes at 1.5M HCOOH formic acid fuel, flow rate of 6ml/h at 25 °C at room temperature.

B. Resistance

For the characterization of resistance, we proceeded as in the characterization of polarization curves, using three testes previously described in the previous section, and found the following results (Fig. 3), in test 1 a resistance of 40 Ω which is within results expected to not be so resistant comparing it with Moreno Zuria [5] finally tests 2 and 3 were performed giving similar values 37 and 32 Ω, respectively. The impedance values practically are similar after the tests therefore the lifetime of membraneless device increase without affecting the performance.

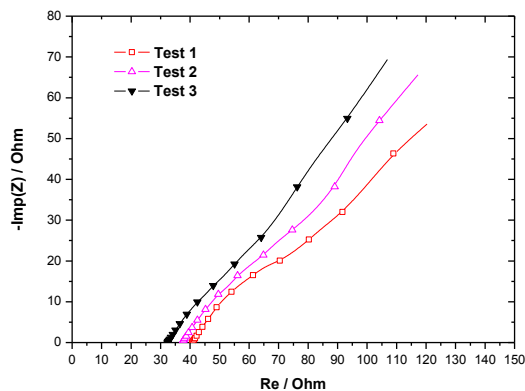


Fig. 3. Impedance curves in four tests at 1.5M HCOOH formic acid fuel in 6ml/h flow rate at 25 °C under atmospheric pressure

C. Chronoamperometry

Finally, stability tests of 20 min. were performed by chronoamperometry in the cell at 450 mV, with flow at 6 mlh⁻¹, to see how is your right through time behavior, demonstrating that formation of CO₂ over time promotes certain loss of current density, which is a challenge to solve to improve stability. (Fig. 4). Likewise a test voltage stability of the microcell connected to the booster was performed. Showing that although the voltage tends to decrease, the device continues to operate in an appropriate way, as can be seen in Fig 5.

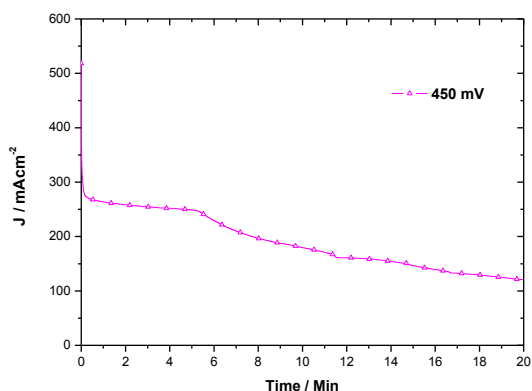


Fig. 4. Chronoamperometry



Fig. 5. - Curves of voltage with booster.

IV. CONCLUSION

In summary, this paper gave an evaluation of how the use of 3D electrodes in membraneless devices allows to increase the availability of catalysts and consequently the output power, so it could give a more tangible fuel cells by adding an elevator application voltage, achieving integration of components into a single device permitting this make way for future more complex applications.. (Fig. 6)

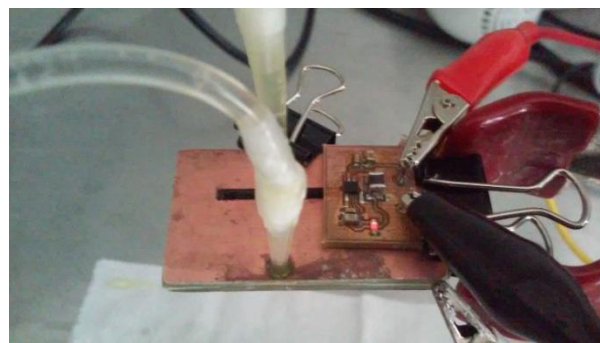


Fig. 6. Fuel cell and booster integrated in a chip lighting a LED

REFERENCES

- [1] Kjeang E., N. Djilali y D. Sinton, 2009, Microfluidic fuel cells: A review, *J. PowerSources*, 186, 353-369.
- [2] J. Clerk Maxwell, *A Treatise on Electricity and Magnetism*, 3rd ed., vol. 2. Oxford: Clarendon, 1892, pp.68–73.
- [3] Cuevas-Muñiz, F. M., et al, 2012, Glucose microfluidic fuel cell based on silver bimetallic selective catalysts for on-chip applications, *J. Power Sources* 216, 297-303.
- [4] Morse J.D., 2007, Micro-fuel cell power sources, *International Journal of Energy Research*, 31, 576–602.
- [5] Moreno-Zuria, A., et al, 2014, Direct formic acid microfluidic fuel cell design and performance evolution, *J. Power Sources* 269, 783-788.
- [6] Kundu A, et al, 2007, Micro-fuel cells—Current development and applications, *J. Power Sources* 170, 67–78.
- [7] Wu, Peter K., 2011, A low power DC/DC booster circuit designed for microbial fuel cells. *Process Biochemistry*, DOI: 10.1016/j.procbio.2011.06.003.
- [8] Du, Yang, et al, 2011, Battery-integrated boost converter utilizing distributed MPPT configuration for photovoltaic systems. *Solar Energy*, 85, 1992–2002.
- [9] E. Ortiz-Ortega, et al, 2014, A nanofluidic direct formic acid fuel cell with a combined flow-through and air-breathing electrode for high performance. *Lab on a chip*. DOI: 10.1039/c4lc01010h

Synthesis of hydroxyapatite nanostructures by microwave assisted hydrothermal method

Luis A. Baltazar^{#1}, Velázquez-Castillo R.^{#2}, Alanís-Gómez R.^{#2}, Cabrera-Torres J.L.^{#3}, Néstor Méndez^{#4}

^{#1} *Facultad de Ingeniería, Universidad Autónoma de Querétaro, Cerro de las Campanas s/n, C.P. 76010 Querétaro, Qro., México*

¹ luis.armandoo10@gmail.com

^{#2} *División de Investigación y Posgrado, Facultad de Ingeniería, Universidad Autónoma de Querétaro, Cerro de las Campanas s/n, C.P. 76010 Querétaro, Qro., México*

² rodrigo.velazquez@uaq.mx

² j.rafael.alanis@gmail.com

^{#3} *CENAM, km 4.5 Carretera a los Cués, C.P. 76246, El Marqués, Querétaro, México*

³ j.cabrera@cenam.mx

^{#4} *Centro de Física Aplicada y Tecnología Avanzada, Universidad Nacional Autónoma de México, A. P. 1-1010, Querétaro, Qro. 76000, México*

⁴ nestorm_3@yahoo.com.mx

Abstract— Hydroxyapatite (HAp) nanofibers have been synthesized by microwave heating using $\text{Ca}(\text{NO}_3)_2$, glutamic acid, K_2HPO_4 and KOH as precursors. The precursor concentration was the same in all experiments, also was varied temperature, heating time, the ramp and the retting time in each reaction. Quartz tubes were used to place the precursor mixture to microwave heating, which makes it easier to obtain such Hap nanostructures. The following characterization techniques X-ray Diffraction (XRD), X-ray fluorescence (XRF), Scanning Electron Microscopy (SEM) and Transmission Electronic Microscopy (TEM) were used to assess the HAp phase obtained, the Ca/P ratio, morphology and nanostructure of the synthesized structures were used.

Keywords—hydroxyapatite; microwave heating; nanofiber; nanostructure

I. INTRODUCTION (HEADING 1)

Synthetic Hydroxyapatite (HAp), $\text{Ca}_{10}(\text{PO}_4)_6(\text{OH})_2$, is a bioactive material that is chemically compatible with biological apatite in both, composition and structure. This is the main mineral constituent of hard human tissues such bones and teeth, and possesses excellent biocompatibility and bioactivity, HAp has been widely used in health-related fields as a material for damaged bones or teeth, important implant and scaffold materials and drug delivery agents [3]. Bioactivity is influenced by several factors such as the Ca/P ratio, content of carbonate or other ions, crystal size, morphology and sample texture [1].

Natural bone minerals are nanostructured non-stoichiometric Hap of dimensions 20 nm in diameter and 50 nm long. Nanocrystalline HAp has proved to be of greater biological efficacy in terms of osteoblast adhesion, proliferation, osseo-integration and formation of new bone on its surface [1].

Different methods have been used for nanocrystalline HAp synthesis such as hydrothermal, mechanochemical, electrospinning, chemical precipitation, and microwave irradiation can be effectively used for fabrication of Nanostructures HAp. Depending upon the technique, materials with various morphology, stoichiometry, or level or crystallinity have been obtained [1-2].

Even though various synthesis methods have been used to fabricate nanosized HAp structures, there are intensive interests to find mild and rapid ways for synthesis of pure HAp nanoparticles. Microwave synthesis is a fast, simple and efficient method to prepare nanosized inorganic materials. Compared with conventional methods, microwave synthesis has the advantages of rapid growth, small particle size and narrow particle size distribution due to fast homogenous nucleation. Microwaves play an important role in reactions in aqueous media, increasing the yield of precipitations, and have been used for preparing HAp in less than 45 min. Precipitation of nanosized HAp using microwave irradiation has also been reported. The thermal stability of microwave synthesized HAp increases with increases in the aging time, microwave irradiation time and power [1-3].

Many efforts have been aimed to produce HAp with controlled morphology and dimension using this type of energy source. In addition, the used of pressured Teflon or quartz vessels in combination with a heating by microwaves helps maintaining homogeneous temperature and pressure in the whole reacting mixture bulk and as a consequence, the crystal growth is easier to control obtaining HAp nanostructures with controlled dimension and with a preferential crystal orientation [3].

The main objectives of this research are the obtaining of HAp nanofiber with diameters in the order of nanometers and lengths of micrometers. The HAp nanostructures will be used for the synthesis of a composite biomaterial which has potential applications in medicine and odontology [3].

II. MATERIALS AND METHODS

A. Synthesis

For the synthesis of HAp by microwave assisted hydrothermal method, the reacting mixtures were prepared in two steps. Initially, one solution made of glutamic acid [$C_5H_9NO_4 \cdot H_2O$] and calcium nitrate [$Ca(NO_3)_2 \cdot 4H_2O$] was prepared in tri-distilled water. The two components were dissolved by mechanical agitation during 2 hours at $60^\circ C$ [2]. In other hand, other solution of monobasic potassium phosphate [KH_2PO_4] mixed with potassium hydroxide [KOH] was prepared in tri-distilled water

Finally, both solutions were mixed and this reacting mixture was spilled inside quartz vessels at once. Each vessel contained 50 mL of the mixture which were closed immediately and placed within a microwave oven (Synthos 3000 by Anton Paar). The power used in the oven was 1200 W. All synthesis reactions were carried out at $170^\circ C$. The concentration of all reagents remained constant in the reacting mixture to evaluate its possible effect on the morphology and microstructure of HAp nanostructures. The Table I summarizes the chemical composition of the different reacting mixtures used in this research.

The heating rate, the reaction time and the cooling time as shown in Table X, these conditions were varied to observe possible changes in the morphology of the HAp nanostructures. After heat treatment the samples were oven dried at room temperature for 24 h for further characterization.

B. Characterization

In order to identify which HAp crystal phase was obtained, each of the HAp nanostructures synthesized were analyzed by X-Ray diffraction by powder (XRD) using a D8 Advance diffractometer built by Bruker. The operation condition in the diffractometer were 30 kV and 30 mA using the CuK_{α} radiation with a wavelength of $\lambda = 1.5406 \text{ \AA}$. The measurements were made from 10° through 90° on a 2θ scale with a step size of 0.05° .

In addition, observations of the morphology and microstructure of the samples were made using a scanning electron microscope JEOL JSM-6390 LV. The accelerating voltage employed in the microscope was 20 kV and all the images were formed from secondary electrons.

Morphology and microstructure were observed using a JEOL JEM-2100F using 120 kV as accelerating voltage. Moreover most of the images were analyzed using the software Digital Micrograph by Gatan in order to analyze the HAp nanostructure of nanofibers.

TABLE I.
FORMULATION OF REACTING MIXTURES AND REACTION CONDITIONS

Reacting	Quantity (gr)	Heating rate (min)	Cooling time (min)
Glutamic acid	1.144	15	10
Calcium nitrate	4	10	15
Monobasic potassium phosphate	0.9272	15	15
Potassium hydroxide	0.736	15	10

XRF analysis was performed to determine the Ca / P ratio of HAp samples and to determine the presence of any impurity substance or residual precursors. The samples were dispersed in 1 mL of isopropyl alcohol as dispersing agent and iron was added as internal standard.

III. RESULTS AND DISCUSSION

The XRD results confirmed the obtaining of synthetic HAp crystals. Phase identification was made by comparison with some powder diffraction files (PDF's) corresponding to different synthetic HAp phases. The more similar phases were those corresponding to the PDF's 86-1199 and 86-1203. All samples synthesized produced alike XRD results which showed in the fig. 1. The most relevant is the signal at 32.65° of 2θ which is related to the planes (300). This signal is more intense than that at 31.60° corresponding to the planes (211) which is the most intense signal in the PDF's. As a consequence, the abundance of planes (300) is indicative that there is a preferential crystal orientation in the [300] direction in the HAp nanostructures.

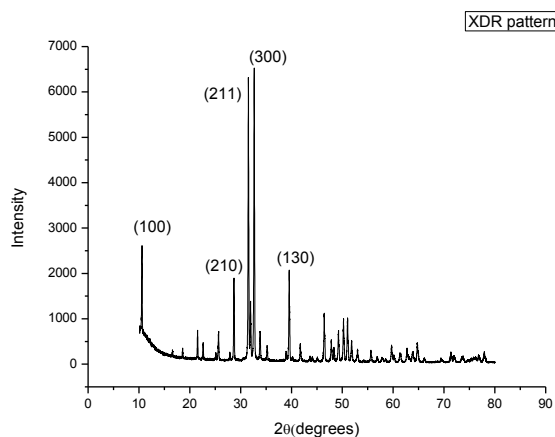


Fig 1 X-Ray diffraction pattern by powders of the HAp samples by identification of the HAp phases.

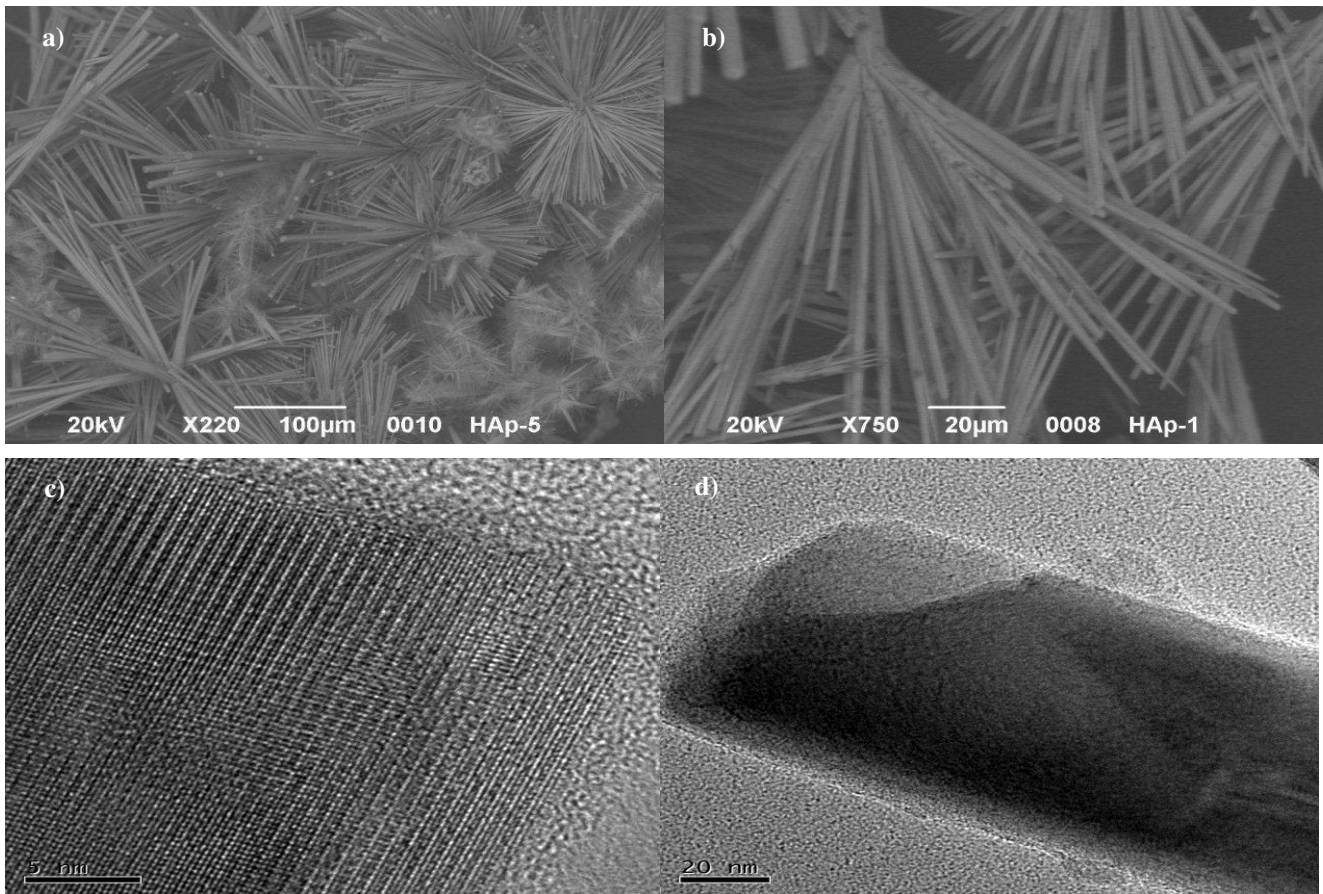


Fig 2 Micrographs of Nanofibers obtained by: SEM a) and b) showing morphology and topology of Nanofibers, and HREM c) displaying the atomic array of the HAp crystal structure and d) a detail of one nanofiber morphology.

Observations through SEM revealed that from all the synthesis reactions, nanofiber structures were obtained with a homogeneous diameter as can be seen in figures 2a and 2b. The length of the nanofibers varied as a function of reaction time, the longer of reaction time, the larger of length in the nanofibers. The thickness also showed a small variation with the reaction time.

Samples of HAp nanofibers were observed by TEM. In the figure 2c is possible to see a periodic arrangement of lines which correspond to the HAp crystal structure. The regularity in the lines distribution is an evidence of a high crystallinity structure. Using the software Digital Micrograph by Gatan it was possible to determinate the distance between lines in the images and they were of 2.72\AA which corresponds to the interplanar distance among the (300). This result agrees to that found in the X-Ray diffraction.

The samples were analyzed by XRF to determine the Ca / P ratio, which is important in HAp structures. All the samples analyzed showed similar Ca / P ratios as those portrays in Table II.

TABLE II. Ca/P RATIO OF THE SYNTHESIZED SAMPLES

# Sample	%P	%Ca	Ca/P ratio
1	32.54	67.46	2.073
2	33.20	66.80	2.012
3	33.02	66.98	2.091
4	34.04	65.92	1.934

IV. CONCLUSIONS

HAp nanostructures were synthesized using the microwave assisted method. The reaction conditions used in the synthesis processes helped to obtain a reproducible structure (nanofibers) and a preferential crystal orientation in the [300]. The Ca / P ratio present in all synthesized samples was similar and the average is about 2, indicating that the variations on the

synthesis reactions conditions were not significative to affect the Ca / P ratio.

ACKNOWLEDGMENT

The authors thank the financial support of Fondo de Salud CONACyT-IMSS-ISSSTE-SSA 2013-1 201329. The authors also acknowledge to José Luis Cabrera Torres for the technical assistance on Electron microscopy.

REFERENCES

- [1] Siddharthan, A., Seshadri, S.K. y Sampath, T.S. 2006. Influence of microwave power on nanosized hydroxyapatite particles, India, Scripta Materialia 55, 175–178.
- [2] Cabrera, J.L., Velázquez, R. y Rivera, E.M. 2011. Synthesis of Hydroxyapatite Nanostructures Using Microwave Heating, Qro., Mx., Journal of Nanoscience and Nanotechnology 11, 1 –7..
- [3] Arami, H., Mohajerani, M., Mazlounia, M., Khalifehzadeh, R., Laka, A. y Sadrnezhad, S.K. 2008. Rapid formation of hydroxyapatite nanostrips via microwave irradiation, Iran, Journal of Alloys and Compounds 469, 391–394.

Synthesis, and functionalization of silica nanoparticles with quercetin, a physicochemical characterization of novel nano-antioxidants.

Granados Segura Luis Oscar^{a1}, Nava Mendoza Rufino^{b1}, Reyes Pool Héctor Paul^{c2*}

¹División de Investigación y Posgrado, Facultad de Ingeniería, Campus Aeropuerto, Universidad Autónoma de Querétaro, Circuito Vial Fray Junípero Serra S/N (Antiguo Aeropuerto), Santiago de Querétaro, Querétaro, México

²CINVESTAV, Unidad Querétaro, Libramiento Norponiente No. 2000, Frac. Real de Juriquilla, Querétaro, Qro. 76230, México.

^a luillilimon@gmail.com

^b rufino@uaq.mx

^c hectorpool@gmail.com

Abstract— The interest for the biological properties of several antioxidants has increased within the medical, pharmaceutical and food industries. Flavonoids, a class of dietary antioxidants, have demonstrated that possess many properties that are beneficial for human being, including anticancer, anti-inflammatory, antiviral, antibacterial, and anti-aging properties. Strong evidences have showed that quercetin, the most abundant flavonoid in plant kingdom, have the capability to inhibit free radical and metal ions that acting as precursors of many chronic degenerative diseases related to oxidative stress. However, the use of quercetin to exert its biological properties is limited by its low water solubility and instability under different conditions (temperature, light and pH). The use of nanocarriers in order to protect and to carrier different biomolecules has been used lately. Nevertheless, biomolecules need to be delivered in order to exert their biological activities; thus, there is a need for the creation of new nanocarriers in order to let the antioxidant act immediately. The aim of this work was to conjugate quercetin in the surface of silica nanoparticles, evaluating its physicochemical properties. Electrochemical analyses were carry out to evaluate that quercetin is able to develop antioxidant activities. Results showed that we obtained small silica nanoparticles and that quercetin was successfully conjugated on silica nanoparticle's surface. Electrochemical studies indicated that the conjugation of quercetin did not affect their ability to exert antioxidant activities.

Keywords— quercetin (Qc), silica nanoparticles (SiNP), conjugation, physicochemical characterization.

I. INTRODUCTION

Today, the increase of chronic degenerative diseases such as obesity, cardiovascular disease, hypertension and cancer, are the order of the day, so, crate a product that can prevent and helps us to fight against these diseases is of great interest, and the system synthesized in this work (SiNP-Qc) would be very helpful to society.

The interest for antioxidant have been increased, since have been demonstrated to possess the ability to prevent many chronic degenerative diseases, such as cancer, diabetes, obesity, neurological diseases and cardiovascular diseases [1].

Flavonoid a subclass of dietary antioxidant, have many strong evidences that can exert the biological properties mentioned above [2]. Among them, quercetina (3, 3', 4', 5, 7-pentahydroxy flavone, Figure 1) is a flavonoid that has been reported to have a particularly high antioxidant activity [3, 4, 5], is abundantly found in edible fruits, vegetables and medicinal plants [6, 7]. It has a wide range of chemotherapeutic activities for many diseases such as anti-cancer, anti-inflammatory, anti-viral and anti-oxidant [8]. However, the strong anti-cancer therapeutic behavior is well exhibited in colon, breast, ovarian and lung cancer cells [9, 10].

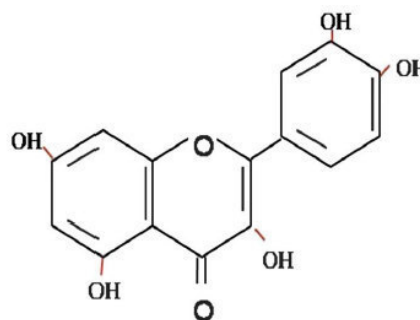


Figure 1. Chemical structure of quercetin [11].

Many flavonoids have been shown to inhibit tumor formation, but quercetin has always stood out as the most effective. Quercetin not attack directly to tumors. Instead acts by preventing cancer cells from dividing. Quercetin was the first compound inhibitor of tyrosine kinase (these proteins are located on the cell or close to membrane, when activated tyrosine kinases send powerful signals to the nucleus informing cancer cells is time divided) tested in a human trial, as a potential treatment for breast cancer, the quercetin appears to act uniquely [12, 13], quercetin is also used to treat malaria, HIV and cardiovascular diseases in addition to the cancer cells [14–16].

The solubility in aqueous media, permeability, oral bioavailability and biodegradation are poor for the quercetin which limits its applications in pharmacology [17].

This Flavonoid is unstable under conditions encountered during food/Pharmaceutical products processing (temperature, light and pH), in the gut (pH, enzymes, presence of other nutrients) or during storage (light, oxygen) [18, 19]. These factors limit the beneficial properties and potential health benefits of this compound in functional food or pharmaceutical products [20]. Consequently, it is necessary to develop a way to give stability and resistance to external agents who could affect this biomolecule, that's why in this work we functionalized silica nanoparticles with quercetin.

The aim of nanotechnology applied to medicine is develop tools to diagnose, prevent and treat some advanced disease or at the onset of development using devices, systems and technologies including nanostructures able to interact at the molecular level and which are interconnected at cell. Some showing these advantages is that nanosystems are more stable, more reactive and more surface contact with. The silica-based nanoparticles have a dominant role because of its fundamental characteristics, such as size (usually 5-1000nm), unique optical properties, high surface area, low density, adsorption capacity, capacity encapsulation, low toxicity and biocompatibility [21]. These features lead to SiNPs to be used as a matrix of inert solid support or entrapment. The surface of the silicon nanoparticles is easily modified with various chemical agents which enable the bio-conjugation addition that these particles are able to penetrate cell membranes and nuclei [22].

Therefore, the aim of this work was synthesized silica nanoparticles by the modified Stöber method, the process was discovered in 1968 by the scientist Werner Stöber [23], who developed a simple method for obtaining silica nanoparticles through the polycondensation of TEOS (tetraethyl orthosilicate) in half alcohol and ammonia catalyzed. This with the purpose to attach the quercetina to the silica nanoparticles and confer them resistance to environmental factors, without affect the anti-oxidant activity of the quercetin.

II. METHODOLOGY

A. Materials

TEOS (tetraethyl orthosilicate), distilled H₂O, ammonium hydroxide (NH₄OH), ethanol (C₂H₆O), APTES (3-Aminopropyl)triethoxysilane, quercetin.

B. Methods

1. Synthesis of silica nanoparticles (SiNP).

The synthesis of the silicon nanoparticles was performed by the technique of Stöber modified, mixed 20ml of ethanol, 1 ml of distilled H₂O and 0.32 ml of NH₄OH, is put under stirring and then 5 ml of TEOS were added with stirring 5 hours.

After the solution was placed in a crucible and in the hood to remove the solvent, after drying is crushed with mortar, suspended in water and filtered, subsequently placed in the oven for 12 hours at 80 ° C.

2. Adding the amine coupling to the SiNP (SiNP-NH₂).

0.2 g sample of SiNP are suspended in 150 ml of H₂O, and after stirring for 5 minutes, were added 0.2 ml of APTES (1: 1), stir at 65 ° C for 24 hours, filtered and washed with distilled H₂O and dried in oven at 80 ° C for 12 hours.

3. Functionalization of SiNP-NH₂ with quercetin (SiNP-Qc).

100 mg of SiNP-NH₂ and 10 mg of quercetin (10% ww) are suspended in 150 ml of H₂O with stirring for 12 hrs at room temperature, avoiding the entry of light and oxygen could result in some degradation in the reaction of flavonoids. After this time, the SiNP-Qc are suspended in water and freeze at -201 ° C for 12 hrs. After this time of freezing, the samples were subjected to a freeze drying for 48 h. The dried samples were stored in amber vials and in environments without oxygen to prevent degradation. The figure 2 show a scheme that represents the path of synthesis to get the SiNP-Qc.

III. RESULTS AND DISCUSSION

The particle size was determined by the technique of laser light scattering using a Zetasizer (Malvern Nano-S Instruments® model). A small portion of nanoparticle powder was put in deionized water and dispersed by ultrasound for 20 minutes, the clear dispersion was placed in its light scattering and measured with the following parameters: position measuring 4.65 nm, attenuator 11 measurement time 20 seconds, 3 replicates were made with three replications (TABLE 1).

TABLE 1. Nanoparticle size.

System	1° test (nm)	2° test (nm)	3° test (nm)	Average size (nm)
SiNP	112.3	110.1	106.7	109.7
SiNP-NH ₂	131.3	144.5	149.8	141.866
SiNP-Qc	165.3	165.2	163	164.5

The zeta potential (ζ) of the systems was determined with a Zetasizer 4 (Team AcoustoSizer II s/m, Brand Colloidal Dynamics), equipment units are expressed in millivolts (mV). Sample was dispersed in deionized water previously adjusted to a pH of 7.2-7.4 using dilute HCl or NaOH to reach a final concentration of 0.5% (0.25 g sample in 50 ml water) solution. The samples were dispersed by magnetic stirring and placed on your computer. The sample was recirculated in the team for 1 minute and 3 replicates were performed with three replicates to evaluate the zeta potential (TABLE 2).

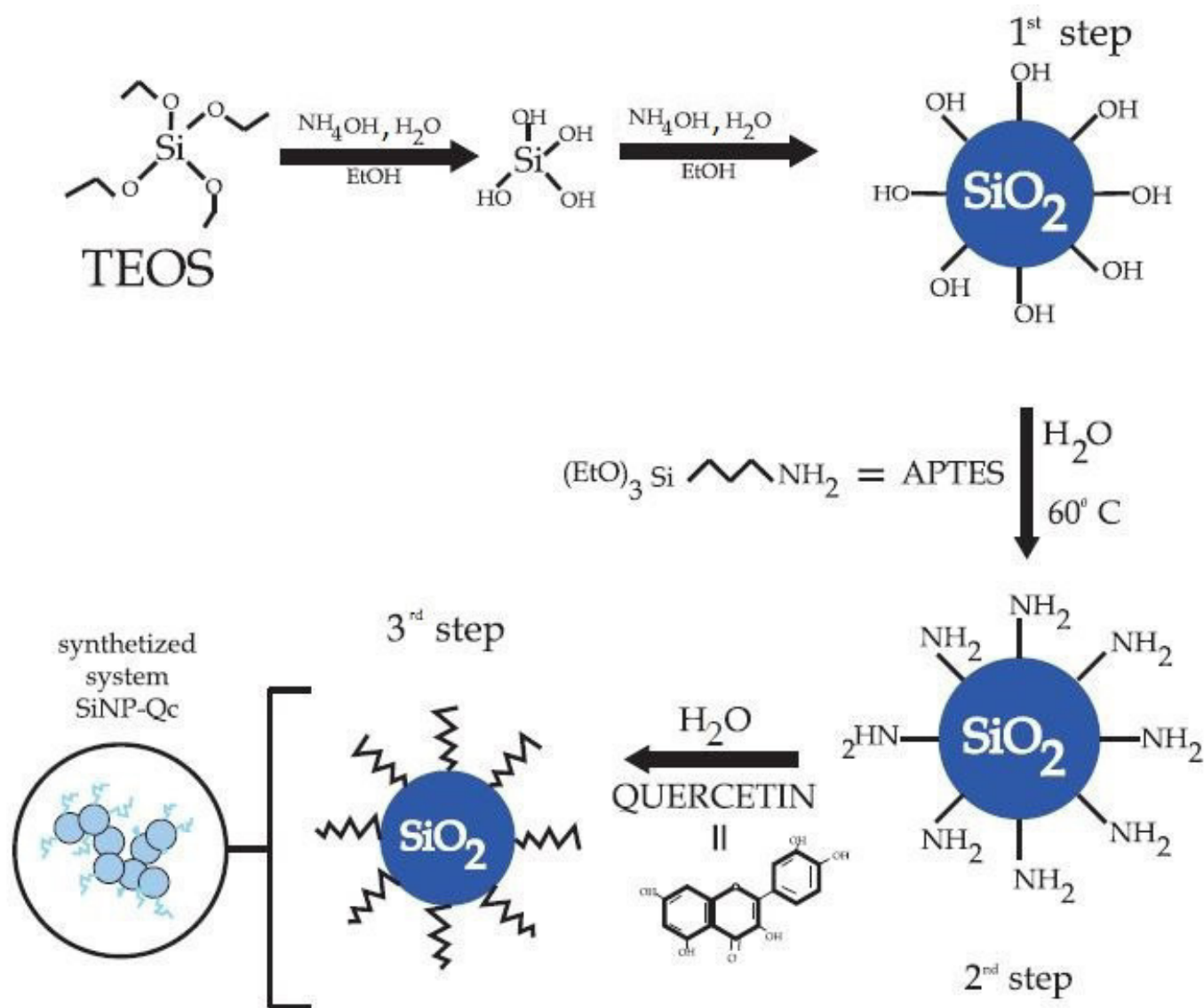


Figure 2. Preparation of SiNP-Qc, as can be seen, the process consist in three steps, first get de SiO₂ nanoparticles, second, add the amine coupling to the SiNP and finally functionalized them with the quercetin.

TABLE 2. ζ potencial.

System	1 ^o test (mV)	2 ^o test (mV)	3 ^o test (mV)	Overall charge (mV)
Qc	-19	-16	-20	-18.333
SiNP	+34.7	+27.3	+26	+29.33
SiNP-NH ₂	-29.6	-29.9	-30.1	-29.866
SiNP-Qc	-20.6	-19.6	-23.7	-21.3

The analysis of the FT-IR spectra (Figure 3) confirm the introduction of the different functional groups onto the surface of SiO₂. It shows the bare SiO₂, the absorption peak at 1020 - 1110 cm⁻¹ is assigned to the Si-O-Si asymmetric stretching vibration, and the peaks at 960 cm⁻¹ are ascribed to the asymmetric bending and stretching vibration of Si-OH, respectively. Figure 2 also shows the asymmetrical deformation vibration of the amino group at 1425 and 900 cm⁻¹, indicating the amino groups were fixed onto the SiO₂ particle surface successfully [24].

The FT-IR spectrum of Qc is shown in Figure 2 too; where the OH stretching ($3700-3000\text{ cm}^{-1}$), characteristic absorption band of the group $\text{C}=\text{O}$ (1662 cm^{-1}), observed bands groups CC stretching (1618 cm^{-1}) bands push- CH (1456.1383 and 866 cm^{-1}) bands allocated to stretch the bond between the oxygen and the ring C (1272 cm^{-1}) and stretches of links CO ($1070-1150\text{ cm}^{-1}$) [25].

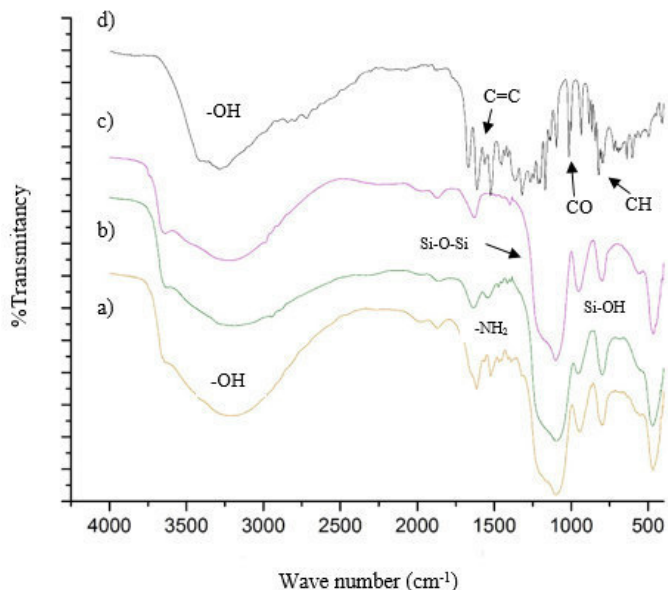


Figure 3. FTIR spectra (a) SiNP-Qc, (b) SiNP-NH₂, (c) SiNP, (d) Qc.

We arrived at the conclusion that the link between the SiNP-NH₂ and the Qc is through their electrostatic charges and by hydrogen bonds. Figure 4 show the representation link between the molecules mentioned [22]. The antioxidant activity of a flavonoid is due to the donation of hydrogen and electrons, and the number, position and conjugation of the hydroxyl groups. The free hydroxyl groups, together with the carbonyl group are electrons donors.

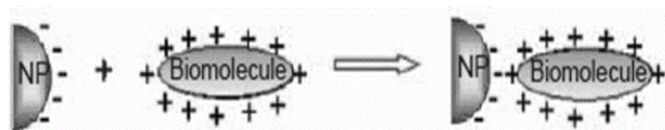


Figure 4. Representation of the link from our system [22].

To determine the antioxidant capacity of our compound we used two techniques, cyclic voltammetry and TBARS test. The cyclic voltammogram is between the Qc and the SINP-Qc (Figure 5), is an electronic transfer of the two compounds. In the pure Qc the oxidation of the catechol 3', 4'-dihydroxyl electron-donating groups, occurs first, at very low positive potentials, and is a two electron two proton reversible reaction [26], the slipping in the SINP-Qc system first peak indicates that electron donation catechol group of quercetin is faster than

Qc, hence increases its antiradical activity; the second peak of the SINP-Qc is delayed relative to the pure Qc, this is related to decrease in the antioxidant activity of OH groups.

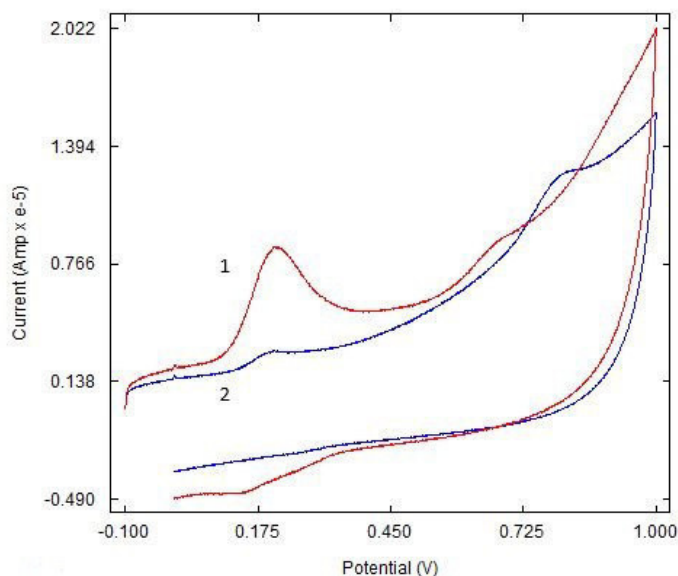


Figure 5. Cyclic voltammograms of Qc (1) and the quercetin coupled to the surface of silica nanoparticles, SiNP-Qc (2).

TBARS test is in phosphatidylcholine liposomes that are made into (lipid present in the human body) size of 100 nm using min extrusion, then reacted with Fe: EDTA and H₂O₂. The union between Fe and H₂O₂ creates free radicals HOO, affecting the liposome membrane. When liposomes are oxidized, degradation product is generated, the malondialdehyde (MDA). In this test we observe a lower production of MDA using our system SINP-Qc than the Qc alone, which proves that our system is more reactive and effective (Figure 6).

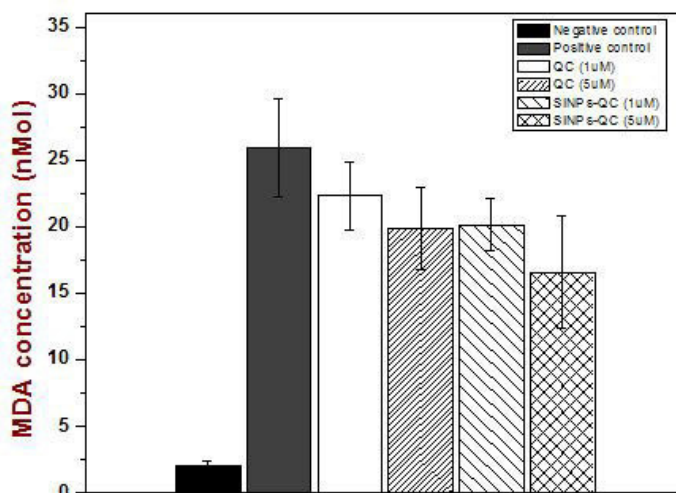


Figure 6. MDA concentration produced by the oxidation of phosphatidylcholine liposomes by peroxy radicals after 24 hrs. The treatments evaluated were quercetin in concentrations of 1

and 5 μM quercetin and silica nanoparticles coupled with quercetin at concentrations of 1 and 5 μM = 10 mM PBS negative control. Positiv Control = PC + H_2O_2 (1 μM) + Fe: EDTA (1 μM) + PBS 10 mM.

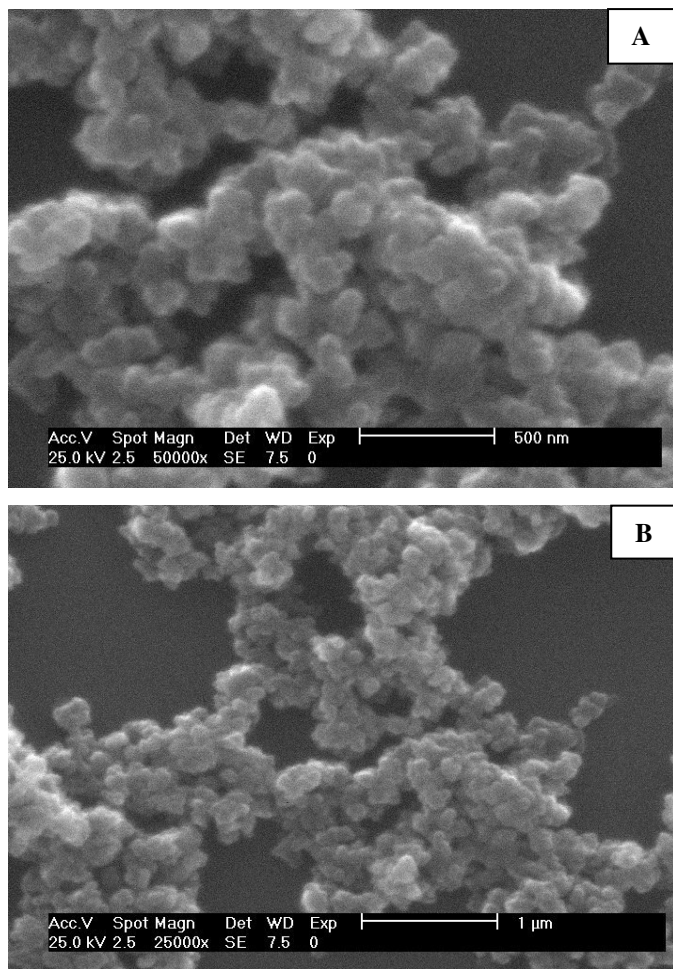


Figure 7. SEM images of the synthesized system SiNP-Qc.

Figures 7 'A' and 'B' shown the micrographs corresponding to the formation of the silica nanoparticles functionalized with quercetin (SiNP-Qc), as can be seen, the particles are semi spherical and are slightly agglomerated, but how the SiNP are spherical this are the expected results.

IV.CONCLUSIONS

The coupling of quercetin on silica nanoparticle was successful, the electrochemical tests show that the antioxidant activity of quercetin is not compromised with the link between the silica nanoparticles and the quercetin, however antioxidant capacity enhancement and the nanoparticles are stable at a pH of 7.4. The synthesized system SiNP-Qc would be useful in biomedicine by the properties of the flavonoid, moreover, the flavonoid would have a longer shelf life thanks to the silica nanoparticles. With this biofunctional system we have hope to create products that help us to have a better quality of life, preventing oxidative stress related diseases. Besides this

system could be a potential anticancer agent for treating breast cancer particularly, for their properties previously identified in this work, which would be projected to create a drug for this cancer.

REFERENCES

- [1] The New Nutrition: a medicine for the next millennium. Michael Colgan. 155-165.
- [2] Azam et al., 2004; Choi et al., 2009; Guardia et al., 2001; Lu et al., 2006; Morel et al., 1993; Pignatelli et al., 2000; Schlachterman et al., 2008.
- [3] M.L. Calabrò, S. Tommasini, P. Donato, D. Raneri, R. Stancanelli, P. Ficarra, R. Ficarra, C. Costa, S. Catania, C. Rustichelli, G. Gamberini, J. Pharmaceut. Biomed. 35(2), 365–377 (2004).
- [4] S. Scalia, M. Mezzena, J. Pharmaceut. Biomed. 49(1), 90–94 (2009).
- [5] Polymeric Nanoparticles as Oral Delivery Systems for Encapsulation and Release of Polyphenolic Compounds: Impact on Quercetin Antioxidant Activity & Bioaccessibility. Food Biophysics.
- [6] A. Kumari, S.K. Yadav, Y.B. Pakade, B. Singh, S.C. Yadav, Colloids Surf. B: Biointerf. 80 (2010) 184.
- [7] T.H. Wu, F.L. Yen, L.T. Lin, T.R. Tsai, C.C. Lin, T.M. Cham, Int. J. Pharm. 346 (2008) 160.
- [8] S. Chakraborty, S. Stalin, N. Das, S.T. Choudhury, S. Ghosh, S. Swarnakar, Biomaterials 33 (2012) 2991.
- [9] M. Kakran, N.G. Sahoo, L. Li, Colloids Surf. B: Biointerf. 88 (2011) 121.
- [10] P. Wang, D. Heber, S.M. Henning, Food Funct. 3 (2012) 635.
- [11] Encapsulation and release of hydrophobic bioactive components in nanoemulsion-based delivery systems: impact of physical form on quercetin bioaccessibility. Food & Functio, 2013. The Royal Society of Chemistry 2013.
- [12] Quercetin conjugated superparamagnetic magnetite nanoparticles for in-vitro analysis of breast cancer cell lines for chemotherapy applications. S. Rajesh Kumar, S. Priyatharshni, V.N. Babu, D. Mangalaraj, C. Viswanathan, S. Kannan, N. Ponpandian.
- [13] Cancer Cure: Natural Methods. Tim Birdsall, Joseph E. Pizzorno, Paul Reilly. 170-175.

- [14] Y. Gao, Y. Wang, Y. Ma, A. Yu, F. Cai, W. Shao, G. Zhai, *Colloids Surf. B: Biointerf.* 71 (2009) 306.
- [15] H. Patir, S.K.S. Sarada, S. Singh, T. Mathew, B. Singh, A. Bansal, *Free Rad. Biol. Med.* 53 (2012) 659.
- [16] M.Y. Wong, G.N.C. Chiu, *Nanomed: Nanotechnology, Biol., Med.* 7 (2011) 834.
- [17] A.R. Patel, P.C.M. Heussen, J. Hazekamp, E. Drost, K.P. Velikov, *Food Chem.* 133 (2012) 423.
- [18] P. Ader, A. Wessmann, and S. Wolfram, "Bioavailability and metabolism of the flavonol quercetin in the pig," *Free Radical Biology and Medicine*, vol. 28, no. 7, pp. 1056–1067, 2000.
- [19] L. Bell, "Stability testing of nutraceuticals and functional foods," in *Handbook of Nutraceuticals and Functional Foods*, pp. 501–516, CRC Press, 2001.
- [20] G. S. Borghetti, I. S. Lula, R. D. Sinisterra, and V. L. Bassani, "Quercetin/ β -Cyclodextrin solid complexes prepared in aqueous solution followed by spray-drying or by physical mixture," *AAPS PharmSciTech*, vol. 10, no. 1, pp. 235–242, 2009.
- [21] Silica-based nanoparticles for biomedical applications, *Drug Discovery Today Volume 17, Numbers 19/20, October 2012*. Clarke 2006, Eckhoff 2006, Buriak 2002.
- [22] Bioconjugated Silica Nanoparticles: Development and Applications. *Nano Res* (2008) 1: 99 115.
- [23] Synthesis and Functionalization of Silica Nanoparticles with Spherical Morphology. Mauricio Echeverrie. *Scientia et Technica* Año XIII, No 36, Septiembre de 2007. Universidad Tecnológica de Pereira.
- [24] Silica nanoparticles for the layer-by-layer assembly of fully electro-active cytochrome c multilayers. Sven C Feifel and Fred Lisdat. Feifel and Lisdat *Journal of Nanobiotechnology* 2011.
- [25] Dias et al. 2008; Kumari et al., 2011.
- [26] Electrochemical Oxidation of Quercetin. Ana Maria Oliveira Brett, Mariana-Emilia Ghica. Universidade de Coimbra, Portugal.

Wastewater treatment by fixed biomass, using PET bottles within a biological aerobic reactor.

M. Y. Mendoza-Burguete¹, J. A. Rodríguez-Morales*², M. Lopez-Velarde S.³

¹*Facultad de Química, Universidad Autónoma de Querétaro, Campus Aeropuerto, Santiago de Querétaro, Qro, C. P. 76010, México.*

³*Facultad de Ingeniería, Universidad Autónoma de Querétaro, Campus Aeropuerto, Santiago de Querétaro, Qro, C. P. 76010, México. Kassel University, Faculty of Organic Agricultural Sciences. Germany.*

¹men_bur@hotmail.com

³mlopezvelarde@uni-kassel.de

²*Facultad de Ingeniería, Universidad Autónoma de Querétaro, Centro Universitario, Cerro de las Campanas, Santiago de Querétaro, Qro, C. P. 76010, México.*

*²josealberto970@hotmail.com

Abstract—The study presents results from a dynamic analysis of an aerobic bioreactor trickling filter type using polyethylene terephthalate bottles on a laboratory scale, which was used for producing biofilm for wastewater treatment. The data presented can be useful for modeling biofilm systems and provide a base for further experiment designs. The main objective was to determine the effect of the microorganisms through the effluent quality and level of adhesion of the biofilm to the polyethylene terephthalate bottle. With the results, control strategies to improve the performance of these processes were established.

Keywords—dynamic analysis, biofilm, wastewater treatment, polyethylene terephthalate.

I. INTRODUCTION

Biofilm has been successfully used in water treatment for over a century [1]. It was not until the early 1980s, however, that the advantages of this type of process became of interest to a considerable number of researchers, not only in the field of water and wastewater treatment, but also in many other areas related to biotechnology [2]. A large number of research projects are currently being conducted on biofilm reactors for the production of bioactive substances, for plant and animal cell cultures, drinking water production, and wastewater treatment.

One key advantage of biofilms is the positive influence of solid surfaces on bacteria. This activity was observed over 50 years ago [3] and confirmed recently by other researchers ([4] [5] [6] [7]). There is considerable discussion about the mechanism, direct or indirect, that induces greater activity of fixed biomass [8]. Some authors [9] [7] attribute this phenomenon to physiological modifications of attached cells. It has been demonstrated that fixed cultures are less strongly affected than suspended cultures by changes in environmental

conditions (temperature, pH, nutrient concentrations, metabolic products and toxic substances).

Biofilm activity is not proportional to the quantity of fixed biomass, but increases with the thickness of biofilm up to a determined level, known as the "active thickness" [10] [11]. Above this level, the diffusion of nutrients becomes a limiting factor, thus differentiating an "active" biofilm from an "inactive" biofilm. A stable, thin and active biofilm therefore offers numerous advantages in water and in wastewater treatment. In order to achieve this objective, it is important to develop methods for fixed biomass activity estimation-which not only is simple and rapid, but also sensitive, precise and representative.

II. EXPERIMENTAL.

A. Selection of form, characteristics and dimensions of the PET bottle.

For proper collection of polyethylene terephthalate (PET) bottles, they should be examined for their effectiveness for fixing to the surface of microorganisms and accommodate the shape of the material within the reactor to maximize the contact area and take into account the size of the reactor to be used.

B. Sampling and analysis of wastewater.

This project was designed as a pilot plant for future use in industrial plants, however, this model-can be used to conduct studies on domestic scale. Sampling was conducted with various waste types, in which physical-chemical analysis was conducted and a preliminary characterization was obtained. With this information, the dimensions of the reactor were designed. For this it was necessary to take into consideration the flow, how to accommodate and set the PET bottles, the

contact area, and the recirculation mechanism of the collected wastewater in order to start the cultivation of microorganisms and consequently, fixing the of the biomass biofilm.

III. MATERIALS AND METHODS

A. Construction of the fixed biomass biological reactor.

PET bottle collection of 2, 1.5, 1, 0.6 and 0.5 liters, as shown in figure 1.



Fig. 1. PET bottle collection.

B. PET bottle preparation.

The bases of the PET bottle were removed, as shown in figure 2 and figure 3, then the bottles were placed inside one another in order from lowest to highest volume. It is important to mention that all the pillars of bottles were similar, it is to say with the same number of bottles with the same amount of volume .



. Fig. 2. Bases of PET bottles



Fig. 3. Pillar of PET bottles

C. Preparing the reactor.

- The pillars of bottles were fixed to the reactor as shown in figure 4.



Figure 4. PET bottles inside to the reactor.

- Sludge was poured into the reactor for it adecuation and the fixed biomass and biofilm production, as shown in figure 5. For the fixation of the biofilm, the wastewater was recirculated.



Fig. 5. Acclimatization and production de fixing biomass and biofilm.

D. Sampling

10 samples were taken, which were obtained from the Chemistry Faculty of Universidad Autónoma de Querétaro.

E. Analytical techniques

- physicochemical.

For the analysis of the samples technical standard methods were followed. For the analysis of water and wastewater, 2005 [12], following the methods numeric and parameters were used (see table 1 and 2).

TABLE 1. METHODS NUMBERS AND PARAMETERS.

Parameters	Method number
BOD	5210A
COD	5220D
Total suspended solids (SST)	2540D, 2540E
pH and Conductivity	2320A
Fats and oil	5520C

- Microbiological.

According to the sección of microbial examination of from the SMAWW 2005 book. These methods and parameters were followed:

TABLE 2. METHODS NUMBERS AND PARAMETERS.

Parameters	Method number
Total coliform bacteria	900
Fecal coliform bacteria	900

IV. RESULTS.

Textual results of water quality of the effluent from aerobic biological trickling filter type reactor were shown in Table 3. These results were obtained with a retention time of 2.75 hours, removing 94% of the contaminants with respect to the wastewater inlet and were compared with the NOM-003-SEMARNAT-1997 [13] [14]. Some of these parameters are not included in the Mexican Official Standar, yet. These parameters were included in the table for comparison in a clear high pollutant removal from wastewater input to the output of treated water.

TABLE 3. COMPARISON OF RESULTS AND PARAMETERS ANALYSIS.

Parameter	Value of Wastewater	Treated water by fixed biomass	Value of the standar
	mg/l	mg/l	mg/l
Total suspended solids	300	18	20
BOD	200	19	20
COD	450	25	
Fats an oil	25	13	15
Total coliforms	10^{24}	10^3 Without Chlorine	10^3

V. DISCUSSION

The support material used was very successful for development and fixing microorganisms PET plastic. It showed good adherence of microorganisms diversity of these, thus favoring the transport of nutrients . While there are rules and parameters for processes and technologies covering the recycling of PET for the production of fibers, films, non-food bottles, as well as greater control treatment if food contact [14] [15] [16] [17] , there is no history or a standardized support for the reuse of PET systems biological treatment of wastewater with information required to be applied as a base methodology in implementing such systems. However there is research on biofilm adhesion to plastic PET in marine waters, in which successful results were obtained [18] . Due to the good adhesion, good population of microorganisms and good water quality obtained is continuing to investigate new prototype with PET plastic as support for biofilm, and whether it is possible to improve the quality of water leaving with a minimal cost.

VI. CONCLUSIONS

The results of the effluent quality by means of the parameters analyzed were satisfactory compared to the Official Mexican Standards: NOM-002-SEMARNAT-1996 [19] y la NOM-003-SEMARNAT-1997[20]; obtaining a high removal of contaminants, high efficiency with low cost of construction and operation. However, more studies are needed to develop more accurate analytical methods for bacterial growth and activity, and biofilm adhesion to PET bottles for better removal of these pollutants.

ACKNOWLEDGMENT.

The authors would like to thank the Universidad Autónoma de Querétaro for the use of their laboratories and equipment.

REFERENCES

- [1] Atkinson B. (1975) Biochemical Reactors. Pion Press, London.
- [2] Adler I. (1987) Proc. Int Eur. Congr. on Biotechnology, Vol. 1, p. 1. Amsterdam, The Netherlands.
- [3] ZoBell C. E. (1943) The effect of solid surfaces upon bacterial activity. J. Bact. 46, 39-56.
- [4] Hattori R. and Edeline F. (1981) Growth rate and growth yeild ofE. coli adsorbed on an anion exchange resin. J. gen. appl. Microbiol. 27, 287-298
- [5] Audic J. M., Faup G. M. and Navarro J. M. (1984) Specific activity of Nitrobacter through attachment on granularmedia. Wat. Res. 18, 745-750.
- [6] Doran P. M. and Bailey J. E. (1986) Effects of immobilization on growth, fermentation, properties and macromolecular composition of S. cerevisiae attached to gelatin. Biotechnol. Bioengng 28, 73-87.

- [7] Klein J. and Ziehr H. (1990) Immobilization of microbial cells by adsorption. *J. Biotechnol.* 16, 1-16.
- [8] Van Loosdrecht M. C. M., Lyklema J., Norde W. and Zehnder A, J. B. (1990) Influence of interfaces on microbial activity. *Microbiol. Rev.* 54, 75-87.
- [9] Fletcher M. and Flodgate G. D. (1973) An electronmicroscopic demonstration of an acidic polysaccharide involved in the adhesion of a marine bacterium to solid.
- [10] Kornegay B. H. and Andrews J. F. (1968) Kinetics of fixed film biological reactors. *J. War. Pollut. Control Fed.* 40, 460 -468
- [11] LaMotta E. J. (1976) Kinetics of growth and substrate uptake in a biological film system. *Appl. env'it. Microbiol.* 31,286-293.
- [12] Standar Methods for the Examination of Water and Wastewater. (2005) American Public Health Asociation/American Water Works Association / Water Environment Federation. Washingtons D. C. USA. 21th Edition.
- [13] NMX-AA-113-SCFI-2010 Water analysis – Determination of Herminth egg – test method. Secretary of Economy. General Directorade of Standars
- [14] NMX-E-060-CNCP-2010 Industria del plástico-Terminología de los plásticos. Declaration of validity published in official Journal of the Federation on May 4, 2010.
- [15] Directiva 97/129/CE del Parlamento Europeo y del Consejo, relativa a los envases y residuos de envases. Establishing the identification system for packaging materials, January 28 .
- [16] Enciclopedia del plástico, Instituto Mexicano del Plástico Industrial, Chapter 29, México, D.F., 2000. Volume 3.
- [17] Technical Bulletin. Resin ID Codes. SPI Material Container Coding System. Society of the Plastics Industry Inc. (SPI).
- [18] Hayden K., Russell J. Crawford, Tomoo Sawabe and Elena P. Ivanova. (2009) Poly (ethylene terephthalate) Polymer Surfaces as a Substrate for Bacterial Attachment and Biofilm Formation. *Microbes Environ.* Vol.24, No. 1, 39-42.
- [19] Mexican Official Standard NOM-002-SEMARNAT-1996. Establishes the maximum permissible limits in wastewater discharges in urban systems or municipal water. Official Journal of the Federation, published on June 3th, 1998.
- [20] Mexican Official Standard NOM-003-SEMARNAT-1997 . Establishes the maximum permissible levels of contaminants for treated wastewater reused in public service. Official Journal of the Federation, published on August 21st, 1998.

Hysteresis Cycles and its Behavior in Expansive Soil-Water Retention Curve

Galaviz-González Roberto¹, Horta-Rangel Jaime², Rojas-González Eduardo³, Pérez-Rea Luz⁴, Robles-Sotelo Jaime⁵

¹ *División de Investigación y Posgrado, Facultad de Ingeniería, Universidad Autónoma de Querétaro, Cerro de las Campanas, 76160, Santiago de Querétaro, Querétaro, México.*

¹ btoviz@hotmail.com

² horta@uaq.mx

³ erg@uaq.mx

⁴ perea@uaq.mx

² *División de Ingenierías, Centro Universitario de Ciencias Exactas e Ingeniería, Universidad de Guadalajara, Boulevard Marcelino García Barragán 1421, 44430, Guadalajara, Jalisco, México.*

⁵ jaime.robles.sotelo@gmail.com

Abstract— Unsaturated expansive soils experience a volume change by physic-chemical reaction produced by variations on its water content. Stress-strain behavior of these soils are very sensitive to this variations. For that reason, buildings founded on expansive soils present structural problems due to repetitive stresses produced by shrink-swelling cycles, caused through drying-wetting cycles that generate suction, water content variations, and hysteresis cycles. This latter is a phenomenon that occurs by the water flow through the soil, causing drying-wetting paths. Because of that, it is necessary to know the real cycles that the soil has been exposed. Theoretical indirect models have been developed with which the Soil-Water Retention Curve (SWRC) is fitted, in order to estimate the hydraulic behavior of soil. However, the adjustments have low correlation with experimental SWRC. This paper presents a comparison of most common methods for determining the secondary hysteresis cycles based on the adjustment of SWRC. Two of them based on predetermined expressions and other used a polynomial fit based on an arrangement table that use methods of interpolation with variable increments and Lagrange's interpolation, resulting a polynomial adjustment that generates the numeric SWRC. The results obtained were compared with experimental and calculated results reported by methods from other authors. Results show that the main and secondary cycles were consistent with those reported by other authors for sandy and silty soils, but, for clayey soils, only the polynomial method was capable to show the hysteresis phenomenon, also the adjusting process of the SWRC is avoided with the polynomial method, concluding in a quick and easy tool to get very consistent results.

Keywords— Unsaturated soils; hysteresis cycle; indirect method; soil-moisture model; soil-water retention curve

I. INTRODUCTION

It is known that the behavior of an unsaturated soil depends heavily on suction changes generated by changes in the water content [1], produced by wetting-drying cycles. This has led to the use of numerical and computational models to predict these cycles through Soil-Water Retention Curve. This is of great interest since the use of the SWRC is used as a

basis for the prediction of parameters unsaturated soils. These models reduce the time and cost to obtain these parameters.

It have been developed to predict numerical procedures hysteresis cycles SWRC. Among the most used models is the shown in [2], in which the main wetting-drying curves are obtained. The methods developed in [3] and [4] are based on the van Genuchten's method in order to adjust the main curves of the SWRC, from this it can predict the secondary cycles. These methods have proven to be feasible and practical in sandy and silty soils. However, in some cases the SWRC adjusted with these equations have low correlation with experimental SWRC (clay), this can cause that the secondary cycles are not correct. Therefore, obtaining parameters from the SWRC not be accurate, yielding inaccurate results of the unsaturated soil hydromechanical behavior.

This paper presents the prediction of the hysteresis cycles of an unsaturated expansive soil, through the SWRC, using the methods [3], [4] and the procedure shown in [5]. This in order to demonstrate the effectiveness of these methods, the behavior and effect that occurs in predicting the hysteresis cycles in expansive soils.

II. ANTECEDENTS

A. Expansive Soils

Expansive soils often contain minerals, such as montmorillonite [6], and are recognized as problematic as they severely compromise the civil structures built on them [7], while even lightly loaded structures built on these soils may develop structural damage as a result of changes in soil water content [8]. The main problems caused by these soils can be attributed to a poor understanding of the volume changes caused by variations in water content [7]. Expansive soils are capable of adsorbing water in their internal structure, and when water content increases, so does soil volume. This change in volume can exert sufficient pressure on the structure to cause damage (see Fig. 1b). When dry, expansive soils shrink, causing a contraction that can affect building supports

and give rise to adverse subsidence (see Fig. 1a). The wetting-drying process produces shrink-swell cycles that subject structures to repetitive stress [6].

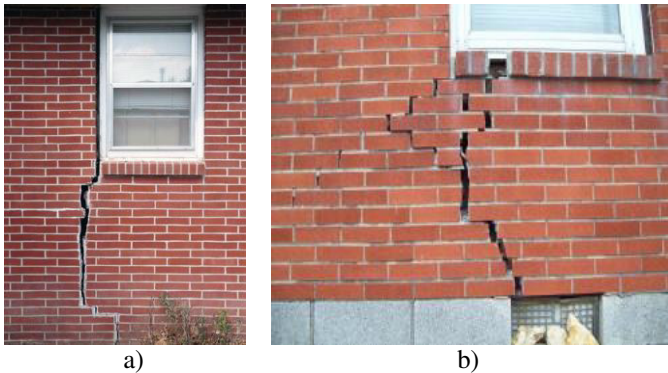


Fig. 1. Building damage: a) produced by shrink movement [9], b) produced by swelling displacement [10].

B. Soil-Water Retention Curve (SWRC)

Soil water flows from one point to another with the greatest potential to lower potential energy. This is defined as the potential energy per unit of water, it means, is the work required to bring the unit from a standard reference state to the point under consideration. Soil water is subject to force field resulting from attraction of the solid matrix, the presence of solutes, the action of the external pressure, the gravitational pull among others. The gravitational potential is measured from the surface of the soil (-z) and the pressure is a function of water content (θ). This pressure potential is considered positive if the water pressure in the soil is greater than atmospheric and negative if is less than the atmospheric pressure. The latter is called matric potential and, when taken in absolute value is called matric suction (ψ). This results from capillary forces and adsorption due to soil structure [11].

Several techniques for measuring matric suction of soil were developed, these can be divided into direct and indirect methods. Direct methods measure the negative water pressure in the soil pores (u_w), then the matric suction ($u_a - u_w$), where (u) is the air atmospheric pressure into the pores. Among the most used direct methods are tensiometers and axis translation technique. Indirect methods include filter paper technique in contact with the soil, and sensors thermal and electrical conductivity [12].

Thus, the relationship between the soil water content (ω or θ) or degree of saturation (S_r) with its respective matric suction (ψ) is known as Soil-Water Retention Curve (SWRC) [12].

SWRC can be used to estimate various parameters used to describe unsaturated soil behavior [13]. Its use has become an important aspect in unsaturated soil mechanics because these materials have a natural hydromechanical coupling, it means, volumetric behavior and shear strength depend not only on applied stress and soil suction, but also their degree saturation (S_r) which depends on its water content (or ω or θ) [14]. SWRC

is not unique to a soil, its shape and position are not the same, it means, wetting and drying paths are different, this phenomenon is called hysteresis [12]. This phenomenon is dictated by the texture and soil structure, the higher the clay content is greater water retention for a given suction value (ψ) and the slope of the curve is smoother [11]. This, is due to its pore size distribution (PSD), because it has a great diversity of pores. Furthermore, for sandy soils slopes are stronger, because its PSD is more homogeneous.

The hysteresis phenomenon can be explained by a porous model that considers interconnected pores and randomly distributed. Figure 2 shows that the start of a wetting process, it is considered that all the pores are dried, the suction is very large, which is reduced in steps. The first pores (P) that are saturated are the smaller along with their interconnections (cavities B) until the end with larger pores, it means, the smallest pore is at the border (cavity B7), subsequently, the cavities B5 and B4, continuing this process until saturate the larger pores (P2 and P1). Moreover, in a drying process all the pores are saturated and suction increases stepwise. The first pores that are drying are large pores, ending with the smallest pores. Similarly, the drying process starts when the larger pores are empty (P1, P2, etc.), continuing this process with smaller pores and ending with the smallest (cavity B7) [15].

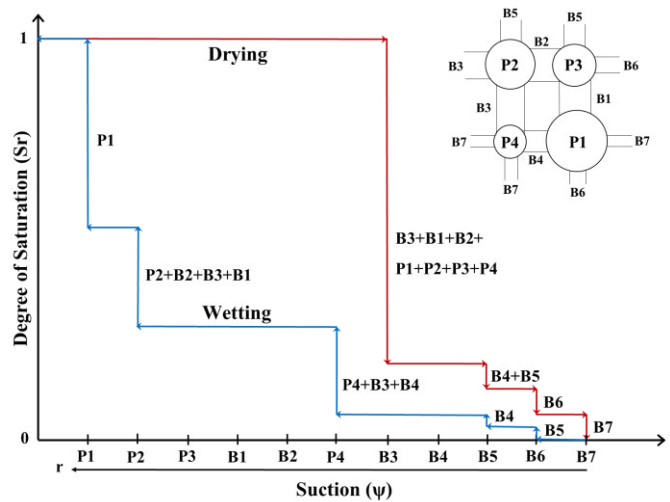


Fig. 2. Hysteresis phenomenon generated by wetting-drying cycles due to soil PSD.

SWRC hysteresis is an important factor the soil behavior, which must be take into account during the drying-wetting process [16]. Because the stress-strain relationship is affected by changes in the water content of an unsaturated soil. These rely on a complicated hydrological process as infiltration, evaporation and evapotranspiration which produce wetting and drying cycles, which cause primary drying curves (from a saturated state to a dry state) and primary wetting curves (from a dry state to the saturated state). Furthermore, from primary curves can be generated other curves like primary, secondary, tertiary wetting-drying cycles (see Fig. 3) [3]. These cycles represent actual cycles to the soil exposed due to hydrological process.

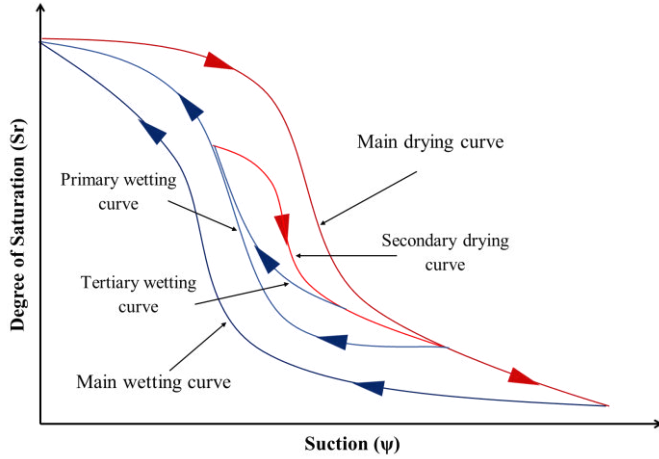


Fig. 3. Wetting-drying paths for unsaturated soils [3].

The measurements in the laboratory and the field can be slow, cumbersome, and difficult to perform [17]. Therefore, it have been developed alternative procedures to estimate the SWRC [18] and of these models have been derived other methods to determine the secondary hysteresis cycles from the SWRCs. However, in some cases SWRC adjustment cannot be performed accurately, so that the primary and secondary curves do not have high correlation with experimental SWRC.

1) Hysteresis cycles prediction

At present there are various models on the relationship of SWRC. The most popular model is the van Genuchten [3].

van Genuchten [2] proposed an equation (1) to adjust the SWRC. This equation is derived from the procedure developed by [19] to simulate the SWRC.

$$\Theta = \frac{\theta - \theta_r}{\theta_s - \theta_r} \quad (1)$$

$$\Theta = \left[1 + |\alpha\psi|^n \right]^{-m} \quad (2)$$

$$m = 1 - \frac{1}{n} \quad (3)$$

where: θ_s = saturated volumetric water content, θ_r = residual volumetric water content, θ = volumetric water content, α , n , and m are not determinate parameters, and $\Theta(\psi)$ is the degree of saturation that is a function of the soil suction. Equation (2) provides a new effective degree of saturation (Θ) with which the SWRC or suction experimental values are adjusted. This procedure is usually referred to as modeling or SWRC adjustment.

Moreover, Han-Chen et al. [3] showed a procedure to model or predict the hysteresis secondary cycles, based on the model proposed by [2] from (2), where parameters θ_s , θ_r , α , and n are unknowns to be determined such that the main wetting curve $\theta^w(\psi,1)$ is described by parameters $[\theta_s^w(1), \theta_r^w(1), \alpha^w, n^w]$. In order to eliminate the effect of pumping, the relations $\theta_r^d(1) = \theta_r^w(1) = \theta_r$ y $\theta_s^d(1) = \theta_s^w(1) = \theta_s$ imposed to close the main hysteresis cycle. Thus, the description of the main wetting and drying curves $\theta^w(\psi,1)$ y $\theta^d(\psi,1)$ for revising $[\theta_s, \theta_r, \alpha^w, n^w]$ and $[\theta_s, \theta_r, \alpha^d, n^d]$, respectively. Additionally, α^w, n^w and α^d, n^d being equal to the description of several wetting and drying curves.

Then, the starting point is the primary path (ψ_i, θ_i) and requires $\theta(\psi,2)$ to meet:

$$\frac{\theta(\psi,2) - \theta_r(2)}{\theta_s(2) - \theta_r(2)} = \left[1 + |\alpha\psi|^n \right]^{-m} \quad (4)$$

Thus, the primary curve $\theta(\psi,2)$ also passes through the points investment (ψ_i, θ_i) and (ψ_f, θ_f) . Substituting (ψ_i, θ_i) y (ψ_f, θ_f) in (4), we have;

$$\frac{\theta_i - \theta_r(2)}{\theta_s(2) - \theta_r(2)} = \left[1 + |\alpha\psi_i|^n \right]^{-m} \quad (5)$$

$$\frac{\theta_f - \theta_r(2)}{\theta_s(2) - \theta_r(2)} = \left[1 + |\alpha\psi_f|^n \right]^{-m} \quad (6)$$

Solving the equations system with two unknowns, formed by (5) and (6), we find $\theta_s(2)$ and $\theta_r(2)$ with their respective shape parameters α , n , and m (wetting and drying). The above process can be applied analogously to the i -th path [3].

Furthermore, Zhou et al. [4] proposed another model that is based on shown in [2]. They consider a simple nonlinear boundary scanning rule to describe the scan cycles (wetting-drying) between the main wetting-drying, it means, main paths are considered borders.

$$S_e = \left[1 + \left| \frac{\psi}{\alpha} \right|^n \right]^{-m} \quad (7)$$

$$\frac{\partial S_e}{\partial \psi} = -m \left[1 + \left| \frac{\psi}{\alpha} \right|^n \right]^{-m-1} \left(\frac{n}{\alpha} \right) \left(\frac{\psi}{\alpha} \right)^{n-1} \quad (8)$$

As shown in Fig. 4, the wetting or drying process can start in (ψ, S_e) , the scanning gradient is defined by (9):

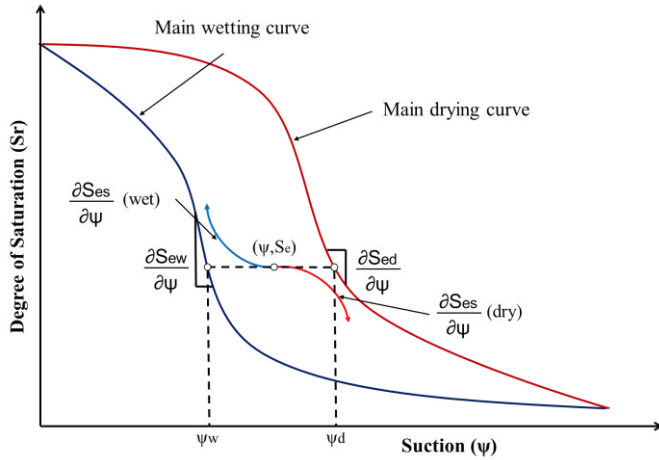


Fig. 4. Main wetting-drying paths and the scanning law [4].

$$\frac{\partial S_{es}}{\partial \psi}(\text{hum}) = \left(\frac{\psi_w}{\psi} \right)^b \left(\frac{\partial S_{ew}}{\partial \psi} \right) \quad (9)$$

with

$$\psi_w = \alpha_w \left(S_e^{-1/n_w} - 1 \right)^{1/m_w} \quad (10)$$

where: ψ_w is the suction corresponding to the wetting boundary to the same effective degree of saturation at the initial point, and the subscript "s" means exploration. Drying from the point (ψ, S_e) , the scanning gradient is defined similarly:

$$\frac{\partial S_{es}}{\partial \psi}(\text{sec}) = \left(\frac{\psi_d}{\psi} \right)^{-b} \left(\frac{\partial S_{ed}}{\partial \psi} \right) \quad (11)$$

with

$$\psi_d = \alpha_d \left(S_e^{-1/n_d} - 1 \right)^{1/m_d} \quad (12)$$

donde: ψ_d is the suction corresponding to the drying boundary to the same effective degree of saturation at the initial point. Here, b is an adjustment parameter (always positive) which adjusts the scanning gradient of the curve [4].

The disadvantage of using this models, is that the adjustment of the SWRC generally has low correlation with experimental SWRC. Due to the foregoing, the proposed method in [5] was used. This method determines the hysteresis cycles of an unsaturated expansive soil using a polynomial

approximation of experimental SWRC, based on an arrangement table, which authors concluded that it is an easy and quick tool to get very consistent results.

III. MATERIALS AND METHODS

Fundamental to the design and construction of any project is the realization of a basic geotechnical characterization site which includes a determination of the index and mechanical properties of the soil. In this study, unaltered samples were obtained from the town of Jurica, Santiago de Queretaro, México, at a depth of between 0.60 m and 0.80 m. The properties corresponding to the index assays were then obtained, which were the Atterberg limits and the soil classification, which were obtained from the granulometric composition and plasticity chart. The results of the soil characterization are summarized in Table II.

TABLE I. SUMMARY OF GEOTECHNICAL PROPERTIES OF JURICA SOIL.

Property	Symbol	Magnitude
Gravimetric water content	ω	33.46%
Specific gravity	γ_m	16.60 kN/m ³
Relative density of solids	Ss	2.35
Void ratio	e	1.31
Porosity	n	0.57
Degree of saturation	G ω	60.01 %
Volumetric water content	θ	34.04%
Liquid limit	LL	74.36%
Plastic limit, (PL)	PL	28.57%
Plastic Index, (PI)	PI	45.79%
Contraction limit, (CL)	CL	16.38%
Lineal contraction, (LC)	LC	18.24%
Gravel content, (G)	G	0.00%
Sand content, (S)	S	6.22%
Fines content, (F)	F	93.78%
Classification	UCSS	CH
Clay activity	A	0.95

For the determination of the hysteresis cycles effect on shrink-swelling soils, suction tests were performed in the laboratory with unaltered material specimens were also made using the filter paper method [20]. Figure 5 shows the relation on soil suction (ψ) and its degree of saturation (Sr) in wetting-drying paths. Samples were taken from the same location from which the soil characterization samples were taken.

The soil suction was measured in unaltered specimens with an initial water content rising in increments of 5.5% from 0% up to 38%. These water contents represent a degree of saturation that rises in increments of 10% from 0% up to 100%.

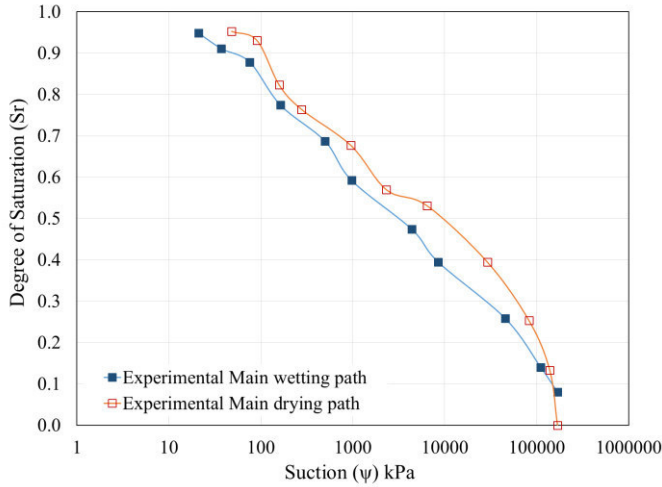


Fig. 5. Soil suction against initial water content of Jurica soil (SWRC).

IV. NUMERICAL AND EXPERIMENTAL COMPARISONS

To assess the ability of the proposed procedure determines the hysteresis secondary cycles through experimental SWRC, have been used experimental data of SWRCs that have been reported by other researchers. The results obtained with the procedure of [5] were compared with those reported by [3] and [4]. The mean absolute deviation (E_m) was used to check the quality of the three procedures, it is defined as:

$$E_m = \frac{1}{n} \sum_i^n \left| \Delta Sr_i \right| \quad (13)$$

Han-Chen et al. [3] determined a SWRC from a sample of compacted sand by vibration using a variable load permeameter (see Fig. 6). Tensiometers and reflectometers were used to measure matric suction and its water content at the same position within the soil specimen.

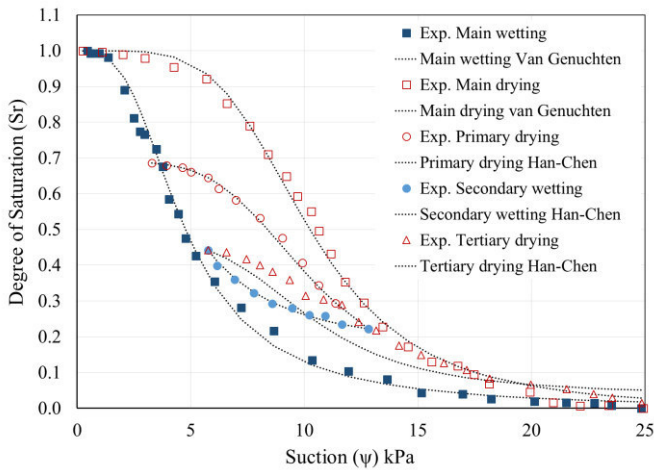


Fig. 6. SWRC from [3] vs hysteresis cycles prediction from [3] method.

Figures 6 to 8 illustrate the experimental SWRC determined in [3] versus the prediction from the hysteresis cycles using the methods of [3], [4], and [5] respectively.

Additionally, Table II lists the mean absolute deviation (E_m) between the experimental data and the results of the three methods using SWRC from [3].

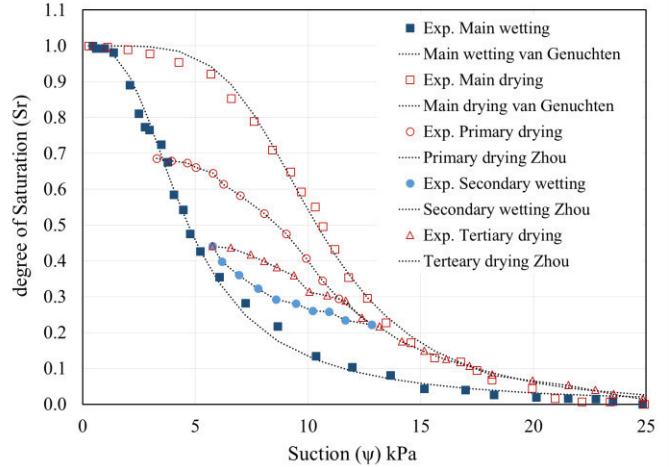


Fig. 7. SWRC from [3] vs hysteresis cycles prediction from [4] method.

Analyzing the Figs. 5 to 7 and Table II, we see that all three methods are very good and through them we can get very consistent results. Furthermore, it is possible to establish that the procedure proposed in [5] provides a significant improvement on the approximation of the SWRC in its main curves. However, other methods presented with lower values of the mean absolute deviation due to the simplicity of the equations that describe its shape.

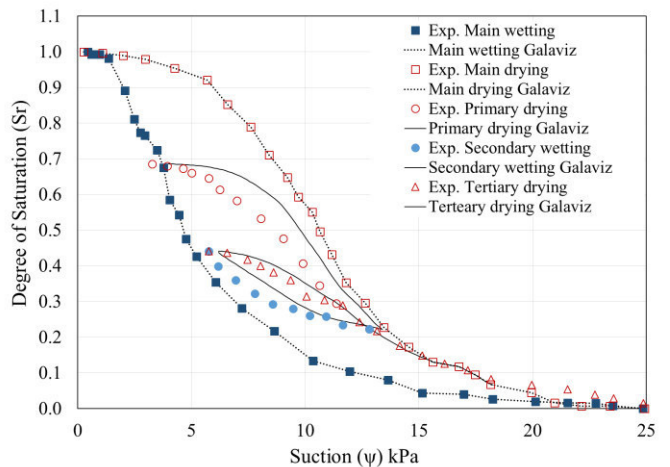


Fig. 8. SWRC from [3] vs hysteresis cycles prediction from [5] method.

TABLE II. MEAN ABSOLUTE DEVIATIONS (EM) BETWEEN EXPERIMENTAL RESULTS AND THOSE OBTAINED WITH THE THREE METHODS USING THE SWRC FROM [3].

SWRC Han-Chen [3]	Method		
	Han-Chen [3]	Zhou [4]	Galaviz [5]
Cycle	Em	Em	Em
Main wetting	0.0179	0.0167	0.0000
Main drying	0.0474	0.0455	0.0000
Primary drying	0.0065	0.0002	0.0482
Secondary wetting	0.0047	0.0002	0.0229
Tertiary drying	0.0706	0.0027	0.0078

Furthermore, it is known that the model shown in [2] is suitable for adjusting SWRC of sandy and loamy soils, but in clays (expansive soil) does not have the same quality. Therefore, this paper presents a comparison of the methods found in the literature that help us predict the hysteresis loops. This in order to assess the effectiveness of procedures to use with expansive SWRC.

From what we observed above, the methods based on the model of [2], using pre-defined equations for setting the SWRC, however, with the method proposed by [5], a predetermined equation of the adjustment process is avoided. Therefore, it is an excellent tool for determining secondary hysteresis cycles for unsaturated soils. The main features we observe the polynomial procedure are: a) the process of adjustment of experimental points for the SWRC with a predetermined equation, is prevented, b) the procedure ensures a 100% correlation between experimental and numerical data, c) this correlation increases the accuracy of the curves leading to unsaturated soils.

Due to the above, it was decided to study the unsaturated expansive soil from Jurica town, of Queretaro valley. This soil has been cause for a large number of investigations due to structural problems in buildings. This is due to volumetric changes caused by variations in water content caused by weather conditions (rainy and dry season).

Figure 9 shows the recognition of changes in water content of Jurica soil in a 12 month period (1992-1993). These data were obtained from moisture profiles reported by [21] and [22]. In Fig. 9 it can see behavior of changes in water content of the soil over time, demonstrating that the dry period for Querétaro city is between the months of October and May, and June to September the rainy season. It is also observed that the greater fluctuations in water content (between 17% and 41%) are very close to the surface (0.30 m) and with increasing depth, changes of water content tend to be constant (between 20% and 30%).

This led us to take these values of water content in order to exemplify and demonstrate the behavior of the hysteresis cycles of expansive soil from Jurica through the SWRC. Therefore, Fig. 10 shows the variation of the water content during the 12 months, corresponding to a depth of 0.30 m.

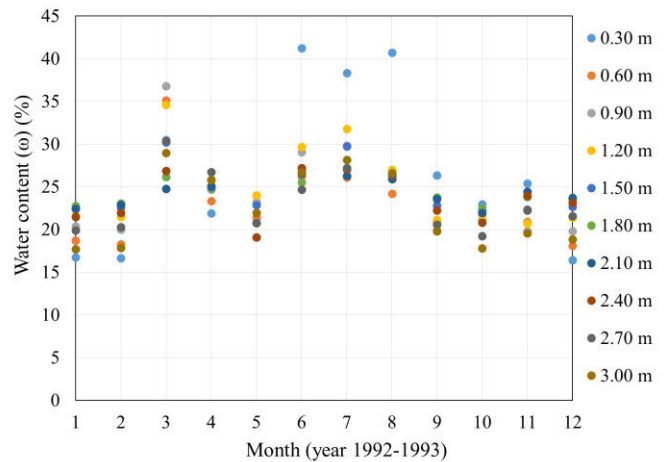


Fig. 9. Jurica's soil water content variations with respect to time and the depth [21, 22].

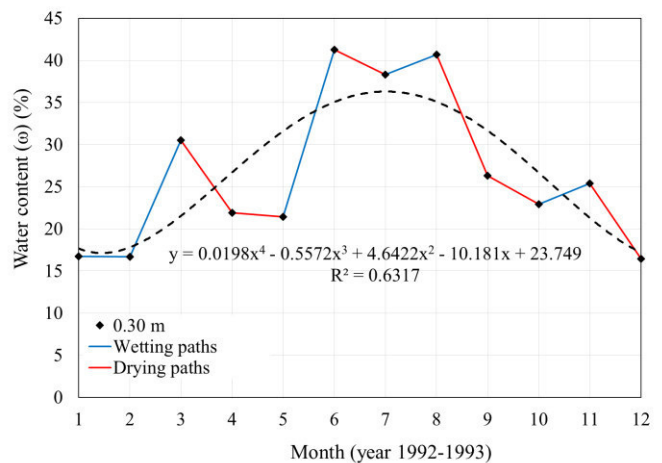


Fig. 10. Jurica's soil water content variations at the depth of 0.30 m.

Through Fig. 10, it can see that from January to March, May to June, July to August and October to November, wetting cycles are presented. Therefore, from March to May, June and July, August to October and November to December drying cycles. Because of this, and in order to show simple and easy way the hysteresis cycles using the SWRC. Only the primary cycle of wetting (January to July) and secondary drying cycle (July to December) are displayed as shown through which the polynomial curve fits the experimental data shown in Fig. 10.

To determine secondary wetting-drying cycles of Jurica soil, it was necessary to use the SWRC shown in Fig. 5. It took into account the minimum and maximum water content values shown in Figs. 11 and 12. Furthermore, in order to demonstrate the effect of adjustment and the correlation of main curves on predicting secondary cycles of wetting-drying, the main curves were adjusted using the method of [3] was performed, and procedure of [5] (see Figs. 10 and 11).

Subsequently, the mean absolute deviations were calculated for comparison adjustments (see Table III).

After analyzing Figs. 11, 12 and Table III, we can see that it is confirmed that the van Genuchten's adjustment is not well suited for clay soils. It was found the lower mean absolute deviation possible, however, it is clear that SWRC adjustment was not very good (see Fig. 11). This led to the prediction of secondary hysteresis cycles were not very successful. Also, it can be seen that the methods based on the model of [2], are not able to reproduce the phenomenon of hysteresis in the secondary paths of an expansive soil. This tells us that the suction values in both secondary cycles are the same for any water content (or degrees of saturation) of the same value. However, it is not properly possible.

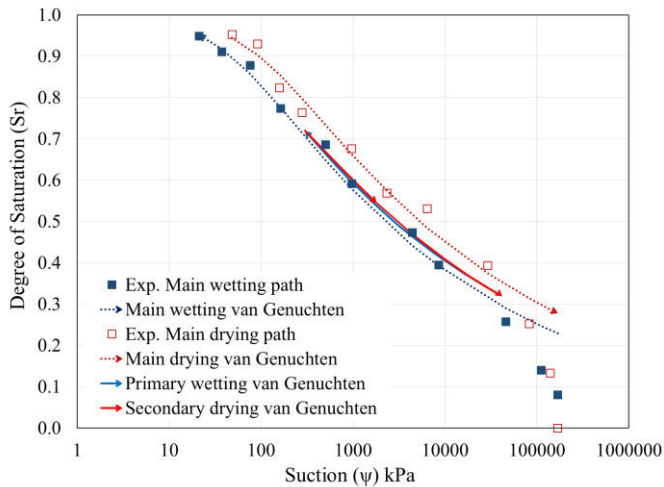


Fig. 11. Jurica SWRC with the fit and cycles prediction using [3] method.

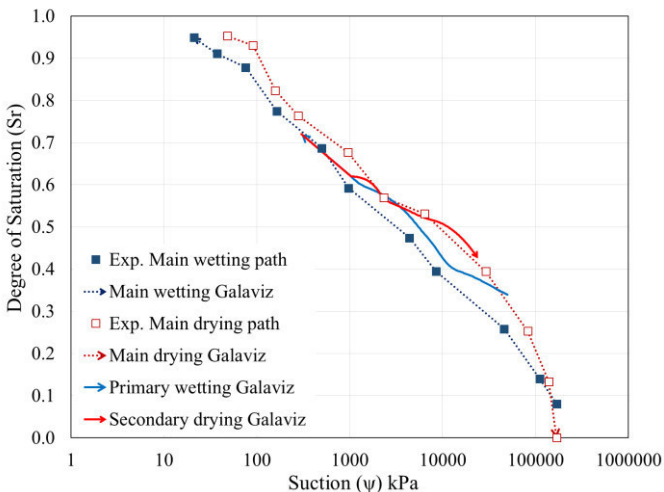


Fig. 12. Jurica's SWRC with the fit and cycles prediction using [5] procedure.

Furthermore, with the procedure proposed in [5] was possible to obtain mean absolute deviations equal to zero,

whereby a 100% fit with the experimental data was obtained (see Fig. 12). In the prediction of secondary cycles, was able to show the hysteresis phenomenon, which allows us to obtain suction values from the various water contents (or degrees of saturation) in various trajectories and the ease to obtain any hysteresis cycle. Otherwise, the methods based on predetermined equations of SWRC, showed that are not able to exhibit the phenomenon of hysteresis in the prediction of secondary cycles. This causes uncertainty in the determination of suction values and subsequent hysteresis cycles.

TABLE III. MEAN ABSOLUTE DEVIATIONS (E_m) BETWEEN EXPERIMENTAL RESULTS AND THOSE OBTAINED WITH THE METHODS USING THE JURICA'S SWRC.

SWRC Jurica	Method	
	Han-Chen [3]	Galaviz [5]
<i>Cycle</i>	E_m	E_m
Main wetting path	0.0185	0.0000
Main drying path	0.0297	0.0000
Primary wetting path	----	----
Secondary drying path	----	----

V. CONCLUSIONS

The procedures used in this paper, in order to predict the secondary cycles through the SWRCs proved viable and capable for sandy and silty soils. However, when used a clayey soil, the methods based on the model of van Genuchten were not able to show or reproduce the hysteresis phenomenon in the secondary cycles. On the other hand, polynomial method shows the hysteresis phenomenon in both primary and secondary cycles, presenting turn advantages over other existing methods: ensures a 100% correlation with the main numerical and experimental curves. Does not require a predetermined equation for the SWRC. The adjustment between the experimental and numerical SWRC is avoided. Finally, comparisons of the hysteresis cycles obtained with the different methods and experimental results, show that the polynomial method is a quick and easy tool to get very consistent results.

ACKNOWLEDGMENT

The authors would like to thank Consejo Nacional de Ciencia y Tecnología (CONACyT) and the Universidad Autónoma de Querétaro for their support and founding the project "Metodología para el diseño de cimentaciones en suelo expansivo por el método de interacción suelo-estructura utilizando el principio de esfuerzos efectivos (FoVin13-T-021)" in which the authors are working.

REFERENCES

- [1] H. Arroyo, E. Rojas, M. L. Perez-Rea, J. Horta and J. Arroyo, "Simulation of the shear strength for unsaturated soils," C. R. Mecanique, vol. 341, pp. 727-742, November 2013.

- [2] M. Th. van Genuchten, "A closed-form equation for predicting the hydraulic conductivity of unsaturated soils," *Soil Sci. Soc. Am. J.*, vol. 44, pp. 892-898, October 1980.
- [3] H. Han-Chen, T. Yih-Chi, L. Chen-Wuing and C. Chu-Hui, "A novel hysteresis model in unsaturated soil," *Hydrol. Process.*, vol. 19, pp. 1653-1665, January 2005.
- [4] A. N. Zhou, D. Sheng, S. W. Sloan and A. Gens, "Interpretation of unsaturated soil behaviour in the stress-saturation space, I: Volume change and water retention behaviour," *Computers and Geotechnics*, vol. 43, pp. 178-187, 2012.
- [5] J. R. Galaviz, J. Horta, E. Rojas, M. L. Pérez-Rea and J. Robles, "Determination of soil suction of Jurica by predictin hysteresis cycles," *Proceedings 8° Coloquio de Posgrado, Universidad Autónoma de Querétaro, Santiago de Querétaro, México, November 2014.*
- [6] King, H. Expansive soil and expansive clay. Available from <http://geology.com/articles/expansive-soil.shtml>. [Cited January 28, 2015].
- [7] J. P. Puppala, T. Manossuthikij and C. S. Chittoori, "Swell shrinkage characterization of unsaturated expansive clays from Texas," *Engineering Geology*, vol. 164, pp. 187-194, 2013.
- [8] E. Jahangir, O. Deck and F. Masrouri, "An analytical model of soil-structure interaction with swelling soils during droughts," *Computers and Geotechnics*, vol. 54, pp. 16-32, 2013.
- [9] Basement systems, <http://www.basementsystems.ca/foundation-repair/wall-cracks-repair/settlement.html>. [Cited February 2, 2015].
- [10] Home general contractor, <http://homegeneralcontractor.com/fixing-a-homes-foundation/>. [Cited February 2, 2015].
- [11] P. Máximo, "Dinámica de la penetración capilar en estructuras complejas," Ph. D. thesis, Universidad Autónoma de Querétaro, Santiago de Querétaro, México, 2012.
- [12] V. Meza, "Suelos parcialmente saturados, de la investigación a la catedral universitaria," *Boletín de Ciencias de la tierra, Medellín, Colombia*, vol. 31, pp. 23-28, 2012.
- [13] D. G. Fredlund and A. Xing, "Equations for the soil-water characteristic curve," *Canadian Geotechnical Journal*, vol. 31, pp. 91-99, 1994.
- [14] J. Horta, E. Rojas, M. L. Pérez-Rea, T. López, J. B. Zaragoza, "A random solid-porous model to simulate the retention curves of soils," *Int. J. Numer. Anal. Methods Geomech.*, vol. 37, pp. 932-944, 2013.
- [15] E. Rojas and O. Chávez, "Volumetric behavior of unsaturated soils," *Can. Geotech. J.*, vol. 50, pp. 209-222, 2013.
- [16] N. Lu and W. J. Likos, "Unsaturated soil mechanics," John Wiley & Sons, Inc. New Jersey, 2004.
- [17] J. R. Galaviz, M. L. Pérez-Rea, H. Arroyo, "Modelos de predicción de curvas de retención de agua para suelos parcialmente saturados," *Proceedings 9° Congreso Internacional de Ingeniería, Universidad Autónoma de Querétaro, Santiago de Querétaro, Querétaro, México, 2013.*
- [18] E. Rojas, "Equivalent stress equation for unsaturated soils, II: solid-porous model," *Int. J. of Geomech*, vol. 8(5), pp. 291-299, 2008.
- [19] Y. Mualem, "Hydraulic conductivity of unsaturated soils: Prediction and formulas," Invited review, Chapter 31, Monograph No. 9 of the ASA: *Methods of Soil Analysis, Part 1*, Edited by A. Klute. 1986.
- [20] ASTM D5298, Standard test method for measurement of soil potential (suction) using filter paper, 2008.
- [21] M. L. Pérez-Rea, "Succión y comportamiento esfuerzo-deformación en suelos expansivos de Jurica y Tejada, Qro.," Mc. Thesis, Facultad de ingeniería, Universidad Autónoma de Querétaro, Querétaro, México, 1993.
- [22] T. López-Lara, "Resistencia al esfuerzo cortante en arcillas expansivas de Querétaro," Mc. Thesis, Facultad de Ingeniería, Universidad Autónoma de Querétaro, Querétaro, México, 1996.

Flow Modelling in Unsaturated Soils

Soto-Reyes L.A. ^{#1}, Cornejo-Pérez O. ^{#2}, Pérez-Rea M. L. ^{#3}

[#] *División de Investigación y Posgrado de la Facultad de Ingeniería, Universidad Autónoma de Querétaro. Cerro de las Campanas S/N, Las Campanas, 76010 Santiago de Querétaro, Qro. México.*

¹ luis_sotoreyes@hotmail.es

² octavio.cornejo@uaq.mx

³ perea@uaq.mx

Abstract— Most of the modelling of flow in porous media is approached through the Richards equation, which is a nonlinear parabolic partial differential equation and due to its complexity, it has been solved by using different methods, and under assumptions that facilitate to obtain its solution. In this paper, a model of flow of moisture in unsaturated soils is presented. The model is inspired by the work of Li in which soil suction potential is used as state variable. For this purpose, data from Jurica Querétaro clays are used to approximate a function that represents the variation of the suction due to weather. Also, an initial distribution which is a function of the soil depth is provided. The model is solved by using the Galerkin method which has been implemented in a MATLAB program, and some results of the suction behavior in the soil substrate are shown in this work.

Keywords—Richards' equation; unsaturated flow; moisture flow; unsaturated soil.

I. INTRODUCTION

Soil mechanics is one of the essential issues in civil engineering because of the important role that it takes when we make any engineering project, mainly due to the soil-structure interaction problems. For too long, saturated soils were extensively studied because of its critical implication to certain infrastructures and the simplicity of the models that explain their behavior, relegated the study of unsaturated soils by the lack of interest and complexity the model needed for study [1]. This makes it more pertinent to research on unsaturated soils.

The limitations of traditional Soil Mechanics or saturated soils are evident when it is necessary to explain the unsaturated soil deformation or supported structures in these soils subject to service loads or total stress states present in situ [2].

In the group of sciences concerned with the behavior of soils, such as Geotechnics, the study of partially saturated soils is of great importance to determine the properties and behavior of the porous body. One of the elements used for the realization of models of unsaturated soils is the Richards equation, which allows to study the flow dynamics from moisture in the soil body [3], [4]. By means of this equation, we are able to observe the variation of moisture content over time and space.

Richards equation has been largely studied in recent decades due to the importance that has taken the unsaturated

soil mechanics in engineering studies. There are a variety of approaches and proposed methods [5]–[9] for the solution of this equation ranging from the simple and suitable to the most complex but with greater resemblance to real phenomena.

There are two main trends to search for the solution of partial differential equations such as the Richards equation. The first approach is the search for a closed solution using analytical tools, which provides a lot of information about the studied phenomenon and gives the possibility to predict the behavior of system. However, for too complicated systems can not exist or turns out to be a very difficult task to find a closed solution. The second approach is to use numerical methods that allow to study the behavior of some a particular model by getting a good approximation of the real phenomenon. An advantage of this approach is that it can be used in solving more complex systems and still provide quite accurate approximations. Also there are works [10], [11] that try to improve the methods used for solve Richards equation.

In this work, the study of a model for the movement of water in Jurica clays by using the Richards equation based on the suction variable, and taking into account a source function, is presented. The numerical approach used to solve the Richards equation allows to observe the variation in water content at different depths and moments.

II. RICHARDS EQUATION

In 1931 Richards first proposed an equation that determines the dynamics of flow in porous media, this is based on two major theories, these are Darcy's law for unsaturated soils and the continuity equation [12],

$$q = -k\nabla H \quad (1)$$

$$\frac{\partial \theta}{\partial t} = -\nabla q \quad (2)$$

where q is the flow rate, k is the coefficient of permeability of soil, θ is the volumetric water content and t is time.

In equation (3), the Richards equation in terms of volumetric water content, is presented. This equation is the bidimensional case of water flow in porous media.

$$\frac{\partial \theta}{\partial t} = \frac{\partial}{\partial x} \left[D_x(\theta) \frac{\partial \theta}{\partial x} \right] + \frac{\partial}{\partial y} \left[D_y(\theta) \frac{\partial \theta}{\partial y} \right] \quad (3)$$

Now we can get the following diffusion equation to describe the flow of moisture in unsaturated soils [13], [14], which introduces the term suction into the equation.

$$\frac{\partial u}{\partial t} = \frac{\partial u}{\partial \theta} \frac{\partial}{\partial x} \left(k \frac{\partial \Psi}{\partial x} \right) \quad (4)$$

The term $\frac{\partial u}{\partial \theta}$ is the slope of the characteristic curve [15], which relates the suction and volumetric water content θ . For most soils, mainly expansive soils, the variable $\frac{\partial u}{\partial \theta}$ can be assumed to be constant over the usual range.

The potential flow Ψ in expansive soils is composed of the full potential of suction u , the gravitational potential z and the potential overload Ω [14], [16].

$$\Psi = -u + z \pm \Omega \quad (5)$$

It has been shown in [17] that the gravitational potential and the overload potential are nearly canceled each other, and the small difference between them is relatively negligible. As we are only interested in evaluating soil movements due to the suction, it is only necessary to consider the potential of suction in (5). Therefore Ψ becomes equivalent to the potential of suction.

Taking the above considerations, and further assuming that the soil is homogeneous and isotropic the Richards equation can be simplified [18] as:

$$\frac{\partial^2 u}{\partial x^2} + \frac{\partial^2 u}{\partial y^2} + \frac{\partial^2 u}{\partial z^2} = \frac{1}{D} \frac{\partial u}{\partial t} \quad (6)$$

Further, if we consider a source of moisture in the soil, equation (6) can be written in the form:

$$\frac{\partial^2 u}{\partial x^2} + \frac{\partial^2 u}{\partial y^2} + \frac{\partial^2 u}{\partial z^2} + \frac{f(x,y,z,t)}{p} = \frac{1}{D} \frac{\partial u}{\partial t} \quad (7)$$

where u is the total suction potential, D is the diffusion coefficient of soil, and x , y and z are the spatial coordinates. Finally, t is the time variable. This equation is the one used by

Li in his work for the flow modelling in Australian soil [19] (Fig. 1), taking the suction as the principal variable.

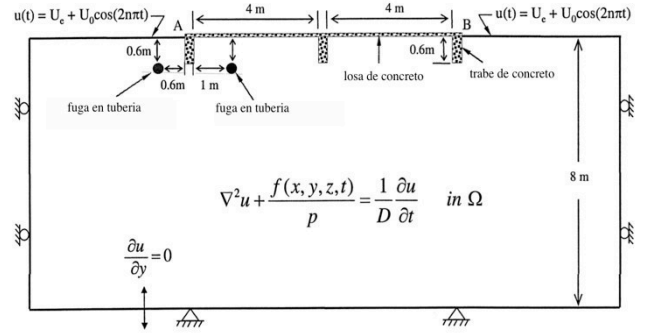


Fig. 1. Model diagram studied by Li [19].

III. MODEL

The proposed model in this work is illustrated in Fig. 2, which shows the boundary conditions, initial conditions and a source of moisture.

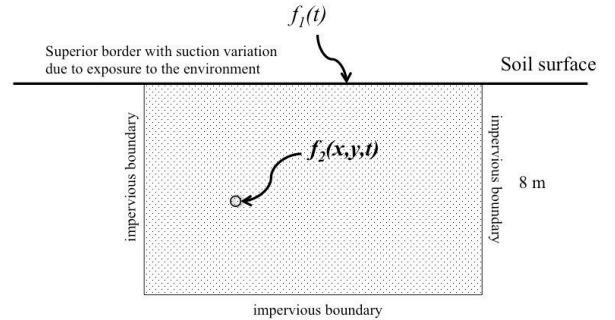


Fig. 2. Proposed model diagram.

In Fig. 2, $f_1(t)$ is a boundary condition determined by the suction variation due to climatic changes in the soil surface and $f_2(x,y,t)$ is a function that represents a source or sink into the soil. Both functions will be described in more detail later in this paper. The spatial domain of the model is two-dimensional, which is of interest, but it can also be extended to three dimensions.

A. Initial and boundary conditions

In order to solve (7) governing the flow phenomenon, it is necessary to specify initial and boundary conditions. Initial conditions specify suction distribution through the entire domain including the borders at the moment that the calculation is started. The boundary conditions can be divided into the following three categories [20]:

- Dirichlet type, where u is suction,

$$u(P, t) = \tilde{u}(P, t) \quad (8)$$

point P is on the border, and $u(P, t)$ is a prescribed function.

- Neumann type, where the gradient is defined as

$$\frac{\partial u}{\partial n}(P, t) = \tilde{q}(P, t) \quad (9)$$

and n denotes the normal to the boundary at point P .

- A convection boundary condition which represents the moisture exchange between the soil mass and the atmosphere,

$$\frac{\partial u}{\partial n}(P, t) = -h'(U_s - U_a) \quad (10)$$

where U_a and U_s are the suction of the atmosphere and the suction in the soil surface, respectively, and h' is a evaporation coefficient which is analogous to the convective heat transfer coefficient used in the heat transfer analysis. The parameter h' can be measured to determine the rate of change of suction at time in a soil specimen with known suction, which is allowed to gain or lose moisture with a suction atmosphere also known.

A boundary condition in which there is a border flow is analogous with thermal insulation, and it can be analyzed mathematically assuming $q = 0$ in (9).

It has been shown that the boundary conditions can be established by suction measurement data [21], [22].

Based on suction data in the field taken from Jurica soil in Querétaro, Mexico [23], [24], it was found that the suction surface could be assumed as a sinusoidal variation in response to climatic cycles, and by using least square method a sinusoidal function we can generate a function to approximate the behavior of the suction climatic changes in the soil surface.

B. Method

The model equation presented in this paper is solved by using the Galerkin method. This method is part of the weighted residual method, and it uses the same functions for weighting functions $W_i(x)$ that were used in the approximating equation [25]

$$\int_0^H W_i(x)R(x)dx = 0 \quad (11)$$

The general procedure consists of evaluation of the Galerkin residual integral with respect to the spatial coordinates for a fixed instant of time. This yields a system of differential equations which are solved to obtain the variation of u with time.

$$[A]\{U\}_b = [P]\{U\}_a + \{F^*\} \quad (12)$$

where A , P and F^* are defined as follows

$$[A] = [C] + \theta\Delta t[K], \quad (13)$$

$$[P] = [C] - (1 - \theta)\Delta t[K], \quad (14)$$

$$\{F^*\} = \Delta t(\theta\{F\}_b + (1 - \theta)\{F\}_a), \quad (15)$$

here $[K]$ is the stiffness matrix, $[C]$ is the capacitance matrix, θ depends on the method used, Δt is the time step, $\{F^*\}$ represents the external forces and $\{U\}$ are suction values.

IV. FLOW PARAMETERS

A. Permeability coefficient

Various techniques exist for determining the coefficient of permeability of a soil, which can be direct or indirect methods. Direct measurement techniques are commonly known as permeability tests, carried out by means of an apparatus called permeameter. The hydraulic gradient and the flow rate is determined by measurement of the water pressure in the pores and water content. In some cases, the pore pressure or the water content is measured, while the other variable is inferred from the characteristic curve [15].

Direct measurement of permeability can be developed in the laboratory and in the field [26]. The non-homogeneity and anisotropy of soils made *in situ* tests give a higher permeability coefficient than laboratory tests. Cracks, fractures, stress cracks and holes roots, commonly found in unsaturated soils cannot be properly represented in laboratory specimens due to their small scale. Furthermore, laboratory samples are subject to changes due to sampling and the methods applied in the field are not as advanced or standardized laboratory methods.

Directly measuring the permeability coefficient for unsaturated soils is often expensive and difficult to perform,

especially in the field. So, attempts have been made to predict it theoretically by using either the permeability coefficient ratio and the degree of saturation, or the soil suction between the volumetric water content and the soil suction [27]. These predictions are generally referred to an indirect method of determining permeability. The saturated permeability coefficient is required when using an indirect method.

Several direct and indirect methods used regularly for permeability coefficient have been described in detail in other papers [15], [26]–[28], so they will not be repeated in this work. The permeability coefficient for a soil obtained from a direct measurement is better since there is no standard theoretical prediction.

B. Diffusion coefficient

The diffusion coefficient of a soil is vital to understand the behavior of water in it. The formal definition of the diffusion coefficient is "ease with which a liquid is passing through a particular medium." It is expressed as the ratio of the permeability coefficient k and the specific water capacity C .

Reference [19] mentions that the diffusion coefficient is analogous to the coefficient of consolidation, in the classical theory of consolidation, further, it is indicated that the magnitude of this coefficient defines the rate of diffusion of moisture under gradients of suction change. The value D is strictly a nonlinear function depending on moisture content, which may be calculated based on test results from saturation.

The diffusion coefficient used in the model of Li, can be determined by the expression,

$$D = \frac{p}{(c\rho_d)}, \quad (16)$$

where

$$c = \frac{\Delta w}{\Delta u}, \quad (17)$$

the parameter c is the characteristic soil moisture, ρ_d is the density dry soil, and p is the unsaturated permeability.

V. RESULTS

The function obtained to approximate the variation of the suction due to climatic changes is shown in Fig. 3.

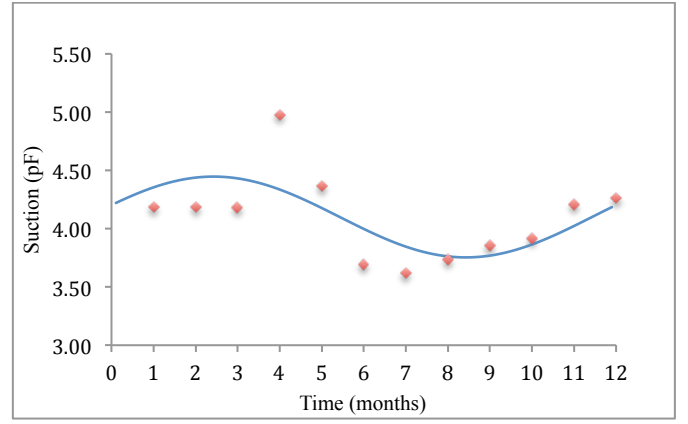


Fig. 3. Fitting of suction data due to seasonal changes to sinusoidal function. The function was an approximation of the experimental data (points) by least squares for a sinusoidal function (solid line).

The approximation was performed by least squares [29] for sinusoidal functions, and the result is presented in the following equation

$$u(H, t) = 4.1 + 0.1 \cos\left(\frac{2\pi}{12}t\right) + 0.3 \sin\left(\frac{2\pi}{12}t\right), \quad (18)$$

where H is the distance from the bottom to the soil surface, u is suction (in pF) and t is the time variable (in months). For the model, we require to make the conversion pF to kPa.

The Fig. 4 shows the fitting of the suction data to an exponential function. Due to the tendency of data for suction variation with depth, a least squares approximation [29] to an exponential function was obtained. Such approximation is given in the following form.

$$u(y, t_0) = 346.15e^{0.0072y} \quad \text{for } y < y_e \quad (19)$$

Although the equation is exponential, suction values in depths larger than y_e are almost constant, i.e., changes in suction values are too small that these can be neglected and the function becomes:

$$u(y, t_0) \approx u_e \quad \text{for } y \geq y_e, \quad (20)$$

where y_e is the depth when the function reaches the equilibrium suction u_e .

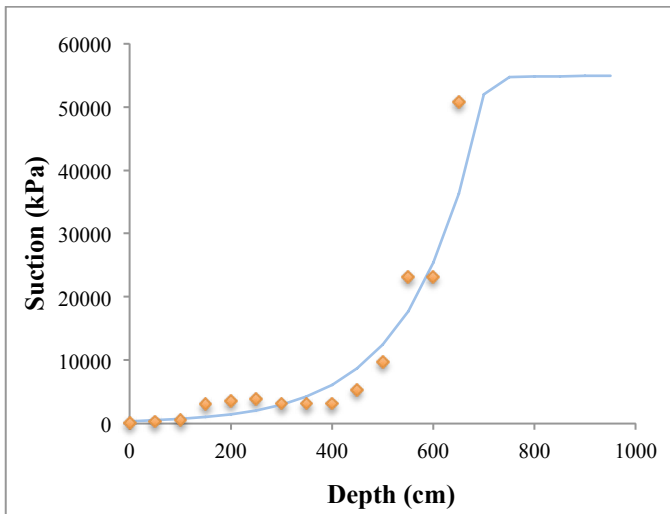


Fig. 4. Fitting of experimental data in different depths to an exponential function. The function was approximated by least squares for an exponential function (solid line) using experimental data (points) from Jurica, Querétaro.

Calculations of functions and graphs shown before were performed in Microsoft Excel. For solving the model with the proposed functions it was used the software MATLAB. The code of the method described above was written in a MATLAB program. In Fig. 5 the results obtained for the model without a source or sink are shown, and the effects from suction changes due to soil-environment interacting on the top boundary are displayed. Finally Figs. 6 and 7 show the suction distribution in a soil substrate where an arbitrary source is acting since the beginning.

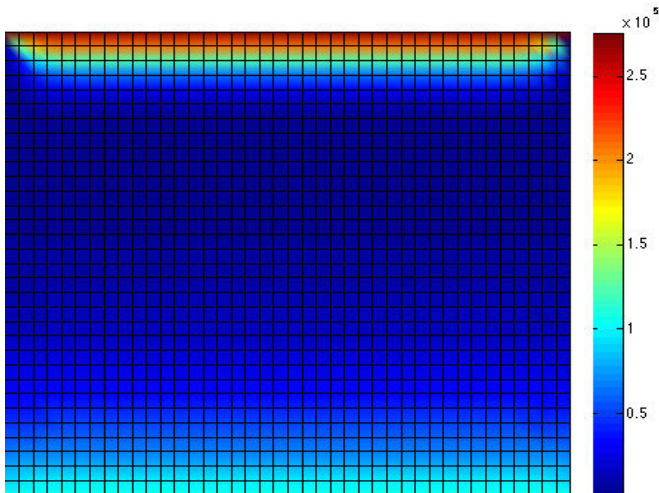


Fig. 5. Matlab graph showing the effects of suction changes (in kPa) due to the soil-environment interaction after 3 months in a soil layer, the initial month was established in January.

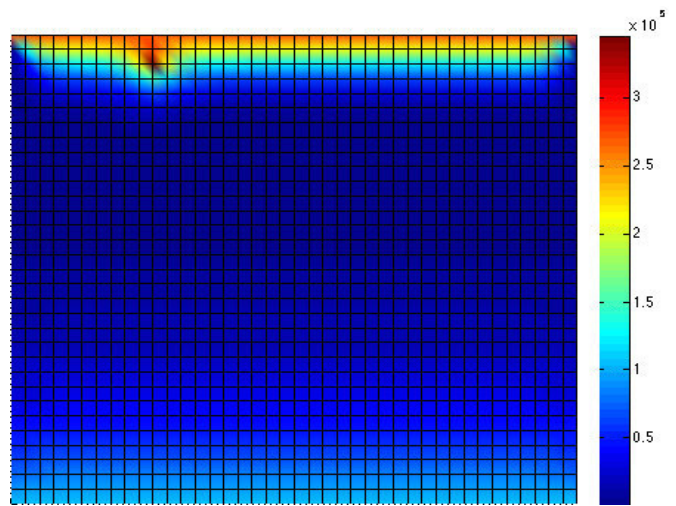


Fig. 6. Matlab graph showing the effects of suction in a soil substrate where a source is acting near the top boundary. Suction distribution (in kPa) after 3 months, the initial month was established in January.

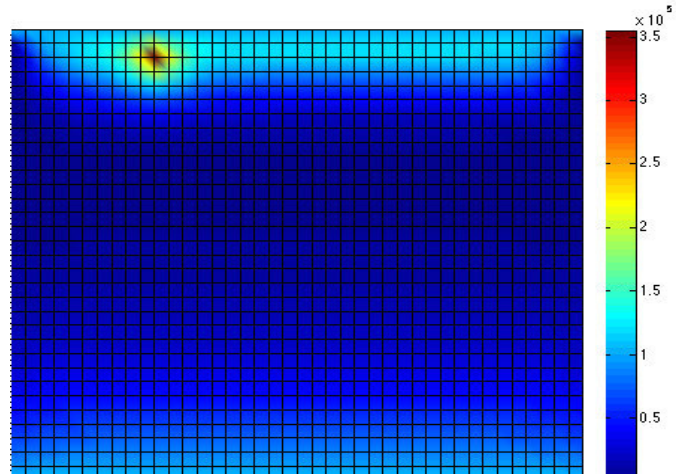


Fig. 7. Matlab graph showing the effects of suction in a soil substrate where a source is acting near of the top boundary. Suction distribution (in kPa) after 6 months, the initial month was established in January.

VI. CONCLUSION

From the obtained results we can see that both changes caused by weather or by the source, do not significantly impact to large depths. On the other hand, both can potentially cause problems when placing structures because they affect the flow on the surface, which influences the behavior of expansion or contraction of the soil. Also, it was found that the dynamics at large depths is mainly defined by the boundary conditions and the initial moisture distribution.

Because we try to model a phenomenon as close as possible to reality, the calculations required to study the model system become quite complicated. In fact, analytical methods require to solve complex equations and therefore, we use numerical methods for their solution.

There are several investigations related to numerical methods, and how to improve its implementation in Richards equation. Although it lacks even further development of flow models in unsaturated soils that can express in a better way the effect of other important state variables, such as sucking and sources of moisture that naturally exist in the system, for instance, moisture leakage and tree roots. Therefore, regarding the fields of geotechnics and mathematical modelling, it is a great opportunity to conduct research on the issues mentioned above.

ACKNOWLEDGEMENTS

The authors wish to thank CONACYT, Mexico, for the support granted for the development of this research which is part of the work done in graduate studies.

REFERENCES

- [1] M. Celia, E. Bouloutas, and R. Zarba, "A general mass-conservative numerical solution for the unsaturated flow equation," *Water Resour. Res.*, vol. 26, pp. 1483–1496, 1990.
- [2] D. G. Fredlund, "Teaching unsaturated soil mechanics as part of the undergraduate civil engineering curriculum," in *Proceedings of the Second Pan American Conference on the Teaching Learning Process of the Geotechnical Engineering. Quayaquil, Ecuador, 2002*.
- [3] D. Titouna and S. Bougoul, "Resolution of the Richards equation for the water transport in a growing substrate," *TerraGreen 13 Int. Conf. 2013 - Adv. Renew. Energy Clean Environ.*, vol. 36, no. 0, pp. 915–922, 2013.
- [4] H. Cao and X. Yue, "Homogenization of Richards' equation of van Genuchten–Muallem model," *J. Math. Anal. Appl.*, vol. 412, no. 1, pp. 391–400, abril 2014.
- [5] J. C. van Dam and R. A. Feddes, "Numerical simulation of infiltration, evaporation and shallow groundwater levels with the Richards equation," *J. Hydrol.*, vol. 233, no. 1–4, pp. 72–85, Jun. 2000.
- [6] A. Barari, M. Omidvar, A. R. Ghotbi, and D. D. Ganji, "Numerical analysis of Richards' problem for water penetration in unsaturated soils," *Hydrol. Earth Syst. Sci. Discuss.*, vol. 6, no. 5, pp. 6359–6385, 2009.
- [7] M. Fahs, A. Younes, and F. Lehmann, "An easy and efficient combination of the mixed finite element method and the method of lines for the resolution of Richards' equation," *Environ. Model. Softw.*, vol. 24, no. 9, pp. 1122–1126, Sep. 2009.
- [8] W. Merz and P. Rybka, "Strong solutions to the Richards equation in the unsaturated zone," *J. Math. Anal. Appl.*, vol. 371, no. 2, pp. 741–749, Nov. 2010.
- [9] H. Sun, M. M. Meerschaert, Y. Zhang, J. Zhu, and W. Chen, "A fractal Richards' equation to capture the non-boltzmann scaling of water transport in unsaturated media," *Adv. Water Resour.*, vol. 52, no. 0, pp. 292–295, Feb. 2013.
- [10] H. An, Y. Ichikawa, Y. Tachikawa, and M. Shiba, "Comparison between iteration schemes for three-dimensional coordinate-transformed saturated–unsaturated flow model," *J. Hydrol.*, vol. 470–71, pp. 212–226, 2012.
- [11] F. A. Radu and W. Wang, "Convergence analysis for a mixed finite element scheme for flow in strictly unsaturated porous media," *Spec. Sect. Multiscale Probl. Sci. Technol. Chall. Math. Anal. Perspect. III*, vol. 15, no. 0, pp. 266–275, Jan. 2014.
- [12] L. A. Richards, "Capillary conduction of liquids through porous mediums," *J. Appl. Phys.*, vol. 1, no. 5, p. 318, 1931.
- [13] B. G. Richards, "Moisture flow and equilibria in unsaturated soils for shallow foundations," *ASTM Symp Permeability Capillarity*, vol. 417, pp. 4–34, 1967.
- [14] R. L. Lytton, "Foundation in expansive soils," in *Numerical method in Geotechnical engineering*, C. S. Desai and J. T. Christian, Eds. McGraw-Hill, 1977.
- [15] D. G. Fredlund and H. Rahardjo, *Soil mechanics for unsaturated soils*. New York: Wiley, 1993.
- [16] J. R. Philip, "Hydrostatics and hydrodynamic in swelling soils," *Water Resour. Res.*, vol. 5, no. 5, pp. 1070–1077, 1969.
- [17] M. Sokolov and J. M. Amir, "Moisture distribution in covered clays," in *Proc. 3th Int. Conf. on expansive soils*, Israel, 1973, pp. 129–136.
- [18] P. W. Mitchell, "The structural analysis of footing on expansive soil," Research Report 1, 1979.
- [19] J. Li, "Two dimensional simulation of a stiffened slab on expansive soil subject to a leaking underground water pipe," in *Unsaturated Soils 2006*, American Society of Civil Engineers, 2006, pp. 2098–2109.
- [20] J. Li, "Finite element analysis of deep beam in expansive clays," presented at the First International Conference on Unsaturated Soils, Paris, France, 1995, pp. 1109–1115.
- [21] A. S. El-Hames and K. S. Richards, "Testing the numerical difficulty applying Richards' equation to sandy and clayey soils," *J. Hydrol.*, vol. 167, no. 1–4, pp. 381–391, May 1995.
- [22] J. Li, "Analysis and modelling of performance of footing on expansive soils," PhD Thesis, University of South Australia, 1996.
- [23] M. L. Pérez-Rea, "Succión y comportamiento esfuerzo-deformación en suelos expansivos," Universidad Autónoma de Querétaro, Querétaro, México, 1993.
- [24] T. López-Lara, "Resistencia al esfuerzo cortante en arcillas expansivas de Jurica, Querétaro," Universidad Autónoma de Querétaro, Querétaro, México, 1995.
- [25] K.-J. Bathe, *Finite element procedures*. Englewood Cliffs, N.J: Prentice Hall, 1996.
- [26] E. J. Badillo and A. R. Rodríguez, *Mecánica de suelos*. Ed. Revista de Ingeniería, 1969.
- [27] D. G. Fredlund, A. Xing, and S. Huang, "Predicting the permeability function for unsaturated soils using the soil-water characteristic curve," *Can. Geotech. J.*, vol. 31, no. 4, pp. 533–546, 1994.
- [28] J. Šimůnek and M. van Genuchten, "Estimating unsaturated soil hydraulic properties from tension disc infiltrometer data by numerical inversion," *Water Resour. Res.*, vol. 32, no. 9, pp. 2683–2696, 1996.
- [29] S. C. Chapra and R. P. Canale, *Métodos numéricos para ingenieros*. McGraw-Hill, 2007.

Study degradation process by cracking in simple concrete through acoustic emission technique and correlation parameters

A.O. Méndez García ^{#1}, M.A. Pérez- Lara y Hernández ^{#2}, S.E. Crespo Sánchez ^{#3}

^{#1} Grad student DEPFI. Facultad de Ingeniería, Universidad Autónoma de Querétaro; Querétaro, México. C. P. 76010

^{#2} Professor-DEPFI. Facultad de Ingeniería, Universidad Autónoma de Querétaro; Querétaro, México

¹jaguar_mega30@hotmail.com

²migperez@uaq.mx

^{#3} Researcher, Instituto Mexicano del Transporte; Querétaro, México. CP. 76703

³screspo@imt.mx

ABSTRACT. All structures gradually accumulate damage during their lifetime. Generally speaking, any structure is likely to behave erratically, since current conditions of service and / or characteristics of materials may differ from those expected by the designer. One of the causes contributing to deterioration, and therefore to the low performance of structures is cracking, which occurs as a natural response to stress conditions specifically developed in them [1]. The progressive cracking in structural elements can lead to failure, since it occurs within the material, which, over a continuous stress, produces the nucleation of these cracks to cause fractures of the material. The Nondestructive Technique NDT of Acoustic Emission AE has proven to be a powerful tool in the detection of damage as well as to assess the current state conditions of structural systems [2]. In this paper, AE technique is used as a tool for identifying and study degradation processes by cracking of simple concrete elements, using as main element the behavior of signals generated in the breaking process. The results show the effectiveness of the AE technique in describing this phenomenon of degradation of concrete and the correlations among its characteristic parameters and the image features of the failure surfaces of the analyzed elements.

Keywords— *Acoustic emission, failure, cracking*

I. INTRODUCTION

Concrete is one of the most used materials in structures such as bridges, dams and buildings [1]. These structures are exposed to damage affecting the conditions and structural performance during their service life. One of the most common damaging issues to concrete is produced by cracking, which is one of the biggest problems of design and durability [3]. This phenomenon is strongly linked to the heterogeneous nature of the material as a result of a natural response to stress conditions generated within it [1]. Such stress may be originated mainly by environmental or load conditions. Depending on their origin, they can be classified as mechanical, physical and chemical effects. Among the

mechanical and physical effects, there are deformations due to volumetric changes, stresses caused by tensile forces, bending moments, shear forces and fatigue effects.

Fracture processes are closely related to degradation by cracking as it is regarded as a continuous propagation process from initial micro –crack propagation, to macro-structural fracture, and complete structural failure [4] which is unpredictable due to the composite materials properties and their complex structure.

Currently certain NDT can give a way to a greater understanding of the deterioration phenomena leading to functional impairment of the structure. Among them the acoustic emissions technique, is a powerful tool for evaluating structural systems without destroying the material conditions, with the advantage of detecting real and irreversible cracking in concrete structures.

AE technique utilizes the elastic stress waves released by dislocation during the incremental loading process. These elastic waves are recorded by a transducer attached to the surface of the concrete structure [2].

II. GENERAL BACKGROUND

The first formal studies of fracture and crack propagation of several materials is given by the Linear Elastic Fracture Mechanics LEFM which was proposed by Griffith in 1920, with its energy criterion of crack propagation. Subsequently, there were major contributions to the LEFM, developing various models of crack propagation. One of the highlights was proposed by Paris [5] and was the foundation for other models such as Walker [6] and the Forman's Law [7], however, were Bazant and Xu [8], who proposed an amendment to the law of Paris for concrete application. Other models have been proposed by Continuum Damage Mechanics CDM, although these have been used frequently by

computational theorists, its main problem is the lack of experimental validation [9].

Currently, there is a growing need of rather than theoretical models, it is necessary a method that allows a more specialized study of cracking, applied not only on the material, but also on the structural assembly that could be used to determine the conditions of service of the structure[10,11], with the effectiveness of a nondestructive evaluation technique (NDE). In some assessments and monitoring systems it is vital to use a non-destructive reliable test (NDT), safe and able to provide real-time information on the conditions of the structure [2]. Experiments have proved the AE technique is a powerful tool for evaluation of some systems without destroying the material conditions [21-30], since this technique is capable of providing information through the analysis of AE parametric or waveform , which helps the understanding of the fracture process in concrete [4], by the fact of detecting cracking within the material . The AE technique has been used in numerous applications for process characterization of material damage, including large concrete structures [2].

A. Acoustic Emission

Acoustic emissions, due to their generation and propagation through a continuous medium, are able to determine according to their intensity, the evolution and behavior of a material in the bearing condition, even without being subject a load [1].

Acoustic emission phenomenon is defined as the elastic wave propagation due to the release of energy in the material produced by micro fractures. Activity sources of EA include processes of plastic deformation such as structural deformation, crack expansion and other kinds of material degradation [12].

The basic principle of the AE is the detection of elastic waves radiated by the crack propagation, occurring not only on the surface but also in the inner section of a structure. Unlike ultrasound tests, AE equipment are designed to monitor acoustic emissions produced within the material during the failure or stress induction, rather than actively transmitting waves. The main components of the EA apparatus include transducers, signal amplifier, signal processor, and a monitor. [4],Fig.1.

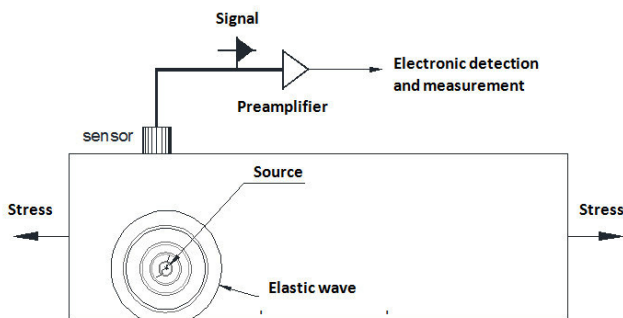


Fig. 3 The basic principle of the AE

Fig. 1 Basic parameters of an acoustic emission waveform

The sensors respond to the dynamic motion caused by an AE event. This is achieved by transducers which convert the mechanical movement into a voltage signal.

The technique of acoustic emissions is based on the analysis of acoustic signals propagating in the form of elastic waves, and also are accompanied by changes in the structure of the material (concrete) which is generated by a local energy release with source located within the material and are commonly cracks or deformations [11]

Initial and subsequent cracks, caused by an external action, result in energy changes, which may be acquired as acoustic waves in the member surface.

EA signals can be recorded by sensors placed on the concrete surface and once recorded the signals (hit) [11] can be calculated certain parameters: amplitude in mV or dB, rise time, duration, signal strength, average signal frequency, number of counts [10] and energy.

These signals can be divided into a classical approach, based on parameters, as well as under a quantitative approach based on waveforms [12]

These approaches are used to determine a type of analysis and treatment for AE. [10]

B. Parametric Analysis.

The implementation of this type of analysis is recommended when the amount of data EA is large in a short period of time, therefore, the acquisition and processing of the waveform is not suitable [13]. In the parametric analysis, amplitude, rise time, duration, signal strength, average signal frequency, number of counts and energy characterize the signal EA (fig.2)[10]. In this approach, the characteristic parameters of the signal are used to assess the damage degree and to identify its nature.

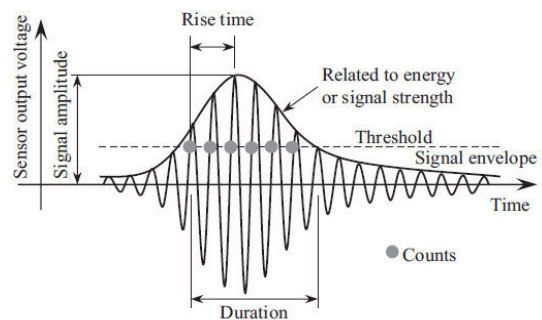


Fig. 2 Basic parameters of an acoustic emission waveform

C. Signal waveform analysis.

In the type of parametric analysis, only some of the parameters of EA are acquired or recorded during monitoring, but not the signal itself. This approach has a fast database, however, may acquire the raw waveforms in multi-channels. The most important feature of this approach is the possibility of obtaining a better performance in noise

discrimination, providing better interpretation in some cases [13].

D. Difference between AE parametric and waveform approach.

In the case of parametric analysis, the premise is that the signal is entirely defined by the parameter settings and storing this relatively small amount of parameter data requires less time and storage space, preferably rather than if entire waveforms are stored. Furthermore, in AE parametric based approach there are possibilities of having high records of data, in addition to high data speed storage so that fast visualization of data would be facilitated. In practice, it can be difficult to discriminate an AE signal from noise (e.g. caused by electronic pulses) after the signal has been reduced to a few parameters. This approach is also very dependent on the material and geometric properties.

On the other hand, implementing AE signal based analysis allows for more comprehensive but time consuming analysis, however it should be noted that AE signal based approach usually offers analysis in a post processing environment whereas AE parametric makes real time monitoring possible. The most important feature of signal based analysis over parametric approach is the capability of signal-to-noise discrimination based on waveform.

Certain parameters alone can provide a quantitative measure of progressive damage in a material, while some should relate to others to provide information on the phenomenon.

In recent studies, the technique has been used in concrete to develop indices of damage to reinforced concrete structures and prestressed by estimating the accumulated energy (parametric analysis), which is associated with plastic deformation energy concrete[11], locating sources of release of this energy[19], behavioral assessments of this material with external reinforcement [20], etc.

III. RESEARCH DESCRIPTION.

In the present study, an analysis of concrete cracking processes through experimental test were performed in the laboratory applying the EA technique in simple concrete specimens following the Standard test method for Flexural strength of concrete(Third-point Loading) ASTM C 78, with monotonous and linear load at break point. The acquisition of AE signals is continuous in time, and records are stored each time when an event exceeds the threshold level set at 35 dB.

Sets of acquired signals in waveform approach are analyzed to obtain the characteristic acoustic parameters (hits, counts, energy, amplitude, etc.) by taking advantage that this approach provides for noise discrimination [13]. The aim of this study is to correlate AE information with the physical properties of failure surfaces of concrete elements tested, and understand the behavior of breaking through these correlations. Among the mentioned properties are estimated moduli of rupture, the percentages of coarse aggregates and distribution of their areas in the failure section. To analyze these properties, algorithms were developed using the technique of artificial vision or

image processing that implies improvement in sharpness and filters that highlights forms, positions, sizes and other features of objects of particular interest.

IV. EXPERIMENTAL PROGRAM

There were made up to 40 prismatic specimens of 15x15cm constant cross section and a length of 50 cm, which were made with simple concrete with an average compressive strength at 28 days $f'_c = 200\text{kg} / \text{cm}^2$ with maximum aggregate size limestone $\frac{3}{4}$ (2cm), and slump of 10 cm. The specimens were cured by immersion in water curing tubs and hydrated lime.

The specimens were tested following the Standard test method for Flexural strength of concrete(Third-point Loading) ASTM C 78, using a servo hydraulic machine Instron 8503 with an application rate monotonic loading increased from 712.37 kgf / min (6986N / min) which was calculated according to (ASTM C -78).

The instrumentation of specimens for the acquisition of acoustic emission signals was performed with 4 piezoelectric transducers (front face S1, S2; posterior face S3, S4), with a sensitivity of 10 mV. Fig.3 shows the position of the specimen, also the location of piezoelectric transducers. The data acquisition was performed with a computer Physical Acoustic PCI-DS using a threshold level of 35 dB acquisition, signal processor (μDispTM), 4 channel capacity bandwidth of 10kHz -2MHz, preamplifier with a gain 40dB.

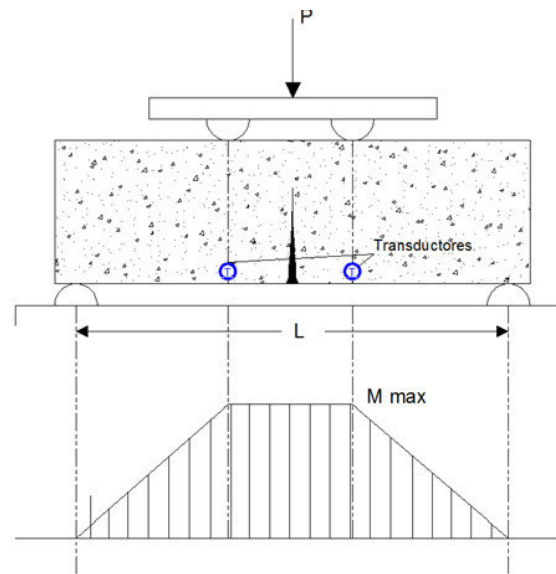


Fig. 4 Test setup, instrumentation and load specimen.

Sensors were mounted by means of a device with mobile clamp to allow the desired location on the front and back of the specimen, and coupled to the surface with an epoxy material to ensure contact with the surface of the specimen, these sensors were established acquisition in a range of 10-400 kHz.

V. DATA ANALYSIS AND PRELIMINARY RESULTS

In order to perform the data analysis, the most significant factors of the experiment, such as Modulus of Rupture, Power signals, accounts, and percentage of aggregates in failure section are taken in account and to related to each other, with the intent of derive behavior relationships . Concrete flexural strength, also known as the modulus of rupture, was estimated using the equation given in ASTM C-78 .

$$R = \frac{PL}{bd^2} \quad \text{Ec. 1}$$

Where R is the modulus of rupture, P is the maximum load applied at the end of test (psi or MPa), L is the span, b is the width dimension (in or mm) and d is the depth of the section (in or mm).

A. AE waveforms analysis

The acquired signals (Fig. 4) were analyzed to obtain various characteristic parameters (Counts, Energy, Amplitude, and Rise Time), for which algorithms are designed in Matlab language. The counts were obtained discriminating events with lower amplitudes at threshold level set at 35 dB equivalent to 0.0056 V, according to the inherent noise in the test conditions. The counting of these events are automatically performed in the databases, the same way it is possible to determine the total or partial time duration of the event from crossing the threshold level.

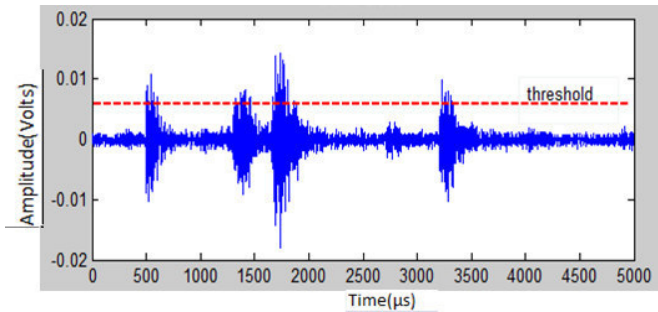


Fig. 4 Acoustic signal processing.

From this analysis, it can be seen that the number of acoustic events that exceed the threshold level in the samples is, in itself, an indicator of progressive damage generated during the test as most counts have each hit, it is assumed that event is generated by a higher crack than a hit with few counts, then each hit serves to characterize a particular crack state while increasing hits over time serve to quantify the progressive damage over time. In the way that increase the percentage of load applied to the bending test, the number hits also suffers substantial increase (Fig. 5).

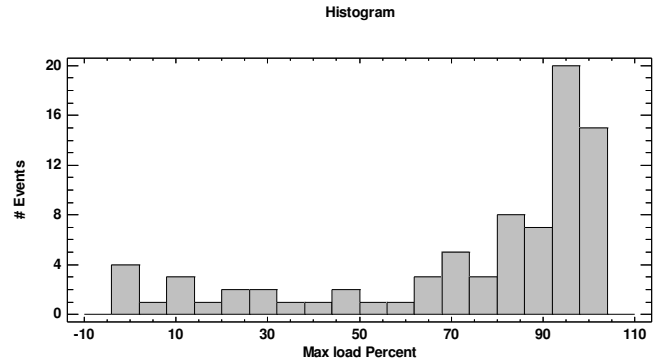


Fig. 5 cracking increment taking in account AE Events

Furthermore, the elastic energy released in each hit is identified in the characteristic parameters of analysis. This parameter is considered as the area under the curve of the signal, taking into account that the ideal is that it is a purified signal Fig. 6

The relationship between the energy and the signal received at the transducer and the strain energy can be affected by factors such as distance from the source, attenuation due to the medium material and the coupling means [13], these factors are not treated in this study, and it can check in references [14-18].

$$E_i = \int_{t_0}^{t_i} V^2(t) dt \quad \text{Ec. 2}$$

Where V is transient voltage of each channel, and t_0 , t_i is the time to start and end respectively of transient voltage.

There were developed algorithms for integration and filtering of signals of acoustic events, and obtain the energy associated with these events.

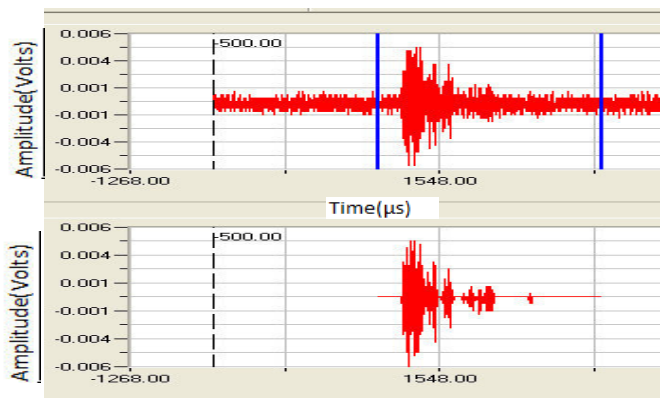


Fig. 6 Signal Reconstruction for integration of energy.

Considering work with a clean signal, a reconstruction of the signal is performed using a Wavelet analysis where the noise band is eliminated, since the software EA (AEwin for DiSP)

allows this type of analysis applies this option to each hit each test performed, obtaining a fully refined noise signal. (Fig.6)

B. Surface analysis failure

The failure surface of each specimen is processed for analysis by Artificial Vision. The process was conducted by the NI Vision Builder (VB) software, which uses a graphical language with a simple linear programming. Through digital photography, VB makes an interpretation of the object of interest, which can be acquired in real time or extracted from a storage medium. With this, a calibration is generated to correct defects of perspective of the lens or the camera and thus achieve a good definition of the edges of the section, since the object of particular interest is located within this area. Filtering of the objects contained within the edges is performed by differences in shades, shape and sizes. Measurement of parameters of interest is carried out by the pixel count conversion to metric units. Data obtained from the processing from the fault surfaces of the area were percentages of aggregates area and cement paste, distribution of these aggregates, and moments of inertia about their centroids.

In Fig. 7 the failure cross-sectional image of a processed specimen with VB is shown.

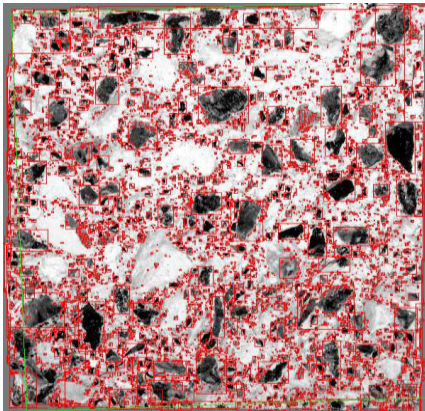


Fig. 7 Rupture cross section processed in VB

Analyzing the failure surfaces, statistical distributions of aggregates surfaces that comprise these surfaces were obtained. It could be seen that as the average of the aggregate areas on this surface increases, also the amount of energy released does it too. Fig 8 shows the accumulated energy for two specimens differing in aggregates sizes in their failure surfaces. In it, T1 has a maximum aggregate size (MAS) of 3.1cm^2 , measured through VB in its failure surface, whereas T2 has a MAS of 2.1 cm^2 in the failure surface.

Among other analyzes it was observed that there is a relationship between the number of registered counts and cumulative energy in simple concrete, this relationship is shown in Fig. 9.

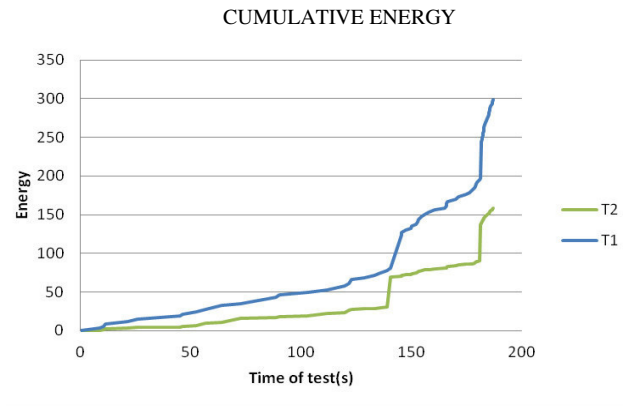


fig. 8 Cumulative Energy in specimens with different aggregate size in the failure surface.

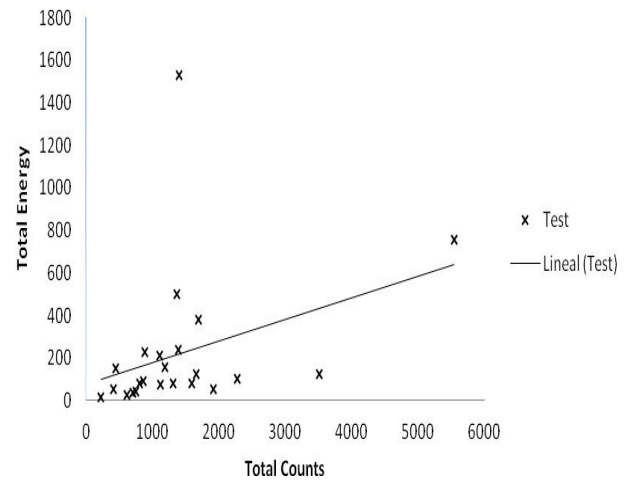


fig. 9 Relationship among counts and Energy

Through the analysis of the initial hits each test, cracking in the initial phase was determined by relating it to the maximum percentage of applied load, since the occurrence of the first hit is related to time and this in turn with the load a given instant. Although there are events occurring in a negligible percentage of damage loads, it is estimated that this is produced by rearrangement of particles of the material, rather than cracks or a micro cracks (Fig.10).

Fig.10 shows that the related load to 15% of the ultimate capacity of the element is the initiation point of cracking damage.

Taking as a reference the point where the first event is recorded in EA different specimens, the relationships shown in Table 1 were obtained.

CRACKING INITIATION

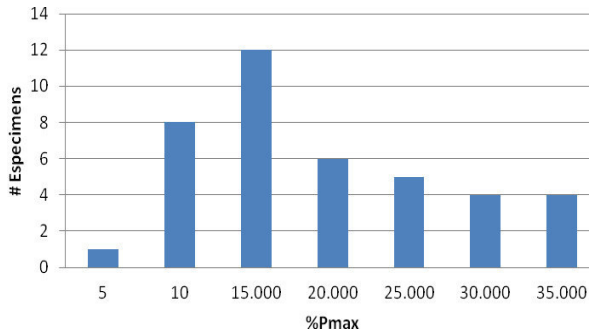


Fig.10 Determination of the onset of cracking through the initial hit

TABLE 1. RELATIONSHIP AMONG CRACKING INITIATION, AGGREGATE AREA AND ENERGY.

Test	% $i_{(P_{max})}$	Aa (cm ²)	A1(cm ²)	A2(cm ²)	R(Mpa)	E
16	8.44	55.33	50.10	60.00	4.59	125.00
20	5.82	56.45	54.04	58.00	4.76	1536.00
3	23.00	53.67	58.84	56.22	3.82	145.00
14	20.00	53.91	53.91	53.14	4.78	137.00
5	28.10	53.17	47.89	58.44	4.11	139.00
10	27.69	47.50	43.41	51.59	3.54	417.00
22	30.00	53.32	55.97	50.67	5.40	1153.00
8	>30.00	61.06	60.89	62.23	3.94	135.00
12		67.69	69.21	76.18	5.03	112.00
23		61.95	55.97	50.67	4.81	107.00

Where % $i_{(P_{max})}$ is the percentage of initiating events in function of the maximum load, Aa is the average aggregate area on the failure surface, A1 and A2 are the areas on the failure surfaces, R is modulus of rupture and E is energy.

This table shows the influence of the aggregate in obtaining energy from EA test. When the variation of areas A1 and A2 is small, a symmetrical fracture of aggregates is assumed, while when the difference is greater, it is assumed detachment at the interface of the aggregate.

Tests 16 and 20 have an onset of activity EA less than 10% with an aggregate average area Aa very similar, but with totally different energies, which explains the difference of areas on the faces of rupture, for 20 A symmetric test aggregate fracture occurs, while the test 16 exists most interface detachment of the aggregate (Fig.11 and 12).

In contrast to the tests 3 and 14 which have an onset of activity after 20% of the load, and equal Aa, they have a similar proportion of energy, just as having a very slight variation in the areas A1 and A2.

Following these analogies can be reviewed other test of table 1.

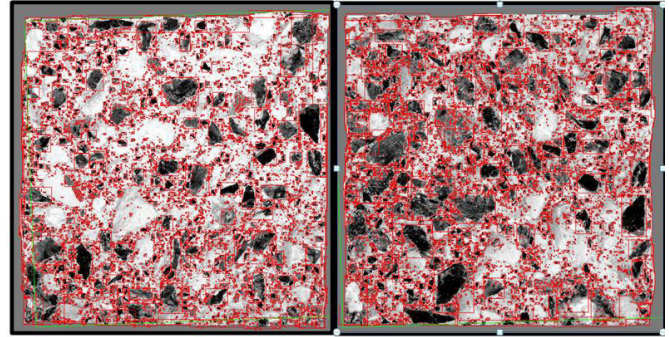


Fig. 11. Test 16, A1 and A2 respective surfaces (aggregate transition zone).

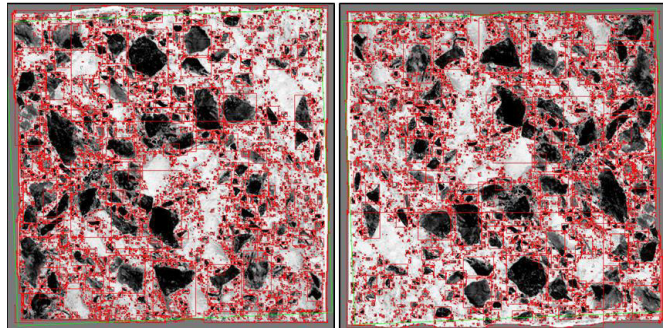


Fig. 12 Test 20, A1 and A2 respective surfaces (Symmetric fracture).

VI. CONCLUSIONS

Based on the results shown, it can be seen that through the analysis of waveform signals and their correlation among AE, mechanical and physical parameters can explain phenomenon related to cracking and concrete failure.

Although the crack initiation process begins at 15% of the maximum load, is from 80% of the maximum load that the element begins to have more severe damage (Fig, 10 and 5 respectively)

The influence the aggregates in the degrading cracking process of degradation is reflected in the energy parameter. The larger aggregates, greater energy is released on a symmetric breaking (A1similar to A2).

Taking as reference the modulus of rupture of Table 1, it is assumed that this value has a relationship with the symmetric rupture or interface detachment of the aggregate, as in a comparative way, specimens that have a symmetrical rupture, also have a larger module of rupture than the specimens with detachment of the aggregate.

The results of the investigation encourage the use of this technique as a possible tool for assessing concrete structural elements under several stress conditions.

VII. ACKNOWLEDGEMENTS.

To the Structural Monitoring group Coordination of Traffic Engineering and Structural Integrity of the Instituto Mexicano del Transporte IMT for their support for the project in their laboratories, technical support and material resources provided for the development of experimental evidence. To CONACYT for the student grant, and to FOMIX project QRO-2012-C01-193364.

REFERENCES

- [1] Gonszczyńska, B., 2014. Analysis of the process of crack initiation and evolution in concrete with acoustic emission testing. *ARCH CIV MECH ENG*, 14: 134–143.
- [2] Shaidan, R. Pulib, N. Bunnori and K. Holford, "Damage classification in reinforced concrete beam by acoustic emission signal analysis," *Const Build Mater*, no. 45, pp. 78–86, 2013..
- [3] S. Yasir Alam, J. Saliba and A. Loukili, "Fracture examination in concrete through combined digital image correlation and acoustic emission techniques," *Construc Build Mater*, pp. 232–242, 2014.
- [4] H. Shaowei, L. Jun and X. Feipeng, "Evaluacion of concrete fracture procedure based on acoustic emission parameters," *Const. Build Mater.*, vol. 47, pp. 1249–1256, 2013.
- [5] P.C, P. & F., E., 1960. A Critical Analysis of Crack Propagation Laws. *Journal of Basic Engineering*, Volumen 85.
- [6] Walker, E. K., 1970. Effect of stress ratio during crack propagation and fatigue for 2024-t3 and 7075-t6 aluminum. *ASTM*.462: 1-14.
- [7] Forman, R. G. & V. E. Kearney. 1967.Numerical Analysis of Crack Propagation in Cyclic-Loaded Structures. *J. Fluids Eng.* 89(3):459-463.
- [8] Bazant, Z. P. y K. Xu. 1991. Size effect in fatigue fracture of concrete. *ACI Mater J.* 88(4): 390–399.
- [9] Zanuy Sánchez, C., 2008. Analisis seccional de elementos de hormigon armado sometidos a fatiga, incluyendo secciones entre fisuras. s.l.:s.n.
- [10] M. ElBatanouny, P. Ziehl, A. Larosche, J. Mangual and F. Mata, "Acoustic emission monitoring for assessment of prestressed concrete beams," *Constr Bild Mater*, no. 58, pp. 46–53, 2014.
- [11] M. Albdelrahman, M. ElBatanouny and P. Ziehl, "Acoustic emission based damage assessment method for prestressed concrete structures:Modified index of damage," *Engin Estruc*, no. 60, pp. 258–264, 2014.
- [12] A. Behnia, H. Chai, M. Yorikawa, S. Momoki, M. Terazawa and T. Shiotani, "Integrated non-destructive assessment of concrete structures under flexure by acoustic emission and travel time tomography," *Const Build Mater*, no. 67, pp. 202–215, 2014.
- [13] Behnia, A., Chai, H. & Shiotani, T., 2014. Advanced structural health monitoring of concrete structures with the aid of acoustic emission. *Const. Buil. Mater.* 65:282–302.
- [14] Salinas V, Vargas Y, Ruzzante J, Gaete L. Localization algorithm for acoustic emission. *Phys Proc* 2010;3:863–71.
- [15] Labuz J, Chang H, Dowding C, Shah S. Parametric study of acoustic emission location using only four sensors. *Roch Mech Rock Eng* 1988;21:139–48.
- [16] Köppel S, Grosse C. Advanced acoustic emission techniques for failure analysis in concrete. In: Proceeding of 15th world conference on nondestructive testing, Roma, Italy; October 2000.
- [17] Ding Y, Reuben R, Steel J. A new method for waveform analysis for estimating AE wave arrival times using wavelet decomposition. *NDT & E Int* 2004;37:279–90.
- [18] Ding Y, Reuben R, Steel J. A new method for waveform analysis for estimating AE wave arrival times using wavelet decomposition. *NDT & E Int*2004;37:279–90.
- [19] B. Goszczyńska, G. S´wit, A. Krampikowska, J. Tworzewska and P. Tworzewski, "Experimental validation of concrete crack identification," *Arch Civ Mech Eng*, vol. 12, pp. 23–28, 2012.
- [20] D. Aggelis, S. Verbruggen, E. Tsangouri, T. Tysmans and D. Hemelrijck, "Characterization of mechanical performance of concrete beams with external reinforcement by acoustic emission and digital image," *Const Buil Mater*, no. 47, pp. 1037–1045, 2013. nondestructive testing, Roma, Italy; October 2000.
- [21] C. Bing and L. Juanyu, "Investigation of effects of aggregate size on the fracture behavior of high performance concrete by acoustic emission," *Constr build Mater*, vol. 21, p. 1696–1701, 2007.
- [22] Kentaro and O. Masayasu, "Crack classification in concrete based on acoustic emission," *Constr. Build Mater.*, vol. 24, p. 2339–2346, 2010.
- [23] R. Lyons, I. Matthew and S. Austin, "Influence of diurnal and seasonal temperature variations on the detection of corrosion in reinforced concrete by acoustic emission," *Corr Sci*, vol. 47, p. 413–433, 2005.
- [24] A. Sagaidak and S. Elizarov, "Acoustic emission parameters correlated with fracture and deformation processes of concrete members," *Constr. Build Mater.*, vol. 21, p. 477–482, 2007.
- [25] G. Santosh and K. Chandra, "Use of acoustic emissions in flexural fatigue crack growth studies on concrete," *Eng Fract Mech*, vol. 87, pp. 36–47, 2012.
- [26] R. Vidya and P. Raghu, "Fracture analysis of concrete using singular fractal functions with lattice beam network and confirmation with acoustic emission study," *Theor. Appl. Fract. Mec.*, vol. 55, p. 192–205, 2011.
- [27] R. Vidya and B. Raghu, "An experimental study on acoustic emission energy as a quantitative measure," *Constr Build Mater*, vol. 25, p. 2349–2357, 2010.
- [28] R. Vidya and B. Raghu, "Damage limit states of reinforced concrete beams subjected to incremental cyclic loading using relaxation ratio analysis of AE parameters," *Constr build Mater*, vol. 35, p. 139–148, 2012.
- [29] S. Yasir Alam, J. Saliba and A. Loukili, "Fracture examination in concrete through combined digital image correlation and acoustic emission techniques," *Construc Build Mater*, pp. 232–242, 2014.
- [30] C. Mukhopadhyay, T. Jayakumar, T. Haneef , S. Suresh , "Use of acoustic emission and ultrasonic techniques for monitoring crack initiation/growth during ratcheting", *Inter jour press vesse piping*, pp27–36,2014.

Application of CCHE2D model to Mexican rivers

Guillermo Cardoso-Landa^{#1}

^{#1}*Land Sciences Department, Instituto Tecnológico de Chilpancingo
Av. Guerrero 81, Col. Ruffo Figueroa, Chilpancingo, Gro., C. P. 39020, Mexico
¹gclanda@prodigy.net.mx*

Abstract—The 39 main rivers of Mexico and the 667 large dams to operate in the country of Mexico, moves a significant amount of sediment, which have not quantified accurately in our country and causing major problems of flooding, disasters and in general, hydraulic, and hydrological problems, which requiring resolved taking as data, among others, through sediment transport. This paper discusses the different current sediment transport models and select models developed by the National Center for Computational Hydroscience and Engineering (NCCHE) of the University of Mississippi, USA, to be applied to the country of Mexico. The governing equations, model closures, empirical functions and numerical methods of sediment transport models in NCCHE are briefly reviewed in this paper. Several verification and application examples are selected to demonstrate the capabilities of NCCHE's models. The amount of sediment transport of the *Papagayo* River was determinate by the CCHE2D model and the results will be used for design of some hydraulic structures at the *Papagayo* River.

Keywords—CCHE2D; river; sediment; transport

I. INTRODUCTION

The rivers in the country of Mexico drain approximately 400 cubic kilometers of water annually, including waters that fall from neighboring countries and discounting departing towards them. Approximately 87 % of this runoff occurs in 39 major rivers whose basins occupy nearly 58 % of the continental territorial extension. Rivers that account for 65 % of runoff are *Grijalva-Usumacinta*, *Papaloapan*, *Coatzacoalcos*, *Balsas*, *Pánuco*, *Santiago*, and *Tonalá* (whose basins together totaled 22 % of the national territory). The Rivers *Balsas* and *Santiago* belong to the Pacific slope and the other five to the slope of the Gulf of Mexico. For its length highlight the *Bravo* and *Grijalva-Usumacinta* rivers.

Some of the water that drains by rivers is currently stored in dams and used, between other purposes, for the production of food, the generation of electric power, flood control, and industrial and domestic uses water supply. Major dams in the country of Mexico began to build before 1920 and had a growth accelerated between 1940 and 1970. Of 4000 existing dams, 667 are classified as large dams in accordance with the criteria of the International Commission of Large Dams. Storage capacity provided is 150 cubic kilometers of water and together would be 37 % of the annual average runoff from the country. However, the average volume storage in 51 major dams in the country between 1990 and 2004 was 61 cubic kilometers.



Fig. 1. Major rivers of México

Of these 39 main rivers of Mexico and the 667 large dams to operate in the country of Mexico, moves a significant amount of sediment, which have not quantified accurately in our country and causing major problems of flooding, disasters and in general, hydraulic, and hydrological problems, which requiring resolved taking as data, among others, through sediment transport.

This paper discusses the different current sediment transport models and select models developed by the National Center for Computational Hydroscience and Engineering (NCCHE) of the University of Mississippi, in the United States, to be applied in the determination of the sediment transport of the Mexican rivers and particularly the *Papagayo* river.

II. STUDY METHODS

A. Comparison of sediment transport models

First, There are many sediment transport models, and each has its strengths and weaknesses. Comprehensive reviews of the capabilities and performance of these models are provided in reports by the National Research Council (1983), and Fan (1988), among others. Fifteen U.S. Federal agencies participated in a Federal Interagency Stream Restoration Working Group (1998) to produce a handbook. They selected eight models for comparison: CHARIMA (Holly et al., 1990), FLUVIAL-12 (Chang, 1990), HEC-6 (U.S. Army Corps of Engineers, 1993), TAS-2 (McAnally and Thomas, 1985), MEANDER (Johannesson and Parker, 1985), USGS (Nelson and Smith, 1989), D-O-T (Darby and Thorne, 1996, and

Osman and Thorne, 1988), and GSTARS (Molinas and Yang, 1986). We aggregated NCCHE models (Wu and Wang, 2002). Tables 1, 2, and 3 summarized the comparisons of these nine sediment transport models.

TABLE I. MODELING CAPABILITIES OF SEDIMENT TRANSPORT MODELS.

Model	1	2	3	4	5	6	7	8	9
Upstream water & sediment hydraulic	Y	Y	Y	Y	Y	Y	Y	Y	Y
Downstream stage specification	Y	Y	Y	Y	Y	N	Y	Y	Y
Floodplain sedimentation	N	N	N	Y	N	N	N	N	Y
Suspended sediment transport	Y	Y	N	Y	N	N	N	N	Y
Total sediment transport	N	N	Y	N	N	Y	Y	Y	Y
Bed load transport	Y	Y	Y	N	Y	N	N	Y	Y
Cohesive sediments	N	N	Y	Y	N	Y	N	Y	Y
Bed armoring	Y	Y	Y	N	N	N	Y	Y	Y
Hydraulic sorting substrate material	Y	Y	Y	N	N	N	Y	Y	Y
Fluvial erosion of stream banks	N	Y	N	N	N	N	Y	Y	Y
Bank mass failure under gravity	N	N	N	N	N	N	Y	N	Y
Straight no prismatic reaches	Y	Y	Y	Y	N	N	Y	Y	Y
Irregular no prismatic reaches	N	N	N	Y	N	N	Y	Y	Y
Branched channel network	Y	Y	Y	Y	N	N	N	N	Y
Looped channel network	Y	N	N	Y	N	N	N	N	Y
Channel beds	N	Y	N	Y	Y	N	Y	Y	Y
Meandering belts	N	N	N	N	N	Y	N	N	Y
Rivers	Y	Y	Y	Y	Y	Y	Y	Y	Y
Bridge crossing	N	N	N	Y	N	N	N	N	Y
Reservoirs	N	Y	Y	N	N	N	N	Y	Y

Model 1, CHARIMA; Model 2, FLUVIAL-12; Model 3, HEC-6; Model 4, TAS-2; Model 5, MEANDER; Model 6, USGS; Model 7, D-O-T; Model 8, GSTARS; Model 9, NCCHE. Y = Yes N = No

TABLE II. DISCRETIZATION AND FORMULATION OF SEDIMENT TRANSPORT MODELS.

Model	1	2	3	4	5	6	7	8	9
Unsteady flow	Y	Y	N	Y	N	Y	N	N	Y
Stepped hydrograph	Y	Y	Y	Y	Y	Y	Y	Y	Y
One-dimensional	Y	Y	Y	N	N	N	Y	Y	Y
Quasi two dimensional	N	Y	N	N	N	N	Y	Y	Y
Two-dimensional	N	N	N	Y	Y	Y	N	N	Y
Depth-average flow	-	-	-	Y	Y	Y	-	Y	Y
Deformable bed	Y	Y	Y	Y	Y	Y	Y	Y	Y
Banks	N	Y	N	N	N	N	Y	Y	Y
Graded sediment load	Y	Y	Y	Y	Y	N	Y	Y	Y
No uniform grid	Y	Y	Y	Y	Y	Y	Y	Y	Y
Variable time stepping	Y	N	Y	N	N	N	N	Y	Y

TABLE III. NUMERICAL SOLUTION SCHEME OF SEDIMENT TRANSPORT MODELS.

Model	1	2	3	4	5	6	7	8	9
Standard Step Method	N	Y	Y	N	N	N	Y	Y	Y
Finite difference	Y	N	Y	N	Y	Y	Y	Y	Y
Finite element	N	N	N	Y	N	N	N	N	Y

B. Research on sediment transport by the NCCHE

The Fundamental research on sediment transport has been conducted at NCCHE in past years. NCCHE researchers proposed formulas for determining the fractional transport capacities of bed load and suspended load, which take into account the hiding and exposure effects among different size classes. In addition, formulas for the calculations of sediment de-posit porosity, settling velocity, movable bed roughness and sediment transport over steep slopes were also developed. These formulas were calibrated using a large data set that included experimental and field measurements.

The newly proposed Wu et al (2000) sediment transport capacity formulas were tested independently against many different experiment and field data, including Brownlie (1981) data sets, and Toffaleti (1968) data sets. Wu et al. formulas were also compared with some existing formulas, such as Ackers and White (1973) formula and its modification by Proffit and Sutherland (1983), Engelund and Hansen (1967) formula, Yang (1973) formula, and the SEDTRA module (Garbrecht, et al. 1995). Wu et al. formulas can provide reliable predictions for the fractional discharges of bed load, suspended load, and bed-material load.

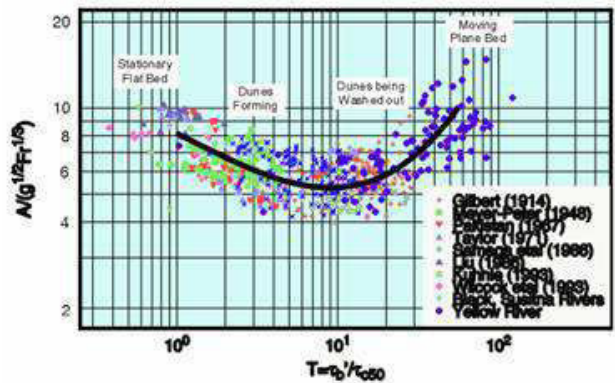


Fig. 2. Formulas for movable bed roughness, (Wu and Wang)

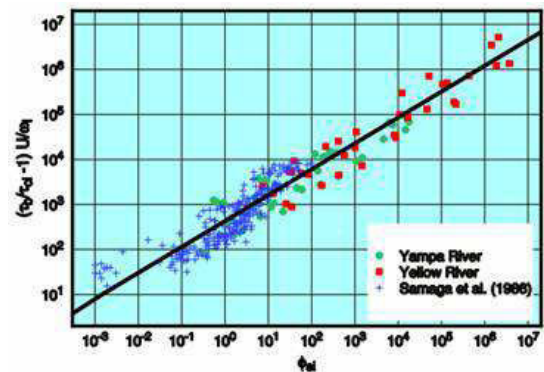


Fig. 3. Formulas for fractional suspended-load discharge (Wu, Wang and Jia)

C. Governing equations

Because many open channel flows are of shallow water problems, the effect of vertical motions is usually of insignificant magnitude. The depth integrated two-dimensional equations are generally accepted for studying the open channel hydraulics with reasonable accuracy and efficiency.

The momentum equations for depth-integrated two-dimensional turbulent flows in a Cartesian coordinate system are:

$$\frac{\partial u}{\partial t} + u \frac{\partial u}{\partial x} + v \frac{\partial u}{\partial y} = -g \frac{\partial \eta}{\partial x} + \frac{1}{h} \left(\frac{\partial h \tau_{xx}}{\partial x} + \frac{\partial h \tau_{xy}}{\partial y} \right) - \frac{\tau_{bx}}{\rho h} + f_{Cor} v \quad (1)$$

$$\frac{\partial v}{\partial t} + u \frac{\partial v}{\partial x} + v \frac{\partial v}{\partial y} = -g \frac{\partial \eta}{\partial y} + \frac{1}{h} \left(\frac{\partial h \tau_{xy}}{\partial x} + \frac{\partial h \tau_{yy}}{\partial y} \right) - \frac{\tau_{by}}{\rho h} + f_{Cor} u \quad (2)$$

Where u and v are depth-integrated velocity components in x and y directions, respectively; t is the time; g is the gravitational acceleration; η is the water surface elevation; ρ is the density of water; h is the local water depth; f_{Cor} is the Coriolis parameter; τ_{xx} , τ_{xy} , τ_{yx} , and τ_{yy} are depth integrated Reynolds stresses; and τ_{bx} and τ_{by} are shear stresses on the bed and flow interface. The shear stress terms at the water surface are dropped since wind shear driven effect is not considered in this version of the model.

Free surface elevation for the flow is calculated by the depth-integrated continuity equation:

$$\frac{\partial \eta}{\partial t} + \frac{\partial uh}{\partial x} + \frac{\partial vh}{\partial y} = 0 \quad (3)$$

Where η is the free surface elevation, h is the water depth. Because bed morphological change is a much slower process than hydrodynamics, this equation is widely accepted and utilized for computing free surface elevation with two-dimensional models. One may note in cases when the bed elevation changes fast due to erosion or deposition, equation 2 should be applied.

The turbulence Reynolds stresses in the equations (1) and (2) are approximated according to the Boussinesq's assumption that they are related to the main rate of the strains of the depth-averaged flow field with a coefficient of eddy viscosity: surface elevation for the flow is calculated by the depth-integrated continuity equation:

$$\tau_{ij} = -u_i' u_j' = \nu_t (u_{i,j} + u_{j,i}) \quad (4)$$

$$\tau_{xx} = 2\nu_t \frac{\partial u}{\partial x} \quad (5)$$

$$\tau_{xy} = \nu_t \left(\frac{\partial u}{\partial y} + \frac{\partial v}{\partial x} \right) \quad (6)$$

$$\tau_{yy} = 2\nu_t \frac{\partial v}{\partial y} \quad (7)$$

$$\tau_{yx} = \nu_t \left(\frac{\partial u}{\partial y} + \frac{\partial v}{\partial x} \right) \quad (8)$$

As it is well known, that eddy viscosity is a function of the flow, and it can be related to the flow properties in different ways.

Another important problem regarding both mixing length model and parabolic model is the wall effect. Very close to the wall, the distance to the wall should be used as the length scale instead of that to the bed. Otherwise, the depth integrated coefficients for the eddy viscosity would be too large when the interior nodes are close to the wall.

In the CCHE2D model the normal distance from a node to the wall (d_w) is used to calculate the mixing length in the region $d_w/h < 0.3245$. And it is also used to calculate the parabolic profile in the range $d_w/h < 0.21$. The number 0.3245 and 0.21 are the relative distances where mixing length and the parabolic profile are equal to their depth averaged values, respectively. This approach avoids the prediction of very large eddy viscosity near the wall.

III. RESULTS

A. Field investigations

In this study, the amount of sediment transport was determinate in the *Papagayo* river basin area, a region pertaining to the 20th hydrological region located close to the coast of the state of Guerrero in the country of Mexico. The *Papagayo* river basin includes in its territory the capital of the State of Guerrero, *Chilpancingo*, and therefore, possible changes in the future use of sediment transport, (i.e. irrigation, storage, supply populations, industrial and eco-logical use) are of major political relevance to this region. Indeed, the impact on the hydrological cycle by current climate changes will only aggravate social conflicts between populations disputing for water both locally and regionally.

The State of Guerrero is located south of Mexico facing the Pacific Ocean, between the 16°18' and 18°48' north latitude and the 98°03' and 102°12' west longitude. Although the whole of its territory is in the intertropical area, its complex geography makes possible the existence of multiple climate types.



Fig. 4. Map of the geographical region of study located at the State of Guerrero in the country of Mexico

The *Papagayo* river basin is the most important of the south-west region in Mexico and brings together the waters of the *Omitlán*, *Azul* or *Petaquillas* and *Papagayo* rivers. The later, flows into the waters of the Pacific Ocean, and in this basin is located *La Venta* hydroelectric dam.



Fig. 5. Papagayo river basin

B. Selection of model

After to revise some sediment transport models and the characteristics of the *Papagayo* river in the country of Mexico, it concludes that the best sediment transport models to apply to this Mexican river are the models developed by the National Center for Computational Hydroscience and Engineering (NCCHE) of the University of Mississippi, in the United States, which apply the next diagram.

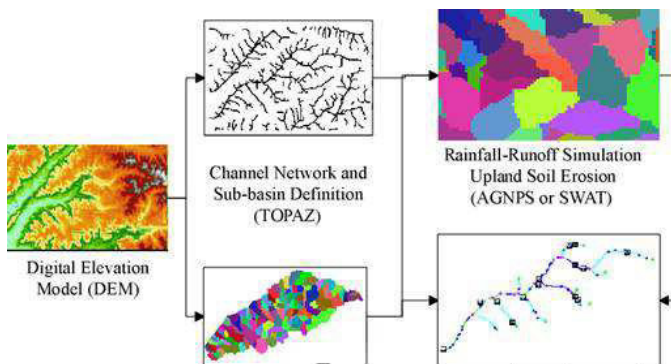


Fig. 6. Process used by the NCCHE's models

The software package proposed is the CCHE2D model to simulate the sediment transport in dendritic channels networks of the Mexican rivers.

C. Results of modeling

The first step was to obtain the digital elevation model (DEM) of *Papagayo* river, which was acquired in the National Institute of Statistics and Geography (INEGI) in Mexico.

The next step was the importation of DEM with ASCII codification into the CCHE-MESH to generating the necessary mesh.

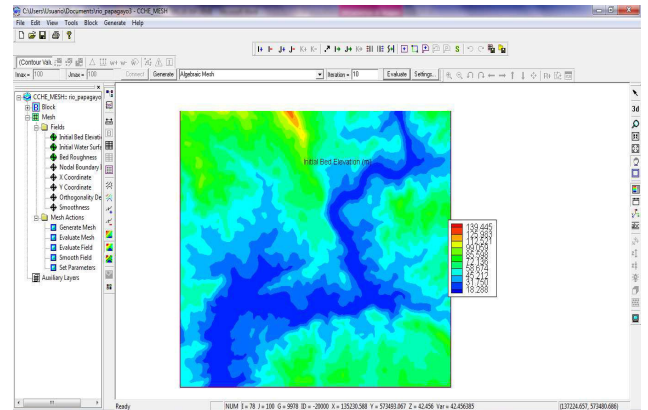


Fig. 7. Generated mesh of *Papagayo* river

The next step was the generation of the algebraic mesh, to apply the numerical methods to resolve the differential equations system.

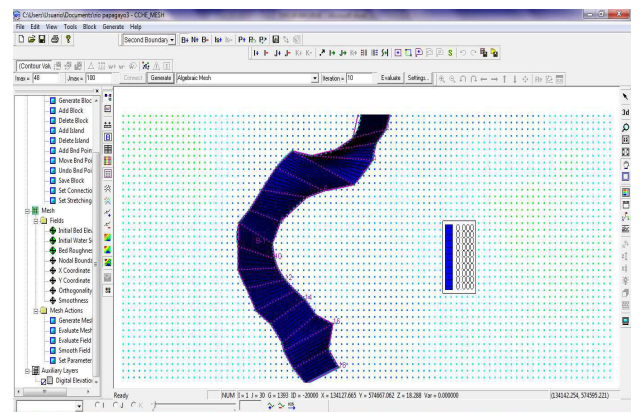


Figure 8. Algebraic mesh of *Papagayo* river

It was necessary select the numerical method to apply, between 7 proposed by the CCHE2D:

1. RL Orthogonal Mesh
2. RL Orthogonal Mesh with smoothness controls
3. RL Orthogonal Mesh with auto smoothness controls, type a
4. RL Orthogonal Mesh with auto smoothness controls, type b
5. Adaptive Mesh
6. TTM Orthogonal Mesh
7. Laplace Conformal Mesh

Next it was selected RL Orthogonal Mesh with smoothness controls and the results it shown in the next figure

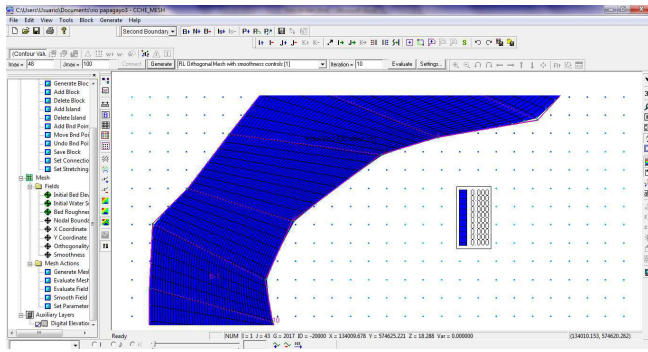


Figure 9. Application of numerical method to algebraic mesh of *Papagayo* river

Finally it was obtained the sediment transport in various sections along this river using the CCHE2D and the results are shown in the next figure

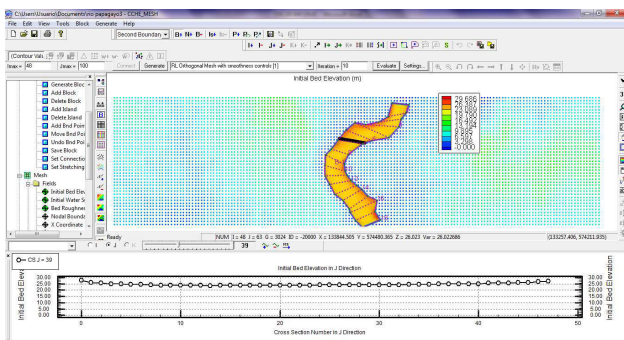


Figure 10. CCHE2D applied to *Papagayo* river

Using all the elements of the model used it was obtained the mean values of the sediment transport in the zone analyzed of *Papagayo* river, near the hydrometric station 3 (CONAGUA).

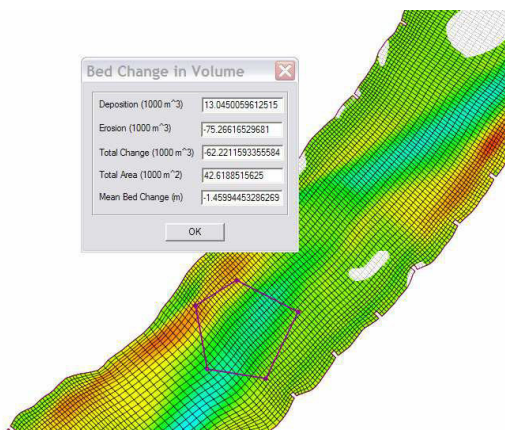


Figure 11. Results of the sediment transport of the *Papagayo* river

D. Measurements of sediments

Measuring of sediments in the Mexican rivers is realized by two federal institutions. The Electricity Federal Commission (CFE), which have 89 hydro-metric stations, with 73 stations with measuring of sediments. The second institution is the Water National Commission (CONAGUA) with 37 hydro-

logic regions and 2, 321 hydrometric stations, which only 398 have equip to do measurements of sediments in rivers.

Hydrometric station number 3 *Agua Salada* is the station more proximity to the application of the model CCHE2D used in this work and the information recollected was between the years 1987 and 2004, with a annual mean of sediments 0.362 kg/m^3 , and the year with more sediments was 1998 with 0.510 kg/m^3 , and the year with less sediments was 1999 with 0.249 kg/m^3 . Next figures and table show the characteristics of sediments of this hydrologic station.

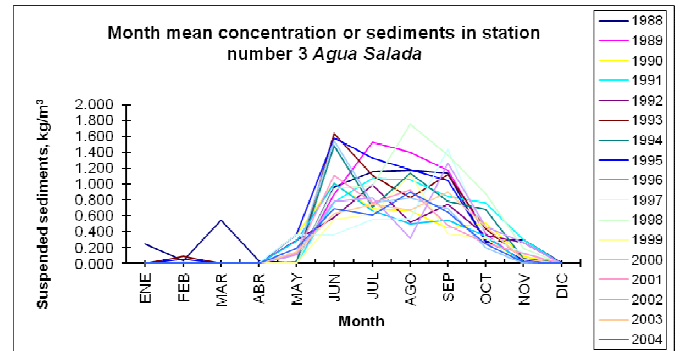


Figure 12. Month variation of the mean concentration of sediments in *Agua Salada* station between 1988 to 2004

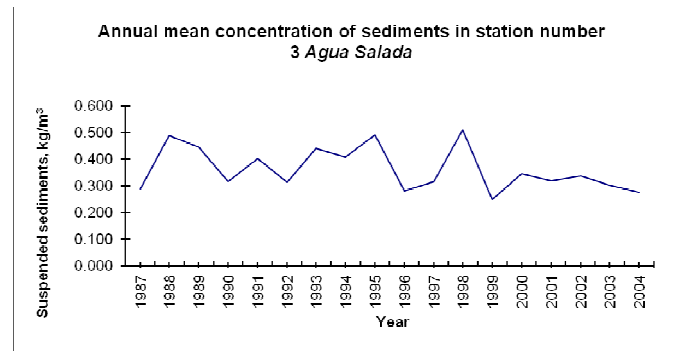


Figure 13. Annual variation of the concentration of sediments in *Agua Salada* station between 1987 to 2004

TABLE IV. VALUES OF THE MONTH AND MEAN CONCENTRATION OF SEDIMENTS IN AGUA SALADA STATION (CONAGUA)

STATION:		<i>Agua Salada</i>				
RIVER:		<i>Papagayo</i>				
WATERSHED:		River <i>Papagayo</i>				
Year	Jan	Feb	Mar	Apr	May	
1987						
1988	0.242	0.038	0.547	0.034	0.000	
1989	0.000	0.000	0.000	0.000	0.000	
1990	0.000	0.023	0.000	0.000	0.366	
1991	0.000	0.000	0.000	0.000	0.000	
1992	0.000	0.000	0.000	0.000	0.288	
1993	0.000	0.092	0.000	0.000	0.000	
1994	0.000	0.000	0.000	0.000	0.019	

1995	0.000	0.058	0.000	0.000	0.364
1996	0.000	0.000	0.000	0.000	0.282
1997	0.007	0.000	0.008	0.012	0.368
1998	0.000	0.000	0.000	0.000	0.000
1999	0.000	0.000	0.000	0.000	0.006
2000	0.000	0.000	0.000	0.000	0.115
2001	0.000	0.000	0.000	0.000	0.133
2002	0.000	0.000	0.000	0.000	0.107
2003	0.000	0.000	0.000	0.000	0.149
2004	0.000	0.000	0.000	0.000	0.195
Mean	0.015	0.012	0.033	0.003	0.141
Min	0.000	0.000	0.000	0.000	0.000
Max	0.242	0.092	0.547	0.034	0.368

1.543	0.763	0.824	0.694	0.201	0.006	0.000	0.346
1.111	0.764	0.931	0.479	0.251	0.133	0.000	0.317
0.780	0.827	0.320	1.266	0.461	0.268	0.000	0.336
0.623	0.744	0.676	0.896	0.467	0.055	0.000	0.301
0.695	0.612	0.897	0.645	0.243	0.018	0.000	0.275
0.971	0.888	0.914	0.863	0.414	0.123	0.006	0.362
0.360	0.551	0.320	0.372	0.201	0.000	0.000	0.249
1.634	1.529	1.750	1.430	0.881	0.300	0.103	0.510

IV. CONCLUSIONS

Comparison between the sediment transport along the *Papagayo* river using the CCHE2D and the measuring of sediments realized by Electricity Federal Commission (CFE) at the hydrometric station number 3 *Agua Salada*, shown a difference of 39% in the mean values for the last year of measurements. It is necessary to work in the another 3 hydrometric station along the *Papagayo* river to obtain more results, which are working at present moment.

It is important emphasize that this is the first application of NCCHE models in a Mexican river.

REFERENCES

- [1] Mexican Institute of Water Technology. Banco Nacional de Datos de Aguas Superficiales (BANDAS in Spanish), 2008.
- [2] Vieira and Wu. National Center for Computational Hydroscience and Engineering (NCCHE). University of Mississippi USA. Technical report No. NCCHE-TR-2002-5, 2002.
- [3] Wu and Wang. Movable bed roughness in alluvial rivers. *Journal of Hydraulic Engineering*, 125 (12), 1309-1312, 1999.
- [4] Wu et al. Nonuniform sediment transport in alluvial rivers. *Journal of Hydraulic Research*, 38 (6), 427-434, 2000.

Jun	Jul	Aug	Sep	Oct	Nov	Dec	Annual
			0.545	0.256	0.246	0.103	0.288
0.962	1.155	1.174	1.139	0.275	0.299	0.009	0.490
0.875	1.529	1.397	1.174	0.369	0.000	0.000	0.445
1.006	0.687	0.668	0.447	0.505	0.092	0.003	0.316
0.775	1.068	1.051	0.846	0.767	0.300	0.000	0.401
0.579	0.991	0.521	0.747	0.353	0.262	0.000	0.312
1.634	1.109	0.830	1.115	0.438	0.067	0.000	0.440
1.482	0.710	1.136	0.778	0.685	0.065	0.000	0.406
1.576	1.330	1.180	1.042	0.296	0.044	0.000	0.491
1.007	0.660	0.503	0.549	0.346	0.017	0.000	0.280
0.360	0.551	0.564	1.430	0.337	0.142	0.000	0.315
0.942	0.982	1.750	1.365	0.881	0.196	0.000	0.510
0.557	0.614	1.118	0.372	0.315	0.004	0.000	0.249

Chilled mirror hygrometer for suction measurement on clays from Queretaro Valley

R. Robles Solís^{#1}, A. Pérez García^{#2}

¹Student of M. C. (Geotechnical Engineering), ²Professor, Faculty of Engineering, University of Querétaro (UAQ), Cerro de las Campanas S/N. Col. Niños Héroes, C.P. 76010, Santiago de Querétaro, Querétaro, México.

¹ ingrobless@hotmail.com

² alfre@uaq.mx

Abstract—Despite the importance of the suction in the behavior of the soils, the current geotechnical engineering have not focused their efforts on improving current methods of measuring suction. This paper presents a comparison between non-contact filter paper method and the chilled mirror hygrometer for measuring suction on clays.

The comparison focuses on three factors; accuracy, easiness and reading time. The relationship between these three factors will show if the chilled mirror hygrometer is a suitable method for measuring suction on unsaturated soil.

Keywords—chilled mirror hygrometer; non-contact filter paper method; suction; unsaturated soils

I. INTRODUCTION

Nowadays and even more in Mexico, the use of chilled mirror hygrometer has been limited to agriculture and food industry. This device utilizes the dew point phenomenon occurred within a sealed chamber where the balance between a sample and the surrounding medium are looking for [1]. This balance occurs just at the time that the first dewdrop is form on a mirror that is cooled by a fan and the temperature is recorded by a thermocouple inside the sealed chamber and is the time it takes to happen which allows relating the dew point with hydric properties of a sample [2].

This knowledge leads us to propose the use of the chilled mirror hygrometer in particular areas of engineering such as unsaturated soils mechanics and determination of soil suction. This is not just because the chilled mirror hygrometer can be used for suction measurement but because the importance of this property on the unsaturated soil mechanics because the behavior of soils can be translated in terms of soil suction, and can be characterized for each particular soil-water retention curve [3].

The main competitors for the chilled mirror hygrometer in suction measurement are the thermocouple psychrometer and the non-contact filter paper method which though it has the advantage of currently being the most commonly used within the geotechnical community for its wide range of suction measuring, also has the disadvantage of being the method with longer reading time, unlike the thermocouple psychrometer which has a short reading time but with a very low range of application because the maximum degree of cooling that can reach this method is 0.6 °C below room temperature, which limits the maximum suction reading psychrometer to 4.9 pF or 8 MPa [4].

These characteristics of the non-contact filter paper method and thermocouple psychrometer turn these methods into a disadvantage when quick results that ensure the accuracy of the suction measured over a wide range of application are desired.

It is well known that suction, as a fundamental element in the behavior of unsaturated soils, has a particular behavior called hysteresis. This property prevents the soil in terms of suction, to behave in the same way under the same conditions, because of the path taken to reach these conditions, for example, if the soil was taken to a moisture state by drying or wetting. Is because this property that for the realization of a characteristic curve are needed at least 10 measuring points for each possible path and 7 to 14 days for the measurement process for each of the measured points required [5], therefor, a final time of at least 1-2 months is required Unlike the chilled mirror hygrometer which reduces time to a period of 2-3 weeks, or even less if you have enough experience using this method.

Therefore, the aim of this paper is to show the advantages of using the chilled mirror hygrometer for measuring suction in CH clays of Querétaro Valley in terms of accuracy, easiness and time of reading. So, this target can be reached only by using one path for reach the moisture state for each

method because if the accuracy, easiness and reading time of the chilled mirror hygrometer are admissible, then also it will be for the other path so it will be used only the drying path.

II. PAST STUDIES

The study of soil suction has been a major topic of interest since the beginning of the "Soil Mechanics" when Karl Terzaghi in 1925 [6], gave birth to the now well-known term [7]. Soil mechanics had the difficult task of finding the relationship between some soil properties such as expansion pressure or volume change of soil and soil water retention curve or soil suction. That is why measuring the suction is a process of high importance for the study of unsaturated soils and their behavior.

Since this is the level of importance that the suction determination on unsaturated soils have, it is essential to find the most accurate method for suction measurement. The optimization of laboratory processes is not a new area of research, from the first laboratory tests, has always looked for optimization of time, cost and application ranges and tests for measuring suction in unsaturated soils are no exception.

An example is the University of Technology, Dalian, China, where Hu Pan [8], made comparative studies of current direct and indirect methods for suction measurement in laboratory where they found a relationship between different laboratory methods, total measured suction or it's matric or osmotic components, the range of suction that are able to measure and the time it takes to reach equilibrium. The results of such research are summarized in Table I [8].

Suction measurement processes can be divided into two main areas, direct and indirect measurements. Direct measurements make use of the theory of suction which states that suction

values were calculated based on the direct measurement of negative pore pressure in the soil, which serve as the basis of existing negative pressures on the soil matrix. For example, with a given pore pressure and by subtracting the air pressure, generally equal to the atmospheric pressure of site [8], we can directly obtain the matric suction of the soil sample. Because of this, in order to make a direct measurement of the suction, it is necessary to perform a phase separation in liquid and gas state in the soil, which is achieved by using ceramic discs, in this case, the air entry value of the ceramic disc will determine the ranges of direct suction measurement.

Moreover, indirect measurement processes vary depending on the method, but the basic principle is to use physical or chemical principles or specially designed sensors for measuring certain properties, which, by mathematical processes can be related to the suction of a soil sample. It means that the suction will be determined using the knowledge obtained from different properties that directly affect the soil in question. Such is the case of measurements made by the filter paper method where by using filter paper circles of 5.5cm diameter placed above a soil sample and inside a hermetically sealed container the equilibrium between the paper filter (pore sensor) and matric soil suction is looked for; therefore the weight of water adsorbed by the pore sensor determines the matric suction of the soil sample [9].

Is important to note that the two processes mentioned above have their role in determining the matric suction, but the component of the total suction can also be determined by indirect methods of measurement based on certain different properties such as the dew point, relative humidity and temperature. The chilled mirror hygrometer is one of these methods. The chilled mirror hygrometer is mainly based in the dew point technique for the determination of the hydric potential of porous materials.

TABLE I Summary Of Suction Measurement Methods

		Technique (Method)	Suction range (kPa)	Equilibrium time	
Direct suction measurement	Matric suction	axis-transition technique	0-1500	hours	
		tensiometer		hours	
		suction probe		minutes	
Indirect suction measurement	Matric suction	time domain reflectometry	0-1500	hours	
		electrical conductivity sensor	50-1500	6-50hours	
		thermal conductivity sensor	0-1500	hours-days	
		in-contact filter paper	all	7-14 days	
	Osmotic suction	squeezing technique	0-1500	days	
		Total suction	psychrometer technique	100-10000	1 h
			relative humidity sensor	100-8000	hours-days
			chilled-mirror hygrometer	150-30000	10 minutes
non-contact filter paper	all		7-14 days		

III. TESTING SAMPLES

In the Valley of Querétaro the predominant type of soils are expansive clays known as CH by SUCS [10]. This type of soil, unaltered, will be the sample for laboratory tests discussed on this paper.

IV. EXPERIMENTAL PROGRAM

A. Preparation of specimens

In order to give greater importance to the results, the research is focused on the use of soil samples from an area with large expansive problems; this area is known as Juriquilla, Querétaro. In this area undisturbed soil samples were obtained [11], from which two types of specimens were made in the laboratory from the initial undisturbed sample.

The first specimen (for non-contact filter paper method or N-C FPM) was styled caring generate rectangular prismatic shapes and trying not to alter the internal structure of the soil. The volume of these specimens have a large variation from sample to sample within a single type of specimen, however, the volume is not a factor since their contribution to the results is only the speed with which equilibrium is generated the sample with the environment that surrounds it inside a sealed chamber. Also all the samples will be left in balancing process for 14 days.

For the second specimen (for chilled mirror hygrometer or CMH) the same conditions were carried out, however, the volume of the specimens of type two is considerably smaller than the type one keeping an approximate ratio of 10 to 1 where the second type of specimens have an estimated volume average of 2 to 3 cm³.

The number of samples for each type of specimen will be 10 units undergo a drying process. It is important to note that both processes, wetting and drying, represent variations in the internal efforts of each sample, which, if they are not done in proper proportion for each increment or decrement could generate cracks in samples in certain cases involve loss of the sample.

B. Experimental Sequence

As mentioned above, there is a line of wetting and drying for each characteristic curve, these paths involve specific process for each one since for the case of this paper only the drying path will be used so for this path is required to completely wet the samples and after dry the samples gradually.

To obtain comparable results, it was proposed to start alongside wetting and drying processes of all samples using a hand sprayer to add water in small amounts once or twice a

day for wetting process and leaving slightly exposed to room temperature samples all day for drying process.

Finally the samples will be submitted to their respective methods efforts to implement each method to each sample at the time this reaches the necessary degree of saturation trying not to allow moisture variations in the sample as these could cause changes in the lines of hysteresis.

V. NON-CONTACT FILTER PAPER METHOD

This test, based on ASTM D5298-10 [9] standard, aims to determine the potential of matric, osmotic and total suction of the soil using filter paper as a passive sensor for measuring energy state (negative pressure) exerted by the water in the pores of a partially saturated soil.

Briefly, the method consists in placing filter paper in an airtight container together with a soil specimen for seven to fourteen days to allow the water vapor pressure of the pores in the specimen, the water vapor pressure of the filter paper and the pressure of water vapor in the air within the container to reach equilibrium.

The weight of the filter papers should be determined before the test and after the end of the equilibrium process. With them, the moistures of the filter papers are determined and by subsequent, the suction of the soil sample is found from a relationship previously calibrated for the filter paper used, between the water content of the paper and the suction.

The calibration procedure should be made to the filter paper used. Complying with ASTM E 832 standard - 81 [12], it could be used these brands as the filter papers: Whatman No.42, Fisherbrand 9-790A and Schleicher and Schuell No. 589 White Ribbon. Commercially filter papers comes in circles, a suitable diameter for this test is 5.5 cm. To calibrate them, the procedure above described to determine the suction a soil sample should be applied, however, to perform a calibration will be necessary to replace the soil sample by a saline solution in which you can use sodium chloride or potassium chloride dissolved in 50ml of distilled water and placing the filter paper on an inert support of stainless steel or PVC. The water used must be at 20 °C to match Table II; otherwise you should consider variations suction produced by the temperature differential.

This procedure is repeated for all salt concentrations for which the osmotic suction developed are known and thus we are able to generate a calibration graph based on the weights obtained from the filter papers used and suctions already known from the salt concentrations.

TABLE II Salt Concentrations And Its Suctions For Filter Paper Calibration

kPa	log kPa	pF	atm	R _b	20° C	
					g NaCl	g KCl
					1000 ml H ₂ O	1000 ml H ₂ O
-98	1.99	3.0	-0.97	0.99927	1.3	1.7
-310	2.49	3.5	-3.02	0.99774	3.8	5.3
-980	2.99	4.0	-9.68	0.99278	13.1	17.0
-3099	3.49	4.5	-30.19	0.97764	39.0	52.7
-9800	3.99	5.0	-96.77	0.93008	122.5	165.0

VI. CHILLED MIRROR HYGROMETHER METHOD

The chilled mirror hygrometer test also requires a calibration process which is similarly to the filter paper calibration. We will use the calibration method of the non-contact filter paper method with the only variant that the volumes used are less because the space available in the chilled mirror hygrometer is limited.

The internal process developed by the chilled mirror hygrometer is primarily similar to that developed by the thermocouple psychrometer as this allows measurement of the temperature by a Peltier device [13], as the hygrometer does. Furthermore the hygrometer uses the dew point technique within an airtight chamber seeking a balance between the liquid phase of the soil and water in the gas phase or water vapor contained in the air above the sample within the airtight chamber. Also a fan is used to cool a mirror inside the chamber and form in it the mirror the first dewdrop and subsequently heating the mirror to eliminate such drop [14].

The temperature of the mirror to which the first dewdrop appears and disappears is measured with a thermocouple. To determine the time of occurrence of the dewdrop an optical device that measures the angle of reflectance of a beam of light incident on the mirror constantly, at the time that this beam resulting reflected at a different angle, this is caused by the appearance of the first dewdrop .

The cooling fan is also used to recirculate air inside the sealed chamber to avoid temperature changes during heat exchange and thus accelerate the process of balance [15].

Once the temperature has stabilized and the first dewdrop has appeared, the instrument determined the relative humidity in the chamber sealed space which will be related to the total suction of the soil sample.

VII. RESULTS AND DISCUSSION

The results obtained after performing the corresponding filter paper tests are presented in suction against degree of saturation graph, as well as the results obtained by using chilled mirror hygrometer.

The first graph shown in the Fig. 1 shows the drying curve obtained using the non-contact filter paper method and a polynomial approximation with the corresponding equation and correlation coefficient with the data obtained from the non-contact filter paper tests.

The Fig. 2 shows the polynomial approximation for the drying curve and the results for some suction measurements using the chilled mirror hygrometer and the Fig. 3 shows the same results of the chilled mirror hygrometer versus the results obtained from the polynomial approximation for the non-contact filter paper method in the same degree of saturation.

The most important factor is the accuracy in the measured value since this value determines whether the data obtained with the chilled mirror hygrometer is accurate and useful for any investigation. These results are shown in the Table III were the results obtained from the chilled mirror hygrometer present an error with respect the ones obtained from the non-contact filter paper method but this percentage of error is relatively small for intermediate values of degree of saturation but for outliers values the percentage increase but it is just because the range of application of the chilled mirror hygrometer originally does not cover this values but even with this error the results obtained are sufficiently good for research purposes.

Finally the details of easiness, execution times and accuracy of both methods will be presented in Table IV. As is shown in Table 4 the use of chilled mirror hygrometer in determining the suction of clays, not only achieves a reduction of over 50% in the total execution time respect the non-contact filter paper method but also achieves facilitate testing process in general.

Using samples of a volume near to 3cm³ resulted in faster drying and wetting process and since having a smaller distance from the center of the sample to its boundaries favors the balance of moisture in the sample therefore the differences in the internal stresses of the soil that appears when the humidity of the soil changes, are minimal in magnitude and duration.

TABLE III Salt Concentrations And Its Suctions For Filter Paper Calibration

Suction Measurement by the Drying Line					
Chilled Mirror Hygrometer Method		Polynomial Approximation for N-C FPM		Variation in CMH Results	
Degree of Saturation	Suction (kPa)	Degree of Saturation	Suction (kPa)	Error (kPa)	Error (%)
0.77	200	0.77	219.8711	19.8711	9.04%
0.71	12170	0.71	13106.4481	936.4481	7.14%
0.64	29120	0.64	30754.4736	1634.4736	5.31%
0.57	48630	0.57	50664.7409	2034.7409	4.02%
0.51	67350	0.51	69531.2441	2181.2441	3.14%
0.42	97620	0.42	100947.3524	3327.3524	3.30%
0.34	126570	0.34	132012.2196	5442.2196	4.12%

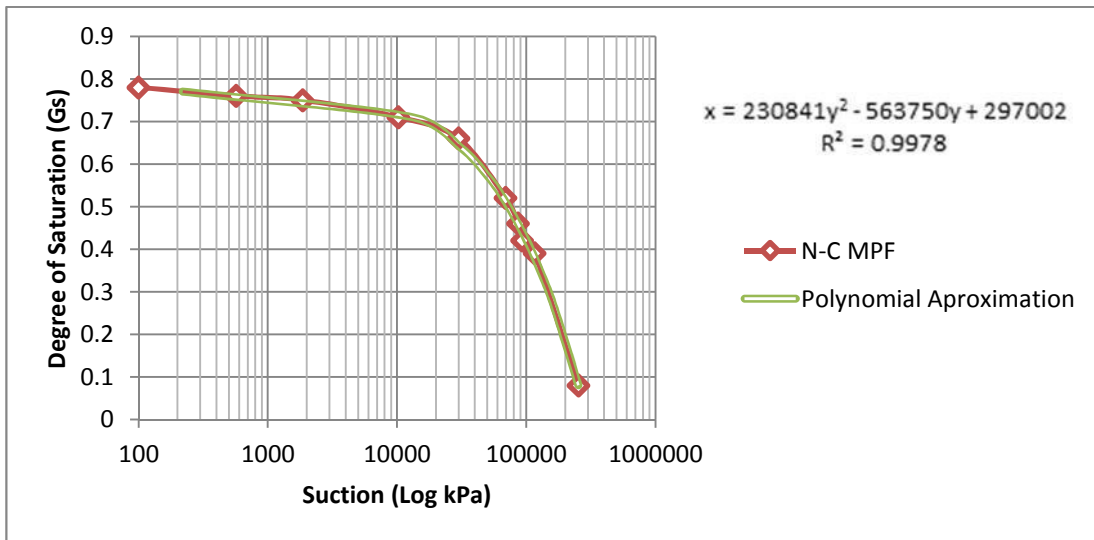


Fig. 1. Drying curve for the non-contact filter paper method and its polynomial approximation.

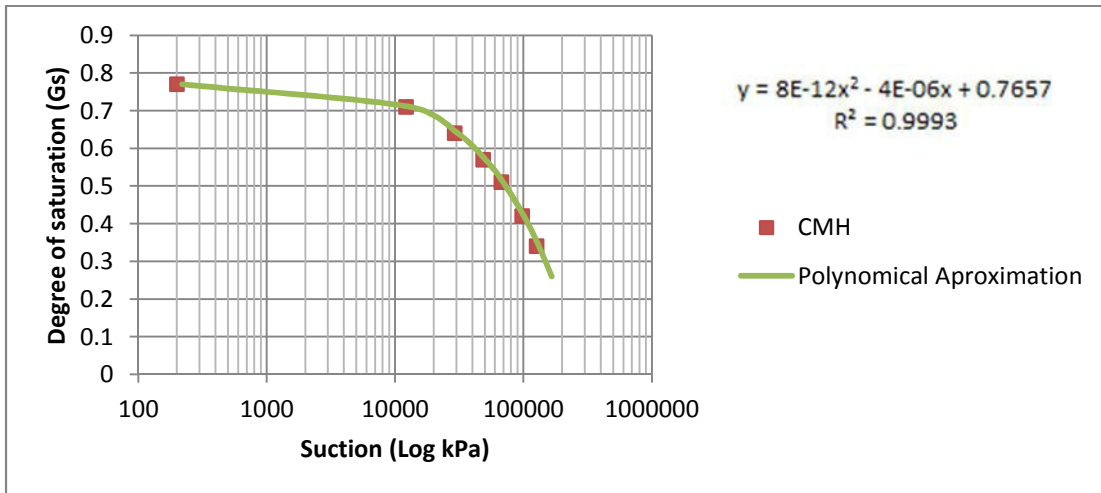


Fig. 2. Drying curve for the chilled mirror hygrometer method and its polynomial approximation.

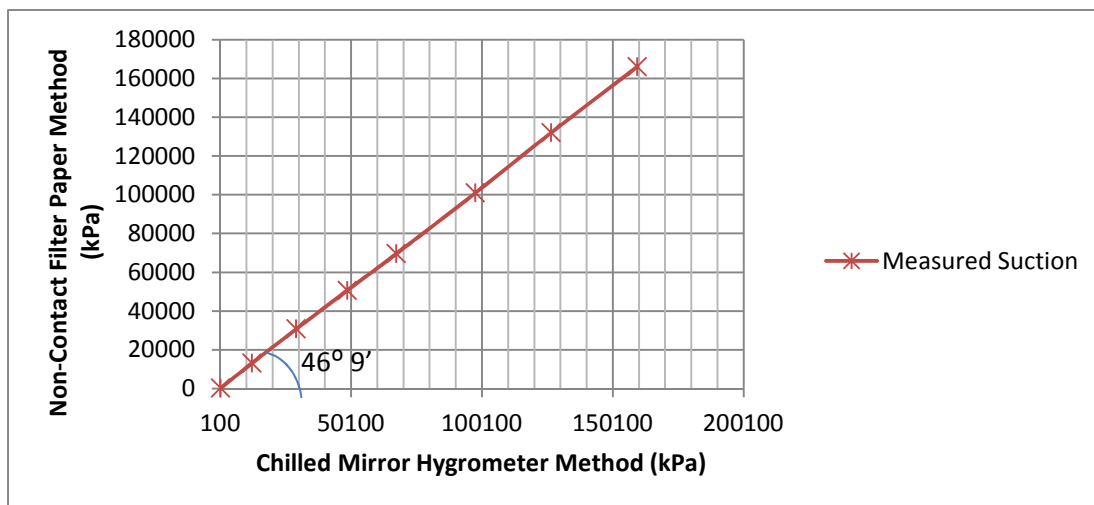


Fig. 3. Non-contact filter paper method vs Chilled mirror hygrometer results.

TABLE IV Evaluation Of Important Factors For Both Methods

Factor	Non-Contact Filter Paper Method	Chilled Mirror Hygrometer Method	Observations
Drying Time	2 - 3 Weeks	1.5 Weeks	The drying process is always more complicated, however, in chilled mirror hygrometer samples the process is greatly facilitated because of the smaller volume of water to dry.
Wetting Time	2 - 3 Weeks	1 Weeks	The wetting process is always the simplest and in the case of samples for chilled mirror hygrometer is even easier because of the low water volume samples required to reach saturation, however, is important to make the process steadily because leaving samples for an extended period under wetting conditions could generate fungus in the samples.
Equilibrium Time	7 - 14 Days	3 - 28 Minutes (It Depends on the suction level).	Time intervals were obtained based on the ASTM D5298-10 standard for the case of the filter paper method and based on the time measured during the tests in the case of `chilled mirror hygrometer method.
Measurement Accuracy	100% (Just for being the most common method).	91 to 97 % (Depending on the suction measured).	The measurement error for the chilled mirror hygrometer was found with the deviations in measurements compared to those obtained with the filter paper method.
Processing Samples	Hard	Easy	Given the size of the samples, processing a larger sample for the filter paper method was more complicated despite previous experience, while the sample for the chilled mirror hygrometer was easier even without previous experience.
Drying Process	Very Hard	Hard	Since this is the most complicated process the benefit of using smaller samples for the chilled mirror hygrometer helped but still remains a process of care.
Wetting Process	Hard	Very Easy	For large samples the wetting process involves some risk of cracking, however, it was noted that in small samples like specimens for chilled mirror hygrometer these risks are minimal.
Total Time	6 - 8 Weeks	2 - 3 Weeks	The reduction in the total time equates to a 50% minimum, being this value that can improve with experience.

VIII. SUMMARY AND CONCLUSIONS

The results herein demonstrate that the factors of interest; accuracy, easiness and reading time, present a considerable improvement. The accuracy factor has minimal variations from the filter paper method that maintain a perfectly acceptable standard for the chilled mirror hygrometer method.

Based on these results and as we can see in Fig , when we compare the results obtained with the chilled mirror hygrometer and the filter paper method it shows a minimal deviation in the results of 1° 09'. This deviation shows that both results are very similar and since the filter paper method has more probability of human error between the processes we consider that the chilled mirror hygrometer results are more reliable.

The results are highly reliable for use on clay soils of Queretaro, however, it is recommended to continue investigating the scope of chilled mirror hygrometer in different soils to confirm their application in various types of unsaturated soils mirror. However, it is highly probable that can extend the use of this method to any other type of soils.

ACKNOWLEDGMENTS

We are grateful to CONACyT and the University of Queretaro to provide support and resources for the preparation of this article.

REFERENCES

- [1] I. Decagon Device, *WP4C Dew Point PotentiaMeter. Operator's Manual*. 2013.
- [2] S. S. Agus and T. Schanz, "Comparison of Four Methods for Measuring Total Suction," *Vadose Zo. J.*, vol. 4, p. 1087, 2005.
- [3] M. Barrera Bucio, "Estudio experimental del comportamiento hidro-mecánico de suelos colapsables." Universitat Politècnica de Catalunya, 04-Jun-2002.
- [4] A. Perez and D. Hurtado, "Manual de utilización del psicrómetro de termopar para medir succión en suelos no saturados,," 2012.
- [5] J. Fenner, R. Lucas, M. Hermínia, F. Tavares, D. L. Cardoso, and F. A. Meira, "Redalyc.CURVA DE RETENÇÃO DE ÁGUA NO SOLO PELO MÉTODO DO PAPEL-FILTRO," *Rev. Bras. Cienc. do Solo*, vol. 35, no. 6, pp. 1967 – 1973, 2011.
- [6] K. Terzaghi, *Erdbaumechanik auf bodenphysikalischer grundlage*. California: Leipzig u. Wien, 1925.
- [7] J. Badillo and R. Rodríguez, *Fundamentos de la Mecánica de Suelos*, Tomo I. México: Editorial Limusa, 2005.
- [8] H. Pan, Y. Qing, and L. Pei-yong, "Direct and indirect measurement of soil suction in the laboratory," *Electron J Geotech Eng*, 2010.
- [9] ASTM D5298-10, "Standard Test Method for Measurement of Soil Potential (Suction) Using Filter Paper," West Conshohocken, PA, 2010.
- [10] A. Trejo, *Estratigrafía y Propiedades Mecánicas Del Subsuelo Del Valle de la Zona Urbana de Querétaro*, Ilustrada. 2008.
- [11] ASTM D7015-07, "Standard Practices for Obtaining Intact Block (Cubical and Cylindrical) Samples of Soils," West Conshohocken, PA, 2007.
- [12] ASTM E832-81(2013), "Standard Specification for Laboratory Filter Papers," West Conshohocken, PA, 2013.
- [13] A. Perez and HurtadoD., "Hydraulic conductivity measurements in two unsaturated soils of Queretaro Valley, Mexico," in *Asian conference on unsaturated soils*, 2000, pp. 427 – 432.
- [14] R. Bulut and E. C. Leong, "Indirect measurement of suction," *Lab. F. Test. Unsaturated Soils*, pp. 21–32, 2009.
- [15] D. Devices, "Measurement of Leaf Water Potential using the WP4(2)," 2006.

Experimental studies on reduction of soil expansion by using reinforced perforations

N.P. Rodriguez-Morales¹, T. Lopez-Lara²

¹⁻² *Department of Research and Graduate Studies of the Engineering Faculty, University of Queretaro, Cerro de las Campanas s/n, Col. Niños Heroes, CP 76010, Queretaro, Qro. Mexico.*

¹ paurodriguez@outlook.com

² lolte@uaq.mx

Abstract—This paper reports the results of laboratory study performed on expansive soil perforated and reinforced with a porous structure and demonstrates that the extraction of volume is useful in restraining the swelling tendency of expansive soils. Swelling characteristics of remolded expansive soil specimens reinforced with hollow tubular and porous structures of various diameters (7mm and 10 mm) were studied. One-dimensional swell-consolidation tests were conducted on oedometer specimens. Reduction in heave was the maximum at using the 10mm diameter structure.

Keywords—*expansive soil; soil stabilization; porous media.*

I. INTRODUCTION

Expansive soil is considered one of the most challenging soil in engineering and construction due to its susceptibility to present volume changes. This material swells, and thus increases in volume when it gets wet and shrinks when it dries. The more water it absorbs the more its volume increases, for most expansive clays, expansions of 10% are not uncommon [1]. This paper focuses on soils that exhibit significant swelling potential.

Because of the mentioned volume changes, either under or nearby to any type of foundation, the structures may be subjected to various degrees of damages. Some of the most common problems associated with expansive soils include buckling of pavements, floor slab on grade cracking, differential movement and cracking of basement walls and buried pipes, wall cracking and even the collapse of one or more elements of the structures [2].

The swell potential of a clay soil is a measure of the ability and degree to which such a soil might swell if its environment were to be changed in some definite way [3].

To know the swelling potential of a soil it is necessary to determine first the expansion degree of it, this can be achieved by wetting an undisturbed soil sample and measuring the volume increment. This test is carried out on an undisturbed sample laterally subject and under normal pressure. If the pressure applied is enough to prevent the swelling of soil it is known as expansion pressure [4].

Among the treatment methods that we can find to solve the expansive soil problem are the following [5] [6]:

- Sub-excavation and removal of expansive soils and replacement with non-expansive soil; requires

removal and replacement of the expansive subgrade soils. The material being put back should not cause problems with respect to the in situ material.

- Application of heavy applied load to balance the swelling pressure; loading the expansive soil with a pressure greater than the swelling pressure avoids the expansion of soil, but setting a pressure of this magnitude can only be achieved with large buildings and not with pavements or small houses.
- Preventing access of water to the soil by encapsulation; isolating the ground from moisture changes using impermeable membranes or through elements such as sidewalks, pavement and drainage.
- Stabilization by means of chemical admixtures; admixtures are used to alter the characteristics of clay mineral and reduce its potential for swelling. Lime is the most effective chemical used to stabilize, but the major limitation is the application of the chemical to sufficient depth.
- Mechanical stabilization; one way is to remold the soil, breaking its structure and relocating the soil compacted to a higher humidity than the original.
- Pre-wetting the soil; theoretically, expansive soils can be wetted and caused to expand prior to construction, but in practice, it is very difficult to achieve uniform moisture penetration in a reasonable time.

Based on the opinion of some authors, the success of some of the above methods has been poor, and repair or overlay is generally required [2][3][4]. Besides, the cost of carrying out some of the presented methods represents between 20% to 25% of the initial cost of a small house and in some cases, one specific method may not be the answer and it might be necessary to combine several different methods, which is why so often it is not taken any special consideration for this type of soil [7].

II. PREVIOUS WORKS

A. Solutions for expansive soil problem

Due to the lack of economic and efficient solutions applicable to small buildings over the years, a large number of investigations seeking to provide solution to the problem of expansive soils have been developed.

In Jordan a study that examined the effect of the temperature under laboratory conditions of clayey soils was conducted. Soils were subjected to four temperature levels (100, 200, 300 and 400 °C) and then their swelling and strength properties were analyzed, the experiment results revealed that heat treatment higher than 100°C resulted in a decrease in swelling potential, but an important decrement in strength properties was also revealed, appearing a loss of 100% of strength in the soil treated at 400°C [8]. Later in Malaysia, a laboratory study was done to determine the behavior of expansive soil mixed with lime and rice husk ash (RHA). Specimens of remolded soil with a 15% of initial expansion were mixed with different percentages of lime and RHA and then their degree and pressure of expansion was measured. A decrease of 90% in the degree of expansion was achieved using 3% of lime and the same amount of RHA. Expansion pressure decreased by 68% [9]. In India, a study was carried to demonstrate that the use of discrete geo fibers placed randomly on expansive soil is useful to restrict their swelling potential. There were studied the expansion properties of remolded and reinforced soil specimens, varying their fiber content from 0.25% to 0.5% and the relationship in size (l/b) in 15, 30 and 45 and subjecting them to expansion and consolidation tests. They managed to reduce the expansion potential by 70% and found that the maximum reduction in the swelling and expansion pressure occurs in specimens with lower ratio of its dimensions (15) in both fiber contents (0.25% and 0.5%) and that reduction increases with increasing fiber content [10]. Finally, in Spain, it was performed an experimental study on a highly expansive clay that was subjected to a treatment through the addition of by-products and waste materials from industry to reduce its swelling potential. The proposed method consisted of mixing dry soil samples with a stablished quantity of dust additive in an industrial mixer and gradually adding the required amount of water to achieve the optimum moisture content; the ingredients were mixed for about five minutes and then the samples were remolded to determine the percentage of expansion. The experiment showed that the use of different additives for specific soil treatments can be very effective, since the expansion potential of various clayey soil was improved by the use of the unconventional additives employed in this test, achieving a reduction of 85% by combining 2% of lime and 1% of magnesium oxide, so the author suggest that the use of these additives, either alone or in a combination, can improve significantly the expansive characteristics of the soil [11].

B. Use of holes in construction

Perforations and their variants have been used extensively over the years in the area of construction and although they are typically used to improve soil properties, there is no method

based on this principle that seeks to reduce the expansive potential of soil.

Since the 80s, in the Soviet Union, it was developed a method for the establishment and strengthening of foundations based on the injection of piles into pre-drilled holes in loess, which are prone to suffer sudden settlements. It was determined that drilling holes and injecting piles increased the load capacity [12]. Later it was proposed to use lime filled perforations to improve the bearing capacity of soft soils by introducing a hollow tube into the soil to the desired depth and putting the lime into the tube under pressure as this is removed [13]. In Egypt, a laboratory model was proposed to study the improvement of soft clay by using holes stuffed with sand with and without confinement. Then there was evaluated the load capacity and the produced settlements and it was found that the improvement in capacity is significant [14]. Also, derived from the use of perforations, there is a method that has been used as an alternative solution to the problem of expansion of soils; the use of inverted hollow structures that are kept in good condition despite the expansion, these are structures that can be supported directly on the expansive soil controlling the direction of swelling [15]. This technique consists in enabling the soil to expand into cavities built into the foundation in order to reduce movement to a tolerable amount. There are different solutions that work under this principle, the principal is the foundation by ribbed slab [16]. The ribbed slab, originally proposed by the Portland Cement Association of California, consists of bulding a raised floor from a ribbed slab, which nerves rest on the expansive soil (Fig.1). The spacing between nerves and slab thickness depend on the expansive potential of soil and the applied load. The holes provide the expansion pressure relief. Although this solution is effective, is costly, and has no experimental studies that support it [17].

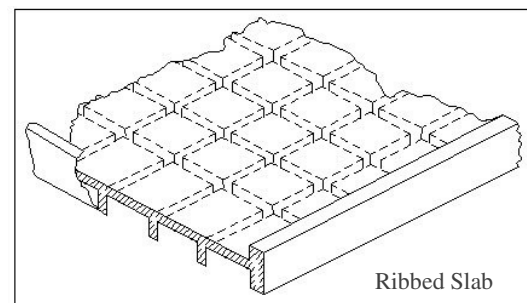


Fig. 1. View of a ribbed slab in which can be appreciated the holes between nerves.

C. Studies on lateral expansion and expansion pressure.

Gromko [3] mentions that soil heave is assumed to occur primarily normal to the surface because lateral swell is largely inhibited by adjacent soil. However, this may not be true in some cases such as when expansive soils undergo severe fissuring on drying, soils on slopes, foundations subjected to differential water content changes beneath central and exterior areas and retaining wall structures subjected to lateral pressures. Also, there is some research [18] that has indicated that undisturbed clay samples have actually shown that lateral swelling can be significant and may, in fact, be greater than swell normal to the surface.

On the expansion pressure, a model test was conducted to measure the lateral pressure of expansive soil exerted on a rigid wall; at the same time, the vertical swelling pressure was also recorded. It was discovered that the ratio of lateral pressure and vertical pressure varies with soil wetting conditions, and that there is a peak value of lateral pressure, which can reach 3.6 times the vertical pressure. Equilibrium was reached when the soil reached complete saturation and the ratio approached 1.

From the principle of the ribbed slab and based on the presented research on lateral expansion, it is proposed a method in which, by using reinforced perforations placed in the soil mass to redirect the soil expansion into the voids, can be achieved the reduce of the vertical expansion degree and the expansive pressure.

III. EXPERIMENTAL INVESTIGATION

A laboratory investigation was conducted to analyze the efficacy of drilling and reinforcement with hollow structures in reducing heave of expansive soils. Swelling behavior of unperforated expansive soil specimens was studied and compared with that of specimens that were drilled. The experimental investigation was conducted on unperforated expansive soil specimens and drilled and reinforced with a hollow structure specimens compacted in oedometer. Swell-consolidation tests were performed.

A. Test Materials

1) Expansive Soil

The soil used in this investigation had a swell index of 27.7% (loaded with 9.8 kPa). The soil was collected from a depth of 1.5m from Jurica, Queretaro, Mexico. Based on the plasticity properties, the soil was classified as CH according to USCS classification. Table 1 shows the index properties of the soil.

TABLE 1. Index properties of the expansive soil.

Property	Value
Specific Gravity	2.6
<i>Consistency properties</i>	
Liquid limit (%)	85
Plastic limit (%)	32
Plasticity index (%)	53
Shrinkage limit (%)	20
Volumetric Weight γ (kN/m ³)	15.41
USCS Classification	CH
Swell index (loaded with 9.8 kPa) (%)	27.7
Expansive pressure (kPa)	686.5

2) Reinforcing Structure

To reinforce the drilling and avoid the collapse of the material within it, it is proposed to use a porous hollow tubular structure for support. To define the material of this structure a finite element analysis was done to determine the stress state to which the reinforcement will be subjected during the laboratory test. The following loads were considered (Fig. 2):

- Normal pressure: 98 kPa
- Expansive pressure (lateral): 686.5 kPa

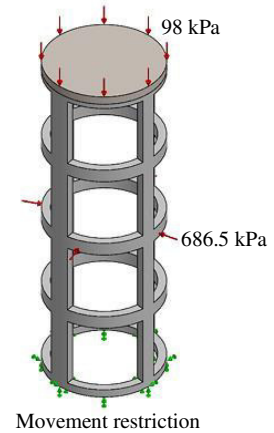


Fig. 2. Model of hollow and porous structure used for finite element analysis.

Based on the presented studies, it was taken the value of vertical expansive pressure to estimate the lateral expansive pressure.

The resulting stress state is shown in Fig. 3. The maximum value of stress and deformation that were found are presented in Table 2.

TABLE 2. Values of stress and deformation of the perforation reinforcement.

	Maximum value	Minimum value
Stress	103 MPa	0.04 MPa
Deformation	0.014 mm	0 mm

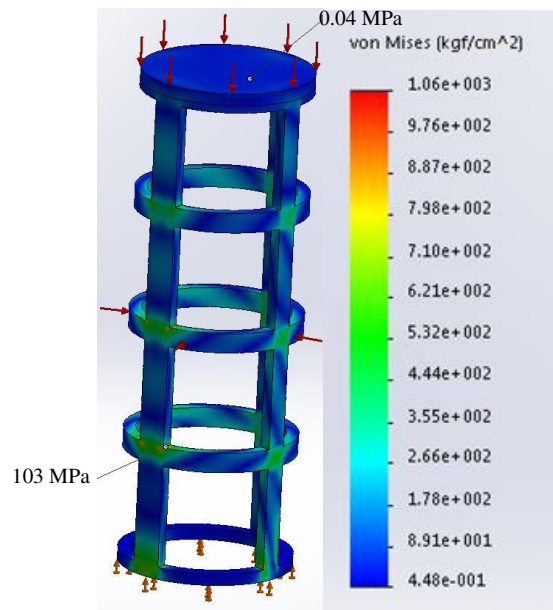


Fig. 3. Stress state of the perforation reinforcement.

After analyzing the obtained data, a comparative between three different materials, PVC, stainless, and galvanized steel (Fig. 4), was done (Table 3).

TABLE 3. Comparative between different materials.

Material	Hollows		Cost (\$/piece)	Resistance (MPa)
	Dimensions	Homogeneity		
Galvanized steel	5x5 mm	High	\$0.50	203.95
PVC	$\varnothing = 2$ mm	Poor	\$0.60	40.7
Stainless steel	$\varnothing = 2$ mm	High	\$20.00	620.5

Since the PVC resistance is not enough for the stresses to which the structure will be subject, this material is discarded. And, between stainless and galvanized steel, galvanized steel is chosen because of its low cost and because it fulfill the presented requirements.

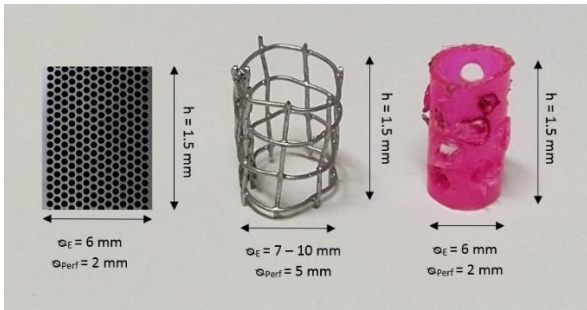


Fig. 4. Structures made by the three different analyzed materials.

3) Laboratory test

One-dimensional swell-consolidation tests were conducted on oedometer specimens (perforated and unperforated). Expansive soil samples were compacted reproducing the volumetric weight in field. Then, using a drill, holes were drilled in soil specimens, some with perforations of 7mm (Fig. 5-a) diameter and the other with perforations of 10 mm of diameter (Fig. 5-b), in each case varying the amount of perforations. Subsequently the reinforcing structures were placed in the holes.

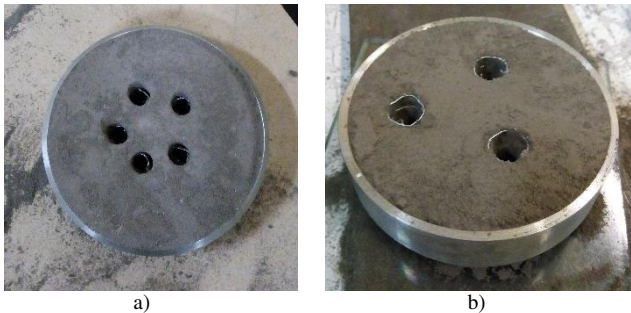


Fig. 5. Perforated soil specimens: a) Diameter of perforation = 7 mm; b) Diameter of perforation = 10 mm.

All the swelling tests were performed with an applied normal load of 98 kPa. The results for tests with perforations of 7 mm diameter are shown in Table 4 and the obtained data for specimens perforated with 10 mm diameter holes can be observed in Table 5.

TABLE 4. Experimental results on the reduction in expansion by drilling with 7mm in diameter.

Diameter of perforation = 7 mm			
Number of holes	Extracted volume (%)	Expansion (%)	Reduced expansion (%)
0	0	27.7	0
2	1.7	20.4	7.3
6	5.2	17.4	10.3
13	11	15.2	12.5

TABLE 5. Experimental results on the reduction in expansion by drilling with 7mm in diameter.

Diameter of perforation = 10 mm			
Number of holes	Extracted volume (%)	Expansion (%)	Reduced expansion (%)
0	0	27.7	0
1	1.7	18.4	9
3	5.2	7	20.7

It can be seen that by using perforations of both diameters is achieved a significant reduction in the percentage of soil expansion. However, the reduction achieved is significantly greater using structures with 10 mm in diameter. The behavior reached in this experimental study on the reduction of the expansive properties of soil is shown in Fig. 6.

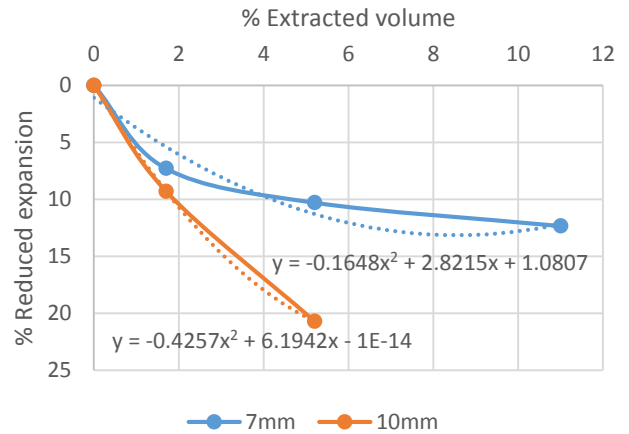


Fig. 6. Effect of extracting volume on reduction of soil expansion.

From the plot, it can be observed that the corresponding line to the 7mm perforations begins to form an asymptote, so that it can be conclude that using this structure diameter, the method would be effective only to reduce approximately 13% of soil expansion. Meanwhile, the corresponding line to the 10mm perforations show no visible limit yet, but due to the size of the perforation it is not possible to further increase the number of holes without sacrificing the strength of soil.

IV. CONCLUSION

The method is feasible and efficient as long as the adequate perforation diameter to be used has been correctly determined, which depends on the degree of expansion of the soil that is been seeking to improve.

V. REFERENCES

- [1] L. Jones y I. Jefferson, «Expansive soils,» de ICE manual of geotechnical engineering: geotechnical engineering principles, problematic soils and site investigation., London, UK, ICE Publishing, 2012.
- [2] B. Kalantri, Construction of foundations on expansive soils, Columbia, Missouri: M.Sc Thesis, Department of Civil Engineering University of Missouri, 1991.
- [3] G. J. Gromko y M. ASCE, «Review of Expansive Soils,» Journal of the geotechnical engineering division, vol. 100, n° 6, pp. 667-687, 1974.
- [4] C. Villalaz, Mecánica de suelos y cimentaciones, México: Limusa, 2004.
- [5] A. Ardani, «Expansive soil treatment methods in Colorado,» U.S. Department of Transportation, Colorado, 1992.
- [6] T. López-Lara y J. F. Romero-Zepeda, «Métodos de prevención para viviendas sobre suelos expansivos,» Reunión Nacional de Mecánica de Suelos: La importancia de la Geotecnia en la Infraestructura de México, vol. 23, pp. 629-642, 2006.
- [7] J. Cabrera-Ramírez y J. Delgado-Hernández, Métodos de remediación de viviendas dañadas sobre suelos expansivos., Querétaro, México: Tesis de Licenciatura. Universidad Autónoma de Querétaro., 2010.
- [8] M. Abu-Zreig, N. Al-Akhras y M. Attom, «Influence of heat treatment on the behavior of clayey soils,» Applied Clay Science, vol. 20, pp. 129-135, 2001.
- [9] A. S. Muntohar, «Swelling characteristics and improvement of expansive soil with rice husk ash,» de Expansive soils: Recent advances in characterization and treatment, London, UK, Taylor & Francis, 2006, pp. 435-451.
- [10] B. V. Viswanadham, B. R. Phanikumar y R. Mukherjee, «Swelling behaviour of a geofiber-reinforced expansive soil,» Geotextiles and Geomembranes, vol. 27, pp. 73-76, 2009.
- [11] A. Seco, F. Ramírez, L. Miqueleiz y B. García, «Stabilization of expansive soil for use in construction,» Applied Clay Science, vol. 51, pp. 348-352, 2011.
- [12] N. V. Dimitriev, V. M. Korolev, L. B. L'vovich, L. I. Malyshev y G. S. Étkin, «Piles injected into predrilled holes in soils prone to slump-tyre settlement,» Soil Mechanics and Foundation Engineering, vol. 25, n° 1, pp. 27-32, 1988.
- [13] C. D. Rogers y S. Glendinning, «Improvement of clay soils in situ using lime piles in the UK,» Engineering Geology, vol. 47, pp. 243-257, 1997.
- [14] A. K. Nazir y W. R. Azzam, «Improving the bearing capacity of footing on soft clay with sand pile with/without skirts,» Alexandria Engineering Journal, vol. 49, pp. 371-377, 2010.
- [15] B. Kalantri, «Foundations on expansive soils: A Review,» Research Journal of Applied Sciences, Engineering and Technology, vol. 4, n° 18, pp. 3231-3237, 2012.
- [16] J. E. Bowles, Foundation Analysis and Design, McGraw-Hill, 1996.
- [17] J. Patrone y J. E. Prefumo, «La acción de los suelos expansivos sobre las cimentaciones: Métodos de prevención y control,» de Primeras Jornadas de Ingeniería de Cimentaciones, Montevideo, Uruguay, 2002.
- [18] J. V. Parcher y P. D. Liu, «Some Swelling Characteristics of Compacted Clays,» Journal of the Soil Mechanics and Foundations Division, vol. 91, n° SM3, pp. 1-17, 1965.

Regionalization of the Dvorak Technique; case study Hurricanes Ingrid and Manuel (13-16th September 2013)

Meza-Ruiz Marilu^{#1}, Herrera-Curiel Libna^{*2}, Gutiérrez-López Alfonso^{#3}

[#] *Hydraulic Laboratory, Engine Faculty, Universidad Autónoma de Querétaro
Cerro de las Campanas S/N Col. Las campanas México*

¹ *mr.marilu@yahoo.com.mx*

³ *third.author@first-third.edu*

Abstract—When there is no technology, like flights and airplanes with radiosondes, which help the scientist and decision makers to know the intensity of a Tropical Cyclone System (TCS) and to prognosticate the future develop of the storm, the Dvorak technique is applied. This technique is based on the analysis of cloud coerture in infrared image from GOES satellite. This analysis include the change in the bright and temperature of the cloud coerture, their distribution in space (circular, spiral among others distribution), the visualization of the “eye” in this case it is possible to use the Visible (VIS) and Infrared (IR) image. This paper discuss this Technique applied in the Mexican territory, different latitude and longitude from where the technique was developed, and it is prove in the two hurricanes Ingrid and Manuel, presented at the same time in 14th September in 2013 in Mexican territory.

Keywords—*Dvorak technique; IR image; GOES; Hurricane intensity; estimation*

I. INTRODUCTION

The latest hurricane Ingrid and Manuel, left in its path 59 thousand people evacuated, many damage to infrastructure (about 93 federal highways, 43 thousand schools, 1 153 hospitals and clinics damaged, to name a few), affected livestock, agriculture and aquaculture in at least five states in Mexico. Is not an official quantification of the damage caused by this phenomenon [1] but September was classified by CONAGUA (National Water Commission) as the wettest month since 1941, the monthly average was 227.3 mm, 60% above the average expected for that month. Total rainfall in September occurred in 1955 was 212.1 mm. [2].

The estimation tracking and forecast of this kind of phenomena is the major goal for meteorologist, hydrologist, hydraulics and civilian protection in order to improve the actions to prevent human losses and minimize the damages produces for this extreme events.

The estimation of Tropical Storm and Hurricane intensity are related with the pressure and sustained winds (Scale Staffir Simpson) although this relations do not gives an estimated of the damages in land, now a day the technique Dvorak made a estimation of this intensity related with the cloud coerture

observed in the IR and VIS image [3] but without direct measurement of convective systems that includes the strength and magnitude, it is difficult to predict how, when and where these intensity changes will occur, this is a challenge for the technique [4]. In this way there is work that related the consolidation of eyewall in the Hurricane with the intensity [5]

The intensity of tropical systems more specific cyclone (TCS) is defined by the maximum sustains winds in 10 m above the level sea or ground. The World Meteorological Organization the intensity is described as the average speed of wind in ten minutes. Is important to have in mind that this parameter is count in knots, one knot is equivalent to 0.5 m/s or 1.85 km/h. Another measure pf the intensity of this kid of TCS is the central pressure; it can be estimated by the relation between wind and pressure. Sometimes there is no available technology, like flights with resonances, that can give important information about the develop or decaying of TCS, that is why the Dvorak technique is the principal methodology used by meteorologist and special researchers to estimate the intensity of cyclone systems since seventies.

Dvorak technic is based on the cloud coerture analysis, the bright of cloud in an infrared image change as the intensity of TCS increase or decay. This intensity changes in T-number units, from 1 to 8, with an increment of 0.5. The word T comes from tropical [6].

II. DVORAK TECNIQUE

A. Localize the tropical cyclone storm (TCS)

The tropical cyclone system is defined by a focal point where all lines and bands of the cloud system are united, in fact is the point where a spiral formation takes place.

B. Cloud patterns

In this part the patterns of cloud coerture are evaluated, is possible to select witch one can be analysed depending on the structure of the storm in the image. There is five kind or different types of pattern; the spiral patterns are estimated with logarithm base 10, it is visible along the axis of a cloud cluster,

the wind shear patterns commonly appear and are visible in the stages pre-hurricane, “eye” pattern is used when a hurricane is formed is an important structure to define if it gets stronger, maintains straight or decay in force, the central dense overcast pattern (CDO) is defined by the formation of a coma band, its temperature are very cold and finally the “embedded” centre pattern, this pattern are analysed when the storm has had a previous history of a T 3.5 or greater intensity [7].

C. T-number estimate from patteredcomparison with model

In this stage is important to identify the CCC pattern (Central Cold Cover), is a well-defined cold overcast mass of clouds covering the storm centre or coma head obscuring the expected signs of pattern evolution. Is necessary to determine the trend of the past 24-hour intensity, comparing the cloud features of current image and last one. In this part is possible to determinate if the storm is strengthening, weakening or remains the same.

D. Forecast 24-hour intensity

In this part the T-number is estimated and given to the storm, a different number is given the CI current intensity, which relates the directly to intensity of storm (mean wind speed and minimum sea level pressure), the T-number and CI are the same in the development stages but is held higher than T-number when the cyclone is weakening [8].

There is an effort in the scientific community, specifically in atmospheric field to improve this methodology. Based on the improvements in spatial technology and the increasing develop in computer science, is possible to improve and innovate the original Dvorak Technique to a converted into a automated computer algorithm that identify, follow and classify correctly the CCO and CCC and decrease the differences and the difficulties of the determination of developing and decay of a storm based on IR image and VIS image all this without the human intervention [9].

III. HURRICANE INGRID AND MANUEL

In 2013 this two weather phenomenon was the most significant, two storms in the same time joined together to hit the two cost of Mexican Republic; while Manuel was developing in the Pacific, Ingrid approached as a hurricane category 1 in the Gulf, this joint of two great masses of air, steam and water, caused heavy rainfalls in the southeast and southwest part of Mexican territory.

A. Ingrid Ingrid from 12th to 17th September

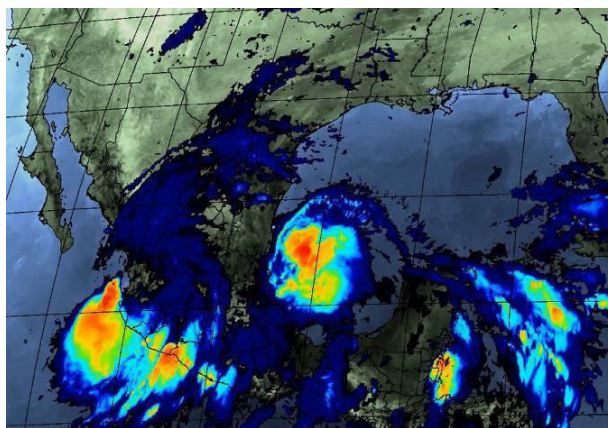
Ingrid became a hurricane category 1 on the scale Saffir-Simpson in the Gulf of Mexico, it made landfall as a tropical storm in the northeast of Mexico. Ingrid began to developing on September 11 due to a low pressure area, began to organize and head toward the Yucatan peninsula at the end of the day. For the 12th it moved very slowly towards Campeche, for 18 00 hours UTC was defined as tropical storm at 250 m from Veracruz. The depression moved initially to the west but turned to the south-west on September 13th while the cyclone

intensified to a tropical storm. On September 14th along with a channel of low pressure at a medium/high level of the atmosphere located in the north of the country and another channel established in the southeast of the United States went to Ingrid north-northeast, although the low pressure channel generated a higher level of Manuel output causing vertical wind in the west intensified by Ingrid which generated that achieved cyclone intensified into Hurricane late on September 14th. Later reached a maximum intensity of 75 knots (38.58 m/s) the early hours of September 15th while the centre was located about 215 nautical miles (398.18 m) south-east of La Pesca, México [10].

B. Manuel from 13th to 19th September

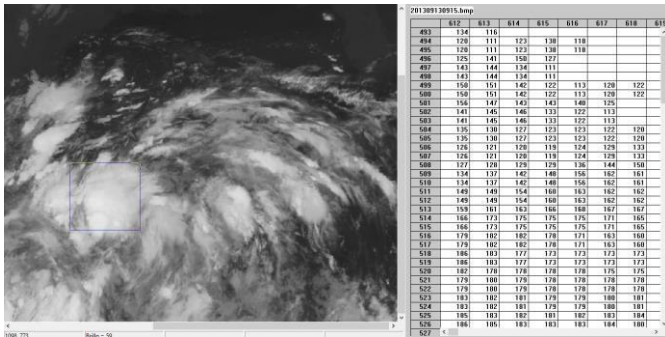
Manuel was a hurricane category 1 scale Saffir-Simpson that made landfall as a tropical storm on the South coast of Mexico and dissipated. Later it regained strength in the Gulf of California and returned to earth for the second time but this time as a hurricane. Manuel caused flooding and landslides, causing at least the death of 120 people in Mexico. Manuel was the first tropical storm developed in the North Pacific (according to records dating back to 1949) which first make landfall in the Mexican territory then reorganize itself into the ocean and later to become hurricane to make a land fall for the second time [11].

Fig.1. Image of the 13th September 2013. Hurricane Ingrid (Gulf of Mexico) and tropical storm Manuel (Pacific)



An executable program was developed in order to get the bright information of each pixel (Figure 2). In IR image the bright value goes from 0 to 255, the coldest superficies are represented with white color and the black ones represent the warmer superficies like land and oceans. In this program we set the minimal bright value of 109, at this value precipitation is reordered in ground stations.

Fig.2. Program to get the bright value of IR image from satellite GOES-13. Image of the 13th September 2013 at 06h15 UTC.



This program allows observe the developing of cloud system formation and at the same time knowing their bright value, this make the estimation of the Dvorak technique easier because we can observe and the same time identify the lowest and the brightest values, identifying the center of the convective cloud system.

IV. RESULTS

A. Information

The image study of the tropical storm Ingrid and Manuel was difficult, because the cluster of clouds was not well defined, the programs developed help us to identify the coldest clouds and select the center of both storms (Fig1).

Dvorak technique uses the images every 24 hours (images from polar satellites, in this case the images comes from geostationary images, available every 15 minutes but in this period of time the change is minimal). At first it was use the two images, for 12 hour period, after we use 6 hour period to observe if there are any difference.

Graphics and Tables I and II, shown the results comparative between the reported by the National Hurricane Center (NHC) from National Oceanographic Atmospheric Administration (NOAA) and the estimation made with the images available and applying the Dvorak Technique.

a) Ingrid (Gulf of Mexico)

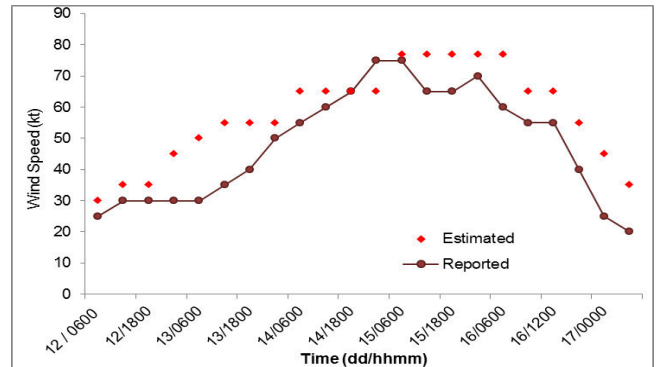
TABLE I. COMPARISON BETWEEN THE ESTIMATIONS FROM DVORAK TECNIQUE AND REPORTED BY NHC FOR INGRID

Date dd/hhmm	Pressure (mb) and Wind Speed (kt)	
	Reported ^a	Estimated
13 / 00 00	1 003 / 30	1 000 / 45
13 / 12 00	1 000 / 35	993 / 55
14 / 00 00	990 / 50	987 / 55
14 / 12 00	898 / 60	987 / 65
15 / 00 00	983 / 75	987 / 65
15 / 12 00	989 / 65	978.5 / 77

Date dd/hhmm	Pressure (mb) and Wind Speed (kt)	
	Reported ^a	Estimated
16 / 00 00	989 / 70	987 / 65
16 / 12 00	991 / 55	987 / 55
17 / 00 00	1006 / 25	1000 / 45
17 / 06 00	1008 / 20	1005 / 35

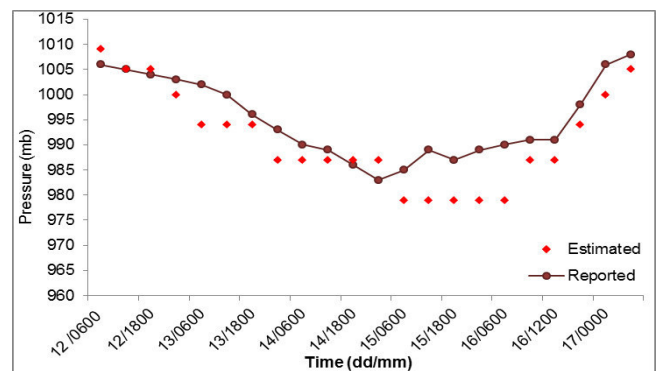
B. John, 2014

Fig 3. Mean Sustained Wind Speed (MSWS) estimated with Dvorak Technique and Reported by NHC for Ingrid.



Ingrid was well developed, and the technique work acceptable to estimate the mean sustained wind speed, the figure 3 shown an normal develop of the Hurricane time lapse, inicaly as depression (with the minime wind speed), then the next stage as tropical storm and finally the maximum stage, corresponding to maximum wind speed as Hurricane, after that it can be observed the storm decay.

Fig 4. Pressure estimated with Dvorak Technique and Reported by NHC for Ingrid



b) Manuel (Pacific)

Comparison between the estimations from Dvorak Technique

TABLE II. TECNIQUE AND REPORTED BY NHC FOR MANUEL

Date dd/hhmm	Pressure (mb) and Wind Speed (kt)	
	Reported ^a	Estimated
13 / 12 00	999 / 30	1 009 / 30
14 / 00 00	997 / 40	1 000 / 30

Date dd/hhmm	Pressure (mb) and Wind Speed (kt)	
	Reported ^b	Estimated
14 / 12 00	993 / 45	987 / 55
15 / 00 00	987 / 55	970 / 90
15 / 12 00	985 / 60	984 / 50
16 / 00 00	1 000 / 30	991 / 45
16 / 12 00	1 003 / 25	1 000 / 30
17/00 00	1004/20	1 000/30
17/12 00	1 003/20	1 000/30
18/00 00	1 000/30	984/50
18/12 00	995/45	966/70
19/00 00	984/65	954/90
19/12 00	984/65	966/70

b. P. Richard, 2014

Fig 5. Mean Sustained Wind Speed (MSWS) estimated with Dvorak Technique and Reported by NHC for Manuel.

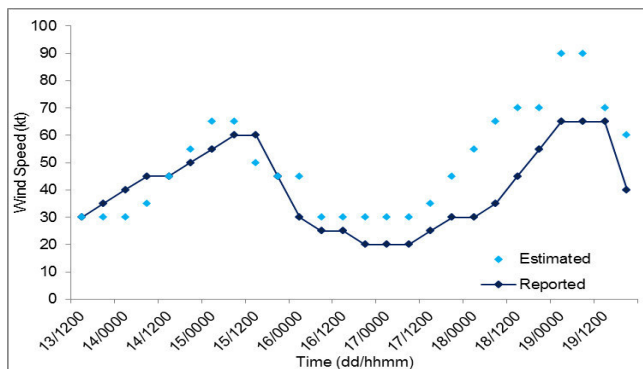
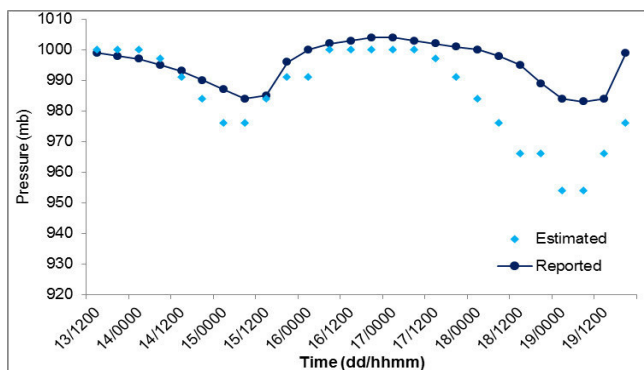


Fig 5 shown difference between the estimated and the recorded, Manuel was interacting with an Hurricane Ingrid (14th September), that could minimize the winds and only register higher winds when Tropical Storm gets the status of Hurricane in 19th September.

Fig 6. Pressure estimated with Dvorak Technique and Reported by NHC for Manuel.

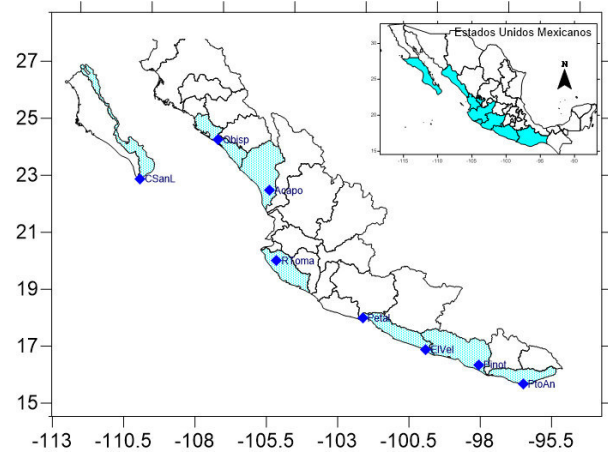


Manuel present a mayor difference between the estimated and the recorded, this is related with the difficulty to

determinate the central cloud system and the methodology in mantain the stage if there is no notable changes in this cloud coverture.

To regionalize the tecnique it was necessary study the Automated Meteorological Estations witch recorderd the event. For this study it was divided in tree parts: The Manuel South (12th to 17th September) and the Manuel North (17th to 19th September), and finally Ingrid (12th to 16 th). The Meterology stasios are shown in Figure 7 for Manuel and Figure 8 for Ingrid.

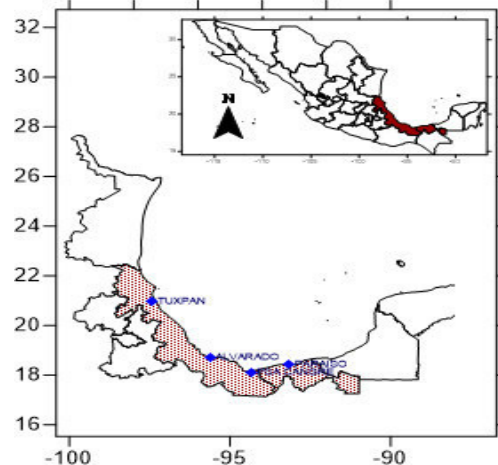
Fig. 7. Map of Meteorological Stasios for Manuel (Pacific)



Three stations in the North; Cabo San Lucas located in 22°52'52" Latitude N, -109°55'35" Longitude W) Obispo (24°15'04" N, 107°11'17" W) and Acaponeta (22° 28' 00" N, -105°23' 07" W). In the South; Río Tomatlán (19°59'54 N, -105°08' 00" W) Petalco (7°59'04" N, -102°07'23" W), El Veladero (16° 53' 03" N, -99° 54' 26" W), Puerto Angel(15° 40' 16" N, -96° 29' 50"W).

Four meteorological station recorderd the event in de Gulf of Mexico. Tuxpan located in 20° 57' 36" Latitude N and -97° 25' 01" Longitude W, Alvarado 18°42' 54" N and -95° 37' 57" W, Presa Cangrejera 18° 06' 21" N and -94° 19' 53" W and Paraiso 18° 25' 23" N and -93° 09' 20" W.

Fig. 8. Map of Meteorological Stasios for Ingrid (Golf of Mexico)



The Dorak technique allows to read the pixel value and related to the pressure and the wind speed, in this case only the pressure was studied. Every 6 hours it was a values for bright value and the pressure record in the differents meorological stations this values were realted. For every meorological station the maximum and minimal value of pressure and bright value was taken in order to related the pressure and the bright value.

The correlation shown to be a exponential relation, the ecuation 1 shown the relation between the bright value and the pressure in mili bares (mb). The $p(b)_{Pacific}$ are the resultl of the three station located in North and four stations located in South (Fig 7) . And the $p(b)_{Atlantic}$ are the resultl of the three station located in Goulf of Mexico (Fig 8).

$$p(b)_{Pacific} = 1199.1b^{-0.039} \quad (1)$$

$$p(b)_{Atlantic} = 1069.9b^{-0.013} \quad (2)$$

As a result the realtion is exponential, there is important to determinate the maxime pressure value recorderd and resplace this value in the highest bright values. In the case of $p(b)_{Pacific}$ the highest value of pressure in North was 1005 mb and 1001 mb in South. For $p(b)_{Atlantic}$ was 1009 mb.

Fig. 10. Estimated by bright value from IR vs Recorderd by NCH (Ingrid)

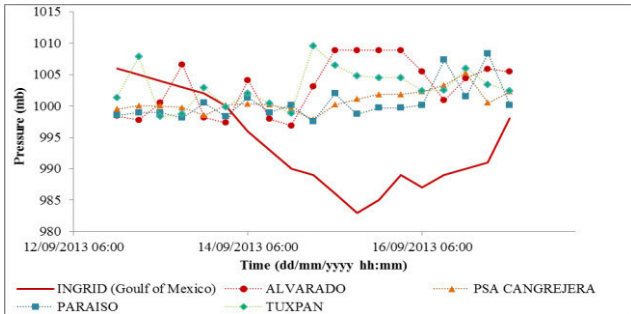


Figure 10 shown the realtion between the recorderd in NHC and the stimated with the ecuation 2 for the Meteorological stations in the Goulf of Mexico for the 12th to 16th September. In this case the differences observed are related with records in meteorological stations, they are near the sea leavel but the difference between the recorder by radiosondes inside the storm is moderate.

Fig. 11. Estimated by bright value from IR vs Recorderd by NCH (Manuel South)

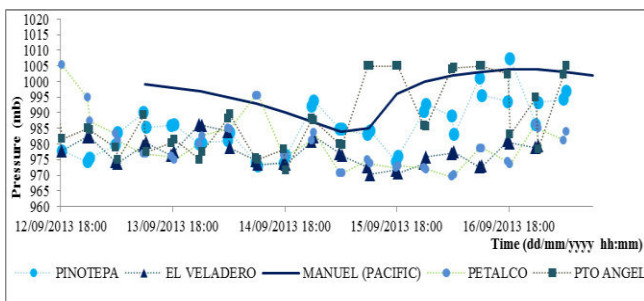
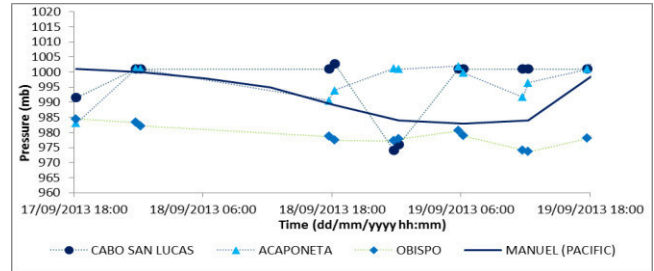


Figure 11 shown the realtion between the recorderd in NHC and the stimated with the ecuation 1 for the Meteorological stations located in the north of Pacific for the 12th to 17th September. In this case the meteorological stations recorderd pressure values below the estimated by radiosondes in the storm.

Fig. 12. Estimated by bright value from IR vs Recorderd by NCH (Manuel North)



In Figure 12 shown the realtion between the recorderd in NHC and the stimated with the ecuation 2 for the Meteorological stations in the North for the period of time 17th to 19th September. In this stage of the Hurricane Manuel the estimations in the meteorologica stations were close to the recorderd by NHC.

There is a difference between the recorderd in the Atlantic (Goulf of Mexico) and the Pacific. The principal differences consist in the region and the time where the storms and Hurricane were located.

In other words, Ingrid was a weak Hurricane and the registers in land are different from those in the storm miles away, Ingrid near to land was awakened by the winds and pressure coming from Manuel in the Pacific. In contrast Manuel was a stronger storm, the stations in ground register values of pressure below the recorderd by NHC and in the north when Manuel become Hurricane by 19th September, the recorderd and the stimations are similar to the reported by NHC.

Based on this information for Hurricanes Ingrid and Manuel, there are a suggest that take all the information and genereate the following Pressure values for Pacific and Atlantic included in the Dvorak Tecnique.

TABLE III. EQUIVALENCE BETWEEN PRESSURE AND THE SCALE SAFFIR SIMPSON AND SUGGESTION

Saffir-Simpson Classification			Suggest	
Pressure Atlantic	Pressure Pacific	Scale	Pressure Atlantic	Pressure Pacific
1009	1000	Depression		
1005	997	Depression	1004	1009
		Tropical Depression	1003	999
994	984	Tropical Storm	1000	984
987	976	1 (64-83 kts)	998	997
979	966	1 (64-83 kts); 2 (84-96 kts)		
970	954	2 (84-96 kts); 3		

Saffir-Simpson Classification			Suggest	
		(97-113 kts)		
960	941	3 (97-113 kts)		
948	927	4 (114-135 kts)		
935	914	4 (114-135 kts)		
921	898	5 (136 kts)		
906	879	5 (136 kts)		
890	858	5 (136 kts)		

These two systems, Ingrid and Manuel, were difficult to study because the kind of developing, the initial formation was easy to determinate, although the developing was difficult to estimate and find the central cloud system, because was not well defined, for hurricane Ingrid was no develop an eye. On the other hand Manuel developed a weak eye for a few hours during the 18th and 19th of September, visible in IR image before made landfall for the second time.

The eye is the consolidation of the hurricane, in this stage the meteorologist know that hurricane is in the climax of develop, and can be a straightening or a weakening of the storm related with the consolidation of the eye in infrared and visible image, but in hurricane Ingrid and Manuel was difficult to determinate this stage, as a result it was difficult to determinate if the storm system was weakening or straightening.

The Dvorak technique is acceptable to use in mayor hurricanes, and even in the developing process, is acceptable, this technique can be adapted with information obtained from Automatic Meteorology Stations located along the cost.

- *Further studies*

With this information is possible to generate a mathematician model that can estimate the T-number and calculate the pressure as a result the status of the storm, depression, Tropical Depression, Tropical Storm and Hurricane from the IR image. This methodology can be applied for every hurricane or Tropical Storm that affects the Pacific and Gulf of Mexico for the last 10 years and develop an auto-learning algorithm improving the forecast of this extreme phenomenon.

There is another kind of images that can be used and can implement more information to the estimations, the Water Vapor image, the sensor of this image, capture 1 mm of water vapor at different altitude of the atmosphere, related with the radiosonde it is possible to compute a 3D image of water vapor and his relation with pressure along the atmosphere.

This methodology can be improved with this information, and extrapolated in the different part of the storm not only in the cost with the meteorological stations but also inside the storm, this information can help us to understand the fluid dynamics in the atmosphere and predict with accuracy the next motion of the storm, this can help us to prevent and evacuate people in order to prevent deaths generated by this disasters.

Is important to mention that this kind of images are in stock in the Servicio Meteorologico Nacional with no practical use, this image can be studied and related with the variables such as wind speed, wind direction, pressure and temperature reordered in ground in order to obtain a relation between the information in the images and the variables in ground. This information can be available for similar conditions and can provide important information to new and developing systems. Also this information can be related with hydrological extreme events and can provide us an important tool to prevention and prognostic.

ACKNOWLEDGMENT

This work was possible to the program developed by José Eduardo Hernández Paulín to L.M.A. Juan Carlos Mota Escamilla for his conversion program from images PCX to BMP (Centro de Investigación en Tecnología y Desarrollo de Software) and the image treatment made by Jesus Abraham Carbajal Ríos. We would like to give a special thanks to SMN (Servicio Meteorológico Nacional) for the information provided, GOES-Infrared image data base and Automated Meteorological Stations (EMA).

REFERENCES

- [1] González V F, Domínguez Mares M, Arriaga Medina JA. 2013. Impactos del huracán “Ingrid” y la tormenta tropical “Manuel” en territorio Mexicano. Red del Agua UNAM. 2013.
- [2] CONAGUA. Reporte del clima en México. Septiembre de 2013. Servicio Meteorológico Nacional. CONAGUA. Año 3 Número 9. 2013.
- [3] Timothy L. Olander, Christopher S. Velden. (2010) Tropical Cyclone Convection and Intensity Analysis Using Differenced Infrared and Water Vapor Imagery. *Weather and Forecasting* 24:6, 1558-1572. Online publication date: 1-Dec-2009.
- [4] V Christopher, H. Bruce, B. John, Z Ray, O Timothy, M Max, G Charles, L Mark, E Roger, A Lixion, B Andrew, T Maiké, A Kikichi, A Christian, C Philippe and M Paul. The dvorak tropical cyclone intensity estimation technique, A satellite-based method that has endured for over 30 years. American meteorological society september 2006. BAMS.
- [5] Elizabeth R. Sanabia, Bradford S. Barrett, and Caitlin M. Fine, 2014: Relationships between Tropical Cyclone Intensity and Eyewall Structure as Determined by Radial Profiles of Inner-Core Infrared Brightness Temperature. *Mon. Wea. Rev.*, **142**, 4581–4599. doi: <http://dx.doi.org/10.1175/MWR-D-13-00336.1>
- [6] Dvorak,V.F. Tropical Cyclone intensity analysis using satellite data, NOAA. Technical report NESDIS 11. Washintong, D.C. September 1984. ftp://satepsanone.nesdis.noaa.gov/Publications/Tropical/Dvorak_1984.pdf
- [7] Dvorak V.F. 1995. Tropical clouds and cloud systems observed in satellite imagery: Volume 2, Tropical Cyclones, (available from NOAA/NESDIS, 5200 Auth Rd Washington, DC, 20333).
- [8] Burton, D. A. Meteorological Note 225. Notes on the application of the Dvorak technique. Australian Government Bureau of Meteorology. Agosto 2005.
- [9] Timothy L. Olander and Christopher S. Velden, 2007: The Advanced Dvorak Technique: Continued Development of an Objective Scheme to Estimate Tropical Cyclone Intensity Using Geostationary Infrared Satellite Imagery. *Wea. Forecasting*, **22**, 287–298. doi: <http://dx.doi.org/10.1175/WAF975.1>
- [10] B. John L. Hurricane Ingrid (AL102013) National Hurricane Centre. 5 February 2014. Tropical Ciclonas Report..
- [11] P. Richard J and Z. David. Hurricane Manuel (EP132013). National Hurricane Centre. 6 January 2014. Tropical Cyclone Report.

Spatial Analysis in real-time of the rainfall season in Queretaro's urban area

ISRAEL RUIZ-GONZALEZ ^{#1}, M. ALFONSO GUTIERREZ-LOPEZ ^{*2}, JAIME ARTEAGA-VARGAS ^{#3}

^{#1,3} *Centro de Investigaciones del Agua Querétaro, Facultad de Ingeniería, Universidad Autónoma de Querétaro, Cerro de las Campanas s/n, C.P. 76010, Querétaro, Qro, México.*

¹ israel.ruiz@uaq.mx

³ jokevargas@hotmail.com

^{*} *Centro de Investigaciones del Agua Querétaro, Facultad de Ingeniería, Universidad Autónoma de Querétaro, Cerro de las Campanas s/n, C.P. 76010, Querétaro, Qro, México.*

² alfonso.gutierrez@uaq.mx

Abstract— A spatial analysis of rainfall allows us to determine its geographic distribution; along with accurate mathematical models, researchers are able to forecast the hydrologic response of a basin. This research is based in data obtained within “Red Cíaq” for August 2012 to November 2012 (rainfall season). Red Cíaq is a project for weather monitoring of the urban area of Queretaro, and has 7 automatic stations transmitting real-time data. Five stations are located over the urban perimeter and two in the center of the city. A Matlab model, based on the Hutchinson algorithm, estimates the isohyets for the city in real-time. It is observed that rainfall spatial patterns differ for each month, i.e. certain areas have more rain in summer than in winter; however, if it is measured the total amount of rainfall, it shows uniform patterns for all the urban area.

Keywords— spatial analysis; isohyet; Matlab; Queretaro; rainfall season

I. INTRODUCTION

A spatial analysis of rainfall allows us to determine its geographic distribution; along with accurate mathematical models, researchers are able to forecast the hydrologic response of a basin. Grimes et. al. affirm that a real-time monitoring of rainfall is vital to allow timely responses to potential disasters. The role of meteorological variables such as precipitation, temperature, evaporation, solar radiation, etc. is crucial for understanding the variation of nature along a basin. [1].

The usage of computational tools affords us a broader and more reliable outlook about how meteorological phenomena act. The geographical information systems (GIS) combined with numerical analysis tools, become essential in the hydrological modeling. With these tools we know simultaneous and in real-time the geomorphological characteristics of a basin and the meteorological events happening over it. However, the shortage of data is a common problem in hydrology, becoming necessary the optimization of available data in certain geographic area [2].

In climatologic research, frequently is needed the classification of variables in homogenous groups, this in order to identify their common characteristics, with the goal of delve into the comprehension of events occurred [3]. Clustering is a

method used for joining meteorological stations in homogeneous regions or time periods (months, years, etc.) into groups that reflect the occurrence of certain events or meteorological patterns [4]. This paper shows the necessity of validate the homogeneity of spatial rainfall behave in the urban area of Queretaro, through instant and cumulative rainfall maps for the rainfall seasons in 2012.

According with the state government, Queretaro's urban area grew, between years 2000 and 2005, 65% in surface cover and 16.5% in population. This urban sprawl increase joined with a bad planning, has altered the hydrological cycle, causing less infiltration and increasing runoff volumes that favour floods. Considering too the lack of proper sewers and the occasional dam of them with thrash, several harms have happened.

With the population increase in the urban area of Queretaro, it is necessary to generate more accurate maps that represent the zones with larger precipitation volumes and those prone to floods, locating where focal risk points in order to prevent damages during Queretaro's rainfall season.

II. MATERIALS AND METHODS

A. Study zone description

The study zone for this paper is the urban area of Santiago de Queretaro, this area belongs to the hydrologic basin of Rio Queretaro, this basin is part of the system Lerma-Santiago, which flows into the Pacific Ocean. The urban area is located in the valley crossed by Queretaro River, and that is defined by a chain of hills and hillocks that are actually urbanized. For the city, the National Commission for Water (CONAGUA) reports an average annual rainfall of 638.3 mm (greater than the average for the state, 575.5 mm) and maximum and minimum average temperatures of 26.4 °C and 11.5 °C respectively.

Querétaro is an industrialized city that concentrates most of the state population, in the urban area of Querétaro lives 60% of the total state's population (INEGI 2010) [5]. The forecast of National Population Council (CONAPO) for 2030 estimates going from 1.75 to 2.30 million residents.

Queretaro is a city with high rates of spatial and population growth; according to the state government, between years 2000 to 2005, Queretaro city grew 65% in land surface and 16.5% in population.



Fig. 1. Study zone

B. Data

The climatologic monitoring network named Red CIAQ has 7 automatic meteorological stations in charge of Queretaro's University. When started, Red CIAQ was projected as a scientific research tool, as several bachelors, master and doctorate degree theses related with hydrology and hydrometeorology are developed in the Engineers school of Queretaro's University. Since data from each measured variable is updated every minute on the network's website, www.redciaq.uaq.mx, the website has been looked up and accepted by the scientific community and population from the city. In this website, downloads of historical data are available. Besides, researchers may use the included tools for temporal and spatial analysis of rainfall; results of these analyses are published in this paper.

The network uses Davis stations model Pro Vantage 2 located strategically around the city; as shown in the Figure 2, 5 stations are placed above the urban perimeter and 2 in the center of the city. Besides, in the image are displayed the assigned names for each station. For data transmitting, each station requires a LAN internet connection; therefore, household locations were selected with two considerations. The first, their geographic placement, and second, an ownership from one person involved in the network. This way is assured the right maintenance and operation of each station.

In the other hand, placing stations on houses, it is present the risk of electric or internet connection failures; in this events, internal memory stores data untransmitted for future recovery, unfortunately real-time transmitting and updating is lost.



Fig. 2. Location of the network Red CIAQ

C. Rainfall spatial analysis algorithm

From data obtained with RedCIAQ, three different analyses are made. The first one is a real-time analysis; the second one is a cumulative rainfall analysis for a certain period of time; and, finally, a spatial and temporal analysis for a single event. To obtain rainfall's spatial distribution along Queretaro's urban area, Delaunay triangulation is applied.

Delaunay triangulation is a geometric method for plotting triangles in two dimensions. The Delaunay's condition states that a triangle net is a Delaunay triangulation if all the circumcircles of all triangles have empty interiors; in other words, no vertexes are inside any circumcircles. Delaunay's condition assures that each internal angle of any triangle is the widest possible, maximizing the smallest triangle's area. According with the intersection areas formed (between triangles and circles), a two dimensional surface is created (latitude and longitude) (See Fig. 3). Rainfall for each point in this surface is calculated as a function of latitude and longitude and interpolated from points with measured data.

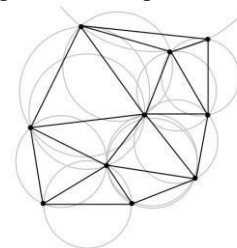


Fig. 3. Location of the network Red CIAQ

The resulting spatial interpolation creates a grid. The points, on the grid, with the same value of precipitation are connected with lines. These lines are called isohyets and they can be of cumulative rainfall or rainfall's intensity.

III. RESULTS

Data from months August through November 2012 were analyzed. According to the records, there were 38 days with rainfall, and events may vary spatially through the city so records may not be recorded in all seven stations. Cumulative rainfall was also analyzed; and spatial and time evolution of two selected rainfalls is presented. These two events were selected since their return period is more than 7 years. In 2012, a severe global meteorological event took place in November, hurricane Sandy. According to historical data presented by CONAGUA from 1981 to 2000, the maximum precipitation in 24 hours for November was 5.6 mm; nonetheless, this year 40.8 mm of rainfall was recorded at ITESM station, this is 7.3 times the data averaged by CONAGUA.

The results of monthly cumulative rainfall are presented for each RedCIAQ station on table 1. Historical average data is compared against the values for 2012; observing that 2012 was a year with far more superior historical records. Only October was a month with less rainfall.

TABLE I. MONTHLY CUMULATIVE RAINFALL IN MM

Station	August	September	October	November	Total
Satélite	170.3	107.1	4.6	31	313
UTEQ	95.8	138.8	0.3	40.2	275.1
ITESM	96.2	131.5	3.1	56.2	287
Candiles	135.4	123.5	1.8	26.8	287.5
Cimatario	141.8	111.8	0	28.3	281.9
Centro Histórico	154.2	117.8	4.6	26.9	303.5
Milenio	136.7	138.9	8.6	25.2	309.4
City's mean	132.9	124.2	3.3	33.5	293.9
CONAGUA's historical mean	73	44.6	34.1	20.8	172.5

* CONAGUA's historical mean refers to the data published by CONAGUA for the period from 1981 to 2000.

The Fig 4 presents the isohyets for monthly cumulative rainfall and the season's cumulative rainfall. It is observed that the lines do not present a defined behaviour throughout time. High and low rainfall zones vary each month, despite of this season's cumulative rainfall seems homogeneous.

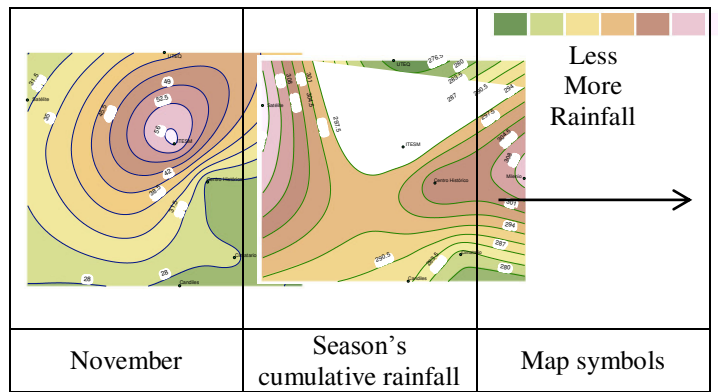
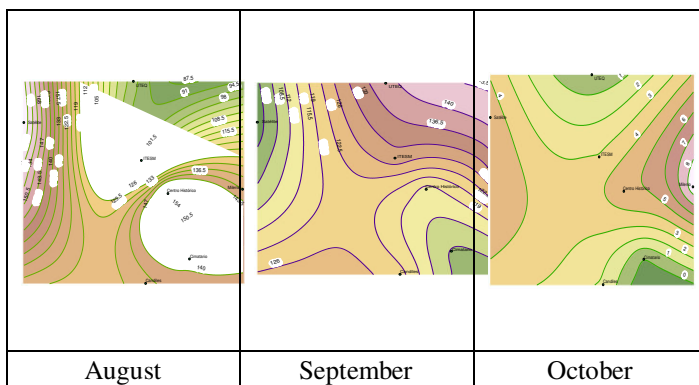


Fig. 4. Monthly isohyets

Finally, intensity isohyets' evolution, in mm/h, in time and space are presented for two selected events. These events are recorded from August 25th and the event from September 16th to 17th, 2012. The first storm had a defined zone for the maximum intensity through time. On the contrary, the second event presents a trajectory that evolves in time. The rainfall originated on the southeast of the city and displaced in a northwest direction.

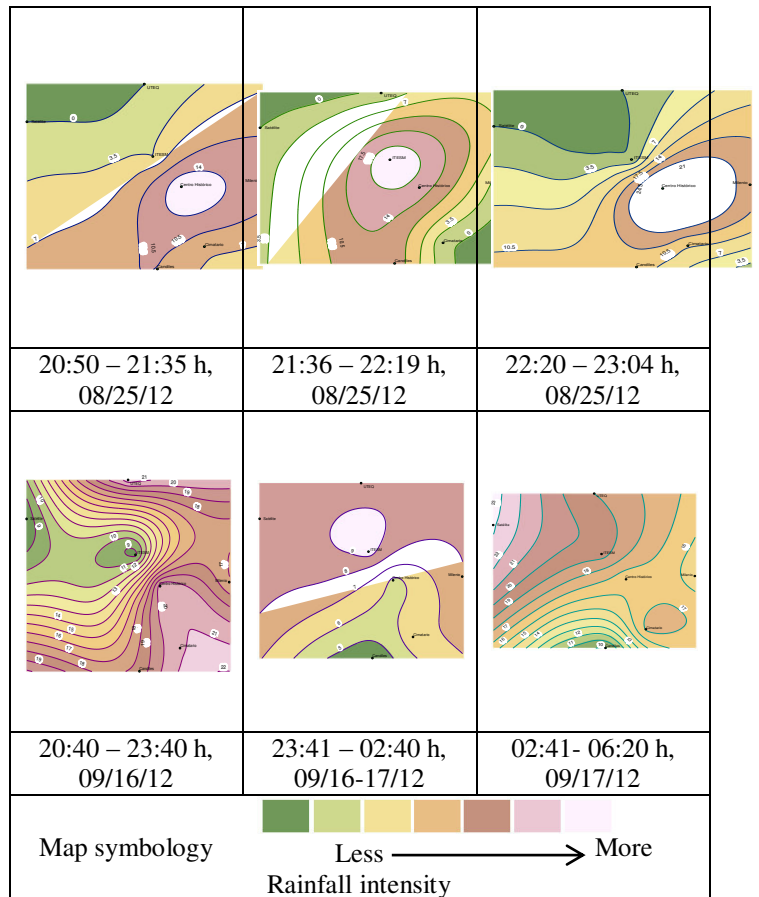


Fig. 5. Monthly isohyets

IV. CONCLUDING COMMENTS

With actual low cost computational tools, it is easy to obtain real-time reliable data for hydrologic purposes. These computational systems can reply and systemize routines like the ones presented in this research, obtaining real-time maps and detailed analysis on the measured hydrological variables.

In order to observe areas with high and frequent intense events, for a real-time alert system, it is necessary to have a meteorological network with a high station density.

If the total rainfall season's cumulative data for each station is considered, homogeneous amount of rainfall is found across the city, UTEQ station has the least with 275 mm and Satélite the highest with 312 mm.

As shown in the rain of August 25th, in urban area of Queretaro City, spatial distribution for a single event prevails. This distribution is not always the same; some events had their maximum intensities at the center of the city, while others have them in the peripheral zones (mostly northwest).

High intensity phenomena, as hurricane Sandy occurred in November, report extreme data in the normal spatial distribution of rain. According to CONAGUA in November, averaging 20 years, the maximum event in 24 hours has 5.6 mm. This year coinciding with hurricane Sandy, 40.83 mm were recorded in 24 hours in ITESM station (7.28 times CONAGUA's averaged).

ACKNOWLEDGMENT

The authors thank the CONACYT for the financial support of this research.

REFERENCES

- [1] Elías, F. and Castellví, F., *Agrometeorología* (2001), Medio Ambiente y Ciencias del Suelo, Ed. Mundi-Prensa, Madrid, Spain, pp. 517, ISBN: 84-7114-973-7.
- [2] Pelczer, I., Ramos, J., Domínguez, R. and González, (2007). Establishment of regional homogeneous zones in a watershed using clustering algorithms. Proc. IAHR, Venice, Italy, 2007, paper 1118.
- [3] Molero, G. (2008). Desarrollo de un modelo basado en técnicas de Minería de Datos para clasificar zonas climatológicamente similares en el estado de Michoacán, M.S. tesis, Ciencia e Ingeniería de la Computación, Universidad Nacional Autónoma de México.
- [4] Muñoz, D. and Rodrigo, F. (2002). Aplicación del análisis clúster para el estudio de la relación Nao-Precipitaciones de invierno en el sur de la Península Ibérica. Universidad de Almería, Spain, pp. 283-292
- [5] Comisión Nacional del Agua (CONAGUA) (2010). Estadísticas del Agua en México, edición 2010, México. D.F., Secretaria del Medio Ambiente y Recursos Naturales, 249
- [6] Grimes, D. I. F., Coppola, E., Verdecchia, M., and Visconti, G. (2003). A neural network approach to real-time rainfall estimation for Africa using satellite data. *Journal of Hydrometeorology*, 4(6), 1119-1133.

Mechanical Design and Development of a Haptic Device

J.M. Hernández Paredes ^{#1}, J. J. Montiel Luna^{#2}, F. J. Valdés Callejas ^{#3}

*# Mechatronics engineering, Instituto Tecnológico Superior de Huichapan,
El Saucillo Huichapan Hidalgo México*

¹ jmhernandez@iteshu.edu.mx

² a10021223@iteshu.edu.mx

³ a10021218@iteshu.edu.mx

Abstract— a human operator, virtual display environment and an electromechanical device called haptic device constitute a haptic interface. This article presents the design and construction of a robotic prototype based on the Phantom Premium device; the mechatronic system is intended to be used as haptic device and programmable manipulator robot. The design is done on a computer, the choice of materials, dimensions and stress analysis is presented for validating the proposed design.

Keywords— development; design; robotics; haptics; machined; Phantom premium, prototype.

I. INTRODUCTION (HEADING 1)

The human-computer interaction requires a virtual environment; usually visual and auditory faculties for feedback of information to interact with other senses are used. The term "haptics" refers to kinesthetic sense. Haptic interfaces (HI) corresponds to a medium in which a human interacting with a virtual visualization environment. The human may change at any time the virtual environment and receives signals in response. Haptics is the study of combining the human sense of touch with a world that is generated by a computer. Virtual reality is the medium that allows interaction between a digital computer and a user [1].

A HI is used as a measuring device and provides tactile kinematics information. The haptic interfaces allow the operator to keep a sense of interaction with the virtual environment [2].

The pioneer of tactile feedback for simulation systems in virtual reality was the MIT (Massachusetts Institute of Technology) with exoskeleton haptic device configuration Dextrous Hand Exoskeleton Master in 1990 [3].

In 2009 Maria Luisa Pinto Salamanca made an analysis of the characteristics of two touch interfaces available on the market, to test theories of force feedback and the development of tools tactile exploration focused on surgical assistance [4].

In 2012 Victor Salas Hilario Méndez developed a mechatronic system that is constituted by two anthropomorphic fingers that reproduce the movements of abduction, adduction,

flexion and extension of the human hand, pneumatic muscles for human arm prosthesis [5].

In 2013 New Granada Military University was developed a training simulator for use surgical instruments to integrate two clips laparoscopy in a haptic device [6].

The dexterity of the human hand when interacting with their environment lets you handle a wide variety of shapes and sizes, perform complex tasks, and adapt its position that must respond to the changes required by the task [7]. With the HI can increase this skill or record tasks in a virtual environment, and allows the robot manipulator performs tasks reduces the risk by eliminating human physical contact with the task increases the safety and efficacy of the process requires.

Thomas Harold designed, manufactured and evaluated haptic interface robot three degrees of freedom. With a finger can "feel" the forces of feedback within the virtual environment created [8].

This paper presented the design and construction a robot of three degrees of freedom with rotational joints for use in a haptic interface as shown in Fig. 1.

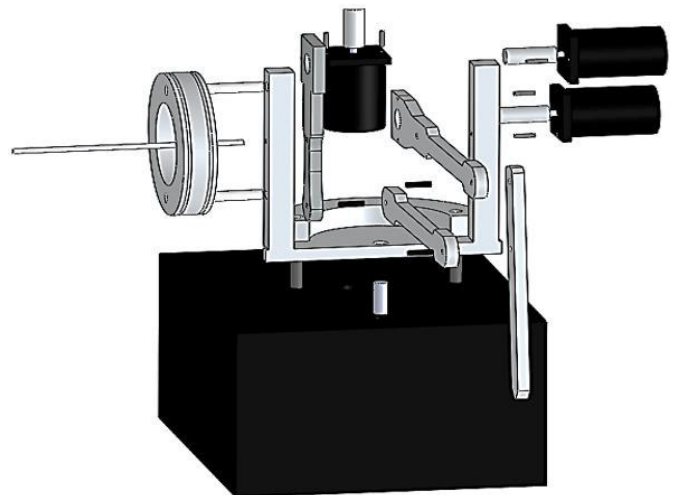


Fig. 1. Explosion view of the haptic interface.

II. MECHANICAL DESIGN

A. Design criteria

The design of a robot serves different functionality and performance criteria such as: load capacity, degrees of freedom, tool use, accuracy, repeatability, ambient operating conditions and development cost of manufacturing, maintenance, flexibility. The materials used in the design are described in Table 1.

TABLE 1 MATERIALS NEEDED TO BUILD THE ROBOT.

Element	Material	Quantity	Measure / Description
Ball bearing	Steel	8	4x12x4 mm
Ball bearing	Steel	1	6.35x19.05x6.35 mm
Board	Aluminum	1	200x250x100 6.35 mm
Motor		3	30x30x51 mm
Axis	Steel	1	3.18mm Ø

B. Calculation of stress links

Is performed 2 kg estimation on the end effector of the robot to know the stress of links respectively, the analysis was performed by designating the center point and fixed point B as q2 and q3 as reflecting the two motors as forces shown in Fig. 2.

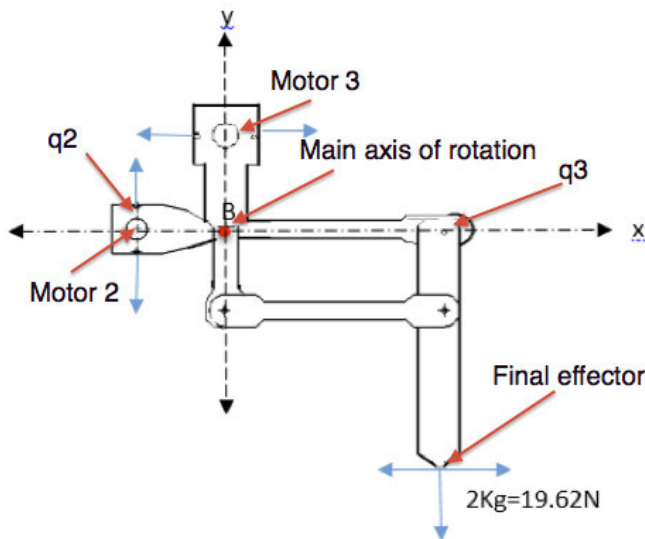


Fig. 2. General diagram of the forces on the links. Where q2 and q3 represent theta rotational joints 2 and 3 respectively.

The movement of the end effector generated forces resulting in the motors as shown in Figure 2, then the calculations of the moments generated about point B. This is first analyzed the link that is carried on the axle x.

As shown in Fig. 3 are two forces acting together about point B which are FC and FA, however the value of the Force is known at point A which is 19.62 N by consistent it is possible C reaction know where q2 is the engine by a sum of moments in point B. from (1) is obtained the force acting in FC, view (2).

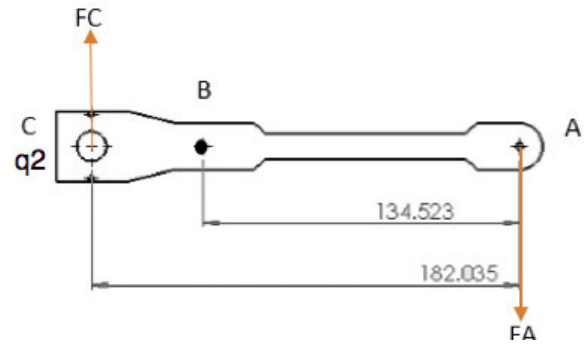


Fig. 3. Free body diagram of motor q2 link.

$$\sum MB = 0 \quad (1)$$

$$Fc(0.0475m) - 19.62N(0.1345m) = 0$$

$$Fc = \frac{19.62N * 0.1345m}{0.0475m} \quad (2)$$

$$Fc = 55.5N$$

Is made an analysis of forces in perpendicular link which holds q3 motor, see Fig. 4.

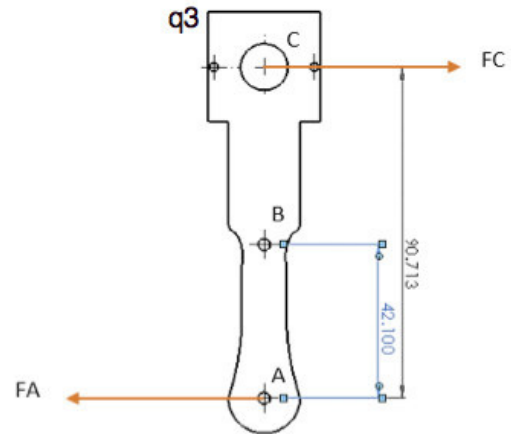


Fig. 4. Free body diagram of motor q3 link.

Motor reactions to a 2 kg load on the end effector are obtained, (3) describes this reaction.

$$\sum MB = 0$$

$$Fc(0.0486m) - 19.62N(0.0421m) = 0$$

$$Fc = \frac{19.62N * 0.0421m}{0.0486m} \quad (3)$$

$$Fc = 16.99N$$

Then in Fig. 5 and Fig. 6 a load analysis was performed using the design software to determine the reaction components to a maximum load shown in main axis of rotation and the base of this.

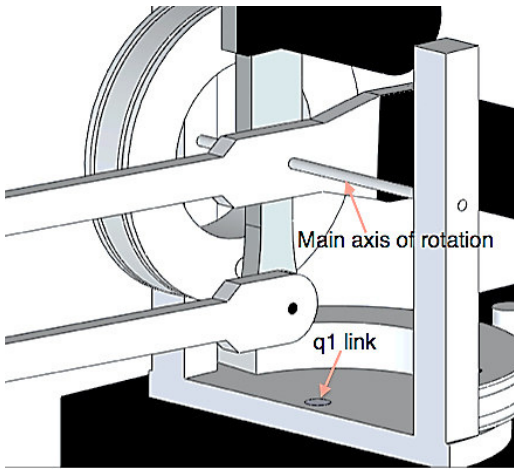


Fig. 5. Main axis of rotation, deformation analysis.

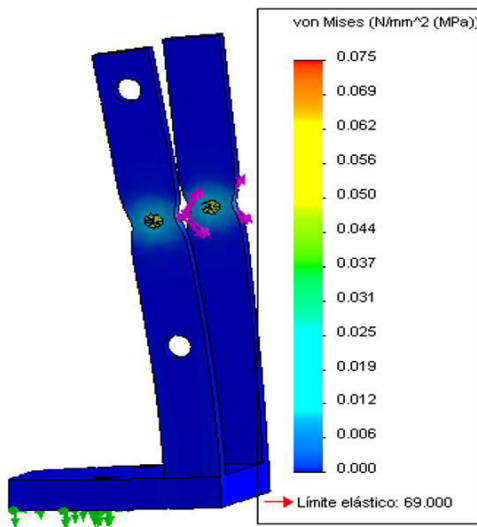


Fig. 6. Results of design software.

As shown in Fig. 6 the stress limit is 69 MPa, this data reveals that the structure supports acceptably the forces exerted by the main axis on the base.

C. Workspace of haptic interface

The length of the links and degrees of rotation of the joints are determined dimensions that the workspace of a robot.

In Fig. 7 (a) and (b) is shown the maximum range of the robot as in Fig. 8 (a) and (b) the minimum extent of the workspace.

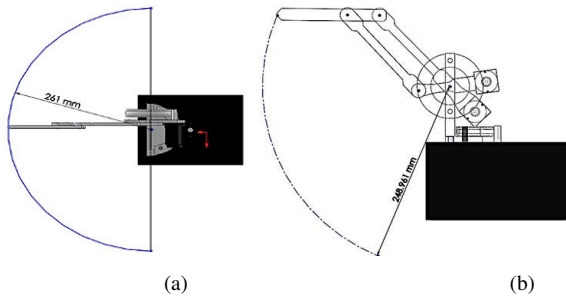


Fig. 7. Maximum workspace.

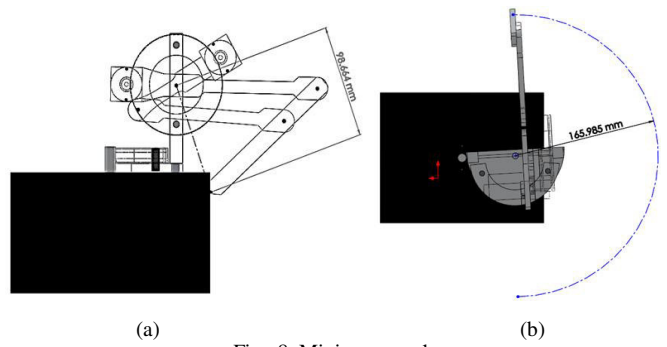


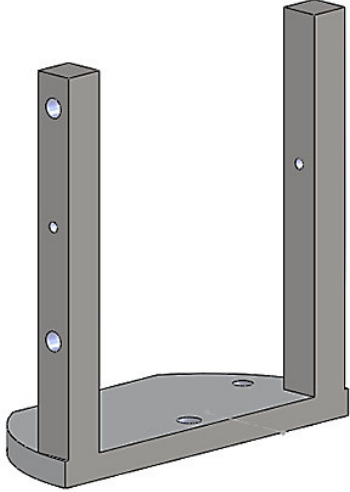
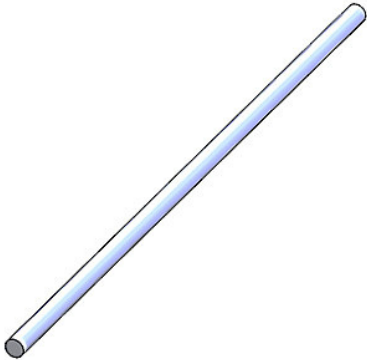
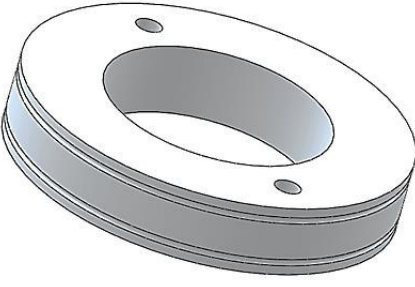
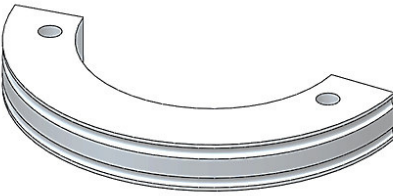
Fig. 8. Minimum workspace.

III. MECHANICAL DEVELOPMENT

For the mechanical development of robot structures the elements shown in Table 2 was machined.

TABLE 2 ELEMENTS MACHINED.

Element	Name
	Base box
	Link 1
	Link 2
	Link 3
	Final effector

	<p>Gyratory Base</p>
	<p>Principal axis</p>
	<p>Transmission circle</p>
	<p>Crescent</p>

Each link has a ball bearing at each end, the bearing carries inside diameter the main axis that previously rectified on a lathe, and by applying this system was reduced vibrations between the joints of the structure.

Once all links are ready the next step is assemble so that the system can rotate on the box that was built, the space below the box was designed for the future development of the control system, the base is composed of 2 posts supporting the main

Identify applicable sponsor/s here. If no sponsors, delete this text box (sponsors).

shaft which serves as the center of rotation for the links, likewise supports the weight of the links and q_2 and q_3 motors, bearings were adapted within each joint to generate fluid movements that do not generate friction or wear.

When were finished painting every element, the structure is mounted so that the main axis passes through the internal diameter of the bearing, the rotary base is assembled which holds a pair of posts that generate the rotary base as illustrated in Table 2, were assembled poles of its lower base by a screw. After bind the links 1, 2 and 3 to the main shaft and likewise the transmission circle.

In Fig. 9 is illustrated as look the links 1, 2, 3 and the end effector together, the circle of transmission must be fixed to the rotating base and its center should be consistent with the main shaft to thereby the q_2 and q_3 motors can traverse the perimeter of the transmission circle a uniform manner.

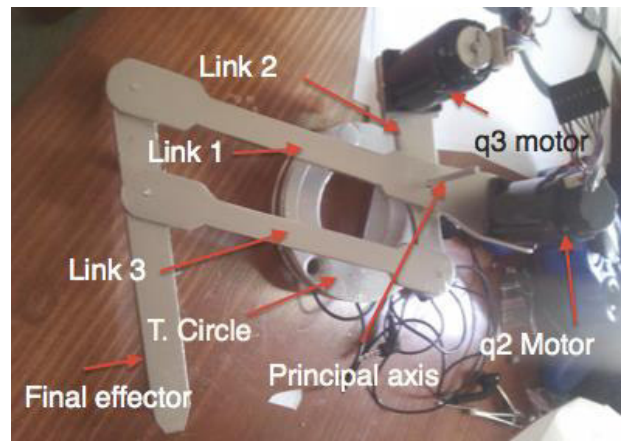


Fig. 9. Attachment of the links to the main axis.

The path through the crescent is completely circular, to be in contact with the motor shaft rotation at any point. Thus three degrees of freedom are generated.

IV. RESULTS

After the process, it resulted a robot with a structure of three degrees of freedom as shown in Fig. 10 and Fig. 11, which allows its easy handling for various haptic interfaces providing versatility of positioning and proper functioning of the motors.



Fig. 10. Haptic interface built.



Fig. 11. Haptic interface built.

As shown in Figure 12 using CAD software can simulate the pre-construction measures were established and thus know any limitation or inconvenience in design.

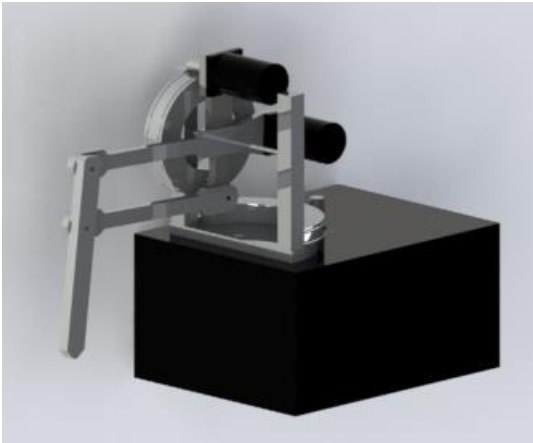


Fig. 12. Final design en CAD of the haptic interface.

V. CONCLUSIONS AND FUTURE WORKS

The haptic interface designed is successfully built thanks to the implementation of manufacturing systems and computer-aided design, achieved its construction prove economical because of the simplicity of its mechanical structure, the workspace is appropriate to use the robot for educational purposes and investigation of haptic interfaces.

This is the first step to built a complex mechatronics system where uses the engineering's mechanical, informatics, electronics and control.

As future work are the following issues:

- Electronics design and development of digital control and power.
- Design and implement robotic control force laws.
- Generates a virtual environment to interaction human-machine.
- Make all the system modular.

REFERENCES

- [1] R. Samperio-Llano, Omar A. Domínguez-Ramírez and V. López-Morales. "Resultados preliminares sobre interacción háptica en laberintos virtuales, con propósitos de diagnóstico en pacientes con discapacidades neuropsicológicas", Día Virtual CUDI: www.cudi.edu.mx, pags 2-12, March 2004.
- [2] A. G. Areli Saray, H. R. Elizabeth and D. R. Omar Arturo, Guiado háptico local con perspectivas de diagnóstico y rehabilitación neuropsicológica, Engineering Thesis, Universidad Autónoma del Estado de Hidalgo, 2006.
- [3] N. J. Patrick. Design, Construction, and Testing of a Fingertip Tactile Display for Interaction with Virtual and Remote Environments, Master Engineering thesis, Massachusetts Institute of Technology, August, 1990.
- [4] Pinto Salamanca, Maria Luisa, Análisis e implementación de una interfaz háptica en entornos virtuales / Analysis and implementation of a haptic interface in virtual environments. Maestría thesis, Universidad Nacional de Colombia, 2009.
- [5] V. H. Méndez Salas. Diseño y Construcción de un Sistema Mecatrónico Articulado de Dos Dedos, Actuado con Músculos Neumáticos, Master Thesis, Centro Nacional de Investigación y Desarrollo Tecnológico, 2012.
- [6] M. Monroy, Maria Oyarzabal, Manuel Ferre, Salvador Cobos, Jordi Barrio, Javier Ortego. Dispositivos Hápticos: Una Forma de Realizar la Interacción Hombre-Máquina. II Congreso Internacional sobre Domótica, Robótica y Telesistencia para Todos, 2007.
- [7] Amanda P. Aldana Suarez, Susana P. Yañez Mantilla. Adaptación de pinzas de Laparoscopia a dispositivos Hápticos Phantom OMNI y Desarrollo de Software de evaluación, Ingeniería Tesis, Universidad Militar Nueva Granada, 2013.
- [8] Thomas Harold Massie, Design of a three Degree of Freedom Force-Refelcting Haptic Interface, Department of Electrical Engineering and Computer Science, Massachusetts Institute of Technology, 1993.
- [9] J. López, J. L. Torres, A. Gimenez, Interfaz Háptica para Tareas de Manipulación, Asociación Española de Ingeniería mecánica, XVIII CONGRESO NACIONAL INGENIERÍA MECÁNICA, 2010.
- [10] Cristina Martín Doñate. Interfaces Hapticos, Aplicaciones en Entornos Visuales, XVI CONGRESO INTERNACIONAL DE INGENIERÍA GRÁFICA, Universidad de Jaén, España, 2, 3 y 4 de Junio, 2004.
- [11] Jones, L.A & Lederman, S.J., Human hand function, New York, published by Oxford University Press, ISBN-13 978-0-19-517315-4, 2006.
- [12] R. E. Ellis, O. M. Ismaeil, M. G. Lipsett, Design and Evaluation of a High-Performance Haptic Interface, Manuscript for article in Robotica, Queen's University at Kingston, Ontario, Canada, vol. 4, pp 321-327. 1996 .

Root Mean Square Voltage Tracking using Analytic Signals

G. Alvarez-Monroy, S. Z. Hernandez-Michel, U. Hernandez-Osornio, D. Camarena-Martinez, M. Valtierra-Rodriguez*, A. Dominguez-Gonzalez

Facultad de Ingenieria, Universidad Autonoma de Queretaro, Campus San Juan del Rio, Rio Moctezuma 249, Col. San Cayetano, 76807, San Juan del Rio, Queretaro, Mexico.

*martin.valtierra@uaq.mx

Abstract— Root-mean-square (RMS) voltage estimation has become a very important task for many power electric applications, such as estimation of power quality indices, power quality disturbances monitoring, electric control, and activation of protections, among others. Although a well-defined way to estimate the RMS value is presented in the Standard IEC 61000-4-30, some issues still remain; for instance, the standard proposes a frame-based RMS estimation technique, where the signal into the analyzed time window is considered stationary which is not true in transient phenomena. Therefore, the results accuracy may be degraded. In this work, a methodology for RMS voltage estimation or tracking (sample to sample) using analytic signals is presented. First, a bandpass filter centered in the fundamental component (60 Hz in Mexico) is applied to remove the rest of the frequency components. Then, the building of its analytic signal by means of filters is carried out. Finally, the instantaneous phase and magnitude of the signal are computed. It is worth noticing that the instantaneous amplitude can be directly related to the RMS value. Some synthetic and real experiments are performed to test the proposal effectiveness.

Keywords—Analytic signal; IEEE Std. 1159; RMS voltage; voltage tracking.

I. INTRODUCTION

Over the past few years, many power applications have used the root-mean-square (RMS) value of voltage or current signals as input parameter to carry out tasks of control, activation of protections, modeling, power quality disturbances monitoring, and estimation of others power quality indices, among others [1-3]. In order to keep or improve the performance of the aforementioned applications, an accurate RMS estimation becomes a primary target. The Standard IEC 61000-4-30 presents a well-defined way to estimate the RMS value [4]. Although it is a simple and efficient approach, some drawbacks are observed when no stationary signals are analyzed. This is because the signal is considered stationary into the analyzed time window, which is not true in transient phenomena [5]. Further, this approach does not provide phase information, which in some applications is required [3].

In general, the RMS value can be estimated in both time domain and frequency domain. In the former, the signal has to be first filtered to remove noise and other frequency components in order to estimate the fundamental component RMS. In the latter, the discrete Fourier transform (DFT) is used to estimate the fundamental component magnitude [6-7]. Both

methods are frame-based techniques and have problems to analyze transient signals. Some improvements can be obtained if the time window is overlapped; however, the computational burden increases. In this regard, several solutions based on recursive (tracking) techniques are reported in the literature. They process sample to sample instead of batch data. Two common techniques for voltage tracking are the adaptive linear network (ADALINE) [8] and the Kalman filter (KF) [1]. Yet, despite being powerful techniques, several aspects have to be contemplated in order to offer a good result. The first point to consider is the selection of the model, generally harmonic-based models, due to that a large or complex model implies a high computational burden and excessive convergence time, but a simple model may lead to wrong results when a frequency component that is not considered on it appears [5]. Further, the updating algorithm, e. g. the least mean square (LMS) algorithm [9], to adjust the model coefficients has to provide a fast convergence time, mainly for fast changes in the signal. Yet, the appropriate value of the learning rate selection is not a straightforward process. From this, it is evident that this topic is still an open issue to propose and develop new techniques and methodologies.

In this paper, the building of the analytic signal of a voltage signal by means of filters for RMS value tracking of the fundamental component is presented. First, to remove other frequency information, a bandpass filter centered in the fundamental component (60Hz in Mexico) is applied. Second, a phase-shifting filter and a delay filter are used to generate the analytic signal. Finally, the coordinate rotation digital computer (CORDIC) algorithm [10] is used to compute its magnitude and phase sample a sample; with that, a tracking of the RMS can be carried out by providing both magnitude and phase information. It is convenient to mention that the proposal is implemented by means of filters and CORDIC operations in order to simplify and facilitate a future hardware implementation. On the other hand, unlike the abovementioned works, the proposal needs neither a harmonic-based model nor an updating algorithm, which simplifies and reduces the computational complexity and the convergence time, respectively, making the proposal an attractive solution for many power applications. For validating and testing the proposal, two scenarios are considered. First, a set of synthetic signals, based on mathematical models, are analyzed. Due to that the original or reference values are known, the estimation error of the proposal can be measured. Second, real

This work is sponsored by UAQ-DIPFI under the FIN201438 project.

measurement data of voltage signals provided by the IEEE work group P1159.3 and the ones monitored of an experimental setup compound of typical electrical loads are also analyzed. The obtained results show the effectiveness and noise immunity, as well as the accuracy of the proposal, which make it a suitable and low complexity tool for RMS voltage tracking (magnitude and phase).

The rest of the paper is organized as follows: section II introduces a brief description of the main topics of this work. Section III and IV shows the methodology and experimentation carried out. Finally, the conclusions appear in section V.

II. THEORETICAL BACKGROUND

A. Analytic Signal

In general, a signal is called analytic signal when it has no negative frequency components [11]. Its representation is a generalization of the phasor concept to define a sinusoidal function with time-variant amplitude, phase, and frequency, which facilitates many mathematical manipulations of the signal. In terms of a time-dependent phasor, the analytic signal of $x(t)$ with its complex conjugate $y(t)$ is defined as:

$$x_a(t) = A(t)e^{j\phi(t)} = x(t) + jy(t) \quad (1)$$

with

$$A(t) = |x_a(t)| = \sqrt{x^2(t) + y^2(t)} \quad (2)$$

$$\phi(t) = \arctan(y(t) / x(t)) \quad (3)$$

where $A(t)$ and $\phi(t)$ are the instantaneous amplitude and the instantaneous phase, respectively. $A(t)$ is also known as the envelope of $x(t)$, which can be used for directly tracking the voltage or current magnitudes as shown in Fig. 1.

B. Voltage Variations

Among electromagnetic phenomena that affect the power quality, short-, and long-duration RMS voltage variations have attracted the interest of many researchers around the world because they can seriously degrade the equipment connected to

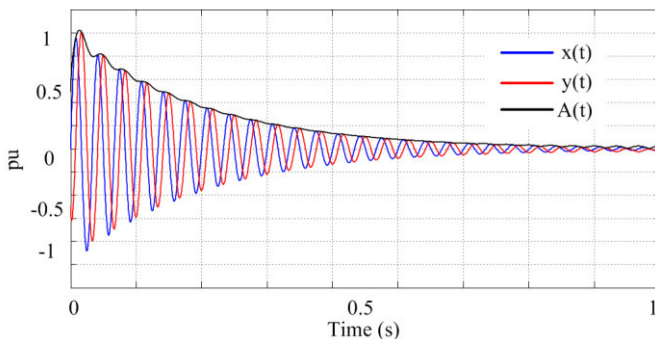


Fig. 1. Tracking of the envelope of a signal $x(t)$.

TABLE I
CATEGORIES AND TYPICAL CHARACTERISTICS OF VOLTAGE VARIATIONS

Category		Typical duration	Typical voltage magnitude
Short-Duration variation			
Instantaneous	Sag	0.5 - 30 cycles	0.1 - 0.9 pu
	Swell	0.5 - 30 cycles	1.1 - 1.8 pu
Momentary	Interruption	0.5 cycles - 3 s	< 0.1 pu
	Sag	30 cycles - 3 s	0.1 - 0.9 pu
Temporary	Swell	30 cycles - 3 s	1.1 - 1.4 pu
	Interruption	3 s - 1 min	< 0.1 pu
	Sag	3 s - 1 min	0.1 - 0.9 pu
	Swell	3 s - 1 min	1.1 - 1.2 pu
Long-Duration variations			
Sustained interruption		> 1 min	0.0 pu
Undervoltages		> 1 min	0.8-0.9 pu
Overvoltages		> 1 min	1.1 - 1.2 pu

The quantity pu refers to *per unit*, which is dimensionless. The quantity 1.0 pu corresponds to 100% [2].

the power supply [3] and, hence, cause economic losses for costumers. The IEEE Std. 1159 establishes the categories and typical characteristics of RMS voltage variations, which are mainly classified by their duration and magnitude as shown in Table 1 [2]. It is worth noticing that these values will be used to test the proposal, since they are the common parameters of real life voltage variations and, hence, real life RMS values. The RMS estimation in time domain is given by:

$$V_{rms} = \sqrt{\frac{1}{n} \sum_{i=0}^n x_i^2} \quad (4)$$

where x_i is the sample value and n the size of the window of analysis, half cycle of the fundamental frequency is suggested.

III. METHODOLOGY

The proposed methodology is presented in Fig. 2. It consists firstly of a bandpass filter to remove other frequency components, which is a finite impulse response (FIR) Gaussian window filter of order 32 centered according to the fundamental component, in this case 60 Hz. Then, $x(t)$ is processed in parallel way by both a phase-shifting and a filter delay filter to obtain $x_a(t)$. The former is a 32 FIR filter designed through Parks-McClellan method to generate a quadrature signal of $x(t)$ (similar to Fig. 1), the latter is only to compensate the sample delay due to the aforementioned filter. Then, its instantaneous amplitude and phase are computed by means of the CORDIC in vectoring mode using the following equations [10]:

$$\begin{aligned} x_{i+1} &= x_i - y_i \cdot d_i \cdot 2^{-i} \\ y_{i+1} &= y_i - x_i \cdot d_i \cdot 2^{-i} \\ z_{i+1} &= z_i - d_i \cdot \tan^{-1}(2^{-i}) \end{aligned} \quad (5)$$

where $d_i = +1$ if $y_i < 0$, -1 otherwise. Therefore

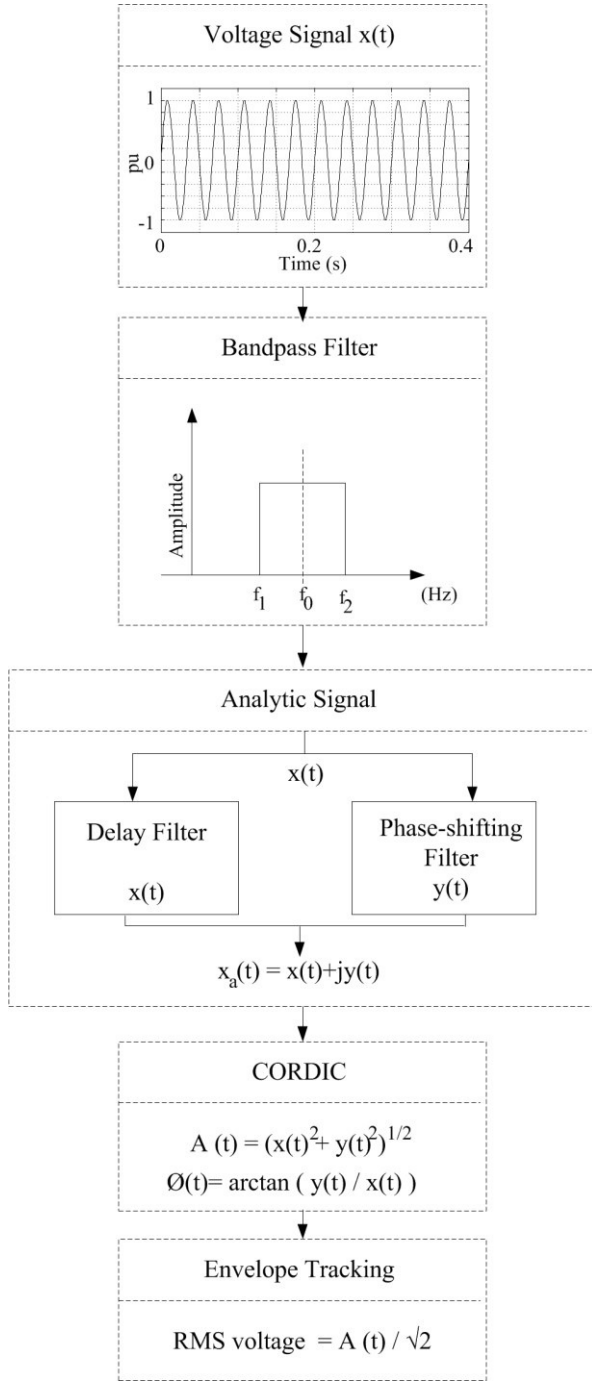


Fig. 2. Proposed methodology.

$$\begin{aligned}
 x_n &= A_n \sqrt{x_0^2 + y_0^2} \\
 y_n &= 0 \\
 z_n &= z_0 + \tan^{-1}(y_0 / x_0) \\
 A_n &= \prod_n \sqrt{1 + 2^{-2i}}
 \end{aligned} \tag{6}$$

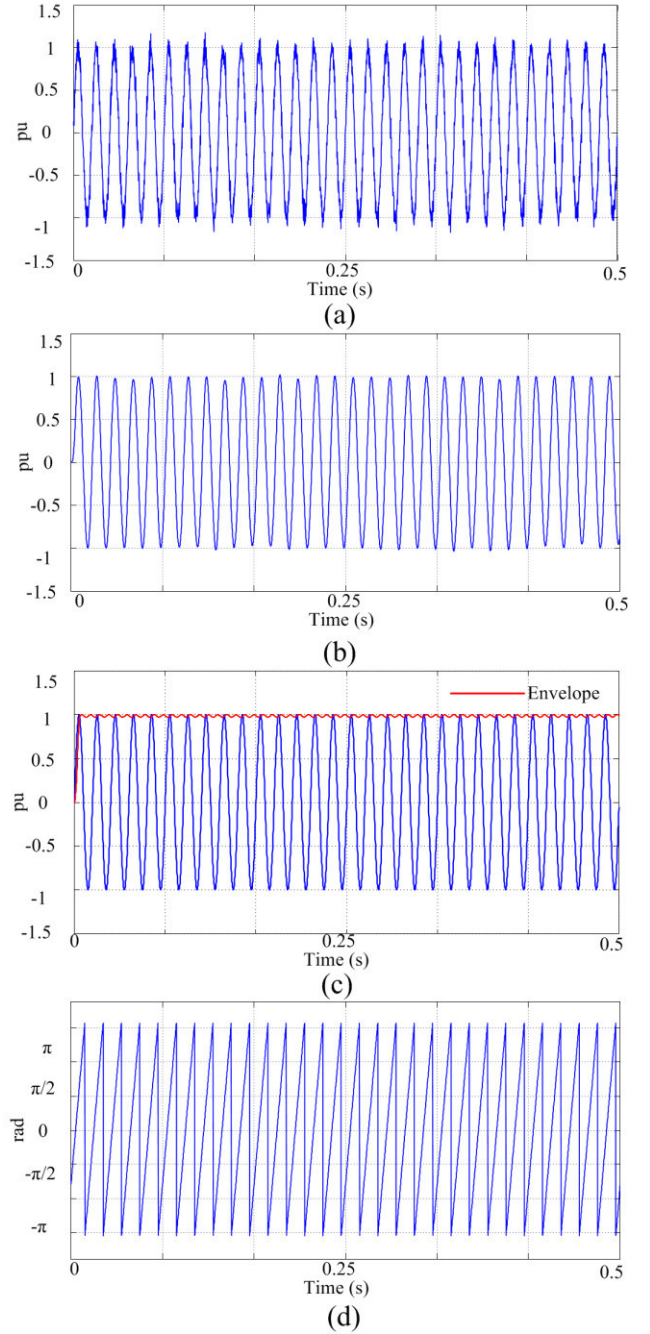


Fig. 3. Signal analysis: (a) original signal, (b) filtered signal, (c) envelope, and (d) phase.

with 16 iterations. This number presents enough good results. Finally, the RMS value can be estimated from the instantaneous amplitude by considering that the envelope is the value of the peak voltage (V_{peak}) as follows:

$$V_{RMS} = V_{peak} / \sqrt{2} \tag{7}$$

Fig. 3 presents the methodology steps for a noisy voltage signal (Fig. 3(a)). The filtered signal appears in Fig. 3(b); as

can be seen, the most of the noise is eliminated. Fig. 3(c) and 3(d) shows the envelope and phase tracking, respectively.

IV. EXPERIMENTATION AND RESULTS

A. Validation

In the validation stage, 10 signals for each short-, and long-duration RMS variations of Table 1 are synthetically generated using a sampling frequency (F_s) of 6000 Hz. Fig. 4 shows the three common categories of voltage variations according to their magnitude, being a sag, swell, and interruption. There, it is seen that the proposal can track the different voltage variations. Further, the tracking of phase is also carried out, which is not possible using standard RMS voltage estimation. The phase value is only a zero value when the signal is zero voltage magnitude as shown in Fig. 4(c). In order to measure the accuracy of the proposal, the relative error (RE) between the known reference value and the obtained with the proposal is computed. The mean RE of all signals is 2.8 % for the proposal and 4.3% for the RMS estimation in time domain according to (7) and (4), respectively. Therefore, a better results accuracy is obtained with the proposal (sample to sample); besides, phase information is also provided. The obtained small RE is mainly due to the light oscillations in the envelope because of the filter-based implementation. Fig. 5 shows a critical voltage variation in magnitude, 0 pu, and duration, half cycle. For comparison purposes, the envelope tracking of the proposal appears in red, whereas the one obtained with Hilbert function (Matlab code) appears in black. In general, Hilbert is a classical phase-shifting operator [11]. From the plot, it is evident that the proposal presents better tracking results.

B. Experimental Results

Regarding the real data, some signals of the IEEE work group P1159.3 are analyzed with the proposal. The aim of this is to observe and analyze the proposal behavior under real power signals. On top, Fig. 6 shows sag, swell, and interruption signals. In the bottom, the signals after filtering and the envelope results are observed. As can be seen, the signals are

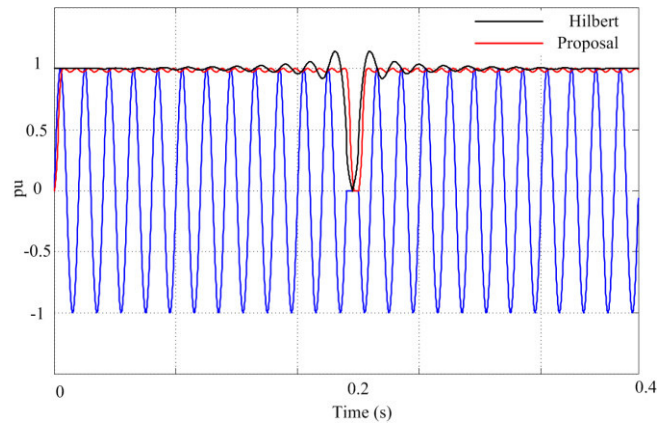


Fig. 5. Hilbert operator and proposal implementation: a comparison.

combined with other electrical disturbances such as transients, notching, and noise, which compromise the accuracy results. It is convenient to mention that the reference values for the signals are not given; therefore, the estimation error is not obtained. However, the abovementioned validation results allow establishing the proposal as suitable and accuracy methodology. On the other hand, real voltage signals acquired from the experimental setup shown in Fig. 7 are also analyzed. It consists mainly of an induction motor and a capacitor bank to generate real voltage variations. The signals using $F_s = 6000$ Hz are sent to the PC by means of a data acquisition system (DAS) and processed by the methodology in Matlab software. Fig. 8(a) shows the monitored voltage signal. There, three voltage changes can be observed: 1) normal, when the electrical loads are deactivated, 2) a voltage drop, when the motor is starting on, and 3) a slight voltage increment, when the capacitor is switching on. Fig. 8 shows the signal after filtering and its envelope. The filtering stage reduces some of the observed peaks or transients when the capacitor is activated or deactivated. In Fig. 8(b), the envelope tracking is observed. At this stage of the work, the experimental tests are only used to evaluate the voltage envelope tracking; however, in the next step of this work, a power quality analyzer such as the Fluke

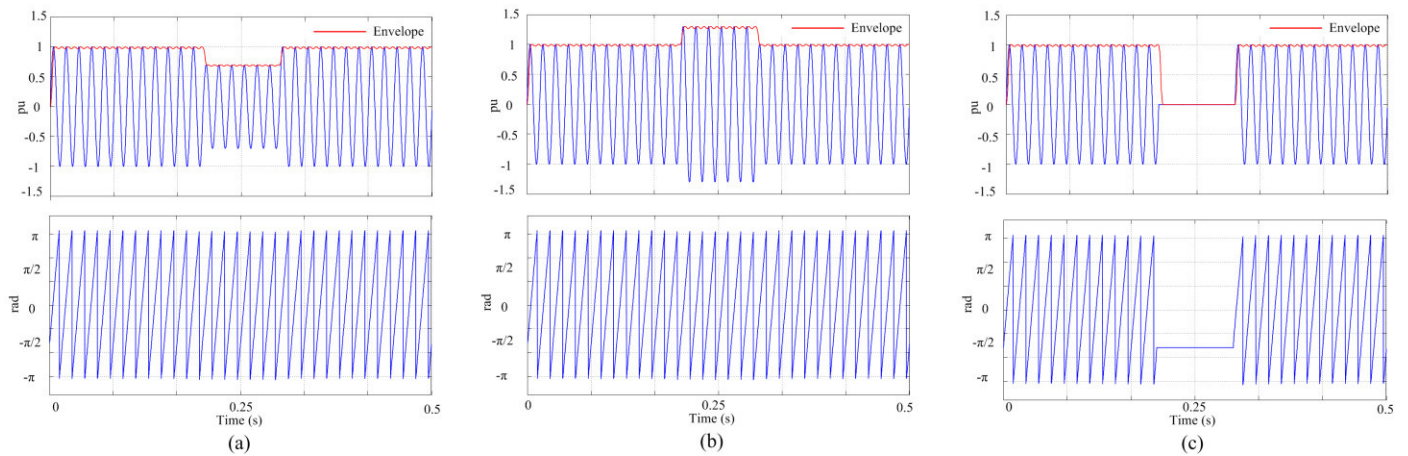


Fig. 4. Envelope and phase tracking for a (a) sag, (b) swell, and (c) interruption.

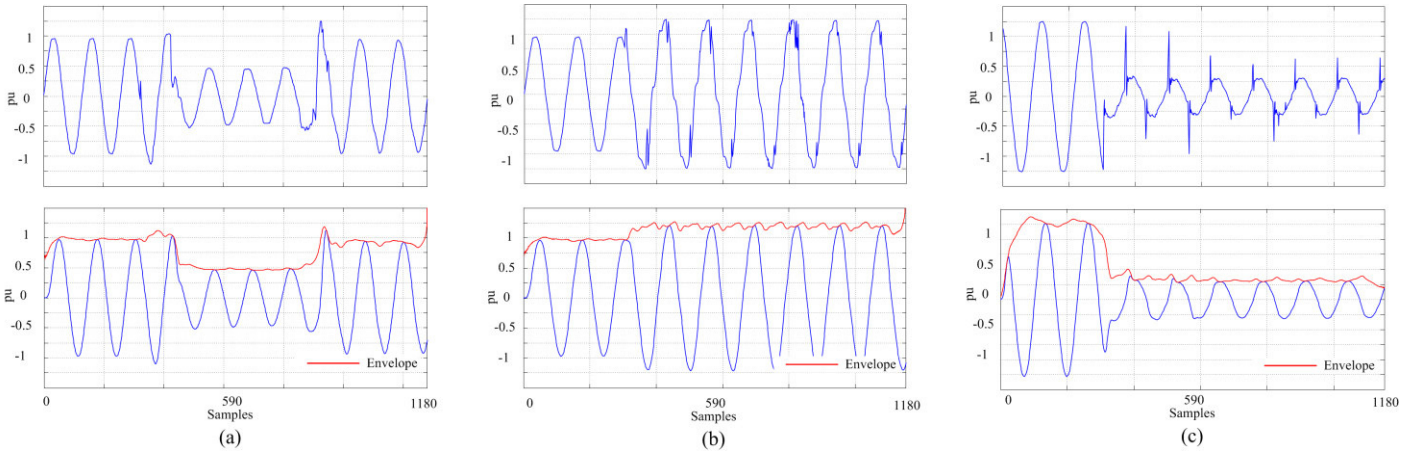


Fig. 6. IEEE work group P1159.3: (a) sag, (b) swell, and (c) interruption.

435 will be used to compare and calibrate the proposed methodology.

V. CONCLUSIONS

In this work, a methodology for RMS value tracking of the fundamental component in voltage or current signals using analytic signals is presented. The proposal development based on filters and CORDIC operations allows offering low computational burden and low complexity for hardware implementation. Thanks to the building of the analytic signal, information of instantaneous magnitude and phase can be obtained. Unlike the frame-based methods, the proposal process a result sample to sample, which may be suitable for control and protection applications.

Synthetic and experimental results show the proposal effectiveness for envelope tracking of voltage variations, even for an interruption of half cycle.

In a future research work, the study of other power quality indices that combines RMS values of voltage and current signals such as the estimation of powers quantities will be researched.

ACKNOWLEDGMENT

Authors thank to UAQ-DIPFI under the FIN201438 project by its financial support for this research work.

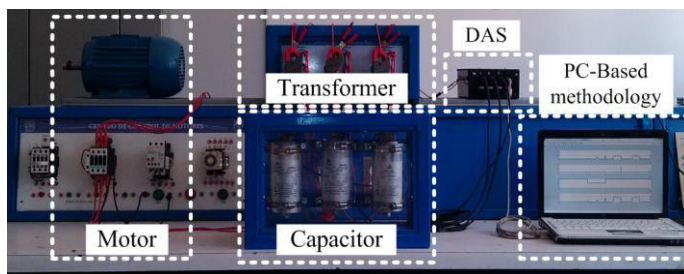


Fig. 7. Experimental setup.

REFERENCES

- [1] M. H. J. Bollen and I. Y. Gu, *Signal Processing of Power Quality Disturbances*, 1st ed., IEEE Press, Piscataway, 2006.
- [2] *IEEE Recommended Practices for Monitoring Electric Power Quality*, IEEE Std. 1159, 2009.
- [3] P. Caramia, G. Carpinelli, and P. Verde, *Power Quality Indices in Liberalized Markets*, 1st ed., John Wiley & Sons Ltd., 2009.
- [4] *IEC 61000-4-30, Electromagnetic Compatibility (EMC). Part 4. Testing and Measurement Techniques. Section 30: Power Quality Measurement*

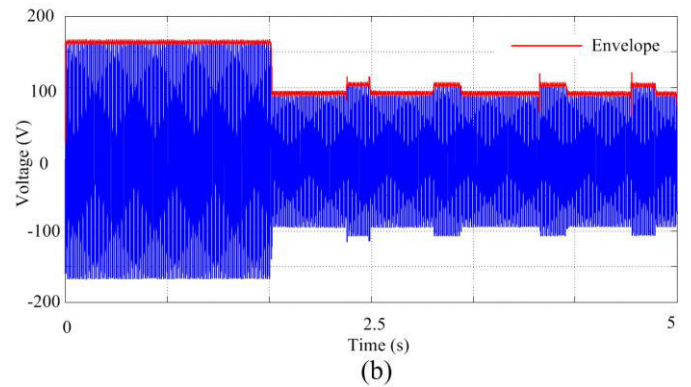
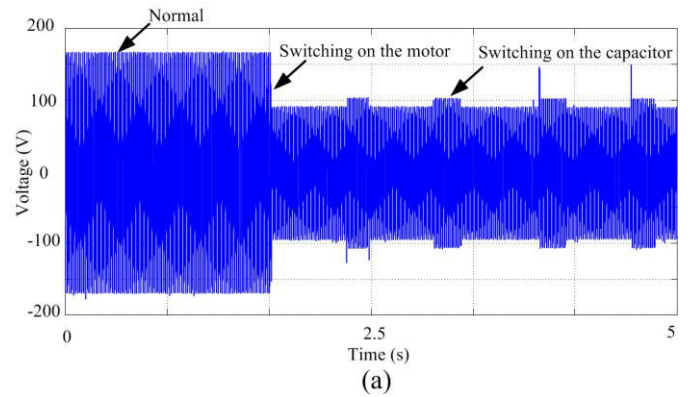


Fig. 8. Real experiment: (a) voltage signal, (b) voltage envelope.

- Methods*, IEC, Switzerland, 2008.
- [5] M. Valtierra-Rodriguez, R. A. Osornio-Rios, A. Garcia-Perez, and R. J. Romero-Troncoso, "FPGA-based neural network harmonic estimation for continuous monitoring of the power line in industrial applications," *Elect. Power Syst. Res.*, vol. 98, no. 1, pp. 51-57, May 2013.
 - [6] E. Oran Brinham, *The fast Fourier transform and its applications*, Prentice Hall international, 1988.
 - [7] Y.H. Gu, and M. H. J. Bollen, "Time-frequency and time-scale domain analysis", *IEEE Trans. Power Deliv.*, vol. 15, no. 4, pp. 1279-1284, Oct. 2000.
 - [8] P.K. Dash, D.P. Swain, A.C. Liew, S. Rahman, "An adaptive linear combiner for online tracking of power system harmonics", *IEEE Transactions on Power Systems*, vol. 11, no. 4, pp. 1730-1735, Nov. 1996.
 - [9] S. Haykin and B. Widrow, *Least-Mean-Square Adaptive Filters*, 1st ed., John Wiley & Sons Inc. 2003.
 - [10] R. Andraka, "A Survey of CORDIC Algorithms for FPGA-Based Computers," *Proc. Sixth ACM/SIGDA Int. Symp. Field Programmable Gate Array*, pp. 191-200, Feb. 1998.
 - [11] L. Cohen, *Time-Frequency Analysis*, 1st ed., Prentice hall PTR, 1995.

Nitrate evaluation on lettuce (*Lactuca sativa* L.) under organic and chemical fertilization in greenhouse conditions

Galicia-Rubio M. ^{#1}, de Santiago-Pérez J. J. ^{#2}, Ávila-Juárez L. ^{#3}, Rodríguez-González A. ^{#4}, Hernández-Puente K.N. ^{#5}

[#] *Engineering Faculty, Autonomous University of Querétaro
Carretera Amealco-Temascalcingo km 1, Col. Centro, Amealco de Bonfil, Querétaro, México.*

¹ galiciarubio.martin@gmail.com

² jjdesantiago@hspdigital.org

³ lucianoavila.j@hotmail.com

⁴ arg_uaq@yahoo.com.mx

⁵ selanginella@gmail.com

Abstract — The world production of vegetables has been increasing in recent years due to the use of technology, intensive use of fertilizers, pesticides and machinery. However, this has created negative side effects such as health issues and soil pollution. Lettuce is one of the most produced plants worldwide, and it is not excluded from the intensive use of those practices. Lettuce is a vegetable that accumulates higher concentration of NO_3^- in its leaf structure; this molecule is reduced to nitrite (NO_2^-) by a segregated enzyme of bacteria contained in human saliva called nitrate-reductase. This substance can affect the health in several ways, from respiratory illness to cancer. In this work, we propose a crop technique based on organic fertilization which intends to produce healthy vegetables without compromising the quality of the product. The experiment was conducted in a greenhouse, and based on the results we found that the organic fertilization shows less nitrate concentration in comparison with chemical fertilization.

Keywords—greenhouse; nitrate concentration; organic fertilizer; vermicompost;

I. INTRODUCTION

The world production of vegetables has been increasing in recent years due to the use of technology the intensive use of fertilizers, pesticides and machinery; however, this has brought side effects that cause damage to the soil. One of the most produced vegetables is lettuce, which is not excluded from the intensive use of those practices. According to the FAOSTAT (2012), China has the first place in lettuce production with 8.42 millions of tons per year (t year^{-1}). The growth of lettuce depends on many different conditions; one of the main factors is fertilization, where elements such as nitrogen (N), potassium (K), phosphorous (P) (called macronutrients), and micronutrients like sulfur (S), calcium (Ca), magnesium (Mg), etc., have an important role for the plant metabolism as the protein synthesis and nucleic acids [1]. The N in nitric form (NO_3^-) in the lettuce is accumulated in the leaf when the absorption surpasses the reduction [2]; only in situations where

the fertilizers are applied in excessive volumes and in a nitric form [3].

The NO_3^- is considered a toxic molecule when is consumed in vegetables with high content of nitrates, but the NO_3^- is not a dangerous substance. The problem is caused when the NO_3^- is reduced to nitrite form (NO_2^-) by a segregated enzyme of bacteria in the saliva of humans [4] called nitrate-reductase; the high consumption of this substance can affect the health in several ways, from respiratory illness to cancer [5].

The radiation, temperature, fertilization, enzymatic activity of nitrate-reductase and genetic variety are the main factors that determine the nitrate accumulation in leaves [6]. Fertilization is one of the more significant in this case as it depends of the N form and the total of fertilizer applied; when the fertilizer is applied in nitric form, this produce a bigger concentration in the soil compared with ammoniac form. This effect is reduced due to N available mainly in the last two weeks before the harvest [4].

The use of organic fertilizers in lettuce production shows less NO_3^- concentration compared with the conventional fertilizers [7]. In the organic fertilizers there are many forms of N as nitric or ammoniac form and other micro and macroelements as sodium (Na), iron (Fe) and molybdenum (Mo), that have an important influence in the enzymatic activity of nitrate-reductase working with no protein molecules called cofactors [8], where the cofactor function is to generate the enzymatic activity accordingly with the structure of the molecule.

The lettuce is one of the vegetables that accumulate higher concentration of NO_3^- in the leaf structure; researches about the content of NO_3^- demonstrate concentrations from 1000 ppm to 4000 ppm of fresh weight. The World Health Organization (WHO) has recommended a daily permitted consumption of NO_3^- of 5 mg kg^{-1} of corporal weight that it is equal to 350 mg day^{-1} for a person with 70 kg of weight. Meanwhile nitrite daily permitted consumption is 0.6 mg kg^{-1} of corporal weight. The European Economic Community has established maximum and minimum contents of NO_3^- of lettuce cultivation in greenhouse

and without greenhouses conditions in different seasons of the year (Table I).

TABLE I. MAXIMUM CONTENTS OF NO_3^- , REGULATED BY THE EUROPEAN ECONOMIC COMMUNITY

Vegetable	Postharvest period	ppm
Lactuca sativa L.	Winter-Spring	
	Greenhouse condition	4500
	Without greenhouse	4000
	Summer-Autumn	
	Greenhouse condition	3500
	Without greenhouse	2500

According to the described problem, is necessary to produce these vegetables, like lettuce, with low concentration of nitrates in the leaf structures in order to reduce the risk of diseases and elevate the nutrimental quality of the food; likewise, we need to increase global production of food considering the health and protection of the environment and the soil.

II. ANTECEDENTS

A study was realized by Sanchez in 2010[8], where they describe the N absorption with nitric and ammoniac forms in relation with the radicular and environmental temperature, concluding that a high temperature increase the N-NH_4^+ and N-NO_3^- absorption, being bigger in N-NO_3^- than N-NH_4^+ . Tarigo *et al.* in 2004 [7], measured the NO_3^- content in lettuce fertilized with biol, urea and cow manure, where no one exceeded the permitted limits; however, the conventional fertilization with urea produced the biggest content of NO_3^- .

Nitrates in lettuce was evaluated by Pavlou *et al.* in 2006 [4], in three seasons of the year with organic nutrition with sheep manure in doses of 0.67, 1.34 and 2.01 kg plant^{-1} and three chemical nutrition with a variation of N, no one surpassed the level of NO_3^- permitted, however, the conventional fertilization produced the biggest content of NO_3^- . Where measured by Sanchez [8], the level of NO_3^- in Cropa lettuce fertilized with 10 and 20 $\text{dm}^3 \text{m}^{-2}$ of cattle manure and urea combined, only the treatment with 10 $\text{dm}^3 \text{m}^{-2}$ had significant differences respect to the others treatments.

According to the cited references, it is relevant the use of organic fertilizers in the production of vegetables with the objective of increasing the global production and the nutrimental qualities with the care of the environment. The least content of nitrates where is compared frequently with the conventional practices as the chemical fertilization where more nitrates are produced in the leaf structure. In this work we propose a crop technique based on organic fertilization which pretends to produce healthy vegetables without compromising the quality of the products.

III. MATERIALS AND METHODS

A. Area of study

This experiment was performed under greenhouse condition in Amealco de Bonfil, Querétaro, México, where the climate condition is sub-humid moderate with a middle temperature of 14.6°C and an annual precipitation of 836.5 mm.

B. Greenhouse conditions

The greenhouse used was cenital type, where polietilene plastic of 800 galgas was used to cover the structure. The structure was produced with ptr tubing of 1.5". The greenhouse had frontal and horizontal ventilation with antiafid mesh. The total area cultivated was 50 m^2 .

C. Preparation of greenhouse

The greenhouse was disinfected with a solution of hypochlorite of sodium with a concentration of 10 mL L^{-1} of water; this solution was applied in the surface of the greenhouse. The treatments were adjusted in four crop beds of 0.6x7.1 m; each crop bed had 13 treatments of 0.6x0.5 m.

D. Production of plant

Seeds of Vulcan lettuce with free polinization were used to produce 208 plants for all the treatments. The seed beds used were disinfected with ammoniac cuaternarium (2%) to prevent pests and diseases. The substrate used was peatmoss (70%) and vermicompost (30%), and finally recovered with vermiculite. When the seeds emerged, they were kept in protected conditions until the transplanted.

E. Transplant

The transplant was realized when the plants developed 4 true leaves or 21 days after the crop seeding. The planting density of lettuce was of 5.05 plants m^{-2} , with a distance between plants of 0.25 m. The organic mulching was used with 0.5 m^3 of straw of barley to cover 40 m^2 of surface.

F. Watering

The consumption of water in lettuce depends of the phenologic stage and the influence of climate conditions, where the lettuce requires 0.5 L day^{-1} in the maturity stage [6].

G. Fertilization

All the treatments were fertilized with solid vermicompost (40 t ha^{-1}) before the transplant with the exception of the control [9].

1) Pre-composting process in manure

Cattle and sheep manure were used to prepare the teas, but were summited to pre-composting where had a duration of 27 days, controlling the temperature, the O₂ incorporation and humid (70%) [10].

2) Organic teas formulation

The teas were made with sheep and cattle manure composted and vermicompost, and were incorporated to humidity during a day; the nutrient concentration was regulated by the electrical conductivity (EC) using 1.5, 2 y 2.5 mS cm⁻¹ for each tea formulation and pH to 5.8 with citric acid. The application was realized foliarly with atomizers until drop point in low radiation conditions.

3) Chemical tea formulation

The chemical tea was prepared according with Steiner (1984), where the elements are showed in Table II, and the nutrient concentration was regulated by the electrical conductivity (EC) using 1.5, 2 y 2.5 mS cm⁻¹ for each tea formulation and pH to 5.8 with citric acid. The application was realized foliarly until drop point in low radiation conditions.

TABLE II. PARTS PER MILLION FOR EACH ELEMENT ACCORDING WITH STEINER (1984).

Element	Ppm
N	180
P	51
K	277
Ca	183
Mg	49
S	96
Fe	3
Mn	1.97
Cu	0.02
Zn	0.11
B	0.44
Mo	0.01

4) Chemical fertilization

The chemical fertilization was applied only to the control treatment, with the objective to do a commercial comparison between the organic and chemical fertilization. The formulation is the same of Table II in fertirrigation way controlling the pH to 5.8 with citric acid, and tezontle was used as substrate like a hydroponic cultivation.

H. Phitosanitarian Control

The pests and diseases control was realized using preventing applications of chili, onion and garlic extracts.

I. Harvest

The harvest was realized in an interval of time of 60 days after the transplant, with duration of 81 days during all the cultivation cycle.

J. Variables to evaluate

Evaluated variables were as the submissiveness per m², weight, fresh and dry matter percentage where they were measured with a platform scale.

1) Fresh and dry matter percentage

The fresh and dry matter percentage was determined with the fresh and dry weight of each sample. The valor was calculated with the follow equations:

$$Pps = \frac{Ps}{Pf} \times 100 \quad (1)$$

$$Ppf = 100 - Pps \quad (2)$$

Where:

Ps= dry weight

Pf= fresh weight

Pps= dry matter percentage

Ppf= fresh matter percentage

2) Nitrate content

The determination of the nitrate content was done cutting a sample of a basal leaf of each treatment of each repetition. The sample was obtained when the leaf was submitted in an extractor sap press, where 10 g of leaf was introduced obtaining 0.75 mL of sap and was submitted to dissolution factor of 1:3 with distilled water and afterwards the sample was collocated with a gradated dropper in the equip Compact NO₃⁻ Meter TwinNO₃⁻ Model B-343, HORIBA, Ltd., in three times of the day: 7:00 a.m., 2:00 p.m. and 7:00 p.m. and in the same time in evolution form, with the objective to determinate the least content of nitrates.

IV. EXPERIMENTATION

A. Experimental design

The experimental method was randomized block design with 4 repetitions and an experimental unit of 4 plants, a total of 12 treatments and a control with chemical fertilization. The factor was the fertilization and 12 levels of application that correspond to doses and concentration, where the organic and chemical tea formulations were realized in atomizers to apply the foliar solution (Figure 1). The description of treatments appear in the follow table (Table III)

TABLE III. TREATMENT DESCRIPTION.

Treatment	Description
T1	FTO D1
T2	FTO D2
T3	FTO D3
T4	FTV D1
T5	FTV D2
T6	FTV D3
T7	FTC D1
T8	FTC D2
T9	FTC D3
T10	FFQ D1
T11	FFQ D2
T12	FFQ D3
T13	CONTROL

V. RESULTS AND DISCUSSION

A. Nitrate content

The low nitrate content of the lettuces in this research was measured in the morning in comparison with the measures in the afternoon and night. This fact was reported by Salinas in his work [6], where it depends of the radiation in first place and the fertilization applied.

Additionally, the nitrate content registered significant differences (ANOVA) among treatments with chemical and organic fertilizations.

The Tukey test showed lower nitrate content in treatments with organic fertilization that corresponds from treatment 1 to 9 and the treatment 10 with chemical fertilization with 1.5 mS cm⁻¹ of concentration, in comparison to the chemical fertilization treatments (treatments 11 and 12), and it is more significant with the control (T13). Figure 3 shows the boxplot of the treatments with their respective fertilizations, where values with the same letter are statistically equals; for example, the treatments 1 to 7 are labeled by el letter 'a' that means they are statistically similar. Only the treatment 13 is significant different respect to all the treatments. It is important to mention that any treatment surpass the maximum limit established by the EU (Europe Union) in the period of summer-autumn.

Where:

FTO: Foliar fertilization with tea of sheep compost

FTV: Foliar fertilization with tea of vermicompst

FTC: Foliar fertilization with tea of cattle compost

FFQ: Foliar fertilization Steiner (1984)

D1: Dose to 1.5 mS cm⁻¹

D2: Dose to 2 mS cm⁻¹

D3: Dose to 2.5 mS cm⁻¹

T13 (Control): 100 % Steiner (1984) fertilization



Fig. 1 Organic and chemical teas formulation in atomizers.

Each treatment was placed in randomized position in the greenhouse, where each fertilization of the treatment was showed on a color paper with its respective concentration on the lettuces (Figure 2).



Fig. 2. Treatment description of fertilization in lettuce.

B. Estadistic analysis

The variations of the variables of each treatment were evaluated with analysis of variance (ANOVA) and test of Tukey with a confidence level of 95% ($\alpha \leq 0.05$).

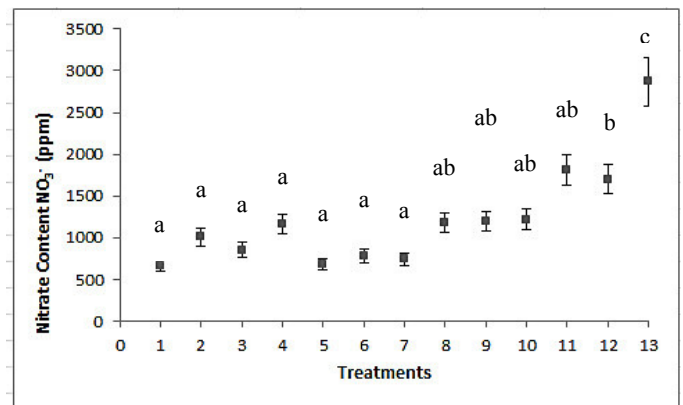


Fig. 3 Nitrate content of the lettuce in each treatment. Values with the same letter are statistically equals. Tukey (0.05)

B. Fresh and dry matter percentage

The fresh and dry matter percentage of the lettuces are presented in Table IV, where there is variability among the treatments. The results show a dry matter percentage less than 10 % to the treatments 2, 3, 4, 5, 7, 8, 10, 11 and 13; where the treatments 1, 6 and 9 with organic fertilization showed a dry matter percentage bigger than 10 % and only the treatment 12 with chemical fertilization with 14.62 % of dry matter.

TABLE IV. FRESH AND DRY MATTER PERCENTAGE OF EACH TREATMENT

<i>Treatments</i>	<i>Dry matter percentage</i>	<i>Fresh matter percentage</i>
T1	10.34%	89.66%
T2	8.03%	91.97%
T3	6.05%	93.95%
T4	6.73%	93.27%
T5	8.83%	91.17%
T6	10.65%	89.35%
T7	9.17%	90.83%
T8	8.18%	91.82%
T9	13.11%	86.89%
T10	6.69%	93.31%
T11	5.28%	94.72%
T12	14.62%	85.38%
T13	9.22%	90.78%

It is important to consider the quality of the lettuces that the population eats, the fresh and dry matter percentage are a way to check the total solids that vegetables contain, but it is necessary to know the origin of the production as if the lettuces are fertilized in a organic manner. In addition to the nitrate content reduction, Pavlou *et al.* in 2006 [4], demonstrated that the organic production of lettuces improve some quality characteristics such as the fenol and flavonoid content and antioxidant capacity.

So, according to the results, we can conclude that the quality of the lettuce is not reduced by using organic fertilization.

VI. CONCLUSION

To determine the quality of lettuces is of great relevance considering the nitrate content and the fresh and dry matter percentage because it is possible to establish a lettuce with a low nitrate content but with a high dry matter percentage. The objective of produce organic lettuces is prevent diseases and eat vegetables of major quality, where it is economically, environmentally and healthy commendable to produce in an organic manner.

In this work, we can verify that the organic fertilizations are commendable to produce lettuces with good quality and low concentration of nitrates; moreover they are a good option to cultivate other kind of vegetables and extend for future experiments in other kind of crops.

VII. ACKNOWLEDGMENT

This research was partially supported by FOFIUAQ-2013 20501155 09.03.02 and PROMEP 103.5/14/10401 projects.

VIII. REFERENCES

- [1] M. D. Raigon, M. D. García-Martínez, C. Guerrero, and P. Esteve, "Actividad de la nitrato reductasa y su relación con los factores productivos en lechuga," Congreso SEAE Zaragoza, N° 157, 2006.
- [2] A. Escalona, M. Santana, I. Acevedo, V. Rodríguez and L. M. Marco, "Efecto de las fuentes nitrogenadas sobre el contenido de nitratos y lecturas "SPAD" en el cultivo de lechuga," *Agronomía Tío*, vol. 59, pp. 99 – 105, 2009.
- [3] L. Ferreras, E. Gomez, S. Toresani, I. Firpo, and R. Rotondo, "Effect of organic amendments on some physical, chemical and biological properties in a horticultural soil", *Bioresource Technology*, vol. 97, pp. 635 – 640, 2006.
- [4] G. C. Pavlou, C. D. Ehaliotis, and V. A. Kavvadias, "Effect of organic and inorganic fertilizers applied during successive crop seasons on growth and nitrate accumulation in lettuce," *Scientia Horticulturae*, vol. 111, pp. 319–325, 2006.
- [5] G. A. Carrasco, and S. W. Burrage, "Diurnal fluctuations in nitrate accumulation and reductase activity in lettuce (*Lactuca sativa* L.) grown using nutrient film technique," *Acta Horticulture (ISHS)*, vol. 323, pp. 51 -60, 1993.
- [6] P. S. Salinas, "Efecto del ácido salicílico sobre la tolerancia a estrés hídrico en lechuga (*Lactuca sativa* L.) Bajo condiciones de invernadero," Thesis degree, Autonomus University of Queretaro, México, 2010.
- [7] A. Tarigo, C. Repetto and D. Acosta, "Evaluación agronomica de biofertilizantes en la producción de lechuga (*Lactuca sativa* L.) a campo," Thesis degree, Republic University, Montevideo, Uruguay, 2004.
- [8] T. M. Sánchez, "Evaluación de la calidad de lechuga (*Lactuca sativa* L.) respecto a su contenido de nitratos y materia seca," *Rev. de la Fac. de Agronomía – UNLPam*, vol. 21, pp. 29-36, 2010.
- [9] M. Tejada, J. L. Gonzalez, M. T. Hernández, and C. García, "Agricultural use of leachates obtained from two different vermicomposting processes," *Bioresource Technology*, vol. 99, pp. 6228 – 6232, 2008.
- [10] C. A. Edwards, N. Q. Arancon, and S. Greytak, "Effects of vermicompost teas on plant growth and disease," *BioCycle*, vol. 47, pp. 28 -31, 2006.

A Finite Element Model to assess flexible pavement – vehicle interaction

José A. Romero Navarrete ^{#1}, Alejandro A. Lozano Guzmán ^{*2}, Guadalupe M. Arroyo Contreras ^{#3}

[#] *Faculty of engineering, Queretaro Autonomous University, Querétaro, Mexico 76000*

¹ jaromero@uaq.mx

³ marroyo@uaq.mx

^{*} *CICATA-IPN Querétaro Unit*

Cerro Blanco 141, Querétaro, México 76090

² alozano@ipn.mx

Abstract—A family of mathematical models has been reported in the literature for analyzing pavement damage due to heavy vehicles. However, no parametric analysis has been carried out of the main conditions and properties affecting pavement response, nor has been possible to simulate real traffic conditions on actual road lengths. In this paper a mathematical scheme is proposed to simulate the pavement response to tire loads as a function of vehicle and pavement properties. The model is based upon finite elements and empirical properties for asphalt mix stiffness. A sensitivity analysis reveals that the pavement temperature is the most influential property for the pavement deflection: 1769 times more influential than pavement roughness; 51 times more influential than the vehicle speed; and 1.6 times more influential than void content. Furthermore, results suggest that superposition effects take place as the spacing of the axles is shortened, and that pavement rebound deeply affects the resulting pavement deflection. The proposed computational scheme makes possible the needed simulation of massive-mixed traffic on real road lengths, under a real-time simulation scheme.

Keywords— *Vehicle-pavement interaction, Flexible pavement, Heavy vehicles, Finite Element Method, Dynamic pavement loading, Computer simulation*

I. INTRODUCTION

Pavement deterioration due to heavy vehicles affects road transportation efficiency in different ways, from augmented road user operating costs due to increased roughness; to traffic disruptions due to road work to repair such increased roughness. A deteriorated road implies vibration of the vehicles and such vibration has implications in different directions, including a faster vehicle degradation, freight damage and driver fatigue [1][2]. It has been reported that using poorly maintained roads can represent an increase in vehicles operating costs up to 30% [3]. The overall effect of such damaging effects finally has to do with road safety [4]. Common needs of road agencies and governments include indicators of the magnitude of the potential road damage caused by heavy trucks, as a function of different operating and design factors [5]. Consequently, investigations have been carried out to assess the potential damaging effect of vehicles on the pavement throughout experimental and analytical approaches [6][7][8][9]. Analytical models of vehicle-pavement interaction that consider the pavement dynamic

response to tire loads, however, are complicated and difficult to utilize in a real traffic environment. That is, in a real world situation, the vehicles use the infrastructure at different traveling speeds and payload conditions, while at the same time the pavement exhibits different levels of vulnerability to such loads. To the knowledge of the authors, such comprehensive model has not been developed yet.

The need for realistic approaches that take into account the massive use of infrastructures has been previously suggested [10]. However, none of the Finite Element Method (FEM) and multilayer models reported in the literature enables the simulation of real traffic on actual pavement lengths. For example, while the variation of pavement stiffness with temperature has been studied both numerically and experimentally [11][7], no parametric analysis has been carried out of the temperature variation effect on pavement damage due to heavy trucks.

In this paper a Finite Element model is proposed to analyze the effect of tire loads on a flexible pavement, by integrating an asphaltic damped beam (asphalt layer), supported by damped-asphaltic bars (Sub-base material). Tire forces are simulated from the response of a lumped mass vehicle model to the pavement profile. A parametric analysis is made and a sensitivity formulation is proposed to identify the most influential factors affecting pavement deflection and potential damage.

II. REVIEW OF EXISTING MODELS

The main modeling approaches reported in the literature to simulate flexible pavement dynamic response to vehicle tire loads include the following: discretized models based on FEM [12] [13] [14] [15] [16]; multilayer models [17]; and discretized uncoupled-lumped models [18]. These models make possible the simulation of passing tires and the superposition of effects due to contiguous axles. However, reported FEM models are difficult to use as they are mostly based on diverse commercial computational platforms [16]. It is thus very difficult to simulate the vast variety of operating conditions and properties of the vehicles and the pavements, so that the use of such models is limited to the analysis of specific aspects of vehicle-pavement interaction. On the other hand, the

multilayer methods run faster, and have been even considered for pavement design methods [19]. The main difference between FEM and multilayer approaches has to do with the local stress distribution around the tire-pavement contact patch, with the FEM being potentially more accurate in that respect.

Other approaches for pavement response simulation that have been reported in the literature include continuous models, fuzzy logic tools, and micromechanical formulations, as described below.

A continuous vehicle-pavement interaction model was proposed by Hardy and Cebon [20], in which the pavement is modeled as an elastic beam resting on a damped elastic foundation. In such a case, a simplified vehicle model (quarter-of-a car) was considered for the analysis of pavement response to vehicle loads. Micromechanical approaches consider the microstructure of the pavement mix, and studies have included the Distinct Element Method (DEM) to analyze the stiffness of the material as a function of loading frequency and temperature [21]; or as a function of the failure modes of the pavements [22]. A fuzzy logic approach has also been proposed to model the pavement response to falling weights [23].

A comprehensive and calibrated model for analyzing rutting in flexible pavements was proposed by Fang et al. [24]. In their model, the authors obtain the evolution of the transverse surface profile of the road as a function of the amount of loading cycles, assuming the tire forces as quasi-static loads that induce uniaxial equivalent stress. The power law formulation for creeping, embedded in a commercial FEM program, was used to simulate the creeping rate for each of the three layers of pavement's structure, as a function of loading speed and level of traffic. A constant tire load was considered, which was divided into FEM model nodes according to tire footprint's geometry. Constant Young's modulus and Poisson's ratio were considered. So, this model neglects the effect that many significant parameters have shown to have on pavement deterioration, including roughness (dynamic loads), cargo level and pavement temperature. Such limitations prevent the application of the model to analyze properties and operating conditions that eventually generate the most pavement damaging conditions. So, to identify which of these factors represent the most influential effect on pavement deterioration a model is needed that based upon physical principles allows the identification of such factors.

III. PAVEMENT MODEL

Fig. 1 illustrates the proposed pavement physical model, consisting of an asphaltic beam supported by a group of bar elements 0.5 m apart. The bar elements combine a damped bar, representing the sub-base of the pavement structure, and an asphaltic bar to reproduce the asphalt layer vertical response.

Fig. 2 illustrates the degree of freedom (DOF) for the beam elements, including vertical positions (w_1 y w_2) and angular displacements (θ_1 and θ_2). In this figure f_i , for $i = 1$ to $i = 4$, represents the forces and moments applied on the beam element. Stiffness $[k]$ and mass $[m]$ matrix expressions for the beam elements are given by the following expressions [25]:

$$[k] = \frac{EI}{h^3} \begin{bmatrix} 12 & 6 & -12 & 6 \\ 6 & 4 & -6 & 2 \\ -12 & -6 & 12 & -6 \\ 6 & 2 & -6 & 4 \end{bmatrix}$$

$$[m] = \frac{m_e h}{420} \begin{bmatrix} 156 & 22 & 54 & -13 \\ 22 & 4 & 13 & -3 \\ 54 & 13 & 156 & -22 \\ -13 & -3 & -22 & 4 \end{bmatrix} \quad (1)$$

where E is the elastic modulus; I is the moment of inertia of the beam element, and m_e the corresponding beam element mass. The damping matrix is proposed as follows:

$$[c] = c_d \begin{bmatrix} 12 & 6 & -12 & 6 \\ 6 & 4 & -6 & 2 \\ -12 & -6 & 12 & -6 \\ 6 & 2 & -6 & 4 \end{bmatrix} \quad (2)$$

where c_d is a damping constant.

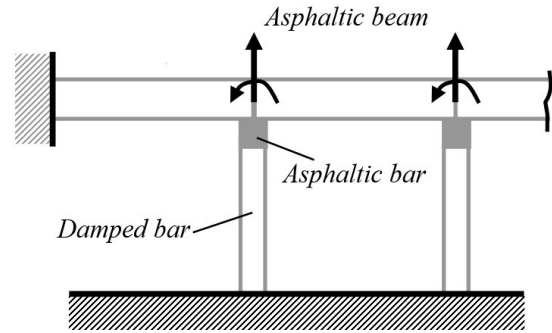


Fig. 1. Finite element model for the pavement.

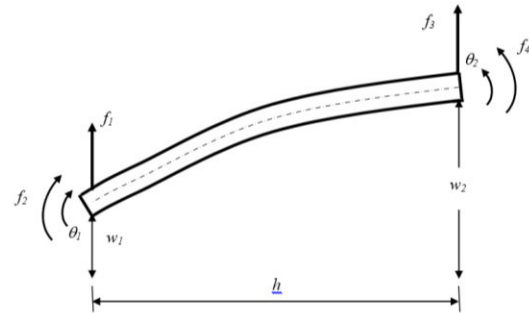


Fig. 2. Degrees of freedom and forces and moments for a beam finite element [25].

For the bar elements, Fig. 3 illustrates the corresponding degrees of freedom (u_1 and u_2), and end forces f_1 and f_2 . The mass and stiffness equations for the bar elements are:

$$[k] = \frac{EA}{h} \begin{bmatrix} 1 & -1 \\ -1 & 1 \end{bmatrix}; \quad [m] = \frac{mh}{6} \begin{bmatrix} 2 & 1 \\ 1 & 2 \end{bmatrix} \quad (3)$$

For the damping matrix, the matrix is assumed as:

$$[c] = c_b \begin{bmatrix} 1 & -1 \\ -1 & 1 \end{bmatrix} \quad (4)$$

where c_b is a damping constant. Vertical stiffness of the bar elements is the equivalent stiffness of an asphalt element and a sub-base element.

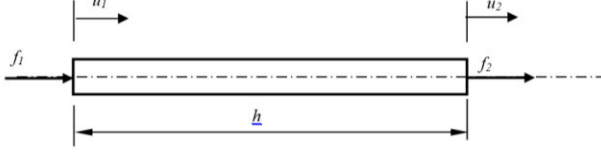


Fig. 3. Degrees of freedom and forces for a bar finite element [25].

The standard procedure of assembling the particular elements was used to realize the equations of motion for the system, as follows [25]:

$$[M] \{\ddot{U}\} + [C] \{\dot{U}\} + [K] \{U\} = \{F\} \quad (5)$$

where $\{F\}$ represents the vector of nodal forces and $\{U\}$ is the state vector containing the degrees of freedom and their derivative (u_i and \dot{u}_i , respectively, for $i = 1$ to $i = \text{DOF}$):

$$\{U\} = \{u_1 \ \dot{u}_1 \ u_2 \ \dot{u}_2 \ u_3 \ \dot{u}_3 \ u_4 \ \dot{u}_4 \ u_5 \ \dot{u}_5 \ u_6 \ \dot{u}_6 \ \dots\}^T \quad (6)$$

Elastic modulus E in (1) and (3) corresponds to the dynamic elastic modulus of asphalt mix [26], which is estimated from the following empirical relation [7]:

$$E = E_b [1 + (257.5 - 2.5 \cdot VMA) / n(VMA - 3)]^n \quad (7)$$

where E_b is the binder's Modulus of Elasticity, the exponent $n = 0.83 \log[(4 \cdot 10^4) / E_b]$ and VMA describes the void content of the pavement expressed in percentage. E thus represents the average stiffness for the full depth of asphalt layer of the pavement. E_b in (7) has been related with the asphalt layer temperature, penetration index (PI) and loading time through the following empirical relation [7]:

$$E_b = 1.157 \cdot 10^{-7} \cdot t_\ell^{-0.368} \cdot 2.718^{-PI^{(R)}} (T_{RB}^{(R)} - T_A)^5 \quad (8)$$

Equations (7) and (8) are valid for $12\% < VMA < 30\%$; and $E_b > 5$ MPa. t_ℓ in the model is calculated on the basis of a constant tire-print length of 300 mm.

IV. VEHICLE MODEL

The forces to be exerted on the pavement model are obtained from simulations of the dynamic response of a vehicle to the pavement profile.

The model was formulated to study its bounce and pitch mode dynamics under excitations arising from measured road surfaces, while the contributions due to roll dynamics are considered negligible [27]. Vehicle dynamics is assumed to be independent from pavement deflection, as the magnitude of deformation in the pavement (in the order of 0.1 mm) is significantly smaller than those deformations observed for the vehicle tires and components [8].

The vehicle is idealized as a set of rigid bodies coupled by massless flexible elements [28][29]. Tires are represented by linear stiffness and damping. Fig. 4 illustrates the in-plane lumped parameter model of the vehicle employed to analyze the response of the FEM pavement proposed to tire loads. The vehicle has six degrees of freedom, associated with the bounce motion of the steering axle z_F ; bounce and pitch oscillations of the sprung mass (z_s and θ_s , respectively); bounce motion of the front axle of the tandem-group $z_{T,F}$; bounce motion of the rear axle of the tandem-group $z_{T,R}$; and swing motion of the equalizing bar in the tandem-group (θ_e).

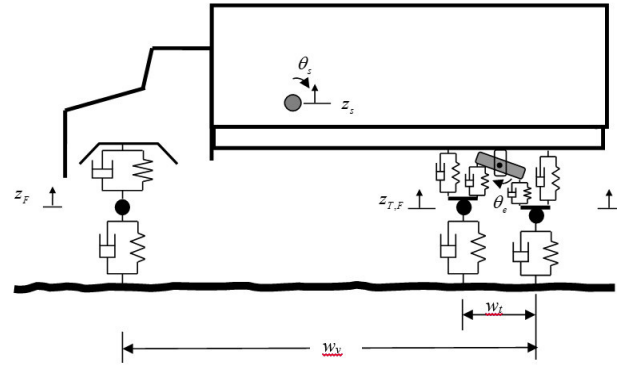


Fig. 4. Schematic representation of vehicle model.

V. SQUEME OF SOLUTION OF THE EQUATIONS

The pavement and vehicle equations of motions are solved throughout the Transition Matrix Approach [25]. According to this approach, equations are expressed as first order systems, as follows:

$$\{\dot{y}(t)\} = [A]\{y(t)\} + [B]\{Y(t)\} \quad (9)$$

where $\{y(t)\}$ represents the state vector containing the different degrees of freedom of the system; $\{Y(t)\}$ constitutes the external perturbation; and $[A]$ and $[B]$ are the coefficient matrices, as a function of vehicle mass, stiffness, damping and geometrical properties. Recursive time solution of first order equation is given by [25]:

$$\{y(t + dt)\} = [\Phi]\{y(t)\} + [\Gamma]\{Y(t)\} \quad (10)$$

where:

$$[\Phi] = e^{[A]t} = [I] + [A]dt + \frac{[A]^2 dt^2}{2!} + \frac{[A]^3 dt^3}{3!} + \dots + \frac{[A]^n dt^n}{n!} \quad (11)$$

$[\Phi]$ is the state transition matrix and $[\Gamma]$ is the particular response, given by:

$$[\Gamma] = \int_0^{\Delta t} e^{[A]t} [B] dt = [A]^{-1} ([\Phi] - [I]) [B] \quad (12)$$

dt in (11) and (12) represents the time step for the simulations, which is as little as necessary to secure the convergence of the Taylor expansion of that equation.

Pavement profile input was discretized in constant elevation segments.

A Computational algorithms

Fig. 5 illustrates the computational scheme to calculate the pavement response as a function of pavement and vehicle properties and conditions of operation. It contains three modules that are sequentially executed: Vehicle > Pavement > Dynamic response. The vehicle module yields tire forces due to every vehicle axle, while the pavement module calculates the transition and particular response matrices, as a function of vehicle speed and pavement temperature and void content. The dynamic response module calculates the pavement response to vehicle tire loads for the pavement length considered.

B Tire forces on the pavement

During the calculation process, the time step dt necessary for the convergence of the Taylor Series (11) (0.001 s), implied that the vehicle did not travel the distance between two consecutive beam nodes of the pavement model (0.5 m apart). Consequently, at any time the resulting tire forces were between nodes, and it was necessary to weight the tire forces on consecutive nodes, as shown in Fig. 6.

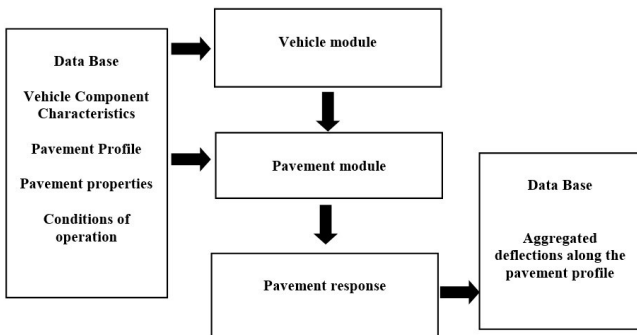


Fig. 5. Computational setup of vehicle and pavement computer programs.

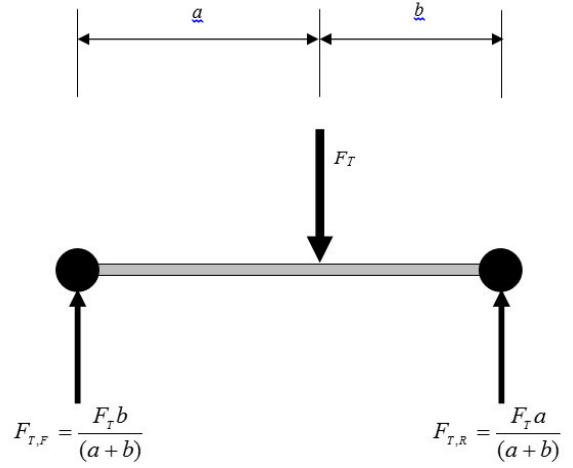


Fig. 6. Weighted forces on beam element nodes.

VI. RESULTS AND DISCUSSION

The pavement response to tire loads under a variety of operating conditions and characteristics is presented. It should be noted that the effect of different levels of static loading is not considered in the analysis, as the relationship of variations of static tire loads and pavement damage obeys contact-stresses power laws [28] [5].

A Calibration of the model

Experimental values of asphalt pavement deflection were considered for calibration purposes of the model. According to Sargand [30], low speed deflection rate of asphalt pavement is as follows: (0.101 mm / 4459 N) for the asphalt layer, and (0.177 mm / 4459 N) for the sub-base.

B Pavement and vehicle nominal conditions and properties

A 25-meter long road segment was considered for the analysis, realizing fifty 0.5-meter long beam elements, with 49 bar elements. The DOF for the system was 98, so that the calculation of the particular response matrix of the transition matrix approach involved operations to inverse matrices containing 196 (98*2) rows and columns.

A sequence of simulations was carried out, considering no roughness pavements and measured pavement profiles to explore the effect of road roughness on pavement response. No-roughness pavement was assumed for analyzing the effect on pavement deflection of diverse parameters including temperature, vehicle speed, axles spacing and asphalt mix void content. Tables I and II describe the pavement and vehicle nominal properties and characteristics.

TABLE I. PAVEMENT MODEL NOMINAL PROPERTIES.

Property	Units	Magnitude
Asphalt pavement temperature (T_p)	$^{\circ}\text{C}$	20
Asphalt pavement softening temperature (T_{RB})	$^{\circ}\text{C}$	60
Void content (VAM)	%	25
Moment of inertia of the viscoelastic beam element	m^4	.000045
Damping constant of the bar elements	Ns/m	14000
Spring constant of the bar elements	N/m	95000000
Beam elements length	m	0.5
Beam elements mass	kg	1000
Bar elements mass	kg	355
Damping constant of the bar elements	Ns/m	140000

TABLE II. VEHICLE PROPERTIES.

Property	Magnitude
Tare mass	5000 kg
Maximum payload	12500 kg
Axle mass (Front/rear)	600 / 1000 kg
Composed front suspension stiffness	1000000 N/m
Composed rear suspension stiffness	2000000 N/m
Composed front suspension damping	10000 Ns/m
Composed rear suspension damping	50000 Ns/m
Truck wheelbase / Axle spacing	5.2 m / 1.3 m

The calculations were performed in a regular computer equipped with an Intel processor at 1.6 GHz with 1.24 GB of RAM memory. The complete single-precision simulation for the 25 meter-road segment, including the transition and particular response matrices calculation, took around 58 seconds. However, if the transition and particular response matrixes, which are a function of the vehicle speed, pavement temperature and void content, are read from an existing file, such simulation took less than one second.

C Pavement time response – no roughness pavement

The first set of results of the model considers the pavement response to constant tire loads, as a function of vehicle speed and tandem group axles spacing.

The corresponding static forces were as follows: 38925 N (Front axle, 19462 N per tire); 76335 N (Front axle of the tandem suspension, 38167 N per dual tire set); 80938 N (rear axle of the tandem suspension, 40469 N per dual tire set). Such axle forces correspond to a vehicle with 20 tons of gross vehicle weight. The pavement temperature (T_p) in these simulations was taken as 20 $^{\circ}\text{C}$, with an asphalt mix void content (VMA) of 25%. So, assuming a perfect lateral symmetry of the vehicle, the pavement loads were split equally on the right and left tires, and the calculated pavement deflections would occur on each of the two tire-tracks.

D Effect of axles spacing of the tandem group / Nominal conditions and properties

Fig. 7 illustrates the time histories of pavement deflection for the node at the middle of the 25-meter long pavement section, as a function of vehicle speed and spacing of the axles of the tandem group. Three values for the axle spacing were considered: 0.7 m; 1.3 m, and 2.2 m. These results suggest a superposition of effects when the tandem axles are closely spaced, while the dynamic response of the pavement influences its maximum deflection. In particular, it is noted that pavement deflection is affected by the rebound of the pavement. Fig. 8 summarizes the combined effect of tandem group axles spacing and vehicle speed on pavement deflection. These results reveal an ambiguous response of pavement deflection to axles spacing: while for the higher speed the maximum deflection consistently decreases with increasing axle spacing, the low and medium ones indicate a minimum deflection at 1.3-m spacing. Such phenomenon is attributed to the dynamic rebound of the pavement, in the perspective of the consecutive axle loading. Such effect would be minimized as the elapsed time between tire loads decreases.

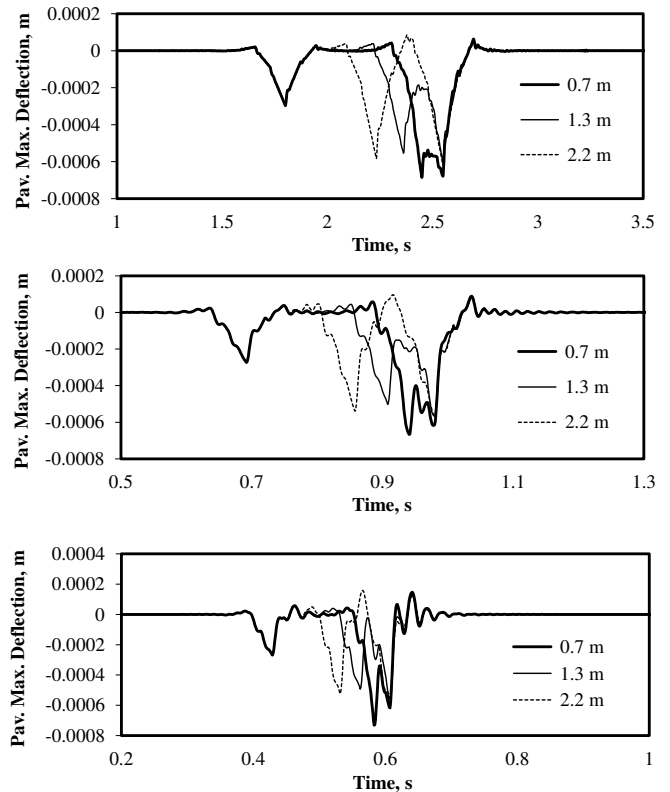


Fig. 7. Time histories of pavement deflection as a function of the vehicle speed and the spacing between axles of the tandem group: (a) 25 km/h; (b) 65 km/h; and (c) 105 km/h (T_p : 20 $^{\circ}\text{C}$; VMA: 25%; No Roughness Pavement).

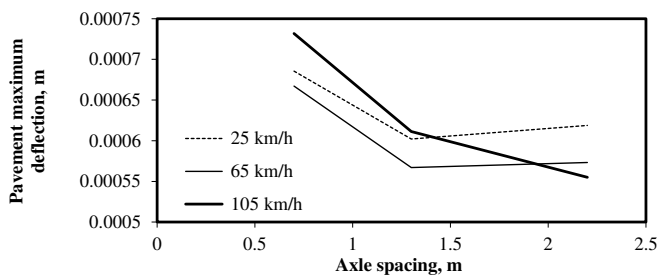


Fig. 8. Effect of vehicle speed and tandem axle separation on maximum pavement deflection (T_p : 20 °C; VMA: 25%; No Roughness Pavement).

VI.5 Effect of road roughness and vehicle speed

Twenty six measured pavement profiles were considered to investigate the effect of road roughness and vehicle speed on the maximum deflection of the pavement, as shown in Fig. 9. The profiles were obtained from the Long Term Pavement Performance program [31]. These results reveal a remarkable level of dispersion of deflection values due to variations in road roughness, further suggesting the importance of pavement profile characteristics on the potential effect of vehicles on the pavement. The linear tendency line in these figures reveals particular effects: while for 45 km/h and 75 km/h the tendency is an increasing pavement deflection with increasing pavement roughness, for 105 km/h the tendency is the opposite.

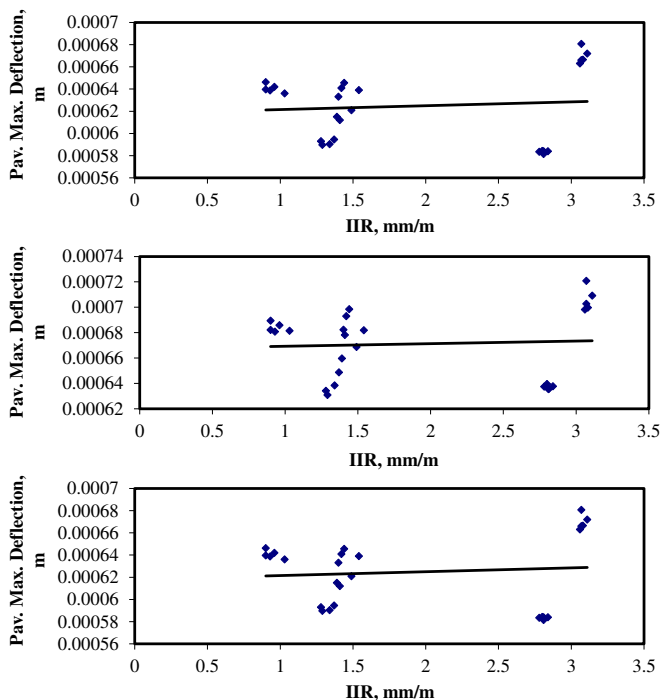


Fig. 9. Effect of vehicle speed and road roughness on pavement deflection (Spacing between axles of the tandem group: 1.6 m; T_p : 20 °C; VMA: 25%).

Fig. 10 reports the average values of the maximum deflections of the pavement as a function of vehicle speed, further suggesting that in spite of the diverse tendencies and dispersion of pavement deflections of Fig. 9, the average

values of pavement deflection consistently decrease with increasing vehicle speed.

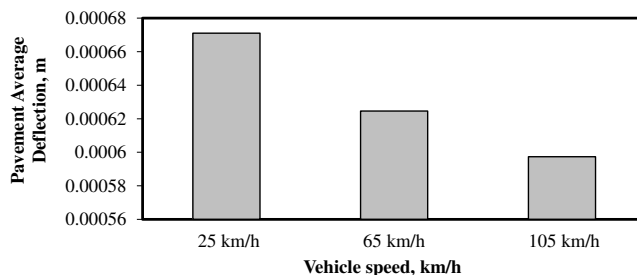


Fig. 10. Average peak deflections as a function of vehicle speed (Spacing between axles of the tandem group: 1.6 m; T_p : 20 °C; VMA: 25%).

VI.6 Effect of pavement temperature – no roughness

Fig. 11 illustrates the effect of pavement temperature on maximum pavement deflection as a function of vehicle speed. The trend shown in this figure would be the result of the nonlinear dependencies of the Elastic modulus E on the loading, loading time rate and pavement temperature, as it is described in (8). As the pavement temperature is increased, the effect of a temperature increase becomes stronger. It is also suggested from these results that increasing pavement temperature and decreasing vehicle speed would induce increases in pavement deflection in the order of 30%.

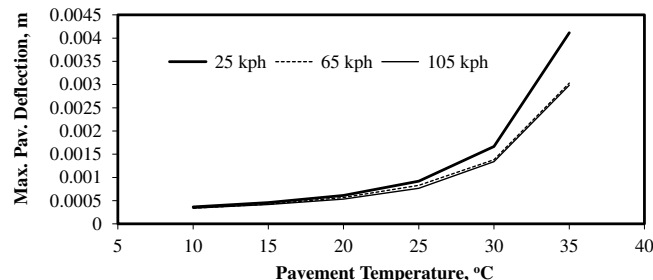


Fig. 11. Effect of pavement temperature and speed on maximum pavement deflection (Axle spacing of the tandem group: 1.6 m; VMA: 25%; No Roughness Pavement).

VI.7 Effect of pavement void content – no roughness

Fig. 12 illustrates the effect of asphalt mix void content VMA on the maximum deflection of the pavement, as a function of vehicle speed. A non-linear sensitivity of pavement deflection to variations in VMA is observed, with the vehicle speed only marginally influencing pavement deflection for low values of VMA.

VI.8 Sensitivity analysis

A sensitivity analysis is presented to assess the relative significance of the parameters considered in this study. A sensitivity function S is formulated upon calculation of the ratio of the relative variations in the output variables divided by the relative variations in the input parameters. Average values

of S for the range of points evaluated is \bar{S} . Fig. 13 illustrates these concepts and the corresponding equations.

VII. CONCLUSIONS

The consideration of the various parameters that potentially affect the pavement response to dynamic tire loads is crucial for understanding road damage due to heavy vehicles. Stiffness of the pavement is affected by a range of factors including environmental, operational and pavement design factors. Environmental factors include temperature, while operational and design concepts are represented by loading speed and void content, respectively. Tire loads are the primary cause of pavement distress and the magnitude of such forces depend on the vehicle response to pavement profile, as a function of vehicle operating conditions and components properties.

Vehicle dimensional characteristics also affect the overall response of the pavement, inducing a superposition of effects when the axle spacing is shortened. The overall effect of the vehicle on the pavement, however, is influenced by the dynamic response of this type of infrastructure and its rebound.

Previous mathematical models have been able to consider several vehicle and pavement properties; however, no parametric analysis has been carried out of the main conditions and properties affecting pavement response, nor has been possible to simulate real traffic conditions on actual road lengths.

The aim of this research was to propose a mathematical model to carry out parametric analyses of the main pavement-related factors affecting the pavement response to tire loads. A continuous model was necessary in order to study the effect of axle spacing. The Finite Element Method was selected as the involved matrix calculations made possible to simulate realistic road lengths with reasonable computer effort. The model output selected as performance measure was the pavement maximum deflection, while empirical relationships reported in the literature were employed to formulate the dependency of asphalt mix elastic modulus to loading speed, temperature and void content.

Parametric analyses were carried out to simulate the effect on pavement maximum deflection of selected pavement and vehicle characteristics and operating conditions. A dimensionless sensitivity analysis was carried out in order to identify the most influential properties.

Results reveal that the most influential factor affecting pavement deflection is the temperature of the pavement, with the less influential factor being the pavement roughness. The average pavement temperature sensitivity is 1769 times greater than the average sensitivity to pavement roughness; 51 times greater than the average sensitivity to vehicle speed; and 1.6 times greater than the average sensitivity to void content.

In relation with the effect on pavement deflection of axle spacing in group axles, results suggest that superposition effects take place as the spacing is decreased, and that the overall response is deeply influenced by the pavement dynamic response, including rebound. As a consequence, only for the highest loading rate considered (150 km/h) it was possible to identify a consistent tendency of increasing pavement deflection with decreasing axle spacing.

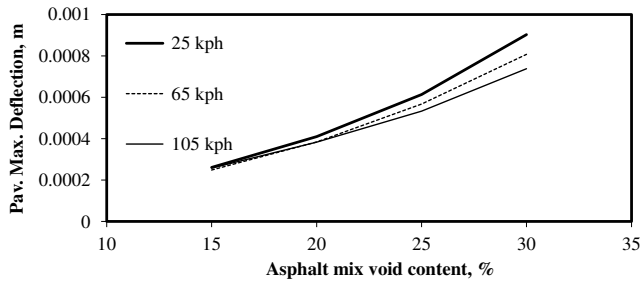


Fig. 12. Effect of asphalt mix void content on pavement temperature and speed on maximum pavement deflection (Spacing between axles of the tandem group: 1.6 m; T_p : 20 °C; No roughness pavement).

In the case of road roughness, the sensitivity calculation proceeded through the use of the linear tendency curves obtained in Fig. 9. Table III lists sensitivity results, suggesting that the sensitivity of pavement deflection to temperature is greater than any of the other parameters. The average temperature sensitivity (2.96) is: 1769 times greater than the average sensitivity to pavement roughness (0.0016); 51 times greater than the average sensitivity to vehicle speed (-0.0571); and 1.6 times greater than the average sensitivity to void content (1.848).

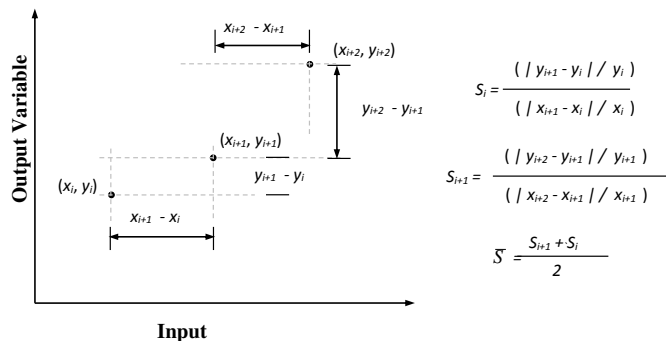


Fig. 13. Description of sensitivity S_i and \bar{S} .

TABLE III. PAVEMENT MODEL NOMINAL PROPERTIES.

Parameter	Speed	Sensitivity S
VMA	25 kph	2.014
VMA	65 kph	1.884
VMA	105 kph	1.646
Pavement Roughness	25 kph	0.00183
Pavement Roughness	65 kph	0.00659
Pavement Roughness	105 kph	-0.00340
Pav. Temperature	25 kph	3.279
Pav. Temperature	65 kph	2.770
Pav. Temperature	105 kph	2.832
Vehicle Speed	25 kph	-0.0432
Vehicle Speed	65 kph	-0.0710

It is considered that the proposed computational scheme contains the parameters and causality to apply such a model in real situations, involving massive heavy-vehicle traffic and actual road lengths. While empirical relationships have been considered in the formulations, a calibration is needed for the specific pavement being assessed, involving low speed force-deflection relationships.

REFERENCES

- [1] DOT, 2004 Status of the Nation's Highways, Bridges, and Transit: Conditions and Performance, Report to Congress, Executive Summary, 31 pp, 2004.
- [2] N.I. Rajapakse, and G. Happawana, "Nonlinear vibration analysis of a heavy truck driver seat for driver fatigue reduction," 9th International Symposium on Heavy Vehicle Weights and Dimensions, The Pennsylvania State University, June 2006.
- [3] T. Watanatada, W. Paterson, A. Bhandari, C. Harral, A. Dhreshwar, and K. Tsunokawa, K., Volume 1 - Description of the HDM III Model, The International Band for Reconstruction and Development, World Bank, Washington, D.C., 1987.
- [4] COST, COST 334 Effects of wide single tyres and dual tyres, Revision of the COST 334 Literature Database and Preparation of the Literature Evaluation, European Commission, Directorate General for Energy and Transport, 1998.
- [5] H. Prem, E. Ramsay, J. Malean, B. Pearson, J. Woodroffe, and J. DePont, Definition of potential performance measures and initial standards, Performance Based Standards - NRTC/AUSTROADS Project A3 and A4, Discussion Paper April 2001, National Road Transport Commission, 2001.
- [6] OECD, Dynamic interaction between vehicles and infrastructure experiment (DIVINE) Technical Report, DSTI/DOT/RTR/IR6(98)1/FINAL, Organisation for economic co-operation and development, 27-oct-1998.
- [7] A.C. Collop, Effects of traffic and temperature on flexible pavement wear, A dissertation submitted to the University of Cambridge for the Degree of Doctor of Philosophy, Department of Engineering, University of Cambridge, June 1994.
- [8] T.D. Gillespie, S.M. Karamihias, D. Cebon, M.W. Sayers, M.A. Nasim, W. Hansen, and N. Ehsan, NCHRP Report 353: Effects of heavy vehicle characteristics on pavement response and performance, Transportation Research Board of the National Academies, Washington, D.C., 1993.
- [9] H.M. Hjelte, "Model for estimating road wear on in-service roads," International Journal of Pavement Engineering, vol. 8(3), pp. 237 - 244, 2007.
- [10] J.A. Prozzi, and F. Hong, "Optimum statistical characterization of axle load spectra based on load-associated pavement damage." International Journal of Pavement Engineering, vol. 8, pp. 323-330. 2007.
- [11] W. Alkasawneh, E. Pan, F. Han, R. Zhu, and R. Green, "Effect of temperature variation on pavement responses using 3D multilayered elastic analysis," International Journal of Pavement Engineering, vol. 8(3), pp. 203 - 212, 2007.
- [12] R.M. Mulungye, P.M.O. Owendea, and K. Mellona, K., "Finite element modelling of flexible pavements on soft soil subgrades," Engineering Structures, vol. 28(3), pp. 739-756, 2007.
- [13] J.M. González, J.M. Caneta, S. Ollera, and B. Miró, "A viscoplastic constitutive model with strain rate variables for asphalt mixtures—numerical simulation," Computational Materials Science, vol. 38(4), pp. 543-560, 2007.
- [14] S.M. Kim, and B.F. McCullough, "Dynamic response of plate on viscous Winkler foundation to moving loads of varying amplitude," Engineering Structures, vol. 25(9), pp. 1179-1188, 2003.
- [15] N. Suleiman, and A. Varma, "Methodology to assess impacts of alternative truck configurations on flexible highway pavement systems," Transportation Research Board, Research Record vol. 1809, pp. 148-159, 2002.
- [16] M.F. Saleh, B. Steven, and D. Alabaster, "Three Dimensional Nonlinear Finite Element Model To Simulate the Pavement Response in the Canterbury Accelerated Pavement Testing Indoor Facility (CAPTIF)." Annual TRB Meeting, Washington, D.C., January 2003.
- [17] F. Wang, F., and R.B. Machedehl, "Mechanistic-Empirical Study of Effects of Truck Tire Pressure on Pavement Using Measured Tire-Pavement Contact Stress Data," Proc. 2006 Transportation Research Board Annual Meeting, Washington, D.C., 2006.
- [18] J.A. Romero, and A. Lozano, "Effect of trucks suspension and tire properties on pavement damage spatial distribution," The Transportation Research Board, Research Record vol. 1949, pp. 148-154., 2006.
- [19] A. Huvstig, A., "The development of a new road design method in Sweden." Proc. 2001 Transportation Research Board Annual Meeting, Washington, D.C., 2006.
- [20] M.S.A. Hardy, and D. Cebon D., "Response of continuous pavements to moving dynamic loads," ASCE J. Eng. Mechanics, vol. 119 (9), pp. 1762-1780, 1993.
- [21] Z. You, and W.G. Buttlar, "Micromechanical Modeling Approach to Predict Compressive Dynamic Moduli of Asphalt Mixture Using the Distinct Element Method," Transportation Research Board 2006 Annual Meeting, Washington, D.C., 2006.
- [22] P. Ullidtz, "Study of Failure in Cohesive Particulate Media using Distinct Element Method," Proc. 2001 Transportation Research Board Annual Meeting, Washington, D.C., 2001.
- [23] M. Saltan, S. Saltan, and A. Sahiner, "Fuzzy logic modeling of deflection behavior against dynamic loading in flexible pavements," Construction and Building Materials, vol. 21, pp. 1406-1414, 2007.
- [24] H. Fang, J.E. Haddock, T.D. White, and A.J. Hand, "On the characterization of flexible pavement rutting using creep model-based finite element analysis," Finite Element in Analysis and Design, vol. 41, pp. 49-73, 2004.
- [25] L. Meirovitch, Elements of vibration analysis, 2nd ed., Mc Graw Hill Int., 1986.
- [26] Y.H. Huang, Fundamentals of Pavement Design and Analysis, McGraw Hill. N.Y., 1993.
- [27] L. Wen-Kan, Y.C. Chen, B.T. Kulakowski, and D.A. Streit, "Dynamic wheel/pavement force sensitivity to variations in heavy vehicle parameters, speed and road roughness," Heavy Vehicle Systems, Special Series, International Journal of Vehicle Design, vol. 1(2), pp. 139-155, 1994.
- [28] D. Cebon, "Interaction between heavy vehicles and roads," SAE SP-951, Society of Automotive Engineers, 85 pp., 1993.
- [29] T.L. Wang, M. Shahawy, and D.Z. Huang, D.Z., "Dynamic response of highway trucks due to roads surface roughness," Computers and Structures, vol. 49(6), pp. 1055-1067, 1992.
- [30] S. Sargand, Determination of Pavement Layer Stiffness on the Ohio SHRP Test Road Using Non-Destructive Testing Techniques. Final Report, Department of Civil Engineering, Ohio University, October 2002.
- [31] E.O. Lukanen, R.N. Stubstad, and M.L. Clevenson, Study of LTPP pavement temperatures, U.S. DOT, Federal Highway Administration, Publication No. FHWA-RD-02-071, 2005.

Development of a Intra-Rumial monitoring system in realtime of physiological variables

A. Ibarra^{#1}, P. García^{*2}, S. Vergara^{#3}, A. Palomino^{#4}, M. A. Vargas^{#5}

[#] *Facultad de Ciencias de la Electrónica, Maestría en Ciencias de la Electrónica opción Automatización, Benemérita Universidad Autónoma de Puebla*

Av. San Claudio y 18 Sur. Puebla, México

¹ *almiux_150385@gmail.com*

³ *svergara2@hotmail.com*

^{*} *Instituto de Ingeniería, Universidad Veracruzana
Juan Pablo S/N, Veracruz, México*

² *jagarcia@uv.mx*

Abstract—In the following work an experimental prototype desing (bolus) is implemented, based on the electronic instrumentation point of view, for real time detection of physiological variables (pH and temperature) on cattle's for being measured in the rumen. A desirable behavior in the cow's health is when the rumen is between 5.5 and 7.0 pH and temperature between 38-40 Celcius degrees. The temperature measuring was implemented using a LM35 IC which presents a linear response of 10 mV/°C and an accuracy of 1°C; in the other hand, for pH measurement a combine electrode SG200C was used which presents a linear response of 41.39 mV/pH and an error of 2.2 mV. The prototype monitoring system was made through IEEE 802.11 wireless technology protocol instrumented with the RN-171-XV module. The obtained data will allow veterinarians to research in the cattle population's ability to adapt to the southeast tropical Mexican weather due to reduced thermal comfort environments.

Keywords—temperature; pH; bovine; acquisition system.

I. INTRODUCTION

In the following work an experimental prototype design is implemented, focused from the electronic instrumentation point of view, for real time detection of physiological variables (pH and temperature) on cattle's for being measured in the rumen. The obtained data will allow veterinarians to research in the cattle population's ability to adapt to the southeast tropical Mexican weather due to reduced thermal comfort environments.

Analyses for cattle bovine vulnerability in Veracruz City; located on the southeast Mexican coast, where there is a tropical weather and most of the year with a temperature around 40°C with a relative humidity of 90%; in front of climate changes shows that the biggest negative impact is during drought season on the north and center of the city, while raining season affects the south. The main species that will be affected is the bovine. Measures about heat stress for long periods of time affects European cattle (*Bos Taurus*), Cebu and the mixes demonstrate affectations in the physiology, heart and respiratory rates, cell packed volume, metabolic acidosis associate to pH sanguine change [1].

In the bovine digestive system the most important organ is the rumen, due in here the food is digested. Some of the features in the rumen are: mixing and wetting of the intake, provide the appropriate environment for the development of ruminal microfiber. The rumen content consists of dry matter on 10-15%, the inside temperature is on 39-40°C, pH is 5.5-7.1 and main variations of pH are due to presence of organic acid on the diet and on the spittle [2].

The traditional method for pH measuring consists on the ruminal fluid extraction across the fistula for a later analyzes. In the other hand, for temperature measurement a thermometer is introduced into the rectal area and these procedures create a stress situation in the cow.

As a solution to early problematic, an experimental prototype design is implemented to be introduced into a rumen's cows with a fistula, the system integrated with: for pH measurement a combine glass electrode was used; temperature measuring was implemented with an LM35 IC; the prototype monitoring systems is made in real time by wireless technology through IEEE 802.11 protocol; the bolus that is a housing that its aim is to protect the electronics of the biochemical environment was realized on SolidWorks™ with a diameter of 9.5 cm and a length of 25 cm; finally transmitted data will be displayed on a workstation display interface designed with LabVIEW2012™.

II. MEXICAN COW CATTLE PRODUCTION

A. Climate impact

Bovine meat is the one with the most economical, social and politic importance in Mexico. Due its productions, processing and marketing which involves more than half of national territory, thousands of producers, providers and business. Veracruz is the most important bovine meat producer city in the country, produces the 15% of the total consumption in Mexico and generates 350 thousands of direct and indirect employees [3].

Climatic changes affect all over the world, and consequences are reflected on forest areas with an increase of

deforestation, reduction in the wildlife and ecosystems, increase on natural phenomenon like earthquakes, drought and big precipitations. For the next 50 years the prognostic is a temperature increase between 2-5%, which leads to a shortage of water and a decreasing on farming area. Climatic changes will affect cattle in four main points: availability and price on the grain to feed cattle; production and quality on pastures and forages; health, growing and production of the animals; and epidemics on cattle [4].

B. Physiological considerations on bovines

The ruminant stomach is integrated of four gastric compartments: rumen, reticulum, omasum and abomasum. The rumen is the most important in the digestion process; due in it is where the food is first separate in solids and liquids. One of the rumen functions is to keep the food mixing and wetting of the semi-degraded food (cud), this with the object to provide and specialized microbe species environment. In order to a correct function in the ruminants it is necessary to maintain some constant conditions like continuous cud; enough liquids; a healthy microbial ecosystem with constant pH, constant temperature, and also to provide a suitable environment for the microorganism to survive. The ruminal contents is compose of 10-15% of dry material, a temperature around 39-40°C, a pH range of 5.5-7.1, and the main variations in it are due the present of organic acid in the daily consumption and the amount of saliva. Some of the rumen disorders are: indigestion, acidosis, alkalosis, omasum impaction, vagal indigestion [2].

III. SYSTEM DESCRIPTION

The following work presents the development of an Intra-Ruminal monitoring system in real time of physiological variables to be used on cattle adaptation researches.

The first part of the system is the physiological variable monitoring inside the rumen; the next stage is the signal conditioning; once it is done, in the next stage it is used a microcontroller to carry on the data processing, data will be transmitted wireless using a WiFi module; and the finally stage is the data display on a workstation for the end user visualization (Fig. 1).

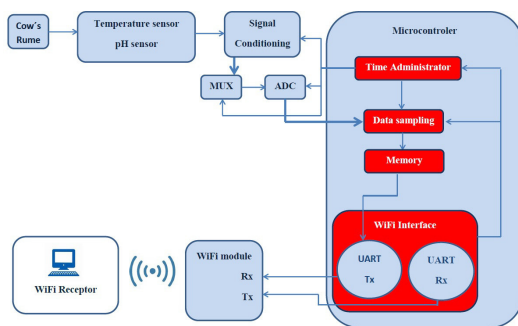


Fig. 1. System block diagram for the physiological variable detection.

On a cow previously fistulated bolus is going to be inserted into cow's rumen. Bolus is a housing to protect from the biochemical environment to the electronic system and also to give a mechanical support. Bolus is going to contain the sensing elements, a microcontroller, WiFi transmission module and a battery.

Animal care and handling practice is going to be over the official Mexican code NOM-062-Z00-1999; with the understanding with the Facultad de Medicina Veterinaria y Zootécnica of the Universidad Veracruzana bioetic rules. Testing stage will be done in the Posta Zootécnica "Torreón del Molino" farm.

IV. HARDWARE SYSTEM

A. Temperature Sensors

A semiconductor temperature sensor provides a transfer functions that is proportional to temperature on °K, °C or °F. In most applications, output signal supply a compare or an A/D converter to transform data temperature into a digital format. A silicon temperature sensor is an integrated circuit (IC) that can contain a circuit to process the signal and handle the cold junction compensation or linearization inside the same IC [5].

LM35 is a precision integrated-circuit temperature device with an output voltage linearly-proportional to the Centigrade temperature, does not require any external calibration or trimming to provide typical accuracies, temperature range is -55°C to 150°C. The device is used with single power supplies, or with plus and minus supplies. And it has a linear +10 mV/°C scale factor [6].

To observe the temperature sensor functionality, it was implemented a comparison between LM35 IC and a mercury thermometer, it was done with a gradual increase (Fig. 2).

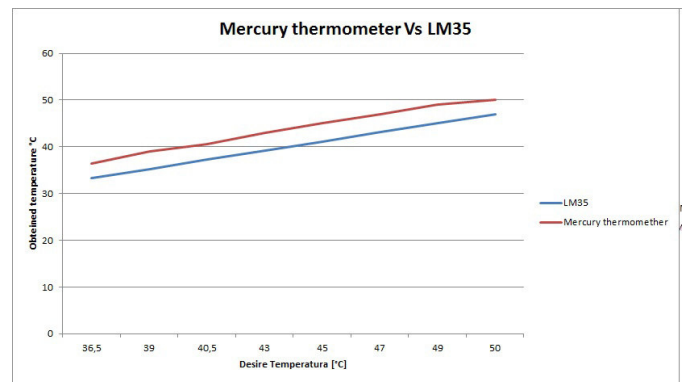


Fig. 2. LM35 and mercury thermometer lineal response.

We can see that the sensor behavior is like expected with a lineal response, but there is an offset that was fixed with a digital adjust with a program on LabView™ (Fig. 3).

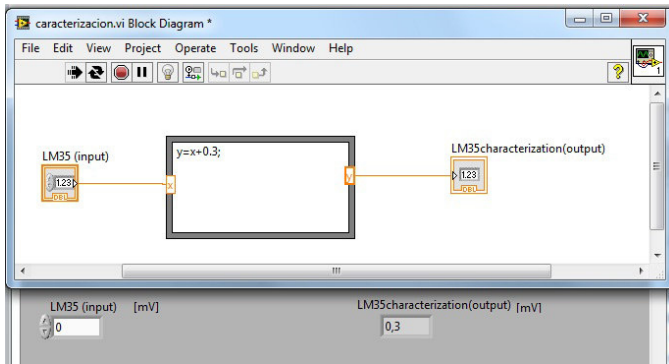


Fig. 3. LabView program for LM35 characterization.

Finally, after LM35 characterization the obtained data is shown on table 1 and lineal response on Fig 4.

TABLE I. TABLE TYPE STYLES

DESIRED TEMPERATURE [°C]	MERCURY THERMOMETER [°C]	LM35 CHARACTERIZED [°C]
36	36.5	36.43
39	39	38.39
40	40.5	40.35
43	43	42.31
45	45	44.27
47	47	46.33
49	49	48.19
50	50	50.15

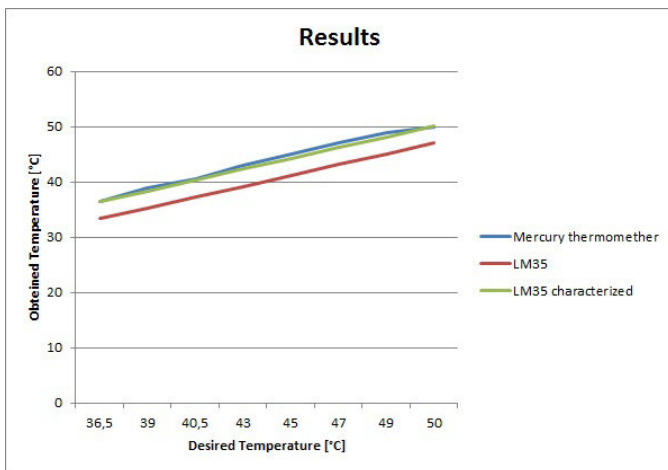


Fig. 4. LM35 characterized response.

B. pH Sensors

pH measuring is based on an electrode sensible to pH, a reference electrode and a temperature element. pH electrodes use a pH sensitive glass bulb that in contact with a solution produces a proportional potential to the pH in the solution. Reference electrode is designed to maintain a constant

potential at any temperature and also to close the loop into the solution. The difference between pH potential and reference electrode proportionate a signal that is in millivolts range directly proportional to pH. Most of the pH sensors are design to produce 0mV in a 7.0 pH, with a slope of -59 mV/pH at 25°C (Fig. 5) [7].

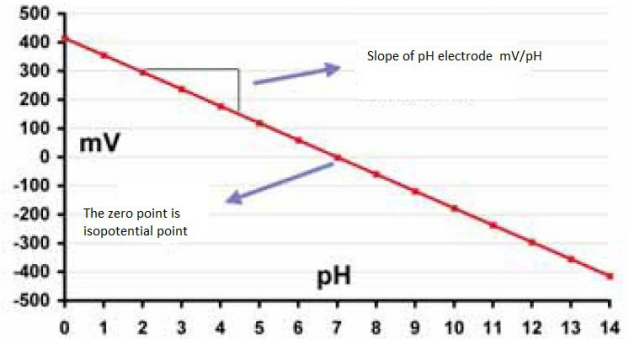


Fig. 5. Theoretical behavior of a glass electrode.

A combined electrode has a concentric space surrounding the measuring electrode is filled with the reference electrolyte and contains the internal reference system. A diaphragm near the bottom of the electrolyte chamber serves as the junction between the KCL solution and the measured medium. As the reference electrolyte is a conductive medium, it acts as a screen to the measuring electrode. The search for a maintenance-free electrode assembly led to the development of the gel reference electrode which chamber is filled with 3 mol/l KCL electrolyte in gel form. The diaphragm is normally made from ceramic. The glass shaft is often reinforced with an outer plastic sleeve or the electrode shaft is made completely out of plastic [8].

A combine electrode was used in this work due the biggest benefits; a combine electrode by Sensorex was purchased. Its main specifications are: SG200C model, 0-14 pH range, isothermal point at pH 7.0 to 0 mV, 12mm diameter, 150mm large, glass body and Ag/AgCl reference (Fig. 6).

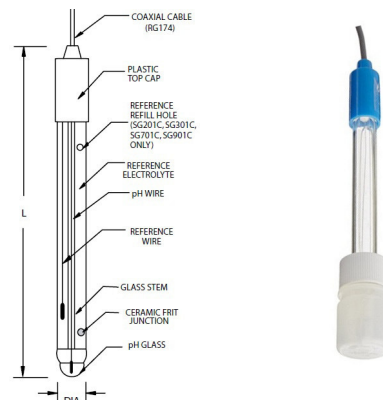


Fig. 6. SG200C combine electrode by Sensorex.

1) SG200C sensor characterization

It is very important to mention that an elemental characteristic of the glass electrode is, that its impedance is in the range of $10M\Omega$ - $100M\Omega$; for this reason it was selected to work with TL084 operational amplifiers due they have a input impedance in the order of $10^{12}\Omega$.

PH measuring was done with buffer solutions of pH4, pH7 and pH10.

- High electrode impedance was mentioned before, for this reason the first stage is the impedance matching with an operational amplifier. A voltage follower configuration is typically used as a buffer to connect a source with high impedance to a low impedance load.

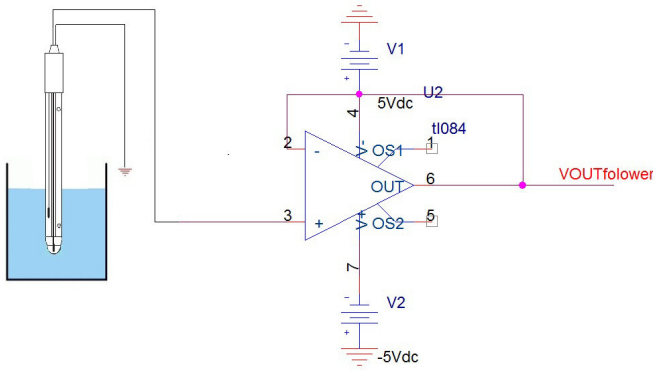


Fig. 7. Impedance matching with voltage follower configuration.

- When working with electrochemical solutions, there are fluctuations in the potential and/or current, this situation added with a high impedance produce higher voltage noises. To solve this situation the next stage was to implement low pass filters in cascaded (Fig. 8), with a frequency of 10Hz. The first order active low pass filter was made with a resistor, capacitor and an operational amplifier.

Cutoff frequency is determined by

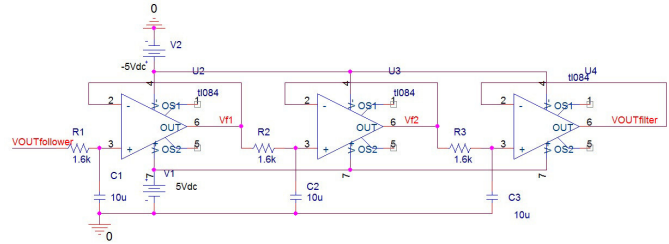
$$f_c = 1/(2\pi RC) \quad (1)$$

Based on the cutoff frequency of 10Hz and a resistor value of $10\mu F$, the resistor value can be calculated as

$$R = 1/(2\pi f_c C) = 1/(2\pi(10Hz)(10\mu F)) = 1592.54\Omega \quad (2)$$

The frequency dependence for the 3 low pass filters in cascaded is described in (3)

$$H(j\omega) = 1/((1 + j\omega R_1 C_1) + (1 + j\omega R_2 C_2) + (1 + j\omega R_3 C_3)) \quad (3)$$

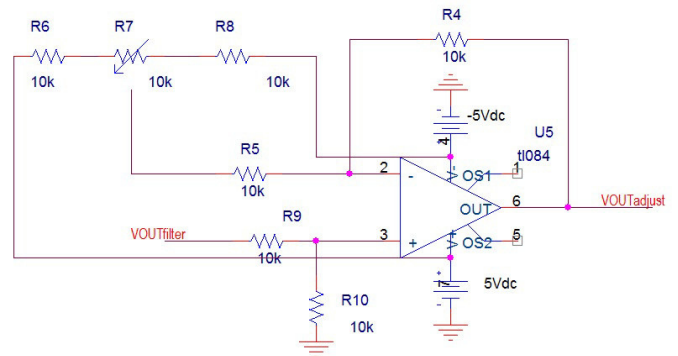


$$\text{Making } C_1 = C_2 = C_3; R_1 = R_2 = R_3$$

The implemented circuit is shown on Fig.8.

Fig. 8. Low pass filters in cascade with a cutoff at 10Hz.

- One of the combined electrode characteristics is the isothermal point is in pH 7.0 at 0mV. For this reason the next stage is to calibrate this point at a pH buffer solution of 7.0.



To set this adjust a differential operational amplifier was designed, with a potentiometer to adjust the isothermal point (Fig. 9).

Fig. 9. Calibration system with a differential operational amplifier.

The equation that describes the calibration system is

$$V_{out\,adjust} = V_{out\,filter} - V_{potentiometer} \quad (4)$$

- Last stage consists of a voltage range fitting, to be in optimal conditions for a digital conversion, also to not saturate the operational amplifier the range is established on 0V to 4V.

The transfer function for this stage is

$$V_{out\,range} = -R_{14}((-V_{out\,adjust} R_{11} / R_{12}) + (V_{out\,2V} / R_{16})) \quad (5)$$

The implemented circuit is in Fig. 10.

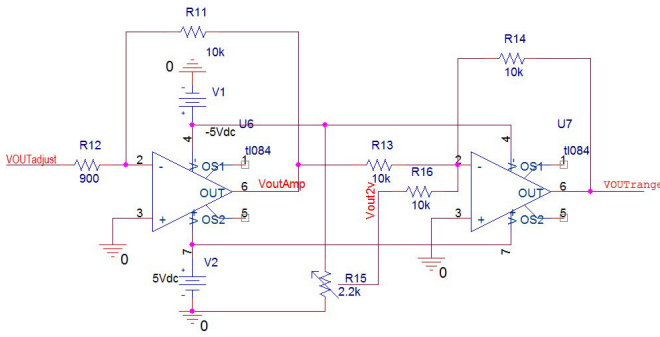


Fig. 10. Fitting voltage range circuit.

The obtained data in the last stage is shown on Table II. The actual measuring system whit the glass electrode presents an average sensitivity of 510 mV/pH.

TABLE II. OUTPUT VALUES AFTER FITTING CIRCUIT

pH	VOUT [V]
4	3.672
7	2.013
10	0.611

C. Signal Digitalization

Now that the signal is in optimal conditions, it can be introduced to an analog to digital converter. An ADC0804 was used, and it has a 8 bits resolution. ADC0804 configuration can be seen on Fig.11. Now the next step is to introduce digitalized signal into a microcontroller.

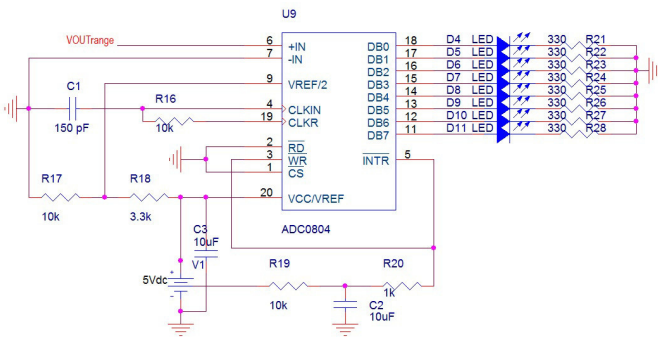


Fig. 11. ADC0804 configuration.

D. Bolus Design

Bolus is a housing to protect the electronic system from the biochemical outside environment and also to give a mechanical support.

The bolus design was made with LabView™ software, some of the parameters to consider are that inside diameter of the cannula is 10.8cm and the omasun conduct has a dimension of 20cm; for this reason for this design dimensions are 9.5 cm of diameter and 25cm of length.

On the cover of the bolus a pocketing was done to facilitate the extraction of the bolus from the rumen inside. Sensors will be in contact with the outside environment through some holes around the walls cover. The inside is divided into four areas: two areas to place the sensors, a compartment to place the battery and the last one for all the electronic (Fig. 11).

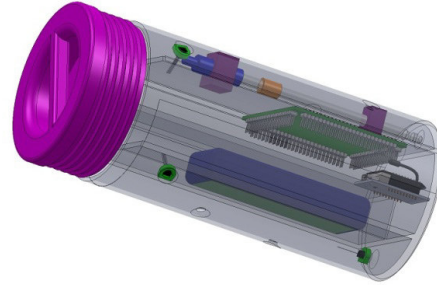


Fig. 12. Bolus design with components distributions.

V. MONITORIN SYSTEM DESIGN

The proposed user interface was designed with LabView™ software. In this interface processed data will be displayed in real time on a workstation (Fig. 13).



Fig. 13. Monitoring software design.

The temperature data is on a range of 25°C to 45°C, for the pH data is on a range of 4.5pH to 7pH.

The interface is divided on two sections:

- 1)Monitoring data: start communication, variable sensyng and information display.
- 2)Storage data: the receveided data will be storage on a text file.

VI. CONCLUSIONS

LM35 precision temperature sensor has an output voltage that is proportional to temperature in Celsius, with the main characteristic that it do not need external adjust, this point is

very important due the application is going to be inside the rumen. LM35 IC presented a good performance in the experimental testing; LM35 IC comparison with the mercury thermometer testing was also done in the laboratory with a regulated temperature increase. Results showed that the LM35IC follows the same response as the mercury thermometer.

In the market there are two classifications for pH measuring systems: optical and electrochemical sensors. Optical sensor (indicator strips) have a low cost and do not proportionate a good precision. In the electrochemical sensors there are some with ISFET technology but the main problem is that they are very expensive; another sensor in this classification are the glass electrode that are more often used in laboratory applications, with a lower cost than the ISFETs. After analyzing pH sensor and the purpose of this application, a glass electrode was the best option to be used. The system has the size limitation, for this reason the best option in the glass electrode area is the use of a combine electrode which includes the electrode sensible to pH, a reference electrode and temperature elements. One disadvantage that this sensor presents is the high impedance, but it was resolved with the appropriate use of elements. On experimental testing combine electrode presented a slope of 46 mV/pH.

Bolus had to be designed considering the environment where is it going to be placed, in this case rumen composition and dimensions. Bolus will be manufactured on a 3D printer with a polylactic acid (PLA) material that is biodegradable thermoplastic aliphatic polyester.

For data transmission is it necessary to use a wireless technology; a RN-171-XV module was choose for this application, which use the 802.11 protocol, on field testing module presented an average transmission of 5.4 meters.

A Microcontroller is proposed to be used for the data processing, the data acquisition board has to fit with the requirements of the applications like low power consumption, UART transmission and the most important with the appropriate size to fit in the electronic are in the bolus.

Finally with this prototype design it will be possible to obtain data from the rumens inside behavior to support veterinarian's research about cattle population's ability against reduced thermal comfort environments.

ACKNOWLEDGMENT

Finally with this the authors would like to thank the support of CONACyT and to Programa de Estudios sobre Cambio Climático de la Universidad Veracruzana, for the fulfillment of this research work.

REFERENCES

- [1] Gobierno del estado de Veracruz, "Programa veracruzano ante el cambio climático", pp. 54-57, 2009. Available from: http://www2.inecc.gob.mx/descargas/cclimatico/e2008a_pvcev2.pdf
- [2] Laboratorios Virbac México S.A. de C.V., "Aspectos generales sobre el rumen y su fisiología", Available from: <http://www.virbac.mx/index.php/especiesanimales/bovinoscarne/publicaciones/224-aspectos-generales-sobre-el-rumen-y-su-fisiologia>.
- [3] H. Román Ponce, R. Aguilera Sosa, and A. Patraca Fernández, "Producción y Comercialización de Ganado y Carne de Bovino en el Estado de Veracruz", 2012.
- [4] Sonia Salazar L. et al., "La ganadería bovina: vulnerabilidad y mitigación", pp. 1-4, Available from: http://peccuv.mx/wp-content/uploads/pdf/reportes_investigacion/Cap%C3%ADtulo%205%20La%20Ganader%C3%ADa%20Bovina.pdf.
- [5] A. Creus, "Instrumentación industrial", 8th ed, México, 2010, pp. 253, Available from: http://www.academia.edu/8286258/Instrumentacion_industrial_-_Creus_8th
- [6] Texas Instruments, "LM35 Precision Centigrade Temperature Sensors", 2013, Available from: <http://www.ti.com/lit/ds/symlink/lm35.pdf>.
- [7] EMERSON Process Managements, "Application Data Sheet", 2010, Available from: http://www2.emersonprocess.com/siteadmincenter/PM%20Rosemount%20Analytical%20Documents/Liq_ADS_43-002.pdf.
- [8] Erich Springer, "HAMILTON the measure of excellence", 2006, Available from: http://www.hamiltoncompany.com/downloads/E_610277_04%20with%20Pathfinder.pdf.
- [9]

Minimum-latency Pipeline Embedded Processor on FPGA

Isaias Cueva-Perez ^{#1}, Jesus Ivan Sanchez-Gomez ^{#2}, Luis Morales-Velazquez ^{#3}

[#] *Facultad de Ingeniería, Universidad Autónoma de Querétaro
San Juan del Río, Querétaro, Mexico*

¹ isaiasc3@hotmail.com

² jesus.sangomez@gmail.com

³ lmorales@hspdigital.org

Abstract—Embedded systems are becoming more and more popular in automation and mechatronics, giving more flexibility and “intelligence” to machines. It is well known that the fundamental unit in an embedded system is the central processing unit (CPU) or processor, then the performance of the system heavily depends on the processor capabilities. In mechatronics, the main system requirements are processing speed, flexibility, and low-cost; thus, field programming gate array (FPGA) devices seem to be a good choice. However, the FPGA world involves a knowledge curve that for some developments is too long. The option is to use an embedded FPGA processor to accelerate the development time. Although not all processors will meet the performance goals for the selected application, due to its internal architecture in most of the cases. This work presents the development of a new embedded processors the xQ116v0, this processor tries to close the gap between high performance and low-cost. The xQ116v0 is a 16 bit Harvard RISC processor with an improved architecture to keep the instruction latency at its minimum. The processor was developed in VHDL code, tested and implemented in FPGA, results demonstrate that the processor works properly by having a reduced resource use as low as 7% at 100MHz in a low-cost Spartan 6[®] device.

Keywords—FPGA; embedded processor; pipeline; minimum-latency

I. INTRODUCCION

In the embedded systems world, there are plenty of processors options, even for target-specific FPGA embedded processors there is an abundance of them. This variety is probably because embedded processors overcomes most of the complexity involved in the low-level digital design. By integrating an embedded processor core and some other special purpose cores, e.g.: I2C, DDR, PWM, among others, the product time-to-market is reduced [1]. In addition, the designer programming expertise is exploited, reducing their training effort to learn a new hardware description language (HDL) such as VHDL or Verilog. Popular embedded processor cores are: 68HC08[®], 8051[®], PIC16F84[®], picoBlaze[®], microBlaze[®], Nios II[®], LEON, SecretBlaze among others; the first four are 8 bits and the last four are 32 bits. Embedded 16-bit processor cores like: C16 [2], Caxton Foster's Blue [3], and some

academic endeavors [4-10] are also available. Most of embedded processors are not designed specifically for FPGA; however, they are synthesizable but utilize many FPGA resources. In the case of embedded processors like picoBlaze[®] and microBlaze[®] from Xilinx and Nios II[®] from Altera, they have an FPGA optimal architecture but they are fixed to their vendor devices. Nevertheless, processors like LEON3 [11] and SecretBlaze [12] are specially designed for FPGA and make an optimal FPGA resource usage in a vendor independent philosophy but for some low-cost applications those processors are quite expensive in area. Although, there exist a vast amount of options in processors, it is difficult to select a low-cost and high performance processor for applications in mechatronics [13] due to its requirements, for instance low latency in the interruption service and low latency in data bus accesses. Most of high performance processors are targeted to multimedia processing that promote processing speed over interrupt handling. While low-cost processors are only for academic or didactic purposes. There is not an option of a processor targeted for mechatronics, thus the challenge is to develop a processor within a good balance between performance and low-cost resource utilization in a didactic design way.

This article presents the development of a new processor with an improved architecture that reduces the latency in the processor pipeline giving high performance at a low-cost. In addition, this new processor is specially designed for low-cost FPGA platforms.

II. PROCESSOR ARCHITECTURE

A. Embedded System Architecture

There are many types of system architectures seen from different points of view [13]. However, from the hardware point of view it is common to represent the system as blocks that are interconnected via a dedicated bus, as depicted in Fig. 1.

Fig. 1 shows a common hardware architecture for an embedded system that consist on a central processing unit (CPU), a memory handler (MMU), a bus interconnection, and many peripheral units. The CPU is the essential core of the system, because it is in charge of the program execution.

This work was partially funded by Universidad Autónoma de Querétaro, FOFI-UAQ 2013, Project number FIN201424.

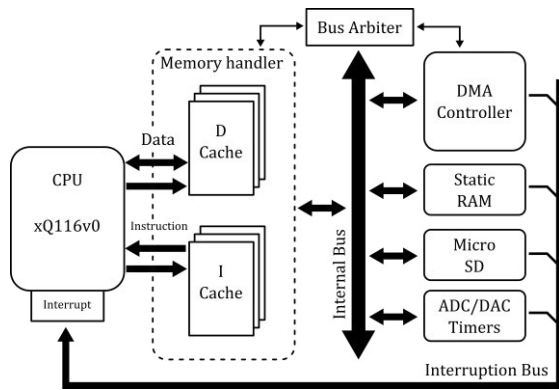


Fig. 1 Embedded system architecture diagram.

The MMU block controls the information access (instructions and data) contained in memory for the process. The bus interconnection is used to transfer data from one module to another. Finally the peripherals are dedicated modules that perform ad-hoc tasks depending on the application of the embedded system such as: storage, digital signal processing (DSP), data acquisition, among others.

This work is centered in the operation of the CPU unit; from this perspective, we apply some constraints to the system to make it simpler and cost-effective. First, the CPU is a reduced instruction set computer (RISC) processor with a Harvard architecture. Second, the memory model uses virtual memory-addressing which requires the MMU unit to decode the address to a physical address. Third, the MMU shall contain two separate caches: instructions and data. Those restrictions aim to isolate the processing task of each unit in the system to increase the parallelism and improve the overall performance.

The performance on a processor is often measured in peak or average number of operations executed per second, in units of millions of instructions per second (MIPS). One way to improve the performance of a processor is to increment the main clock frequency, but physical devices have very strict limits due to the signal propagation time over semiconductors; thus, maximum frequency heavily depends on the semiconductor manufacturing process that is beyond the scope of this work. Other way to improve the performance of a processor is designing a hardware architecture that uses parallelism whenever possible. Earlier processor architectures used a sequential structure while modern ones use a pipelined structure. As an example in Fig. 2a, the process of each instruction is performed sequentially, for each instruction four stages are computed sequentially: writes back the result of the previous instruction, fetches the next instruction, decodes the current instruction, and executes the current instruction. Processors such as Microchip PIC16 family [14] use a sequential approach that takes 4 clock cycles for each machine cycle, most of the instructions are executes in one or two machine instructions. Another example is the Intel 8051 [15] that takes 12 clock cycles per machine cycle, each instruction takes one or two machine cycles to execute. On the other hand, the pipelined architecture processes all stages concurrently one instruction per stage, ideally processing one instruction per each clock cycle, see Fig 2b, the number of stages at the pipeline is named pipeline depth. Modern processors such as

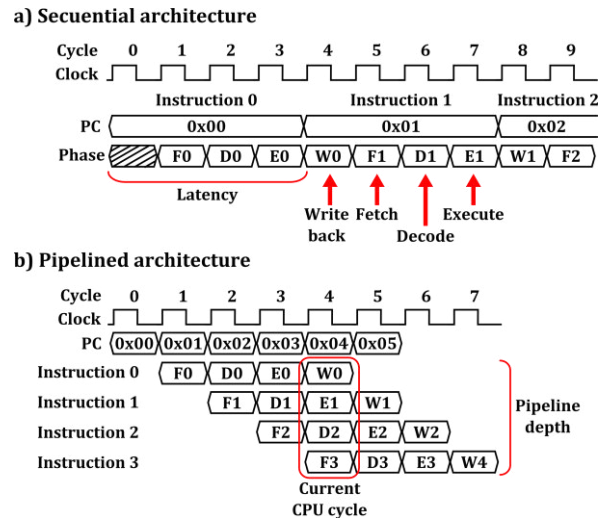


Fig. 2 CPU processing approaches: a) sequential and b) pipelined.

ARM Limited Cortex A8[®] [16] have a pipeline depth of 13 stages. Some embedded processors such as Nios II[®] [17] and MicroBlaze[®] [18] that have a pipeline depth of 5. Processor pipelining have some performance benefits but also have some drawbacks: in deeper pipelines the latency (number of cycles that takes to process an instruction from the first to the last stage) is increased, if the next instruction requires some data that have not been processed the pipeline shall halt to avoid unexpected results. Those mentioned problems impacts the processor performance mainly when the program executes jumps.

The main benefit in using a pipelined architecture is the throughput improvement, as seen in Fig. 2, while a sequential architecture at seventh cycle finishes instruction 1, the pipelined have completed instruction 3. However, in a jump instruction (branch), the flow of the program changes, so the pipeline shall be cleared (flush) introducing latency stages (miss). Modern processors use branch prediction algorithms in order to reduce the miss rate; nevertheless, those algorithms are complex and for low-cost processors are unaffordable. Thus, the alternative is to reduce the pipeline depth to reduce the latency, this requires a processor that implements a compact and efficient structure.

B. Internal architecture

This work presents a new processor (xQ116v0), this has a 16-bit Harvard RISC architecture which uses a pipeline of 3 stages: fetch, execute, and write. As mentioned, the reduction in the pipeline depth reduces the latency, even so the challenge is to perform all calculations on time and orderly. The diagram of Fig. 3 shows the internal architecture of the processor. As shown in Fig. 3, the pipeline has three stages delimited by dashed lines that represent flip-flop (FF) registers. The fetch stage increments the program counter (PC) to get the next instruction from the program memory. At the same time, it selects the register address to be read calculations. The execute stage performs the arithmetic-logic operations in the arithmetic-logic unit (ALU) and sets the virtual address for the data bus. The write stage saves the result value in the destination register.

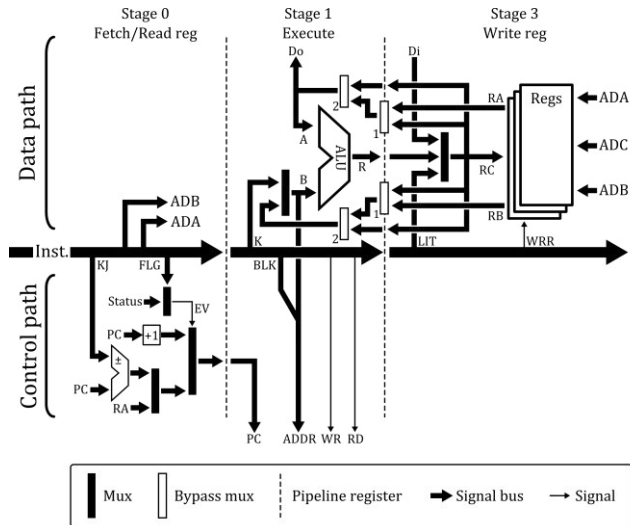


Fig. 3 Internal architecture and pipeline for the xQ116v0 processor.

The proposed processor architecture separates data and control paths. Data path gathers ALU, registers, and data routing. Control path includes PC, address generator (AG) unit, and bus control signals: read (RD) and write (WR). This processor does not have a decode stage because its instructions are decoded on each stage according to a special instruction encoding that simplifies the task.

The data path performs operations on the ALU with the source operands A and B, source operands are selected depending on the instruction by the routing multiplexers (Mux). The registers load the ALU result or a literal encoded in the instruction or data from the bus (D_i). A special routing multiplexers (Bypass mux) were introduced to handle hazards when the current instruction needs a result that is not available yet. In addition, this processor keeps a hardware stack to speed up the context saving process in function calls.

The control path handles data and instruction addresses buses, data address is created by the content of a register and the block segment contained in the instruction; where the program counter is automatically incremented or loaded from a register in the jumps.

C. Instruction set

The xQ116v0 is a RISC processor with only 31 instructions that executes in a single clock cycle. Instructions are divided into four groups: control operations, register operations, load/store operations, and literal operations, as indicated in Table 1.

Instructions in Table 1 have different parameters, each parameter is properly decoded in the corresponding pipeline stage, e.g. control operations are decoded in the first stage of the control path, see Fig. 3. Note that each instruction have a unique identification sequence on the most significant bits named operation code (opcode). In addition, some instructions have option code, e.g. register operations have 4-bits option that are decoded by the ALU, Table 2 shows the complete set of options for arithmetic and logic operations.

Table 1 Instruction set groups.

Description	Encoding
Control operations	
No operation	0000000000000000
Status register	000001p-----aaaa
Interruption handling	00001ppp-----
Cache control	0001ssssbbbbpppp
Jump/call	001kkpppfffffaaaa
Register operations	
Register to register	010-ppppbbbbaaaa
Literal to register	011-ppppkkkkaaaa
Load/store operations	
Load from memory	100pssssbbbbaaaa
Store to memory	101pssssbbbbaaaa
Load literal	
Load literal to register	11pkkkkkkkkkaaaa

a : register A address s : memory segment
b : register B address k : constant
p : instruction option - : do not care

The ALU supports only integer operations, floating point operations should be handled by software routines or by a hardware floating point co-processor.

The instruction set encoding was specifically designed to use a minimum of decoding resources on each pipeline stage, where all registers are orthogonal on behalf of simplicity.

Table 2 ALU option instruction encoding.

Description	Mnemonic	Option	Status	Operation
Addition	ADD	0000	Z,C	$R = A + B$
Carry-in addition	ADDC	0001	Z,C	$R = A + B + C$
Subtraction	SUB	0010	Z,C	$R = A - B$
Borrow-in sub.	SUBC	0011	Z,C	$R = A - (B+C)$
Bit-wise AND	AND	0100	Z	$R = A \& B$
Bit-wise OR	OR	0101	Z	$R = A B$
Bit-wise XOR	XOR	0110	Z	$R = A \wedge B$
Bit-wise NOT	NOT	0111	Z	$R = B'$
Copy register	MOV	1000	Z	$R = B$
Multiply low-byte	MULT	1001		$R = A_l * B_l$
Shift right	SHR	1010		$R = A \rightarrow B_n$
Shift left	SHL	1011		$R = A \leftarrow B_n$
Compare	CMP	11--	L,E,G	$CMP(A,B)$

III. INSTRUCTION EXECUTION PROCESS

This section presents a detailed explanation regarding the way that the processor executes a code segment and the implications of latency.

To make this explanation didactic we have selected a simple algorithm that computes the first ten numbers of the Fibonacci sequence: 1,1,2,3,5,8,13,21,34,55. This sequence can be expressed as in (1), where the next value is the addition of the two previous values in the sequence.

$$f_n = f_{n-1} + f_{n-2} \quad (1)$$

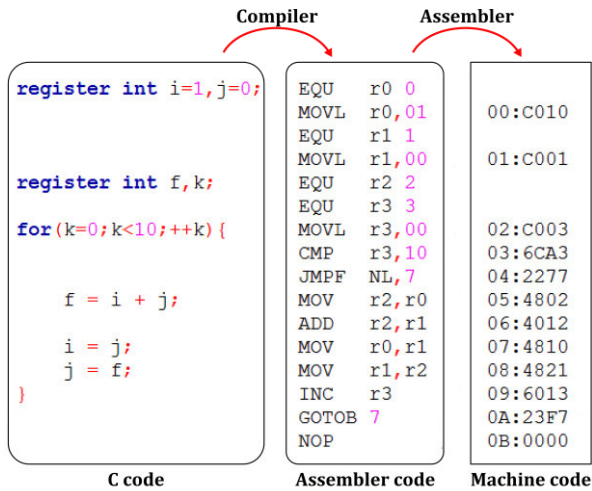


Fig. 4 C-code and its equivalent assembly and machine code for Fibonacci algorithm.

Fig. 4 shows the C-code and its equivalent assembly and machine code for the iterative algorithm in the calculation of the Fibonacci sequence.

Machine code is very difficult to follow by humans, for this reason a high-level tools have been developed to make affordable the programming of computers. The process to translate a C-code expression to its equivalent assembly code is performed by a compiler, then another tool converts assembly code into machine code that can be directly executed in the processor. In Fig. 4 row spacing was inserted to show the equivalence in the three formats. In the machine code segment of Fig. 4, the first datum represents the address separated by a colon and then the instruction code in hexadecimal representation.

When the processor executes a code segment, it is first loaded in the I-Cache, then the fetch stage loads the instruction and starts the process depicted in Fig. 2b. As example, the code execution sequence in Fig. 4 is shown in Fig. 5.

The execution sequence of Fig. 5 shows a time diagram to represent instructions execution for the Fibonacci algorithm. Fig. 5 is structured as follows, the upper region shows the

current clock cycle and the instruction address (PC), the instruction is ready one clock cycle after PC sets. The left region of Fig. 5 shows the instructions in its execution order instead of in the program order as in Fig. 4. The main area of Fig. 5 shows the pipeline status at each clock cycle, there are some marks around the pipeline status that indicates abnormalities in the natural flow of the program that will be discussed in detail.

To begin with, instruction 0 loads a literal straight to the register r0, in spite of this the desired value in the register is obtained at cycle 2 on the third clock cycle due to initial latency in the pipeline; meanwhile, instructions 1 and 2 are loaded in the pipeline. In processors with a deeper pipeline the initial latency increases with pipeline depth so the proposed processor reduces the latency to only 2 clock cycles. When the processor tries to execute instruction 3, the first hazard arises, because instruction 2 has not finished writing register r3 when the instruction 3 request this value for the comparison; so the result of the ALU is directly fed through the bypass mux 1 of Fig. 3 giving the correct result. In the execution of instruction 6 happens the same as in instruction 3 and same solution is applied. On the other hand, at the execution of instruction 8 a different hazard is reached when this instruction needs the value of r2 processed by instruction 6. In this case the value is properly written on register r2 at cycle 10 but the F8 stage takes place at cycle 9, thus a bypass mux 2 must be used to solve the problem. In the execution of instruction 10 an unconditional jump backward is performed, the instruction jumps back 7 instructions to instruction 3 making the comparison of r3 again. If the comparison result is false, then the instruction 4 performs a forward jump of 7 instructions to instruction 11, terminating the *for* loop. When a jump is taken a bubble is generated because fetched instructions must be flushed. This jump latency is only 2 clock cycles long for the xQ116v0 processor, for processor such as Nios II[®] with a pipeline depth of 5 the jump latency is 4 cycles and for ARM Cortex A8[®] with a pipeline depth of 13 is 12 cycles.

IV. TEST AND RESULTS

The proposed processor xQ116v0 was implemented in a VHDL code based on the architecture of Fig. 3, then it was

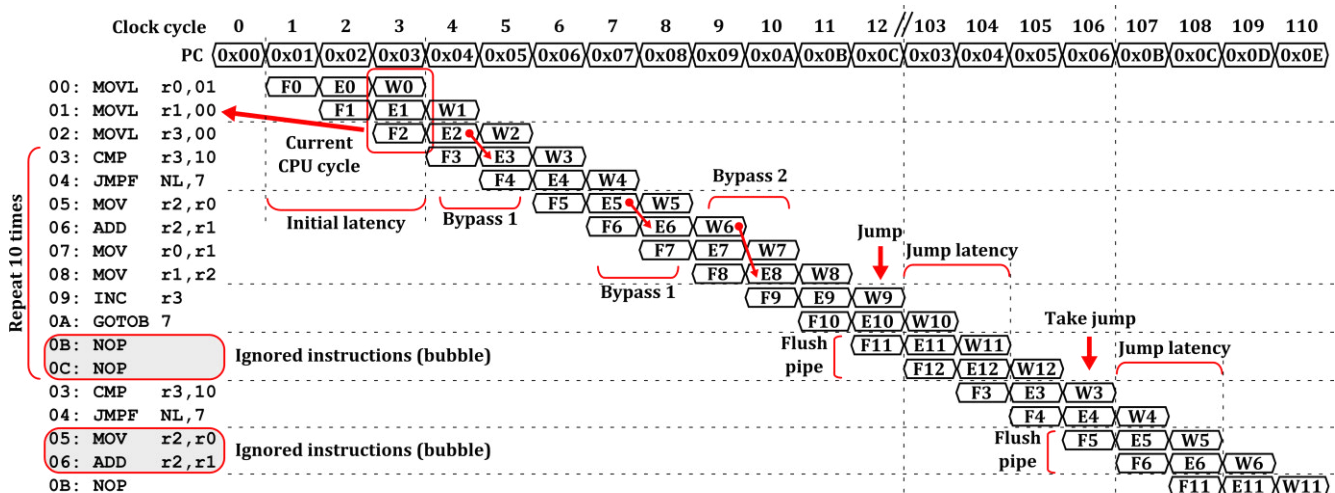


Fig. 5 Execution sequence for the Fibonacci algorithm.

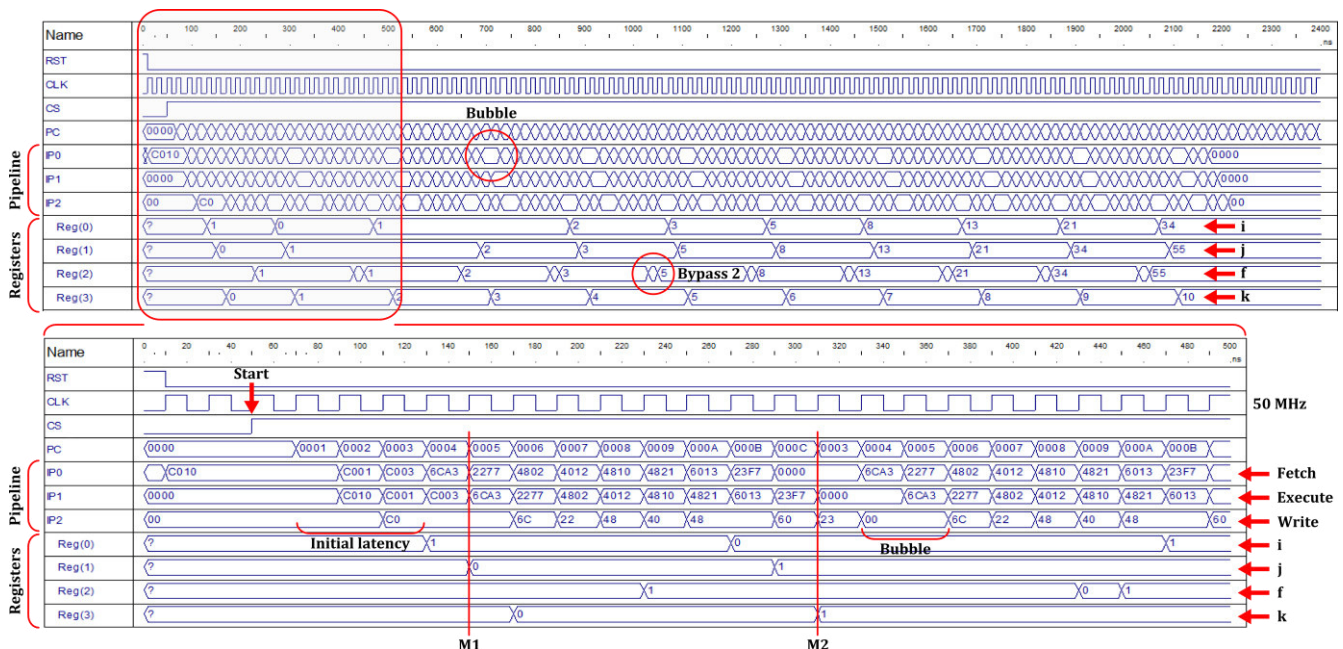


Fig. 6 Simulation result for the Fibonacci algorithm.

implemented in FPGA. It was verified using the AldecHDL[®] simulator and implemented using the Xilinx ISE[®] platform in two Spartan devices. The processor test was performed by using the Fibonacci algorithm discussed in the previous section.

A. Simulation test and results

The processor simulation was done by a test bench described in VHDL with the program generated by the assembler for the Fibonacci algorithm of section III.

The simulation result shown in Fig. 6 presents the complete execution for the 10 iterations of the Fibonacci algorithm that is completed in 2,200 ns by using a 50 MHz clock, giving a final count of 110 machine cycles. The lower half of Fig. 6 presents a zoom for the region from 0 ns to 500 ns for a better visualization of the simulation test. The Fig. 6 shows the following signals: reset (RST), clock (CLK), chip select (CS), the program counter (PC), the pipeline content (IP0, IP1, and IP2) and the content of registers 0 to 3. The RST and CLK signals work as usual for a digital system, CS when goes low the processor stops and when goes high the processor starts. In the pipeline the IP0 corresponds to the fetch stage, the IP1 corresponds to the execute stage, and the IP2 corresponds to the write back stage. Register content correspond to the variables assignation given by the compiler, r0 to *i*, r1 to *j*, r2 to *f*, and r3 to *k*.

There are some things to note in Fig. 6, first we must be sure that the algorithm does computations successfully, take a look to the register 2 aka *f*, it contains the right sequence for the Fibonacci series; thus, the algorithm execution is well done. Second, we check if the process is completed in the expected number of cycles, from Fig. 5 we see that the code inside the *for* loop is repeated 10 times since this code takes 10 instructions giving a total of 100 cycles plus the 3 initial and the last 5 instructions giving a total of 108 cycles plus 2 latency cycles to complete the execution in the pipe, giving 110 cycles for a total computation, at 50 MHz it lasts 2,200 ns. Comparing with the simulation result on Fig.6, it takes 2,200 ns to

complete computations, thus execution time is right. Third, there are some interesting points to observe: just after taking a jump, a bubble is generated and propagated through the pipeline as expected. Another is that a transitory datum is loaded in *f* when bypass 2 is activated because the correct data was fed-backed by the FF in front of bypass 2 in Fig. 3. In addition, mark M1 indicates the moment when instruction 2 is executed and the result of instruction 1 is written in register 1. The mark M2 indicates the moment in which a jump is taken changing the PC to 3 instead of the default PC+1, at the same time in which the jump is taken, a bubble is generated taking 2 cycles to complete.

Since bubbles are used to avoid the execution of miss prefetched instructions they, also represent a performance penalty due to its consumption of time. In the execution of the example code on Fig. 6 the entire algorithm uses 110 cycles and every iteration produces a bubble, this is 20 clock cycles of NOPS that represents the 18% of execution time. In processors with a deeper pipeline the problem grows, thus is a common practice in many processors to implement a branch prediction logic to reduce the time processing NOPS due to pipeline flushes. In the developed processor an optional simple branch prediction algorithm was also implemented to reduce the latency of unconditional jumps from 2 cycles to 1 cycle, this reduction means the introduction to only 12 bubble cycles for the entire process, using only the 11% of the computation time in NOPS instead of 18%; additionally, the total time was reduced to 2 us.

B. Implementation results

The new developed processor was implemented in FPGA to check the proper instantiation of logic blocks from the VHDL code to the FPGA netlist. In addition, the implementation results are compared with another two processors of the same family, previously developed xQ16v3 in [19] and xQ16v7 in [20], those are proprietary processors. By using the Xilinx ISE[®] 14.4 the three processors were implemented in two FPGA devices one Spartan 3E (XC3S500E) and one Spartan 6 (XC6SLX16). The aim of

using this two devices is to find out if there is a real performance improvement with the same architecture. The implementation results are shown in Table 3, where the percentage of device use is reported as well as the maximum frequency reached and the performance peak. The percentage of use refers to the number of occupied slices in relation with the total number of slices present in the device.

The maximum frequency in FPGA devices changes in every design because this is constrained by the longest combinatorial path in the design plus the routing resources used. Then a good design implies a balances between combinatorial and sequential logics to allow largest frequencies. And finally, since the three compared processors use similar instruction sets, a performance comparison is also shown, measured in MIPS.

Table 3 Implementation results for various processors in two FPGAs.

Processor	XC3S500E			XC6SLX16		
	% use	Max. Freq.	P.*	% use	Max. Freq.	P.*
xQ16v3	6%	56.38 MHz	54	4%	78.61 MHz	78
xQ16v7	14%	69.49 MHz	34	7%	94.03 MHz	47
xQ116v0	9%	62.72 MHz	62	7%	100.56 MHz	100

* P.: Performance measured in MIPS.

The results in Table 3 show that the processor with lowest resource use is the xQ16v3 for both devices, but it is a small processor, it is limited to handle 1k of program memory, which for many applications is insufficient. The xQ16v7 is a bigger processor than the xQ16v3, but it uses more than the double of resources; in addition, each instruction takes 2 clock cycles bringing a performance reduction. The new developed xQ116v0 use fewer resources than the xQ16v7 but thanks to its pipelined architecture, it reaches the highest performance in both devices. Although, the xQ116v0 is a 16 bit processor which has similarities with other popular FPGA 32 bit processor cores like Altera Nios II® [17] and Xilinx MicroBlaze® [18] in area and performance within equivalent devices, the main advantage of the xQ116v0 is its vendor independency. The xQ116v0 is a low-cost processor because it occupies a small area, since the price of the tested FPGA devices is below \$30.00 USD a 7% gives an approximate cost of \$2.10USD by the used area. However, there is another associated cost that should be considered in an embedded system design and implementation but they are beyond the scope of this work.

V. CONCLUSIONS

This work presents a new embedded 16-bit processor (xQ116v0) for FPGA with an improved architecture to reach high performance at low-cost. This paper gives a general overview about the way in which a processor works, discussing some common problems in the processors design world. With the intention of making a didactic approach to the processor design world, it was selected a simple example based on the Fibonacci algorithm to illustrate the latency problem and hazards in the pipeline architecture. As a result, it was demonstrated that the xQ116v0 has a minimum latency of 1 or 2 cycles, depending on the optimization level, compared to the 4 to 12 latency cycles in common processors [15-18]. In addition, the FPGA implementation results yield a high

performance and a low resource use of the processor, making it an option for low-cost embedded systems. Nevertheless, to provide a complete platform further work should be done, for instance, tools for compiling, optimization, simulation, etc.; those tools are currently under development. In conclusion, the xQ116v0 processor is a new vendor independent which is a high performance option for FPGA embedded designs.

ACKNOWLEDGMENT

The authors wish to thank Gavina Quintanar who assisted in the language reviewing of the manuscript.

REFERENCES

- [1] W.A. Najjar, "Compiling code accelerators for FPGAs," in Proc. Hardware/Software Codesign and System Synthesis, Int. Conf. on, Salzburg, Oct. 2007, pp. 2.
- [2] OpenCores, <http://www.opencores.org>.
- [3] C.C. Foster, T. Iberall, "Computer Architecture," Van Nostrand Reinhold, 3th Ed., 1985.
- [4] P.H.W. Leong, P.K. Tsang, T.K. Lee, "A FPGA based Forth microprocessor," in Proc. FPGAs for Custom Computing Machines, Symposium on, Napa Valley, CA, Apr. 1998, pp. 254-255.
- [5] Y. Du, "Design of a 16-bit real time stack processor in FPGA," in Proc. ASICON, 6th Int. Conf. On, Shanghai, China, Vol. 2, Oct. 2005, pp. 783-786.
- [6] V. Angelov, V. Lindenstruth, "The educational processor Sweet-16," in Proc. Field Programmable Logic and Applications, Int. Conf. On, Prague, Czech Republic, Aug. 2009, pp. 555-559.
- [7] J.M. Youn, K. Daeho, A. Minwook, K. Yongjoo, P. Yunheung, "Orthogonal instruction encoding for a 16-bit embedded processor with dynamic implied addressing mode," in Proc. High Performance Computing and Communications, Int. Conf. On, Prague, Czech Republic, June. 2009, pp. 545-550.
- [8] E. O' ztu'rk, H. Sedef, "Designing of a 16-bit microprocessor by using FPGA," in Proc. Electrical, Electronics and Computer Engineering, Nat. Conf. On, Bursa, Turkey, Dec. 2010, pp. 349-354.
- [9] S. Sakthikumar, S. Salivahanan, V.S.K. Bhaaskaran, "16-Bit RISC processor design for convolution application," in Proc. Recent Trends in Information Technology, Int. Conf. On, Chennai, India, June. 2011, pp. 394-397.
- [10] J.L.L. Presa, E.P. Calle, "MMP16 a 16-bit didactic micro-programmed micro-processor," in Proc. Computer Research and Development, 3th Int. Conf. On, Shanghai, China, March. 2011, pp. 61-65.
- [11] Aeroflex Gaisler, "GRLIB IP Core Users Manual," v1.1.0-b4104, Nov. 2010. <http://www.gaisler.com/>
- [12] L. Barthe, L. Vitrio Cargnini, P. Benoit, L. Torres, "Optimizing an Open-Source Processor for FPGAs: A Case Study," in Proc. Field Programmable Logic and Applications (FPL), 2011 Int. Conf. On, Chania, Greece, Sept. 2011, pp. 551-556.
- [13] T. Noergaard, "Embedded Systems Architecture," Elsevier, 2005, ISBN: 0-7506-7792-9.
- [14] Microchip, "PIC16F87xA data sheet," 2001, DS39582A.
- [15] Philips, "80C51 8-bit microcontroller family," 2000, 853-0169 24291.
- [16] ARM Limited, "Cortex A8 Technical Reference Manual," 2007, ARM DDI 0344D.
- [17] Altera, "Nios II Processor Reference Handbook," 2014, NII5V1-13.1.
- [18] Xilinx, "MicroBlaze Processor Reference Guide," 2008, UG081 (v9.0).
- [19] L. Morales-Velazquez, R.A. Osornio-Rios, R.J. Romero-Troncoso, "FPGA Embedded Single-cycle 16-bit Microprocessor and Tools," Reconfigurable Computing and FPGAs, Int. Conf. on, Cancún, Mexico, Dic. 2012, pp. 1-6.
- [20] J. I. Sánchez Gómez, A. Valdez Garfias, L. Morales Velázquez, "Robot móvil de exploración implementado con sistema embebido FPGA," 8vo Coloquio, FI-UAQ 2014, in press.

FPGA-based Online Estimation of the Fundamental Frequency (Period) in Civil Structures using a RDT-FFT approach

Carlos Andres Perez-Ramirez*, Juan Pablo Amezcua-Sanchez*, David Camarena-Martinez*,
Martin Valtierra-Rodriguez*, Aurelio Dominguez-Gonzalez[†], Irving Armando Cruz-Albarran*,
Roque Alfredo Osornio-Rios*, and Rene de Jesus Romero-Troncoso[‡]

*HSPdigital-CA Mecatronica, Facultad de Ingenieria, Universidad Autonoma de Queretaro, Campus San Juan del Rio,
Rio Moctezuma 249, Col. San Cayetano, 76807, San Juan del Rio, Queretaro, Mexico

Email: {cperez, jamezcua, mvaltierra, amejia, raosornio}@hspdigital.org

[†]Facultad de Ingenieria, Universidad Autonoma de Queretaro, Campus San Juan del Rio,
Rio Moctezuma 249, Col. San Cayetano, 76807, San Juan del Rio, Queretaro, Mexico

Email: auredgz@uaq.mx

[‡]HSPdigital-CA Telematica, DICIS, Universidad de Guanajuato, Carr. Salamanca-Valle km 3.5 + 1.8,
Palo Blanco, 36885, Salamanca, Guanajuato, Mexico

Email: troncoso@hspdigital.org

Abstract—The fundamental frequency accurate estimation is an important concern since the value allows the correct assessment of the structure behavior during an earthquake. Unfortunately, the value obtained with the formulas provided by current construction codes differ to the one obtained by using an experimental approach, leading to the necessity of exploring other alternatives. Since the measurements of real-life structures are noise-contaminated, signal processing techniques should be able to process the signal without affecting the frequency estimation. In this article, a fusion of the well-known RDT and FFT algorithms is proposed in order to estimate the fundamental frequency of civil structures. The methodology is tested using a synthetic signal and real-life measurements in order to find out its accuracy and performance. Thanks to its low computational burden, an FPGA implementation is developed to offer a low-cost and a system-on-a-chip solution. The results obtained show that the methodology has a great accuracy since the maximum error is 2% from the theoretical value.

Keywords—RDT; FFT; FPGA; Fundamental frequency estimation; Civil structures;

I. INTRODUCTION

The fundamental frequency or period is an important value of the civil structures since it allows assessing its behavior during an earthquake and designing a suitable structure capable of having a better adaptation to the motion caused by external forces [1]. Further, its calculation can be used to implement a structural health monitoring (SHM) scheme in an online way.

Current constructions codes such as ATC (1978), BSSC (2003), CEN (2005), NZSEE (2006), and ASCE (2010) provide empirical expressions for the fundamental period

calculation; however, the results obtained by these usually differ from the ones calculated using the structure experimental data [2]–[4]. This divergence motivates the utilization of other approaches for the aforementioned estimation. To this purpose, strategies based on the use of analytic models (e.g. Finite Element Model, FEM) have been used [5]–[7]; but, a calibration procedure is usually required [7], leading to the utilization of signal processing techniques in order to obtain experimental results. One promising signal processing technique is the multiple signal classification (MUSIC) as it has provided noticeable results in other areas such as electrical machine diagnosis [8], and the structural health monitoring in civil engineering [9] since the technique has excellent capabilities when dealing with noisy signals. However, the technique computational burden is high [10], limiting its utilization in real-time or online applications. Hence, other schemes must be explored in order to achieve similar results to the ones obtained with the MUSIC algorithm but using algorithms with a lower computational burden. For instance, the well-known Fast Fourier Transform (FFT) can be used; but, its capabilities are degraded when noisy signals are processed [10]. Therefore, before using the FFT a pre-processing stage is necessary to filter the signal. To this purpose, the Random Decrement Technique (RDT) is a simple but effective technique used for filtering raw sensor measurements employing statistical properties [11] with a minimum computational burden, allowing its utilization in real-time and online applications. Hence, its use should be explored.

The contribution of this work is to present a methodology for the estimation of the fundamental period based on the fusion of the RDT and FFT algorithms, having the advantage of a lower computational burden than MUSIC algorithm. Another contribution is the implementation of

This work was supported in part by the National Council on Science and Technology (CONACYT). Mexico, under Scholarships: 289377, 229795, and 289369.

the proposal in a Field Programmable Gate Array (FPGA) in order to offer a low-cost and a system-on-a-chip (SOC) solution for the online estimation of the fundamental period. The proposed methodology is validated through a synthetic signal with high-level of noise. Moreover, the methodology implementation is tested using real-life measurements of a Reinforced Concrete (RC) highway bridge located at San Juan del Rio, Queretaro. The results show that proposed methodology can estimate the natural frequency with high accuracy.

II. THEORETICAL BACKGROUND

This section introduces the techniques used in the proposed methodology.

A. Fast Fourier Transform (FFT)

The FFT algorithm is an efficient way to calculate the Discrete Fourier Transform (DFT), as its forward calculation requires N^2 multiplications, whereas the FFT requires only $N \log_2(N)$ operations (where N is the number of points of the analyzed signal) [12].

The DFT operation procedure is defined as:

$$X[k] = \sum_{n=0}^{N-1} x[n] e^{-j2\pi nk/N} \quad (1)$$

Rewriting (1) leads to:

$$X[k] = \sum_{n=0}^{N-1} x[n] W_N^{nk} \quad (2)$$

From (1), it is easy to conclude that the same values of W_N^{nk} are calculated several times as the DFT calculation is carried out. By using the symmetric property of the twiddle factor [12], the DFT computation can be efficiently done by changing (2) as follows:

$$X[k] = \sum_{r=0}^{\frac{N}{2}-1} x(2r) W_N^{2kr} + \sum_{r=0}^{\frac{N}{2}-1} x(2r+1) W_N^{k(2r+1)} \quad (3)$$

By simplifying the indices inside both sums and rearranging the last term, (3) is expressed:

$$X[k] = \sum_{r=0}^{\frac{N}{2}-1} x_1(r) W_{N/2}^{kr} + W_N^k \sum_{r=0}^{\frac{N}{2}-1} x_2(r) W_{N/2}^{kr} \quad (4a)$$

$$X[k] = X_1(k) + W_N^k X_2(k) \quad (4b)$$

Therefore, an N -point DFT can be obtained from two $N/2 - 1$ samples transforms: one on even input data, and the other one on odd input data.

B. Random Decrement Technique (RDT)

The Random Decrement Technique (RDT) is a method that uses environmental excitation responses to obtain the free response from the raw response measurements. The algorithm considers that the random response of any mechanical structure is composed by a random part and a deterministic part. By averaging enough selected responses with a common initial condition a , the random part is removed, allowing its utilization as a filter; hence, the result is the deterministic part associated to the free-decay response [13]. This response is known as Randomdec signature. The RDT vector is obtained as follows:

$$\delta(\tau) = \frac{1}{N} \sum_{i=1}^N y(\tau + t_i) \Big|_{y(t_i)=a} \quad (5)$$

where $y(t)$ is a measurement from the response signal $x(t)$ at the time instant t_i , which satisfies the triggering condition a ; N is the number of the triggering points obtained, and τ is the time variable. The used trigger condition is the level crossing condition, a , and is expressed mathematically as follows [14]:

$$a = \sqrt{2} \sigma_x \quad (6)$$

where σ_x is the measurements standard deviation. In order to illustrate the process used for obtaining the Randomdec

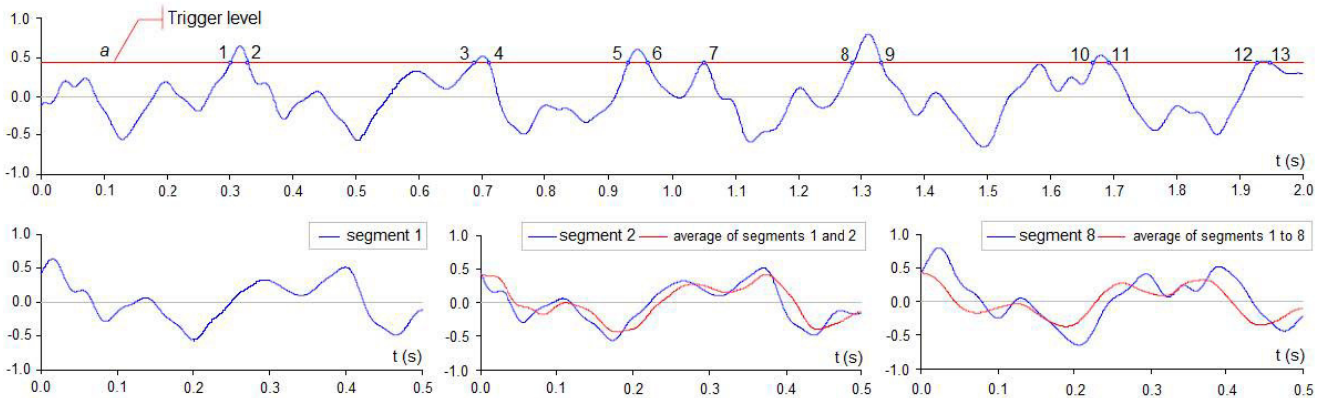


Figure 1. Procedure for obtaining the Randomdec signature.

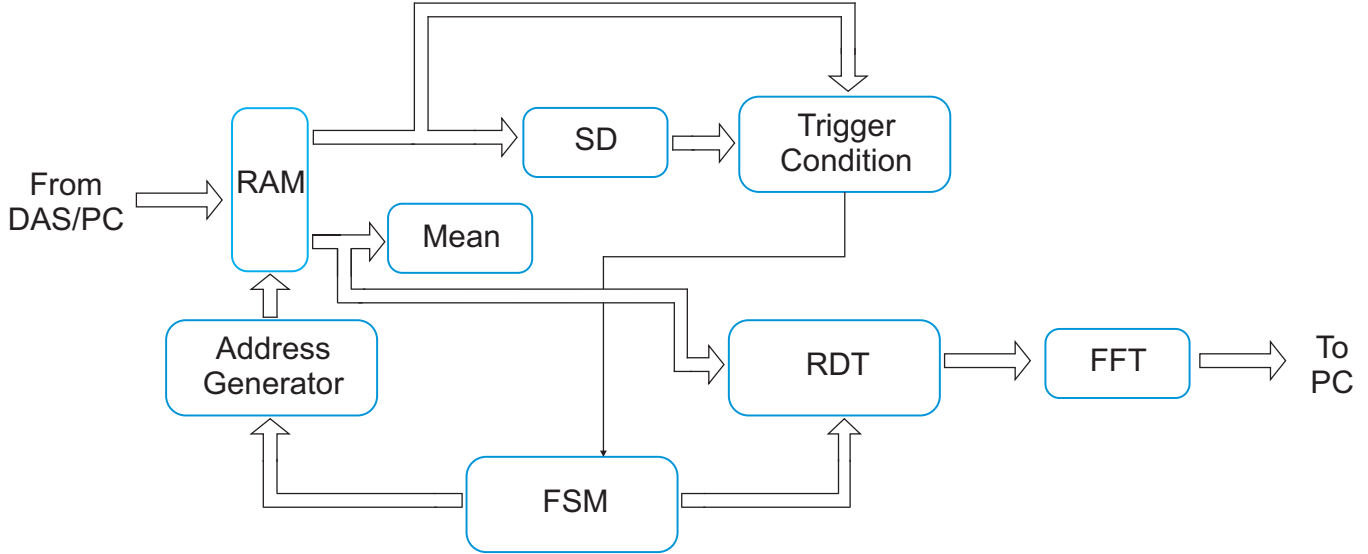


Figure 2. Proposed methodology implementation.

signature, a graphical representation is shown in Figure 1. The process starts using any signal (depicted at the top of the image, with a blue line). Then, the trigger condition, expressed by (6) is calculated and illustrated with the red trace. Next, the samples that accomplish with the trigger condition are located (in this case 13 samples are located, numbered in the figure from 1 to 13). Then, starting from each sample located, a segment or batch of the signal is extracted as shown in the bottom part of the aforementioned figure (512 or 1024 points after each sample located is recommend since it allows generating the best results [14]). Finally, all estimated segments are averaged using (5).

III. METHODOLOGY IMPLEMENTATION

The proposed methodology is depicted in Figure 2. It is based on three steps: (1) the structure dynamic response is measured, (2) the model is estimated using the data acquired, and (3) a comparison between the different models responses is performed.

A. RDT Implementation

Recalling from the theory presented in section II, a batch of raw measurements are required in order to calculate the Randomdec signature (or the free damped response). To this purpose, a dual port Random Access Memory (RAM) is used to store the samples. Since (6) uses the batch of samples standard deviation to calculate the trigger condition for extracting the trigger points, its value has to be calculated. The aforementioned calculation also requires the mean of the batch. Once they are calculated, the threshold value is estimated, allowing the Randomdec signature estimation. This procedure is executed as follows: when the actual sample value is grater or equal to the threshold one, the

next N samples are added arithmetically with the contents of a RAM (whose size is N). The results update the RAM and the aforementioned procedure continues until the batch of data is revised entirely. It should be remarked that if the number of available samples is less than the size selected for the Randomdec signature, the missing positions are filled with zeros in order to avoid a possible miscalculation. Once the entire batch is processed, the contents of the N -sized RAM are arithmetically divided with the number of trigger points founded

B. FFT Implementation

The FFT implementation is made by means of the radix-4 butterfly algorithm presented in [15]. This approach uses a pipelined structure in order to achieve the maximum processing speed. Once the Randomdec signature is calculated, the FFT algorithm to obtain its spectrum, which is transferred to a Personal Computer (PC) by using the Universal Serial Bus (USB) protocol, in order to visualize the calculated spectrum, and therefore, show the fundamental frequency.

IV. EXPERIMENTATION AND RESULTS

In this section, the validation of the proposed methodology is presented and its performance is tested using real-life measurements from a RC bridge.

A. Validation

In order to validate the proposed methodology accuracy, a synthetic signal, representing the free damped response of a 3-DOF system, is used:

$$s(t) = \sum_{i=1}^3 A_i e^{-2\pi\zeta_i f_i t} \sin(2\pi f_{d_i} t + \theta_i) + n(t) \quad (7)$$

where A_i is the amplitude, θ_i is the phase angle, f_i is the natural frequency, ζ_i is the damping ratio of the i th frequency, and $n(t)$ is a sequence of white noise. This signal is composed of a fundamental frequency $f_1 = 2$ Hz, and two additional with values of $f_2 = 5$, and $f_3 = 7$ Hz, respectively. Further, the damping ratio for the fundamental frequency is $\zeta_1 = 0.8\%$, whereas for the others are: $\zeta_2 = 1.0\%$, and $\zeta_3 = 0.5\%$, respectively. Besides, the following parameters are chosen: amplitude $A_i = 1.0$, and a phase angle $\theta_i = 0$ for $i = 1, 2$, and 3 . Finally, a sampling frequency of 100 Hz within a period of 10 seconds is used, obtaining 1000 samples. A high-level noise with a Signal-to-Noise Ratio (SNR=1dB) is used to approximate the signal to a real-life condition.

Once the signal is built, it is analyzed with the proposed methodology. The number of points, N , used for the Randomdec signature, is set to 512. On the other hand, the FFT uses also the same vector for its calculation. Figs. 3a and 3b show the analyzed signal and its spectrum, respectively, whereas Figs. 4a, 4b, and 4c depict the original signal without noise, the noisy signal (SNR=1dB) and filtered signal using RDT method, respectively. From these figures, it is possible to observe that the RDT method is a useful tool to eliminate the noise in the signal.

B. Experimental Setup

The methodology implementation is carried out in a Xilinx Spartan 3EXC3S1600 FPGA proprietary platform running at 48 MHz. Table I summarizes the used resources for its implementation. In the case of the RDT implementation, a 1024-vector is used, whereas the FFT algorithm implementation uses 1024 points. On the other hand, the experimental setup consists of a PC that transfers, using the USB protocol, a batch of raw ambiental measurements from

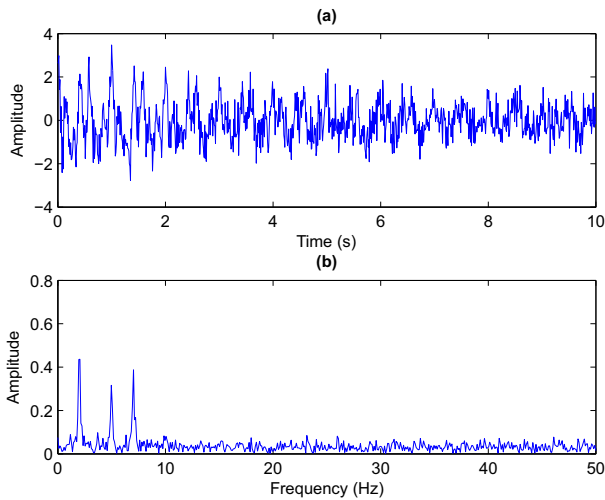


Figure 3. Results obtained using the validation signal, (a) synthetic signal, (b) amplitude spectrum.

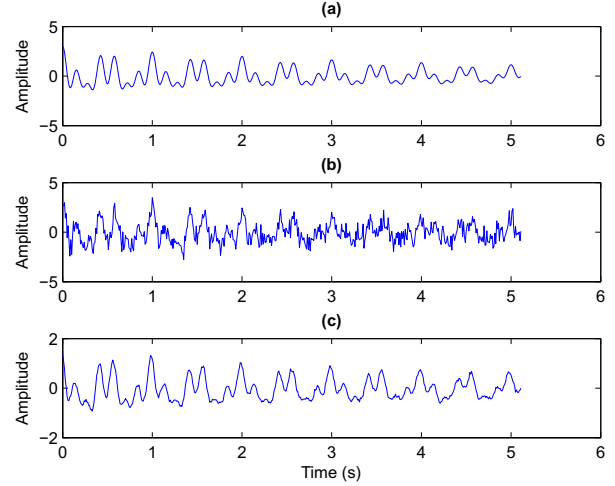


Figure 4. Results obtained using the validation signal, (a) synthetic signal, (b) amplitude spectrum.

a RC bridge located at San Juan del Rio, Queretaro. The aforementioned bridge is used for both highway traffic and pedestrians (depicted in Fig. 5a). The structure is excited by wind and traffic. Its response is online monitored through a tri-axial accelerometer mounted in the middle of the bridge, as shown in Fig. 5b, using a sampling frequency of 100 Hz during 600 s. The sensor is located in the metallic protection in order to secure its position. Further, as the metallic protection is part of the structure, the sensor can be placed in, allowing monitoring of the structure fundamental frequency. It should be noticed that traffic load induces mostly vertical vibration of the bridge; hence, only the data from the accelerometer in the vertical direction is used in the analysis [17]. Once the fundamental frequency is estimated, the results are transferred to the PC by the aforementioned protocol. Figs. 6a to 6c show the recorded responses, the filtered signal, and its spectrum, respectively.

C. Analysis and Discussion

Regarding the validation stage, despite the high level of noise added to the signal, the obtained spectrum (depicted in Fig. 3b) shows clearly the three frequencies of the signal without any other spurious peak. Table II resumes the detected frequencies and the relative error, demonstrating the proposed methodology high accuracy since the maximum error is about 2%, which is desirable for natural frequencies identification [16]. On the other hand, the results obtained

Table I
FPGA RESOURCE UTILIZATION

Resource	Xilinx Spartan 3E XC3S1600E
Logic Cells	16736/29504
18 × 18 Multipliers	4/36
BRAM	2/36

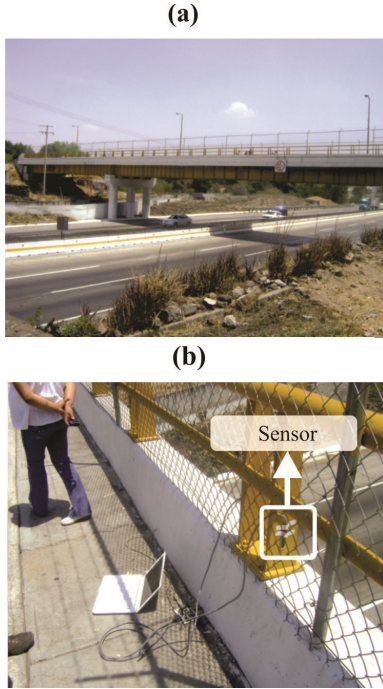


Figure 5. Experimental Setup, (a) analyzed RC bridge, (b) Sensor Location.

from the ambient response also show a clean spectrum, allowing a visual identification of the fundamental frequency without any confusion. Moreover, the RDT filtering properties are demonstrated, as the original and filtered signals (shown in Fig. 4) are remarkable similar, despite the level of noise added to the original signal, which limits the accurate estimation of its amplitude.

A comparison between the RC bridge fundamental frequency obtained with the proposed methodology and other

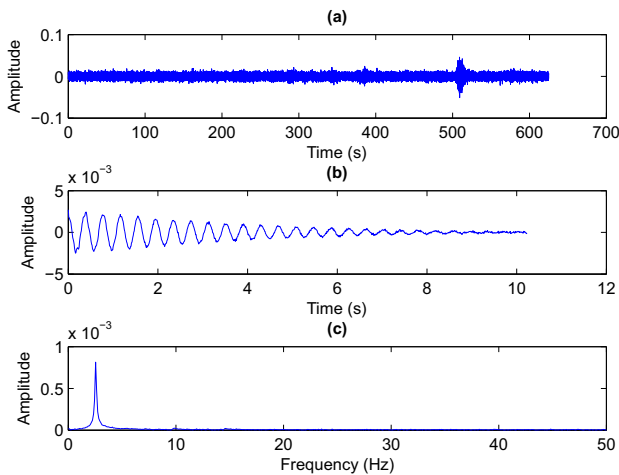


Figure 6. Results extracted from the raw ambient response, (a) measured signal, (b) free damped response, and (c) amplitude spectrum.

Table II
NATURAL FREQUENCIES EXTRACTED

Frequency	Proposed Methodology	Relative Error (%)
$F_1 = 2$ Hz	1.96	2.04
$F_2 = 5$ Hz	5.078	1.54
$F_1 = 7$ Hz	7.031	0.44

approaches is shown in Table III, where the proposed methodology accuracy is validated since the results obtained are quite similar to the ones obtained in [17]; further, its computational burden is lower than the other approaches presented, allowing an online operation.

Regarding the FPGA implementation, it should be noticed that the proposed methodology executing time is about 5 ms whereas the PC time execution is about 175 ms; that is, the FPGA implementation executes 35 times faster than its PC counterpart. This speed up is possible thanks to the proposed methodology simplicity and the inherent features of a FPGA implementation: parallelism and distributed processing. Moreover, this time execution also might allow a real-time operation, as the sampling rate is commonly used at 100 Hz or less; nonetheless, since RDT uses a batch of data, only the online operation of the proposed methodology is achievable

V. CONCLUSIONS

This article presents a methodology based on the fusion of the well-known RDT and FFT algorithms to estimate the fundamental frequency of civil structures. First, RDT is used to filter the signal and obtaining the free damped response (or Randomdec signature) of the batch of raw measurements; then, FFT is applied to the Randomdec signature to estimate the fundamental frequency. The performance and accuracy (as shown in tables II and III) of the proposed methodology is demonstrated through the analysis of a synthetic signal and the measurements of a RC bridge, where the maximum error is about 2%, which is within the limits of an accurate frequency identification [16]. Moreover, thanks to the lower computational burden than other approaches [17], and the inherent parallelism of a FPGA, its online operation is demonstrated. This approach can be used in further structural health monitoring (SHM) schemes for an online condition assessment and structural control approaches.

REFERENCES

- [1] K. Young and H. Adeli, "Fundamental period of irregular moment-resisting steel frame structures," *Struct. Des. Tall*

Table III
FUNDAMENTAL FREQUENCY IDENTIFICATION

Proposed Methodology	EEMD-MUSIC [17]	DWT-MUSIC [17]
2.539 Hz	2.539 Hz	2.50 Hz

- Spec. Build.*, vol. 23, no. 15, pp. 1141–1157, Oct. 2014. [Online]. Available: <http://doi.wiley.com/10.1002/tal.1112>
- [2] F. Vidal, M. Navarro, C. Aranda, and T. Enomoto, “Changes in dynamic characteristics of Lorca RC buildings from pre- and post-earthquake ambient vibration data,” *Bull. Earthq. Eng.*, vol. 12, no. 5, pp. 2095–2110, Jul. 2013. [Online]. Available: <http://link.springer.com/10.1007/s10518-013-9489-5>
- [3] M. R. Gallipoli, M. Mucciarelli, B. Šket Motnikar, P. Zupančić, A. Gosar, S. Prevotnik, M. Herak, J. Stipčević, D. Herak, Z. Milutinović, and T. Olumčeva, “Empirical estimates of dynamic parameters on a large set of European buildings,” *Bull. Earthq. Eng.*, vol. 8, no. 3, pp. 593–607, Jun. 2009. [Online]. Available: <http://link.springer.com/10.1007/s10518-009-9133-6>
- [4] C. S. Oliveira and M. Navarro, “Fundamental periods of vibration of RC buildings in Portugal from in-situ experimental and numerical techniques,” *Bull. Earthq. Eng.*, vol. 8, no. 3, pp. 609–642, Oct. 2009. [Online]. Available: <http://link.springer.com/10.1007/s10518-009-9162-1>
- [5] X. Q. Yao, B. T. Sun, Q. Zhou, Y. K. Chen, and X. L. Yang, “The Seismic Finite Element Analysis of Tianjin Western-Style Dwellings,” in *Adv. Mater. Res.*, vol. 1065-1069, Jan. 2015, pp. 1443–1450. [Online]. Available: <http://www.scientific.net/AMR.1065-1069.1443>
- [6] F. N. Catbas, S. K. Ciloglu, O. Hasancebi, K. Grimmelsman, and A. E. Aktan, “Limitations in Structural Identification of Large Constructed Structures,” *J. Struct. Eng.*, vol. 133, no. 8, pp. 1051–1066, Aug. 2007. [Online]. Available: [http://ascelibrary.org/doi/abs/10.1061/\(ASCE\)0733-9445\(2007\)133%3A8\(1051\)](http://ascelibrary.org/doi/abs/10.1061/(ASCE)0733-9445(2007)133%3A8(1051))
- [7] I. G. Araujo, E. Maldonado, and G. C. Cho, “Ambient vibration testing and updating of the finite element model of a simply supported beam bridge,” *Front. Archit. Civ. Eng. China*, vol. 5, no. 3, pp. 344–354, Sep. 2011. [Online]. Available: <http://link.springer.com/10.1007/s11709-011-0124-8>
- [8] A. Garcia-Perez, R. d. J. Romero-Troncoso, E. Cabal-Yepez, and R. A. Osornio-Rios, “The Application of High-Resolution Spectral Analysis for Identifying Multiple Combined Faults in Induction Motors,” *IEEE Trans. Ind. Electron.*, vol. 58, no. 5, pp. 2002–2010, May 2011. [Online]. Available: <http://ieeexplore.ieee.org/lpdocs/epic03/wrapper.htm?arnumber=5747206>
- [9] J. P. Amezcua-Sanchez, A. Garcia-Perez, R. J. Romero-Troncoso, R. A. Osornio-Rios, and G. Herrera-Ruiz, “High-resolution spectral-analysis for identifying the natural modes of a truss-type structure by means of vibrations,” *J. Vib. Control*, vol. 19, no. 16, pp. 2347–2356, Sep. 2012. [Online]. Available: <http://jvc.sagepub.com/content/19/16/2347>
- [10] J. P. Amezcua-Sanchez and H. Adeli, “Signal Processing Techniques for Vibration-Based Health Monitoring of Smart Structures,” *Arch. Comput. Methods Eng.*, Oct. 2014. [Online]. Available: <http://link.springer.com/10.1007/s11831-014-9135-7>
- [11] J. Rodrigues, R. Brincker, and P. Andersen, “Improvement of Frequency Domain Output-Only Modal Identification from the Application of the Random Decrement Technique,” in *2004 IMAC-XXII Conf. Expo. Struct. Dyn.*, 2004, pp. 1–9.
- [12] J. G. Proakis and D. G. Manolakis, *Digital Signal Processing*, 3rd ed. Upper Saddle River, NJ: Prentice-Hall, 1999.
- [13] J. He and Z. F. Fu, *Modal Analysis*. Butterworth-Heinemann, 2001.
- [14] S. R. Ibrahim, “Efficient Random Decrement Computation for Identification of Ambient Responses,” in *2001 IMAC XIX - 19th Int. Modal Anal. Conf.*, 2001, pp. 1–6.
- [15] J. Vite-Frias, R. de Jesus Romero-Troncoso, and A. Ordaz-Moreno, “VHDL Core for 1024-Point Radix-4 FFT Computation,” in *2005 Int. Conf. Reconfigurable Comput. FPGAs*. IEEE, pp. 24–24. [Online]. Available: <http://ieeexplore.ieee.org/articleDetails.jsp?arnumber=1592506>
- [16] W. C. Su, C. S. Huang, C. H. Chen, C. Y. Liu, H. C. Huang, and Q. T. Le, “Identifying the Modal Parameters of a Structure from Ambient Vibration Data via the Stationary Wavelet Packet,” *Comput. Civ. Infrastruct. Eng.*, vol. 29, no. 10, pp. 738–757, Nov. 2014. [Online]. Available: <http://doi.wiley.com/10.1111/mice.12115>
- [17] D. Camarena-Martinez, J. P. Amezcua-Sanchez, M. Valtierra-Rodriguez, R. J. Romero-Troncoso, R. A. Osornio-Rios, and A. Garcia-Perez, “EEMD-MUSIC-Based Analysis for Natural Frequencies Identification of Structures Using Artificial and Natural Excitations,” *Sci. World J.*, vol. 2014, pp. 1–4, 2014. [Online]. Available: <http://www.hindawi.com/journals/tswj/2014/587671/abs/>

CONIIN 2015

Automation of optoelectronic experiment of the Production of light, Interference, and Quantum entanglement with Orbital Angular Momentum for applications in Optical communications

Jesús López Gómez¹, M. Aurora Vargas Treviño², V. Manuel Velázquez Aguilar³, Sergio Vergara Limon⁴

Facultad de Ciencias de la Electrónica-Maestría en Ciencias de la Electrónica Opción Automatización, Benemérita Universidad Autónoma de Puebla

Ave. San Claudio y 18 Sur, building 109A, Ciudad Universitaria City Puebla, Puebla, Country México

¹ jesuslopez_meca@hotmail.com

² auroravargast@hotmail.com

⁴ svergara@ece.buap.mx

Facultad de Ciencias- Laboratorio de Óptica Avanzada, Universidad Nacional Autónoma de México

Ave. Universidad No.3000, Circuito Exterior S/N, Ciudad Universitaria, Delegación Coyoacán, Distrito Federal, City México, Country México

³ vicvela@ciencias.unam.mx

Abstract— The automation has improved and increased considerably not only in industrial production, but is also present in conducting scientific experiments as part of teaching and research. The aim of this work is the study of the production of single photons with orbital angular momentum (MAO), quantum interference of photons with orbital angular momentum and their spatial distribution (spatial entanglement) with orbital angular momentum. The electronic project is to produce this type of patterns in an automated manner and build a detection system with quantum efficiency for studying counts and spatial correlations of photons with different angular momenta. With an array of five detectors, we are obtained five electrical signals -2-, -1, 0, +1, +2, and we could analyze the photon correlations with orbital angular momentum. Moreover, the study of these photons with MAO involves trying to understand how a particle can propagate with a certain helicity and not a wave.. The experiment consists of an optoelectronic arrangement, which is generating beams Laguerre-Gauss (LG) via holograms (or gratings of diffraction) produced by computer, when this grating is illuminated with a beam of plane waves is generated, a first order the intensity and phase pattern that is required, in particular, to produce a grid Laguerre-Gauss (LG) a fork grating is required. This paper presents the design, development and implementation of a data acquisition system (SAD) via Wi-Fi, which consists of hardware, firmware and application software and characterize a detection system with quantum efficiency and to study counts and spatial correlations of photons with different Orbital Angular Momentum. Also, design and implement three Cartesian robots linear and also using in the axis X a piezoelectric motor with high accuracy.

Keywords— *Quantum optics, Orbital Angular Momentum, Electronic design, mechanical engineering, Software & Hardware, Wi-Fi, FPGA, AHDL programming, system data acquisition, control, robotics, Mechatronics.*

I. INTRODUCTION

The manipulation of individual atoms and photons represents a technological breakthrough with many promises of applications in communications and information. The basis of this technology is the use of the information encoded in the quantum components of these individual entes. So phenomena such as quantum interference and quantum entanglement are concepts that have no classical counterpart, therefore, is very important to understand and manipulate them to their best advantage. In the lab of quantum optics of the Faculty of Sciences of the UNAM, various research experiments are performed, these experiments are complex and it can take several weeks or even months to take the data and then do your analysis. Basically, the experiments consist in the study of the photon correlations properties: frequency, polarization, time, detection position, orbital angular momentum. For these experiments, it is essential to have a source of single photons. Such technology involves the use of quantum phenomena such as quantum entanglement. The entanglement can be used for the quantum encryption information, quantum computing, quantum microlithography, among other applications. For the test correlation of photons we used a beam splitter that only has two options of directionality (transmitted and reflected). In contrast, production of photons with Orbital Angular Momentum, the directionality depends directly on the burden

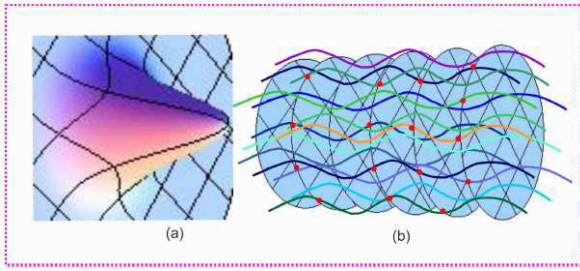


Fig. 1. (a) In the cross section of planar wavefront is observed a Gaussian intensity distribution. (b) The wavefront of a beam of light with orbital angular momentum equal to zero, where points of constant phase are flat

of orbital angular momentum; we study this degree of freedom and its influence on the entanglement. For this reason, it is important to find solutions to all this, and get results in less time and with a minimum of human error, which allows us to automate the experiment. Given the needs of the experiment, the Faculty of Sciences of the Autonomous University of Puebla has gained experience for automation of optical experiments, in the year 2005 Dr. Sergio Vergara and Dra. Aurora Vargas, they designed and they built a data acquisition card. This PCI card was the first version of a photon counter individual and coincidence, the card uses an FPGA MAX7000AETC144-5 and has a resolution of 5-30ns [1]. For this experiment we are going to develop a detection system and it must meet the following: Ability of count, processing data through communication WI-FI and to improve its resolution. It is also necessary to make changes to software and firmware to include the processing of information obtained by the counts process and to perform the photon correlation with Orbital Angular Momentum.

II. FUNDAMENTALS OF THE EXPERIMENT

In the theory of light there are two approaches called, theory: classical and quantum. In classical physics, light is treated as electromagnetic waves; in quantum optics, as photons [2]. In the classical theory is known Maxwell's equations, electromagnetic moment, Leguerre-Gauss modes, Poynting vector, which shows the behavior of light as waves. In the case of quantum optics, the quantum photon sources with Orbital Angular Momentum involves trying to understand how a particle and not a wave can propagate with a certain helicity, which is very similar but is treated with photons.

A. Orbital Angular Momentum

Intuitively, you can think to light with Orbital Angular Momentum equal to zero as a wavefront ordained whose points of constant phase are formed planes perpendicular to the direction of propagation k . The amplitude of the electric field of a plane wave at a given instant can be written as (1).

$$E(r) = E_0 e^{i k r} + c.c. \quad (1)$$

with the wave vector k . The constant phase points r , satisfy the condition (2).

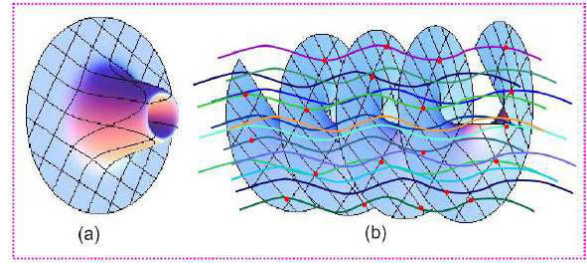


Fig. 2. (a). The transverse intensity distribution of light with orbital angular momentum is no longer Gaussian. In the case shown in this figure, light having angular momentum $L = 1$ unit of orbital angular momentum and the transverse intensity distribution is a Laguerre-Gauss mode. (b) Certain sections of the wavefront are delayed with respect to others and the points of constant phase are another type of surface.

$$k r = \text{constant} \quad (2)$$

which is the equation of a plane orthogonal to k . The transverse intensity distribution of the plane wave is Gaussian, see Fig. 1. Conversely, in the light with orbital angular momentum, some sections of the wavefront are delayed or is coming forward regarding other and the points of constant phase are form another type of surface, see Fig. 2 [3].

B. Production of light with Orbital Angular Momentum

These holograms are generated by computer or grids [4]. Basically, overlapping a Gaussian beam and one of LG [5]. The quantum entanglement using LG beams, but they generate LG beams with a spatial light modulator [6].

The most common technique for generate LG beams is through holograms, produced by computer. So you can practically generate a beam with any value of orbital angular momentum. The Suitable diffraction grating can be produced from the interference pattern between a light Gaussian beam (plane wave front) and a light beam with the desired distribution [7]. When this grating is illuminated with a beam of plane waves is generated the intensity and phase pattern required [8]. In particular, to produce modes leguerre-Gauss is required a grating of fork, as shown in Fig. 3 and that is generated by the expression (3) [9].

$$l(\theta/\pi) = \gamma + (2r/\lambda)(\cos \theta) \quad (3)$$

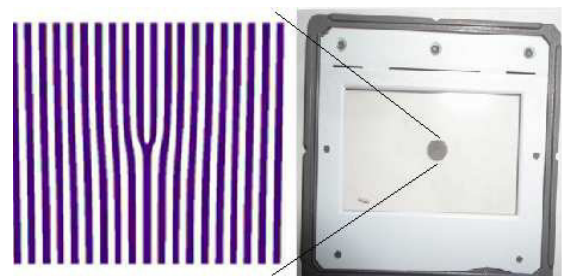


Fig. 3. Diffraction grating with bifurcation + 1s.

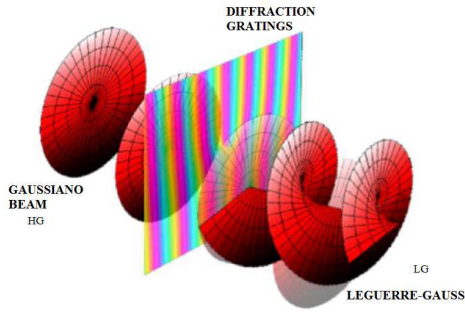


Fig. 4. Diffraction gratings a Gaussian beam overlapping HG and a Gauss-Laguerre LG

With the method of diffraction gratings, a front of Gaussian wave (a laser) is diffracted in the different orders of orbital angular momentum, see Fig. 4. The maximum central not poseé Orbital Angular Momentum ($l = 0$), the first order diffracted with Orbital Angular Momentum has $l = +1, -1$, see Fig. 5, and so forth see Fig. 6. Intuitively, the discontinuity represented by the bifurcation is sufficient to produce a change angular in the distribution of light intensity. This means, that if we let only this bifurcation of light with orbital angular momentum, in which the magnitude of angular momentum would have to do with the order of the bifurcation present (topological charge) at the fork. Thus, a Orbital Angular Momentum l depend on the number of teeth possessed by the fork.

III. AUTOMATION OF THE EXPERIMENT

The experiment consists of studying the production of single photons with Momento Angular Orbital, their spatial distribution (spatial entanglement) and its automation. The study of the production of light with orbital angular momentum there is a method which can produce such beams is computer generated holograms or diffraction gratings basically a Gaussian beam overlapping HG and a Gauss-Laguerre LG see Fig. 4.

A. Characteristics of the experiment

The electronic project is to produce this type of patterns in an automated manner and build a detection system for studying quantum of efficiency counts of photons with different orbital Angular Momentum. The quantum signals are obtained of the optoelectronic array, the detection system are sent to the electronic system for processing and analysis.

Experiments with orbital angular momentum consist of an optoelectronic arrangement with the following components: a laser 405,38nm, 100mW and a bandwidth of 0,78nm, a 50:50 beam splitter, fork grid $l = +1s$, and avalanche photodiodes (APDs, Avalanche photodiode), which generate pulses turning it into a square electrical signal.

1) Arrangement for photon correlation: Optoelectronic

The 50:50 beam splitter splits the incident beam (LG) in a transfer beam and a reflected beam, therefore, the intensities of the transmitted and reflected beams are equal. In the splitter

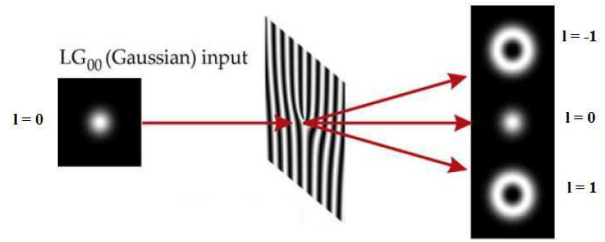


Fig. 5. Input with Orbital Angular Momentum ($l = 0$), the output from an LG phase hologram with Orbital Angular Momentum has $l = +1, -1$.

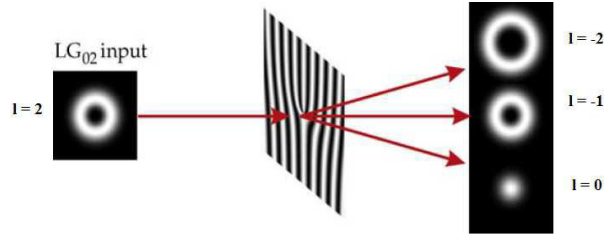


Fig. 6. Input With Orbital Angular Momentum ($l = 2$), the output from an LG phase hologram with Orbital Angular Momentum has $l = 0, +1, +2$.

outputs is mounted robots with light collectors, and is coupled to a multi-mode optical fiber, see Fig. 7.

The manifolds are lenses having an anti-reflection treatment, which makes them suitable to allow maximum transmission in the near infrared region, with this reflection losses are reduced. Robots must be positioned along the horizontal and vertical diameter of the productions with Momento Angular Orbital in the bifurcations $l = +1, -1, +2, -2$, so that the transmitted and reflected beam find their correlation space. The optical fibers are connected to the input ports of avalanche photodiodes by type FC connectors. Thus, the light is sent to the avalanche photodiodes.

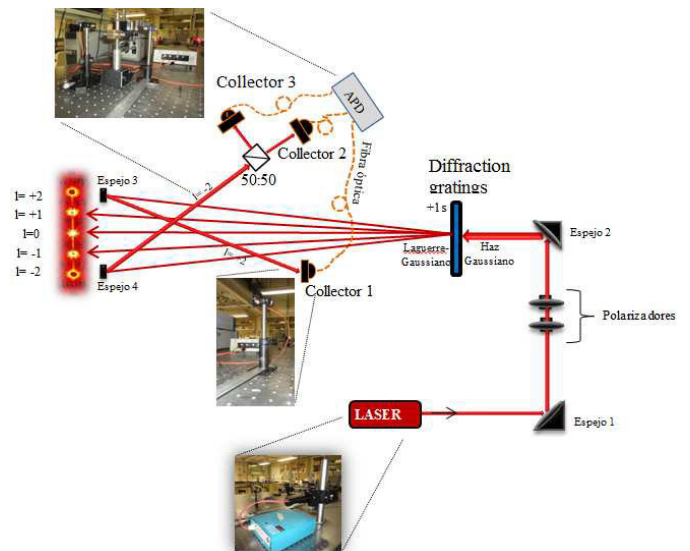


Fig. 7. Optoelectronic arrangement of the experiment

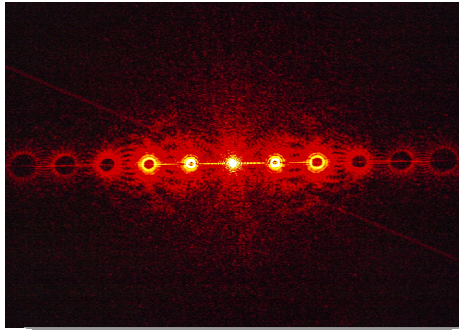


Fig. 8. Laguerre-Gauss distribution produced by a fork-type grid using a classic font.

2) *Analysis and description of the experiment:* The objective of this experiment is to see if there is a correlation between the two symmetric distributions of the first mode of the same pattern, that is, if the spatial distributions of both modes are correlated, if one provides information of the other. Once the detector showing the distribution of LG modes of the Fig. 8, the system is aligned, then we will analyze the number of accounts and coincidences between the rings. We consider, for example, 30 fixed points of distribution LG2 with a distance between these points of 0.5mm. Meanwhile, a detector measures the intensity at each position fixed of the LG2 distribution, a second detector makes a scan of the intensity distribution of LG1 with the positioning system at a speed of 10 microns / sec Fig. 9.

B. Description of the system of detection

1) *Design of three robots with 3gdl :* The Detection system consists of build three robots of high precision with quantum efficiency Fig.10 to receive signals and to study counts of photons with difference of Orbital Angular Momentum.

2) *The configuration of the detection:* The Signals are obtained of the optoelectronic arrangement of the experiment, which of the detection system are sent to the electronic system for processing and analysis, the three collectors are shown in Fig.11 and will instead be three robots linear, to make correlations and corresponding sweeps.

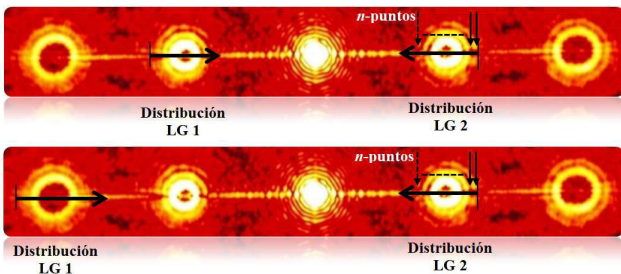


Fig. 9. Diffraction ring with orbital angular momentum, based in the study of dislocations $l = -1, +1$ (LG1, LG2), for observing the correlation.

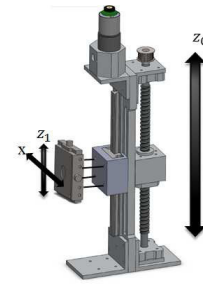


Fig. 10. Robot linear of high precision.

IV. ROBOT DESIGN

A. Kinematic and dynamic model of the robot

Before designing the Cartesian robot we find the dynamic model of the robot for 3gdl, this in order to have a broader view of system behavior of our robot and get a more optimal model in the controller. We have links and joints according to Fig. 12 and we have to get the mathematical equations that describe the kinematics of the robot.

- The direct kinematics of a Cartesian robot is given by (4), (5), (6) [10].

$$\begin{bmatrix} z'_1 \\ x_1 \\ z_1 \end{bmatrix} = \begin{bmatrix} q_1 + l_1 \\ 0 \\ 0 \end{bmatrix}, \quad (4)$$

$$\begin{bmatrix} z'_2 \\ x_2 \\ z_2 \end{bmatrix} = \begin{bmatrix} q_1 + l_1 \\ q_2 \\ l_1 \end{bmatrix}, \quad (5)$$

$$\begin{bmatrix} z'_3 \\ x_3 \\ z_3 \end{bmatrix} = \begin{bmatrix} q_1 + l_1 \\ q_2 \\ q_3 + l_1 \end{bmatrix}, \quad (6)$$



Fig. 11. Configuration of the detection

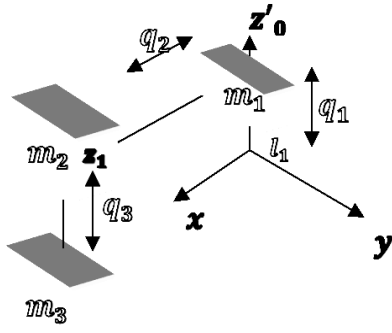


Fig. 12. Cartesian Configuration.

- The speeds of our system it is given for (7), (8), (9).

$$V_1 = \frac{d}{dt} \begin{bmatrix} z'_1 \\ x_1 \\ z_1 \end{bmatrix} = \frac{d}{dt} \begin{bmatrix} q_1 + l_1 \\ 0 \\ 0 \end{bmatrix} = \begin{bmatrix} \dot{q}_1 \\ 0 \\ 0 \end{bmatrix} \quad (7)$$

$$V_2 = \frac{d}{dt} \begin{bmatrix} z'_2 \\ x_2 \\ z_2 \end{bmatrix} = \frac{d}{dt} \begin{bmatrix} q_1 + l_1 \\ q_2 \\ l_1 \end{bmatrix} = \begin{bmatrix} \dot{q}_1 \\ \dot{q}_2 \\ 0 \end{bmatrix} \quad (8)$$

$$V_3 = \frac{d}{dt} \begin{bmatrix} z'_3 \\ x_3 \\ z_3 \end{bmatrix} = \frac{d}{dt} \begin{bmatrix} q_1 + l_1 \\ q_2 \\ q_3 + l_1 \end{bmatrix} = \begin{bmatrix} \dot{q}_1 \\ \dot{q}_2 \\ \dot{q}_3 \end{bmatrix} \quad (9)$$

- We obtain the rapidity of the following way (11), (12), (13).

$$V^2 = \|V\|^2 = V^T V = [V_1 \ V_2 \ V_3] \begin{bmatrix} V_1 \\ V_2 \\ V_3 \end{bmatrix} \quad (10)$$

$$V_1^2 = \begin{bmatrix} \dot{q}_1 \\ 0 \\ 0 \end{bmatrix}^T \begin{bmatrix} \dot{q}_1 \\ 0 \\ 0 \end{bmatrix} = \dot{q}_1^2 \quad (11)$$

$$V_2^2 = \begin{bmatrix} \dot{q}_1 \\ \dot{q}_2 \\ 0 \end{bmatrix}^T \begin{bmatrix} \dot{q}_1 \\ \dot{q}_2 \\ 0 \end{bmatrix} = \dot{q}_1^2 + \dot{q}_2^2 \quad (12)$$

$$V_3^2 = \begin{bmatrix} \dot{q}_1 \\ \dot{q}_2 \\ \dot{q}_3 \end{bmatrix}^T \begin{bmatrix} \dot{q}_1 \\ \dot{q}_2 \\ \dot{q}_3 \end{bmatrix} = \dot{q}_1^2 + \dot{q}_2^2 + \dot{q}_3^2 \quad (13)$$

- There is only energy of translation. Later we get the equations of kinetic energy for each degree of freedom (14), (15), (16).

$$K_1(q, \dot{q}) = \frac{m_1 \dot{q}_1^2}{2}, \quad (14)$$

$$K_2(q, \dot{q}) = \frac{m_2(\dot{q}_1^2 + \dot{q}_2^2)}{2}, \quad (15)$$

$$K_3(q, \dot{q}) = \frac{m_3(\dot{q}_1^2 + \dot{q}_2^2 + \dot{q}_3^2)}{2}, \quad (16)$$

- Add all the energies and we have that the total kinetic energy is expressed as (18).

$$K(q, \dot{q}) = \frac{1}{2} m_1 \dot{q}_1^2 + \frac{1}{2} m_2 \dot{q}_1^2 + \frac{1}{2} m_2 \dot{q}_2^2 + \frac{1}{2} m_3 \dot{q}_1^2 + \frac{1}{2} m_3 \dot{q}_2^2 + \frac{1}{2} m_3 \dot{q}_3^2 \quad (17)$$

- The potential energy is given by the expression (18)

$$K(q, \dot{q}) = \frac{(m_1 + m_2 + m_3)}{2} \dot{q}_1^2 + \frac{(m_2 + m_3)}{2} \dot{q}_2^2 + \frac{(m_3)}{2} \dot{q}_3^2 \quad (18)$$

$$U(q) = (m_3)g(q_3 + l_1) \quad (19)$$

- With the obtained kinetic energy and the potential energy given, we obtain the Lagrangiano (21).

$$L(q, \dot{q}) = K(q, \dot{q}) - U(q) \quad (20)$$

$$L(q, \dot{q}) = \frac{(m_1 + m_2 + m_3)}{2} \dot{q}_1^2 + \frac{(m_2 + m_3)}{2} \dot{q}_2^2 + \frac{(m_3)}{2} \dot{q}_3^2 - (m_3)g(q_3 + l_1) \quad (21)$$

- The equation of motion Euler-La Grange is the following (22).

$$\frac{d}{dt} \left[\frac{\partial L(q, \dot{q})}{\partial \dot{q}_i} \right] - \frac{\partial L(q, \dot{q})}{\partial q_i} = \tau_i, \quad i = 1, \dots, n \quad (22)$$

- Finally, the dynamic equations that model the forces applied on each joint of the robot are expressed as (23), (24), (25).

$$\tau_1 = (m_1 + m_2 + m_3)\ddot{q}_1 \quad (23)$$

$$\tau_2 = (m_2 + m_3)\ddot{q}_2 \quad (24)$$

$$\tau_3 = (m_3)\ddot{q}_3 + (m_3)g \quad (25)$$

B. Features of the robot

- 1) *Mechanical structure*: Cartesian type.
- 2) *Degrees of freedom (GDL)*: 3GDL.
- 3) *Range of motion*: Axis Z (vertical) and axis X (horizontal).
- 4) *Feedback*: Encoder in quadrature with a resolution of 8400 pulses per revolution of the output of the motor shaft.

- 5) *Actuators:* Motor C.D. 12VDC with a gearbox of metal 131.25 :1 (Axes Z), Piezoelectric Motor 6VDC (axes X).
- 6) *Accuracy in linear motion:* Transmission with pulleys and bands for acople, rail for linear guide 15mm, linear block for guide 15mm, screw packed with nut 16 mm.
- 7) *Height of the robot:* 0.40m .
- 8) *Maximum load.:* Axis Z (vertical) and axis X (horizontal) .
- 9) *Travel Range (eje Z,X) Piezomotor:* 12mm .
- 10) *Total weight of the robot:* 3.2Kg

V. CONTROL SYSTEM

A. Hardware

The following block diagram shows Fig. 13, the connection of the phases of our system for the experiment, each motor has two signals (A and B), and is connected to the FPGA for their control, this FPGA in turn is coupled to a module WiFi as acquisition system, this card is to be able to send and receive data via WiFi from computer to the FPGA, and thus, to make the process of our signs of the Encoders and the engines on our, the FPGA card designed previously in the Faculty of Sciences of the electronic (BUAP).

1) *Motorreductor 37DX57Lmm:* The gear motor 37DX57L is a powerful dc motor 12V with a gearbox of metal 131.25 : 1 and a quadrature encoder integrated that provides a resolution of 64 pulses per revolution of the motor shaft, which corresponds to 8.400 counts per revolution of the output shaft of the gearbox. These units have an output shaft of 0.61in, 6mm in diameter in the form of D, [11].

2) *Encoder:* The encoder is based on Hall sensors, detects the rotation of the motor shaft. The wiring consists of six wire colors of about 28 cm cables are peeled with the terminals and without any connector, so that it can be welded or put a few connectors depending on the need we have. The Hall sensor requires a voltage (Vcc) of between 3.5V and 20V and a maximum current of 10mA. The A and B outputs are square waves from 0V up to Vdc with a lag of 90 °C. The frequency of the transitions tells you the speed of the motor and the order gives you the address [11].

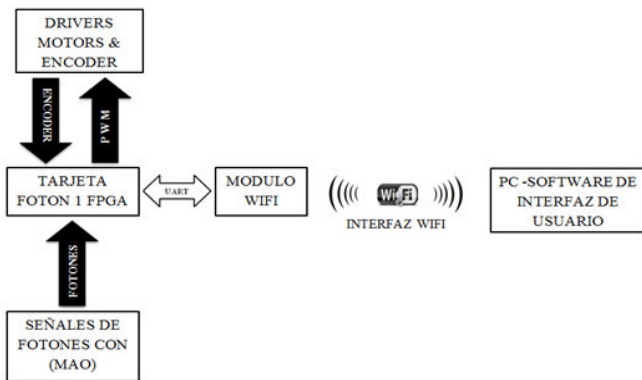


Fig. 13. Blocks of the implementation of the hardware.

a) *Incremental Encoder:* This type of encoder is characterised because it determines your position, count the number of impulses that are generated when a ray of light, and traverses by dull marks on the surface of a disc attached to the shaft [2]. The output of an encoder signals can be a train of pulses, in the form of square signal, where the number of impulses generated in a return match the number of impulses from the disk encoder inside, we are referring to a single channel (A signal) encoders. A second signal B to supply a pulse train identical to that supplied the outdated but signal 90 ° with respect to this, refers to a two-channel encoder [12].

b) *Theoretical resolution of the system.:* One of the biggest questions we have in the manufacture of the system is to know if we can obtain the accuracy desired in our degree of freedom of the system, we need to check if we can theoretically obtain the accuracy desired precision 10µm, can perform theoretical calculations to know if even theoretically this precision can be predicted. The theoretical resolution that includes this axis is determined by the following equation (27) [12].

$$\Delta z = (Lz)/(MRC) \quad (26)$$

$$\Delta z = 0.22m / ((17)(131)(8400)) = 11.76 \text{ nm} \quad (27)$$

Where:

Δz = theoretical resolution in the z-axis.

L z = total effective length of the Z axis.

M = number of turns needed to displace Lz.

R = reduction of the box of gear motor.

C = resolution of counts per turn of the motor.

c) *Power stage.:* For control of the rotation of our motors he is needed a power circuit, which will consist of a H-bridge with power transistors, this in turn will control the rotation and will have another entry that will receive a signal in the FPGA, PWM, on the other hand, the H bridge will serve to characterize our engine and get the ideal frequency for optimum performance of the engine Fig. 14.

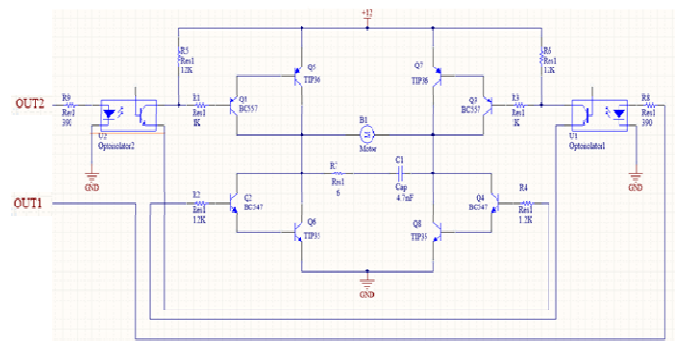


Fig. 14. Power Stage.

3) *Characterization of the motorreductor:* The motor torque or torque is the moment of force exerted on a motor shaft power transmission. If a body is able to rotate on an axis, the result of the force is a combination of the applied force and the distance to the rotational axis, as can be seen in Fig. 15 [13]. The function of the characterization is that it allows us that the C.D. motor should be modified its frequency of work, in order to which the motor works like an motor of direct transmission. We cannot modify the voltage, because the voltage that we need is 12v, therefore it is constant and to to be modifying the voltage it begins working to 3.5V, and the torque necessary for this one is not sufficient, the current cannot also be modified since the current only consumes it, so, what we must modify is the work cycle across an ideal frequency of the motor and that we will be modifying to obtain different forces without forcing the efficiency of the engine. To obtain the force with which the motor works, uses a dynamometer digital Fig 16.

4) *Control electronic card:* The electronic card consists of: a Cyclone III FPGA, 4 connectors 50 pin header of each one, a reset circuit, a crystal oscillator with their respective resistors and capacitors. The card is as a processing core Cyclone III EP3C10F207C6 alters, is responsible for reading and processing the information from the encoders and WiFi interface, as well as the processing of the counts of photons Fig. 17.

5) *WiFi Module:* The module RN-XV is based on the module-Roving Networks RN-171 [14]. Since the RN-XV module has a built-in firmware Fig. 17. This version also includes the mode of operation of the access point and the settings default access point are created by the module [14].

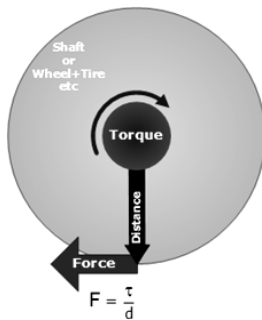


Fig. 15. Graphical representation of the Torque.



Fig. 16. Characterization of the motorreductor.

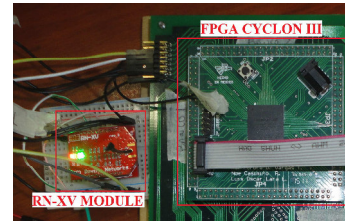


Fig. 17. WiFi module.

a) *SSID:* is the name of the access point that the module transmits.

b) *Canal:* is the channel that is being used by the module. It is recommended that the nearby access points use different channels to avoid interference; channel 1 is used for this project.

c) *DHCP:* (Dynamic Host Control Protocol) enabled and your job is auto assign / re-assign IP devices that connect to the access point

d) *Project management IP:* logical address of the module, IP 1.2.3.4.

e) *Network Mascara:* 0 is used to specify the bits of the IP address of the network that can be used to assign IP addresses to the devices that are in the network, for example 255.255.255.0.

f) *Link gate:* is the address of the router that manages the network in this case through the point of access 1.2.3.4.

6) *UART:* The Universal Asynchronous Receiver Transmitter or Receiver/Transmitter Universal Asynchronous enables you to establish a serial communication between two devices. You can be 2 lines, or 4 if it makes use of the flow control. The wiring is simple See Fig 18. The basic communication of the UART is shown in Fig 19. Choose a reading speed increased 16 times, where there is a counter that sets the tone to read the bit to reach half of its count. Should be noted that despite that sent packages where understood by package start/stop bits more of data, even if there is a deviation, this only brings the end bit is received, since each home (getting a bit of home) resyncs transfer and so on, is shown in Fig 20 .

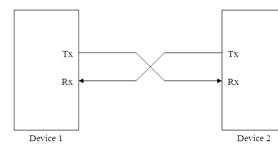


Fig. 18. UART Communication.

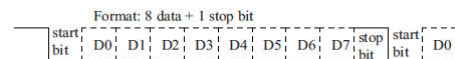


Fig. 19. UART.

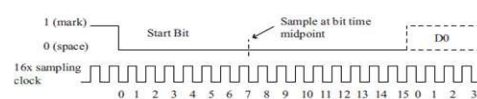


Fig. 20. Sampling of the data to a period of 1/16 of the time per bit.

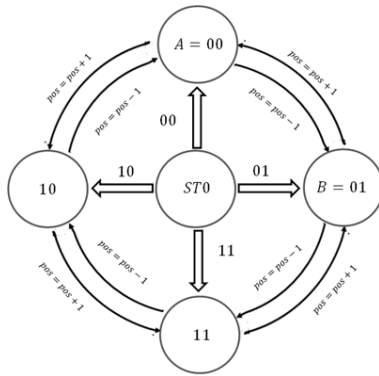


Fig. 21. Encoder reading.

B. Firmware

1) *Motor Frequency*: To use the technique of speed control PWM needs to work with certain frequencies. each engine works with different frequencies, although the same type of with the same mechanical properties does not work with with the same frequency. For this, was done the characterization of the engine, and the frequency to M1 is 350 Hz , 330Hz M2, and M3 of 240 Hz. To perform the control of the motor in our FPGA, is necessary generate this frequency, our FPGA works with an internal clock of 100Mhz, therefore, we need to realize a delay in exit of the signs to generate the frequency for every motor.

a) *PWM*: If half of the PWM to input is required you will be provided the data of 128 and if required a quarter of the final value of the PWM is provided 64 and so on to generate the value delivered by the PWM.

2) *Encoder Implementation*: The flow diagram of Fig 21 shows the signals from the encoder with precision without losing accounts, ensuring the maximum performance of our system.

3) *UART protocol*: The UART Protocol has been implemented in the FPGA, particularly in AHDL language (Altera Hardware Design Language), in Fig. 22 is observed the UART firmware block diagram [15].

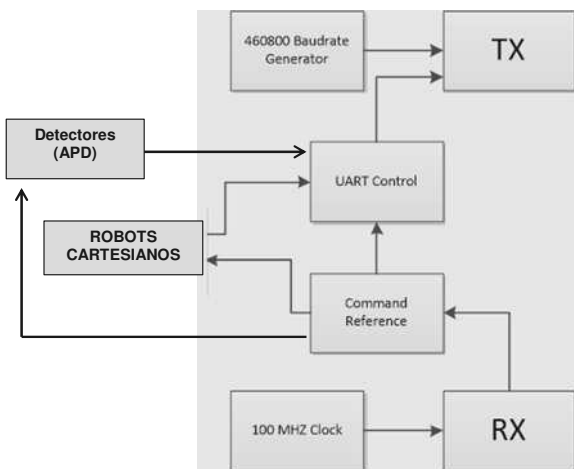


Fig. 22. Control WiFi.

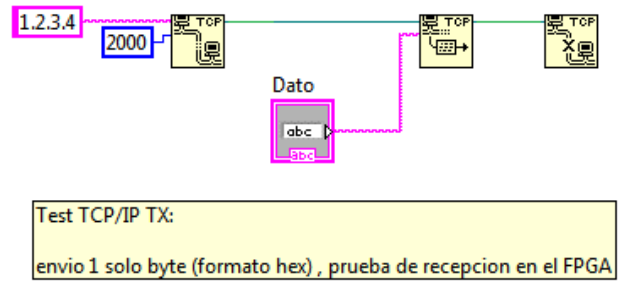


Fig. 23. TCP/IP Writing.

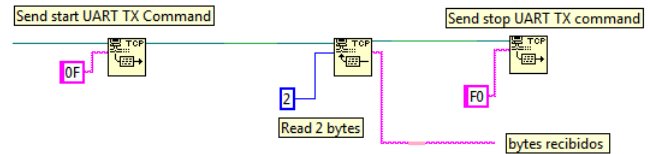


Fig. 24. Commands sending.

C. Software

1) *WiFi writing*: the unspecified parameters take default values. The process is simple, once the computer is connected to the access point created by the RN-XV module, Fig. 23 shown the software connected to RN-XV module that operates as a server, waiting requests through your IP (1.2.3.4) and by port 2000, then writes the data using the TCP Write function and finally closes the connection.

2) *Commands sending*: Since the user interface must allow the user send commands to the FPGA to indicate that action should be performed. The description is shown in Fig. 24. the 0F Hex command is written to instruct the FPGA to initiate data transmission via WiFi. Then, it reads two-byte package and ultimately sends the command F0 indicating to stop the transmission of data to the FPGA.

3) *WiFi reading*: The description is shown in Fig. 25. For the reading opens a connection, the function TCP read and wait to receive the 2 bytes that indicated that they received, then timeout by default and there are 25 seconds to receive them, in case of not receiving the bytes, an error message is generated. Once we receive the bytes, the connection is closed. The bytes are received in format string and they are converted to an array of 8-bit elements. Subsequently with array index function separates array elements in order to obtain each byte separately.

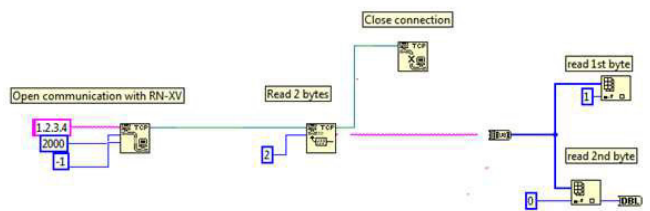


Fig. 25. WiFi reading.

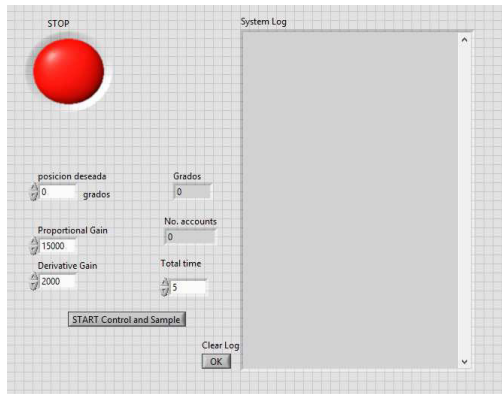


Fig. 26. Software Monitoring.

4) *Software monitoring*: Once obtained the necessary parameters, such as the reading of the encoder, the error of the system, the positions, velocities, only send the desired position and earnings and the robot performs its task properly, software to perform the experimentation of control and feedback is shown in Fig. 26.

VI. RESULTS

Given the results of this project have been realized tests and simulations , Fig. 27 shows the experimental evidence obtained in the experiment of the array optoelectronic manually and they carry much time make them and are not exact sometimes, for this motive it is necessary to automate. In the Fig. 28 shows an image constructed of the Cartesian robot and that will be used for the route with the optical fibre to realize the photons correlation. In the Fig. 29 shows the tests of the encoders to observe the signal that it provides our sensors and to observe the behavior of the signal applying 3.2v to the source of the encoders and that the exit of the sensors also is of 3.2v and to introduce without problems the FPGA, since the alone FPGA supports voltage of 0 to 3.3v, once the signal of the encoder are obtained, adds a capacitor of 100pf in parallel with the signal and ground of the system, this in order to that the obtained signal should avoid to have noise, voltage peaks and this way to avoid to damage the FPGA. On the other hand, the frequency of the motors obtained in the characterization verifies the work cycle and we find the ideal frequencies and verifying wich one is the most linear, in the M1=330HZ, M2=350, M3=240HZ, in the Fig. 30 shows the M2 and we design the firmware in AHDL of the Fig. 31.

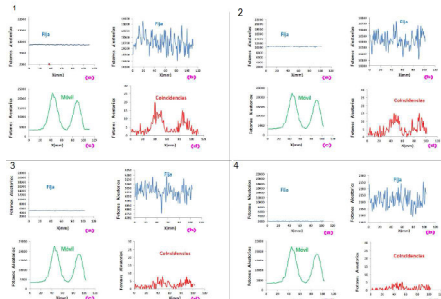


Fig. 27. Experimental evidence photon detection manually.



Fig. 28. Cartesian robot built.

For the design of the firmware of the encoder of position they were realized in AHDL together with the position block how appears in the Fig. 32, with this block it is already possible to do the count of the signs of the encoder with all precision without losing accounts, guaranteeing the maximum performance of our system, the simulation shows itself in the Fig. 33. Finally, in the Fig. 34 we have the design to blocks WiFi, one finds the blocks of transmission and recipient, the transmission module is provided with a clock formed to 460800 bauds. It is provided with an entry of fitting out and entry of information and an exit that it indicates that the module is busy. The reception module takes the information to 100Mhz, being synchronized to the transmission bauds by means of delays. To carry out a reliable reading, the information is read to half of the transmission of every bit. Its exits are the received byte and an indicator (dataRdy) who generates a pulse from which the fact has been received. THE module of (UART Control) is the manager of sending the information towards the UART TX and of this form that they are sent by WiFi to the user. The sent information is the current position and the applied pair. It has an entry to determine if the transmission module is occupied and other one of fitting out to initiate a transmission originated from the module (Command Reference), this module receives from Labview a byline header from 32 bits.

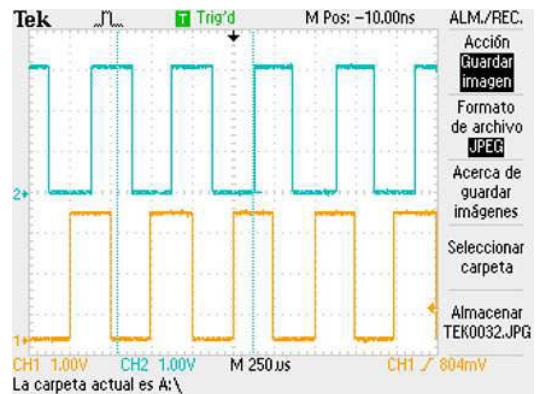


Fig. 29. Encoder signal with oscilloscope.

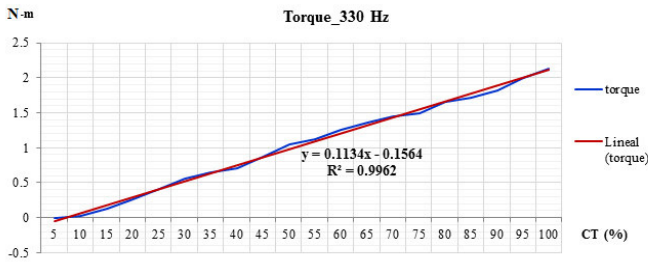


Fig. 30. Frequency ideal of the motor 2 (M2).

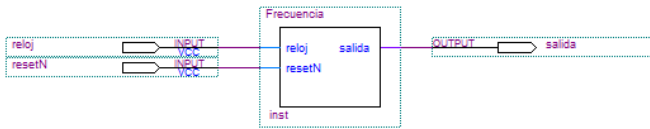


Fig. 31. Block firmware of the frequency ideal of the motor.

VII. CONCLUSIONS

Before starting work, the experiment was understood, by what, one of the needs that are important is the precision linear motion and, so it was decided to design and implement three Cartesian robots that perform these functions. The robots designed is implemented to move in the Z axis using rails and precision screws, this will give us the desired position and accuracy in the movement. For the movement in the X-axis is going to be mounted a motor piezoelectric ultrasonic already that we want greater accuracy and that does not have vibration or other obstacles, the positioner should have a resolution in Nm and move to a distance of approximately 1cm which is the approximate diameter of the interference pattern of the ring. In our dynamic model is based on the study of a Cartesian robot type, so it is not complicated its development and there are many research studies on the dynamic model. In characterizing our engine, means that it is essential to understand and meet our engine, as we predict if our engine is efficient and meets the requirements. Tests were carried out with the engine and we could see that it is efficient in 12v and then we opted to find the best frequency, in order that our motor works as direct transmission motors and thus achieve its behavior linear, we as 50% of the working cycle and frequencies given are carried out the firmware design. Tests were conducted on the robot by closing a control loop (via Wi-Fi) and we observe that if you move to your desired position, with this we are going to be managing to assemble our finished system to realize the experimental tests of the optoelectronic array.

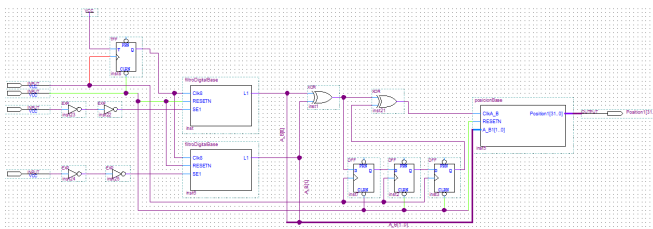


Fig. 32. Block Firmware of the Encoder position.

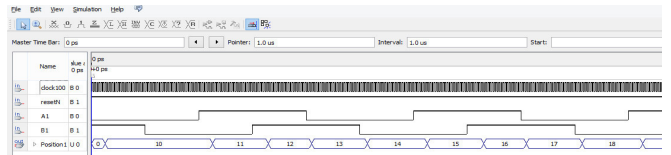


Fig. 33. Simulation Encoder of position

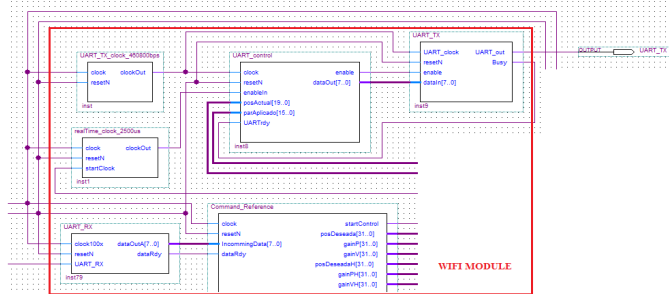


Fig. 34. Firmware WiFi modules of communication.

ACKNOWLEDGMENT

The authors of this article want express his thanks to the jury of this work, contribute their comments and support. Likewise wish to thank the anonymous reviewers who have contributed their comments to improve the final version of this article.

REFERENCES

- [1] Vergara S., Vargas M.A., Paic G., Tejeda G., Fernandez A., León I., Reyes F., and Villaseñor L. *Characterization of the ACORDE scintillator counters using a PCI electronic card*, volume 53 (2) 120-125. Revista Mexicana de Física, México, Abril 2007.
- [2] Fox Anthony Mark. *Quantum Optics An Introduction*. Department of Physics and Astronomy, University of Sheffield, 2005.
- [3] E. J. Galvez, *Gaussian beams in the optics course*, American Association of Physics Teachers, 74, 2006, 355-361.
- [4] L. Allen, M. W. Beijersbergen, R. J. C. Spreeuw, and J. P. Woerdman *Orbital angular momentum of light and the transformation of Laguerre-Gaussian laser modes*, Phys. Rev., 45, 1992, 8185-8189.
- [5] M. W. Beijersbergen, L. Allen, H. Van der Veen and J. P. Woerdman, *Asig-matic laser mode converters and transfer of orbital angular momentum* Opt. Commun., 96, 1993, 123-132.
- [6] E. Yao, S. Franke-Arnold, J. Courtial and M. J. Padgett, *Observation of quan- tum entanglement using spatial light modulators*, Optics Express, 14, 2006, 1389-13094.
- [7] M. Padgett, J. Courtial and L. Allen, *Light_s Orbital Angular Momentum*, Phys. Today, 57, 2004, 35-40.
- [8] J. Arlt, K. Dholakia, L. Allen and M.J.Padgett, *The production of multiringed Laguerre-Gaussian modes by computer-generated holograms*, J. of Mod. Opt., 45, 1998, 1231-1237.
- [9] D. L. Andrews, *Structured Light and Its Applications: An Introduction to Phase- Structured Beams and Nanoscale Optical Forces*, Academic Press, 2008.
- [10] Reyes Cortés Fernando, *Robotica: Control de Robots Manipuladores*, 1ra Ed. 2011.
- [11] Pololu Documentation: 131:1 Metal Gearmotor 37Dx57L mm with 64 CPR Encoder. <https://www.pololu.com/product/1447>. 2001–2015 Pololu Corporation.
- [12] Josep Balcells, José Luis Romeral, *Autómatas Programables*, marcombo, 1997.
- [13] Roving Networks Inc., *WiFly Command Reference, Advanced Features & Applications User's Guide*, Version 1.1r 3/27/13.
- [14] Reese Robert, *Microcontrollers From Assembly Language to C Using the PIC24*, Charles River Media, 2005.

Enhancement of the photoactivity RuO₂ doped nanoparticles TiO₂ supported on disordered mesoporous silica as photocatalysts for methylene blue photodegradation

Y.J. Acosta-Silva^{*,1}, R. Nava², A. Méndez-López³

¹ Depto. de Física, Centro de Investigación y de Estudios Avanzados del Instituto Politécnico Nacional, Avenue IPN No. 2508, 07360 Mexico City, DF, Mexico.

¹ yuliacoss@gmail.com

² División de Investigación y Posgrado, Facultad de Ingeniería, Universidad Autónoma de Querétaro (UAQ), Centro Universitario, 76000 Querétaro, Qro., Mexico

² rufino@uaq.mx

³ Sección de Electrónica del Estado Sólido (SEES), Depto. de Ingeniería Eléctrica, Centro de Investigación y de Estudios Avanzados del Instituto Politécnico Nacional, Avenue IPN No. 2508, 07360 Mexico City, DF, Mexico

³ amendez@cinvestav.mx

Abstract— RuO₂ doped nanoparticles TiO₂ supported on disordered mesoporous silica (DMS-1) was synthesized by the sol-gel method, its ex-situ modification with TiO₂ nanoparticles. The photoactivity was examined for methylene blue photodegradation in aqueous medium. To assist in interpreting the photocatalytic behavior of 0.76%RuO₂-40%TiO₂/DMS-1 and 0.79%RuO₂-30TiO₂/DMS-1, reference systems consisting of x%TiO₂/DMS-1 photocatalysts undoped RuO₂ and TiO₂ pure (Degussa P-25). The load RuO₂ <1.0 wt% was prepared by impregnation method and vary amount of TiO₂ (30 and 40 wt.%). The photocatalysts were characterized by N₂ adsorption-desorption isotherms, X-ray diffraction (XRD), UV-vis diffuse reflectance spectroscopy (UV-vis DRS) and transmission electron microscopy (TEM). The results showed that RuO₂ on TiO₂ present greater activity photocatalytic due to the presence of RuO₂ that promoting efficiently charge separation, causes inhibition of recombination of electron-hole pairs.

Keywords— Methylene blue; Photocatalysts; DMS-1; x%RuO₂-x%TiO₂/DMS-1; x%TiO₂/DMS-1.

I. INTRODUCTION

Photodegradation of dyes by metal oxide has seen a remarkable improvement due to the environmental necessity that arises as large quantities of dyes are released as waste into the environment. Thus, the release of dyes in the environment will affect the bio-diversity. Among the various dyes, methylene blue (MB) is the most commonly employed dye

that finds enormous applications in printing and dyeing industry [1]. Dye effluents can be treated by biological methods, flocculation, reverse osmosis, adsorption on activated charcoal, chemical oxidation methods and advanced oxidation processes [2]. Heterogeneous photocatalysis is one of the feasible methodologies that can be effectively exploited for the complete degradation of various dye pollutants present in natural environment. Among the different metal oxide semiconductors, TiO₂ has been widely used as a photocatalyst because of its relatively high photocatalytic activity, biological and chemical stability, low cost, nontoxicity, and long-term stability against photocorrosion and chemical corrosion [3].

However, the high recombination rate of photoinduced electron-hole pairs produced during photocatalytic processes limits the application of TiO₂. Among the different approaches, surface modification by coating noble metal on TiO₂ surface is one of the effective methods to reduce electron-hole recombination in the photocatalytic process [4]. Along noble metals like gold or platinum, other metallic compounds can also be associated with TiO₂ to enhance its photocatalytic performances. As an example, ruthenium (IV) oxide (RuO₂), which belongs to the family of transition-metal oxides with rutile-like structure, shows an interesting variety of properties.

Because of its high chemical stability, electrical (metallic) conductivity, and excellent diffusion barrier properties. RuO₂ exhibits an excellent metallic conductivity related to its partially filled metal (d)-oxygen (p) π^* band [5]. Sakata *et al* [6] showed that RuO₂ is an efficient hole and electron transfer catalyst on TiO₂ and seems to improve the efficiency of charge separation at the metal/semiconductor interface, when deposited in small quantity, as an excessive amount may act as recombination center. In addition, RuO₂ has a high work function, situated in the band gap above the valence band of

TiO₂ [7]. In contact, electrons will be transferred from TiO₂ to RuO₂ in order to equalize the Fermi level at thermal equilibrium. As a consequence, an upward bending of energy bands is expected from TiO₂ to RuO₂ which favors an efficient charge separation at the RuO₂/TiO₂ interface under illumination. Another important beneficial effect of RuO₂ loading on TiO₂ is the increase in conductivity, which ultimately allows more efficient charge transfer within the photocatalyst and makes it kinetically faster when it is involved in the redox processes [8]. However, small particles RuO₂-TiO₂ particles exhibit two disadvantages. Firstly, trend to agglomerate into large particles, making against on catalyst performance. Secondly, the separation and recovery of catalyst is difficult [9]. Recently, introducing titanium species into mesoporous silicate materials has attracted much interest because the titanium containing mesoporous materials have much higher active surface areas (>200 m²/g) in comparison to pure titania, which makes them more effective [10].

The disordered mesoporous silica (DMS-1) has the disordered arrangement of its mesoporous, wormhole pore morphology (small path left by a worm). This material is characterized as a material composed of silica nanoparticles agglomerates which have a spherical shape, resulting in the formation of a high textural porosity and with high surface area (in the 600-1000 m²/g range) [11]. The immobilization and stabilization of the nanoparticles of RuO₂-TiO₂ in the DMS-1 eliminates the majority of the problems associated with slurries such as particle aggregation allows with a suitable mean pore size induce controlled oxide particle growth, uniformity of size, as well as to stabilize and prevent agglomeration of the particles.

In this research study, we use RuO₂ doped nanoparticles TiO₂ supported on disordered mesoporous silica for methylene blue photodegradation. DMS was synthesized using sol-gel method, TiO₂ nanoparticles for ex-situ method and doped with ruthenium for impregnation. Furthermore, the structural characterization of the photocatalysts doped with RuO₂ (x%RuO₂-x%TiO₂/DMS-1) and undoped (x%TiO₂/DMS-1) has been performed using several techniques such as N₂ adsorption-desorption isotherms, X-ray diffraction (XRD), UV-Vis diffuse reflectance spectroscopy (UV-Vis DRS) and transmission electron microscopy (TEM).

II. EXPERIMENTAL

2.1. Preparation of the support DMS-1

The support DMS-1 was synthesized according to the procedure described by Zhao *et al.* [12]. The Pluronic F127 was dissolved in a mixture of water and 2M hydrochloric acid solution vigorously stirred for 1 h. Subsequently, the TEOS was added. After 48 h stirring at 298 K and then the mixture was subsequently transferred into polypropylene bottles and heated at 353 K for 48 h. Afterwards the solid product was filtered, washed with distilled water and dried at 383 K for 18 h and finally was calcined at 823 K for 4 h to remove the organic template.

2.2. Modification of mesoporous DMS-1 with TiO₂ particles

The modification of support material is based in the method described by Peza-Ledesma *et al.* [13]. Different amounts of titanium (IV) isopropoxide (97%, Aldrich, IPOTi), were added gradually to 2-propanol (99.5%, Sigma-Aldrich), the solution was formed at room temperature under constant stirred in an inert atmosphere of N₂ for 45 min. The support material DMS-1 was added and the mixture was stirred for 1 h at room temperature. Then, deionized water was slowly added and the liquid suspension was stirred for 30 min. Finally, the solids were dried at room temperature and later at 383 K for 18 h before being calcined at 823 K for 4 h.

2.3. RuO₂ doped TiO₂/DMS-1 photocatalysts

RuO₂ doped TiO₂ particles supported on disordered mesoporous silica were prepared at room temperature by incipient wetness impregnation method. The modified materials mesoporous x%TiO₂/DMS-1 were impregnated with an aqueous solution of ruthenium trichloride trihydrate (RuCl₃, 99%, Aldrich) with appropriate amount of the precursor corresponded to the theoretically necessary loading of <1 wt%. The synthesized samples were dried at 110 °C for 18 h, and there after calcined at 500 °C for 4 h.

III. CHARACTERIZATION METHODS

3.1. N₂ adsorption-desorption isotherms

The textural properties of the photocatalyst doped and undoped with RuO₂ were determined from the nitrogen adsorption isotherms recorded at 77 K with a Micromeritics TriStar 3000 apparatus. The samples were previously degassed at 423 K for 24 h under a vacuum (10⁻⁴ mbar) to ensure a clean, dry surface, free of any loosely bound adsorbed species. The specific areas of the samples were calculated according to standard BET procedure using nitrogen adsorption data collected in the relative equilibrium pressure interval of 0.03 < P/P₀ < 0.3. Pore size distributions were calculated from the adsorption and desorption branches of the corresponding nitrogen isotherm using the BJH method. The total pore volume (V_{total}) was estimated from the amount of nitrogen adsorbed at a relative pressure of 0.99.

3.2. X-ray diffraction (XRD)

X-ray diffraction (XRD) patterns of photocatalysts doped and undoped with RuO₂ were obtained on a Bruker D8 Advance diffractometer using Cu K α radiation ($\lambda = 1.5406 \text{ \AA}$) over the scan range of 2θ between 10 and 80 at 295 K, in order to identify the phase present.

3.3. Diffuse reflectance spectroscopy (DRS)

The UV-Vis diffuse reflectance spectra of the photocatalysts were recorded at room temperature using an Ocean Optics Inc. spectrometer First in Photonics (Mini-DT 2) in the 200-400 nm range. The respective support of each photocatalyst was used as a reference.

3.4. TEM measurements

Transmission electron microscopy (TEM) studies were carried out on a JEM 2100F microscope operating with a 200 kV accelerating voltage and fitted with an INCA X-sight (Oxford Instruments) energy dispersive X-ray microanalysis (EDX) system employed to verify the semi quantitative composition of solids.

3.5. Photocatalytic activity

The photodegradation of methylene blue (MB) was performed in order to evaluate the photocatalytic activity of prepared $x\%Ru-x\%TiO_2/DMS-1$ and $x\%TiO_2/DMS-1$ photocatalysts. For all photocatalysts, the adsorption and catalytic activity were investigated. Therefore, the MB concentration (initial concentration of 40 mg/L) was measured at distinct time intervals by means of UV-vis spectroscopy (Varian Cary 5000 Scan UV-vis-NIR spectrophotometer). The amount of photocatalyst undoped and doped with RuO_2 used in each experiment was adjusted to achieve the same loading 30.0 mg. Commercial pure TiO_2 (P-25, Degussa Co., Germany) as those of reference sample. The mixture was first stirred for 15 min in the dark at room temperature to assure that the adsorption equilibrium was reached. Then the reaction solution was placed perpendicularly to a 125 W medium pressure mercury lamp inside cold water and the solution was bubbled with air under magnetic agitation in a cylindrical double wall jacket glass reactor.

The concentration of the remaining MB was analyzed in fixed time intervals in 5 mL volume following centrifugation. The photocatalytic degradation of methylene blue was determined by means of UV-vis spectrophotometry through monitoring of color disappearance. Unfortunately, there is no way to evaluate the extent of mineralization the MB into harmless gaseous CO_2 , NH_4^+ and NO_3^- using UV/vis technique employed. The concentration of MB was obtained by converting absorbance of the solution to MB concentration (Beer-Lambert's law, $A = \epsilon bC$, where A: absorption, ϵ : proportion constant, b: light length, C: concentration). A calibration curve of MB solution absorbent was obtained at 665 nm wavelength at different concentrations prepared. A standard calibration curve (not shown here) was built by adjusting a different concentration of MB solution and the absorption at 665 nm. This calibration curve refers to the situation of the absence of by-products co-adsorption.

IV. RESULT AND DISCUSSION

4.1 Surface area and pore volume

The textural properties of RuO_2 doped photocatalysts were studied using the adsorption-desorption isotherms of N_2 at 77K. The adsorption-desorption isotherms of N_2 of the materials are shown in Figure 4.1. Similarly to the materials $x\%TiO_2/DMS-1$ [14], all photocatalysts doped RuO_2 $x\%Ru-x\%TiO_2/DMS-1$ exhibit hysteresis curves with two stages of capillary condensation with P/P_0 in the ranges from 0.4 to 0.6 and 0.8-0.9. The low pressure hysteresis loop is probably an artifact due to the lack of equilibrium in the adsorption branch whereas the second hysteresis loop, which starts at a relative

pressure of 0.8, is due to textural interparticle mesoporosity or macroporosity. This clearly indicates that the photocatalysts $0.79\%Ru-30\%TiO_2/DMS-1$ and $0.76\%Ru-40\%TiO_2/DMS-1$ exhiben in addition to the porosity provided by (structural porosity) an additional porosity (textural porosity), as evidence the adsorption step at $P/P_0 > 0.8$ [15]. This result is typical of a disordered mesoporous material, probably with an arrangement of pores as small path left by a worm, wormhole. The disordered structure of the mesoporous silica is maintained after doped with RuO_2 which is highly dispersed on TiO_2 particles supported on the DMS-1.

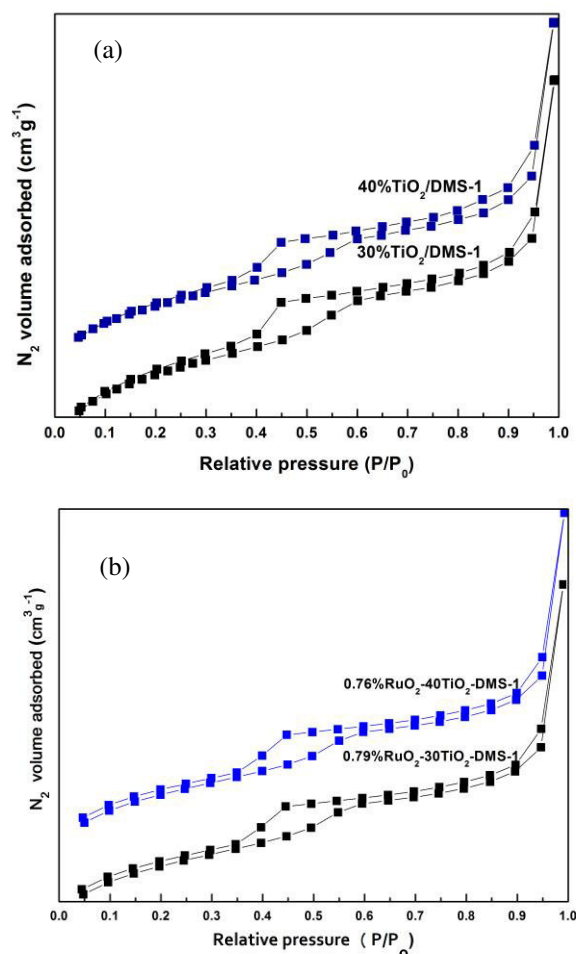


Fig. 4.1. N_2 adsorption-desorption isotherms (a) $40\%TiO_2/DMS-1$ and $30\%TiO_2/DMS-1$ (b) $0.76\%RuO_2-40\%TiO_2/DMS-1$ and $0.79\%RuO_2-30\%TiO_2/DMS-1$ mesoporous samples.

Figure 4.2 shows the pore size distribution of the photocatalyst $x\%RuO_2-x\%TiO_2/DMS-1$, using the information in the adsorption-desorption isotherms of nitrogen calculated by the BJH method. All photocatalysts $0.79\%RuO_2-30\%TiO_2/DMS-1$ and $0.76\%RuO_2-40\%TiO_2/DMS-1$ shows mesopore distribution around 3.4 nm due to the mesoporous structure, photocatalysts have a uniform and narrow distribution of pore size.

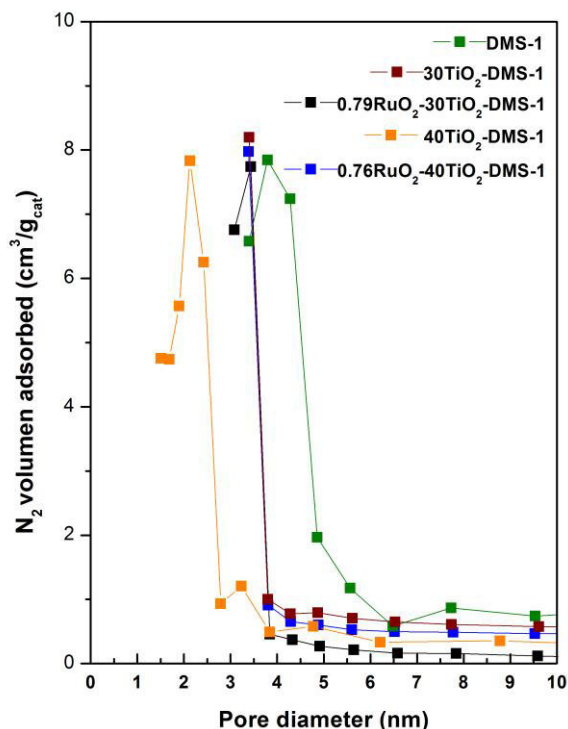


Fig. 4.2. Pore size distribution of the $x\%TiO_2/DMS-1$, $x\%RuO_2-x\%TiO_2/DMS-1$ and $DMS-1$ samples calculated from the adsorption branch of the N_2 isotherm using the by BJH method.

RuO_2 doped photocatalysts not show decreased diameter and pore volume after the addition of the metal, due to its low concentration and high dispersion. RuO_2 doped photocatalysts have a decrease in BET surface area due to the incorporation of RuO_2 on TiO_2 particles supported on the $DMS-1$ compared to the corresponding supports $x\%TiO_2/DMS-1$. This indicates that a part of TiO_2 particles are doped with RuO_2 in the pores of the $DMS-1$. The BET surface area values of the materials $x\%RuO_2-x\%TiO_2/DMS-1$ are in the range ($328-403\text{ m}^2\text{g}^{-1}$). The surface areas of the doped and undoped photocatalysts and pore parameters are summarized in Table 4.1.

TABLE I. CHEMICAL^a AND TEXTURAL^b PROPERTIES OF $X\%TiO_2-DMS-1$ AND $X\%RuO_2-X\%TiO_2/DMS-1$ MESOPOROUS MATERIALS.

Samples	S_{BET} (m^2/g)	d (nm)	V_{total} (m^3/g)	RuO_2 (wt.%)
40% $TiO_2/DMS-1$	377	2.5	0.35	0
0.76% $RuO_2-40TiO_2/DMS-1$	403	3.4	0.37	0.79
30% $TiO_2/DMS-1$	456	2.5	0.35	0
0.79% $RuO_2-30TiO_2/DMS-1$	393	3.4	0.39	0.76

^a As determined by ICP technique.

^b Specific BET surface area (S_{BET}), total pore volume (V_{pore}) and pore diameter (d) as determined by N_2 physisorption at $196\text{ }^\circ\text{C}$.

4.2. Transmission electron microscopy (TEM)

The morphology of the photocatalysts $x\%RuO_2-x\%TiO_2/DMS-1$ can be observed by TEM, Figure 4.3 shows the TEM

image of the photocatalyst $0.79\%RuO_2-30\%TiO_2/DMS-1$, which presents both ordered parallel channels and a disordered mesoporous structure. This result shows that TiO_2 particles are doped with RuO_2 incorporated in the mesoporous structure of the surface of the $DMS-1$, and this leads to a disordered mesoporous region near the surface of the particle and an ordered mesoporous region within particle.

The inset shows the image of the Fast Fourier Transform (FFT), figure 5.4 of the marked area where the plane corresponding reflection (110) shown with interplanar distance of 3.32 angstroms, identified according to PDF # 71-1166 as ruthenium silicide ($RuSi$). These results agree with those of X-ray diffraction.

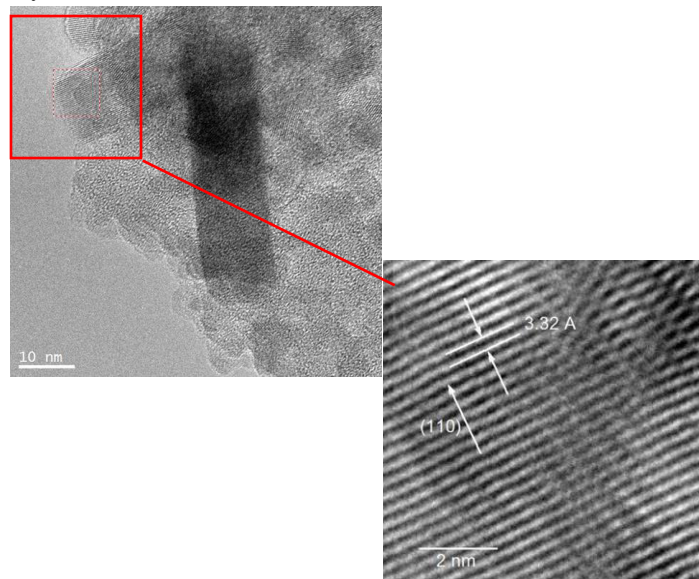


Fig. 4.3. (a) Inverse Fast Fourier Transform box area after applying a filter using the Gatan Digital Micrograph © software for $0.79\%Ru-30\%TiO_2/DMS-1$ photocatalyst (b) Plano (110) for the $RuSi$ PDF # 71-1166 of $0.79\%Ru-30\%TiO_2/DMS-1$ photocatalyst.

4.3. X-ray diffraction (XRD)

Diffraction patterns of the materials $x\%TiO_2/DMS-1$ $x\%RuO_2-x\%TiO_2/DMS-1$ are shown in Figure 7.5. Diffraction patterns show that all materials the anatase crystalline phase is present as indicated by reflections 25.3° , 37.7° , 48.0° , 53.9° , 55.1° , 62.7° , 68.6° and 75.0° (JCPDS 00-004-0477). For photocatalysts doped $x\%RuO_2-x\%TiO_2/DMS-1$ plus a small peak is observed at $2\theta=35^\circ$, which could indicate the presence of RuO_2 [16] which is not observed in but micrographs revealing the presence of said structure. And another small peak at $2\theta=26.8^\circ$ assigned to $RuSi$ (PDF # 83-0145). For all photocatalysts, no peak of (1 1 0) rutile reflection at 27.4° was detected.

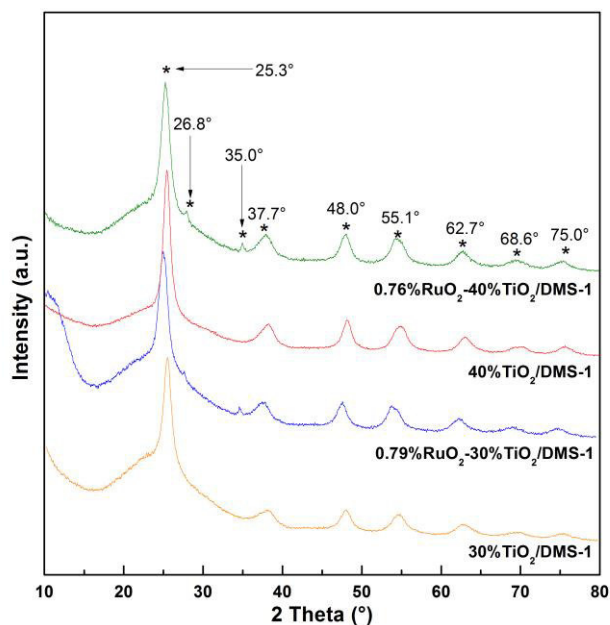


Fig. 4.4. XRD patterns of $x\%TiO_2/DMS-1$ and $x\%RuO_2-x\%TiO_2/DMS-1$ photocatalysts.

4.4. UV-vis diffuse reflectance spectra (DRS)

The diffuse reflectance spectra show a large absorption band below 400 nm Figure 7.6. The spectra exhibited a narrow absorption band at 212 nm attributed to species isolated from [17] Ti (IV) in tetrahedral coordination and broadband 330 nm indicates the anatase phase of TiO_2 . Absorption in the UV range is due to the charge transfer process from the valence band (mainly 2p orbitals) oxide ions to the conduction band (orbital T_{2g}) of Ti^{+4} ions. Comparing the diffuse reflectance spectra of TiO_2 particles doped and undoped Ru remained almost unchanged after dopant, except in increased absorption of visible light with the RuO_2 loading and no detectable phase.

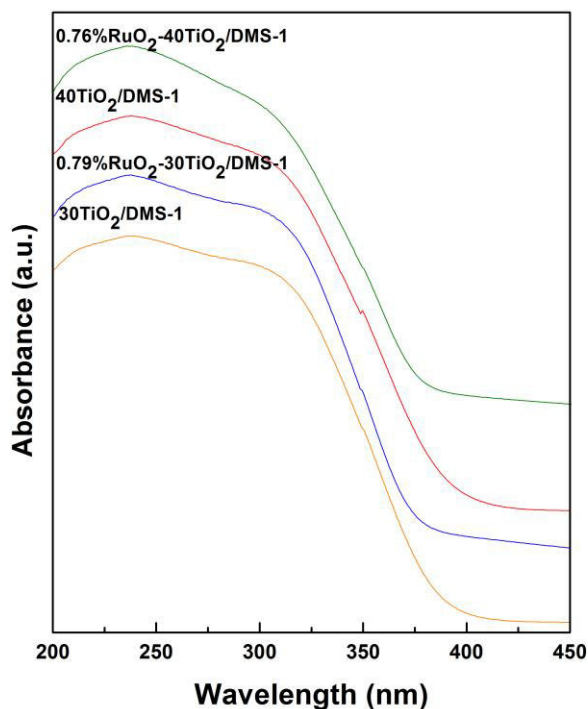


Fig.4.5. DRS UV-vis spectra of $x\%TiO_2/DMS-1$ and $x\%RuO_2-x\%TiO_2/DMS-1$ samples collected at ambient conditions.

4.5. Photocatalytic activity

Figure 4.6. shows the degradation curves of MB with UV light by $x\%RuO_2-x\%TiO_2/DMS-1$, $x\%TiO_2/DMS-1$ and TiO_2 pure samples, without UV irradiation, during the initial 60 min the concentration of MB rapidly decreased and 50-60% is discolored, which was due to the adsorption of dye on photocatalyst surface [17]. The adsorption amount of MB on (adsorption capacity of 50% in the presence of ($x\%RuO_2-x\%TiO_2/DMS-1$, $x\%TiO_2/DMS-1$)) is much higher than that Degussa P-25 (10%), because these photocatalysts have larger surface area and pore volume

Blank experiments were also carried out in the presence of DMS-1, no obvious photodegradation was observed, all the samples show photocatalytic activity, and the MB conversion depends on the Ti and RuO_2 content in the $x\%RuO_2-x\%TiO_2-DMS-1$ materials. The MB was photocatalytic decomposed by $x\%RuO_2-x\%TiO_2-DMS-1$ at higher Ti loading which demonstrated that Ti in the silica is also active for photocatalytic reaction. Besides the adsorption ability of photocatalysts, other factors, such as crystal phase, surface area, crystalline size and crystallinity, also play an important role in influencing photoactivity [18].

Introducing transition metals causes a change in the electronic environment of TiO_2 . Based on the results of XRD and UV-vis. RuO_2 is adsorbed on the surface of TiO_2 , as a small island of metal particles serving as the active sites for photocatalytic reaction [19]. And may promote efficient charge separation, inhibition of recombination of electron-hole pairs and ultimately causing the increased reactivity of the materials $x\%RuO_2-x\%TiO_2/DMS-1$. The increased activity of $x\%RuO_2-x\%TiO_2/DMS-1$ ruthenium doped materials is attributed to the separation of the charge carriers by forming barriers Schottky [20].

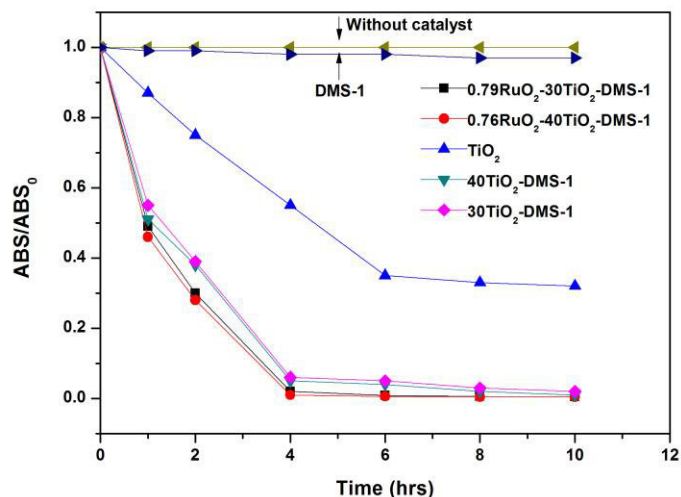


Fig.4.6. Photocatalytic decomposition of methylene blue on $x\%RuO_2-x\%TiO_2/DMS-1$, $x\%TiO_2/DMS-1$ and TiO_2 pure samples.

V. CONCLUSIONS

Photocatalytic degradation of methylene blue in the presence of ultraviolet light is produced in the first instance

through a synergistic effect of the coupling of the methylene blue adsorption on the surfaces of the photocatalysts followed by a second step, the surface photocatalytic oxidation.

The highest crystallinity in the crystalline anatase phase and high surface area, even at high TiO₂ contents and thus have a strong ability to surface adsorption of the dye molecules. Therefore, the photogenerated radicals such as superoxide and hydroxyl radicals readily react with molecules adsorbed on the surface AM catalysts.

The RuO₂-doped materials x%TiO₂/DMS-1 generates more photocatalysts with high activity in the degradation of methylene blue. This is attributable to the presence of RuO₂ on TiO₂ nanoparticles favors charge separation efficiently, causes inhibition of recombination of electron-hole pairs and ultimately causing the increased reactivity of the materials x% RuO₂-x%TiO₂/DMS-1.

REFERENCES

- [1] X. Wan, M. Yuan, S.L. Tie, and S. Lan, "Effects of catalyst characters on the photocatalytic activity and process of NiO nanoparticles in the degradation of methylene blue", *Appl. Surf. Sci.*, vol. 277, pp. 40-46, 2013.
- [2] Y.M. Slokar, and A.M. Le Marechal, "Methods of decoloration of textile wastewaters", *Dyes Pigm.*, vol. 37, pp. 335-356, 1998.
- [3] M.A. Ahmeda, Emad E. El-Katorib, and Zarha H. Gharnib, "Photocatalytic degradation of methylene blue dye using Fe₂O₃/TiO₂ nanoparticles prepared by sol-gel method", *J. Alloy. Compd.*, vol. 553, pp. 19-29, 2013.
- [4] X.Z. Li, and F.B. Li, "Study of Au/Au³⁺-TiO₂ Photocatalysts toward Visible Photooxidation for Water and Wastewater Treatment", *Environ. Sci. Technol.*, vol. 35, pp. 2381-2387, 2001.
- [5] J. Riga, C.T. Noel, J.J. Pireaux, R. Caudano, and J.J. Verbist, "Electronic Structure of Rutile Oxides TiO₂, RuO₂, and IrO₂, Studied by X-ray Photoelectron Spectroscopy", *Phys. Scr.*, vol. 16, pp. 351-354, 1977.
- [6] T. Sakata, K. Hashimoto, and T. Kawai, "Catalytic Properties of Ruthenium Oxide on N-type Semiconductors under Illumination" *J. Phys. Chem.*, vol. 88, pp. 5214-5121, 1984.
- [7] R. Schafranek, J. Schaffner, and A. Klein, "In situ Photoelectron Study of the (Ba,Sr)TiO₃/RuO₂ Contact Formation", *J. Eur. Ceram. Soc.*, vol. 30, pp. 187-192, 2010.
- [8] J. Blondeel, A. Harriman, G. Poter, D. Urwin, and J. Kiwi, "Design, Preparation and Characterization of Ruthenium Dioxide/Titanium Dioxide Catalytic Surfaces Active in Photooxidation of Water", *J. Phys. Chem.*, vol. 87, pp. 2629-2636, 1983.
- [9] J.C. Yu, J.G. Yu, and J.C. Zhao, "Enhanced photocatalytic activity of mesoporous and ordinary TiO₂ thin film by sulfuric acid treatment", *Appl. Catal. B: Environ.*, vol. 36, pp. 31-43, 2002.
- [10] L. Liang, Y. Meng, L. Shi, J. Ma, and J. Sun, "Enhanced photocatalytic performance of novel visible light-driven Ag-TiO₂/SBA-15 photocatalyst", *Superlattices Microstruct.*, vol. 73, pp. 60-70, 2014.
- [11] A. Bahaumik, S. Samanta, and N. Kishor Malet, "Highly active disordered extra large pore titanium silicate", *Microp. Mesop. Mater.*, vol. 68, pp. 29-35, 2004.
- [12] D. Zhao, J. Feng, Q. Huo, N. Melosh, G.H. Fredrickson, B.F. Chmelka, and G.D. Stucky, "Triblock copolymer synthesis of mesoporous silica with periodic 50 to 300 angstrom pores", *Science*, vol. 279, pp. 548-552, 1998.
- [13] C.L. Peza-Ledesma, L. Escamilla-Perea, R. Nava, B. Pawelec, and J.L.G. Fierro, "Supported gold catalysts in SBA-15 modified with TiO₂ for oxidation of carbon monoxide", *Appl. Catal. A: Gen.*, vol. 375, pp. 34-78, 2010.
- [14] J. Y.J. Acosta-Silva, R. Nava, V. Hernández-Morales, S.A. Macías-Sánchez, and B. Pawelec, "TiO₂/DMS-1 disordered mesoporous silica system: Structural characteristics and methylene blue photodegradation activity", *Micropor. Mesopor. Mat.*, vol. 170, pp. 181-188, 2013.
- [15] A. Bhaumik, S. Samanta, and N.K. Mal, "Highly active disordered extra large pore titanium silicate", *Micropor. Mesopor. Mat.*, vol.68, pp. 29-35, 2004.
- [16] M. Senthilnathan M,D.P. Ho, S. Vigneswaran, H.H. Ngo, and H.K. Shon, "Visible light responsive ruthenium-doped titanium dioxide for the removal of metsulfuron-methyl herbicide in aqueous phase", *Separ. Purif. Technol.*, vol. 75, pp. 415-419, 2010.
- [17] R. van Grieken, J. Aguado, M.J. Lopez-Munoz, and J. Marugan, "Synthesis of size-controlled silica-supported TiO₂ photocatalysts", *J. Photochem. Photobiol. A: Chem.*, vol.148, pp. 315-322, 2002.
- [18] J. Yang, J. Zhang, L. Zhu, S. Chen, Y. Zhang, Y. Tang, Y. Zhu ,and Y. Li, "Synthesis of nano titania particles embedded in mesoporous SBA-15: Characterization and photocatalytic activity", *J. Hazardous. Materials. A*, vol. 137, pp. 952-958.
- [19] S. Ozkan, M.W. Kumthekar, and G. Karakas, "Characterization and temperature-programmed studies over Pd/TiO₂ catalysts for NO reduction with methane", *Catal. Today*, vol. 40, pp. 3-14, 1998.
- [20] N. Sasirekha, S.J.S. Basha., and K. Shanthi, "Photocatalytic performance of Ru doped anatase mounted on silica for reduction of carbon dioxide 2, *Appl. Catal. B: Environ.*, vol. 62, pp. 169-180, 2006.

Image Generation Method for Geographic Information Systems with PHP & MySQL

J. A. de Jesús Osuna-Coutiño^{#1}, Elías N. Escobar-Gómez^{#1}, Horacio I. Solís-Cisneros^{#1},
L. Fernando Taracena-Sanz^{#2}, Sabino Velázquez-Trujillo^{#1}, Abiel Aguilar-González^{#1}

^{#1} Instituto Tecnológico de Tuxtla Gutiérrez
Tuxtla Gutiérrez, Chiapas, México

^{#2} Instituto Tecnológico de Querétaro
Querétaro, Querétaro, México

¹ 08270144@ittuxtlagutierrez.edu.mx, ² eescobar@ittg.edu.mx, ³ 09270588@ittuxtlagutierrez.edu.mx,
⁴ fertaracena@yahoo.com.mx, ⁵ svelazquez1@ittg.edu.mx, ⁶ 13270869@ittuxtlagutierrez.edu.mx

Abstract— A current trend for companies dedicated to product distribution is the use of software tools to determine the shortest route. Effective use of this techniques is essential in order to achieve optimal delivery. However, in most of the cases the route optimization analysis is presented in matrix form, which complicates the interpretation, forcing the user to know software nomenclature and technical terms partially. An alternative to solve this problem is to provide results in graphical form facilitating information to product distribution staff such as distribution division managers, logistics managers, drivers, etc. In this paper, we proposed a three-equation system to transform intersections and flows in image coordinates. These equations work with any route selection model and due to their low mathematical complexity, they allow to process scenarios with a large number of nodes and arcs in seconds. A Geographic Information System (GIS) is presented for product distribution using linear programming with PHP & MySQL.

Keywords— GIS; image generation; linear programming; shortest route; PHP; MySQL.

I. INTRODUCTION

Route selection aims to determine both the minimum distance as the graphical representation that facilitates comprehension. Its application extends to different areas such as: aerial vehicles routes [1], robot routes [2], data transmission [3], attack path [4], etc.

The interpretation of results in the most of mathematical models is based on graph theory [5]. Network optimization [6], and specialized algorithms for selecting routes [7-9], are also based on graph theory to visualize the junctions between two nodes, even present the optimal routes of all possible paths in a graph. Linear programming models [10, 11] are an alternative to obtain the shortest route.

In recent times graphic representation has been used to exhibit results on route selection algorithms such as improved Floyd Algorithm [12], Fuzzy Dijkstra algorithm [13] and new fuzzy algorithms [14].

A Geographic Information System is a system designed to capture, store, manipulate, analyze, manage and present all types of geographical data. These are widely used in presentation of elements of the urban environment [15], transportation service optimization [16], route optimization [17], etc.

The graphic structuration in the route selection models facilitates their understanding. Furthermore, GIS are an alternative for product distribution improvement. In this research, an equation system, in order to provide necessary coordinates for structuring graphics according to route selection models is proposed.

The principal motivation of this research to using PHP & MySQL in a GIS, is the benefits that an online system provides such as high-speed communication, availability and accessibility.

A. Linear Programming Formulation of the Shortest-Route Problem

Consider a directed network or a digraph G , consisting of a finite set of nodes (vertices or points) $\mathcal{N} = \{1, 2, 3, \dots, n\}$ and a set of directed arc (links, branches, edges or lines) $\mathcal{A} = \{(i, j) : i, j \in \mathcal{N}, i \neq j\}$ joining pairs of nodes in \mathcal{N} , see Fig. 1.

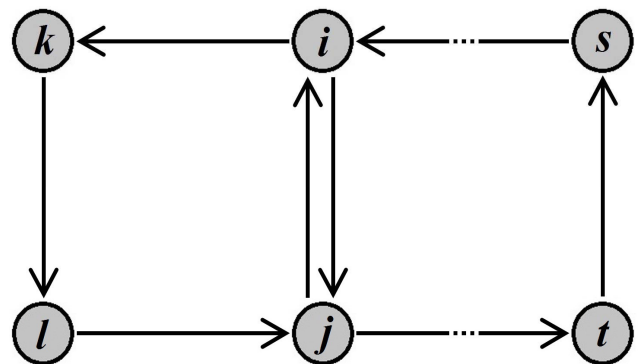


Fig. 1. Digraph G

A linear programming formulation of the shortest-route is shown below, where $x_{i,j}$ are indicator variables and $c_{i,j}$ the distance of the arc (i,j) for $i \neq j$ [10, 11].

$$\min: Z = \sum_{i=1}^n \sum_{j \neq i}^n c_{i,j} x_{i,j} \quad (1)$$

$$s.t. \sum_{j \neq i}^n x_{i,j} - \sum_{j \neq i}^n x_{j,i} = b_i, \quad i=1,2,3,\dots,n \quad (2)$$

$$x_{i,j} \geq 0 \text{ for all } i,j \quad (3)$$

In the conservation equations (2), $\sum_{j \neq i}^n x_{i,j}$ represents the total flow out of node i , while $\sum_{j \neq i}^n x_{j,i}$ indicates the total flow into node i . Where each node i in G is associated to one number b_i . Nodes with $b_i > 0$ are called sources, and nodes with $b_i < 0$ are called sinks. For $b_i = 0$, node i is called a transshipment (or intermediate).

Non-negativity constraint in (3), indicates that the decision variable $x_{i,j}$ is set either 0 or a positive integer number.

II. THE PROPOSED METHOD

The notation used along this proposed method is summarized in Table I.

TABLE I. NOMENCLATURE

Symbol	Description
a	Subscript of vertical intersection position
b	Subscript of horizontal intersection position
m	Number of vertical intersections
n	Number of horizontal intersections
P	Horizontal intersection lengths matrix
Q	Vertical intersection lengths matrix
U	Matrix of lengths of horizontal-upper flows of the block
V	Matrix of lengths of vertical-left flows of the block
$p_{a,b}$	Length horizontal of intersection
$q_{a,b}$	Length vertical of intersection
$u_{a,b}$	Lengths of horizontal-upper flows of the block
$v_{a,b}$	Lengths of vertical-left flows of the block
x	Abscissa of a pixel
y	Ordinate of a pixel
$(x,y)^1_{a,b}$	Left upper intersection pixel coordinates
$(x,y)^2_{a,b}$	Right lower intersection pixel of horizontal flow coordinates
$(x,y)^3_{a,b}$	Right lower intersection pixel of vertical flow coordinates

This method employs four elements $(p,q,u,v)_{a,b}$ of a set of blocks in a graph, to classify them, a matrix structure is used (P,Q,U,V) . The initial elements $(p,q,u,v)_{1,1}$ are in the upper-

left block, called pivot block. For each block the elements $(p,q,u,v)_{a,b}$ scroll down from pivot block, subscript a will increase by one. Similarly, for each block the elements $(p,q,u,v)_{a,b}$ scroll right from pivot block, subscript b will increase by one. Classification of elements (P,Q,U,V) is presented in Fig. 2.

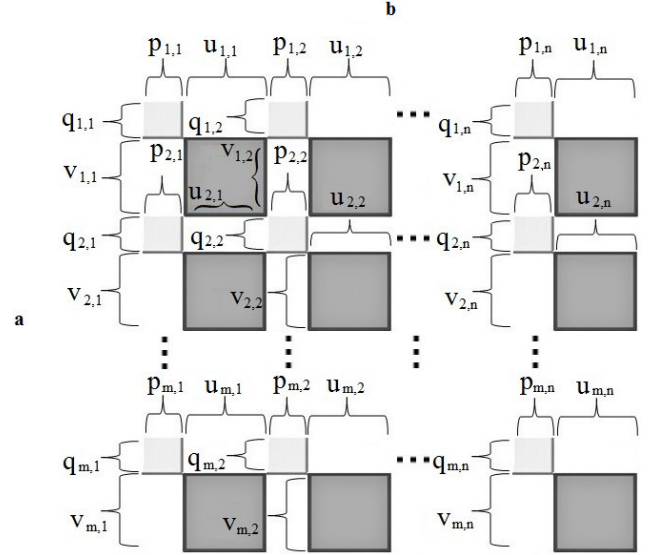


Fig. 2. Classification of elements of (P,Q,U,V)

The proposed method is developed in the following four steps:

Step 1. Storage lengths of elements $(p,q,u,v)_{a,b}$ into one m rows and n columns matrix as shown in Table II.

TABLE II. LENGTHS MATRIX

	1				2			...	n		
1	$p_{1,1}$	$q_{1,1}$	$u_{1,1}$	$v_{1,1}$	$p_{1,2}$...	$v_{1,2}$...	$p_{1,n}$...	$v_{1,n}$
2	$p_{2,1}$	$q_{2,1}$	$u_{2,1}$	$v_{2,1}$	$p_{2,2}$...	$v_{2,2}$...	$p_{2,n}$...	$v_{2,n}$
⋮	⋮	⋮	⋮	⋮	⋮	...	⋮	...	⋮	...	⋮
m	$p_{m,1}$	$q_{m,1}$	$u_{m,1}$	$v_{m,1}$	$p_{m,2}$...	$v_{m,2}$...	$p_{m,n}$...	$v_{m,n}$

Step 2. Obtain coordinates $(x,y)^1_{a,b}$, $(x,y)^2_{a,b}$ and $(x,y)^3_{a,b}$ by applying equations (4-6) to the elements in Table II, see Fig. 3.

$$(x,y)^1_{a,b} = (\sum_{i=1}^b [p_{a,i-1} + u_{a,i-1}], \sum_{i=1}^a [q_{i-1,b} + v_{i-1,b}]) \quad (4)$$

$$(x,y)^2_{a,b} = (\sum_{i=1}^b [p_{a,i} + u_{a,i}], \sum_{i=1}^a [q_{i,b} + v_{i-1,b}]) \quad (5)$$

$$(x,y)^3_{a,b} = (\sum_{i=1}^b [p_{a,i} + u_{a,i-1}], \sum_{i=1}^a [q_{i,b} + v_{i,b}]) \quad (6)$$

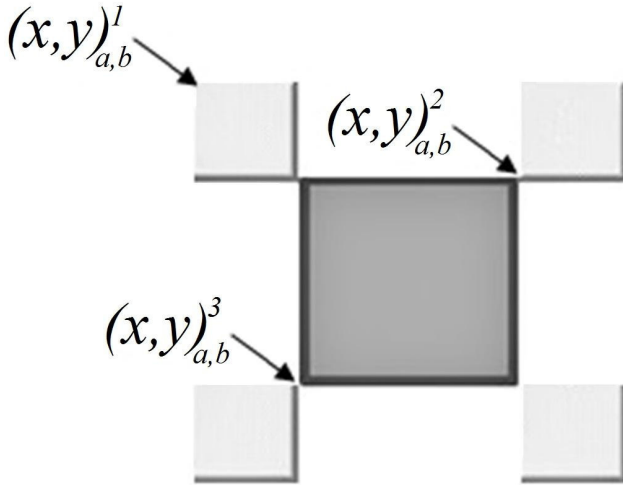


Fig. 3. Pixel coordinates

Step 3. Using $(x,y)_{a,b}^1$, $(x,y)_{a,b}^2$ and $(x,y)_{a,b}^3$ five additional coordinates corresponding to both intersection corners and flows are obtained. Then, this coordinates are storage into one m rows by n columns matrix. Table III presents the coordinates matrix graph.

Step 4. Using a programming language for imaging based on ordered pairs, a figure with information in Table III is structured.

III. PHP & MySQL IMPLEMENTATION

PHP & MySQL implementation disposes 3 forms: **Flow Storage**, **Flow Deletion** and **Source & Sink Route Nodes Storage**. Six modules: **Nodes & Flows Entry/Deletion**, **Initial Linear Programming Matrix Structuration**, **Linear Programming Solution**, **Map Lengths Matrix Structuration**, **Coordinates Matrix Structuration** and **Map Structuration**. Six Tables: **Flows Table**, **Nodes Table**, **Initial Linear Programming Matrix**, **Route Time & Flows Table**, **Map Length Matrix** and **Coordinates Matrix**. Two reports: **Route Time & Flow Routes** and **Map**. Fig. 4 presents a GIS Block Diagram.

Flow Storage form features two panels called **Linear Programming Data** and **Map**. Elements in **Linear Programming Data** are **Flow Time**, **Source Node** and **Sink Node**. Elements in **Map** are **Projection**, **(z)**, **(p)**, **(q)**, **(a)**, **(b)** and **Projection Omission**.

TABLE III. COORDINATES MATRIX

	l								...	n		
1	$(x,y)_{1,1}^1$	$(x,y)_{1,1}^2$	$(x,y)_{1,1}^3$	$(x^3,y^1)_{1,1}$	$(x^1,y^2)_{1,1}$	$(x^3,y^2)_{1,1}$	$(x^2,y^1)_{1,1}$	$(x^1,y^3)_{1,1}$...	$(x,y)_{1,n}^1$...	$(x^1,y^3)_{1,n}$
2	$(x,y)_{2,1}^1$	$(x,y)_{2,1}^2$	$(x,y)_{2,1}^3$	$(x^3,y^1)_{2,1}$	$(x^1,y^2)_{2,1}$	$(x^3,y^2)_{2,1}$	$(x^2,y^1)_{2,1}$	$(x^1,y^3)_{2,1}$...	$(x,y)_{2,n}^1$...	$(x^1,y^3)_{2,n}$
3	$(x,y)_{3,1}^1$	$(x,y)_{3,1}^2$	$(x,y)_{3,1}^3$	$(x^3,y^1)_{3,1}$	$(x^1,y^2)_{3,1}$	$(x^3,y^2)_{3,1}$	$(x^2,y^1)_{3,1}$	$(x^1,y^3)_{3,1}$...	$(x,y)_{3,n}^1$...	$(x^1,y^3)_{3,n}$
\vdots	\vdots	\vdots	\vdots	\vdots	\vdots	\vdots	\vdots	\vdots	...	\vdots	...	\vdots
m	$(x,y)_{m,1}^1$	$(x,y)_{m,1}^2$	$(x,y)_{m,1}^3$	$(x^3,y^1)_{m,1}$	$(x^1,y^2)_{m,1}$	$(x^3,y^2)_{m,1}$	$(x^2,y^1)_{m,1}$	$(x^1,y^3)_{m,1}$...	$(x,y)_{m,n}^1$...	$(x^1,y^3)_{m,n}$

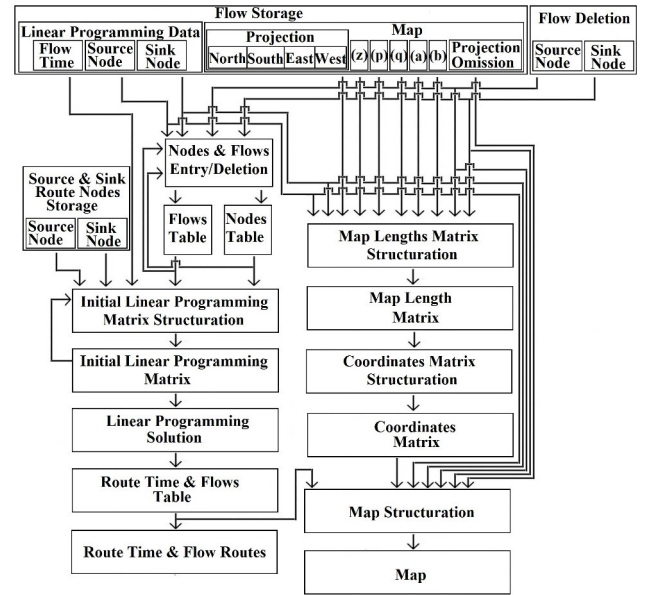


Fig. 4. GIS block diagram

A. Route Time & Flows Routes Report

Linear Programming Data panel sends information to three modules **Nodes & Flows Entry/Deletion**, **Initial Linear Programming Matrix Structuration** and **Map Lengths Matrix Structuration**. **Nodes & Flows Entry/Deletion** module analyze both flows and nodes in **Flows Table** and **Nodes Table** respectively, if elements that enter are not in these, they are stored, otherwise omitted. **Initial Linear Programming Matrix Structuration** elaborates the initial linear programming matrix based on **Flows Table**, **Nodes Table**, **Flow Time**, **Initial Linear Programming Matrix** feedback and **Source & Sink Route Nodes Storage**.

Thereafter **Initial Linear Programming Matrix** stores information from **Initial Linear Programming Matrix Structuration**. Table IV provides **Initial Linear Programming Matrix** table in general form.

Flows that form the delivery route become the decision variables entering into the basic variables column. Route time is located in objective function-solution cell.

TABLE IV. INITIAL LINEAR PROGRAMMING MATRIX

	$x_{i,j}$	$x_{k,l}$...	$x_{s,t}$	A_i	A_j	A_k	A_l	...	A_s	A_t	Solution
z	$c_{i,j}$	$c_{k,l}$...	$c_{s,t}$	0	0	0	0	...	0	0	0
A_i	1	0	...	0	0	0	0	0	...	0	0	1
A_j	-1	0	...	0	0	0	0	0	...	0	0	0
A_k	0	1	...	0	0	0	0	0	...	0	0	0
A_l	0	-1	...	0	0	0	0	0	...	0	0	0
\vdots	\vdots	\vdots	\vdots	\vdots	\vdots	\vdots	\vdots	\vdots	\vdots	\vdots	\vdots	\vdots
A_s	0	0	...	1	0	0	0	0	...	0	0	0
A_t	0	0	...	-1	0	0	0	0	...	0	0	-1

Delivery route flows in this solution are disordered and not all variables in basic variables column for route structuration are used. In order to solve these details, **Linear Programming Solution** module orders the flows and ignore route useless variables, then, sends information **Route Time & Flows Table**. This is shown in a general structure in Table V.

TABLE V. ROUTE TIME & FLOWS TABLE

$C_{i,t}$
$x_{i,j}$
$x_{k,l}$
\vdots
$x_{s,t}$

B. Map Report

In panel **Map**, flow length of one block is given by (z) , and based on element entering to **Projection** flow orientation is obtained. **Map Lengths Matrix Structuration** module utilizes this information to classify length of flows of one block in $u_{a,b}$ if it is **East** or **West**, otherwise in $v_{a,b}$ if it is **North** or **South**. Element (p) expresses the horizontal axis length of intersections as $p_{a,b}$ and (q) the vertical axis length as $q_{a,b}$.

In addition this module elaborates a matrix with $(p,q,u,v)_{a,b}$, and there after sends all information to **Map Length Matrix**. The general form of this matrix is shown in Table II.

Coordinates Matrix Structuration module with equations (4-6), transforms the information into pixels coordinates in **Map Length Matrix** and then sends this new data to **Coordinates Matrix**. Table III presents a general form of **Coordinates Matrix**.

Coordinates Matrix table is used to generate images of flows and intersection of streets in **Map Structuration** module; blocks are represented by free space. In more complex blocks case, the horizontal or vertical flows visualization is omitted in **Projection Omission** element from panel **Map**.

Finally, **Map Structuration** provides information to the report based on panel **Map**, **Source Node**, **Sink Node**, **Coordinates Matrix** and **Route Time & Flows Table** to **Map** report, this elaborates one image of the digraph and route in .jpg format. If **Route Time & Flows Table** is not sent to **Map Structuration**, **Map** only presents an image of the graph without any route.

IV. EXAMPLE

In **Source & Sink Route Nodes Storage** form, it is entered 97 as source node (representing the delivery company) and 1 as sink nodes as customer. Then, GIS develops all necessary analysis in order to present to the user **Route Time & Flow Routes** report, see Fig. 5, the route time is provided in hours, minutes, seconds format.

Time:
00:10:58
Route:
X97,90
X90,89
X89,88
X88,87
X87,86
X86,80
X80,79
X79,78
X78,71
X71,46
X46,45
X45,44
X44,43
X43,18
X18,15
X15,9
X9,3
X3,2
X2,1

Fig. 5 Route Time & Flow Routes

Then, with information in **Route Time & Flow Routes**, **Map** report is able to present the developed route, see Fig. 6.

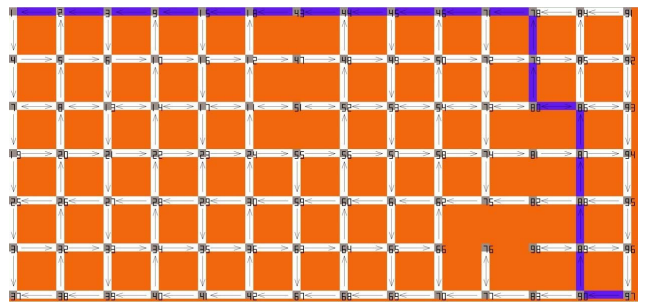


Fig. 6 Map

Considering the requirements regarding to distribution of a soft drink company, the proposed method was implemented in a sector of the distribution area of them. The sector is bounded by 2nd North and 4th South Avenues, and 5th West and 8th East Streets in Tuxtla Gutiérrez Mexican municipality of the state of Chiapas, see Fig. 6.

V. EXPERIMENTAL RESULTS

5 samples were used in order the processing times of the proposed model based on the time which **Map** report generate the image, using different flows as shown in Table VI, this time is provided in minutes, seconds, hundredths of a second format.

TABLE VI. PROCESSING TIME ESTIMATION

Flows	Processing Time
48	00:05:18
65	00:06:24
105	00:06:47
142	00:06:54
181	00:07:12

Using Excel, a statistical analysis was developed, obtaining the regression equation in (7).

$$y = 0.0117x + 5.2463 \quad (7)$$

An average distribution area consists in 1,000 flows. Estimated processing time of proposed GIS is 16.57 seconds. Samples using an Aspire E1-421 computer were developed.

VI. CONCLUSIONS

The three-equation system presented in this paper provides information to generate distribution area images, processing 1,000 flows in 16.57 seconds. These equations are compatible with route selection models.

A Geographic Information System is a system designed to capture, store, manipulate, analyze, manage and present all types of geographical data.

Implementation of the developed system in this study to a productive system allows the user to present images that support distribution division staff such as distribution division managers, logistics managers, drivers, etcetera. Improving decision making and optimizing product delivery. In addition,

the user would be able to broadcast information clearly for different appropriated levels.

REFERENCES

- [1] H. Zhonghua and Z. Min and Y. Min, "Cooperative Attack Path Planning for Unmanned Air Vehicles Swarm Based on Grid Model and Bi-level Programming", Journal of Information & Computational Science, 2011, pp. 671-679.
- [2] S. Anthony, "Optimal and Efficient Path Planning for Partially-Known Environments", Proc. of the IEEE International Conference on Robotics and Automation, 1994, pp. 3310-3317.
- [3] S. Chung Il and C. Tae Ho, "Path Selection Method for Reliable Data Transmission in Sensor Networks using GA", International Journal of Computer Science and Network Security, 2011, pp. 208- 212.
- [4] S. Khaitan and S. Raheja, "Finding Optimal Attack Path Using Attack Graphs: A Survey", International Journal of Soft Computing and Engineering, 2011, pp. 33-36.
- [5] D. Reinhard, "Graph Theory". Springer, 2000, pp. 1-28.
- [6] R. K. Ahuja, T. L. Magnanti and J. B. Orlin, "NetworkFlows: Theory, Algorithms, and Applications". Prentice Hall, Englewood Cliffs, NJ, 1993, pp. 1-22.
- [7] E. W. Dijkstra, "A Note on two problems in connexion with graphs, Numerische Mathematik", 1959, pp. 269-271.
- [8] F. Robert W., "Algorithm 97: Shortest Path", Communications of the ACM, 1962, p. 345.
- [9] W. Stephen, "A theorem on Boolean matrices", Journal of the ACM, 1962, pp. 11-12.
- [10] H. A. Taha, "Operations Research: An Introduction", Pearson Education, 2007, pp. 257-258.
- [11] M. S. Bazaraa, J.J. Jarvis and H.D. Sherali, "Linear Programming and Networks Flow", John Wiley & Sons, New York, 1990, pp. 453-455.
- [12] W. Da-chuan, "Implementation of Route Selection Function Based on Improved Floyd Algorithm", ASE International Conference on Information Engineering, 2010, pp. 223-227.
- [13] D. Yong, C. Yuxin, Z. Yajuan and M. Sankaran. "Fuzzy Dijkstra algorithm for shortest path problem under uncertain environment", Applied Soft Computing, 2012, pp. 1231-1237.
- [14] K. Amit and K. Manjot, "A New Algorithm for Solving Shortest Path Problem on a Network with Imprecise Edge Weight". Applications and Applied Mathematics, 2011, pp. 602-619.
- [15] X. Juan, "Design of Urban Basic Traffic Management System Based on Geographic Information System", Control Conference, 2010, pp. 5353-5357.
- [16] M. Advani, B. Srirama and S.K.Pathan, "Improvement in Transit Service using GIS – Case study of Bhavnagar State Transport Depot", ESRI National Conference, 2005, pp. 1-7.
- [17] R. R. Puente and M. L. Cortés, "Graph-reduction Algorithm for Finding Shortest Path in Geographic Information Systems", IEEE Latin America Transactions, 2012, pp. 2201-2208.

Modification with Lime and its Effect on Hydraulic Conductivity of Expansive Soils

Vásquez-Nogal Ismael¹, Galaviz-González Roberto², Horta-Rangel Jaime², Rojas-González Eduardo², Pérez-Rea Luz²,

¹ *Autonomus University of Querétaro, Cerro de las Campanas, 76160, Santiago de Querétaro, Querétaro, México.*
¹isvano_5@hotmail.com

² *Department of research and graduate of the Faculty of Engineering, Autonomus University of Queretaro, Cerro de las Campanas, 76160, Santiago de Querétaro, Querétaro, México.*
btoviz@hotmail.com; horta@uaq.mx; erg@uaq.mx; perea@uaq.mx

Abstract— For more than 50 years, soil mechanics has been developed in the analysis of saturated and dry mechanical behavior of soils. Since 1960's, the mechanical behavior of unsaturated soils has been growing its interest, this is defined by negative pore pressures (soil suction).

Within their classification are the expansive soils which often contain minerals such as montmorillonita. These kinds of soils are very problematic, because they produce failures on foundations of civil structures built over that kind of soils. That is the main reason of the development of techniques to improve the mechanical behavior of expansive soils and to avoid the volumetric changes by the insertion of additives such as lime, Portland cement, polymers, etc.

Nevertheless, most of the problems related with civil structures built over expansive soils improved by insertion of lime, came from the deficient quality control when lime is added to the expansive soil. For that reason people have resorted solutions like injections of whitewash. It must be remembered that an expansive soil has a very low hydraulic conductivity, and because of that is necessary to estimate the behavior of the hydraulic conductivity in the improvement soil.

In the literature are mixed results, like rise of the hydraulic conductivity and decrease of it in the improvement soil.

Key words: *Hydraulic conductivity, expansive soils, improvement soils*

I. INTRODUCTION

The soil is a skeletal structure of solid particles in contact, forming an interstitial system of interconnections among the pores. Those pores could be complete filled, or partial filled with water [1]. And can be:

- ✚ Saturated soils with water and zero air among their pores.
- ✚ Dry soils with only air in their pores.
- ✚ Partial saturated soils with water and air among their pores.

For more than 50 years the soil mechanics has been developed in the analysis of the mechanical behavior of saturated and dry soils. The dry condition was an implicit

supposition and in the other hand the saturated condition was commonly used to obtain conservative results. Until the 1960's remain that analysis, and the interest of the mechanical behavior of unsaturated soils, defined by the negative pore pressures (suction) has been growing [2].

The unsaturated soils contain three phases: solid, liquid and gas phase; within their classification are the expansive soils which often contain minerals such as montmorillonita [3] known to be very problematic, because they can cause failures in the foundations of civil structures built over that kind of soils [4]. Some lightweight structures built over expansive soils can develop structural damage caused by variations of water content product of flow of water through the soil [5].

The main problem could be attributed to the bad compression of volume changes caused by the variations of water content [3]. This kind of soils can adsorb water into their inner structure and cause a volume increase, with the sufficient pressure to damage the structure. Also when the soil is dry it shrinks and affects the support of buildings resulting in subsidence. Cyclic drying and wetting of expansive clayey soils causes repetitive stresses [2].

For that reason techniques have been developed to improve the mechanical behavior of expansive soils and to avoid the volumetric changes by the insertion of additives such as lime, Portland cement, polymers, etc. into the unsaturated soils.

The hydraulic conductivity of unsaturated soils is a function of a set of variables that describes the pore structures like the void ratio and porosity, the properties of liquid into the pore like density and viscosity, and the relative fluid content in the system like water content and degree of saturation.

The flow of water through the soil describes a characteristic dependence in the quantity of pore fluid in the system. And it can be described in terms of the matric suction $k(\Psi)$, degree of saturation $k(S_r)$, or in terms of the volumetric water content $k(\theta)$. Because of this the hydraulic conductivity is directly related to the Soil-Water Retention Curve (SWRC) [7].

II. BACKGROUND

A. Soil Water Retention Curve (SWRC)

Water movement in unsaturated soils flows from one point with a large amount of potential energy to other one with a small amount of potential energy. This is defined as the potential energy per unit of water, that is, it is the work required to bring the unit from a standard reference state to the point under consideration. Thus, water in the soil is subject to field forces resulting from the attraction of the solid matrix, the presence of solutes, the action of the external pressure, the gravitational pull, among others. The gravitational pull is measured from the ground surface, the external pressure is considered positive if the water is at a higher pressure than the atmosphere and negative if it is at a lower pressure. The latter is called matric potential and, when taken in absolute value is called matric suction (ψ). Then, matric suction is produced from capillary forces and adsorption due to soil structure [8].

From this way, SWRC is strongly affected by the texture and structure of the soil, that is, the higher the clay content is increased water retention by a given suction value and the slope of the curve is smoother [8]. This is because of the pore size distribution (PSD) due to which has pores of very different sizes from very large to very small.

Every SWRC has different shape and position; also the wetting curve and the drying curve are not the same, this phenomenon is called hysteresis [9].

The SWRC can be used to estimate various parameters used to describe the soil behavior [10] and its use has become an important aspect in unsaturated soil mechanics because these materials have a hydromechanical coupling, it means, the volumetric behavior and the strength depend not only on the applied stress and the suction, but also its degree of saturation (S_r) that depends on the water content (ω or θ) [11].

B. Models used to determinate the SWRC (Soil Water Retention Curve)

Among the techniques there are two categories: empirical models and physical models. With the empirical models the difference in the equations of the SWRC are related to parameters like specific gravity, percent sand, organic matter and other properties of the soil using an statistical regression [12]. Among the mathematical expressions used to describe the SWRC, there are equations developed by van Genuchten (1980) and Fredlund and Rahardjo (1993).

C. Models used to determinate HCF (Hydraulic Conductivity Function)

Van Genuchten develop an empirical mathematical form of the SWRC, nowadays this equation is largely used.

This method is suitable to make an adjustment to relax the SWRC and not to predict it, just proved by [13]. He proved that this equation is a function of suction and three empirical parameters: α , n and m (eq. 2). In the other hand, from the SWRC can be estimated an equation that describe the

behavior of HCF, and is also a function of the soil suction and the same parameters α , n and m (eq. 4). Due to the above, van Genuchten developed a relationship between the SWRC and HCF. The last one is important to estimate precisely in problems related to the water flow, contaminant transport, cyclical wetting and drying, and others.

The volumetric water content is used in its normalized form, and referred to the degree of saturation.

$$\Theta = \frac{\theta - \theta_r}{\theta_s - \theta_r} \quad (1)$$

$$\Theta = \left[1 + |\alpha\psi|^n \right]^{-m} \quad (2)$$

$$m = 1 - \frac{1}{n} \quad (3)$$

where: Θ = volumetric water content normalized or effective degree of saturation, θ_s = saturated volumetric water content, θ_r = residual volumetric water content.

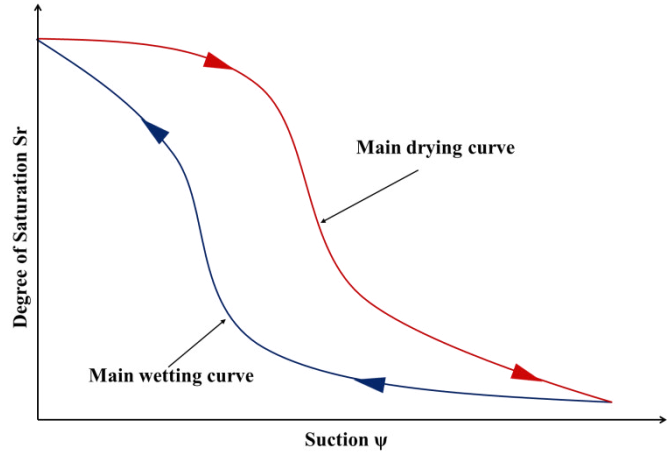


Fig. 1. Wetting and drying curves of clayey soils showing the hysteresis phenomenon [14].

If the parameters α , n and m are known as well as the saturated water content, the soil suction can be calculated. The use of this equation is limited between the air entry value and the residual soil suction, because of the nature of the equation.

$$k_r(\psi) = \frac{\left\{ 1 - (\alpha\psi)^{n-1} \left[1 + (\alpha\psi)^n \right]^{-m} \right\}^2}{\left[1 + (\alpha\psi)^n \right]^{m/2}} \quad (4)$$

According to [5] the HCF can be obtained from the SWRC an equation that comes from the Poiseuille equation. The next equation has a similar form of the presented by Kunze *et al.*,

(1968) and has been modified to be used with IS units and the matric suction.

$$k_w(\theta_w) = \frac{k_s}{k_{sc}} \frac{T_s^2 \rho_w g \theta_s^p}{2\mu_w N^2} \sum_{j=1}^m \left\{ \frac{(2j+1-2i)}{(\psi_j)^2} \right\} \quad (5)$$

where: the wetting and drying curves are divided into (N) equal intervals of the volumetric water content ($\Delta\theta$), $i=1$ identifies the first interval which is close to the saturated volumetric water content (θ_s), $i=m$ identifies the last interval corresponding to the lowest volumetric water content on the experimental SWCC (θ_r), j is a counter from i to m ; (k_s) is the measured saturated coefficient permeability; (k_{sc}) is the theoretic saturated permeability coefficient (calculated from the SWCC); (T_s) is the surface tension of water, (ρ_w) is the water density, (g) is the gravitational acceleration, (μ_w) is the absolute viscosity of water, (θ_s) is the saturated volumetric water content, (p) it was considered equal to 1, ($N=M$) total number of intervals computed between the saturated volumetric water content and zero volumetric water content, (ψ_j) is the matric suction to the j th interval, the term $\sum_{j=1}^m \{(2j+1-2i)(\psi_j)^{-2}\}$ describes the shape of the permeability function.

The above expression can be written as:

$$k_w(\theta_w) = \frac{k_s}{k_{sc}} A_d \sum_{j=1}^m \left\{ \frac{(2j+1-2i)}{(\psi_j)^2} \right\} \quad (6)$$

where: A_d is an adjustment constant and is equal to:

$$A_d = \frac{T_s^2 \rho_w g \theta_s^p}{2\mu_w N^2} \quad (7)$$

$$k_{sc} = \frac{T_s^2 \rho_w g \theta_s^p}{2\mu_w N^2} \sum_{j=1}^m \left\{ \frac{(2j+1-2i)}{(\psi_j)^2} \right\} \quad (8)$$

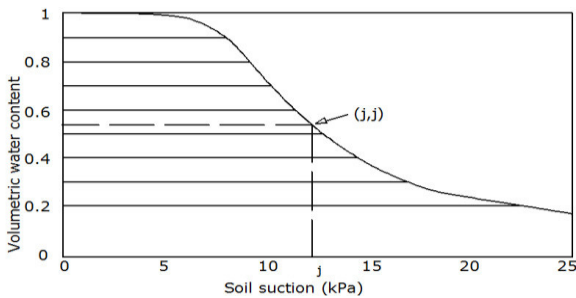


Fig. 2. Typical characteristic curve of the prediction of the function of permeability, θ_f as middle point of interval j of the water content ψ_f from the suction. θ_f [10].

Is well known that van Genuchten method is suitable for adjustment of sandy and silty soils, but in clayey soils it lacks of accuracy. Due to the above [14] have developed a procedure to estimate the SWRC and its secondary cycles of hysteresis in unsaturated soils without using an adjustment equation. Results given by [14] shows advantages like: a) its avoided the adjustment process over the experimental data with equations, b) their procedure give a correlation of 100% between the experimental and numerical points, c) this correlation rises the accuracy of the main curves for unsaturated soils.

This procedure has three steps: in the first one, the user introduce the number of points and its respective data for each curve (drying and wetting), in this step it's necessary to convert the water content in degree of saturation. When the first step is finished all the data is stored in an array called "table", later a polynomial of degree "n" is generated for each curve. This procedure is based on the interpolation of Lagrange and interpolation with variable increments methods. This allows generating a degree of saturation for any suction value. The second step the secondary cycles of hysteresis are evaluated with the procedure of Zhou *et al.* (2012) with certain modifications. Later it's generated a slope and the suction value of the main curve for the degree of saturation evaluated. Finally it's generated the secondary cycle and its corresponding differential of degree of saturation. And finally the third step consist in evaluate the next secondary cycle starting with the previous value. This procedure is shown in figure 3.

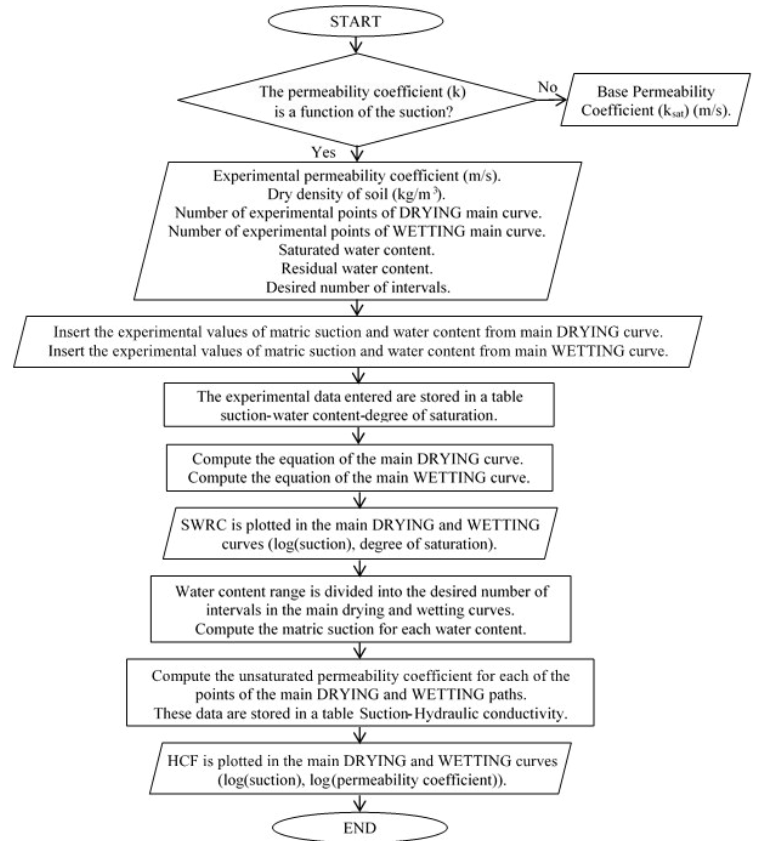


Fig. 3. Flow chart of the determination of HCF given by [15]

D. Soil improvement through the addition of lime

The addition of lime is the most common technique to improve the mechanical behavior of the clayey soil, it change the geotechnical properties immediately after lime is added to soil, this treatment makes the soil behave like a granular material, and lost its cohesive properties: plastic index and expansion pressure are reduced while the permeability increases.

The spreading of lime should be uniform in a specific percentage and there are two methods:

1) Dry method.

This method consists in the application of lime over the roadway. The lime shouldn't be placed in windy days, and it is necessary to spread water into the roadway to reduce dust.

The lime must be applied in areas where could be mix with soil in the same day, and need to be mixed in maximum six hours after its application.

Usually is applied with tanks trucks and generally are self-unloading bulks.

2) Lime slurry method

In this method, the hydrated lime and water are mixed, and should be placed over the roadway though gravity or pressure sprayers. Need to take care that lime solids don't settle in lime slurry.

One typical proportion of slurry is 1895 liters per ton. This slurry could be prepared in two ways; mixed in a central tank or add a specific amount of water and lime to truck tanks and mix while moving.

This method has and disadvantage because is limited only to works that require a small amount of lime (4% or less) due to the amount of water needed to have the lime in suspension [16].

E. Effects of soil improvement through lime

Soil improvement through lime leads to changes into the structure and texture of clayey soils, and irreversible changes into the hydromechanical behavior. These changes can be described in three general phenomena:

Cation Exchange: Take place after the lime is in presence of water. In this reaction produces ions lime (Ca^{++}) and pH increase in the mix soil-lime.

Pozzolanic reaction: is provoques the flocculation of the particles, further lowering soil plasticity. Moreover, it leads to the formation of cementitious compounds through pozzolanic reaction that bind soil particles together, and improve mechanical characteristics [17].

Carbonation: this reaction happens when lime reacts with carbon dioxide present in the air, mostly associated with hot-dry climates where control of curing is difficult; it is a phenomenon that should be avoided because it inhibits the formation of cementitious products that hence reduces the material strength [18].

The results obtained from several investigations proved that the optimum percentage of lime required to improve the mechanical behavior is between 4 and 6 [19, 20, 21]. And a minimum of 4% lime is necessary to activate the pozzolanic reaction according to pH measurements, and swelling pressure is almost eliminated by 6% of lime added [21].

Even when this kind of soil improvement is commonly used in the roadways and the construction of foundations in civil structures, the consequences caused by adding lime in the clayey soil over the hydraulic conductivity are not well known, from qualitative and quantitative points of view. Plenty of results are in the literature, [22] have reported different results that proved the rise of hydraulic conductivity shown by Brandl (1981), Nalbantoglu y Tuncer (2001). They have also reported that the hydraulic conductivity decreases being the case of Terashi *et al.* (1980). Even further there are results that shown the rise of the hydraulic conductivity and the decrease with time, being the case of Locar *et al.* (1996) and Merelková *et al.* (2011).

Even more, the hydraulic conductivity depends of its microstructure, and its pore size distribution, and the last one is a direct function of the compaction conditions [17, 23].

III. DESCRIPTION OF THE PROCEDURE

The study of hydraulic conductivity of clayey soils and its procedure could be done by evaluating methods like [5,14] or the van Genuchten's equation. The procedure of [5] requires as data the saturated permeability coefficient (k_s), intervals number (M) at which given water content range is divided, surface tension of water (T_s), absolute viscosity of water (μ_w), and water density to estimate the HCF in wetting and drying paths. The procedure is performed by few steps:

The first step is the intervals of equal volumetric water content and its respective suction, the eq. (8) gives us how to obtain k_{sc} , in this case it will be calculated in the first point where we can see k_s , note that the hydraulic conductivity only depends on the coefficient of permeability test (k_s) and the parameter A_d (8) doesn't take place in the eq. (6).

$$k_w(\theta_w) = \frac{k_s}{k_{sc}} A_d \sum_{j=1}^m \left\{ \frac{(2j+1-2i)}{(\psi)_j^2} \right\} \quad (6)$$

$$A_d \frac{T_s^2 \rho_w g \theta_s^p}{2\mu_w N^2} \quad (7)$$

$$k_{sc} = \frac{T_s^2 \rho_w g \theta_s^p}{2\mu_w N^2} \sum_{j=1}^m \left\{ \frac{(2j+1-2i)}{(\psi)_j^2} \right\} \quad (8)$$

In the other hand van Genuchten equation (4) gives how to obtain HCF and has important steps. The first one is that is

necessary to obtain an adjust of the SWRC and is given by (1) and (2), being (1) dependent of the volumetric water content (θ), saturated volumetric water content (θ_s), and residual volumetric water content (θ_r) given by the intersection of the tangents of the curves, Fig. 4 Shows the procedure.

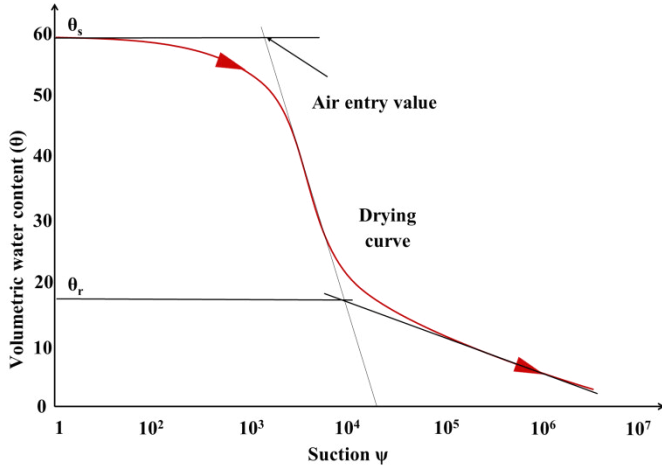


Fig. 4. Drying curve of clayey soil, θ_s = saturated volumetric water content, θ_r = residual volumetric water content [14].

To obtain the best fit of the SWRC given by (2) different results of α , m and n are obtained, however it's necessary to have strong correlations ($R^2 > 0.95$), this correlation is given by the least square method or other procedures. Fig. 5 gives us the values of α , m and n of the SWRC of a certain sandy soil with very acceptable correlations. However the correlation could give us inadequate results of the hydromechanical behavior of unsaturated soils.

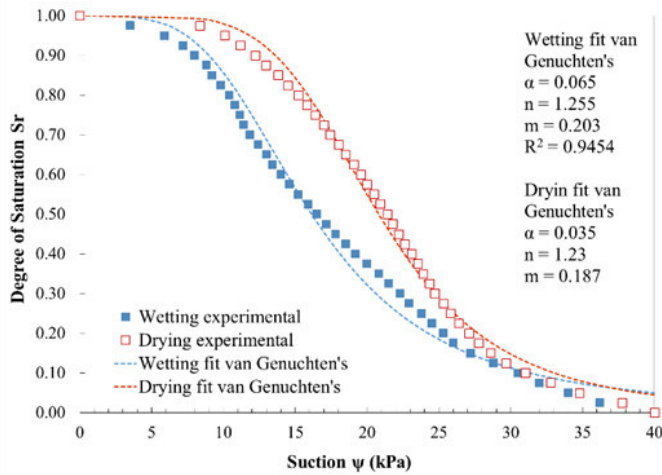


Fig. 5. Wetting and drying curves of sandy soil, and its best fit of α , m and n [14].

$$\Theta = \frac{\theta - \theta_r}{\theta_s - \theta_r} \quad (1)$$

$$\Theta = \left[1 + |\alpha\psi|^n \right]^{-m} \quad (2)$$

$$m = 1 - \frac{1}{n} \quad (3)$$

Finally, to obtain the hydraulic conductivity is necessary to evaluate (4) and multiplying the result by k_s to relate it with the saturated permeability.

$$k_r(\psi) = \frac{\left\{ 1 - (\alpha\psi)^{n-1} \left[1 + (\alpha\psi)^n \right]^{-m} \right\}^2}{\left[1 + (\alpha\psi)^n \right]^{m/2}} \quad (4)$$

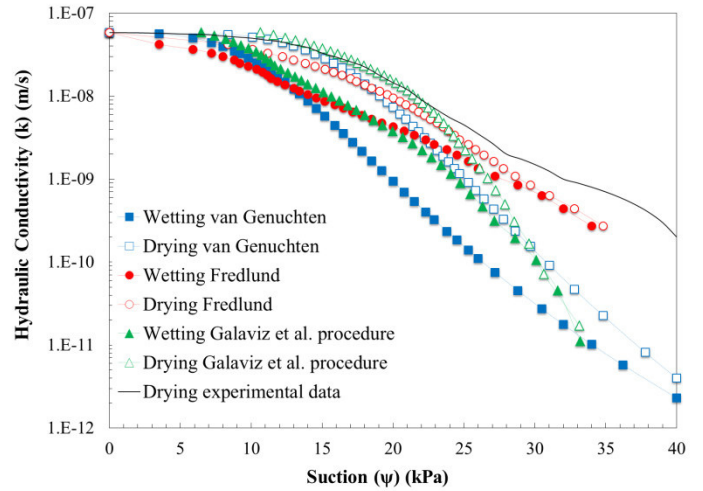


Fig. 6. Comparison of the Hydraulic conductivity vs Suction plotted in log scale [15].

Figure 6 shows the result of comparison of the HCF using the drying and wetting path of the SWRC through different methods, where the saturated coefficient of permeability is $5.83 \times 10^{-8} m/s$. It is to be noted that all the results seems to be very similar, and it's to be noted that [14] have consistent results and also the precision can be chosen depending of the number of intervals. It is essential to observe that those results given by different procedures (e.g. Fredlund and Rahardjo, van Genuchten) are not the same; this is because the need of adjustment of their own equations, due to the above the obtaining of parameters such as the hydraulic conductivity are not precise.

The hydraulic conductivity is shown to be essentially constant throughout the capillary zone and equal to the saturated coefficient of permeability. As the soil starts to desaturate as a result of the increase in matric suction, the coefficient of permeability also decreases and takes the form of a function that various over several orders of magnitude as the soil suction is increased. It also shows that hydraulic flow appears to continue until the residual suction of the soil is reached [24].

To evaluate the impact on the hydraulic conductivity it is necessary to obtain the SWRC with the optimum content of lime and the use of the procedures described above in order to observe the effect when lime is added and later compare with the results reported by [22]. Also this analysis will be matched with porosimetry where the hydraulic conductivity is a function of the pore structure.

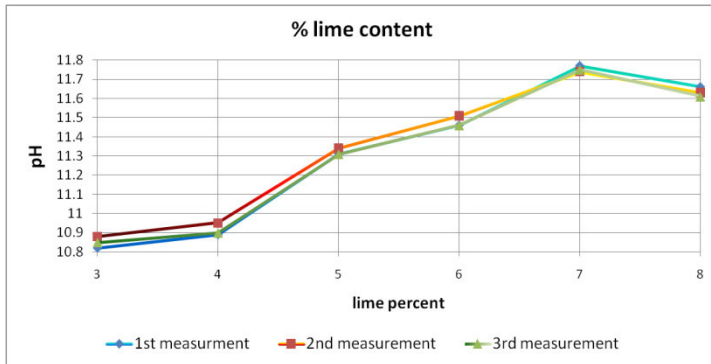


Fig. 7. Optimum lime content for the soil of study according to nom-021-semarnat-2000.

Figure 7 shows the lime content of the study soil obtained from the Hacienda of Juriquilla, located at north of Queretaro, which is recognized for the existence of expansive soils in the city. The test were carried out by the nom-021-semarnat-2000 procedure, and can be noted in the figure that the optimum lime content is 7 % where the pH reaches the maximum value, and above that value the soil has a pH decrease. As a result of that the three phenomenons described before takes place.

IV. CONCLUSIONS

This research tries to evaluate the impact in the hydraulic conductivity product of the modification with lime in clayey soils, determining the hydraulic conductivity function of the clayey soil through the soil water retention curve not only in clayey soil but also in improvement soil (with optimum lime content). Even when the clayey soil has a very low hydraulic conductivity it is necessary to estimate it to judge if the slurry method is suitable to solve problems in foundations over the clayey soils. To continue with the investigation of the effect of the lime in the hydraulic conductivity procedures such as porosimetry need to be done in order to explain if there is a change in the interconnection of pores.

ACKNOWLEDGEMENT

The authors would like to thank Consejo Nacional de Ciencia y Tecnología (CONACyT) and the Universidad Autónoma de Querétaro for their support, with which the realization of this research was possible.

REFERENCES

- [1] D. G. Fredlund, H. Rahardjo, "Soil mechanics for unsaturated soils", Wiley-Interscience, New York, 1993.
- [2] F. Hoyos, "Implementación de la Mecánica del Suelo Parcialmente Saturado en la práctica de la Ingeniería Geotécnica". Editorial Litoimpresos, Colombia, 2003.
- [3] M. L. Pérez-Rea, T. I. Ayala, J. R. Galaviz-González, y E. Rojas-González, "El cambio volumétrico en la predicción de asentamientos, análisis y diseño de cimentaciones", XXVI Reunión Nacional de Mecánica de Suelos e Ingeniería Geotécnica, Cancún, Quintana Roo, México, 2012.
- [4] A. J. P. Puppala, T. Manossuthikij, B. C. S. Chittoori, "Swell shrinkage characterization of unsaturated expansive clays from Texas", *Engineering Geology*, vol.164, 2013, pp. 187-194.
- [5] E. Jahangir, O. Deck and F. Masrouri, "An analytical model of soil-structure interaction with swelling soils during droughts", *Computers and Geotechnics*, vol. 54, 2013, pp. 16-32.
- [6] T. D. Trinh, Y. J. Cui, A. M. Tang, M. Audiguier, R. Cojean, "Effects of lime treatment on the microstructure and hydraulic conductivity of Héricourt clay", *Journal of Rock Mechanics and Geotechnical Engineering* (in press).
- [7] N. Lu, W. J. Likos, "Unsaturated soil mechanics", John Wiley & Sons, Inc. New Jersey, 2004.
- [8] P. Máximo, "Dinámica de la penetración capilar en estructuras complejas", Ph. D. thesis, Universidad Autónoma de Querétaro, Santiago de Querétaro, México, 2012.
- [9] V. Meza, "Suelos parcialmente saturados, de la investigación a la cátedra universitaria, *Boletín de Ciencias de la tierra*, Medellín, Colombia, vol. 31, 2012, pp. 23-28.
- [10] D. G. Fredlund, A. Xing, S. Huang, "Predicting the permeability function for unsaturated soil using the soil-water characteristic curve", *Canadian Geotechnical Journal*, vol. 31(3), 1993, pp 521-532.
- [11] J. Horta-Rangel, E. Rojas-González, M. L. Pérez-Rea, T. López-Lara, J. B. Zaragoza, "A random solid-porous model to simulate the retention curves of soils, *Int. J. Numer. Anal. Methods Geomech.* 37, 2013, pp. 932-944.
- [12] A. Maqsood, B. Bussière, M. Aubertin, M. Mbonimpa, "Predicting hysteresis of water retention curve from basic properties of granular soils", *Geotechnical and Geological Engineering* 30(5), 2012, pp. 1147-1159.
- [13] J. R. Galaviz-González, M. L. Pérez-Rea, H. Arroyo, "Modelos de predicción de curvas de retención de agua para suelos parcialmente saturados, En memorias 9º Congreso Internacional de Ingeniería, Universidad Autónoma de Querétaro, Santiago de Querétaro, Querétaro, México, 2013.
- [14] J. R. Galaviz-González, J. Horta-Rangel, E. Rojas-González, M. L. Pérez-Rea, J. Robles, "Un nuevo procedimiento para predecir los ciclos secundarios de histéresis de los suelos no saturados", XXVIII Reunión Nacional de Mecánica de Suelos e Ingeniería Geotécnica, Puerto Vallarta, Jalisco, México, 2014.
- [15] J. R. Galaviz-González, J. Horta_Rangel, E. Rojas-González, M. L. Pérez-Rea, J. Robles, "Computational Model to Estimate Hydraulic Conductivity Function", X Congreso internacional de Ingeniería, Universidad Autónoma de Querétaro, Santiago de Querétaro, Querétaro, 2014.
- [16] T. Lopez-Lara, "Estudio fisicoquímico de la modificación de suelos arcillosos", Ph. D. thesis, Universidad Autónoma de Querétaro, Santiago de Querétaro, México, 2002.
- [17] O. Cuisinier, J. Auriol, T. Le Borgne, D. Deneele, "Microstructure and hydraulic conductivity of a compacted lime-treated soil", *Engineering Geology*, vol. 123, 2011, pp 187-193.
- [18] D. Ciancio, C. T. S. Beckett, J. A. H. Carraro, "Optimum lime content identification for lime-stabilised rammed earth", *Construction and Building Materials*, vol. 53, 2014, pp 59-65.
- [19] F. G. Bell, "Lime stabilization of clay minerals and soils", *Engineering Geology*, vol. 42, 1996, pp 223-237.

- [20] A. Seco, F. Ramírez, L. Miqueleiz, B. García, “Stabilization of expansive soils for use in construction“, *Applied Clay Science*, vol 51, 2011, pp 348-352.
- [21] M. Al-Mukhtar, A. Lasledj, J. Alcover, “Behaviour and mineralogy changes in lime-treated expansive soil at 20 °C”, *Applied Clay Science*, vol 50, 2010, pp 191-198.
- [22] T. D. Trinh, Y. J. Cui, A. M. Tang, M. Audiguier, R. Cojean, “Effects of lime treatment on the microstructure and hydraulic conductivity of Héricourt clay”, *Journal of Rock Mechanics and Geotechnical Engineering* (in press).
- [23] H. Noureddine, S. Ezzeddine, “Hydraulic conductivity study of compacted clay soils used as landfill liners for an acidic waste”, *Waste Management*, vol. 33, 2013, pp 60-66.
- [24] D. G. Fredlund, “Teaching unsaturated soils mechanics as part of the undergraduate civil engineering curriculum”, *Proceedings of the second Pan American Conference on the Teaching and Learning Processes of Geotechnical Engineering*, Quayaquil, Ecuador, 2002.

BLDC Motor Drive based on Current Shaping Cell Converter

Alonso Jimenez-Garibay ^{#1}, Member, IEEE, Juvenal Rodriguez-Resendiz ^{*1}, Senior Member, IEEE, J.C. Jáuregui-Correa ^{#1}

^{#1} Universidad Autónoma de Querétaro
Cerro de las Campanas S/N, Las Campanas, Santiago de Querétaro, Qro, Mex.

¹ alonso.jimenez-garibay.1979@ieee.org

³ juvenal@ieee.org

¹ juancarlosjauregui2007@gmail.com

Abstract— The Brushless Direct Current (BLDC) motor has advantages like high efficiency and torque, low electromagnetic interference and maintenance, this make it suitable for low power applications, however, the addition of an electronically switching driver induces problems with power quality standards in a PI closed-loop based on Hall effect sensors. This paper presents a typical BLDC drive modified with a cell based on a discontinuous current mode converter with an active shaping technique to manage the DC voltage to feed the IGBT-VSI, power factor and Total Harmonic Distortion (THD) is improved to comply with the IEC 61000-3-2 standard. As a result, stresses on the IGBT semiconductor are reduced. Proposed cell converter design and experimental results are presented.

Keywords—Brushless Direct Current, power quality, power factor, total harmonic distortion.

I. INTRODUCTION

The BLDC motor is a type of permanent magnet machine, in comparison with a Brushed DC machine, the BLDC incorporates rare earth rotor magnets which improve the flux density and therefore the efficiency. The BLDC needs an electronic commutation rather than mechanical to change the phase currents at the appropriate times to produce rotational torque. Fig. 1 shows a typical BLDC speed control drive composed of three main stages: first, the AC – DC converter, in this case, a non-controlled diode full bridge plus a bulky filter capacitor to establish the DC bus, secondly, a DC-AC converter composed by three IGBT branches, and finally, a controller to manage the feedback signals from the BLDC motor and generate the PWM signals to control each IGBT in order to achieve the proper switching sequence.

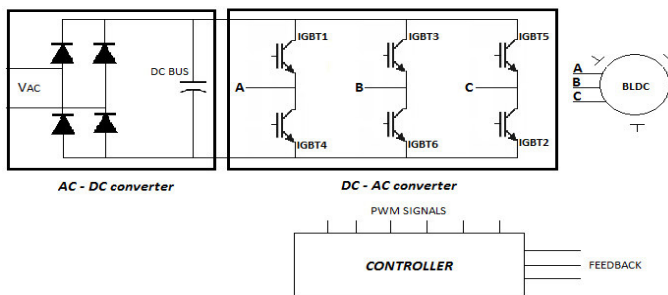


Fig. 1. Typical single-phase-input BLDC drive.

From a power quality requirement stand point, the typical drive has a poor performance [1], literature reported many topologies that use DC-DC converters instead of bulky capacitors to reduce the harmonic content and comply with the IEC 61000-3-2 standard [2]. Boost, buck – boost, sepic, cuk, zeta converters in continuous, discontinuous or front-end conduction modes are implemented in order to achieve a good tradeoff between power factor, THD, and semiconductor switching losses [3-8]. This paper proposes a DC-DC cell based on a flyback converter to improve the power factor, reduce the THD and semiconductor stresses, via an active current shaping technique [9].

II. PROPOSED OF CELL CONVERTER

Fig. 2 shows the proposed cell which emulates the controlled resistor characteristic of a flyback converter operated in discontinuous current mode (DMC), with the addition of an auxiliary branch to the transformer to return part of the energy in order to shape the input current.

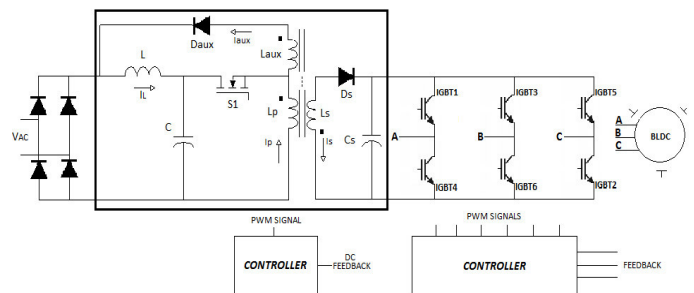


Fig. 2. Proposed cell converter

A. Operating stages

The proposed cell has three stage behaviors that depend on the duty cycle:

1. Fig. 3 shows the first operating stage. the main semiconductor switch S_1 turns on, the result is an energy charge into the input inductor L and primary inductor L_p , for this instance the current of the input inductor i_L is equal to the current of the auxiliary inductor i_{aux} , at this time the converter does not demand energy to the AC mains.

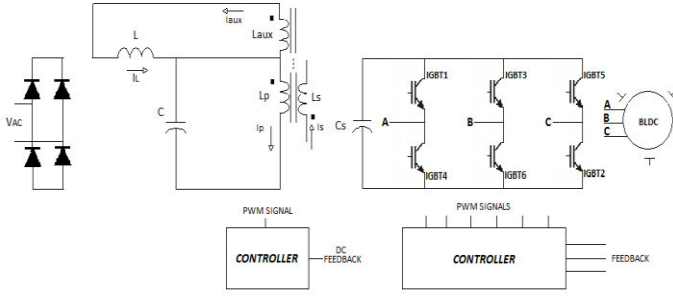


Fig. 3. First stage

- Fig. 4 shows the second operating stage, S_1 is turned off, L is completely discharged, and the secondary inductor L_s discharges its energy through the output capacitor, at this moment the current i_{aux} is equal to zero, and the current i_L demands energy from the AC main line.

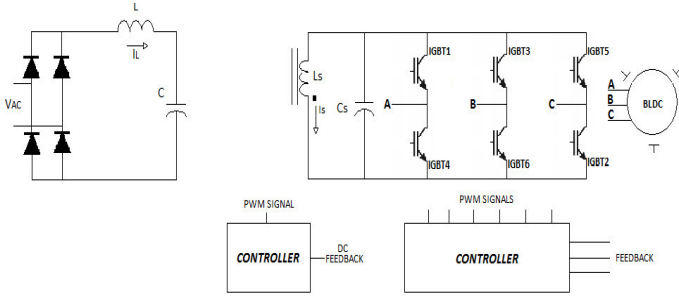


Fig. 4. Second stage

- Fig. 5 shows the third operating stage, S_1 remains turned off, the energy in the inductor L is totally discharged, and the converter does not demand energy to the AC main line.

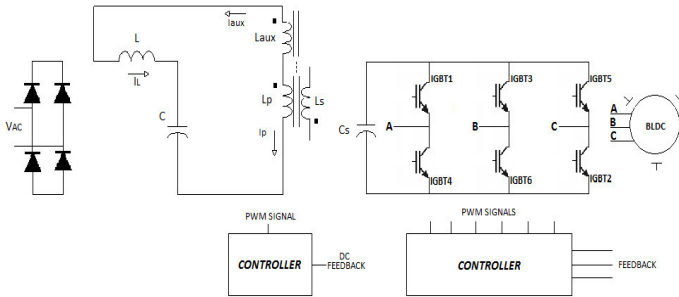


Fig. 5. Third stage

The key of the input current shape is the quantity of energy returned into the input, the following section describes the procedure design and considerations.

III. DESIGN OF CELL CONVERTER

Equation (1) shows a typical output power of a Flyback converter in DCM, which depends on the duty cycle (D) and input voltage (V_{AC}) magnitude, the inductor value (L), transformation ratio (n), and switching frequency (T_s) remains constant, for the aforementioned condition the flyback converter presents a controlled resistor behavior [10].

$$P_O = \frac{V_{AC}^2}{\frac{2Ln^2}{D^2T_s}} \quad (1)$$

Equation (2) defines the output power of the proposed cell based on a steady-state analysis taking into account the triangular shape of the input power at turn-off switching semiconductor condition.

$$P_O = \frac{V_{AC}}{V_C - V_{AC}} \frac{i_L^2 L}{2} \quad (2)$$

In comparison with the output power of (1), if the inductor current (i_L), and the inductor value remain constant on (2), the denominator term of (2) tries to emulate the square V_{AC} behavior of (1) by means of the capacitor voltage (V_C), in order to get an approximately sinusoidal behavior.

A. Design conditions and procedure

Equation (3) describes an equality proposed for the modified flyback transformer, where the subscript c and aux make reference to capacitor and auxiliary wound, N and V represents the number of turns and voltage respectively.

$$\frac{N_p}{N_{aux}} = \frac{V_c}{V_{aux}} \quad (3)$$

Hence the transformation ratio n is given as:

$$n = \frac{N_{aux}}{N_p} \quad (4)$$

Therefore the auxiliary voltage equals:

$$V_{aux} = nV_c \quad (5)$$

The peak input inductor current at turn-on time i_{Lon-pk} is:

$$i_{Lon-pk} = \frac{V_{aux}}{L} t_{on} = \frac{nV_c}{L} DT_s \quad (6)$$

where the turn-on time t_{on} is equal to duty cycle D for the switching period T_s .

For turn-off time t_{off} the peak input inductor current is defined as:

$$i_{Loff-pk} = \frac{V_c - V_{AC}}{L} (1 - D)T_s \quad (7)$$

Due to the triangular shape of the peak current into the input inductor at t_{on} and t_{off} :

$$\frac{nV_c}{L} DT_s = \frac{V_c - V_{AC}}{L} (1 - D)T_s \quad (8)$$

Now, resolving in terms of D and to ensure discontinuous behavior:

$$D < \frac{1}{1 + \frac{nV_c}{V_c - V_{AC}}} \quad (9)$$

The input inductor average current equation are given in (10) as:

$$\langle i_L \rangle = \frac{1}{T_s} \int_0^t i_{L-pk} dt \quad (10)$$

for t_{on} and t_{off} the expression for average inductor current are defined by:

$$\langle i_{Lon} \rangle = \frac{nV_c}{2L} D^2 T_s \quad (11)$$

$$\langle i_{Loft} \rangle = \frac{V_c - V_{AC}}{2L} (1 - D)^2 T_s \quad (12)$$

Now, Fig. 6 shows the power block diagram, where P_r is the rectified power, P_o is the output power of the flyback transformer, and P_p is the partial power returned to the input which is function of the quantity of recycled energy K and rectifier power.

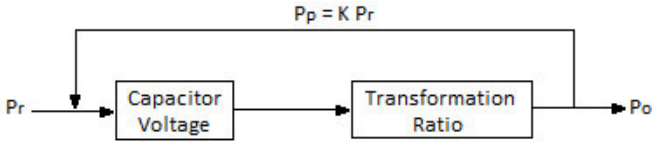


Fig. 6. Block diagram of power flow into the cell

Partial power can be written as (13) and is related to average inductor current at turn-on time, transformation ratio, capacitor voltage, and duty cycle.

$$P_p = \frac{1}{\pi} \int_0^\pi \langle i_{Lon} \rangle nV_c D d\theta \quad (13)$$

And, rectified power is related to average inductor current at turn off time, and AC main line.

$$P_r = \frac{1}{\pi} \int_0^\pi \langle i_{Loft} \rangle V_{AC} \sin \theta d\theta \quad (14)$$

For equations (13)-(14), θ is the variable of integration

In order to shape the current, the quantity of recycled energy returned to the input, will then become

$$K = \frac{P_p}{P_r} = \frac{D\sqrt{(V_c^2 - V_{AC}^2)}}{V_c - \sqrt{(V_c^2 - V_{AC}^2)}} \quad (15)$$

IV. BLDC CONTROL SYSTEM

Fig. 7 shows a common six-step sequence, the IGBT gates are triggered to produce one signal per phase with a displacement of 120° with respect of each other into the three

phase inverter, a typical PI closed-loop with hall effect sensors was performed.

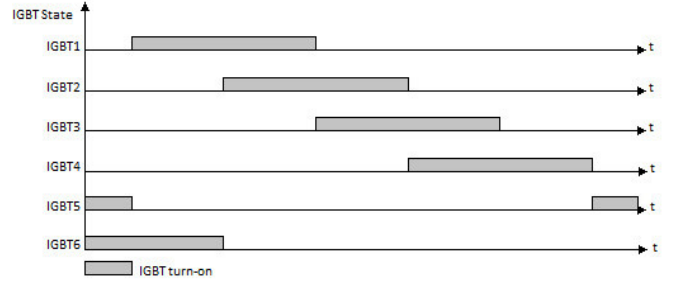


Fig. 7. Six-step trigger gate sequence.

V. EXPERIMENTAL RESULTS

Table 1 shows the cell design values, AC input voltage, output voltage, switching period, input inductor, primary inductance, secondary inductance, auxiliary inductance, capacitor, and output capacitor.

Table 1. Cell Design Values

Variable	Value
$V_{AC} =$	120 V
$V_o =$	48 V
$T_s =$	10 us
$L =$	190 uH
$L_p =$	418 uH
$L_s =$	17 uH
$L_{aux} =$	268 us
$C =$	100 uF / 400 V
$C_o =$	47 uF / 100 V

Fig. 8 shows the inductor discontinuous current which is related with the duty cycle and is the first design consideration by this time the duty cycle is equal to 0.27.

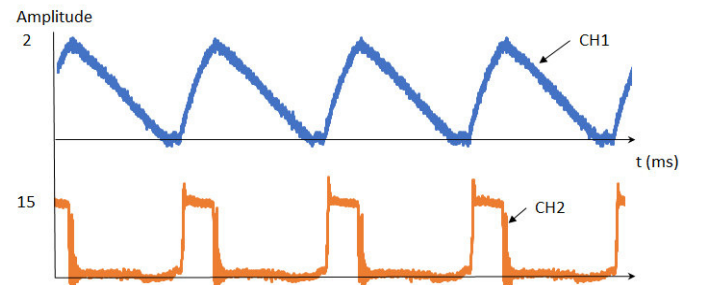


Fig. 8. CH1 – Input inductor current; CH2 – Duty cycle of 0.27, $f=100$ KHz

According to the design, a duty cycle upper to 0.27 generates a continuous current into the inductor, in which case, the cell converter behavior changes as shown in Fig. 9.

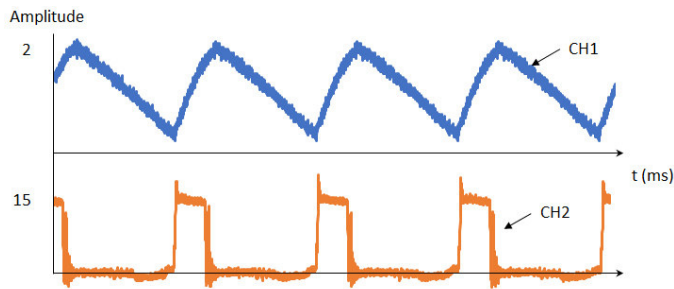


Fig. 9. CH1 – Input inductor current; CH2 – Duty cycle of 0.32, $f=100$ KHz.

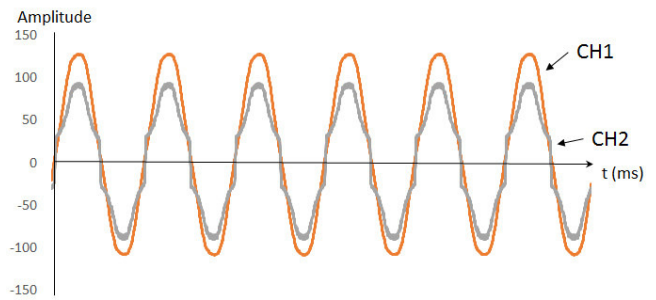


Fig. 12. CH1 – AC input voltage 120Vpeak, 60 Hz; CH2 – AC input current (with amplification factor).

A typical flyback converter deals with the drawback stresses from the semiconductors at DCM, a proposed cell gets a good trade-off between a discontinuous current and switching semiconductor losses are obtained, Fig. 10 shows the drain-source signal and the control signal with a duty cycle of 0.27.

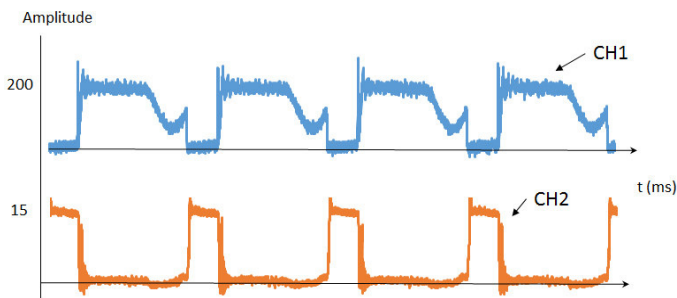


Fig. 10. CH1- Drain-source semiconductor voltage, CH2 - Duty cycle of 0.27, $f=100$ KHz.

A 48 Volts, BLM-N23-50-1000-B BLDC motor is used for experimental testing. Fig. 11 shows the maximum output voltage for $D=0.27$ to feed the three-phase IGBT bridge versus capacitor voltage or DC bus.

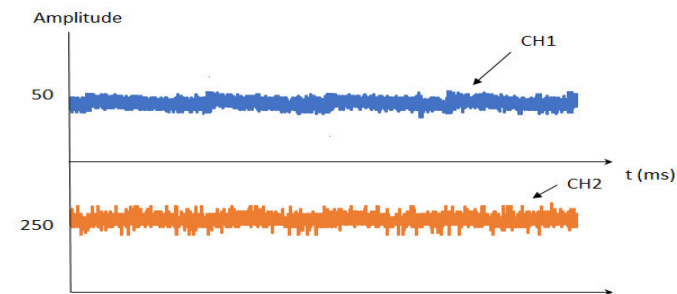


Fig. 11. CH1 – Output voltage of cell converter; CH2– DC bus voltage.

Design requirements for the proposed cell were: a specific duty cycle limit to ensure the discontinuous current mode and a controlled capacitor voltage in order to emulate a typical flyback DCM behavior. Fig. 12 shows the experimental result of the input current shape versus AC main voltage.

A power factor of 0.98 has been obtained. Fig. 13 shows a comparison between Total Harmonic Distortion (THD) IEC 6100-3-2 D class standard and the harmonic content of the proposed driver.

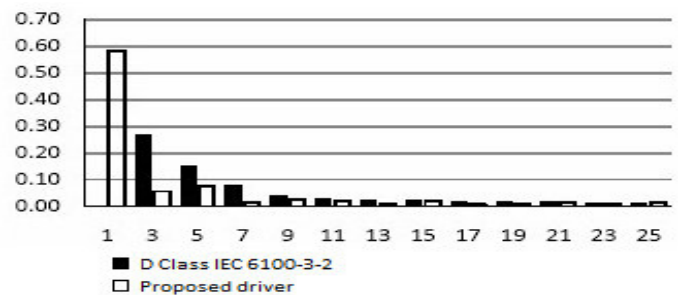


Fig. 13. Harmonic content of the proposed driver.

VI. CONCLUSION

Ideally BLDC speed drives strive to reduce the complexity and comply with set power quality requirements. This paper presents a cell converter based on a typical flyback converter operated in DCM, with an input current shaped in order to feed a BLDC via a three phase inverter. Design and control were described through the results analysis. The proposed cell converter gets an approximately sinusoidal behavior in order to achieve a good commitment between simplicity of cell control, power factor, THD, and switching semiconductor losses.

References

- [1] C. L. Xia, Permanent Magnet Brushless DC Motor Drives and Controls. Hoboken, NJ, USA: Wiley, 2012.
- [2] Limits for Harmonic Current Emissions Hoboken, International Standard IEC 61000-3-2, 2000.
- [3] V. Bist and B. Singh, "PFC Cuk Converter-Fed BLDC Motor Drive", IEEE Transactions on Power Electronics, vol. 30, no. 2, Feb. 2015.
- [4] V. Bist and B. Singh, "An Adjustable-Speed PFC Bridgeless Buck-Boost Converter-Fed BLDC Motor Drive", IEEE Transactions on Industrial Electronics, vol. 61, no. 6, Jun. 2014.
- [5] B. Singh, S. Singh, A. Chandra, and K. Al-Haddad, "Comprehensive study of single-phase ac-dc power factor corrected converters with high frequency isolation," IEEE Trans. Ind. Informat., vol. 7, no. 4, Nov. 2011.
- [6] T. Gopalarathnam, H.A. Toliyat, "Input current shaping in BLDC motor drives using a new converter topology", The 27th Annual Conference of the IEEE, Industrial Electronics Society, 2001. IECON '01., vol. 2, Nov. 2001.

- [7] V. Bist, B. Singh, "A Brushless DC Motor Drive With Power Factor Correction Using Isolated Zeta Converter", *IEEE Transactions on Industrial Informatics*, vol.10, no. 4, Nov. 2014.
- [8] V. Bist, B. Singh, "A PFC-Based BLDC Motor Drive Using a Canonical Switching Cell Converter", *IEEE Transactions on Industrial Informatics*, vol. 10, no. 2, May. 2014.
- [9] N. Vazquez, J. Lopez, J. Arau, C. Hernandez, E. Rodriguez, "A different approach to implement an active input current shaper", *IEEE Transactions on Industrial Electronics*, vol.52, no.1, Feb. 2005.
- [10] L Jong-Jae, K. Jung-Min, K. Eung-Ho, C. Woo-Young, K. Bong-Hwan, "Single-Stage Single-Switch PFC Flyback Converter Using a Synchronous Rectifier", *IEEE Transactions on Industrial Electronics*, vol. 55, no. 3, Mar. 2008.

Influence of pre-activation of type “F” fly ash on the compressive strength of mortars with short curing periods.

A. Naranjo Curiel ^{#1}, J.L. Reyes Araiza ^{#2}, R. Ramírez Jiménez ^{#3}, A. Manzano Ramírez ^{#4}, J. Pérez Bueno ^{#5}

Universidad Autónoma de Querétaro, engineering department, Cerro de las Campanas S/N, Las Campanas, 76010 Santiago de Querétaro, Querétaro, México

^{#1} ing.naranjocuriel@hotmail.com

^{#2} araiza@uaq.edu.mx

^{#3} ruraji@uaq.edu.mx

CINVESTAV, Libramiento Norponiente 2000, Real de Juriquilla, 76230 Santiago de Querétaro, Querétaro, México.

^{#4} amanzano@gro.cinvestav.mx

CIDETEQ, Parque Tecnológico Querétaro S/N, San Fandila, 76703 Pedro Escobedo, Querétaro, México.

^{#5} jperez@cideteq.mx

Abstract—Different research works have documented that mortars and concretes with type-F fly ash achieve their maximum compression capacity in long curing periods. This work presents the evolution study of the strength of the mortars with fly ash with two pre-activation periods, with the objective of establishing a simple method to obtain compression strengths in early ages for these mortars. In order to achieve that 4 mixes were designed, one control mix and another mix replacing 20% of the Portland cement with fly ash, the other two mixes were elaborated with pre-activated fly ash in sodium hydroxide, with 3 and 5 days of pre-activation respectively. As a result of this investigation we can observe that when fly ash is activated an increase in the compression strength in early ages with longer activation periods is noted. In addition, it can be perceived that a better water control is needed due to the fact that both fly ash and sodium hydroxide have affinity with the water, and that can affect the mixes reducing their compression strength

Keywords—Fly Ash, Pre-activation, Type-F, Compression Strength.

I. INTRODUCTION

The high volume of solid wastes generated by the industry demands adequate solutions for the final dispose of these wastes, in order to prevent negative environmental impacts [1]. The concrete, up to these days, has been the most used material in the construction of any kind of infrastructure in the whole history of civilization [2]. The concrete absorbs natural mineral resources and should be decreased its use in order to reduce the consumption of energy during the construction [3] it generates larges emissions of CO₂ SO₂ and NO_x, responsible gases of the greenhouse effect [4], The fly ash is a industrial residue generated by the combustion of pulverized coal in coal burning electric plant [5], and it has been

considered as a mineral additive for mortars and concretes due to his puzolanic activity. Is the most available supplementary cementitious element in the entire world [6, 7, 8]. In some cases, high volumes (>40%) of fly ash are used to achieve desired concrete properties and lower the production cost of the concrete. However, as a puzolanic reaction is a slow process where its contribution to the strength occurs only in late ages [9, 10].

The possibility of activation of fly ash lie son breaking its vitreous phases. [11] Considered that the required pH value to dissolve the alumina and sílica is closed to 13.3 o greater. Then, is impossible to make the fly ash to rise its activation speed in the fly ash – Ca (OH)₂ system because its pH is lower than 13. The usual way to achieve a high pH value is adding NaOH (sodium hydroxide) or any other alkalinity in the fly ash.

According to the past arguments, in this paper the evolution of the strength of mortars with fly ash with different pre-activation periods was observed, with the purpose of achieving a simple method to obtain compressive strengths in early ages for these mortars. Is worth indicating the reported work is part of a sequence of local studies related to the topic [12-15], that has served as a theoretical base for the development of this work.

TABLE 1. Chemical composition (%) of fly ash.

Óxides (%)	Cement	Fly Ash
SiO ₂	18.08	58.89
Al ₂ O ₃	5.58	24.84
Fe ₂ O ₃	2.43	4.94
CaO	61.94	3.23
MgO	2.43	0.87
SO ₃	2.54	1.12
Na ₂ O	0.18	0.45
K ₂ O	0.99	1.18
TiO ₂	--	1.0

II. EXPERIMENTAL WORK

A. Materials.

Composed Portland cement CPC-30R was used in all the mortars mixes (Mexican standard for cements [16] whose chemical composition is shown in table 1. Region mine sand was used as light aggregate with a dry loose volumetric weight of 1,180 kilograms per cubic meter and a fineness module of 4.9.

The fly ash was obtained from the coal burning electric plant Río Escondido in Piedras Negras, Coahuila, México. Its chemical composition was obtained by X-ray fluorescence (XRF) technique and is exhibited in table 1. We can observe that its calcium content is low and based on [17] it can be classified as a type F fly ash.

A solution with an 8M molar concentration was prepared with sodium hydroxide (NaOH) industrial grade with a purity of 98% and distilled water. Subsequently the portion of fly ash was mixed in such solution to pre-activate it; the solution was labeled as NaOH-FA and the time of activation was established as 3 and 5 days.

B. Specimens Preparation.

Four different mixes were designed and prepared under the guidelines of [18]. In specific the dosage was ensured to meet a cement-sand relation of 1:3, with the right amount of water to accomplish the fluidity recommended by [19] and [20]. It is mentioned in this guidelines that the mixes with fly ash must accomplish a fluidity of $.172 \pm .005$ meters (m).

The control mixes M1-1 y M1-2 contains only Portland cement and light aggregate in the previously specified proportion. In contrast, in mixes M2-1 y M2-2 an amount of 20% of Portland cement was replaced with fly ash. The mixes M3-1, M3-2 y M4 are similar to the mixes M2-1 y M2-2 with the difference that those mixes (M3-1, M3-2 y M4) include pre-activated fly ash. Mixes M3 and M4 differ in their activation periods, being 3 and 5 days respectively.

In the case of mix M3-1 the NaOH-FA solution was used to elaborate the mix. In contrast, for the mixes M3-2 y M4, the pre-activated fly ash was separated from the NaOH-FA solution and subsequently mixed with the other constituents, adding the right amount of water to obtain the mix.

The mixes were elaborated in the laboratory at a temperature of 24 ± 2 Celsius degrees in standardized moulds of 0.05 meters of diameter and 0.10 meters height, keeping the relation of diameter-height of 1:2. For all the compositions the materials were mixed in their dry state in order to achieve a good homogenizing for a period of 120 seconds and then adding the corresponding amount of water to obtain a the fluidity consistent with the standard.

TABLE 2. Proportions of the mixes per cement unit.

Mix.	Materials Proportions					No. Specimens	
	C	S	FA	PFA (3D)	PFA (5D)	7 D	14 D
M1-1	1	3	-	-	-	9	9
M1-2	1	3	-	-	-	9	9
M2-1	0.8	3	0.2	-	-	9	9
M2-2	0.8	3	0.2	-	-	9	9
M3-1	0.8	3	-	0.2	-	9	9
M3-2	0.8	3	-	0.2	-	9	9
M4	0.8	3	-	-	0.2	9	9

C = cement, S = sand, FA = fly ash, PFA = pre-activated fly ash, 3D = 3 days.

Fig. 1. Homogenizing of dry materials.

Dry materials were mixed in a tray in order to homogenize them before adding the water.

Fig. 2. Solution (NaOH + H₂O) 8M.



Sodium hydroxide was prepared by adding .320 kilograms of NaOH per each lite.001 m³ of water (or 1 kilogram of water) so the relation (water/NaOH) was approximately of 1:3 in order to achieve de 8 molar solution.

Fig. 3. Fly Ash + Solution.



After the preparation of the NaOH solution and one day of repose the type-F fly ash was poured inside the solution in order to activate it in the periods previously mentioned.

Fig. 4. Collocation of pre-activated fly ash.



Finally the solution with the fly ash previously activated is mixed with the dry materials to fabricate the mortar mix.

C. *Mechanic Tests.*

The compressive strength of the specimens was determined in accordance with [21] and using a Tinius Olsen universal machine equipped with a loading cell of 500 kilo Newtons to test the specimens. 9 specimens were tested for each of the mixes at the ages of 7 and 14 days, and such tests were executed at a room temperature of de 23 ± 2 Celsius degrees and a relative humidity of 50 ± 5 %.

III. RESULTS AND DISCUSSIONS.

The specimens elaborated with the solution of sodium hydroxide and fly ash (mix M3-1) required more time to be unmolded in contrast with the rest of the mixes, this can be due to the presence of a great quantity of sodium hydroxide in the mix.

A. *Fluidity of the Mixes.*

The results of the fluidities for each mix are shown in table 3. It can be observed that big water/cement (w/c) relations were obtained but all of the fluidities are in congruence with [19]; big water/cement relation obtained in the mixes is due to the water retention of the hydroxide and the fly ash.

With the purpose of studying the effect that the amount of water has over the mechanic properties in these mixes it was considered that M1-1 and M2-1 mixes were elaborated with such an amount of water that the fluidity would be in the lower limit. In contrast, the mixes M1-2 and M2-2 were elaborated with such an amount of water that the fluidity would be in the upper limit. In the other hand, mix M3-1 was elaborated with the total amount of the alkali solution in which the fly ash was pre-activated so that his fluidity would be in the upper limit and finally the mixes M3-2 and M4 were decanted, leaving only a small portion of sodium hydroxide in the fly ash paste.

TABLE 3. Fluidity relation of the mixes.

	w/c	FLUIDITY (meters)				
		1	2	3	4	Average
M1-1	0.44	.150	.150	.145	.145	.148
M1-2	0.55	.170	.170	.172	.172	.171
M2-1	0.90	.160	.165	.165	.170	.165
M2-2	1.20	.177	.178	.179	.176	.178
M3-1	1.15	.170	.170	.170	.170	.170
M3-2	1.23	.170	.170	.170	.170	.170
M4	1.23	.178	.177	.178	.178	.178

In reference to the mixes with fly ash, the superficial area contributes to an acceleration of the hydration of the mixes with fly ash, however, it also increases the amount of water required. Such effect can be appreciated when looking at the (w/c) relations of the mixes M2, M3 and M4 that needed more water to achieve the lower limit of fluidity, and all this because of their fly ash content. Furthermore, as established before, is convenient to keep a control of the water content of the mixes avoiding the presence of a large amount of water to prevent lower compressive strengths.

B. Compressive strength of the specimens.

The results to the compressive strength test are given in tables 4 and 5. It can be observed that the compressive strength for all the mixes increases over the time.

TABLE 4. 7 days compressive strength.

	Arithmetic Mean (kg/cm ²)	Standard Deviation (kg/cm ²)
M1-1	92.29	14.95
M1-2	79.19	7.31
M2-1	52.16	8.36
M2-2	59.20	2.70
M3-1	19.84	1.47
M3-2	58.00	6.05
M4	48.06	2.63

TABLE 5. 14 days compressive strength.

	Arithmetic Mean (kg/cm ²)	Standard Deviation (kg/cm ²)
M1-1	87.24	13.89
M1-2	82.94	7.34
M2-1	54.96	9.61
M2-2	71.70	4.01
M3-1	25.22	1.26
M3-2	58.45	2.40
M4	60.56	6.96

Compressive strength of the mixes fluctuates due to their constituents and their curing periods. It can be noticed that the specimens that contains fly ash without pre-activation have a lower compressive strength for short-term curing periods in contrast with the control mix. Such effect has already been proved in previous works that have contributed to the state of the art.

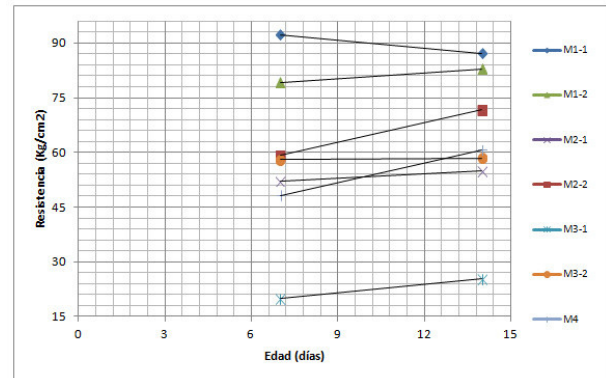
Paying attention to the 14 days-compressive strength we can observe that the mix M3-2 with pre-activation of the fly ash acquires a mayor strength compared to the mix M2-1 which had no previous activation. This continues to be concordant with other author's works in relation to the pre-activation of fly ashes in short activation periods.

In comparison between the mixes M3-2 and M4 it can be observed an increase in the compressive strength in a longer pre-activation period, which makes us infer that greater strengths can be achieved with longer pre-activation periods

In the case of the mix M3-1 some specimens were let to a 40 days curing period which reflected a lower compressive strength.

TABLE 6. 40 days compressive strength.

	Arithmetic Mean (kg/cm ²)	Standard Deviation (kg/cm ²)
M3-1	41.78	3.98

Fig. 5. Compressive strengths.

The ASTM C109 and ASTM C39 mention that two or three specimens from a batch of mortar must be tested for each period of test or test age, all this for mortars and concretes with a Portland cement base. In our case the quantity of specimens tested is associated with a 90% confidence in the results, having in mind that these materials are too heterogeneous and anisotropic, and using this to determine a design compressive strength that ensures that the applied mortar is trustworthy.

IV. CONCLUSIONS

This study showed that mixes that contain fly ash present lower strength compared to those of a conventional mix in short curing periods, however, when the pre-activation of the fly ash is done the compressive strength of the mixes raised over the time, is necessary to take into consideration some important points:

- The pre-activation time is an important factor to achieve greater strengths, as we saw in figure 5, because a greater gain of strength is perceived due to a longer pre-activation time. Is advisable to gather data of the compressive strengths of mortars with fly ash pre-activated for a longer period of time and with prolonged curing periods.
- Is most likely that the existence of the sodium hydroxide inside the fly ash paste have inhibited the hydration reactions between the particles of the Portland cement and the fly ash, not allowing the crystalline microstructures that have influence in the mechanic resistance of these materials to be generated (calcium silicate hydrates-CSH and ettringite). Such effect can be observed by comparing the compressive strength between the mixes M3-1 and M3-2 where the first mix contained the mayor quantity of sodium hydroxide.

KNOWLEDGEMENTS

Special thanks to CONACYT and the Government of the State of Querétaro for the support offered through the project QRO-2012-C01-193364 from the convening FOMIX 2012-01: Strengthening through the Laboratories of the Master Degree in Science of the engineering faculty of the Universidad Autónoma de Queretaro.

REFERENCES

- [1] Pelegrini, M., G. Pinheiro y J.A.B. Valle. 2010. Plates made with solid waste from the recycled paper industry. *Waste Manage* 30 (2010) pp. 268-273.
- [2] Mehta Kumar, Monteiro Paulo, 1998, *Concreto Estructural y Materiales*, IMCYC.
- [3] Zong, L., Z. Fei, S. Zhang. 2014. Permeability of recycled aggregate concrete containing fly ash and clay brick waste. *Journal of Cleaner Prod.* xxx (2014) pp. 1-8.
- [4] Gamero D. P., 2008, Programa Nacional para la prevención y gestión integral de los residuos, Saltillo Coahuila: CINVESTAV.
- [5] Yilmaz, A. N. Degirmenci. 2009. Possibility of using waste tire rubber and fly ash with Portland cement as construction materials. *Waste Manage* 29 (2009) pp. 1541-1546.
- [6] Arezoumandi, M., J.S. Volz, C.A. Ortega y J. Myers. 2013. Effect of total cementitious content on shear strength of high-volume fly ash concrete beams.
- [7] Glasser, F.P. 1996. Properties of cement waste composites. *Waste Management* 16 (1996) pp. 159-168.
- [8] Neville, A.M. 1994 *Properties of concrete*. Great Britain: Pitmann Publishing Ltd (1994) pp. 628-645.
- [9] Palomo, A., M.W. Grutzeck M.T. Blanco. 1999. Alkali-activated fly ashes a cement for the future. *Cement and Concrete Res.* 29 (1999) pp. 1323-1329.
- [10] Poon, C.S., S.C. Kou, L. Lam, Z.S. Lin. 2001. Activation of fly ash/cement systems using calcium sulfate anhydrite (CaSO₄). *Cement and Concrete Res.* (2001) pp. 873-881.
- [11] Fraay, A.L.A., J.M. Bejen. 1989. The reaction of fly ash in concrete: A critical examination. *Cement and Concrete Res.* 19 (1989) pp. 235-246.
- [12] Bernal Elias Vladimir. 2008. "Efecto de la ceniza volante en morteros fabricados con cemento Portland". Tesis de grado M. en C. (Construcción), Facultad de Ingeniería, UAQ.
- [13] Baltazar Méndez Mauricio. 2010. "Contribución de la ceniza volante tipo "F" sobre las propiedades físicas y mecánicas de los concretos de cemento Portland". Tesis de grado M en C. (Construcción), Facultad de Ingeniería, UAQ.
- [14] Mendoza Santiago Juan Francisco. 2014. "Efecto de la ceniza volante tipo F y del hule reciclado de neumáticos en las propiedades mecánicas del concreto". Tesis de grado M en C. (Construcción), Facultad de Ingeniería, UAQ.
- [15] Vega Nieto Hugo. 2014. "Mejoramiento de las Propiedades Mecánicas del Tabique Rojo Recocido mediante la Adición de Ceniza Volante tipo F". Tesis de grado M en C. (Construcción), Facultad de Ingeniería, UAQ.
- [16] NMX-414-ONNCE. 2009. *Industria de la construcción –cementos hidráulicos–especificaciones y métodos de prueba.*
- [17] ASTM C618. Standard specification for fly Ash and raw or calcined natural pozzolan for use as a mineral admixture in portland cement concrete
- [18] ASTM C109/C109M. Standard test method for compressive strength of hydraulic cement mortars (using 2-in. or [50mm] cube specimens).
- [19] ASTM C1437. Standard test method for flow of hydraulic cement mortar.
- [20] ASTM C593. Standard specification for fly ash and other pozzolans for use with lime for soil stabilization
- [21] ASTM C39/C39M. Standard test method for compressive strength of cylindrical concrete specimens.

Optimization of gearbox dynamic by a continuous genetic algorithm

S.V. Camacho^{#1}, J.C. Jauregui^{#2}, A. Dominguez^{#3}

[#] *Division de Estudios de Posgrado, Facultad de Ingenieria, Universidad Autónoma de Querétaro, Centro Universitario, Cerro de las Campanas S/N, Las Campanas, C. P. 76010, Querétaro, Qro., México.*

¹ scamacho21@alumnos.uaq.mx

² jc.jauregui@uaq.mx

³ auredgz@uaq.mx

Abstract— The conventional design of a gearbox is deficient because it dismisses the effects of dynamic iterations between components as external excitations due to defects on thereof, which can cause early failure. In this paper, a methodology based on a continuous genetic algorithm and a dynamic model is presented in order to minimize vibrations or to eliminate resonances on a simple gearbox by maximizing the distance between their excitation frequencies which often-overlap. Also, there were proposed two objective functions to deal with the optimization problem, a weighted sum of cost functions and a maximum minimum distance. The results show that the function objective maximum minimum distance improve the distribution between the excitation frequencies, therefore, they can be applied for the design of a gearbox.

Keywords—*optimization; gearbox dynamic; continuous genetic algorithm.*

I. INTRODUCTION

In this paper, a methodology for the optimal design of a simple gearbox based on their dynamic model is presented. This is performed by a continuous genetic algorithm that finds the best distribution between the excitation frequencies (due to defects in the elements), additionally, a comparison among two different objective functions was made. So that the noise is minimized and the resonances are eliminated.

Because of the need to transmit power and motion, gearboxes are present in a wide range of machines. However, the methodology used in the conventional design of a transmission is based on the selection of components using standards and above all, in the experience of the designer. Therefore, the dynamic interactions between its components are scarcely considered.

The literature reports several studies related to the optimal design of gears, bearings and gearboxes. Many of them focused on minimizing the volume, as Gologlu and Zeyvali [1] who minimized the volume of gear trains by a genetic algorithm. It were used restrictions related to the geometry of the gears and the normal module, the number of teeth and the face width were chosen as design variables. Rajiv [2] also used a genetic algorithm to optimize volume in crowded cylindrical roller bearings, he used design constraints to improve the life of bearings. Huang et al. [3] reduced the volume of medium sized motor truck based on structural features and design

requirements, they used a sequential quadratic programming. Zhang et al. [4] optimized the volume of a spiral bevel helical gear. They took into account 14 design variables mainly related to the geometry of the gears. Qimin and Qili [5] optimized a planetary gear reducer to minimize their volume using particle swarm optimization.

Moreover, vibration studies have only focused on minimizing the transmission error and noise. Bonori et al. [6] used a genetic algorithm to optimize spur gears by micro-geometric modifications and minimization of the static transmission error which causes vibrations. Faggioni et al. [7] used profile modifications in spur gears in order to reduce gear vibrations related to static transmission error and dynamic transmission error by a mean Random–Simplex optimization. Kong et al. [8] suggested the use of optimization algorithms of a single parameter. They proposed the Quasi-Newton method for minimizing the starting torque and torque fluctuations that may cause noise and vibrations in a magnetic planetary gear transmission.

All these works had positive results using different optimization methods. However, genetic algorithms and particle swarm optimization stand out because they are simpler to implement and they always find a solution even if the model is discontinuous or the solution space has abrupt changes. Nowadays, there is a discussion about which optimization algorithm is the best. But, in this work a genetic algorithm was chosen because there are more implementation references.

II. DYNAMIC MODEL

The dynamic interactions between the components of a mechanical transmission cause external excitations due to defects from thereof. These excitations generate vibrations, therefore, it is necessary to prevent frequencies overlapping, so as to prevent early failure. The natural frequencies of the system are not considered because usually found far from the excitation frequencies. Case study corresponds to a one stage gearbox.

The goal of this work is to minimize the vibrations of a gearbox by maximizing the distance between their excitation frequencies that commonly overlap. From [9], four excitation frequencies (1-4), due to the kinematics of each bearing, were taken.

$$\omega_{ir}=N/2[1+d/D*\cos(\alpha)]\omega_i \quad (1)$$

$$\omega_{or}=N/2[1-d/D*\cos(\alpha)]\omega_i \quad (2)$$

$$\omega_c=1/2 [1-d/D*\cos(\alpha)]\omega_i \quad (3)$$

$$\omega_{re}=D/d[1-(d/D*\cos(\alpha))^2]\omega_i \quad (4)$$

The frequency ω_{or} corresponds to the contact frequency between the roller element and the internal track, ω_{or} is the contact frequency between the roller element and the external track, ω_c is the casing frequency and ω_{re} is the roller spin frequency. These frequencies are multiplied by the rotational speed ω_i . N is the number of rolling elements, d is the rolling element diameter, D the pitch diameter and the axial contact angle α .

Additionally, the frequency of the pinion ω_p (5), the gear frequency ω_g (6) and the gear mesh frequency ω_{gm} (7) were taken into account. ω is the excitation frequency of gearbox, r is the reduction ratio and N_g is the number of teeth of gear. The pinion teeth number N_p is determined by the variables N_g and r .

$$\omega_p=\omega \quad (5)$$

$$\omega_g=\omega_p/r \quad (6)$$

$$\omega_{gm}=\omega_g*N_g=\omega_p*N_p \quad (7)$$

III. DEFINING THE OPTIMIZATION PROBLEM

Genetic algorithms (GA), which were invented by John Holland in 1975, are a heuristic method based on ‘‘Survival of the fittest’’. They combine the persistence of the strongest with a random exchange of information arranged to form a search algorithm. In every iteration, a new generation is created using data of the fittest previous set. However, genetic algorithms are not just a random path, they efficiently take advantage of historical information to speculate new search points with an expected improvement in performance [10].

In this optimization problem a continuous genetic algorithm was proposed as it provides many advantages over binary genetic algorithm [11]. First, in a continuous genetic algorithm the design variables are represented by floating point numbers with the machine precision rather than have precision limited by their binary representation. Second, the continuous GA requires less storage than binary GA because a single floating number represents the variable instead of N bits integers. Finally, the continuous genetic algorithm is naturally faster than binary GA since the chromosomes do not have to be decoded prior to the evaluation of the cost function.

A. Objective function

The goal of optimization is to maximize the distance between the frequencies which usually overlap. To achieve this, two objective functions were proposed, a weighted sum of cost functions and a maximum minimum distance.

1) Weighted sum of cost functions

This objective function lies in maximizing the weighted sum [11] of the differences between consecutive frequencies. The weight values w_n were determined experimentally.

$$cost=\sum_{n=1}^{10} w_n |\omega_{n+1}-\omega_n| \quad (8)$$

2) Maximum minimum distance

This objective function consists on maximizing the minimum difference between among all consecutive frequencies as shown (9).

$$cost= \min |\omega_{n+1}-\omega_n| \quad (9)$$

B. Design variables

The excitation frequencies of each bearing were determined by the number of rolling elements, the rolling element diameter, the pitch diameter and the axial contact angle (Fig. 1). Nevertheless, these parameters are encompassed in the first and second design variables, $b1$ and $b2$, inasmuch as the values of these parameters are extracted from a database of 192 actual bearings.

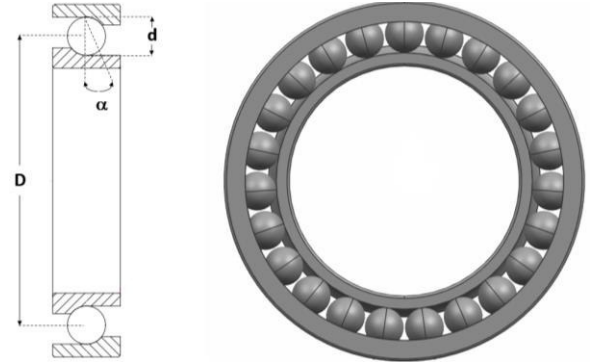


Figure 1 Bearing parameters.

The third and fourth design variables, N_g and r , equate to the number of teeth of gear and the reduction ratio. Finally, the design variable vector (chromosome) is expressed as:

$$X = \{b1, b2, N_g, r\} \quad (10)$$

C. Constraints

In a genetic algorithm can be observed different kind of restrictions as inequality constraints, equality constraints and domain constraints. The latter establishes the lower and upper bounds on the variables, in this case, the bounds are expressed in (11-14). The values of $b1$ and $b2$ are limited by the size of the database bearings. In order to ensure that the minimum number of the pinion teeth is 4, the minimum value of N_g is 13 and the maximum value is 152 according to standard. Non-limiting pinion-gear options, a slight variation was added in the reduction ratio r .

$$1 < b1 < 192 \quad (11)$$

$$1 < b2 < 192 \quad (12)$$

$$13 < N_g < 152 \quad (13)$$

$$2.99 < r < 3.1 \quad (14)$$

On the other hand, for this case, it is only necessary to define a restriction of inequality, the difference between consecutive distances must be greater than 2.5 Hz [12] (15).

$$|\omega_{n+1} - \omega_n| > 2.5 \text{ Hz} \quad (15)$$

IV. PROGRAMMING THE GENETIC ALGORITHM

The genetic algorithm is composed of four main modules and its flowchart can be seen in Fig. 2. To start, the population size, N_{pop} , the generation number, N_{ger} , the rates of mutation, N_{mut} , and the probability of crosses, N_{mat} , are established.

Subsequently, the first population is generated with random values between the upper and lower limits. Thus, the algorithm begins to iterate until it reaches the set number of generations.

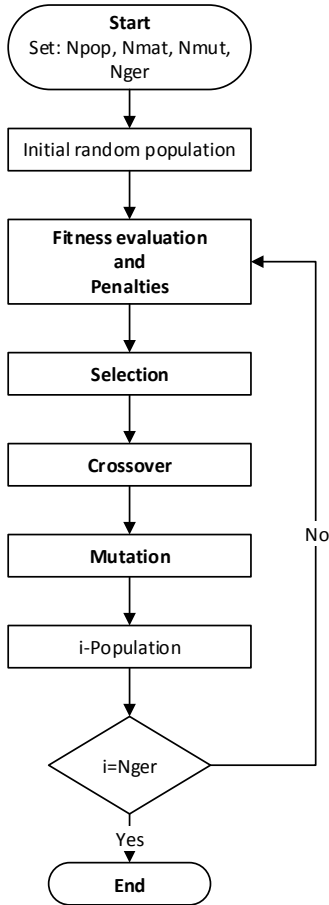


Figure 2 Flowchart of genetic algorithm.

A. Fitness evaluation and penalties.

The fitness evaluation is conducted for each individual (chromosome) of the population as follows:

- Find mechanical transmission frequencies that commonly overlap (1-7).
- Sort frequencies.
- Get the cost (8) or (9).

The penalty method from [13] was used to apply the limitation of the minimum distance, so, the optimization problem with a weighted sum of cost functions becomes:

$$\sum_{i=1}^{10} w_n [|\omega_{n+1} - \omega_n| - p\Phi] \quad (16)$$

With the objective function maximum minimum, the optimization problem turns into:

$$\min[|\omega_{n+1} - \omega_n| - p\Phi] \quad (17)$$

In both cases, Φ is the penalty function and p is the penalty coefficient, which are applied each time the constraint is violated.

$$\Phi = |\omega_{n+1} - \omega_n| \quad (18)$$

$$p = (150 - w_n |\omega_{n+1} - \omega_n|) / 150 \quad (19)$$

B. Selection and Crossover.

According to the mating rate, the highest values from fitness evaluation and penalties are selected to be parents and the offspring are combination of them. Next, a point crossover α is chosen randomly (18).

$$\alpha = \text{round}(\text{random} * \text{size chromosome}) \quad (18)$$

Then, the variables after point crossover are combined, as shown (19 and 20), to form new variables that will appear in the children. p represents the variables after point crossover, β is a random number between 0 and 1, d and m distinguish between the dad and the mom parent [11].

$$Off_1 = p_{m\alpha} - \beta(p_{m\alpha} - p_{d\alpha}) \quad (19)$$

$$Off_2 = p_{d\alpha} - \beta(p_{d\alpha} - p_{m\alpha}) \quad (20)$$

C. Mutation

The mutation operator produces spontaneous random changes in various chromosomes [14]. In order to do this and avoid a global minimum, random numbers are elected to select the row and columns of the population matrix to be mutated [11]. A mutated variable is replaced by a new random variable between upper and lower limits.

V. RESULTS

The case of study corresponds to single-stage gearbox, ie with four bearings (two equal), two shafts and two gears (Fig. 3). In order to implement the continuous genetic algorithm the following parameters were defined:

$$N_{pop} = 25$$

$$N_{ger} = 500$$

$$N_{mat} = 0.4$$

$$N_{mut} = 0.1$$

$$r = 3$$

$$\omega = 26.166667 \text{ Hz}$$

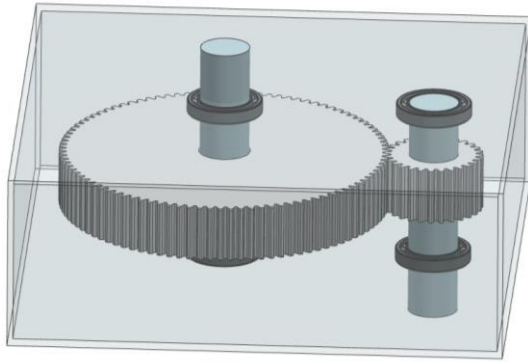


Figure 3. Single-stage gearbox

A. Continuous genetic algorithm with a weighted sum.

The values of the initial design are shown on table 1 and they correspond to the best design variables from first generation of genetic algorithm. The excitation frequencies of the input bearing and the output bearing are noted on table 2 and 3, respectively. The frequencies associated with the gears are shown in table 4.

Table 1 Best design variables values

Initial values			
$b1$	$b2$	Ng	r
12	146	136	3.0891465

Table 2 Input bearing

Initial values (Hz)			
ω_{ir}	ω_{or}	ω_c	ω_{re}
503.5304	429.8028	13.4313	354.4204

Table 3 Output bearing

Initial values (Hz)			
ω_{ir}	ω_{or}	ω_c	ω_{re}
118.9256	98.1086	4.2655	88.3430

Table 4 Gears

Initial values (Hz)		
ω_p	ω_g	ω_{gm}
29.16667	9.4362	1283.3333

The frequency spectrum of the initial design of the gearbox is shown in Fig. 4. In this spectrum, it can be seen that the distance between consecutive frequencies are fairly distributed. The minimum distance between frequencies was 3.9896 Hz.

After implementing the algorithm, the maximum weighted sum was obtained. The final values design are shown on table 5. The excitation frequencies of the input bearing and the output bearing are noted on table 6 and 7, respectively. The frequencies associated with the gears are shown in table 8.

The frequency spectrum of the final design is shown in Fig.5. The convergence of the genetic algorithm is shown in Fig. 6.

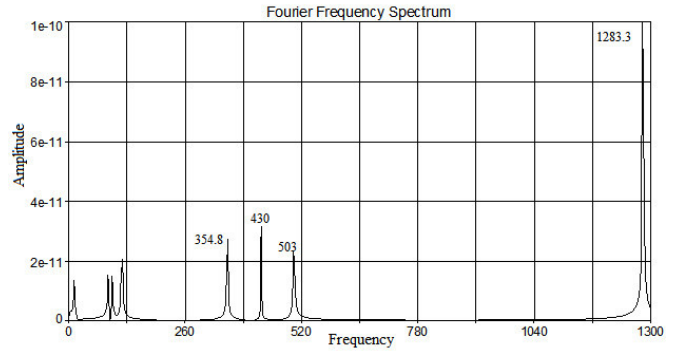


Figure 4. Initial design

Table 5 Best design variables values

Final values			
$b1$	$b2$	Ng	R
8	191	150	3.0050

Table 6 Input bearing

Final values (Hz)			
ω_{ir}	ω_{or}	ω_c	ω_{re}
532.7629	458.9037	13.4971	376.1624

Table 7 Output bearing

Final values (Hz)			
ω_{ir}	ω_{or}	ω_c	ω_{re}
64.0523	42.8920	3.8992	45.6038

Table 8 Gears

Final values (Hz)		
ω_p	ω_g	ω_{gm}
29.16667	9.7222	1458.3333

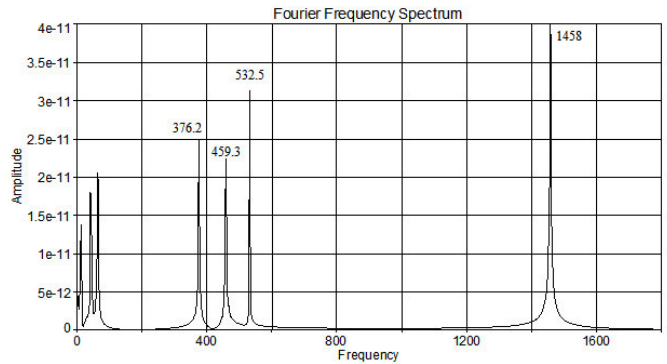


Figure 5. Final design

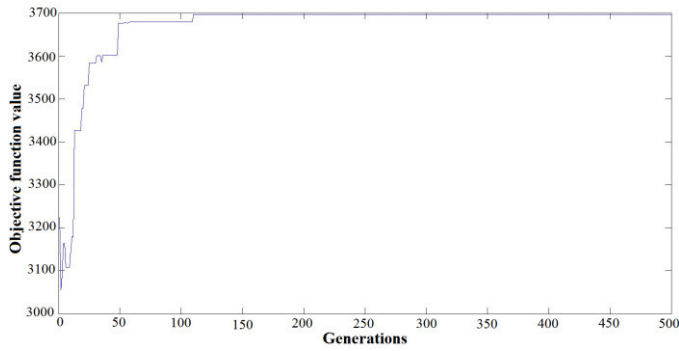


Figure 6. Convergence of the genetic algorithm

B. Continuous genetic algorithm with maximum minimum distance.

The values of design variables from first generation are shown on table 9. The excitation frequencies of the input bearing are noted on table 10 and the output bearing on table 11. The frequencies related with the gears are shown in table 12.

TABLE 9 Best design variables values

Initial values			
$b1$	$b2$	Ng	r
9	112	91	3.0047

Table 10 Input bearing

Initial values (Hz)			
ω_{ir}	ω_{or}	ω_c	ω_{re}
530.4836	461.1830	13.5642	376.4135

Table 11 Output bearing

Initial values (Hz)			
ω_{ir}	ω_{or}	ω_c	ω_{re}
132.4791	107.9054	4.3162	89.9050

Table 12 Gears

Initial values (Hz)		
ω_p	ω_g	ω_{gm}
29.16667	9.6153	875

The frequency spectrum of the gearbox in its initial configuration is shown in Fig. 7. Despite being the first generation, distribution of frequencies is quite good, the minimum distance between frequencies was 3.9488 Hz.

Lastly, the maximum minimum distance between adjacent frequencies was found. The final design variables are in table 13. The excitation frequencies due to bearings are shown in table 14 and 15 and the frequencies of the gears are in table 16. The spectrum frequency of the final design of the gearbox is

shown in Fig. 8. The convergence of the genetic algorithm is shown in Fig. 9.

Table 13 Best design variables values

Final values			
$b1$	$b2$	Ng	r
9	42	10	3.0335

Table 14 Input bearing

Final values (Hz)			
ω_{ir}	ω_{or}	ω_c	ω_{re}
530.4836	461.1830	13.5642	376.4135

Table 15 Output bearing

Final values (Hz)			
ω_{ir}	ω_{or}	ω_c	ω_{re}
102.3501	81.3998	3.8761	68.6498

Table 16 Gears

Final values (Hz)		
ω_p	ω_g	ω_{gm}
29.16667	8.75	87.5

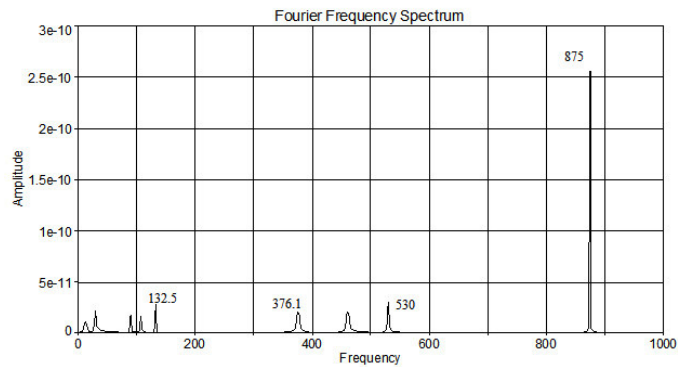


Figure 7. Initial design

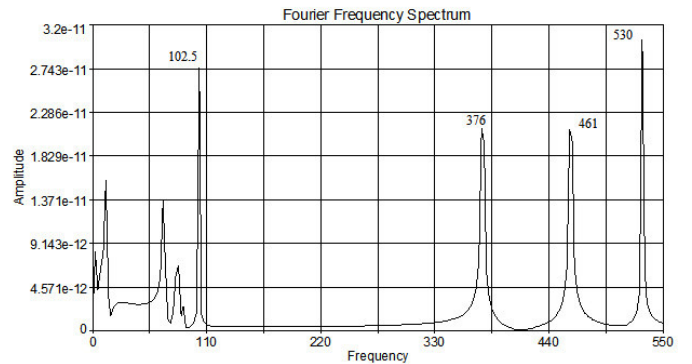


Figure 8. Final design

VIII. REFERENCES

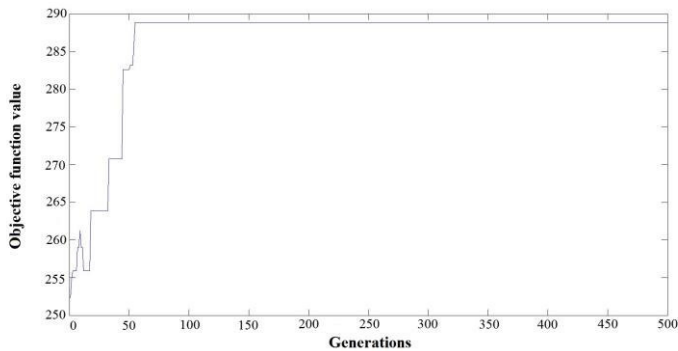


Figure 9. Convergence of genetic algorithm.

VI. DISCUSSION

Fig. 5 shows the distribution of gearbox excitation frequencies after implementing the genetic algorithm. Although the maximum sum was obtained, the minimum distance between frequencies was decreased to 3.7912 Hz compared with the Fig. 4 with the initial values. This is because the values of the weights are not suitable when there is a significant change in the values of the design variables, so that would require a dynamic adjustment of weights.

Fig. 7 shows the initial distribution of gearbox excitation frequencies, which differ from the values of Fig. 4 because the initial values are random. Fig. 8 shows the distribution of gearbox excitation frequencies after implementing the genetic algorithm with the maximum minimum distance. It can be seen that the frequencies of the optimum design (Fig. 8) are much better than the original design (Fig. 7). The minimum distance between consecutive frequencies was 4.8142. This ensures that the gearbox frequencies are not in resonance.

VII. CONCLUSIONS.

The dynamic interactions between the elements of a gearbox are hardly considered in the conventional design, however, there are external excitations due to the defects on the components that it could decrease the life of them. The results of the proposed method show that it is possible to optimize the design of gearboxes in order to minimize vibrations and to eliminate resonances because of external excitations.

Two objective function were proposed, a weighted sum and a maximum minimum distance. Both algorithms found the optimal solution but the weighted sum require a dynamic adjustment of weights because of the significant changes in the values of the design variables decreased the minimum distance between adjacent frequencies. In contrast, the maximum minimum distance improve smoothly the minimum distance between consecutive frequencies.

- [1] C. Gologlu y M. Zeyveli, «A genetic approach to automate preliminary design of gear drives.,» *Computers & Industrial Engineering*, vol. 57, pp. 1043-1051, 2009.
- [2] K. S. K. Rajiv Tiwari, «An optimum design of crowned cylindrical roller bearings using genetic algorithms.,» *Journal of mechanical design*, vol. 131, Mayo 2009.
- [3] W. Huang, L. FU, X. Liu, Z. Wen y L. Zhao, «The estructural optimization of gearbox based on sequential quadratic programming method.,» *2009 Second International Conference on Intelligent Computation Technology and Automation.*, pp. 356-359, 2009.
- [4] Z. Zhang, D. Chen, Y. Bai, Z. Yang y M. Feng, «The optimization design of triple gear-box assembled with spiral-behaviour of helical-spur gear.,» *Computer-Aided Industrial Design & Conceptual Design, 2009. CAID & CD 2009. IEEE 10th International Conference on*, pp. 2078-2081, 2009.
- [5] X. Qimin y X. Qili, «Study on optimal design planetary gear reducer based on particle swarm algorithm and matlab.,» *2010 Sixth International Conference on Semantics, Knowledge and Grids*, pp. 391 - 394, 2010.
- [6] G. Bonori, M. Barbieri y F. Pellicano, «Optimum profile modifications of spur gear by means of genetic algorithms.,» *Journal of Sound and Vibration 313*, pp. 603-616, 2008.
- [7] S. F. B. G. P. F. Faggioni M, *Dynamic optimization of spur gears*, vol. 46, Elsevier, 2011, pp. 544-557.
- [8] F. Kong, X. Zhu, L. Quan, Y. Ge y L. Qiao, «Optimizing design of magnetic planetary gearbox for reduction of cogging torque.,» *Vehicle Power and Propulsion Conference (VPPC), 2013 IEEE*, pp. 1 - 5, 2013.
- [9] J. C. Jauregui-Correa, «The effect of nonlinear traveling waves on rotating machinery.,» *Mechanical Systems and Signal Processing*, pp. 129-142, 2013.
- [10] D. E. Goldberg, *Genetic Algorithms in search, optimization, and machine learning.*, Addison-Wesley Publishing, 1989, p. 412.
- [11] H. S. Haupt Randy, *Practical genetic algorithms*, Hoboken, New Jersey: Wiley Interscience Publication, 2004.

- [12] A. A. Lozano Guzmán y J. C. Jáuregui Correa, Las vibraciones mecánicas en el mantenimiento predictivo, Santiago de Querétaro: UAQ/Fundap/IPN, 2013.
- [13] D. S. N. Sivanandam S. N., Introduction to Genetic Algorithms, TN: Springer, 2008.
- [14] R. C. Mitsuo Gen, Genetic algorithms and engineering optimization., Ashikaga: Wiley-Interscience publication, 2000.

Determination of the moisture active zone in expansive soils of Jurica, Querétaro, obtained by numerical solution of the diffusion equation.

C. D. Mendoza Solórzano¹, J. M. Horta Rangel^{*1}, E. Rojas Gonzales^{#1}, J. C. Leal Vaca²

¹*Division of research and graduate of the Faculty of Engineering. Autonomous University of Querétaro, Cerro de las Campanas, S/N, 76010, Santiago de Querétaro, Qro., México.*

¹ mendozacivil.c@gmail.com

^{*1}horta@uaq.mx

^{#1}erg@uaq.mx

²*Division of engineering of the Faculty of Engineering. University of Guanajuato, Calle Juárez No. 77; Col. Centro; C.P. 36000; Guanajuato, Gto., México.*

²jcesarlealv@hotmail.com

Abstract—A two-dimensional moisture diffusion model is solved. The model is capable of predicting soil suction changes in expansive soils under a waterproof surface (e.g., flexible slab model) with respect to time when the supporting soil mass is subjected to climatic boundary conditions that cause moisture changes. The moisture movement in unsaturated soils model was based on Mitchell's diffusion equation for soil suction. A program written in APDL language that runs Ansys environment was developed that allows the solution of the problem with 2-D Thermal transitory finite element with 4 linear degrees of freedom, characteristics for potential problems; the analogy of fields included solving a problem of suction base to a thermal transient model. The period of time considered into the analysis was of 2 years, obtaining suction profiles over the time, finding that Jurica soil suction remains constant at depth of 4 (four) meters describing the moisture active zone.

Keywords—Diffusion; soil suction; Mitchell's equation; ANSYS; 2-D Thermal transient finite element.

I. INTRODUCTION

Within the study of unsaturated soils, exist a group of soils with a peculiar problem when their state of moisture varies; called expansive soils. Expansive soils suffer volumetric deformations due to the change of the gravimetric moisture; these alter the internal structure suffering swelling when absorb moisture, and likewise, shrinkage at lose moisture.

Suction is the potential of pressure having the soil to retain water in its interior, the suction is intrinsically related to changes of humidity in soil mass, thus, suction is the most important property to relate the cycles of moisture that are shown in a specific region. There is thus a depth that defines a region who presents volumetric distortions due to the change

of suction over time in expansive soils, called moisture active zone.

In this paper a proposal is conducted to determine the depth of the active zone in expansive soils by the numerical solution of Mitchell's diffusion equation [13] to analyze the moisture flow in unsaturated soils, using suction as the state variable for a 2D finite element model similar than [6], [8] and [18].

II. NUMERICAL SOLUTION OF THE DIFFUSION EQUATION

A unsaturated soil volumetric change is caused by changes in its efforts, either by the net normal stress or the matric suction; matric suction changes can occur as a result of the variation in climatic conditions, the water taken by the vegetation, the depth of groundwater level change, the excess of irrigation in the gardens up to extraordinary agents as the leak in pipes within the medium [5].

Through the application of the law of Darcy and moisture flux continuity equations can be obtained the following diffusion equation to describe unsaturated moisture flux [10], [15]:

$$\frac{\partial u}{\partial t} = \frac{\partial u}{\partial \theta} \frac{\partial}{\partial x_i} \left(k_{ij} \frac{\partial \psi}{\partial x_j} \right) \quad (1)$$

where:

(u) is the total suction, (θ) volumetric water content, (ψ) is the potential of mass flow, (t) is the variable time, (k_{ij}) is the hydraulic conductivity, (x_i, x_j) spatial coordinates.

If it is assumed that the soil is homogeneous and isotropic body, differential former ruler the equation can be written as [7], [12]:

$$\frac{\partial^2 u}{\partial^2 x} + \frac{\partial^2 u}{\partial^2 y} + \frac{\partial^2 u}{\partial^2 z} = \frac{1}{D} \frac{\partial u}{\partial t} \quad (2)$$

where: (u) is the total suction, (D) the coefficient of diffusion, $c = \Delta\theta / \Delta u$ is the characteristic humidity, (k) is the hydraulic conductivity, (ρ_d) is the dry density of the soil, (θ) the volumetric water content, (x, y, z) spatial coordinates, (t) time variable.

Being D equal to:

$$D = \frac{k}{\frac{\Delta\theta}{\Delta s} \rho_d} \quad (2.a)$$

The phenomenological equation (2) putting in two-dimensional form, can be analyzed under the Galerkin method [16], [19], which consists of evaluating the integral waste weighted with respect to the spatial coordinates for a fixed time.

$$\{R^{(e)}\} = - \int_A [W]^T \left(k_x \frac{\partial^2 \phi}{\partial x^2} + k_y \frac{\partial^2 \phi}{\partial y^2} - \lambda \frac{\partial \phi}{\partial t} \right) dA \quad (3)$$

Where $u = \phi$ and Galerkin weighted residues are assimilated to the shape functions of the finite elements $[W]^T = [N]^T$, separating integral is:

$$\{R^{(e)}\} = - \int_A [N]^T \left(k_x \frac{\partial^2 \phi}{\partial x^2} + k_y \frac{\partial^2 \phi}{\partial y^2} \right) dA + \int_A [N]^T \left(\lambda \frac{\partial \phi}{\partial t} \right) dA \quad (4)$$

The derivative terms of second grade can express themselves differently in accordance with the chain rule, if the following amount is taken into account:

$$\frac{\partial}{\partial x} \left([N]^T \frac{\partial \phi}{\partial x} \right) \quad (5)$$

Evaluating (5) is then:

$$\frac{\partial}{\partial x} \left([N]^T \frac{\partial \phi}{\partial x} \right) = [N]^T \left(\frac{\partial^2 \phi}{\partial x^2} \right) + \frac{\partial [N]^T}{\partial x} \frac{\partial \phi}{\partial x} \quad (5.a)$$

Similarly to the term derivative in the direction 'y' is evaluated, and thus replaced (5.a) (4) obtaining:

$$\begin{aligned} \{R^{(e)}\} &= - \int_A [N]^T \left(\frac{\partial}{\partial x} \left(k_x \frac{\partial \phi}{\partial x} \right) + \frac{\partial}{\partial y} \left(k_y \frac{\partial \phi}{\partial y} \right) \right) dA \\ &+ \int_A \left(k_x \frac{\partial [N]^T}{\partial x} \frac{\partial \phi}{\partial x} + k_y \frac{\partial [N]^T}{\partial y} \frac{\partial \phi}{\partial y} \right) dA \\ &+ \int_A [N]^T \left(\lambda \frac{\partial \phi}{\partial t} \right) dA \end{aligned} \quad (6)$$

Equation (6) can be written in a final form replacing the following relations of ϕ :

$$\phi^e = [N]\{\Phi^e\} \quad (7)$$

Deriving (7) with respect to t :

$$\frac{\partial \phi}{\partial t} = [N]\{\dot{\Phi}^e\} \quad (7.a)$$

Replacing the terms (7) and (7.a) in (8) and regrouping the equation we get:

$$\begin{aligned} \{R^{(e)}\} &= - \int_A [N]^T \left(\frac{\partial}{\partial x} \left(k_x \frac{\partial \phi}{\partial x} \right) + \frac{\partial}{\partial y} \left(k_y \frac{\partial \phi}{\partial y} \right) \right) dA + \int_A \left(k_x \frac{\partial [N]^T}{\partial x} \frac{\partial [N]}{\partial x} + \right. \\ &k_y \frac{\partial [N]^T}{\partial y} \frac{\partial [N]}{\partial y} \left. \right) dA \{\Phi^e\} + \int_A \left(\lambda [N]^T [N] \right) dA \{\dot{\Phi}^e\} \end{aligned} \quad (8)$$

Which (8) has the general form:

$$\{R^e\} = \{R_D^e\} + \{R_\lambda^e\} \quad (9)$$

Where $\{R_D^e\}$ is equivalent:

$$\{R_D^e\} = \{I^e\} + [k^e]\{\Phi^e\} \quad (10)$$

And also:

$$\{I^e\} = - \int_A [N]^T \left(\frac{\partial}{\partial x} \left(k_x \frac{\partial \phi}{\partial x} \right) + \frac{\partial}{\partial y} \left(k_y \frac{\partial \phi}{\partial y} \right) \right) dA \quad (10.a)$$

being the inter-element that defines the residue of the integral, it is the value that the integral reduces to zero; This element has been practically omitted since its boundary conditions will be subsequently included in the global matrix of rigidities; its omission is not material so it can be said that the solution is approximate.

$$[k^e] = \int_A \left(k_x \frac{\partial [N]^T}{\partial x} \frac{\partial [N]}{\partial x} + k_y \frac{\partial [N]^T}{\partial y} \frac{\partial [N]}{\partial y} \right) dA \quad (10.b)$$

The equation (10.b) can be defined more compactly by taking into account:

$$[D] = \begin{bmatrix} k_x & 0 \\ 0 & k_y \end{bmatrix} \quad (10.c)$$

And the gradient vector $\{gv\}$:

$$\{gv\} = \begin{Bmatrix} \frac{\partial \phi}{\partial x} \\ \frac{\partial \phi}{\partial y} \end{Bmatrix} = \begin{Bmatrix} \frac{\partial [N]}{\partial x} \\ \frac{\partial [N]}{\partial y} \end{Bmatrix} \{\Phi^e\} = [B]\{\Phi^e\} \quad (10.d)$$

Stiffness matrix (10.b) of the problem is then written by substituting (10.c) and (10.d) as:

$$[k^e] = \int_A [B]^T [D] [B] dA \quad (11)$$

And finally the quasi dynamic term is:

$$\{R_\lambda^e\} = \int_A (\lambda [M]^T [N]) dA \{\Phi^e\} = [c^e] \{\Phi^e\} \quad (12)$$

When the elementary matrices are coupled with other arrays of other elements and summed over all the elements using the procedure of direct stiffness, it has resulted in a system of differential equations of the first order given by:

$$[C] \{\dot{\Phi}\} + [K]\{\Phi\} = \{0\} \quad (13)$$

where $[C]$ is called the capacitance matrix which houses the λ factor that defines the quasi-dynamic process. The array $[K]$ is the global stiffness. Being the vector:

$$\{\dot{\Phi}\}^T = \left[\frac{\partial \Phi_1}{\partial t} \quad \frac{\partial \Phi_2}{\partial t} \quad \dots \quad \frac{\partial \Phi_p}{\partial t} \right] \quad (14)$$

The system of equations described in eq. (13) can be solved similarly to the methods associated with the solution to the problems of heat transfer [16] using the approximation of finite difference time domain to generate a numerical solution.

Referring to the fig 2.1 several relationships can be obtained, using the mean value theorem, the slope at time ξ is obtained and can thus approach the value of $\phi(\xi)$ in terms of $\phi(a)$ and $\phi(b)$.

$$\frac{d\phi}{dt}(\xi) = \frac{\phi(b) - \phi(a)}{\Delta t} \quad (15)$$

Coming to the expression:

$$\phi(\xi) = (1 - \theta)\phi(a) + \theta\phi(b) \quad (16)$$

where:

$$\theta = \frac{\xi - a}{\Delta t} \quad (16.a)$$

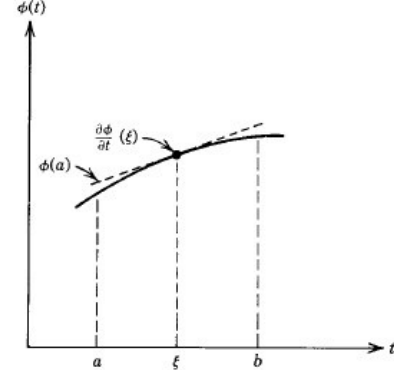


Fig. 2.1 Approximation of $\phi(a)$ given $d\phi/dt$.

The above equations can be generalized to a set of values nodal replacing $\phi(a)$ and $\phi(b)$ by column vectors containing the nodal values. For which the equation (13) can be rewritten by combining equations (15) and (16) to vector, resulting form:

$$([C] + \theta \Delta t [K])\{\Phi_b\} = ([C] - (1 - \theta)\Delta t [K])\{\Phi_a\} \quad (17)$$

Regardless of the value taken for θ , the final set of equations has the general form:

$$[A]\{\Phi\}_b = [H]\{\Phi\}_a \quad (18)$$

III. MODEL ANALYSIS AND RESULTS

For the numerical-computational solution was developed a program written in APDL language that runs Ansys environment, and allows the solution of the problem, so it used finite element 2-D Thermal transient with 4 linear degrees of freedom [3], characteristics for potential problems; the analogy of fields included solving a problem of suction base to a thermal transient model. The 2D (fig. 3.2) model to solve was a region with 16 meters of length with 8 meters of depth and a waterproof membrane at the midpoint of the surface, with 8 meters of length; it is positioned to simulate the presence of a foundation. The passage of time in the transient model has been established according to the relationship between their dimensions and their constituent properties [16]. Establishing that the minimum dimension of the finite element used has been 0.25 m.

For the solution of the transient model is initially defined an array with initial values of suction in the soil, initiated a process with the suction of balance. At each interval of time distribution of suction in the soil inside as on the borders thereof is calculated. The equation that characterizes the boundary conditions of the model that relates the variation of suction of soil due to climatic changes during the time should be defined according to each region.

According to [8] the climatic conditions of the northeast of Adelaide, South Australia, finding that the suction surface can vary from sinusoidal in response to climate cycles way is:

$$u(0, t) = U_e + U_0 \cos(2n\pi t - P) \quad (19)$$

Being U_e suction of balance (pF), U_0 the amplitude of the cycle of suction or the maximum change of suction on the surface of the soil (pF), n is the rate of climate change, P is the phase angle which is used to set the starting point and t the time variable. Being $\text{pf} = \log_{10}[u(\text{kPa}) + 1.01]$.

According to the surface values of suction measured by [9] and [14] during the months of March to November, to the expansive soil of Jurica, Querétaro, a curve was adequate with sinusoidal shape (eq. 20) based on the parameters that defines L_i [7], [8], shown in Fig. 3.1 it graphical representation.

$$u(0, t) = 4.4 + 0.24 \cos\left(\frac{\pi}{180} t - \frac{\pi}{6}\right) \quad (20)$$

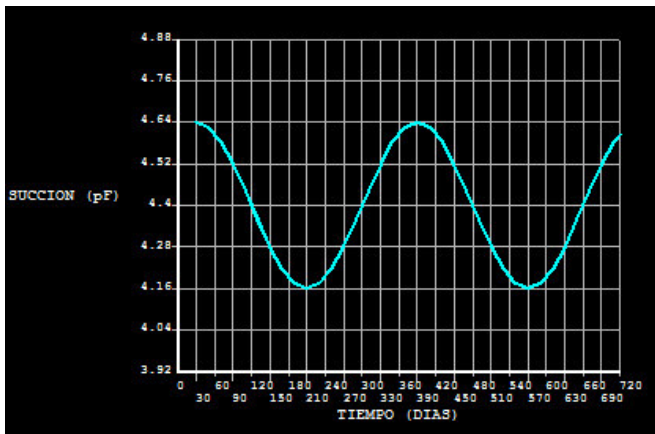


Fig. 3.1. Variation of the surface suction (pF) vs time (days) in Jurica soil, Qro.

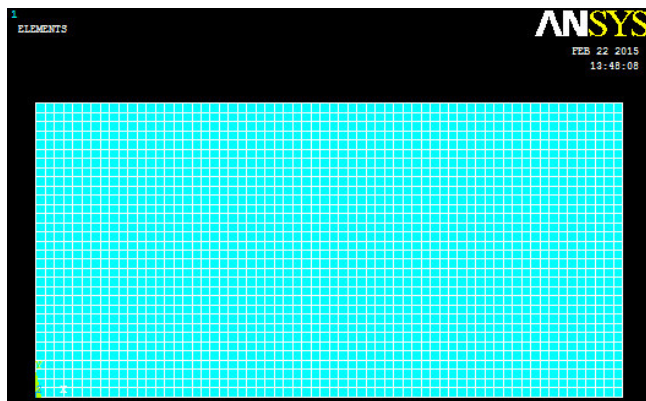


Fig. 3.2. (2-D) Thermal transient Finite element model solved.

The permeability (k) in unsaturated soils is not constant, varies respect soil suction, this parameter can be

defining into the model with hydraulic conductivity ($k(s)$) equations proposed by [4], [12] and [17] using the soil water retention curve (SWRC), therefore each node of the finite element model will have a certain value $k(s)$ which can be included in eq. (3) as a similar form that in [11].

According to [13] the diffusion coefficient (D) is assumed constant over a small suction change, therefore in the model, D was obtained from the wetting tests; the results can be seen in table 1. Likewise a constant permeability coefficient $k_x = k_y = k$ was used with value of $1.32E-07$ m/seg from tests.

The factor $T = 0.3$ was obtained from adjusting the values obtained in the test with Figure 3-1 from [6], hence the diffusion coefficient can be calculated as:

$$D = \frac{L^2 T}{t} \quad (21)$$

Therefore:

$$D = \frac{(.1243m)^2 (0.3)}{2días} = 2.32 \times 10^{-3} m^2 / día \quad (21.a)$$

Table 1 Diffusion coefficient, D.

x (mm)	x/L	u (kPa)	u (pF)	A	T= 0.3
18.9	0.152	700	3.86	-0.579	t= 172800 s
28.46	0.229	690	3.85	-0.575	L= 124.3mm
50	0.402	450	3.66	-0.478	$U_0 = 4.5$ pF
71.54	0.576	360	3.57	-0.427	$U_L = 2.75$ pF
18.9	0.152	700	3.86	-0.579	$\Delta u = -1.75$ pF

In [1] a new technique to determine the coefficient of unsaturated diffusivity is given by the similarity to determine D in the laboratory in a similar way to the coefficient of consolidation laboratory determination.

Following results of analysis shows the variation of suction within the soil mass through time (fig. 3.3 to 3.9). It was plotted at 60 days, 120 days, 240 days, 360 days, 480 days, 600 days and 720 days respectively.

As we can see in figures 3.3, 3.4, 3.5, 3.6 and 3.7 the suction distribution beneath the waterproof surface maintains constant suction value around 3.38 ± 0.01 pF over the time in an approximate depth of 0.25 m. Similarly suction is maintained constant at the bottom of the model grid which indicates a non- flow of moisture under a certain depth (limit of active zone). Also it can be observed how the suction changes drastically around the waterproof surface, where indeed the phenomenon of evapotranspiration exists.

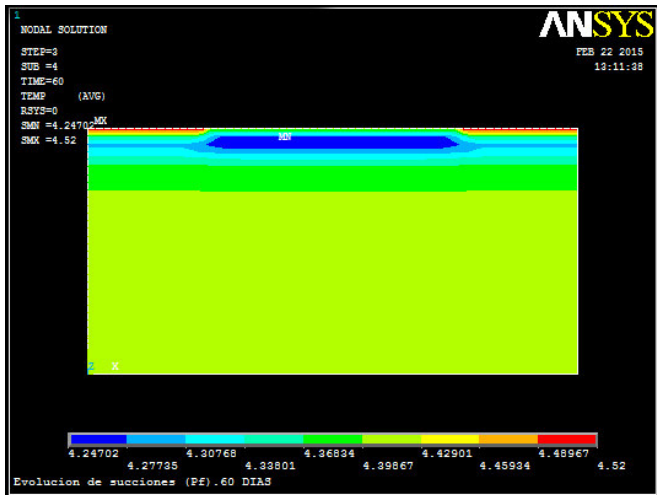


Fig. 3.3. Suction variation (pF) at 60 days.

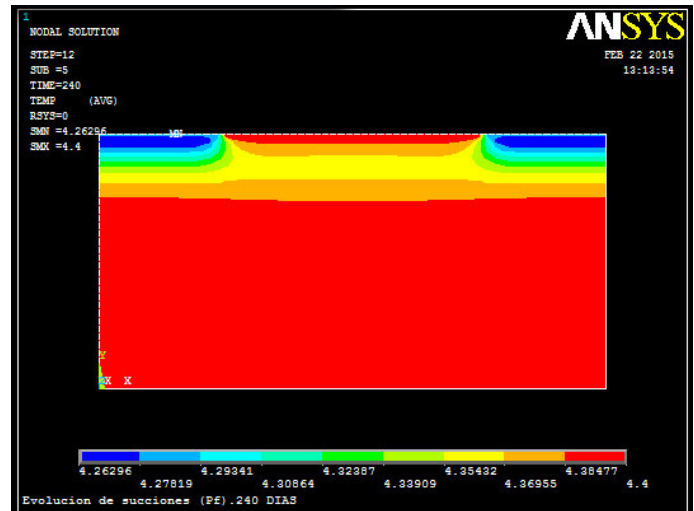


Fig. 3.5. Suction variation (pF) at 240 days.

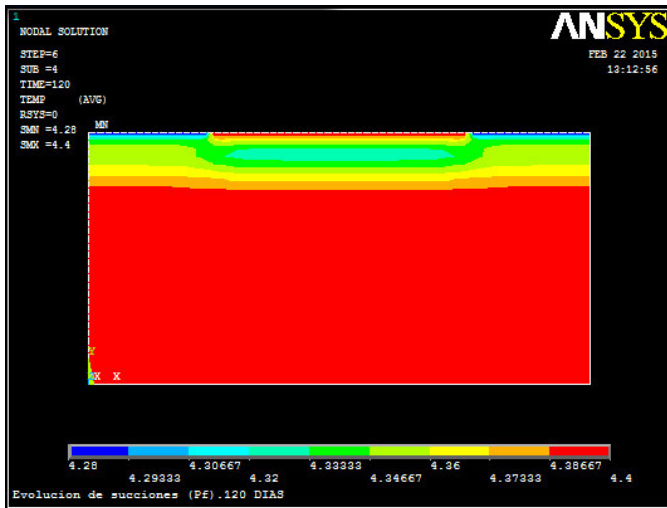


Fig. 3.4. Suction variation (pF) at 120 days.

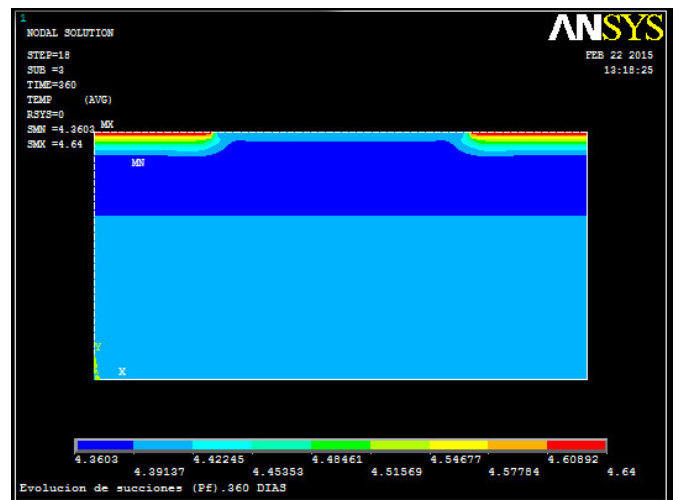


Fig. 3.6. Suction (pF) variation at 360 days.

In figures 3.10, 3.11 and 3.12 shows the relationships obtained from suction change in time with respect to depth to a point located at 2.0 m, 4.0 m and 8.0 m from the left superior corner of the mesh in x axis.

We can observed that the soil suction below the center of the waterproof surface (fig. 3.12) has a minimum suction range of variation, from 4.34 pf to 4.40 pf, compared with the free area (fig. 3.10) subject to climatic changes from 4.16 pf to 4.64 pf, but preserving in but cases a constant value of soil suction at a depth of approximated 4.0 meters which according with [10] describes the moisture active zone.

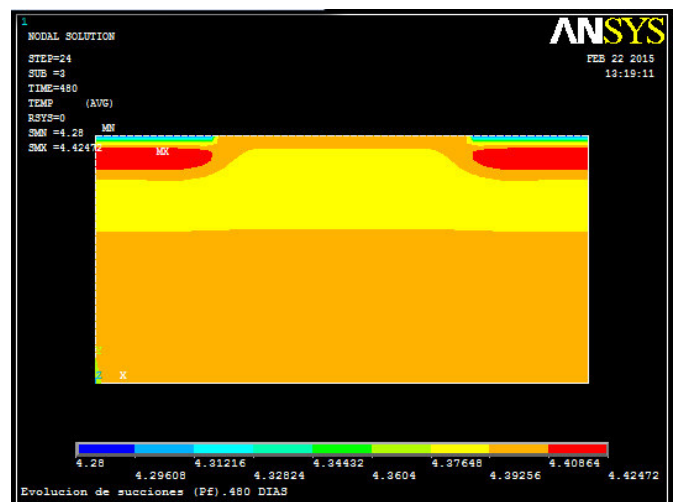


Fig. 3.7. Suction (pF) variation at 480 days.

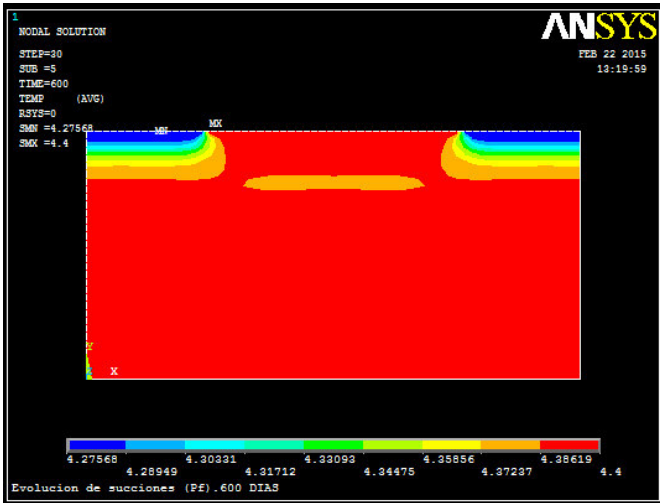


Fig. 3.8. Suction (pF) variation at 600 days.

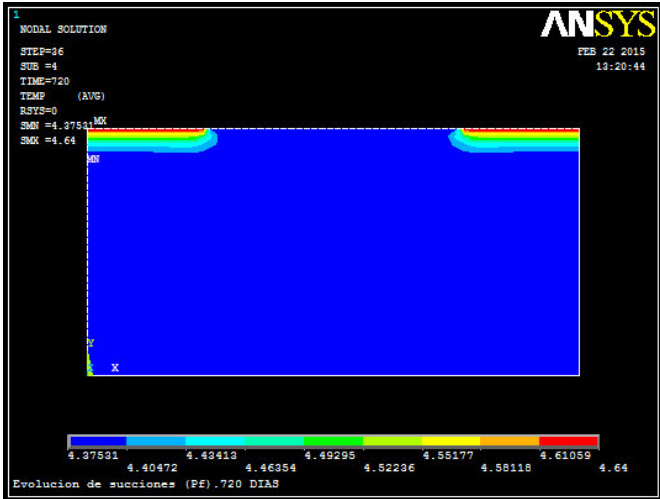


Fig. 3.9. Suction (pF) variation at 720 days.

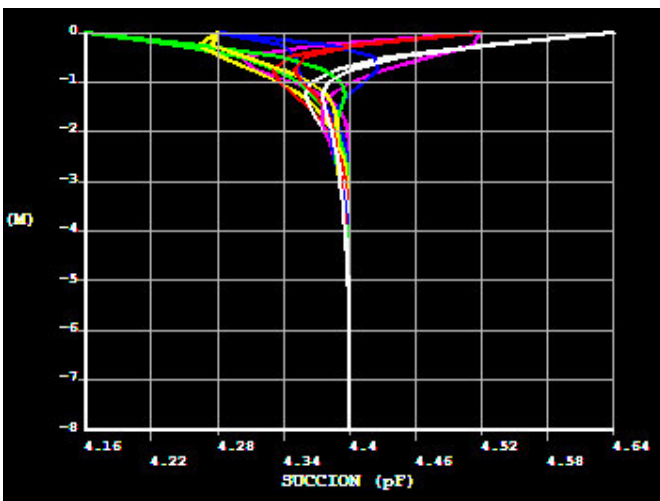


Fig. 3.10. Suction vs depth in $x=2.0\text{m}$ (free area) [Days / Mag(60): Blue(120): Green(180): Yellow(240): Red(300): White(360)].

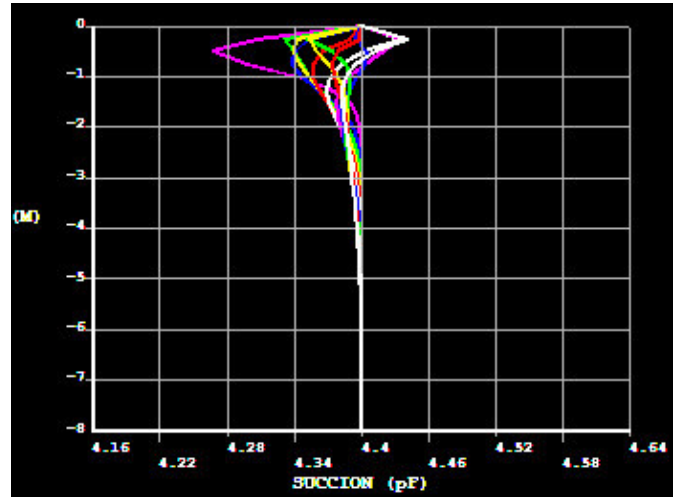


Fig. 3.11. Suction vs depth in $x=4.0\text{m}$ (left corner of waterproof surface) [Days / Mag(60): Blue(120): Green(180): Yellow(240): Red(300): White(360)].

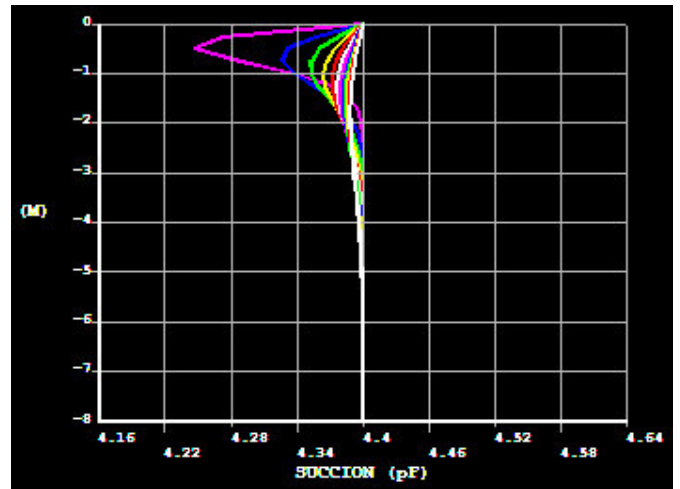


Fig. 3.12. Suction vs depth in $x=8.0\text{m}$ (center of the waterproof surface) [Days / Mag(60): Blue(120): Green(180): Yellow(240): Red(300): White(360)].

The free surface soil suction behaves in an harmonic way over the time, as we see in figure 3.13, in a point located at 2.0 m from the left top corner of the model grid, it can be shown that a depth of zero meters the soil suction has a sinusoidal shape (magenta color) equal to the governing equation (20) of the boundary conditions, and its reduces in a similar way according the depth increases. In the case of the center of the covered area (fig. 3.15) it can be shown that the soil suction gets a constant value after a certain value of time, having a asymptote tendency.

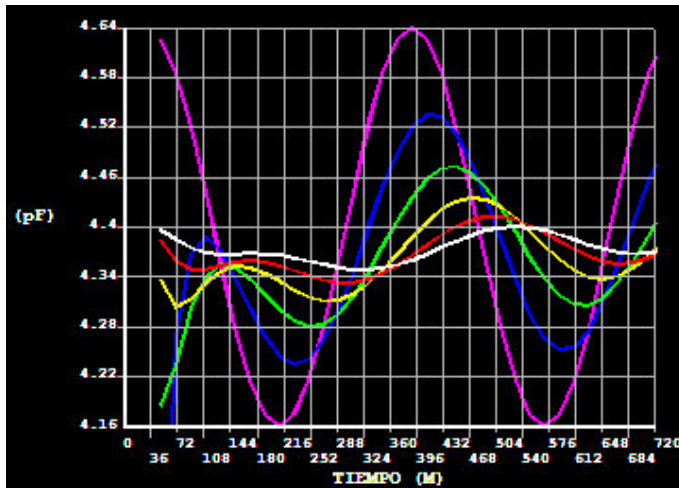


Fig. 3.13. Suction vs time at $x = 2.0\text{m}$ (free area)
[color (depth) / Mag(0.0m): Blue(0.25m): Green(0.5m):
Yellow(0.75m): Red(1.0m): White(1.25m)].

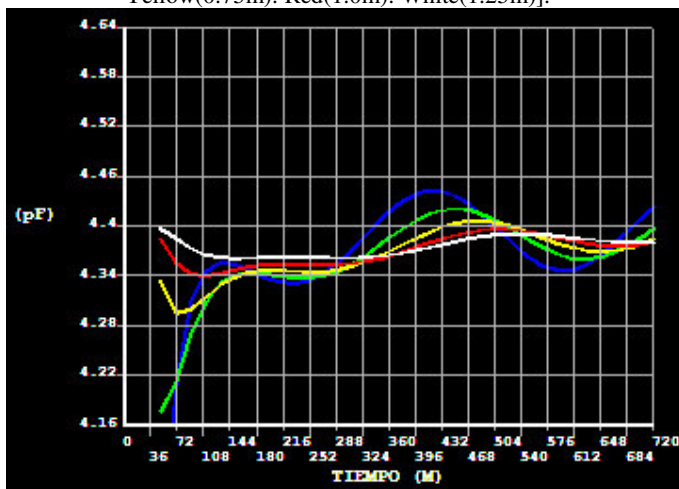


Fig. 3.14. Suction vs time at $x = 4.0\text{m}$ (left corner of waterproof surface)
[color (depth) / Mag(0.0m): Blue(0.25m): Green(0.5m):
Yellow(0.75m): Red(1.0m): White(1.25m)].

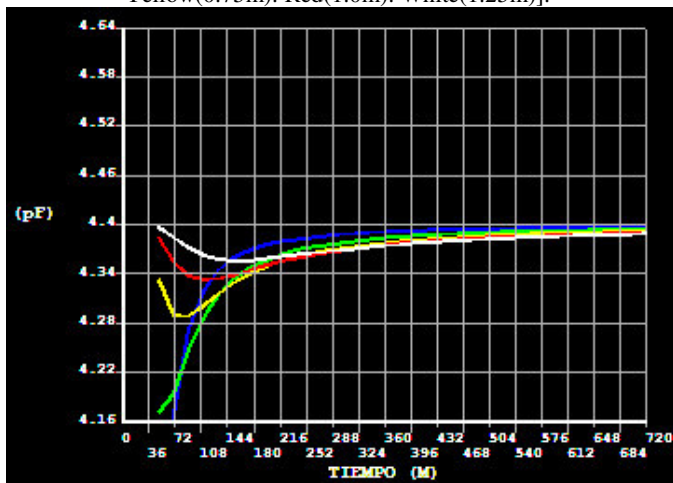


Fig. 3.15. Suction vs time at $x = 8.0\text{m}$ (center of waterproof surface)
[color (depth) / Mag(0.0m): Blue(0.25m): Green(0.5m):
Yellow(0.75m): Red(1.0m): White(1.25m)].

IV. CONCLUSIONS

The finite difference method is an approximate tool for solve the diffusion equation of unsaturated soils, reducing the in-situ research work for defining the suction profiles over time for a specific region. Otherwise this problem can be solved with Method of Lines (MOL) or Lax-Fredich scheme like in [2] where MOL proved to be the most appropriate. With numerical techniques the researcher can have a widely view of behavior of the phenomenon, who results in an advantage for future investigations. The model may be validated by comparing the measured suction values of the soil zone, a covered area also can be constructed by a waterproof surface, so that the soil suction at various periods of time can be recorded for a better data description. [18] proposes an equation to describes the accumulative moisture beneath the impermeable surface because the evapotranspiration of the soil.

Also by comparing the results obtained from the analysis, we can observed how the covered area by a waterproof surface affects the distribution of soil suction into the mass reducing the wide range obtaining on the free surface. The suction stays virtually constant from a depth of 4.0 m, indicating that from the surface up to that depth is the zone susceptible to volumetric distortions due the climatic changes in region.

All the analysis give an a idea for future investigations knowing that waterproof area reduces the change in suction, so it can be proposed the use of vertical screens around the foundation for determinate the soil suction behaves.

ACKNOWLEDGEMENT

The authors would like to thank Consejo Nacional de Ciencia y Tecnología (CONACyT) and the Universidad Autónoma de Querétaro for their support, with which the realization of this research was possible.

REFERENCES

- [1] Abdelmalak Remon I., (2007). Soil structure interaction for shrink-swell soils "A new design procedure for foundation slabs on shrinkswell soils" Ph. D. Dissertation, Texas A&M University.
- [2] Álvarez Sierra, E. et al., (2006). Una nueva alternativa numérica para la solución de la ecuación unidimensional de Richards: estudio de drenaje e infiltración de fluidos en la zona no saturada. UBP-Investigación & Desarrollo 6:133-143, ISSN 1814-6333.
- [3] ANSYS, (2013). Mechanical APDL Thermal Analysis Guide. ANSYS Workbench, Release 15.0, Canonsburg, PA 15317.

- [4] Fredlund, D. G. et al., 1994. Predicting the permeability function for unsaturated soils using the soil-water characteristic curve. *Canadian Geotechnical Journal*. Vol. 31, pp. 533-546.
- [5] Fredlund M, Stianson J, Vu H and Thode RC (2006) Numerical modeling of slab-on-grade foundation. Unsaturated soils. Geotechnical Special publication. 147(2) ASCE, USA.
- [6] Hung V and Fredlund D (2000) Volume Changes Predictions in Expansive Soils Using a Two-Dimensional Finite Element Method. *Unsaturated Soils for Asia*, Rahardjo, Tool & Leong (eds). Balkema, Rotterdam.
- [7] Li, J. 1996. Analysis and modelling of performance of footing on expansive soils [PhD Thesis]. University of South Australia.
- [8] Li, J. 2006. Two dimensional simulation of a stiffened slab on expansive soil subject to a leaking underground water pipe. In: *Unsaturated Soils 2006*. American Society of Civil Engineers. p. 2098–2109.
- [9] López-Lara, T. (1996) Resistencia al esfuerzo cortante en arcillas expansivas de Jurica, Querétaro. Tesis de maestría. Universidad Autónoma de Querétaro.
- [10] Lytton, R. (1997). “Engineering structures in expansive soils.” Keynote address, Proc. 3rd International Symposium on Unsaturated Soils, Rio de Janeiro, Brazil, 1, 3-15.
- [11] Martinez, J. L. et al., (2013). Aproximación en diferencias finitas a la ecuación de Richards para transporte de agua en suelos no saturados. *Mecánica Computacional Vol. XXXII*, Mendoza, Argentina, págs.. 2779 – 2793.
- [12] Mualem, Y., (1976). A new model for predicting the hydraulic conductivity of unsaturated porous media. *Water Resources Research*, 12(3), p.513. doi:10.1029/WR012i003p00513.
- [13] Mitchell, P. W. (1979). “The structural analysis of footings on expansive soil.” Kenneth W.G. Smith and Associates Research Report No. 1, pp. 1-159, Newton, South Australia.
- [14] Pérez-Rea, M.L. (1993) Succión y comportamiento esfuerzo-deformación en suelos expansivos de Jurica y Tejada. Tesis de maestría. Universidad Autónoma de Querétaro.
- [15] Richards, L. A. 1931. Capillary conduction of liquids through porous mediums. *J. Appl. Phys.* 1:318.
- [16] Segerlind J. L. (1984). *Applied Finite Element Analysis*. 2nd ed. Jhon Wiley and Sons, New York.
- [17] Van Genuchten, M. T. 1980. A closed-form equation for predicting the hydraulic conductivity of unsaturated soils. *Soil Sci. Soc. Am. J.* 44:892–898.
- [18] Wray, W.K., El-Garhy, B.M. and Youssef, A.A. 2005. Three-dimensional model for moisture and volume changes prediction in expansive soils. *Journal of Geotechnical and Geoenvironmental Engineering*, 131(3): 311–324.
- [19] Zienkiewicz, O. C., and Taylor, R. L. (1989). *The finite element method – basic formulation and linear problems*. 4th ed. McGraw-Hill, New York.

EXPANSION ANALYSIS IN HIGH COMPRESSIBILITY UNSATURATED CLAY.

R. Zazueta-Rodríguez¹, E. Rojas-González²

^{1,2} DIPFI, Facultad de Ingeniería, UAQ, Universidad Autónoma de Querétaro, Cerro de las Campanas S/N, Las Campanas, 76010 Santiago de Querétaro, Querétaro, México.

¹raulzr@hotmail.com

²erg@uaq.mx

ABSTRACT- This paper presents evidence and data analysis in terms of effective stress, suction and volume change, showing the volumetric behavior (either by reducing suction or net stress).

Keywords: volumetric behavior, unsaturated soil, effective stress, suction.

I. Introduction:

Being able to predict the expansion of expansive soils due to the large presence of these in our environment is a fundamental building aspect. This is the case of Querétaro Valley, where much of the urban area of the city is set on expansive clay [1] When this material is wetted and it expands causes serious damage to civil engineering works [2]. Such damage can be mild or severe depending on the structure of the case.

The effective stress Bishop's equation [3], represents the most efficient way to model the soils behavior due to its simplicity and ease of use. This equation combines the net stress apply on the soil mass, the suction and the saturation degree. The saturation degree (G_s) is introduced as the factor " χ " [4]. Suction values are related to soil moisture through the soil-water retention curve [5].

Is possible to predict the behavior of the soil, as several authors have already expressed with models using independent variables of effort: the net stress and suction. For example, the Barcelona Basic Model [6] reproduce multiple aspects of the behavior of unsaturated soils. This type of models is of great interest being [7]. Other models are based on effective stress to predict the behavior of unsaturated soils. Where both types of models have been applied to the behavior of collapse in the soil [6], [8]. And other methods are based on variables as the deviator stress, the net stress and suction [9] where the net stress is defined as the difference between the total stress and the air pressure.

In this research preparing tests were performed in increments of controlled humidity to determine the soil expansion. It began with a completely dry material to full saturation. Also net stress controlled releases were performed to produce expansion in the material. The results are reported in terms of void ratio, and effective stress and suction to

obtain a more consistent behavior with what the soil matrix undergoes.

II. Actual methods.

There are some models that have been proposed on the basis of the theory of critical state. Others are based on thermodynamic considerations, for example models based on plastic potential [10]. Others use principles of hydraulic behavior [11] or volumetric behavior [8]. Some of the most used models and considerations that apply in their formulation are mentioned.

A. Barcelona Expansive Model.

The BExM (Barcelona Expansive Model)[9] is an BBM (Barcelona Basic Model) extension which is based on independent stress variables. These variables are the net stress, suction and deviator stress. This model explains the expansive phenomenology produced by suction cycles or changes of stress. Referred to BExM, the independent stress variables are combined with the critical state theory to obtain a yield surface to delimit the expansion condition of soil.

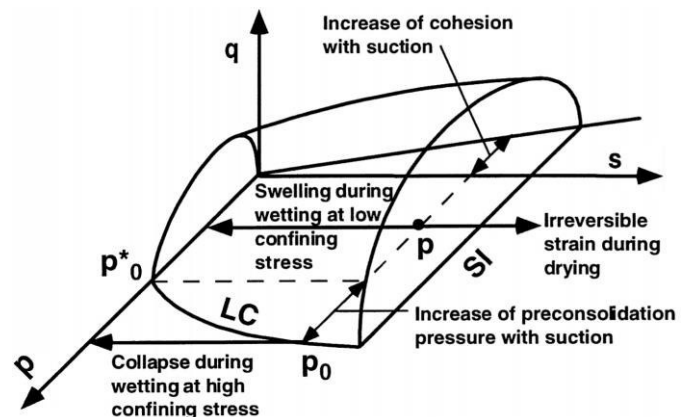


Fig. 1. BBM yield Surface.

In the mechanical-expansive behavior of unsaturated soils plus consideration of the 3 phases of soil has been considered two levels of structure: macrostructure or large pore [6] and microstructure or small pores [12].

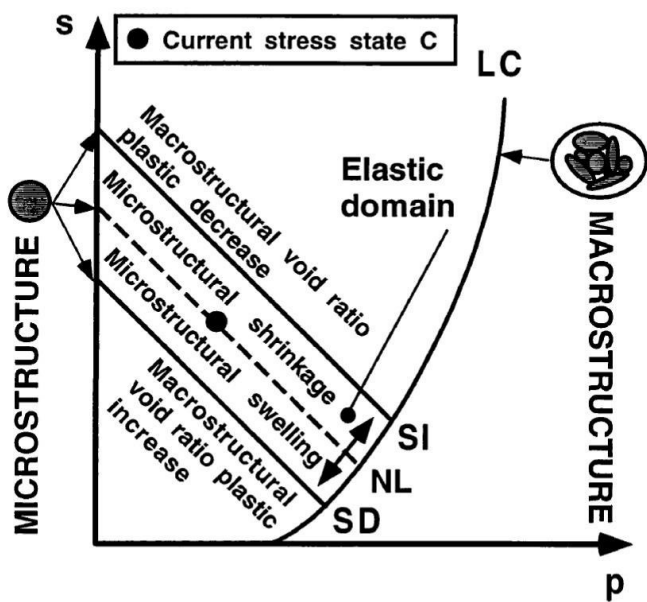


Fig. 2. Effects of micro and macro structure in soil behavior.

B. Modified Cam Clay.

Numerous theories have been developed to calculate and predict the plastic deformations in soils, one of the most important being developed at the University of Cambridge in the 60s [13], who described the original Cam-Clay, and the modified Cam-Clay [14]. This theory was developed for normally consolidated soils and slightly over-consolidated, and in the practice should apply only to them, though not always the case. Historically, one can consider the Cam-Clay model as the first plastic hardening model was widely adopted for soils.

One of the basic assumptions in the modified Cam-Clay model is considered that the yield surface (or plasticizing) coincides with the plastic potential, which implies an associated flow rule and acceptance criteria for normality (increasing plastic deformation it is normal, in any point, to the flow curve or plasticizing). Furthermore, the hypothesis assumes isotropic stiffening, namely that successive yield surfaces, which appear at increase the loads on the sample, are homothetic.

Yield surfaces are elliptical centered on the axis p , which intersection with the critical state line (CSL) is produced in the surface maximum (point where the slope of the tangent is null and therefore, presents a state of elasto-plasticity perfect). To the left of that point, a loss of volume and hardening occurs, while on the right an expansive behavior, increased volume and softening occurs. Thus, a simple model fairly representative of the actual behavior of certain soils is obtained, and although not predict an exact behavior, if you set the dual behavior of contraction-expansion of the field.

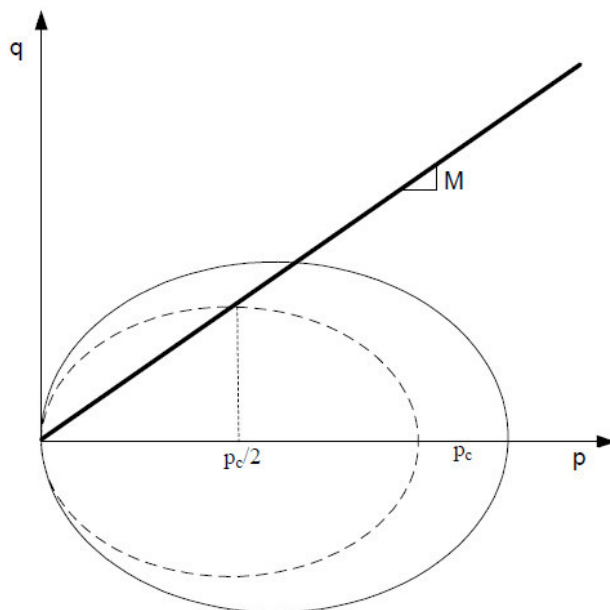


Fig. 3. Yield surface in the p - q plane and hardening function [14].

C. Effective stress.

Various geotechnical properties used in the calculation and analysis of problems, including settlements or load capacity are dependent on the effective stress, so this concept is of great importance [15].

In traditional soils mechanics (saturated soils mechanics) the effective stress is defined as a combination of external stress applied and the internal pressure developed in the liquid phase, which makes valid the equivalence of a porous medium of several phases to continuum phase [16].

Today does not exist an expression that set the behavior of unsaturated soils [3]. The Bishop's equation (equation 1) sets the effective stress in the soil in terms of net stress (σ) and the suction in the soil ($u_a - u_w$), it contains a parameter (χ), which does not have a procedure to determine it [16]. The experimental results show that the value of the parameter (χ) depends on various factors such as: a history of wetting-drying, void ratio and soil structure. Based on experimental evidence, it was proposed that for granular materials and degrees of saturation above 50%, the parameter (χ) can take the value of the degree of saturation (G_s)[4]. Some authors have proposed other empirical expressions for the parameter (χ) and these are related to water retention curve of the soil [5], [17].

$$\sigma' = \sigma - u_a + \chi(u_a - u_w) \quad (1)$$

D. Zhou model [11].

The constitutive modeling of unsaturated soil generally involves a constitutive model extension for the saturated case. Such inclusion is done by adding the suction to stresses space. By doing this suction acts as a fundamental variable in the mechanical and hydraulic behavior of unsaturated soils, like previous models suction is used as variable stress (external) or variable hardening (internal). Suction models as external

variable, are in net stress-suction space [6], [18]; while others are in the space of effective stress and suction [7].

In this model, a hydromechanical coupling is between the main functions of drying and wetting predicting the volumetric soil behavior with the degree of saturation, replacing the variable suction by the degree of saturation in relation to cycles, primary and secondary, of hysteresis relating to the drying and wetting (Fig.4).

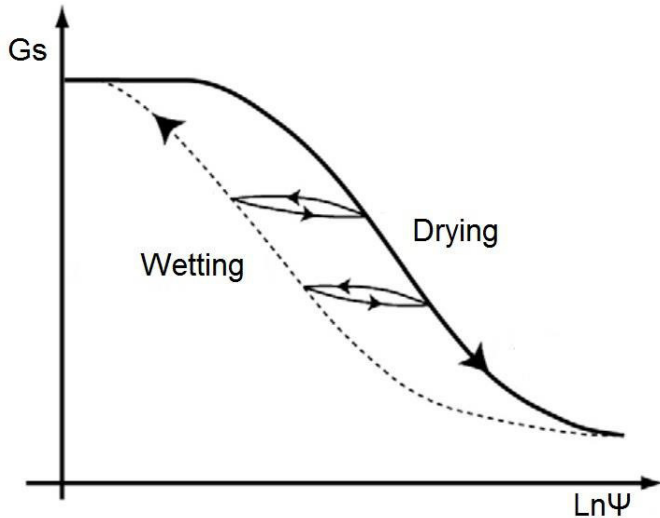


Fig. 4. Approach to determine the secondary cycles of wetting-drying [11].

III. Experimentation

In the city of Querétaro, the urban area is located mainly on expansive clay [1]. Therefore an adequate prediction of expansive behavior would be a useful tool.

Unaltered samples of clay (expansive) in the community of Jurica, located in the city of Santiago de Querétaro, Querétaro, Mexico were. The samples were characterized by getting its moisture [19], Atterberg limits [20], specific gravity [21], soil density [22], soil-water characteristic curve [23], and also obtained its one-dimensional behavior [24].

Taking geotechnical soil parameters for volumetric behavior, we proceed to design a test expansion by varying the suction and restricting their volume change, reviewing expansion pressure generated at different moisture based on the evidence for expansion pressure existing and normed [24]. To sample the addition of quantities of water controlled using Figure 5 ring design by applying moisture increased as shown in the same figure. To determine the accumulated moisture and using the characteristic curve of the material, it is possible to know the value of the suction. The expansion of the ground is allowed until the deformation is stabilized. At that time, it is considered that water content has homogenized within the sample.

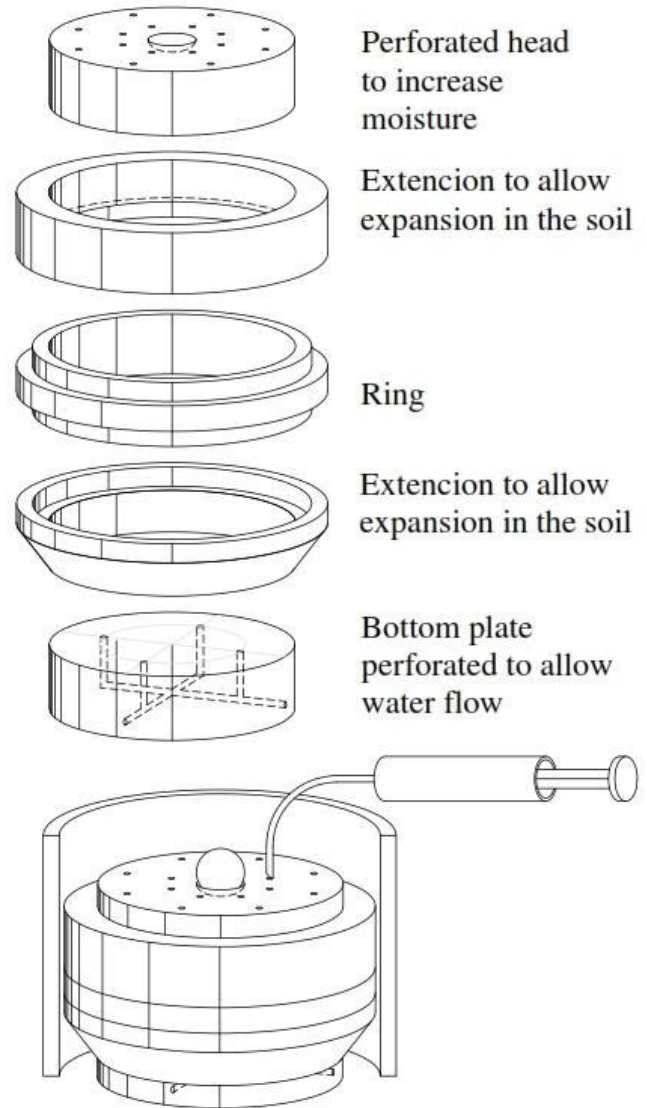


Fig. 5. Ring for consolidation and plates for variable water content tests.

Once the increase in humidity in the test you get an expansion graph where you can appreciate the behavior of clay to expand and at the top of the curve plotted when clay goes to a secondary expansion for a change of moisture can be seen (the slope of the curve is reduced at the end as shown in Figure 6).

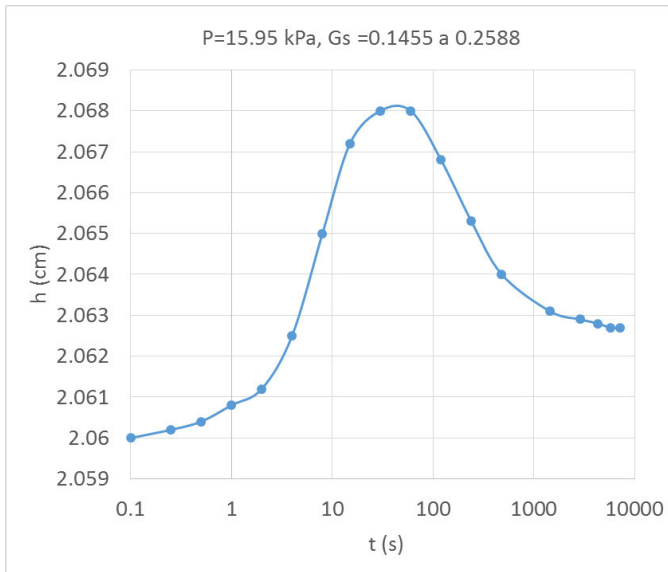


Fig. 6. Graph of expansion in unsaturated soil

Also testing for changes in humidity from the dry state to the saturated for increases in the degree of saturation. This is done to constant net stress to determine the state of internal stresses required to present expansion in the soil mass. For each increment of moisture (like in the figure 6) gets a point to graph and are made the needed increases moisture to cover the entire range (from dry to saturate for the graph against expansion percentage moisture content as in Figure 7).

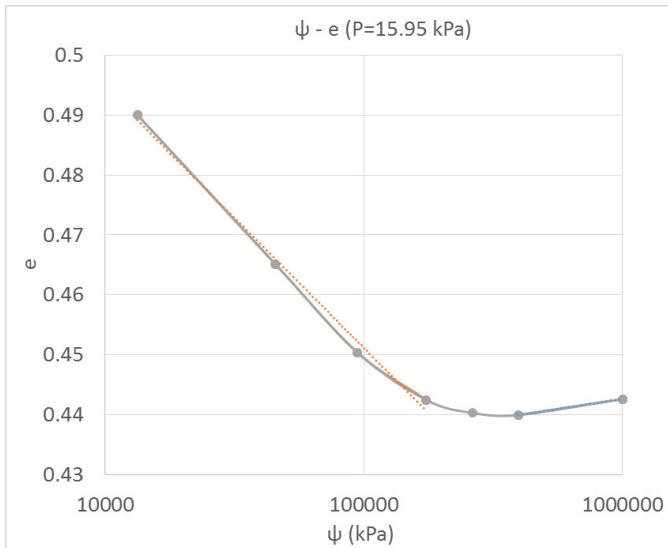


Fig. 7. Expansion for suction changes graphic.

Finding the suction from which arises the expansion with different pressures (as in Figure 7 is obtained for a net stress of 15.95 kPa is expanding to a suction of 200581 kPa) and join with those points a graphic effective effort against suction Gets a non-linear curve in the plane (line of expansion "LEx") that predicts when the expansion occurs in the soil as shown in Figure 8.

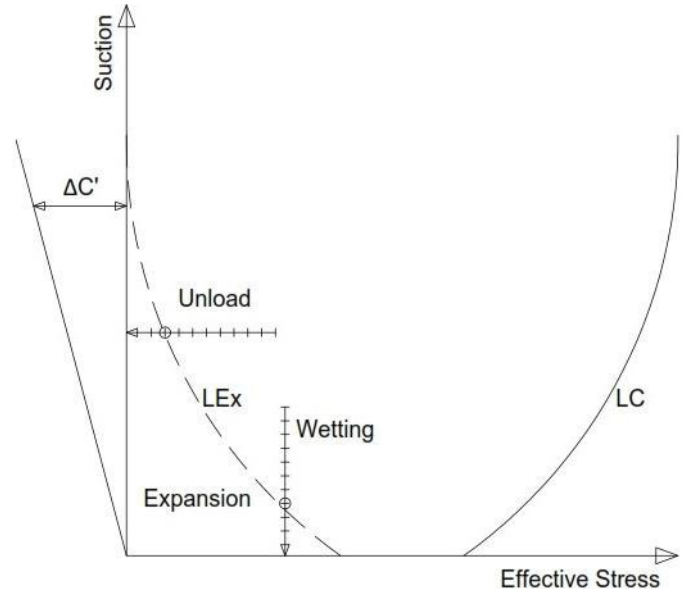


Fig. 8. Scheme of surface collapse (LC), expansion (LEx) and increase in cohesion with the suction ($\Delta C'$) in the plane, as well as routes to be followed so that the expansion is presented in the plane σ' - ψ .

IV. Discussion

When considering the behavior of the expansion in the plane of effective stress against suction and not in the plane net stress against suction like other authors, one can understand the behavior of the soil in a more precise manner, as effective efforts are those which supports the soil matrix. On the other hand, the net stress is the load applied to the soil and not take into account the effect of suction, as it is the case of the Barcelona expansive model (BExM)[9]. In this case of the plane net stress against suction, the line of expansion is linear but does not adequately represent the behavior of the soil.

V. Conclusions

In general, volumetric behavior of expansive soil is established from a curve in the plane effective stress-suction called yield surface in expansion, which when passed either by download or wetting the soil expansive behavior is triggered. That is, if the soil is subjected to a stress state and this state is lower than the limit condition represented by the yield surface expansion, then the soil increase its volume.

VI. Acknowledgements

Thanks to my family, to my classmate in the master, as well as my teachers by their guide, to CONACYT for the financial support and the UAQ for the financing of the project "Metodología para el diseño de cimentaciones en suelo expansivo por el método de interacción suelo-estructura utilizando el principio de esfuerzos efectivos (FoVin13-T-021)" in which I am participating.

VII. References

- [1] CONCYTEQ, "Uso actual y potencial del suelo en los municipios conurbados de Querétaro," Querétaro, 2002.
- [2] A. T. Sudjianto, M. Cakrawala, and C. Aditya, "The Effects of Water Contents on Free Swelling of Expansive Soil.," *Int. J. Civ. Environ. Eng.*, vol. 12, no. 06, pp. 13–17, 2012.
- [3] A. W. Bishop, "The principles of effective stress," *Tek. Ukebl.*, vol. 106, no. 39, pp. 859–863, 1959.
- [4] A. L. Öberg and G. Sälfors, "A rational approach to the determination of the shear strength parameters of unsaturated soils," in *First International Conference on Unsaturated Soils*, 1995, pp. 151–158.
- [5] M. Nuth and L. Laloui, "Advances in modelling hysteretic water retention curve in deformable soils," *Comput. Geotech.*, vol. 35, no. 6, pp. 835–844, Nov. 2008.
- [6] E. E. Alonso, A. Gens, and A. Josa, "A constitutive model for partially saturated soils," *Géotechnique*, vol. 40, no. 3, pp. 405–430, Jan. 1990.
- [7] D. Sheng, "Review of fundamental principles in modelling unsaturated soil behaviour," *Comput. Geotech.*, vol. 38, no. 6, pp. 757–776, Sep. 2011.
- [8] E. Rojas and O. Chávez, "Volumetric behavior of unsaturated soils," *Can. Geotech. J.*, vol. 222, no. January, pp. 209–222, 2013.
- [9] E. E. Alonso, J. Vaunat, and A. Gens, "Modelling the mechanical behaviour of expansive clays," *Eng. Geol.*, vol. 54, pp. 173–183, 1999.
- [10] E. Rojas, "Modelos constitutivos para suelos no saturados a partir de potenciales plasticos," in *Memorias de la XVIII Reunión Nacional de Mecánica de Suelos e Ingeniería Geotécnica*, 1996.
- [11] A.-N. Zhou, D. Sheng, S. W. Sloan, and A. Gens, "Interpretation of unsaturated soil behaviour in the stress – Saturation space, I: Volume change and water retention behaviour," *Comput. Geotech.*, vol. 43, pp. 178–187, Jun. 2012.
- [12] A. Gens and E. E. Alonso, "A framework for the behaviour of unsaturated expansive clays," *Can. Geotech. J.*, vol. 29, no. 6, pp. 1013–1032, Jan. 1992.
- [13] A. Schofield and P. Wroth, *Critical state soil mechanics*. McGraw-Hill, 1968.
- [14] K. H. Roscoe and J. B. Burland, "On the generalized stress-strain behaviour of wet clay," *Cambridge University Press*, Cambridge, England, pp. 535–609, 1968.
- [15] K. Terzaghi, "A fundamental fallacy in earth pressure computations," *Bost. Soc. Civ. Eng. J.*, 1936.
- [16] M. Nuth and L. Laloui, "Effective stress concept in unsaturated soils: clarification and validation of a unified framework," *Int. J. Numer. Anal. methods Geomech.*, vol. 32, pp. 771–801, 2008.
- [17] A. Alanís, "Deformación volumétrica en suelos no saturados," Universidad Autonoma de Querétaro, 2012.
- [18] C. F. Chiu and C. W. W. Ng, "A state-dependent elasto-plastic model for saturated and unsaturated soils," *Géotechnique*, vol. 53, no. 9, pp. 809–829, Jan. 2003.
- [19] ASTM Standard D2216, *Standard Test Method for Laboratory Determination of Water (Moisture) Content of Soil and Rock by Mass*, no. January. West Conshohocken, PA, 2010.
- [20] ASTM Standard D4318, *Standard Test Methods for Liquid Limit , Plastic Limit , and Plasticity Index of Soils*. West Conshohocken, PA, 2010.
- [21] ASTM Standard D4531, *Standard Test Methods for Bulk Density of Peat and Peat Products*, vol. 04, no. Reapproved. West Conshohocken, PA, 2008.
- [22] ASTM Standard D854, *Standard Test Methods for Specific Gravity of Soil Solids by Water Pycnometer*. West Conshohocken, PA, 2014.
- [23] ASTM Standard D5298, *Standard Test Method for Measurement of Soil Potential (Suction) Using Filter Paper*, no. November 1994. West Conshohocken, PA, 2010.
- [24] ASTM Standard D4546, *Standard test methods for one-dimensional swell or collapse of soils*. West Conshohocken, PA, 2014.

Some geometrical properties of noncircular gears

González Edgar ^{#1}, Garibay-Díaz Jorge ^{*2}, Jerónimo-Castro Jesús ^{#3}

[#]Facultad de Ingeniería, Universidad Autónoma de Querétaro, Centro Universitario Cerro de las Campanas s/n, C. P. 76010; Santiago de Querétaro; Qro., México.

¹ gonzalez_a_edgar@live.com.mx

³ jesusjero@hotmail.com

^{*}Unidad Académica de Matemáticas, Universidad Autónoma de Guerrero, Calle Carlos E. Adame 54, C. P. 39650; Acapulco; Gro., México.

² arturo_dz@hotmail.com

Abstract—Circular gears are well known and have a lot of applications in mechanical systems, however, there are systems where circular gears are not the best option because of the especial requirements of the process. Wunderlich and Zenow (1975) proposed a construction of elliptical gears using "the Reuleaux's method", which with some modifications, may be used to build gears that have the shape of any given convex figure. The main purpose of this work is to deepen in the study of some geometrical properties of non-circular gears.

I. INTRODUCTION

Construction of non-circular pulleys have been widely studied in several works because of the necessity of generate variation in the velocity of transmitting movement from one pulley to the other. A clear example where this variation of velocity is need is in some mechanical press. It is possible to increase its efficiency if the velocity of movement is bigger when the mechanism is not pressing the object under work. Even now, it is not clear what kind of curves can be used as pulleys in a belt drive with belt of constant length, however, for a given pair of curves it is possible to calculate the variation in length for the belt surrounding both curves [1].

Wunderlich and Zenow [2] had developed a non trivial crossed belt with a pair of pulleys whose shape are ellipses. The length of the belt in this case is constant (see Fig. 1); moreover, using the Reuleaux's method they construct a pair of elliptical gears, rotating at two fixed points A and A' , respectively. Another work about belt drives is due to H. Stachel [3] where he gave a more wide view on the geometric properties need for constructing this kind of pulleys.

The main purpose of this work is to prove that the pulleys in a strict and uniform belt drive need to be Euclidean discs.

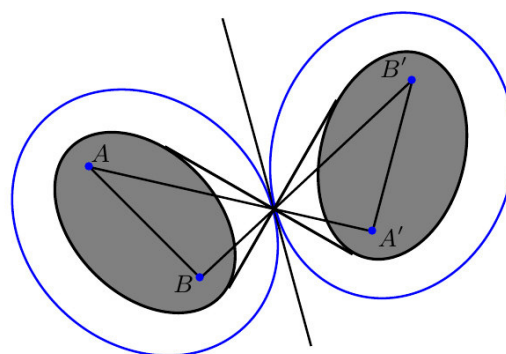


Fig. 1. A pair of elliptical gears.

II. SOME NOTATION AND KNOWN RESULTS

In this section we will introduce the basic notions and some notation. Consider two convex figures γ_1 , γ_2 , and two points O_1 , O_2 contained in the interior of γ_1 and γ_2 , respectively. Now, a belt is wrapped around the two pulleys and suppose γ_1 is the driving pulley. This pulley will transmit motion to the belt and the motion of the belt in turn will give a rotation to γ_2 . In an open belt drive system, the rotation of both pulleys is in the same sense, whereas, for a crossed belt drive system, the pulleys have opposite sense of rotation. The driving pulley γ_1 is rotating about the center O_1 through the angle ϕ_1 , while the output wheel γ_2 rotates about O_2 through an angle ϕ_2 . Then the pole O_{12} , collinear with O_1 and O_2 , divides the segment O_1O_2 in a ratio equal to that of the instantaneous angular velocities, i.e.,

$$\frac{\overline{O_1O_{12}}}{\overline{O_2O_{12}}} = \frac{\dot{\phi}_2}{\dot{\phi}_1} = \frac{\omega_2}{\omega_1}.$$

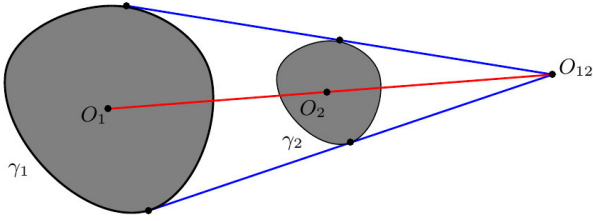


Fig. 2. A uniform belt drive.

A belt drive whose surrounding belt has constant length is named a *strict belt drive*, and when the pole O_{12} is a fixed point, it is named a *uniform belt drive*. Through this paper we will be concerned with belt drives which are at the same time uniform and strict.

One important and classical theorem for strict belt drives is the following due to Hoschek [4].

Theorem 1. *At each instant the upper and the lower common tangents of the two pulleys are aligned with the relative pole O_{12} .*

The following fact is also known.

Theorem 2. *For any transmission function and any driving pulley γ_1 there is a unique conjugate pulley γ_2 . However, γ_2 is not necessarily convex.*

So, it is interesting to know what conditions should be added to the belt drive in order to ensure that γ_2 is also a convex curve.

III. SOME NEW RESULTS

An interesting question about belt drives is the following: *to know whether or not there is a uniform and strict belt drive whose pulleys are not circles.* We don't yet know the answer, however, if we add an extra hypothesis the answer is no. In what follows, we will denote the convex hull of two sets A, B as $[A, B]$, also, we will denote the perimeter and area of a given region K as $P(K)$, and $A(K)$, respectively. The main result of this paper is the following.

Theorem 3. *Let γ_1 and γ_2 be a pair of convex curves such that the belt drive consisting on the pair γ_1 and γ_2 is uniform and strict. If $P([\gamma_1, O_{12}])$ is constant then γ_1 and γ_2 are circles.*

In order to give the proof of Theorem 3, we need to give some definitions and prove some auxiliary lemmas.

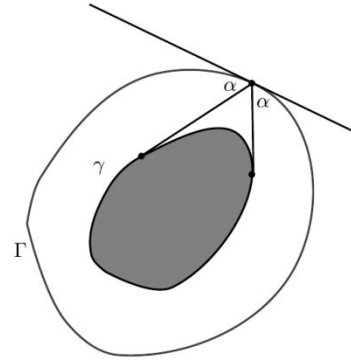


Fig. 3. A billiard ball table and its caustic.

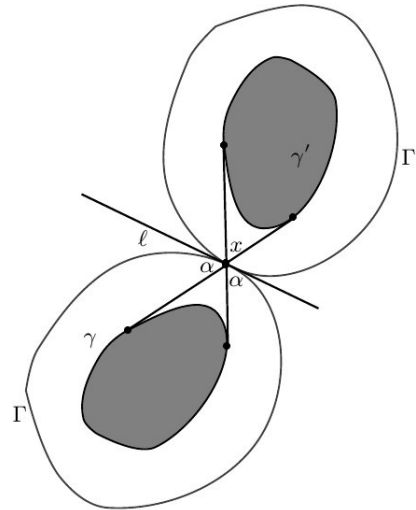


Fig. 4. A pair of non-circular gears.

Definition 1. A *mathematical billiard* consists of a domain, say in the plane (a billiard table), and a point-mass (a billiard ball) that moves inside the domain freely. This means that the point moves along a straight line with a constant speed until it hits the boundary. The reflection on the boundary is elastic and subject to a familiar law: *the angle of incidence equals the angle of reflection.*

Definition 2. A *caustic* is a curve inside a plane billiard table such that if a segment of a billiard trajectory is tangent to this curve, then so is each reflected segment.

To every convex curve we can associate a curve with similar properties of the ellipse. Such a curve can be obtained by the so called *gardener's construction*: wrap a closed non-stretchable string around γ , pull it tight at a point and move this point around γ to obtain a curve Γ . Then the billiard inside Γ has γ as its caustic.

Using the gardener's construction is possible to construct crossed belt drives, in an analogous way to that given by Wunderlinch and Zenow, however, instead of an ellipse we use a given convex figure γ as follows: by the Gardener's construction we get a convex figure with boundary Γ which

have the optical property of the ellipse. In other words, let x be a point in Γ and consider the two tangents to γ from x . These tangents make equal angles with respect to the tangent line l to Γ at x . Now, reflecting γ and Γ with respect to l we obtain the two figures γ' and Γ' (see Fig. 4). The length of the crossed belt around γ and γ' has constant length.

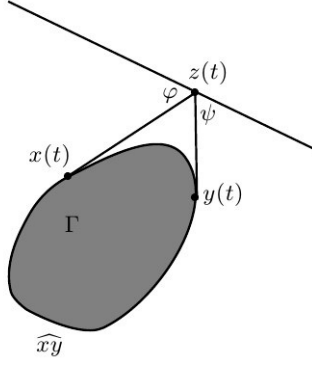


Figure 5. Length of the belt wrapping Γ .

However, we don't know if the rotation of γ and γ' can be both done through single points. We conjecture that if this is the case then γ must be an ellipse.

Now we give some words about billiards in a circle. It is well known that the circle has rotational symmetry, and a billiard trajectory is completely determined by the angle α made with the circle. This angle remains the same after each reflection. Each consecutive impact point is obtained from the previous one by a circle rotation through angle $\theta = 2\alpha$. If $\theta = 2\pi p/q$, then every billiard orbit is q -periodic and makes p turns about the circle; it is said that the *rotation number* of such an orbit is p/q . If θ is not a rational multiple of π , then every orbit is infinite. We denote the circle rotation through angle θ by T_θ .

The following theorem is classical in the theory of billiards.

Theorem 4. (see [5]) *If α is π -irrational, then the T_α -orbit of every point is dense. In other words, every interval contain points of this orbit.*

In order to prove lemma 2 we need to prove first the following lemma. In lemma 1, $\text{arc}(x(t)y(t))$ denotes the arc belonging to Γ from $x(t)$ to $y(t)$.

Lemma 1. *Let Γ be a given convex curve and let $P(t) = \|x(t) - z(t)\| + \|y(t) - z(t)\| + \text{arc}(x(t)y(t))$ be the length of the curve, as shown in Fig. 5, then*

$$\frac{dP}{dt} = \left\| \frac{dz}{dt} \right\| (\cos \varphi - \cos \psi). \quad (1)$$

Proof. Denote the curve describing the arc $\text{arc}(x(t)y(t))$ in the clockwise sense as $\alpha(t)$ with $t \in [t_0, t_1]$, where $y(t) = \alpha(t_0)$ and $x(t) = \alpha(t_1)$. Since $P(\alpha(t)) = \int_{t_0}^t \|\alpha'(t)\| dt$, differentiating with respect to t , we have

$$\begin{aligned} \frac{d(\text{arc}(x(t)y(t)))}{dt} &= \frac{dP(\alpha(t))}{dt} \\ &= \frac{d}{dt} \left[\int_{t_0}^t \|\alpha'(t)\| dt \right] \\ &= \|\alpha'(t_1)\| - \|\alpha'(t_0)\| \\ &= \|x'(t)\| - \|y'(t)\|. \end{aligned} \quad (2)$$

Now, differentiating $\|x(t) - z(t)\|$ and $\|y(t) - z(t)\|$, we obtain

$$\begin{aligned} \frac{d\|x(t) - z(t)\|}{dt} &= \frac{d}{dt} \left[\sqrt{\langle x(t) - z(t), x(t) - z(t) \rangle} \right] \\ &= \frac{\langle x'(t) - z'(t), x(t) - z(t) \rangle}{\|x(t) - z(t)\|} \\ &= \langle x'(t) - z'(t), n_x \rangle; \end{aligned}$$

where $n_x = \frac{x(t) - z(t)}{\|x(t) - z(t)\|}$, then

$$\begin{aligned} \langle x'(t), n_x \rangle - \langle z'(t), n_x \rangle &= \|x'(t)\| \cos \pi \\ &\quad - \|z'(t)\| \cos(\pi - \varphi) \\ &= -\|x'(t)\| \\ &\quad + \|z'(t)\| \cos \varphi. \end{aligned} \quad (3)$$

We proceed in a similar way with the segment $\|y(t) - z(t)\|$ and considering $n_y = \frac{y(t) - z(t)}{\|y(t) - z(t)\|}$, then

$$\begin{aligned} \frac{d\|y(t) - z(t)\|}{dt} &= \langle y'(t) - z'(t), n_y \rangle \\ &= \|y'(t)\| \cos 0 - \|z'(t)\| \cos \psi \\ &= \|y'(t)\| - \|z'(t)\| \cos \psi. \end{aligned} \quad (4)$$

It follows from (2), (3) and (4) that

$$\begin{aligned} \frac{dP}{dt} &= \|x'(t)\| - \|y'(t)\| - \|x'(t)\| + \|z'(t)\| \cos \varphi \\ &\quad + \|y'(t)\| - \|z'(t)\| \cos \psi \\ &= \left\| \frac{dz}{dt} \right\| (\cos \varphi - \cos \psi). \end{aligned} \quad (5)$$

□

We denote by $B(x, \lambda)$ the disc with center at x and radius λ . The result established in the following lemma, as far as we know, seems to be new.

Lemma 2. Let K be a convex figure in the plane with the origin O in its interior. Let r be a positive number such that $K \subseteq \text{int } B(O, r)$ and for every $x \in \text{bd } B(O, r)$ we have that $P([K, x])$ is constant, then K is a circle.

Proof. Since $P([K, x])$ is constant for all $x \in \text{bd } B(O, r)$, we have that K is the caustic of the billiard table $B(O, r)$. To see this, notice that since $\frac{dP}{dt} = 0$, we get from Lemma 1 that $\cos\varphi - \cos\psi = 0$ which implies that $\varphi = \psi$, in other words, the boundary of $B(O, r)$ have the reflection property of the ellipse. If for every $x \in \text{bd } B(O, r)$ we have the same angle of reflection α , it is not difficult to see that K is also a circle.

Consider now that α is not constant, then by the compactness of K there is an interval $[\alpha_{\min}, \alpha_{\max}]$ such that α takes every value in $[\alpha_{\min}, \alpha_{\max}]$. Clearly, there exists $\alpha_0 \in [\alpha_{\min}, \alpha_{\max}]$ such that $\frac{\alpha_0}{\pi}$ is irrational. Consider a point $x_0 \in \text{bd } B(O, r)$ such that the angle of reflection is α_0 . By theorem 4 we have that the $T_{2\alpha_0}$ -orbit of x_0 is dense in the boundary of $B(O, r)$ that is, the orbit $x_0, x_1, x_2, x_3, \dots$ have the property that every segment $[x_i, x_{i+1}]$ is tangent to K and the set of points $\{x_0, x_1, x_2, \dots\}$ is dense in $\text{bd } B(O, r)$. On the other side, since the angle α_0 is constant we have that the envelope of the segments $[x_i, x_{i+1}]$ is a circle. We conclude that K is a disc.

□

Now we are ready to give the proof of Theorem 3.

Proof of theorem 3. Since the belt drive is strict and uniform we have that $P([\gamma_1, \gamma_2])$ is constant and O_{12} is a fixed point. We know that

$$P([\gamma_1, \gamma_2]) = P([\gamma_1, O_{12}]) - P([\gamma_2, O_{12}]) + P(\gamma_2).$$

By hypothesis we know that $P([\gamma_1, O_{12}])$ is constant, hence $P([\gamma_2, O_{12}])$ must also be constant. It follows from lemma 2 that γ_1 and γ_2 are circles. □

REFERENCES

- [1] E. Zheng, F. Jia, H. Sha, and S. Wang, "Non-circular belt transmission design of mechanical press," *Mechanism and Machine Theory*, vol. 57, pp. 126–138, 2012.

- [2] W. Wunderlich and P. Zenow, "Contribution to the geometry of elliptic gears," *Mechanism and Machine Theory*, vol. 10, no. 4, p. 273–278, 1975.
- [3] H. Stachel, "Gears and belt drives for non-uniform transmission," in *Proceedings of EUCOMES 08*, M. Ceccarelli, Ed. Springer Netherlands, 2009, pp. 415–422.
- [4] J. Hoschek, "Konstruktion von kettengetrieben mit veränderlicher Übersetzung mit Hilfe von Bezier-Kurven," *Forschung im Ingenieurwesen*, vol. 48, no. 3, pp. 81–87, 1982.
- [5] S. Tabachnikov, "Geometry and Billiards." *American Mathematical Soc.*, 2005.

Implementation of an Automatized Photoluminescence System Using LabView

A. Bejarano-Rincón ^{#1}, J. A. Villada ^{*2}, M. E. Rodríguez-García ⁺³

[#] *Facultad de Ingeniería, Departamento de posgrado, Universidad Autónoma de Querétaro, C.U.*

Querétaro, Qro., México

IEEE Member

¹ abejarano17@alumnos.uaq.mx

^{*} *Departamento de Ingeniería, Universidad del Valle de México, Campus Querétaro,*

Querétaro, Qro., México

² jhon.villadavi@uvmmnet.edu

⁺ *Departamento de Nanotecnología, Centro de Física Aplicada y Tecnología Avanzada,*

Universidad Nacional Autónoma de México, Querétaro, Qro., México.

³ marioga@fata.unam.mx

Abstract— The design and implementation of a automatized photoluminescence system at low temperature is presented for the optical characterization of semiconductor materials. The function, selection and connection for each component of the system is described. The control of the equipment and the data acquisition is made by software developed in LabView. Each block of the software is described explaining the used libraries.

Keywords — *Photoluminescence, Automation System, LabView, Temperature Control, Semiconductors Characterization, Optical Properties of Semiconductors.*

I. INTRODUCTION

The principal characteristic of the semiconductor materials is the ability to change its conductivity by changing an external parameter such as the temperature, radiation, pressure, among others [1]. Nowadays the development of new semiconductors and the study of the properties of the existing ones have great interest for the scientific community due to the development of new electronic devices based on these materials. As an example, the photo-detectors used in the CD players or in movement sensors are made of GaAs [2]. This semiconductor material has the property to emit or to absorb electromagnetic radiation. The principal parameter of a semiconductor material is the energy gap, defined as the minimum energy required changing the conductivity of the semiconductor. In order to describe the behavior and properties of the semiconductor materials, different characterization techniques are used. Each characterization technique is implemented to measure a particular property. The Photoluminescence is a very common technique employed to study the optical properties of materials [3]. This technique has different components such as monochromator, photodetector, Lock-In amplifier, etc., all of them can be controlled by computer software. LabView is a common environment employed to control process [4], [5], [6].

In this work it is presented the design, implementation and automation of a system to measurement photoluminescence at low temperature realized in the “Centro de Física Aplicada y

Tecnología Avanzada (CFATA)” into “Universidad Nacional Autónoma de México (UNAM)” using LabView.

II. PHOTOLUMINESCENCE TECHNIQUE (PL)

PL is a nondestructive optical characterization technique. It means that the samples studied by this technique are not affected in the process and it can be used for further studies. Fig. 1 shows the energy diagram and the different stages of the PL process. Fig. 1a shows the initial state of the system. In this estate the electrons are in atomic or molecular orbitals. The energy of these electrons is in the range of the so called “Valence Band”. Fundamentals of PL involve the excitation of electrons (Fig. 1b). After the excitation, electrons have the enough energy to move through the material. This energy corresponds to the “Conduction Band”. A monochromatic laser with energy larger than the band gap of the material is used as the excitation source. Following excitation various relaxation processes occur in which the energy absorbed by electrons is released. Fig. 1c shows the first relaxation process where electrons release the energy in a thermal way until reach the thermal equilibrium with the material; this process is called “Thermalization”. When electrons have energy equal to the minimum energy of the conduction band, they release its remained energy in electromagnetic form (photons). This process is represented in Fig. 1d. This radiation is namely PL and is collected by a special photo-detector. The intensity and energy of PL contains information about the band gap of the materials, crystalline quality, and composition of the material.

The voltage of the photodetector is proportional to the intensity of the radiation. To determine the energy of the radiation, a monochromator device is used.

The temperature of the experiment must be as low as 10 K, to prevent thermal excitation and noise. The temperature must be controllable from 10K to room temperature with a precision of 0.1 K.

In summary a PL system has several variables to be controlled and measured. For this reason it is necessary to

develop an automation system that allows to the user to measure and to control each variable with accuracy and facility. In addition the system must facilitate the interpretation of the results by graphics or other visualization options.

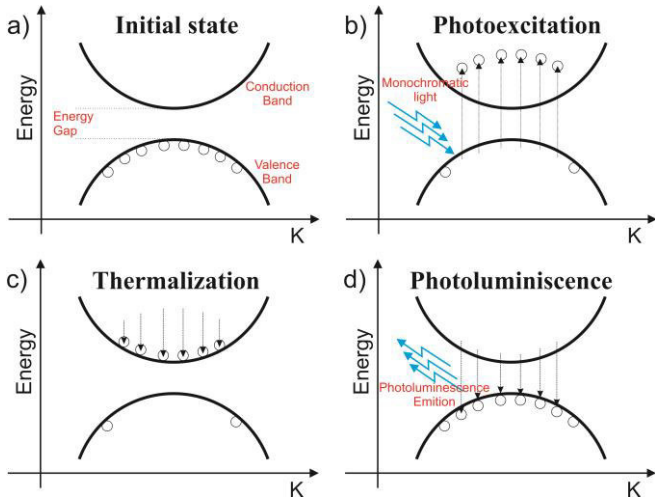


Fig. 1. Energy band diagram for a photoluminescence emission in a semiconductor.

III. PL SYSTEM DESING

Fig. 2 shows the functional diagram used as a tool to design the PL System. In this figure the input and output of each component of the system is presented. A monochromatic coherent light is used to excite the sample. The energy of the light must be higher than the band gap of the studied material. The most common light source is a laser. The light must be modulated in order to filter it subsequently. The beam is focused and directed by a set of lens and mirrors in order to obtain a nondispersed laser beam point on the sample. The sample is placed on the cold finger of a cryostat with a controlled temperature from 11K to room temperature. The temperature control consists of a heating device, a cooling device and a temperature sensor. To avoid the water condensation at low temperature, the pressure into the cryostat should be as low as 10^{-3} Torr.

After the excitation, the PL generated by the sample is collected by a lent and directed to a monochromator. This device consists of different mirrors and diffraction gratings and is able to do a frequency sweep to find the frequency at which the PL is. To sense de PL a semiconductor photo-detector is placed at the exit of the monochromator.

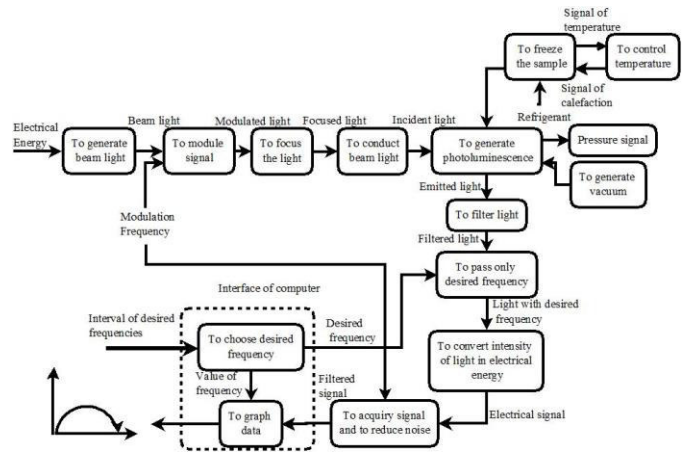


Fig. 2. Functional diagram for the implemented photoluminescence system.

The photo-detector converts the PL signal into voltage which is amplified by the Lock-In amplifier. In addition, the Lock-In works as a filter that uses the modulation frequency to discard other electromagnetic signals different than the ones produced by the sample. The signal generated by the Lock-In has two components, the amplitude and the phase. Both of them are acquired by a computer using a GPIB interface from National Instrument. To facilitate the interpretation of the PL measurements, a user interface was developed using LabView.

IV. PL SYSTEM IMPLEMENTATION

The selection of each component and interconnection of the system is presented in this section. All the components are grouped in five subsystems as shown in Fig. 3. Each subsystem consists of different devices. The subsystems are described as follows:

- A. Vacuum system
- B. Temperature control system
- C. Excitation system
- D. Detection system
- E. Control and acquisition system

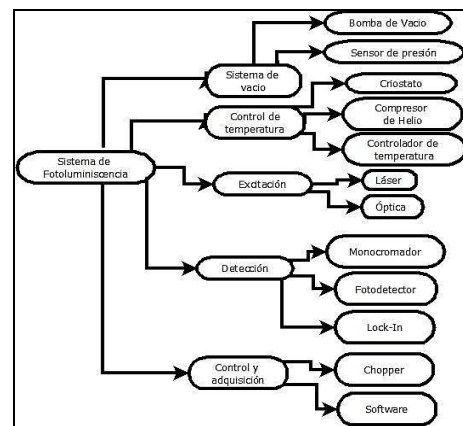


Fig. 3. Subsystems and components for a photoluminescence system.

A. Vacuum system:

Due to the system is designed to work at low temperatures, it is necessary to lower the pressure. In this way, heat transfers by conduction or convection are avoided. Only energy by radiation can cross the wall of the cryostat. A cryostat is a closed chamber with several electrical and gas connections. A cryostat model DE-202, from Advanced Research Systems, Inc was used in this work.

The low pressure is obtained by a mechanical vacuum pump coupled to the system. In this case we choose a rotary vanes vacuum pump (RV5, from Edwards Vacuum Inc.), obtaining a minimum pressure of 1.5 mTorr. A DP-20 sensor, from Sunx, Inc, was used to measure the pressure.

B. Temperature control system:

To lower the temperature, the cryostat is connected to a Helium compressor ARS 2HW, from Advanced Research System. At high pressure helium passes from solid to liquid state. When liquid the temperature of the Helium is about 4K. In order to control the temperature a heating element is required. In this case the cryostat has electrical resistors around the cold finger. To measure the temperature a type K thermocouple was used. The resistors and the thermocouple are connected to an auto-tuning PID temperature controller (330-4X, from LakeShore).

C. Excitation system:

There are two kinds of laser: Gas and solid state. A solid state laser (Compass 415M from Coherent Inc) was used as excitation source for this work. This laser has energy of 2.3 eV (532nm), enough to excite the most of the semiconductor materials. A mechanical chopper, (SR 540, from Stanford Research System) was used to modulate the light. The modulation frequency is controlled by a Lock-in Amplifier SR830 from Stanford Research System.

The light is directed by a mirror and then is focused by a spherical lens. The cryostat has special quartz windows to allow the laser to reach the sample with no lost pressure. Before the quartz windows, a cylindrical lens is placed to distribute the light into a line in order to avoid damages in the sample.

D. Detection system:

After radiation, the PL is emitted by the sample in all directions. A spherical lens collects the most of this radiation and focuses into a monochromator. This device can select a narrow band from the wide range of wavelengths available at the input. A Horiba - Jobin Yvon iHR320 was used in this system. From the LabView software the user can select the range of wavelength and the desired step to do a search for the radiation from the sample. At the exit of the monochromator a photodetector (H9307-2, from Hamamatsu) with a bandwidth from 200 to 800 nm, is placed to transform the PL into an electric signal which is carried to the Lock-In amplifier. This device selects only signals with the same frequency used for the chopper, working as a filter for the electromagnetic radiation.

E. Control and acquisition system:

Labview 2010 was used to develop the software for the technique. This software receives data from the photodetector. These data are received through of a Lock-In amplifier. It is connected to a computer using a GPIB-USB interface by National Instruments.

The *SR830.LLB* and *API Toolkit.LLB* libraries were used in the software for the development of the control of Lock-In amplifier and the Monochromator respectively. Both of these libraries are provided by the manufacturers. The user interface of the software is shown in the Fig. 4. This interface allows to the user selecting the range of wavelength, the step, the slit aperture, and the diffraction grid. In other section of the same window it is shown the collected data as a function of the wavelength and as a function of the energy. The information can be saved in a “.txt” file containing three columns (PL amplitude, wavelength and energy).

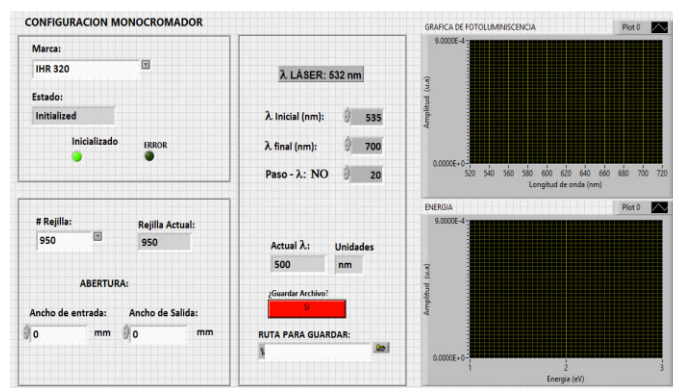


Fig. 4. Interface user for the software designed.

The programing in blocks was carried over the structure "Stacked Sequence". This structure allows executing the code sequentially and it does not enable to pass the data from a block to other if these are not complete. Fig. 5 shows the hierarchy of the software. The software is divided into two stages; the first one is the configuration stage used to establish the communication with all devices. The second stage is used to present and to save the PL data obtained from the experiment.

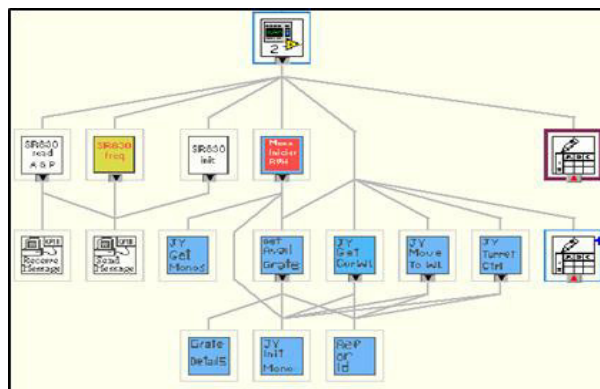


Fig. 5. Hierarchy of blocks involved in the software.

In the first stage, the first step of the code is the configuration of communications with the monochromator and the Lock-In. The block *SR830init* (shown in Fig. 6) sends the initial configuration to the GPIB interface to communicate with the Lock-In amplifier using a sub-function called *SendMessage*.

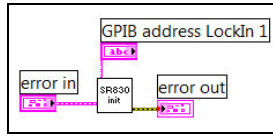


Fig. 6. Initialization SR830.

The second step is to establish the communication frequency for the Lock-In amplifier using the block *SR830_freq*. Then the monochromator is configured using the block *JYGetMonos Start RVH* shown in Fig. 7. The block *JYGetMonos* is into the *Mono Star RVH* and it is used to get the ID of the monochromators that are connected and it shows the connection in the user interface.

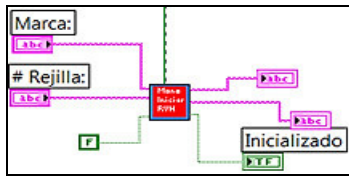


Fig. 7. To configure monochromator.

Each monochromator have a different number of grids. The block *GetAvailGrate* obtains information about the current grid selected on the monochromator.

The block *JYTurretCtrl* is used to choose the grid required according the PL signal. In the monochromator used it is possible to select one of three options: 1200, 900, 150. These numbers refer to the number of grids per millimeter.

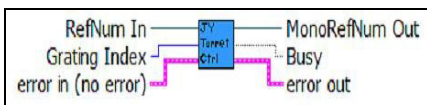


Fig. 8. To choose grid.

The block *JYMoveToWL* is used to move the grid to the wavelength chosen.

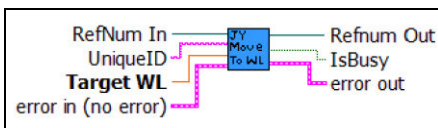


Fig. 9. To move grid.

In the second stage of the code the first step is to check the settings and command sent to the devices. Then the data obtained from PL signal are plotted and saved in a “.txt” file.

At this stage the first block is *JYCurGetWL*. It is used to ensure that the value of the grid is according to the value of the wavelength chosen by the user. After, using the block

SR830read, (Fig. 10) the amplitude and the phase of the PL signal is acquired from the Lock-In amplifier.

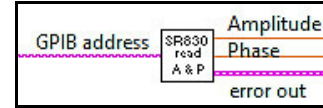


Fig.10. SR830 block used to acquire the amplitude signal.

The acquired data and the wavelength are plotted and displayed on the user interface. These data can also be stored in a “.txt” file in a route selected by the user.

V. CONCLUSION

A system of photoluminescence is obtained as result of this work for the radiometry laboratory at “Centro de Física Aplicada y Tecnología Avanzada (CFATA)” into “Universidad Nacional Autónoma de México (UNAM)” using LabView.

The system was calibrated and proven in a sample of GaAs. This proof throws similar results to the reported in the literature, which validates the good performance of the system. In addition a reduction of costs is obtained in the implementation of system in approximately 1000 USD, it is due to design and fabrication of some elements as the voltage source to the photodetector, or coupling elements of the optics device.

ACKNOWLEDGMENT

This work was supported by project PAPPIT in115113, Universidad Nacional Autónoma de México. A. Bejarano-Rincón wants to thanks to engineering faculty and the vice rector of research, Universidad del Quindío, Colombia, for the financial support for the trip from Colombia to Mexico. J.A. Villada wants to thank the National Science and Technology Council of Mexico, CONACYT for the financial support to develop this research, through the SNI program. Authors want to thank to Rosa Maria Jimenez Aguilar, from the language department of the Universidad del Valle de Mexico, campus Querétaro, for the English review of this paper.

REFERENCES

- [1] A. Rockett. *The materials science of semiconductors*. Illinois, USA: Springer. 2008.
- [2] German, T. D. *Desing and realization of novel GaAs based laser concepts*. Berlin, Germany: Springer, 2012, pp. 5.
- [3] J. N. Demas, G. A. Crosby, “Measurement of photoluminescence quantum yields. A review”. *Journal of Physical Chemistry*, Vol. 75, 991–1024, 1971.
- [4] J. Balderas-Zapata, M. Zapata-Torres, F. Chale-Lara y H. Peraza-Vazquez. “Automatizacion del control térmico de un sistema de evaporación de películas delgadas usando Labview. 2008.
- [5] C. Elliot, V. Vijayakumar, W. Zink and R. Hansen. “National Instruments LabView: A Programming Enviroment for Laboratory Automation and Measurement”. 2007.
- [6] A. Garg, R. Sharma and V. Dhingra. “Automating Energy Bandgap Measurements in Semiconductors Using LabView”. 2010.

Comparative study of methods for segmentation of thermographic images of the soles of the feet in patients with diabetes

M. A. Jiménez-Arthur^{#1}, L. A. Morales-Hernández^{#2}, R. A. Osornio-Ríos^{#3}

[#]Facultad de ingeniería, Universidad Autónoma de Querétaro, Campus San Juan del Río
Río Moctezuma 249, San Cayetano, C.P. 76807, San Juan del Río, Querétaro, México.

¹ jasshem@hotmail.com

² luis_morah@yahoo.com

³ raosornio@hspdigital.org

Abstract— This paper presents a comparative study of methodologies used in the pre-processing focused on the automatic segmentation of critical spots on the soles of the feet. The methodologies that are compared are: Otsu, Thresholding of minimum error and Hamadani, which due to their characteristics are used in order to separate the region of interest of the rest of the image that does not provide useful information for automatic segmentation of critical spots. The comparative study, based on the results, carried out in this work, allowed to evaluate what is the most appropriate methodology to detect with greater reliability and speed the regions with thermal anomalies in the plantar, in order to assist in the early detection of ulcerations in the soles of people with diabetes.

Keywords—Otsu; Thresholding of minimum error; Hamadani; Segmentation; Critical spots.

I. INTRODUCTION

One of the main issues that concern society today is health, and prediction techniques are essential when it is time to diagnose diseases and to act accordingly as soon as possible. One of these techniques is the use of thermography since it provides information that can help in the diagnosis of diseases, being one of its main applications in the study of diabetic foot. This is because the temperature and relative risk of ulceration is well known in the field of medicine. In the human body, the use of thermography allows to visualize and quantify in noninvasive and quick changes of surface skin temperature based on the infrared radiation emitted by the body, being a noninvasive technique that can be repeated as often as necessary and without contraindications. Living beings emit heat at a temperature above 0 °K (-273 °C), which corresponds to a radiation over the electromagnetic spectrum of visible light, so that the human eye is not sensitive to this called infrared radiation, however, there are thermal cameras capable of measuring infrared radiation to these wavelengths [1].

Thermographic analysis can be performed by means of digital image processing, applying necessarily a segmentation method to separate an image into significant regions, which are similar according to a specific property or feature extraction measurements [2]. For the segmentation, pre-processing tools are required to isolate the region of interest of the rest of the image that does not provide information for this purpose. That is why it is vital to the analysis and evaluation of different methodologies focused on the pre-processing of images, in this case with thermal image application in patients with diabetes.

The following works are related to image processing of the soles so as to assist in the early detection of ulcerations are addressed. One paper developed intensity levels as in [3], wherein a genetic algorithm combined with thermal imaging analysis asymmetry is developed through early detection of neuropathy ulcerations. Another intensity level based on work is [4], in which a computer software performs a standard automated temperature diagnosis by pattern recognition system of digital images IR and set geometry. In [5] separation algorithm which extracts different areas of thermal images of the foot by geometrical methods and separates temperatures by assigning colors to make a comparison between the areas proposed to contribute in the detection of diabetic foot. Another work is [6], in which a quantitative methodology to obtain temperature differences in the plantar of diabetic foot ulceration detecting risks, which is based on the proposed concept of angiosome. However, the division of the image by regions of interest was performed manually, and a temperature estimation of an angiosome was calculated by identifying these regions of assigned color. Temperature results were analyzed using statistical methods, but not thresholding and classification are performed. Works [3], [4] and [5] are made intensity levels, whereby there is no precise temperature management by proposing behaviors temperature which contribute to the accurate detection of a possible condition in the plant of the foot. Also, the methodology used by [5] for the extraction is not the best, as it is done manually and there is no segmentation, because the areas related to the metatarsals and toes are overlapping.

Although they are focused on the detection of hot spots or critical work sole, none addresses the use of a pre-processing based on any of the methodologies that are considered a case study in this paper.

In the present work, a comparative study appears focused to determine which is the most suitable methodology of Pre-processing used as tool in the process of segmentation for the detection of thermal anomalies in the sole of people with diabetes. In the study, the methodologies Otsu, Thresholding of minimum error and Hamadani are analyzed, which are evaluated by means of the results of the first segmentation inside a process for the detection of thermal anomalies. The methodologies are programmed and evaluated by means of termografic images of patients with diabetes.

II. THEORETICAL FOUNDATIONS

A. Diabetes

Diabetes is a chronic disease that occurs when the pancreas does not produce enough insulin or when the body does not effectively use the insulin it produces. Insulin is a hormone that regulates sugar in blood. The effect of uncontrolled diabetes is hyperglycemia (high blood sugar). When blood glucose levels remain high for a considerable time, organs such as the heart, kidneys, eyes and especially the nerves and blood vessels [7] are affected.

B. Infrared Thermography

The electromagnetic spectrum is composed of a set of visible and non-visible electromagnetic radiation. The infrared radiation on the electromagnetic spectrum is not visible [8]. Heat or thermal radiation is the main source of infrared radiation, so that the hotter the object is the more infrared radiation emits. Infrared thermography is the art of transforming an image into a radiometric infrared image that allows read temperature values, thus, each pixel of a radiometric image is in fact a temperature measurement [9]. In medicine, the thermogram or thermal image is the image that reflects the values of body temperature **Figure 1**, illustrating a drawing temperature of the areas of study that can be analyzed in both ways qualitatively and quantitatively [1]. Qualitatively, in which relative values of temperature of a hot spot are taken with respect to other parts of an object, with normal environmental factors. This type of measurement is widely used in most industrial, electrical, medical applications, among others. Quantitatively, in which the exact value of temperature of the object is taken. This method was unusual during thermal inspection because accuracy was affected by environmental factors, however, these factors will be controlled during the development of for this work. Therefore, the quantitative measurement is adopted to analyze the temperature values captured by an infrared camera. For both methods the aim is to analyze abnormalities in high temperatures.



Fig.1. Thermographic image of the soles of the feet.

C. Image Processing

The digital image processing is born due to the availability of technology to capture and manipulate large amounts of spatial information in the form of arrays of values. This distinction puts the digital image processing as a technology associated with computer science and, therefore, as a projection of the term artificial vision, within the field of artificial intelligence [10].

D. Steps for the detection of thermal anomalies

The diagram in **Figure 2** shows the most common steps in a process used to detect thermal anomalies, which involves making initially capturing the thermal image.

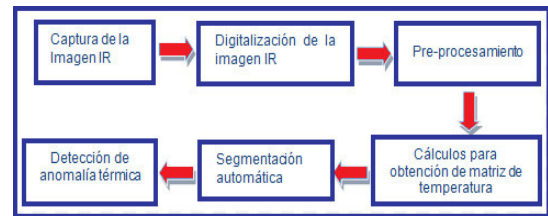


Fig.2. General block diagram of a detection process of thermal anomalies.

In the digitalization step, a conversion of the original image is performed in RGB format grayscale, obtaining **Figure 3** matrix whose row and column indices identify a point in the captured image whose value matches a gray level intensity hue in a range of between 0 and 255.

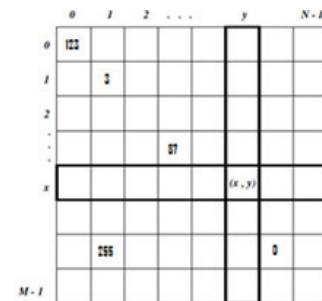


Fig. 3. Matrix grayscale image.

In the pre-processing step a first segmentation is to separate the area of interest of the rest of the image that does not provide useful information. The pre-processing that is the case study of this work, is of great importance because a first

segmentation is carried out by extracting only the region of interest, a better detection of thermal anomalies is achieved in the segmented plantars. In the next step, mathematical calculations are performed to acquire the temperature of the matrix of **Figure 4** segmented image.

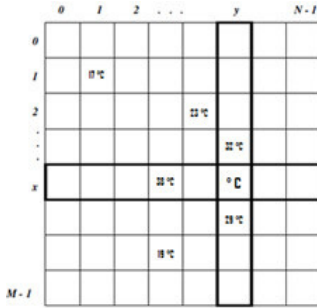


Fig. 4. Matrix temperature.

A search for maximum temperature values in this matrix is also performed and compared with temperature pattern already established to carry out a second automatic segmentation of the critical spots that allow the detection of thermal anomalies in the last stage.

III. COMPARATIVE STUDY OF THERMOGRAPHIC IMAGE SEGMENTATION METHODOLOGIES

In this section, segmentation methodologies focused on pre-processing thermal images of the soles of the feet in order to make a comparison are discussed, such as: Otsu, Thresholding of minimum error and Hamadani. The pre-processing of images is of vital importance as it allows images to be treated in order to deliver an image that has the right to be processed in a specific application features.

A. Otsu Method

The Otsu method [11] maximizes the variance between classes, the goal is to find the threshold value at which the sum of the pixels of the object and the background image are at their minimum.

For this method first the histogram of the image is obtained, denoting the components of the histogram as p_i , where $i=0,1,2, \dots, L-1$, and $k=0,1,2, \dots, L-1$:

Cumulative sums $P(k)$ are calculated by the following equation:

$$P_1(k) = \sum_{i=0}^k p_i \quad (1)$$

Cumulative average $m(k)$ are calculated, using:

$$m(k) = \sum_{i=0}^k ip_i \quad (2)$$

The overall average current is calculated m_G , Obtained by:

$$m_G = \sum_{i=0}^{L-1} ip_i \quad (3)$$

Is calculated variance between classes $\sigma_B^2(k)$, given by:

$$\sigma_B^2(k) = \frac{[m_G P_1(k) - m(k)]^2}{P_1(k)[1 - P_1(k)]} \quad (4)$$

Otsu threshold, k^* , is obtained as a value of k for which the variance is maximum. If the maximum value is not unique, k^* is obtained to average them.

B. Thresholding of minimum error method

The method Thresholding of minimum error [12] considers the histogram as an estimate of a probability of density function $p(g)$, which is a mixture of distributions for the foreground and background, where these have a normal distribution with mean and standard deviation.

Initially the probability density functions are calculated from the following form:

$$p_f(t) = \frac{1}{\sigma_f \sqrt{2\pi}} e^{-\frac{(t-\mu_f)^2}{2\sigma_f^2}} \quad (5)$$

$$p_b(t) = \frac{1}{\sigma_b \sqrt{2\pi}} e^{-\frac{(t-\mu_b)^2}{2\sigma_b^2}} \quad (6)$$

The probability density function of the histogram Is calculated as:

$$p(t) = P_f(t) \cdot p_f(t) + P_b(t) \cdot p_b(t) \quad (7)$$

The minimum error is achieved when as a threshold value is selected, for which:

$$P_f(t) \cdot p_f(t) = P_b(t) \cdot p_b(t) \quad (8)$$

Applying logarithm of both sides, solving equations and substituting values $\mu_f, \mu_b, \sigma_f^2, \sigma_b^2$:

$$\mu_f(t) = \sum_{g=1}^t g \frac{p(g)}{P_f(T)} \quad (9)$$

$$\mu_b(t) = \sum_{g=t+1}^{255} g \frac{p(g)}{P_b(T)} \quad (10)$$

$$\sigma_f^2(t) = \sum_{g=1}^t (g - \mu_f)^2 \cdot p(g) \quad (11)$$

$$\sigma_b^2 = \sum_{g=t+1}^{255} (g - \mu_b)^2 \cdot p(g) \quad (12)$$

Finally, a criterion function is defined, which seeks the minimum error given by the equations:

$$J(t) = 1 + 2(P_f(t) \log \sigma_f(t) + P_b \cdot \log \sigma_b(t)) - 2(P_f(t) \log P_f(t) + P_b \cdot \log P_b(t)) \quad (13)$$

$$T^* = \text{Min}\{J(t)\} \quad (14)$$

C. Hamadani Method

The Hamadani method [13] is a statistical method first order defined on a histogram, its importance relies on being an automated method.

Initially the image histogram was obtained in a grayscale by the following equation:

$$h(i) = \frac{n}{NP} \quad (15)$$

Where h corresponds to the intensity histogram, the number of pixels n of intensity i and NP the total number of image pixels. Then the probability distribution of the histogram of the image obtained was calculated by:

$$p(i) = \frac{n_i}{N} \quad (16)$$

Being n_i the frequency of gray level i , and N the total number of pixels. The average intensity level of the image is also determined using the following formula:

$$\mu = \sum_{i=0}^{G-1} i * p(i) \quad (17)$$

In addition, the standard deviation of the image, given as the square root of the variance was obtained, which describes the variation of the intensity around the mean:

$$\sigma^2 = \sum_{i=0}^{G-1} (i - \mu)^2 * p(i) \quad (18)$$

Therefore the probability distribution, the average intensity value and standard deviation of the image is calculated to determine an optimal threshold T by the following equation:

$$T = (k1 * \mu) + (k2 * \sigma) \quad (19)$$

$k1$ and $k2$ are constants, to which are assigned a value between 1 and 2.

IV. RESULTS AND DISCUSSION

Methods of Otsu, Thresholding minimum error and Hamadani were programmed in the programming language C++, the GTK platform library was used with the objective of developing graphical user interface, plus the free library computer vision OpenCV (Open Source Computer Vision). The capture of infrared images was made using a camera FLIR A-310, the captured image was for both feet with the rainbow palette, in RGB format size 320x240 pixels of patients suffering from diabetes.

Then comparison of results obtained when performing a segmentation of a thermal image of the soles of the feet using the methods under study is shown.

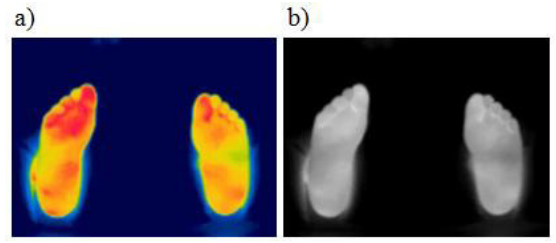


Fig.5. a) Original Thermographic image. b) grayscale image.

In **Figure 5**, clause a) the thermal image captured from the soles of the feet with the FLIR A-310 camera is displayed, where shows color variants designated by the camera according to the detected infrared radiation are, being white for the highest temperature and dark blue for the lowest. In paragraph b) conversion of the thermal image of the soles is shown in an image intensity levels in gray, which was obtained to calculate the histogram of the image and based on this power segment the region interest.

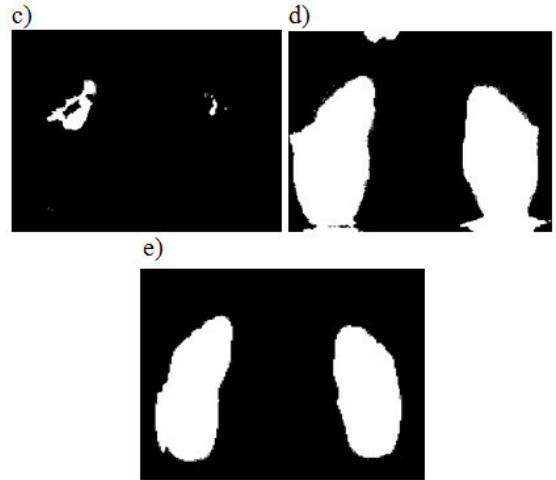


Fig. 6. c) Segmentation by Otsu, threshold value of $k = 183$. d) Segmentation by Thresholding of minimum error, threshold value $T = 77$. e) Segmentation by Hamadani, threshold $T = 56$.

In **Figure 6**, clauses c), d) and e) show the application of the methods studied in the segmentation of soles. It is noted that the segmentation by Otsu method, valuable information from the region of interest is lost, whereas in the segmentation method of minimum error, some background regions that should be eliminated are remained, and this would provide information that at the time of processing it would generate false results compared with Hamadani method with the best patterns by segmenting region of interest from the rest of the image.

Once completed the pre-processing of the image by applying a first segmentation by Hamadani method, mathematical calculations were performed to acquire the matrix temperature of the segmented image and then conducted a second automatic segmentation of the critical spots found based on the values of maximum temperature of the temperature matrix, thereby detecting areas with thermal anomalies in the soles of the feet.



Fig. 7. Areas of the foot with thermal anomalies.

In **Figure 7** is shown in dark gray hue in a yellow circle critical spots detected in the soles of the feet of a patient with diabetes study. **Table 1** shows the parameters of mean temperature \bar{T} of the area with thermal anomalies found, σ the standard deviation around the mean temperature and the percentage of area $\%A$ with abnormal temperatures, the parameters were calculated for each foot.

TABLE 1. Parameters of interest

	Left sole	Right sole
\bar{T}	31.25°C	31.37°C
σ	0.23	0.39
$\%A$	18.89	3.68

According to information of the parameters of interest, left foot has small areas with thermal anomalies of 18.89%, unlike the right foot which presents only a minimum of 3.68%, however, the average temperature of the areas with thermal anomalies is very similar and slightly higher at 31 °C, so that a possible reduced risk of ulceration was observed in both feet.

V. CONCLUSIONS

In this paper, the implementation of three methods focused on pre-procesamiento thermographic images within a process of detecting thermal anomalies in soles of the feet in patients with diabetes is presented. The Otsu, Thresholding of minimum error and Hamadani methods were programmed and evaluated through real images of patients with diabetes. After applying the methodologies programmed in the thermal images a visual comparison of images processed to determine the best performance of the methods is performed. The results showed that the method was Hamadani allowing more efficiently segmenting images, properly separating the region of interest in this case the sole. Subsequently methodology Pre-processing Hamadani in the entire process of detecting thermal anomalies reporting reliable results in detection was used.

VI. ACKNOWLEDGEMENTS

The first author is grateful to "Consejo Nacional de Ciencia y Tecnología" (CONACYT) by support for shoolarship received. Also like to thank M.E.S. Gavina Quintanar Martínez Language Services department of the School of Engineering Campus San Juan del Río, University of Querétaro, México for provide the English language editing of this paper.

REFERENCES

- [1] E. L. Salazar, "Aplicación de la Termografía a la Psicología Básica". Tesis doctoral, Universidad de Granada, 2013.
- [2] N. Montiel et al., "Segmentación adaptativa de lesiones isquémicas cerebrales a partir de imágenes de difusión de resonancia magnética", 2009.
- [3] N. Kaabouch, W. Hu, Y. Chen, J. W. Anderson, F. Ames, R. Paulson, "Predicting neuropathic ulceration: analysis of static temperature distributions in thermal images", *Journal of Biomedical Optics*, 15(6), 061715 1-6, 2010.
- [4] M. L. Brioschi, J. E. Fouto Matias, M. Jacobsen Teixeira, J. Viriato Vargas, "Automated Computer Diagnosis of IR Medical Imaging", *InfraredMed - Medical Infrared Imaging Diagnostic, Brazil*, 2010.
- [5] P. R. Vázquez y L. H. Morales, "Algoritmo para separación de áreas de temperaturas en el pie diabetic", Tesis Maestría en Instrumentación y Control Automático. Universidad Autónoma de Querétaro, 2013.
- [6] H. Peregrina-Barreto, L. A. Morales-Hernández, J. J. Rangel-Magdaleno, J. G. Avina-Cervantes, J. M. Ramírez-Cortes, R. Morales-Caporal, "Quantitative Estimation of Temperature Variations in Plantar Angiosomes: a study case for diabetic foot", 2013.
- [7] World Health Organization. Diabetes, Nota descriptiva N°312; Septiembre de 2012. Obtained: <http://www.who.int/mediacentre/factsheets/fs312/es/>
- [8] J. A. S. Jaramillo, "Física, Óptica", Editorial MAD, S. L., España. 388-401, 2003.
- [9] FLIR. 2011. Guía de Termografía para Mantenimiento Predictivo. Revised on April 7, 2014, obtained: http://www.flirmedia.com/MMC/THG/Brochures/T820264/T820264_ES.pdf
- [10] J. J. E. Esqueda, L. E. M. Palafox, "Fundamentos de procesamiento de imágenes", Universidad Autónoma de Baja California. 9-11, 2005.
- [11] D. Sanchez and V. Ponomaryov, "Diseño e implementación de algoritmos de segmentación basados en lógica difusa con aplicaciones en imágenes biomédicas", IPN, 2010.
- [12] C. Cattaneo, L. Larcher, A. Ruggeri, A. Herrera and E. Biazoni, "Métodos de umbralización de imagines digitales basados en entropía de Shannon y otros", *Mecánica Computacional Vol XXX*, págs. 2785-2805., 2011.
- [13] N. L. Palomino, W. Contreras, M. E. Ruíz, "Procesamiento digital de textura: Técnicas utilizadas en aplicaciones actuales de CBIR", *RISI* 7(1), 57-64, 2010.

Vibration Analysis of ABB IRB 140 Industrial Manipulator using Moving Average Filter and FIR Filter

Elvira-Ortiz D. A. ^{#1}, Romero-Troncoso R. J. ^{*2}, De Santiago-Pérez J.J. ^{#1}, Morales-Velázquez L. ^{#1} and Osornio-Ríos R. A. ^{#1}

HSPdigital CA-Mecatrónica, Universidad Autónoma de Querétaro, Facultad de Ingeniería, Campus San Juan del Río Río Moctezuma 249, Col. San Cayetano, San Juan del Río, Querétaro, 76807, México

¹ delvira@hspdigital.org

³ jjdesantiago@hspdigital.org

⁴ lmorales@hspdigital.org

⁵ raosornio@hspdigital.org

** HSPdigital, Universidad de Guanajuato, División de Ingenierías Campus Irapuato-Salamanca*

Carretera Salamanca - Valle de Santiago Km. 3.5 + 1.8. Comunidad de Palo Blanco Salamanca, Gto. C.P. 36885

² troncoso@hspdigital.org

Abstract— This work presents a methodology to perform an analysis of vibrations on an industrial manipulator, through signals acquired from three-axis accelerometer and digital signal processing by using a moving average filter and a FIR filter (finite impulse response). In order to test the efficiency of this methodology, two cases of study are performed, emulating a welding task and a painting one on a robot ABB IRB 140. A report containing all the vibration levels, which are obtained from the methodology developed, is presented for both tasks with the purpose of assess the vibration levels in a commercial manipulator.

Keywords: *Moving Average Filter, Industrial Manipulator, FIR Filter.*

I. INTRODUCTION

Nowadays, industry tries to automate most of its processes as part of an update which is focused, inter alia, on improving quality standards by developing tasks in which a robotic system can directly supervise that the process takes out properly and correct problems that may arise along the way. Industrial robots or robotic arms are a relatively young technology within the industry, but their popularity has considerably increased because of its capability to perform difficult tasks presenting repeatability in a quick and easy way to control. However, there are several factors that can affect the proper performance of a robotic manipulator, one of the most important is vibration. Vibrations are present in any industrial process, because the action between elements of any mechanism generates forces that make one or more elements oscillate around its equilibrium point, so, many works have been developed around the identification and measuring of vibration on industrial machines. Several methods have been proposed for acquisition, processing and analysis of vibrations in Robotic structures. The

use of accelerometers is well established to obtain kinematic parameters [1-4], or to measure vibrations [5]. The acceleration signal in an accelerometer contains merged information from the inclination with respect to gravity and about vibrations, therefore it is desirable to have methods that allow to separate the vibration parameter from the inclination one and from some other factors like noise. The extraction of vibrations allows failure detection [6] that affects the industrial processes in which repetitive tasks have been delegated to a robotic structure. As mentioned above, the accelerometer provides vibration and inclination information which should be separated. Given that the inclination signal is principally low frequency [7] whereas vibration is high frequency [8], they can be separated with properly tuned filters. In this paper, a methodology that focuses on the evaluation of vibrations on a commercial robotic structure ABB IRB 140 [9] is developed. This methodology is based on the combination of a high-pass FIR filter and a moving average filter. The high-pass FIR filter allows to separate the vibration signal from the inclination one, both of them present in the accelerometer signal. Due to noise is also a high frequency signal, the use of a moving average filter is proposed to isolate vibration from noise contamination. The effectiveness of the methodology is demonstrated through its implementation in two cases of study in a robotic structure ABB IRB 140, emulating a task of painting and another one of welding.

II. THEORETICAL BACKGROUND

Now some of the concepts required for the development of this project are introduced.

This work was partially supported by CONACYT scholarship (296549) and by projects SEP-CONACYT 222453-2013 and PROMEP 103.5/14/710401.

A. Robotic Manipulators

Two types of robotic manipulators are primarily used on industry: serial and parallel manipulators. In [10] it is mentioned that serial manipulators are the most used on industry because they are relatively simple to analyze. For this reason in this work the attention is focused on a serial manipulator, specifically the ABB IRB 140 manipulator [9]. This is a 6 degrees of freedom serial manipulator, i.e. that six articulation parameters or variables are required to completely describe the configuration of the manipulator [11]. **Figure 1** shows the manipulator ABB IRB 140.



Figure 1. ABB IRB 140 manipulator.

B. Moving Average Filter

According to [12], moving average filter is the most common in digital signal processing (DSP), mainly because it is very easy to understand and use. In addition to its simplicity, the moving average filter is optimal for the task of reducing white noise, which is one of the most common tasks in DSP. As its name suggests, the moving average filter works by averaging a number of points of the input signal to obtain a value in the output signal and it is described by (1)

$$y[n] = \frac{1}{M} \sum_{k=0}^{M-1} x[n-k] \quad (1)$$

where:

y is the output signal;

M is the number of samples of the signal to be averaged; and

x is the input signal.

C. Finite Impulse Response Filter (FIR)

According to its impulse response, filters can be classified into finite impulse response or FIR filters and infinite impulse response or IIR filters. Thus, a FIR filter has an impulse response that is zero outside a finite interval. A FIR filter whose

input is $x(k)$ and output $y(k)$, can be described by a difference equation with finite terms of the form presented in (2).

$$y(k) = \sum_{i=0}^n a_i x(k-i) \quad (2)$$

where $\{a_i\}$ is the set of filter coefficients [13]. There are different methods to design FIR filters, being the most common the use of windows. There are also many different windows to do the filter design, just to name a few there are the rectangular window, the Hann window, the Blackman window, etc. In this work a Hann window is used to develop a high pass filter of order 256, with a sampling rate of 1000 Hz and a cutoff frequency of 100 Hz.

III. METHODOLOGY

The general diagram of the methodology proposed in this work is presented in **Figure 2**. It can be seen that it was necessary to carry out the instrumentation of the manipulator ABB IRB 140. From the sensors on the robot, signals were acquired through the RS-485 protocol and sent to an FPGA based data acquisition system. Then the signals were sent to the PC via USB protocol. On the PC the process starts with a filtering stage using a moving average filter to remove the noise components present on the signal. Once the smoothed signal was obtained, another filtering stage is carried out to isolate the vibration signal, but this time using a high-pass FIR filter of order 256.

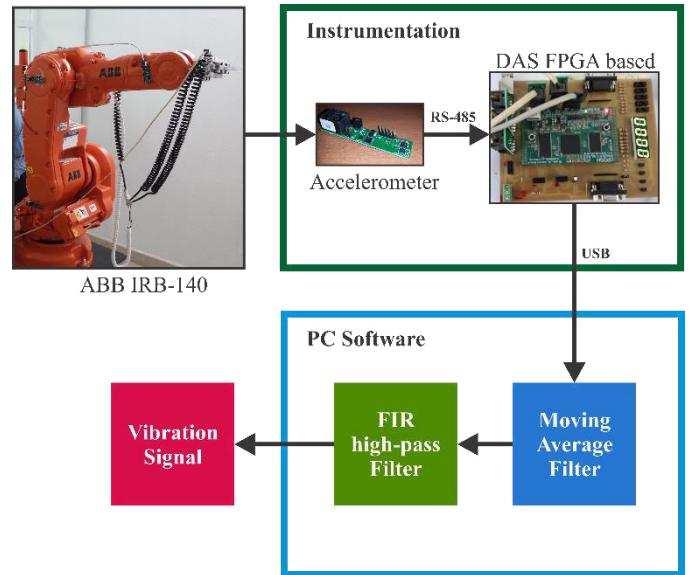


Figure 2. Methodology

A. Instrumentation

To perform the instrumentation task, 5 accelerometers LIS331DLH [14] were used. These are three-axis digital accelerometers that provide the output data through SPI communication protocol. These accelerometers are mounted on a board of own development, which contains a microcontroller PIC to perform the acquisition of the signals and to allow communication between the microcontroller and other devices via RS-485 communication protocol. It is through the latter

protocol that data are sent to the FPGA device. Then data are extracted from the FPGA for being processed with the proposed methodology which is developed on a PC. **Figure 3** shows the location of the 5 sensors on the manipulator ABB IRB 140 .

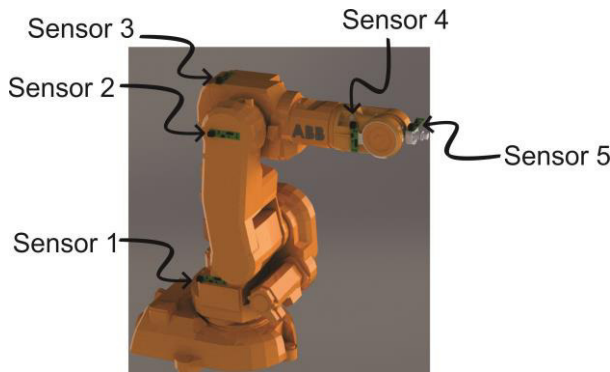


Figure 3: Location of the sensors on ABB IRB 140 robot.

B. Moving Average Filter

To apply the moving average filter a Matlab script was implemented to execute the task described by (1). **Figure 4** shows the flowchart of the implementation of this step.

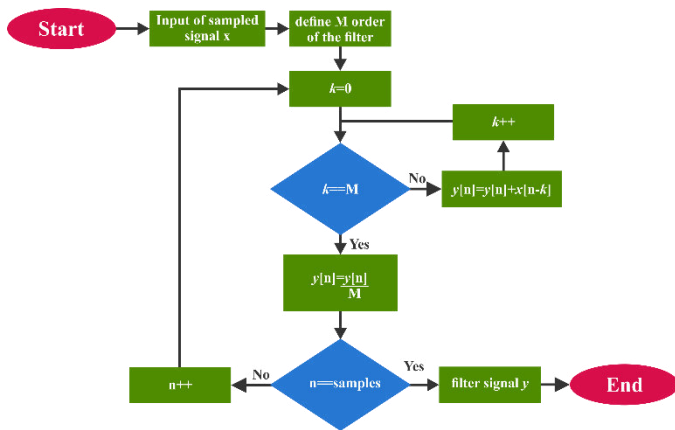


Figure 4. Flowchart of the moving average filter.

C. FIR Filter

The next step was to implement the FIR filter. This filter was also developed using a Matlab script. As mentioned, the filter design parameters were a sampling frequency of 1000 Hz, a cut-off frequency of 100 Hz and 256 as the order of the filter. **Figure 5** shows the flowchart followed to implement this filter represented by (2).

Through the union of the two models described above the vibration signal presented on every axis of the manipulator ABB IRB 140 could be obtained.

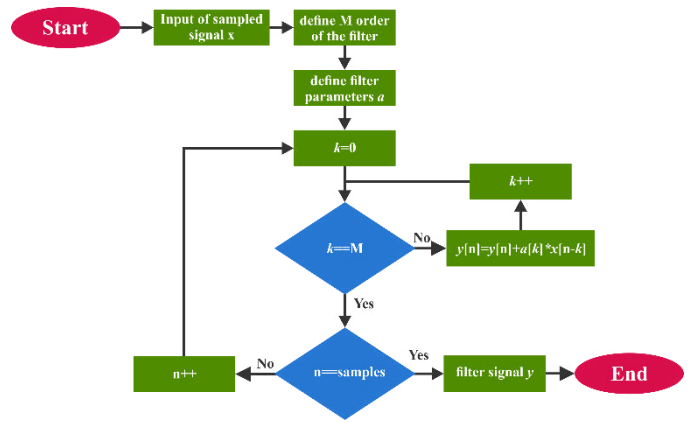


Figure 5. Flowchart of the FIR filter.

IV. EXPERIMENTAL SETUP

Two cases of study are presented with the intention to test the proposed methodology and evaluate the vibration levels on the manipulator. This methodology was programmed using a script developed in Matlab and hosted on a PC with an AMD A-8 processor. These tests were developed to evaluate the performance of the ABB IRB 140 manipulator which is considered to be used in an industrial environment. In the first case of study the manipulator was programmed to perform a welding task on a flat surface and a circular path in the YZ plane. In the second case of study a painting task was performed on a path in the XZ and YZ planes. In each case study the movement starts from a HOME position and once the task has been completed the manipulator is returned to the same HOME position. **Figure 6** shows the programmed paths as cases of study.

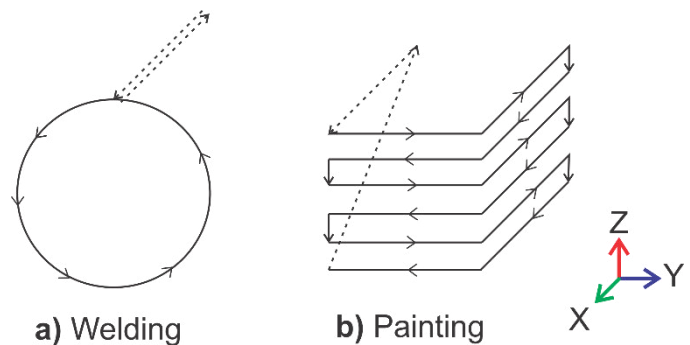


Figure 6. Cases of study.

Due to the tasks that were programmed and the way these tasks were performed, one of the axes that presented longer and sharper movements was the axis 2 of the manipulator, for this reason, the figures presented in this work show the results obtained for this particular axis but the tables present the results obtained for all of the manipulator axes and for each axis of the accelerometers. **Figure 7** shows one of the original signals acquired from the accelerometers when the welding task was performed and the signal after being passed through the moving

average filter. It can be clearly seen that the signal is smoothed in a good way and also that the amplitude of the largest peaks of the signal were decreased.

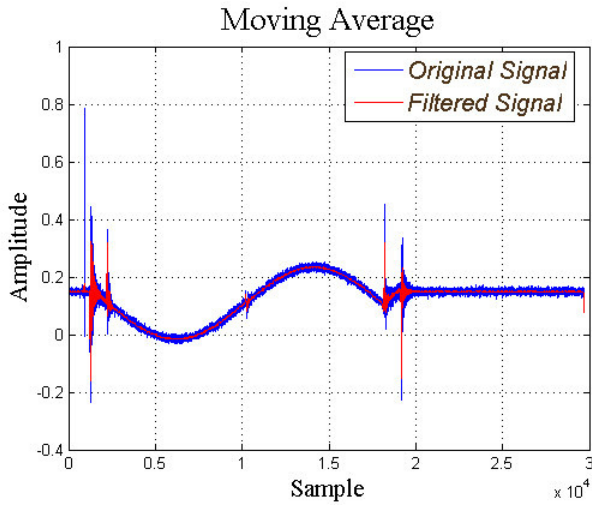


Figure 7. Original and smoothed signals on the welding task

Figure 8 shows the vibration signal obtained for the y-axis of the accelerometer placed on the second axis of the manipulator, while the task of welding on a circular surface (first case of study) was performed. It can be seen that there are two areas where the amplitude of vibration clearly stands. The biggest vibration amplitude is near the beginning of the task, because the movement starts from the rest and it is necessary to apply a greater torque to initiate the movement of the axes than to keep them moving. After this, the vibration zones presented are due to the way the circular path is generated. This path is obtained through two semicircular paths and the manipulator has to apply the brakes twice, one after each trajectory, which are reflected in the graph in these two areas of vibration. In addition a final vibration region appears indicating the end of the task, i.e. the manipulator finishes the work and completely stops.

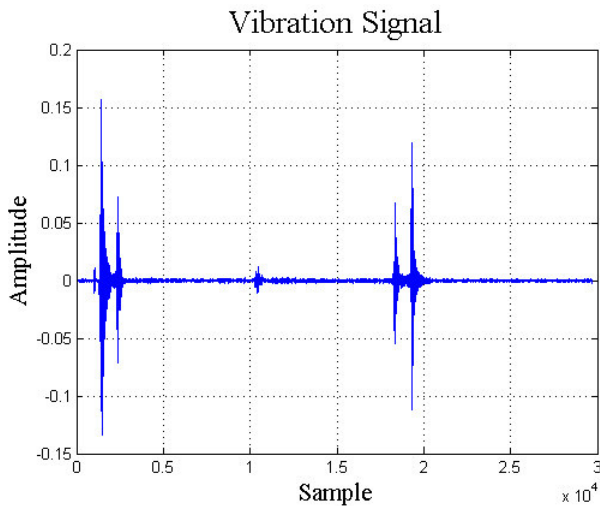


Figure 8. Vibration signal on weldind task.

Moreover, in **Figure 9** is presented one of the accelerometers signals before and after the moving average filter acquired while the robot performed the painting task. Just as in the previous case of study, noise components are clearly diminished, proving that it is fulfilling its purpose.

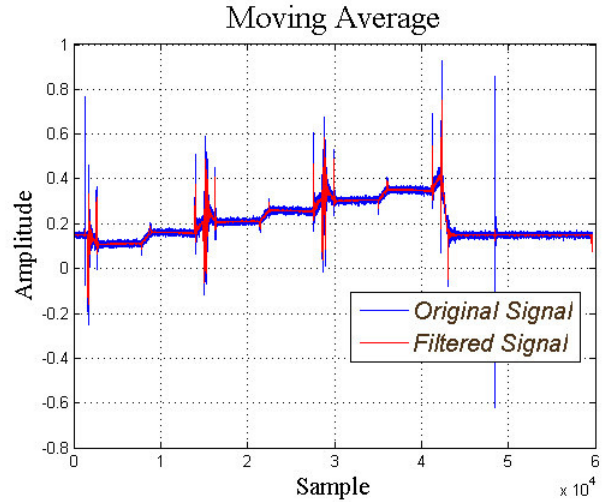


Figure 9. . Original and smoothed signals on the painting task.

In turn, in **Figure 10** is observed the vibration signal obtained for the y-axis of the accelerometer positioned on the second axis of the manipulator while the painting task (second case of study) was made. On the painting task more areas with vibration amplitude peaks are observed. This is because the task is more complex than the earlier one and has more abrupt changes in direction.

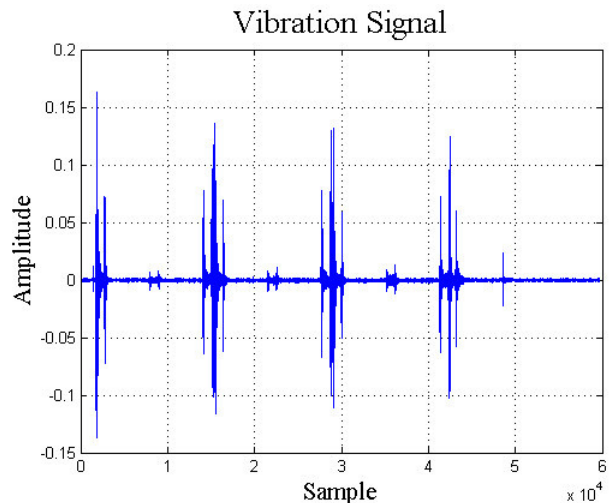


Figure 10. Vibration signal on painting task.

Table 1 below shows the analysis for the three axes of each accelerometer in the manipulator when the welding task is performed in the circular surface.

Table 1. Vibration analysis on welding task.

Robot Axis	Sensor Axis	Amplitude (G)		
		Min.	Max.	Mean
1	X	-6.3x10 ⁻⁸	-0.4051	-0.0011
	Y	-7.8x10 ⁻¹¹	0.0330	-8.8x10 ⁻⁷
	Z	-2.8x10 ⁻⁹	-0.0067	-1.9x10 ⁻⁵
2	X	1.4x10 ⁻⁹	0.0176	3.6x10 ⁻⁵
	Y	-2.5x10 ⁻⁹	-0.1563	1.4x10 ⁻⁴
	Z	-1.2x10 ⁻⁷	-0.4106	-0.0011
3	X	-7.9x10 ⁻⁸	-0.4068	-0.0010
	Y	-1.3x10 ⁻⁸	-0.1355	-1.8x10 ⁻⁴
	Z	-1.9x10 ⁻⁸	-0.0401	-2.9x10 ⁻⁵
4	X	-6.7x10 ⁻⁵	-0.1107	-2.4x10 ⁻⁴
	Y	-6.7x10 ⁻⁵	-0.4059	-6.3x10 ⁻⁴
	Z	6.5x10 ⁻⁵	0.0364	9.1x10 ⁻⁴
5	X	1.9x10 ⁻⁸	0.1263	-1.4x10 ⁻⁵
	Y	-1.3x10 ⁻⁸	-0.0461	-5.1x10 ⁻⁵
	Z	-5.3x10 ⁻⁸	-0.3841	-0.0011

The table shows the minimum amplitude value of the vibration for each axis (it can be negative or positive), the maximum amplitude value of vibration and the average of vibration recorded during the task. It may be noted that, as expected by the characteristics of the manipulator, the vibrations presented a very small amplitude.

Finally, in **Table 2** the vibration analysis for painting task is presented. Despite being a more complex task and recorded higher levels of vibration, the amplitudes remain low in this task. Although the maximum amplitudes become much greater than the minimum amplitudes, the average remains below the peaks due to the vibration is presented for very short periods.

Table 2. Vibration analysis on painting task.

Robot Axis	Sensor Axis	Amplitude (G)		
		Min.	Max.	Mean
1	X	2.6x10 ⁻⁸	-0.4041	-0.0011
	Y	-1.6x10 ⁻¹⁰	0.0554	-3.7x10 ⁻⁷
	Z	-3.1x10 ⁻⁹	0.0073	-1.9x10 ⁻⁵
2	X	-4.8x10 ⁻¹⁰	0.0366	3.5x10 ⁻⁵
	Y	-2.6x10 ⁻¹⁰	0.1631	-2.3x10 ⁻⁴
	Z	7.9x10 ⁻⁸	-0.4027	-0.0011
3	X	-1.9x10 ⁻⁷	-0.4072	-0.0010
	Y	-1.4x10 ⁻⁸	-0.1354	-2.3x10 ⁻⁴
	Z	7.5x10 ⁻⁹	-0.0271	-2.9x10 ⁻⁵
4	X	-2.9x10 ⁻⁸	-0.0650	4.5x10 ⁻⁵
	Y	-1x10 ⁻⁸	0.0229	-4.9x10 ⁻⁴
	Z	1.8x10 ⁻⁷	0.0415	2.6x10 ⁻⁴
5	X	-1.2x10 ⁻⁸	0.1277	-1.7x10 ⁻⁵
	Y	-2.3x10 ⁻⁸	-0.0455	-4.9x10 ⁻⁵
	Z	-5.9x10 ⁻⁸	-0.3951	-0.0011

V. ACKNOWLEDGMENT

Vibration analysis on industrial manipulators becomes of great importance to the industry today, because automation is important in the production system and any failure in this

system translates into losses for the company. Having a system based on a proper methodology to monitor vibration can become a vital factor on detecting faults, not only in robotic manipulators, but in many other industrial systems. The combination of finite impulse response filter and the moving average filter is efficient for extracting vibration in a robotic structure as shown by the results, because the characteristics of the FIR filter allow to isolate the tilt component from the acceleration obtained from the accelerometer, while the moving average filter prevents noise contamination in the results. The two proposed cases of study were selected based on the difference in the dynamic motion that generate on the manipulator, the welding trajectory follows the path on a soft and smooth way with little braking situations, while the path for painting presents abrupt changes in speed and direction of movement, which allows different vibration levels.

REFERENCES

- [1] Väliiviita, S.; Ovaska, S.J. Delayless acceleration measurement method for elevator control. *IEEE*
- [2] Liu, H.H.S.; Pang, G.K.H. Accelerometer for mobile robot positioning. *IEEE T. Ind. Appl.* 2001,37, 812-819.
- [3] Jassemi-Zargani, R.; Neculescu, D. Extended kalman filter-based sensor fusion for operationalspace control of a robot arm. *IEEE T. Instrum. Meas.* 2002, 51, 1279-1282.
- [4] Dumetz, E.; Dieulot, J.Y.; Barre, P.J.; Colas, F.; Delplace, T. Control of an industrial robot using acceleration feedback. *J. Intell. Robot Syst.* 2006, 46, 111-128.
- [5] Ohta, T.; Murakami, T. A stabilization control of bilateral system with time delay by vibration index-application to inverted pendulum control. *IEEE T. Ind. Electron.* 2009, 56, 1595-1603.
- [6] Trendafilova, I.; van Brussel, H. Condition monitoring of robot joints using statistical and nonlinear dynamics tools. *Meccanica* 2003, 38, 283-295.
- [7] Miro, J.V.; White, A.S. Modelling an industrial manipulator a case study. *Simulat. Pract. Theor.* 2002, 9, 293-319.
- [8] Karagülle, H.; Malgaca, L. Analysis of end point vibrations of a two-link manipulator by Integrated CAD/CAE procedures. *Finite Elem. Anal. Des.* 2004, 40, 2049-2061.
- [9] ABB [online]. IRB 140 Small, powerful and fast 6-axes robot. Available: <http://new.abb.com/products/robotics/industrial-robots/irb-140>.
- [10] J. Angeles, *Fundamentals of Robotic Mechanical Systems: Theory, Methods, and Algorithms*, 2nd ed. Springer 2003.
- [11] M. W., Spong, S., Hutchinson, and M. Vidyasagar. *Robot Modeling and Control*. John Wiley and Sons INC 2007.
- [12] Smith, S.W., "The Scientist & Engineer's Guide to Digital Signal Processing", 1997, California Technical Pub.
- [13] J., Proakis and D., Manolakis, *Tratamineto digital de señales*, 3rd Ed. Prentice Hall. 1998
- [14] ST Electronics [Online]. Datasheet LIS331DLH Available: <http://www.st.com/web/en/resource/technical/document/datasheet/CD00213470.pdf>. [fecha de consulta 24 de octubre de 2014].

Supported Gold Catalyst in Al₂O₃-TiO₂ for Oxidation of Carbon Monoxide

Rufino M. Nava¹, Abigail Moreno-Martell^{*2}, Bárbara Garcia-Pawelec³

¹ *División de Investigación y Posgrado, Facultad e Ingeniería, Universidad Autónoma de Querétaro (UAQ)
Cerro de las Campanas s/n, 76010, Querétaro, México*

³ *Instituto de Catálisis y Petroleoquímica, CSIC
Cantoblanco, 28049 Madrid, Spain*

¹ rufino@uaq.mx

² bgarcia@icp.csic.es

^{*2} *División de Investigación y Posgrado, Facultad e Ingeniería, Universidad Autónoma de Querétaro (UAQ)
Cerro de las Campanas s/n, 76010, Querétaro, México*

² morenomartell@gmail.com

Abstract— The strong influence of the support properties on the activity of gold catalysts has been observed in many publications. Gold metal dispersed on metal oxides has been applied to a number of catalytic reactions including complete oxidation of hydrocarbons, hydrogenation, NO reduction and CO oxidation. It is established that the catalytic performance of supported gold catalysts in the low temperature CO oxidations is highly sensitive to the catalyst preparation procedure and the nature of support. Considering the nature of support many reducible oxides substrates have been tested as supports for gold nanoparticles but many of them were found to be less stable than that supported on mixed oxide supports.. The influence of metallic mixed oxides on the catalytic response of supported gold catalysts in the CO oxidation reaction was investigated.

In this work, supports based on Al₂O₃-TiO₂, Al₂O₃ and TiO₂ were prepared by sol-gel method for dispersing gold nanoparticles. Gold nanoparticles were deposited on mixed oxides and reducible oxides by deposition-precipitation (DP) using HAuCl₄. The gold supported catalysts were characterized by several techniques: X-ray diffraction (XRD), UV-vis diffuse reflectance spectroscopy (UV-vis DRS) and thermogravimetric analyses (TGA), and N₂ adsorption-desorption isotherms. The XRD characterization of gold catalysts supported showed the presence of XRD peaks from metallic Au, anatase as the TiO₂ crystalline phase and hexagonal gamma alumina as the Al₂O₃ crystalline phase. For UV-vis spectra of catalysts, has been observed the peak position of Au in the metallic state. The Au/Al₂O₃-TiO₂ catalysts manifested the highest catalytic activity between Au/Al₂O₃ and Au/TiO₂.

Keywords: metallic mixed oxides, gold catalysts, gold nanoparticles.

I. INTRODUCTION

In the past decades highly dispersed gold Nanospecies supported on various metal oxides have been reported to be active in many reactions. Since the discovery on the high activity of extremely fine gold nanoparticles in a low temperature CO oxidation [1] and reactivity of gold catalysis supported on different materials were extensively studied. The catalytic activity of these gold catalysts strongly depends on the gold particle size, method of gold deposition, pretreatment conditions and nature of the supports [2]. The gold containing

catalysts have been found more active when metal gold particles are smaller than 5 nm and the method used for preparation of the gold catalyst significantly influences the size of gold nanoparticles. One of the methods most often used for gold catalyst preparation is the deposition-precipitation technique which allows a control of particle size depending on pH and the precipitation inducing agent (urea, hydroxides). At pH of the solution of gold chloride between 6 and 10 it is possible to obtain gold particles smaller than 4 nm [2], [3], [4]. The other principal factor which has a decisive influence on the activity of gold catalysts is the nature of the support. Most of the catalytic supports require a combination of high surface area and good thermal stability [5]. Among the potentially interesting solids, zirconia, alumina and titania have recently attracted considerable attention not only for their remarkable properties in the materials fields, but rather by its potential use as catalyst support. These support, ZrO₂, Al₂O₃, and TiO₂, are most frequently studied because these oxides demonstrated to be “active” in CO oxidation reaction due to their high oxygen storage capacity and well known catalytic and redox properties. The reducible support plays a decisive role in the formation and distribution of oxygen vacancies as well as in gold particle dispersion and shape, which are directly reflected on catalytic activity [2]. Unfortunately, gold nanoparticles supported on ZrO₂, Al₂O₃, and TiO₂ exhibits a low specific area. As a consequence, the gold particles supported on these reducible oxides were found to be less stable than that supported on mixed oxide supports [6]. Mixed oxides are the main supports for gold [2], [3]. The synthesis of mixed oxides by sol-gel is well known to confer important structural, textural and chemical characteristics to noble metal catalysts, due to better control of oxide-oxide interactions at the molecular scale. In addition, the sol-gel process permits to obtain highly homogeneous materials by incorporation of several components in a single-step synthesis [7]. Furthermore, application of the sol-gel technique enhances the formation of structural defects in oxides used as supports thus improving the catalytic activity [8]. The aim of the present work was to investigate the effect of Al₂O₃-TiO₂ mixed oxide prepared by sol-gel on the behavior of Au/Al₂O₃-TiO₂ catalyst in the CO oxidation.

II. EXPERIMENTAL

A. Preparation of the $\text{Al}_2\text{O}_3\text{-TiO}_2$, Al_2O_3 and TiO_2 Support

$\text{Al}_2\text{O}_3\text{-TiO}_2$ support was prepared by a sol-gel method from organo-metallic precursors. For the preparation of $\text{Al}_2\text{O}_3\text{-TiO}_2$ support, the required amount of aluminum isopropoxide $\text{Al}[(\text{CH}_3)_2\text{CHO}]_3$ (98%, Aldrich) was taken and dissolved in 150 mL of 1 propanol (99.5% Sigma-Aldrich) under continuous stirring for 30 minutes. Titanium was incorporated by gently adding to the solution an exact amount of Titanium (IV) isopropoxide ($\text{C}_{12}\text{H}_{28}\text{O}_4\text{Ti}$) (97%, Aldrich) under continuous stirring for 30 minutes. Hydrolysis was attained by addition of deionized water. After 24 hours with moderate agitation, the precipitated solution was filtrated and dried at room temperature for 1 day and at 110°C for 15 h in an oven, and calcined for 6 h at 500°C . For the preparation of Al_2O_3 and TiO_2 supports, the same procedure described above was used.

B. Preparation of the $\text{Au}/\text{Al}_2\text{O}_3\text{-TiO}_2$, Au/TiO_2 , $\text{Au}/\text{Al}_2\text{O}_3$

Gold catalysts were prepared by deposition-precipitation (DP), method using HAuCl_4 (98%, Aldrich) as source of the Au. To obtain the gold concentration corresponding to a theoretical Au loading of 3 wt. %, the appropriate amount (50 mL) of aqueous solution of 3×10^{-3} M of HAuCl_4 was prepared. In order to ensure the complete gold deposition, the

pH of solution was adjusted to 11 with a solution 0.1 M NaOH. This high pH value allows us to control the deposition species and concentration [9]. After this, 1 g of each support was dispersed in HAuCl_4 solution at 70°C for 1 h. In order to avoid the negative effect of chlorine ions on the catalyst activity [10], the solids obtained were several times washed with deionized water. Finally, the samples were dried overnight at 110°C . The references $\text{Au}/\text{Al}_2\text{O}_3$ and Au/TiO_2 , samples were prepared by the DP method employing the same washing and drying conditions as above.

C. Characterization Methods

1) *X-ray diffraction (XRD)*: The determination of the crystalline phases was carried out by X-ray diffraction (XRD). Powder X-ray diffraction measurements of the dried catalysts were carried out using $\text{CuK}\alpha$ radiation ($\lambda=1.5415\text{\AA}$) and a scan rate of $0.5^\circ \text{min}^{-1}$ with step size of 0.009 degree in the range $5^\circ \leq 2\theta \leq 80^\circ$ in a Bruker D8 Advance diffractometer.

2) *UV-vis diffuse reflectance spectroscopy (DRS)*: The characteristic absorption bands of the electronic transition metal derivative were observed by Uv-Vis. UV-vis diffuse reflectance spectra of the dried catalysts were recorded in the 200-800 nm range at room temperature, using a Varian Cary 3 UV-vis spectrometer.

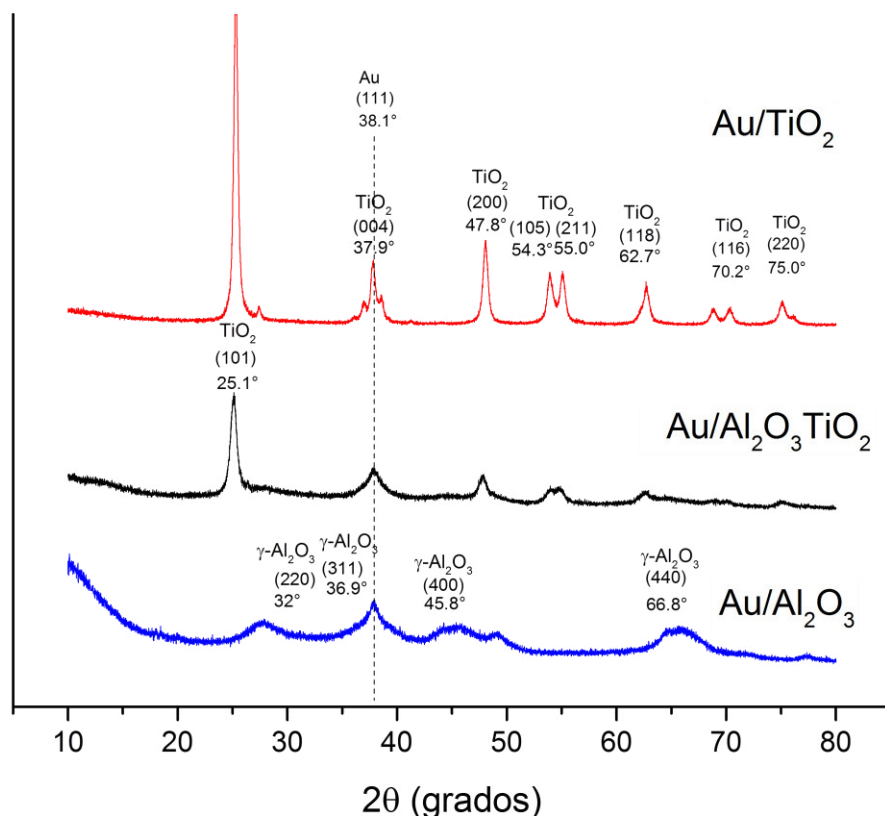


Fig. 1. XRD patterns of the catalysts: $\text{Au}/\text{Al}_2\text{O}_3$, $\text{Au}/\text{Al}_2\text{O}_3\text{-TiO}_2$, and Au/TiO_2

3) *Analysis termogravimetric (TGA)*: The decomposition behavior and weight loss steps were observed in TG curves. TGA analyses of the supports and catalyst were carried out in a TGA Q500 TA Instruments. The samples were performed with 4-8 mg samples on a platinum pan under nitrogen atmosphere and scanned from 25 to 800 °C with a heating rate of 10°C/min. The derivative thermogravimetry (DTG) profiles were obtained from TGA profiles by derivation calculus.

4) *N₂ adsorption-desorption isotherms*: The textural properties (The specific surface area, pore volume and mean pore diameter) of the catalysts were determined from the nitrogen adsorption isotherms recorded at 196 °C with a Quantachrome Autosorb iQ₂ instrument. The samples were previously degassed at 200°C for 10 h under a vacuum (10⁻⁴ mbar) to ensure a clean dry surface, free of any loosely bound adsorbed species. The specific areas of the samples were calculated according to standard Brunauer-Emmett-Teller (BET) equation [11] for data collected in the relative equilibrium pressure interval of 0.03<P/P₀<0.3. Pore size distributions were calculated from the adsorption branch of the corresponding nitrogen isotherm using the Barret-Joyner-Halanda (BJH) method. The total pore volume (V_{total}) was estimated from the amount of nitrogen adsorbed at a relative pressure of 0.99 [12], [13].

5) *Catalytic activity measurements*

Catalytic measurements of CO oxidation were carried in a fixed-bed reactor using ≈40 mg de Au/Al₂O₃- TiO₂ catalysts, accurately weighed for each sample. The catalysts were previously treated with air at 473 K for 4h. After thermal treatment, the reactor was cooled down to 268 K and the air was replaced by a gas mixture consisting of 1 vol.% CO, and 1% O₂ balanced with N₂ to 1 atm (80 mL/min). The molar flow rate of the CO in this gas mixture was 4.36 x 10⁻⁷ mol/s. CO was analyzed at the outlet of reactor with an Agilent Technologies 6890N, Network System gas chromatograph.

The catalytic stability of the gold catalysts for CO oxidation was carried out at 308 K for 8 h. Activities are

described in terms of the total CO conversion as well as the specific reaction rates calculated according to the Eq. (1):

$$r = \frac{X_{CO} \cdot F_{CO}}{m_{cat}} \quad (1)$$

Where r is the specific reaction rate [mol/(g_{cat} s)], X es CO conversion, F_{CO} is the molar flow rate of the CO (mol s⁻¹) and m_{cat} es the catalyst weight (g).

III. RESULTS AND DISCUSSIONS

A. *Characterization of Supports and Catalysts*

1) *X-ray diffraction (XRD)*: XRD patterns were recorded with the aim to investigate the presence of any crystalline in supported gold catalysts. XRD patterns of the studied catalysts are presented in Fig. 1. The pattern of Au/Al₂O₃-TiO₂, Au/Al₂O₃ and Au/TiO₂ are characteristic by the presence of XRD peaks from metallic Au, anatase as the TiO₂ crystalline phase and hexagonal gamma alumina as the Al₂O₃ crystalline phase. The Au/Al₂O₃-TiO₂ and Au/Al₂O₃ catalysts reveals diffraction pattern of alumina by the presence of four theta peaks at 32°, 36.9, 45.8 and a more intense peak at 66.8 corresponding to the (222), (400) and (440) crystallographic planes, respectively (JCPDS reference No. 00-010-0425) [14]. The anatase is the only titania phase present in this material, as indicated by the peaks at 2θ ≈ 24.5°, 38°, 48°, 54.5°, 62.5°, 70° and 75° (JCPDS-ICDD 21-1272). Only one peak of (110) rutile reflection at 27.4° was detected. As seen in Fig. 1 the gold catalysts only show a narrow peak of FCC gold lattice in 38.1° corresponding to (111). This peak is clear in Au/Al₂O₃, but in Au/TiO₂ and Au/Al₂O₃-TiO₂ is overlapping with the peak of anatase reflection at 27.9°. All the catalysts don't exhibit diffraction lines at 2θ= 44.2°, 64.6°, 77.5° and 81.4° corresponding to the (200), (220), (311) an (222) planes, (JCPDS-ICDD 04-0784). These results indicate that the gold nanoparticles are highly dispersed, with a particle size lower than 4 nm (according to the detection sensitivity of this technique).

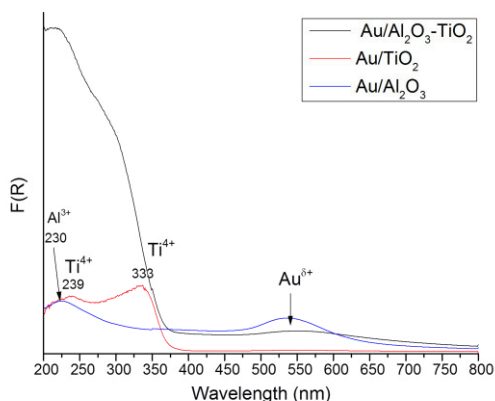


Fig. 2. DRS UV-vis spectra of the dried catalysts: Au/Al₂O₃, Au/TiO₂, and Au/Al₂O₃-TiO₂.

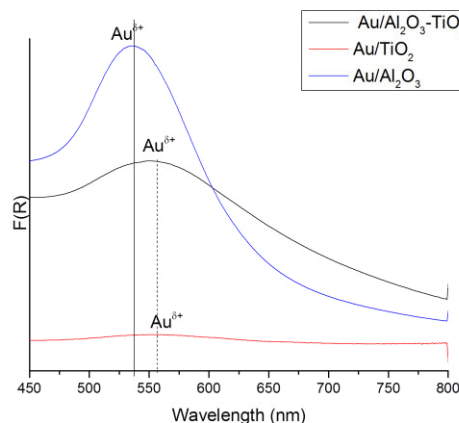


Fig. 3. DRS UV-vis spectra of the dried catalysts in the 400-800 nm: Au/Al₂O₃, Au/TiO₂, and Au/Al₂O₃-TiO₂.

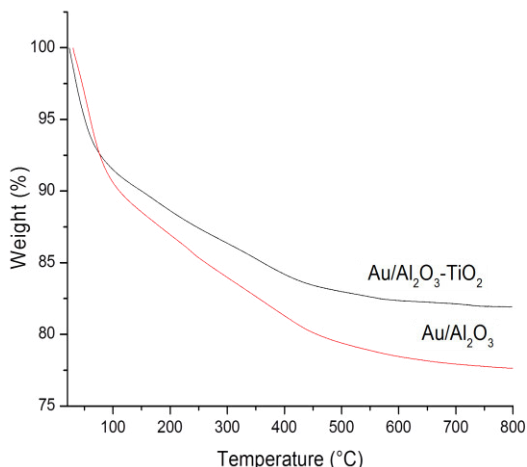


Fig. 4. TGA curves of the Au catalyst: Au/Al₂O₃ and Au/Al₂O₃-TiO₂.

2) *UV-vis diffuse reflectance spectroscopy (DRS)*: The UV-vis diffuse reflectance spectra of the dried gold catalysts are presented in Figs. 2. The Ti-containing gold catalysts exhibit two absorption bands centered at ca. 230 and 330 nm. The former bands are associated with the charge transfer caused by the electron migration between tetrahedral site of Ti⁴⁺ and O²⁻ [15], [16]. Also, the Al₂O₃-containing catalysts exhibit an absorption band at ca. 220 nm. In addition to the charge-transfer bands due to Al₂O₃ and TiO₂, the UV-vis spectra of the gold catalysts show a wide band in the 450-700 nm region originated by the excitation of surface Plasmon vibration due to the presence of gold nanoparticles..

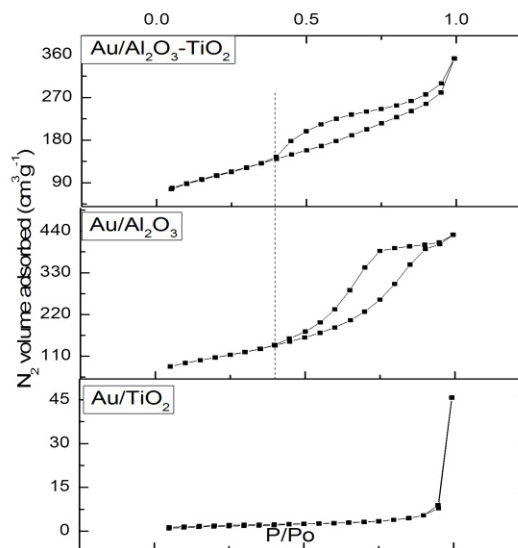


Fig. 6. N₂ adsorption-desorption isotherms of the gold catalysts: Au/Al₂O₃, Au/TiO₂ and Au/Al₂O₃-TiO₂.

This plasmon did not appear of the naked supports (figure not shown here). It is known that this band is affected by the dispersed metal particle size and shape and the dielectric properties of the environment that surround it (Fig. 3) [17]. Thus, a shift to larger wavelength in the longitudinal Plasmon vibration is an indication of the extent of aggregation of the gold nanoparticles. For the Au/Al₂O₃ catalysts, the typical plasmon band of small Au particles centered at 535 nm appears very clearly in figure 3. As seen, there is a small shift of the longitudinal plasmon vibration due to the presence of TiO₂. One probable explanation of this phenomenon is that TiO₂ has the potential to alter the local environment of gold, inducing shifts in the position of the band.

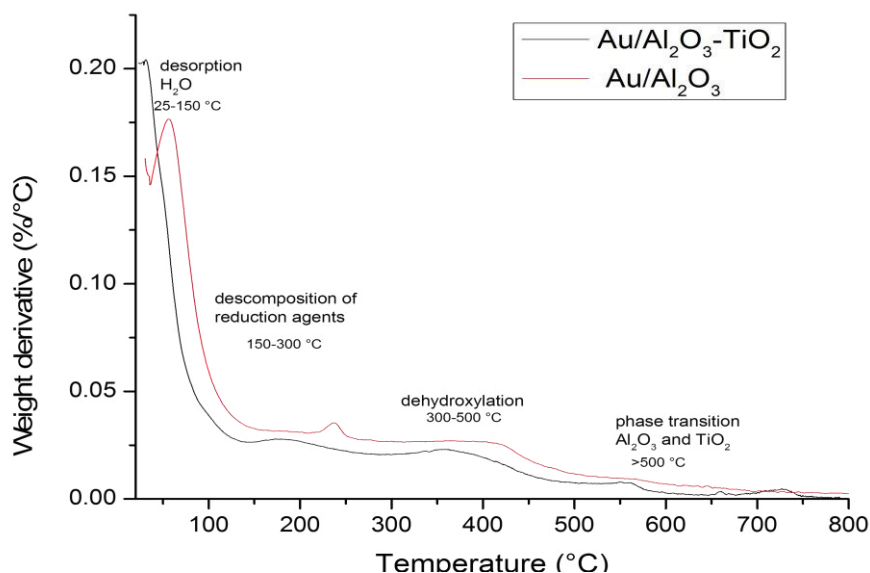


Fig. 5. DTG curves of the Au catalysts: Au/Al₂O₃ and Au/Al₂O₃-TiO₂.

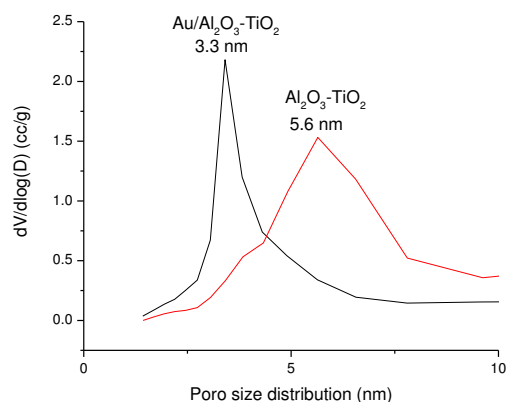


Fig. 7. Pore distribution of the gold catalysts as determined from adsorption branch of the N_2 adsorption-desorption isotherm using the BJH methodology.

3) *Analysis termogravimetric (TGA)*: TGA and DTG curves of the Au catalysts supported are shown in Fig. 4 and 5. The catalysts show that the weight loss mainly occurs in four stages: (i) from room temperature to ca. 150°C , due to the desorption of physically bonded water and residual solvent; (ii) from ca. 150°C to 300°C , due to the desorption of chemically bonded water and also the decomposition of reducing agents used; (iii) between 300 and 500°C due to a dehydroxylation caused by the decomposition of the phase $\gamma\text{-Al}_2\text{O}_3$; (iv) above 500°C due to surface dehydration and subsequent phase transitions (from $\gamma\text{-}$ to $\theta\text{-Al}_2\text{O}_3$) [5], [12], [18]. In addition, the weight loss observed in $\text{Au/Al}_2\text{O}_3\text{-TiO}_2$ catalyst (19%) is less than $\text{Au/Al}_2\text{O}_3$ catalyst (23%). This demonstrates the superior thermal stability of the $\text{Al}_2\text{O}_3\text{-TiO}_2$ support.

4) *Textural properties*: The textural properties of the dried supported Au catalysts were evaluated by N_2 adsorption-desorption isotherms at -196°C . The N_2 adsorption-desorption isotherms and the corresponding pore size distributions (Fig. 6 and 7) were calculated from the adsorption branch of N_2 isotherm by using the Barrett-Joyner-Halenda model. According to IUPAC'S classification, the $\text{Au/Al}_2\text{O}_3$ and $\text{Au/Al}_2\text{O}_3\text{-TiO}_2$ isotherms show a typical type IV and II shape and display H3 and H2-type hysteresis loops respectively [19], [20].

And the Au/TiO_2 show a typical type I shape and display H4-type hysteresis loops. This indicates that the support change the form of hysteresis loop. Thus, in addition to structural porosity, all samples have a textural porosity.

The Fig. 7 shows the pore size distributions of support and catalyst expressed as the plot of $dV/d\log(D)$ versus pore diameter applied to the adsorption branch of the nitrogen isotherm. As seen in this figure, the catalyst shows a uniform, narrow pore size distribution centered at about 3.3 nm, while the support is about 5.6 nm. The pore volume decrease by $\approx 55\%$ is due to the Au incorporation onto support.

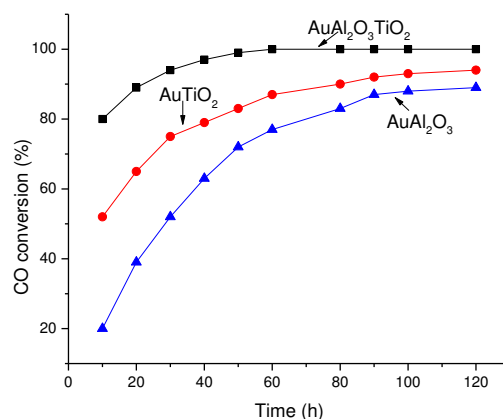


Fig. 8. Catalytic activity the Au catalyst: $\text{Au/Al}_2\text{O}_3$, Au/TiO_2 and $\text{Au/Al}_2\text{O}_3\text{-TiO}_2$

5) *Catalytic activity*: The catalytic activity of Au catalysts was investigated by temperature-programmed CO oxidation reaction performed in temperature range 20°C . The stability of catalysts, Au/TiO_2 , $\text{Au/Al}_2\text{O}_3$ and $\text{Au/Al}_2\text{O}_3\text{-TiO}_2$, is compared in Figure 8. As seen in this figure the catalysts Au/TiO_2 and $\text{Au/Al}_2\text{O}_3$ shows lower stability than $\text{Au/Al}_2\text{O}_3\text{-TiO}_2$. Considering the time-on stream stability trend is: $\text{Au/Al}_2\text{O}_3\text{-TiO}_2 > \text{Au/TiO}_2 > \text{TiO}_2$. Thus, one might suppose that the large stability is one of the factors contributing to the superior activity of the $\text{Au/Al}_2\text{O}_3\text{-TiO}_2$ in the reaction of total CO oxidation (Figure 8).

IV. CONCLUSION

We have shown that the $\text{Al}_2\text{O}_3\text{-TiO}_2$ oxides metallic mixed could be successfully used as supports for the preparation of gold catalysts for CO oxidations. This catalysts $\text{Au-Al}_2\text{O}_3\text{-TiO}_2$ has a large stability and a superior activity that $\text{Au/Al}_2\text{O}_3$ and Au-TiO_2 in the reaction of total CO oxidation. The Au catalyst supported on oxides metallic mixed obtained by the sol-gel method suggests a low mobility of the Au nanoparticles, probably due to the higher thermal stability (by TGA). The oxides metallic mixed improved the catalytic performance of supported gold catalysts. This could be due probably a synergetic effect between the gold nanoparticles and the $\text{Al}_2\text{O}_3\text{-TiO}_2$ nanoparticles (by XRD and UV-vis).

ACKNOWLEDGMENT

The authors would like to express their gratitude to CONACYT for the financial support. The authors are greatly thankful to Dr. R. Velázquez for their technical support in thermogravimetry and DRX studies.

REFERENCES

- [1] M Haruta, T. Kobayashi, H. Sano, and N. Yamada, "Novel Gold Catalysts for the Oxidation of Carbon Monoxide at a Temperature far Below 0 °C", *Chemistry Letters*, vol. 16, pp. 405-408, 1987. doi:10.1246/cl.1987.405
- [2] G.C. Bond, and D.T. Thompson, "Catalysis by Gold", *Catalysis Reviews: Science and Engineering*, vol. 41, pp. 319-388, 1999. Doi:10.1081/CR-100101171
- [3] G.C. Bond, C. Louis, and D.T. Thompson, "Catalysis by Gold", *Catalytic Science Series*, vol. 6, Graham J. Hutchings (Ed.) Imperial College Press, London, 2006.
- [4] I. Sobczak, K. Jagodzińska, and M. Ziólek, "Glycerol oxidation on gold catalysts supported group five metal oxides – A comparative study with other metal oxides and carbon based catalysts", *Catalysis Today*, vol. 158, pp. 121 – 129, December 2010.
- [5] T. Klimova, M.L. Rojas, P. Castillo, R. Cuevas, and J. Ramírez, "Characterization of Al₂O₃-ZrO₂ mixed oxide catalytic supports prepared by the sol-gel method", *Microporous and Mesoporous Materials*, vol. 20, pp. 293-306, 1998.
- [6] F. Moreau, G.C. Bond, B. van der Linden, B.A.A. Silberova, and M. Makkee, "Gold supported on mixed oxides for the oxidation of carbon monoxide," *Applied Catalysis A*, vol. 347, no. 2, pp. 208–215, 2008.
- [7] J.B. Miller, and E.I. Ko, "Homogeneously Dispersed Silica Dopant for Control of the Textural and Structural Evolution of an Alumina Aerogel", *Catalysis Today*, vol. 43, pp. 52-67, August 1998.
- [8] A. Vazquez, T. Lopez, R. Gomez, and X. Bokhimi, "Synthesis, characterization and catalytic properties of Pt/CeO₂-Al₂O₃ and Pt/La₂O₃-Al₂O₃ sol-gel derived catalysts, *Journal of Molecular Catalysis A: Chemical*, vol. 167, pp. 91-99, February 2001.
- [9] S.J. Lee, and A. Gavrilidis, "Supported Au Catalysts for Low-Temperature CO Oxidation Prepared by Impregnation", *Journal of Catalysis*, vol. 206, pp. 305-313, March 2002.
- [10] L. Escamilla-Perea, R. Nava, B. Pawelec, M.G. Rosmaninho, C.L. Peza Ledesma, J.L.G. Fierro, "SBA-15- supported gold nanoparticles decorated by CeO₂: Structural characteristics and CO oxidation activity", *Applied Catalysis A: General*, vol. 381, pp. 42-53, 2010.
- [11] S. Brunauer, P.H. Emmett, and E. Teller, "Adsorption of Gases in Multimolecular Layers", *Journal of the American Chemical Society*, vol. 60, pp. 309-319, February 1938.
- [12] A.P. Ferreira, D. Zanchet, R. Rinaldi, U. Schuchardt, S. Damyanova, and J.M.C. Bueno, "Effect of the CeO₂ content on the surface and structural properties of CeO₂-Al₂O₃ mixed oxides prepared by sol-gel method", *Catalysis A: General*, vol. 388, pp. 45-56, 2010.
- [13] S.F. Galata, D. Tsoutsou, G. Apostolopoulos, P. Tsipas, A. Sortiropoulos, G. Mavrou, Y. Panayiotatos, and A. Dimouls, "Stabilization of a veri high-k tetragonal phase in Ge-doped ZrO₂ films grown by direct doping with Germanium", *Microelectronic Engineering*, vol. 86, pp. 1226-1628, September 2009.
- [14] J. Yu, R. Huo, C. Wu, X. Wu, G. Wang, and P. Jiang, "Influence of Interface Structure on Dielectric Properties of Epoxy/Alumina Nanocomposites", *Macromolecular Research*, vol. 8 (20), pp. 816-826, 2012.
- [15] A. Tuel, and L.G. Hubert-Pfalzgraf, "Nanometric monodispersed titanium oxide particles on mesoporous silica: synthesis, characterization, and catalytic activity in oxidation reactions in the liquid phase", *Journal of catalysis*, vol. 217, pp. 343-353, July 2003.
- [16] C.L. Peza-Ledesma, L. Escamilla-Perea, R. Nava, B. Pawelec, J.L.G. Fierro, "Supported gold catalysts in SBA-15 modified with TiO₂ for oxidation of carbon monoxide", *Applied Catalysis A: General*, vol. 375, pp. 37-48, 2010.
- [17] P.Claus, A. Brückner, Ch. Mohr, and H.Hofmeister, "Supported Gold Nanoparticles from Quantum Dot to Mesoscopic Size Scale: Effect of Electronic and Structural Properties on Catalytic Hydrogenation of Conjugated Functional Groups", *Journal of the American Chemical Society*, vol. 122, pp. 11430- 11439, 2000. doi:10.1021/ja0012974
- [18] P.D.L. Mercera, J.G. van Ommen, E.B.M. Doesburg, A.J. Burggraaf, and J.R.H. Ross, "Stabilized tetragonal zirconium oxide as a support for catalysts: evolution of the texture and structure on calcination in static air." *Applied Catalysis*, vol.78 (1), pp. 79-96, 1991.
- [19] G. Leofanti, M. Padovan, G.Tozzola, and B. Venturelli, "Surface area and pore texture of catalysts, *Catalysis Today*, vol. 41, pp. 207-219, 1998.
- [20] K.S.W Sing, D.H. Everett, R.A.W. Haul, L. Moscou, R.A. Pierotti, J. Rouquerol, and T. Siemieniewska, "Reporting physisorption data for gas/solid systems with special reference to the determination of surface area and porosity". *Pure and applied chemical science*, vol. 57, pp.603–619, 1984. doi:10.1351/pac198557040603

A Speed Performance Comparative of Field Oriented Control and Scalar Control for Induction Motors

Martinez-Hernandez M. A.¹, Gutierrez-Villalobos J. M.², Malagon-Soldara S. M.³, Mendoza-Mondragon F.⁴ and Rodriguez-Resendiz J.⁵

^{1,2} *Mecatrónica, Facultad de Ingeniería, Universidad Autónoma de Querétaro
Cerro de las Campanas Col. Las Campanas s/n CP76010, Querétaro, Qro.*

¹ moises.martinez@uaq.mx

² marcelino.gutierrez@uaq.mx

³ smalagon@uaq.mx

⁴ fmendoza@uaq.mx

⁵ juvenal@uaq.edu.mx

Abstract— Many schemes have been proposed to control induction motors, however all these systems this kind of motors consist in complex systems. One of the most precise control schemes is the Field Oriented Control (FOC), although Scalar Control (SC) is simple compared to the construction of the FOC and others. In this work a SC and a FOC for induction motors are implemented. The goal of this study is to identify the advantages and disadvantages of each controller in conditions such as: load changes, open loop, with or without encoder in a speed profile. Each controller was implemented on the same motor with commercial equipment. Each response is analyzed and explained by graphics considering the performance in different speeds and the response to compensate changes in load.

Keywords— induction motor; scalar control; field oriented control; comparison.

I. INTRODUCTION

The three-phase AC Induction Motors (3ϕ IM) are commonly used in many speed applications, the use of these motors is due to its high performance, quiet operation, low cost, and low maintenance cost; allowing its use in pumps, compressors, conveyors, fans, automated processes, and different mechatronic systems. The common control techniques for 3ϕ IM are [1]:

- Scalar Control or Voltage/frequency (V/f).
- Field Oriented Control (FOC).
- Direct Torque Control (DTC).

DTC and FOC are the most used techniques to control for 3ϕ IM [2]. Both controllers are used in applications that were exclusive for DC motors, where a fast dynamic response is required [3]. FOC and DTC are techniques to decouple the magnetic flux and current using mathematical transformations in order that flux and current are controlled independently and reoriented to obtain a good performance [4].

Despite these techniques are widely used, the FOC is the most popular control method for 3ϕ IM in applications where high performance is required [5].

Some applications such as economical speed control can be achieved using the SC method, where the V/f ratio is kept constant to maintain the stator flux linkage. SC is commonly implemented in commercial drives, due to their simplicity.

On other hand, in this work are considered a commonly methodology, with the use of transducers and a methodology free of transducers to measure the signals. Sensorless technique has been widely adopted in many industry applications, because of the advantages of reduced cost and increased reliability by eliminating the position sensor and related cabling connections [6]. Although, FOC and SC have been analyzed previously to test its stability and fault tolerance in [7] and [8]. It is important to know the Induction Motor (IM) response using a basic control, without observers or complex algorithms. This work presents a methodology for analyzing the responses of sensorless FOC and SC, both operating in open and closed loop, with load changes in speed profile.

II. SCALAR CONTROL

SC does not use a vector controlled drive scheme. The scalar variable speed is obtained by a direct measurement or calculation, and it is used in closed loop and open loop feedback formats. Although its transient behavior is not ideal, a scalar system tends to a satisfactory steady state response.

SC process consists in controlling IM speed by means of the adjustable magnitude of stator voltages and frequency and tries to maintain the air gap flux at the desired steady-state value. The circuit in the Fig. 1 describes how this technique works by trying to emulate a simplified version of the steady-state.

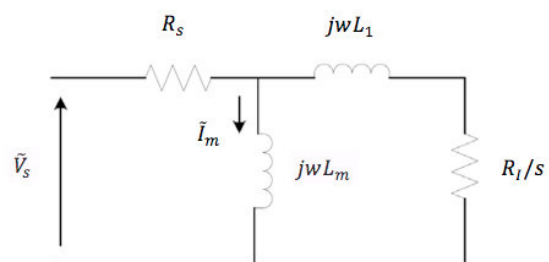


Fig. 1. Induction motor equivalent circuit.

Where R_s is the stator resistance and its value is zero by convention, L_{ls} is the stator leakage inductance and is embedded into the rotor leakage inductance L_{lr} . The air gap flux is represented by the magnetizing inductance, and its equation is represented by:

$$L_l = L_{ls} + L_{lr}$$

As a result, the magnetizing current that generates the air gap flux can be approximately the stator voltage to frequency ratio, with the next phasor equation for steady-state analysis:

$$\tilde{I}_m \cong \frac{\tilde{V}_s}{j\omega L_m}$$

The equation can be simplified whether IM is operating in the linear magnetic region, thus L_m is:

$$I_m = \frac{\Lambda_m}{L_m} \cong \frac{V_s}{(2\pi f)L_m} \Rightarrow \Lambda_m \propto \frac{V_s}{f}$$

The magnetic flux remains constant and torque becomes independent from the power supply frequency whether ratio V_s/f ratio remains constant at any frequency change. At different speeds the V_s/f ratio keeps constant and it is possible to maintain Λ_m constant. For that reason the stator voltage must increase proportionally to the speed, in order to keep V_s/f ratio. The slip compensation is added in the system with the speed measurement. In the Fig. 2 is shown the closed-loop V/Hz system with a speed sensor. There are three speed ranges in the V/Hz profile as shown in the Table I.

TABLE I. SCALAR CONTROL PROFILES

Hz	Properties
$0-f_c$	<p>A voltage is required, so the voltage drop across the stator resistance cannot be neglected and must be compensated for by increasing the V_s</p> <p>Not linear</p> <p>The cutoff frequency f_c and the suitable stator voltages may be analytically computed from the steady-state equivalent circuit $R \neq 0$</p>
f_c-f_{rated}	<p>It follows the constant V/Hz relationship</p> <p>The slope actually represents the air gap flux quantity</p>
$>f_{rated}$	<p>The constant V_s/f ration cannot be satisfied because the stator voltages would be limited at the rated value in order to avoid insulation breakdown at stator windings</p> <p>The resulting air gap flux would be reduced, and this will unavoidably cause the decreasing develop torque correspondingly.</p> <p>This region is called "field weakening"</p>

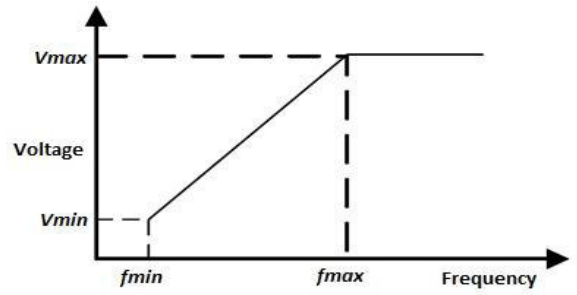


Fig. 2. Stator voltage versus frequency profile.

A reference at as a lower limit on frequency is acceptable to applications such a fan and blower drives where the speed response is not critical. Since the rated voltage and maximum frequency information are needed to implement the profile. The command frequency is allowed to go below the minimum frequency f_{min} , with the output voltage saturated at a minimum value V_{min} . Also, when the command frequency is higher than the maximum frequency f_{max} , the output voltage is saturated at a maximum value V_{max} .

The overall system implementing a 3 ϕ IM with V/f drive is depicted in Fig. 3. The IM is driven by the conventional voltage-source inverter.

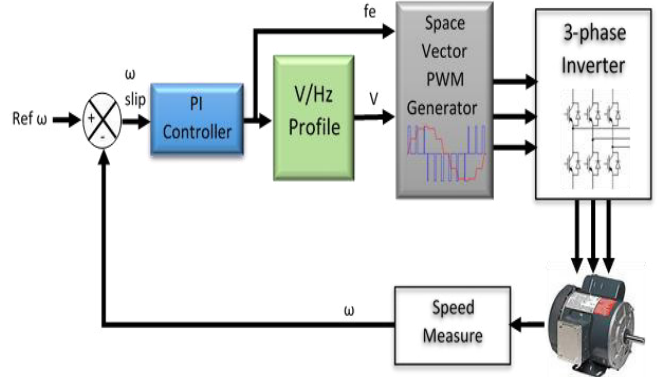


Fig. 3. Standar scalar control for Induction Motor.

III. FIELD ORIENTED CONTROL

The induction machine control scheme is more difficult than a DC motor control, due to its non-linear nature of the relationship between the stator current and torque or flux. An accurate representation of the real behavior of the IM is given by a field oriented model, whose principle is based on a control vector system.

FOC lets us decouple torque and magnetization flux; stator flux components are produced by this decoupling, so it is used such as independent torque control. FOC consist of controlling stator currents represented by a vector whose projections transform a 3 phase and speed dependent system into a two coordinates (q and d) with a time invariant system. Thus, two constants inputs are needed by FOC which are the torque component and the flux component, those must be aligned respectively with the q and d coordinates.

Working with projections mean that instantaneous electrical quantities are used by the control structure and it is possible to solve typical scalar control problems such as the ease of reaching constant reference torque component and stator current flux components.

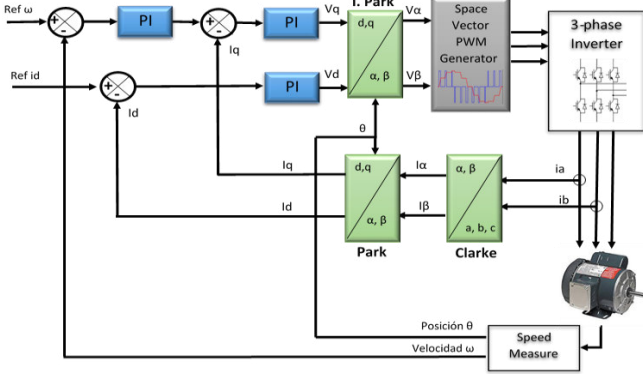


Fig. 4. IM standar field oriented control.

The three phase voltages, currents and fluxes of AC-motors are analyzed in terms of complex space vectors. With regard to the currents, space vector is defined as shown in equation below. Assuming that i_a, i_b, i_c are stator-phase instantaneous currents, then the complex stator current vector \vec{i}_s is defined by:

$$\vec{i}_s = i_a + \alpha i_b + \alpha^2 i_c$$

Where $\alpha = e^{j\frac{2}{3}\pi}$ and $\alpha^2 = e^{j\frac{4}{3}\pi}$ represent the spatial operators. The Fig. 5 shows the stator current complex space vector.

Where a, b and c are the three phase system axes. This current space vector depicts the three phase sinusoidal system. It still needs to be transformed into a two time invariant coordinate system. This transformation is split into two steps:

- Clarke transformation which outputs a two co-ordinate time variant system, $(a,b,c) \Rightarrow (\alpha, \beta)$.
- Park transformation which outputs a two co-ordinate time invariant system, $(\alpha, \beta) \Rightarrow (d,q)$.

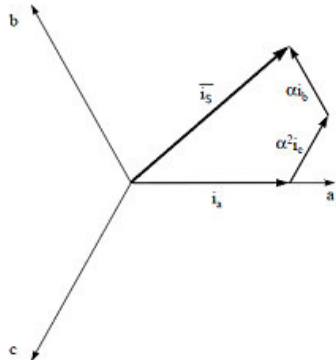


Fig. 5. Stator current space vector and its component in (a,b,c).

IV. DESCRIPTION OF EXPERIMENTAL SYSTEM

Tests were performed with a 3φIM whose characteristics are shown in Table II, the motor was supplied with TMDSHVMTRPFCKIT kit, which contains a Texas Instruments (TI) DSC TMS320C28035. Using Space Vector PWM technique, the DSC produces 6 PWM signals to control the inverter and control the rotor speed, these changes are controlled from a PC with Code Composer Studio. The implementation of the algorithms was using Digital Motion Control (DMC) libraries from TI, using the basic elements of each control as shown in Fig. 3 and Fig. 4. In order to obtain an analysis of each control, tests were conducted on a bench are shown in Fig. 7. The Conditions and tests are summarized in Table IV.

a) Sensorless

Algorithms of DMC libraries were used to carry out speed estimation, where two motor phases are measured to estimate the motor electric flux, and then, it is used to estimate the speed as shown in Fig. 6.

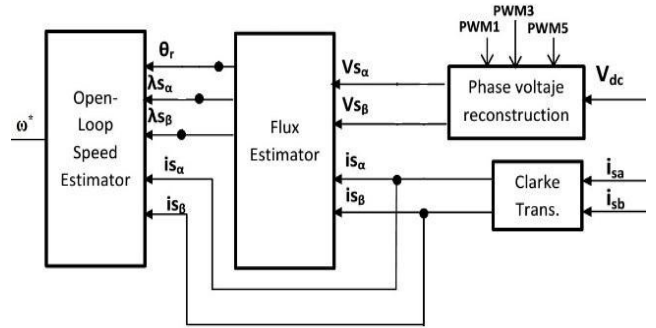


Fig. 6. IM speed estimation scheme [9].

b) Close Loop and Open Loop

The variable speed drive provides a current of 10 A, as a security system, it is protected by a fuse in the power input, in addition, the software protects IM from currents above 8 A. To close the control loop, tests were made with speeds under 40% of rated speed, due to the current demand.

c) Load

A DC motor, Table III, was used to produce mechanic loads on the IM. A load cell was incorporated between both motor shafts, load cell signal was introduced to a data acquisition card (DAQ) and processed by National Instruments (NI) LabView software. Finally, the torque applied was plotted to monitor this signal.

The load was applied an instant time when the engine was at steady state in a defined speed, this was to see the current drawn by the motor and test the efficiency of the controller in speed.

d) Speed Profiles

Functionality algorithms of the controller are used to monitor motor efficiency at different speeds, especially under conditions explained above.

Three speeds were applied: low, medium and high speed. Low speed at 10% of the nominal value, 50% as average speed and 90% as high speed, except for the closed loop where speeds

were 10% and 30%, because the current drawn by the motor to compensate the load exceeded protection capabilities.

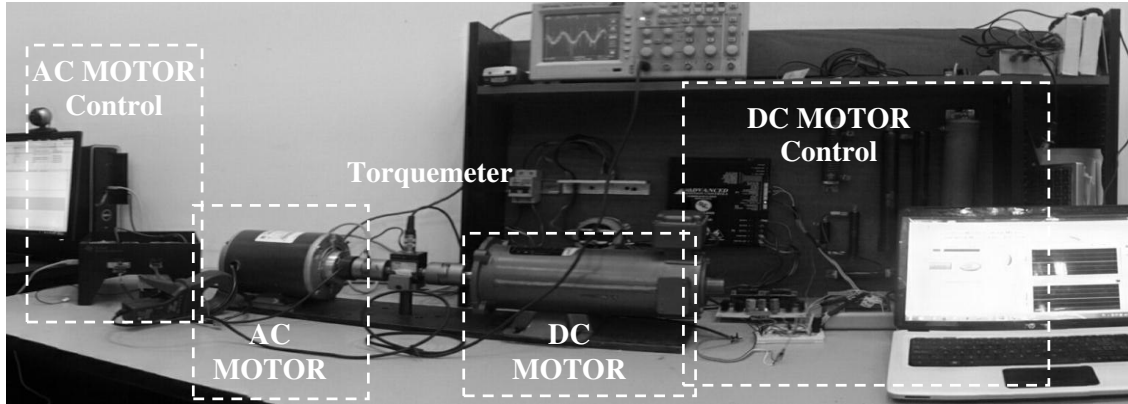


Fig. 7. Test Bench for IM control.

TABLE II. INDUCTION MOTOR PARAMETERS

1/4 HP, 1800 rpm, 208-230 V, 10 A, 3 phase, 4 pole, 60Hz
Stator Resistance R_s : 11.05 Ω
Stator Inductance L_s : 0.316423 H
Rotor Resistance R_r : 6.11 Ω
Rotor Inductance L_r : 0.316423 H
Mutual Inductance L_m : 0.293939 H

TABLE III. DIRECT CURRENT MOTOR PARAMETERS

Power : 1/2 Hp
RPM: 1750
Voltage (dc): 180 V
Current: 2.5 A
Torque Constant (Kt): 1 Nm/A
Torque Max: 2.5 N

TABLE IV. TEST BENCH LIST

Fiel Oriented Control		
Sensorless		
Open-loop		
Close-loop		
Low Velocity	Low Velocity	Medium Velocity
Scalar Control		
Sensorless		
Open-loop		
Close-loop		
Low Velocity	Low Velocity	Medium Velocity

V. RESULTS

Sensorless FOC was the first algorithm tested in open loop with a specific velocity profile (as previously explained). Fig. 8 shows an error in the velocity estimated at low revolution, however, as speed increases, estimation algorithm gets closer to the actual value, which was measured with a QD200 encoder.

The profile shows four speeds that are: 180, 540, 1260 and 1440 rpm. A 1-Nm torque with a DC motor is applied; due it is open-loop, disturbance directly affected IM speed, which decreases when applied load was returned to the desired value when removed. Similarly, because there is no control loop, the current drawn by the motor is approximately 2 A as shown in Fig. 9. The current frequency only changes as the engine speed rises.

When the control loop is closed as seen in Fig. 10, the velocity estimator shows erroneous values when a load is applied, then the motor change its direction to the load rotation, for an instant, in order to compensate and a current consumption with amplitudes of 2 Amp and 1 Amp of noise, as shown in Fig. 11.

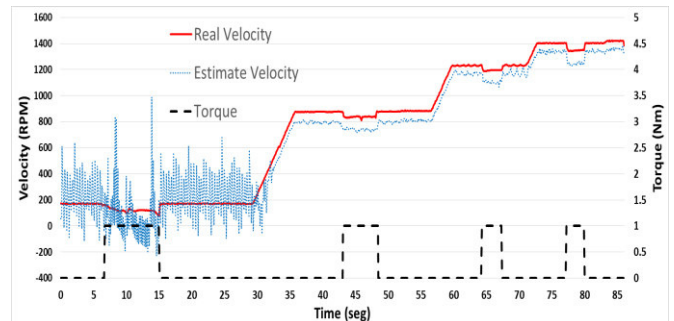


Fig. 8. Sensorless FOC open-loop response.

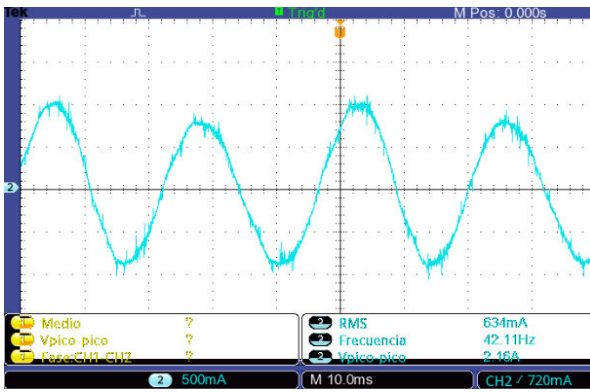


Fig. 9. FOC Sensorless open-loop current.

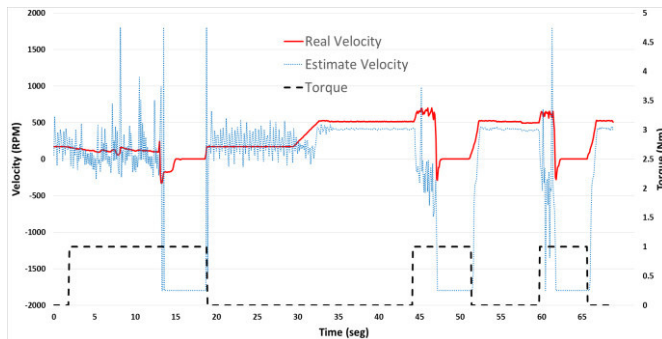


Fig. 10. FOC Sensorless closed-loop response.

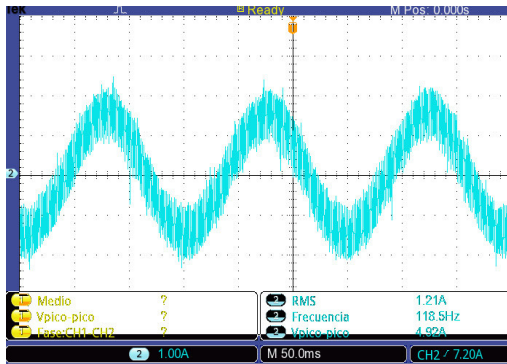


Fig. 11. FOC Sensorless closed-loop current.

With this observed behavior, it is understood that the estimation algorithm will not allow closing the loop without forcing the motor, therefore, a closed loop test with sensed scheme was performed.

Fig. 12 shows the load disturbance in speed and how it is compensated. The current consumption is higher if the speed increases. Fig. 13a shows the current consumption without load and Fig. 13b shows the consumption with load, consumption is twice the current. Considering the characteristics of the motor, Table II, only 2 speeds were tested, as a safety measure to avoid damaging the AC motor.

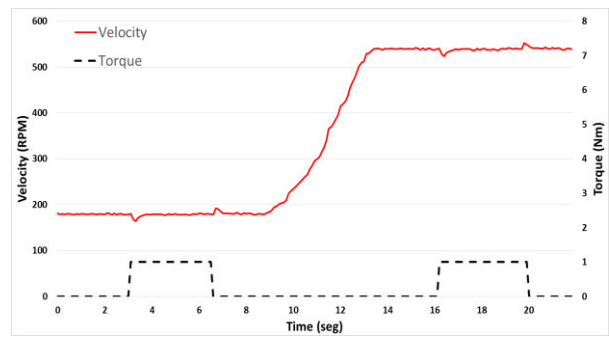


Fig. 12. Sensed FOC close-loop response.

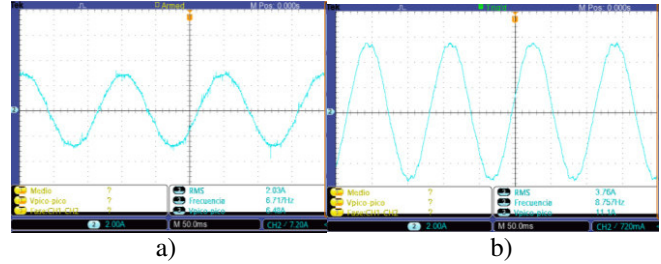


Fig. 13. Sensed FOC close-loop currents a) without load b) with load.

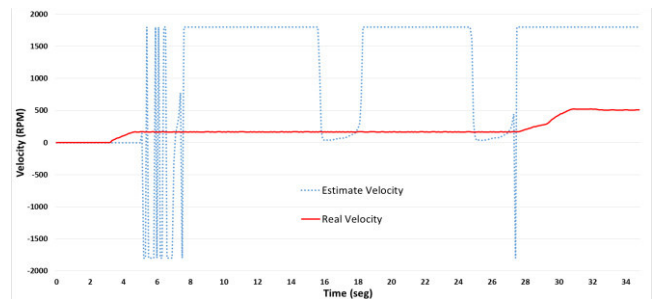


Fig. 14. Sensorless scalar open-loop response.

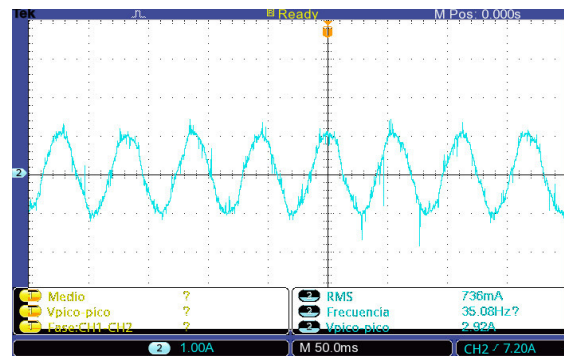


Fig. 15. Scalar Sensorless open-loop current.

In SC testing, greater error was observed in the speed estimator, compared to FOC, this is caused by a saturation in the variable speed. This result does not affect the current consumption, due the use of open-loop. At this point the use of the peed estimator for testing the SC closed-loop is discarded.

Fig. 16 shows the results of implementing the sensed SC, similarly in FOC, the open-loop does not compensate the speed error when a load is applied. However, a noise is observed in the motor current Fig. 17.

VI. CONCLUSIONS

This work presents two testings under different control technique conditions, the tests were performed in order to make a comparison in IM speed performance, it is incorrect to say that one technique is better than the other one.

Although the sensorless technique simplifies the installation by saving a sensors installation, it has disadvantages in SC both open and closed loop, however, the FOC is more useful when used in open loop. In this paper an estimate algorithm of DMC libraries was used, however, there are currently various schemes to estimate the speed, such observers, fuzzy control, genetic algorithms, and neural networks, among others. It would have to be consider using a robust estimator to load changes.

For both techniques a sensor was required to obtain better results. The performance of both controllers in closed-loop was similar, except for the current consumption, the SC had higher consumption compared to FOC, and in addition, at low speed SC was more sensitive to disturbances. It is important to consider to use a motor with more features to support high currents and try it at high speeds. As mentioned above, the tests were limited by security of motor and control system, however, literature has reported some works based on classical schemes control with good speed performance without high power consumption.

Also, it is important use a platform with greater power capacity, the employed kit was only for test and learn the control schemes, not for industrial use, the platform must meet the requirements based on the demand of the application.

Therefore, the SC is useful in medium and high speeds, in open-loop has a speed close to the desired one and the main advantage, is the control simplicity, on an another hand, the FOC offers excellent performance in closed loop and open loop with sensor, quickly compensates disturbances and can operate with lower currents than SC.

A methodology that allows testing innovations in techniques of control was presented, because it shows the basic elements for speed performance criteria, and perform an appropriate comparison IM controller key points.

Acknowledgement: The authors would like to thank CONACyT and UAQ for economic support.

REFERENCES

- [1] H. Toliyat, E. Levi, and M. Raina, "A review of RFO induction motor parameter estimation techniques," *Energy Conversion, IEEE*, vol 18, pp. 271–283, 2003.
- [2] M. Naouar, E. Monmasson, A. Naassani, I. Belkhdja, and N. Patin, "FPGA Based Current Controllers for AC Machine Drives - A Review," *IEEE Transactions on Industrial Electronics*, vol 4, pp. 1907-1925, 2007.
- [3] X. Garcia, B. Zigmund, P. Terlizzi, and L. Salvatore, "Comparison Between FOC and DTC Strategies for Permanent Magnet Synchronous Machines," *Advances in Electrical and Electronic Engineering*, pp. 76-81, 2011.
- [4] M. Merzoug, and F. Naceri, F, "Comparison of Field Oriented Control and Direct Torque Control for Permanent Magnet Synchronous Motor (PMSM)". *Proceedings World Academy of Science, Engineering and Technology*, vol 45, pp.299–304, 2008

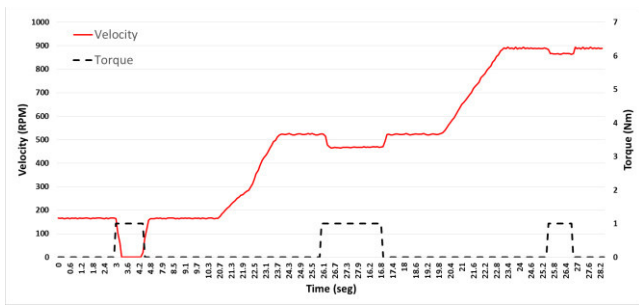


Fig. 16. Sensored scalar open-loop response.

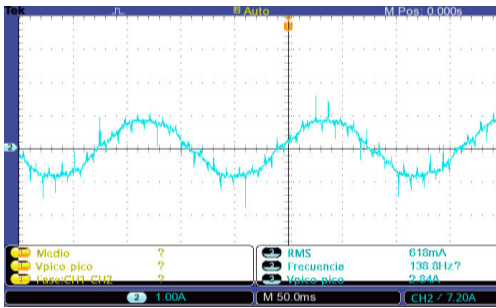


Fig. 17. Sensored scalar open-loop current.

When the SC was implemented in closed-loop, a better performance was observed, to compensate the disturbances in speed as shown in Fig. 18, unlikely in sensored FOC closed-loop, the disturbance at low speed is more noticeable, and similar at high speed. The difference is the current consumption, Fig. 19a shows the consumption with motor unloaded, in contrast at Fig. 19b where current spikes are observed. These high current values might damage equipment, consequently, only results at speeds of 180 and 540 rpm are shown, similar to the FOC test in closed-loop.

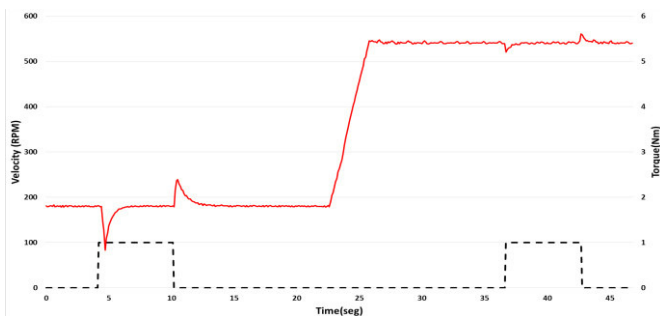


Fig. 18. Sensored scalar close-loop response.

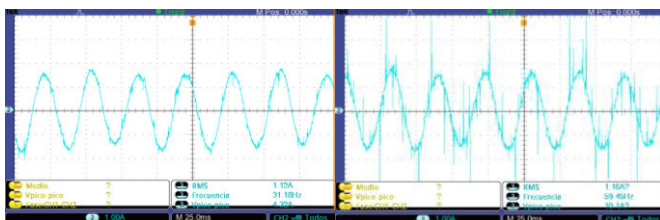


Fig. 19. Scalar Sensored open-loop currents a) Without load. b) With load.

- [5] C. Korlinchak, and M. Comanescu, "Sensorless field orientation of an induction motor drive using a time-varying observer," *IET Electric Power Applications*, vol 6, pp. 353-361, 2012.
- [6] K. Ide, S. Sato, S. Morimoto, H. Iura, H. Stefan, and C. Schreiter, "A robust sensorless AC motor drive based on simple flux observer with voltage error compensation," 2009 13th European Conference on Power Electronics and Applications, pp 1-9, 2009.
- [7] A. Oteafy, and J. Chiasson, "A study of the Lyapunov stability of an open-loop induction machine," *IEEE Trans. Control Syst. Technol.*, vol. 18, pp. 1469-1476, 2010.
- [8] A. Sayed-Ahmed, and N.A.O. Demerdash, "Fault-tolerant operation of delta-connected scalar- and vector-controlled AC motor drives," *IEEE Trans. Power Electron.*, vol 27, pp. 3041-3049, 2012
- [9] M. A. Martinez-Hernandez, F Mendoza-Mondragon, J. Resendiz; R. Rodriguez-Ponce and J. Gutierrez-Villalobos, "On-line rotor resistance estimation for an induction motor drive based on DSC," *European DSP Education and Research Conference (EDERC12)*, pp. 233-237, Sep. 2012

Productivity appraisal of Lettuce (*Lactuca sativa* var. *Vulcan*) and Nile Tilapia (*Oreochromis niloticus* var. Spring) of three aquaponic systems under greenhouse conditions.

Arellano-Márquez J.A.¹, García-Trejo J.F.², Soto-Zarazúa G.M.³

¹ *Facultad de Ingeniería, Universidad Autónoma de Querétaro, C.U. Cerro de las Campanas s/n. Col. Las campanas. C.P. 76010, Qro., México. armajaal@hotmail.com*

² *División de investigación y posgrado, Facultad de Ingeniería, Universidad Autónoma de Querétaro. C.U. Cerro de las campanas s/n. Col. Las campanas. C.P. 76010, Qro., México.*

³ *Cuerpo Académico de Sistemas Embebidos y Asociados, Facultad de Ingeniería. Universidad Autónoma de Querétaro. C.U. Cerro de las campanas s/n. Col. Las campanas. C.P. 76010, Qro., México.*

Abstract—Tilapia growth and productive parameters were evaluated in aquaponic systems, as well as lettuce growth in aquaponic systems. Each aquaponic system was made of a 6m³ fish tank and a growing bed. In aquaponic systems biomass was initially adjusted with 1080 fish of 2.3g mean weight. Fishes were feed three times a day at 8:00 am, 13:00 pm and 16:00 pm with Api-Tilapia 1 MaltaCleyton Brand adjusted to 8% of total biomass at the beginning and 5% at the end. Every 20 days, fish wet weight, total length, standard length, minimum and maximum height were obtained, and at the end of the harvest productive parameters were calculated. Every 20 days a sample of 25 g of plants were taken and fresh weight were obtained. In each aquaponic system, 150 plants/system were seeded, and followed for growth length and wet weight. Some photographic images were taken in order to establish lettuce nutritional deficiencies and make a database. Every day pH, temperature, dissolved oxygen and visibility values were taken, and every 15 days values of ammonia, nitrite, nitrate, calcium and potassium were obtained. Significant differences were observed in growth of fish and lettuce in the different systems. Treatment 1 (NFT) fish did exhibit better productive parameters than the other ones. Also Treatment 3 (Soil culture) lettuce did present larger wet weight and larger leaf height. In all systems, plants did present Ca, K and Fe deficiencies. Fish growth was good with productive parameters, also the best with survival percentages. Main factors for the differences observed were temperature changes and dissolved oxygen. NFT system (T1) was better in terms of productive parameters than Bed Growth system (T2) and soil irrigated with fish water system (T3).

Key words—Aquaponic systems, lettuce and tilapia culture, productivity appraisal.

I. INTRODUCTION

According to [1] aquaponics refers to the culture of fish and plants in a closed recirculation system, which is the result of the integration of techniques used in hydroponics and aquaculture. These systems have been

widely used throughout the history of mankind, because all great civilizations had been established near rivers or the sea, generating tools and techniques for fishing and aquaculture, as an example the Chinese culture has a tradition of more than 3000 years regarding fish farming refers [2]. Aquaponics try to build systems that resemble natural conditions in a lake or river where the waste produced by an aquatic organism serve as a nutrient source for plants. Of course, this requires the action of intermediary microorganisms as nitrifying bacteria that facilitate the flow of essential nutrients like nitrogen. Plants turn these compounds into nitrates that they can assimilate, by taking them clean the water avoiding crop eutrophication. The basic components of an aquaponic system are: aquatic organisms, plants and recirculation system.

Reference [3] says that aquaponics is gaining attention as a biointegrated food production system, which is done in closed recirculation aquaculture systems. Reference [4] indicates that this is due to the advantages of the system which includes: prolonged water reuse and minimizing discharges; further integration of the production systems of fish and plants allows cost savings so that the profitability of aquaculture systems is improved. Reference [1] indicates that technological advances in recirculating aquaculture systems stimulated a big interest in it as a potential means to increase profits while some of the waste products are used. In this regard [5] report that conventional treatments of aquaculture discharges represent a significant additional cost; thus aquaponics becomes an alternative treatment of discharges from aquaculture, more economical and profitable.

Also Reference [6] indicates that the aquaculture effluent typically supplies 10 of the 13 required plant nutrients in adequate amounts, with only Ca, K and Fe needing supplementation. Continuous generation of nutrients from

fish waste prevents nutrient depletion while uptake of nutrients by the plants prevents nutrient accumulation, extends water use, and reduces discharge to the environment.

II. MATERIALS AND METHODS

A. Location of the Experiment

The experiment was conducted under greenhouse conditions. The greenhouse was located in Campus Amazcala with dimensions of 15 m long x 7 m wide and where four black plastic tanks were installed with a capacity of 6 m³ equipped with submersible pump of 1/6 hp Little Giant brand for water recirculation and the aeration was provided with an oxygen generator Topaz brand of 1 hp. The experiment was conducted over a period of 20 weeks.

B. Biological Material

For horticultural crop seeds of Vulcan Lettuce (*Lactuca sativa* var. *Vulcan*) were used and for aquaculture Nile tilapia (*Oreochromis niloticus* var. *Spring*) organisms were used.

Each tank initially received 1080 tilapia of 2.3 g mean wet weight and each culture bed initially received 150 plants of lettuce.

C. Design of Experiments

The experimental design was a 3 x 2 design, where the three treatments interact. The number of replicates per treatment was one (or two experimental units by type of crop) to finally had a total of six experimental units.

The experimental units consisted of:

- T1. Tilapia-lettuce aquaponic system using nutrient film technique (NFT).
- T2. Tilapia-lettuce aquaponic system using the technique of inert substrate in growing bed.
- T3. Tilapia-lettuce aquaponic system using soil irrigated with water fish.

D. Associated variables with the measurement of environmental conditions inside the greenhouse.

The response variables were measured in water at noon on a daily schedule through the following determinations: temperature (°C) relative humidity (%) and radiation (watts / m²).

E. Associated variables with the measurement of physical-chemical parameters of water.

Determinations of the different forms of nitrogen in water were made, such as; ammonia nitrogen (NH₃-N), nitrate (NO₃), nitrite (NO₂), also phosphorus (PO₄) and potassium (K⁺) determining them systematically every 8 days.

F. Associated variables with fish biometrics

Measurements in fish were obtained through biometrics of a sample of the population every 20 days and the parameters were; minimum height (Amin) in mm, total length (Lt), standard length (Lp), maximum height (Amax) and wet weight (Phum) in grams. At the end of this period a determination of the standard aerobic metabolism to a sample of organisms was made, and measured daily oxygen consumption (QO₂ day-1g-1), humidity (%), total ash (%), ammonia nitrogen (obtained NH₃-N), nitrate (NO₃), nitrite (NO₂), phosphorus (PO₄) and potassium (K⁺) all in mg / L. The estimation of the amount of food that would be provided to fish (8% of total biomass at baseline and after 5%) was calculated with biometric data obtained.

G. Associated variables with lettuce biometrics

The response variables in lettuce culture were performed through biometrics, initially all organisms that were in treatment were measured, the measures taken were: total length of leaf (Lthoja), root length (Lraíz), stem diameter (Amax) and minimum (Amin) in millimeters, wet weight (Phum) in grams. Systematically the same data were taken every 20 days and a sample was took having a wet weight of 25 g biomass to make determinations like: humidity (%), total ash (%), ammonia nitrogen (NH₃-N) was selected, nitrate (NO₃), nitrite (NO₂), phosphorus (PO₄) and potassium (K⁺).

H. Analysis of collected data

A descriptive analysis expressed as the mean and standard deviation of fish growth (weight, total length and standard) in aquaponic systems was performed.

The same procedure was used for growth in plant height in aquaponic systems, so the dynamic behavior associated with each measured variable and crop yield was determined. Statgraphics Centurion XV, ver. 15.2.06 software was used to analyze the collected data.

I. Productive parameters

Productivity parameters were determined according to the parameters proposed by De Silva and Anderson (1986) using the following equations:

$$\text{Weight gain (g)} = 100 (P1-P0) \quad (1)$$

$$\text{Daily average weight gain (g)} = (P1-P0) / t \quad (2)$$

$$\text{Specific Growth Rate (\%/day)} = ((LnP1-Lnp0) \times 100) / t \quad (3)$$

$$\text{Survival rate (\%)} = Ni \times 100 / N0 \quad (4)$$

Where: P0 = initial wet weight; P1 = final wet weight; t = time (days); N0 = initial fish number; Ni = final fish number.

J. Identification of nutritional deficiencies

During the experiment, a weekly record was performed and symptoms of deficiencies in lettuce plants were determined.

III. RESULTS

A. Water Quality

A sample was taken every 15 days during the experiment; the data collected is shown in Table 1. The results of the statistical analysis show that the variation for this experiment could be attributed to dissolved oxygen (44.43%) and temperature (17.26%) between these two parameters and the remaining 38.31% of the variance is explained by the other factors (Table 2).

TABLE 1. Values of physicochemical parameters of water in different treatments during the experiment. Minimum (Min), maximum (Max) average (Avg) and Standard deviation (Std.D.)

Dissolved oxygen (O ₂ mg/L)												
	1	2	3	4	5	6	7	8	Avg.	Std.D.	Min.	Max.
T1	7.5	7.2	7	6.9	6.8	5.2	5	5.5	6.39	± 0.988	5	7.5
T2	7.6	7.1	6.8	6.6	6.4	5.3	5.2	5.1	6.26	± 0.950	5.1	7.6
T3	7.5	7	6.8	6.5	6.6	5.4	4.3	4.6	6.09	± 1.174	4.3	7.5
Temperature (°C)												
T1	29.6	28.4	30	26	28	29	31	32.3	29.2	± 1.925	26	32.3
T2	30.5	29.4	32	28	29	29	32	31.4	30.1	± 1.529	28	32
T3	30	30.2	31	28	28	28.5	31.5	31.3	29.8	± 1.461	28	31.5
Hydrogen potential (pH)												
T1	8.5	8.8	9.3	9	8.6	8.8	8.7	8.8	8.8	± 0.247	8.5	9.3
T2	8.4	8.8	9.5	9.5	8.8	9	8.8	9.1	8.9	± 0.376	8.4	9.5
T3	8.5	8.9	9.8	9.4	8.9	9.1	9.1	9.1	9.1	± 0.382	8.5	9.8
Nitrate (NO ₃ ⁻ mg/L)												
T1	1.3	0.11	2.3	2.2	2.4	2.9	3.6	3.7	2.31	± 1.185	0.11	3.7
T2	1.4	0.15	2.5	2.5	3.6	3.1	4.7	4.6	2.82	± 1.546	0.15	4.7
T3	1.3	0.15	2.5	2.3	3.8	3.8	3.65	5.8	2.91	± 1.742	0.15	5.8
Nitrite (NO ₂ ⁻ mg/L)												
T1	0.03	0.11	0.11	0.12	0.15	0.16	0.14	0.13	0.12	± 0.040	0.03	0.16
T2	0.03	0.2	0.13	0.15	0.15	0.85	0.8	0.9	0.4	± 0.376	0.03	0.9
T3	0.03	0.22	0.15	0.18	0.18	1.16	1.18	1.16	0.53	± 0.528	0.03	1.18
Ammonia (NH ₃ -N ⁺ mg/L)												
T1	0.05	0.11	0.06	0.5	0.7	0.8	0.7	0.75	0.46	± 0.331	0.05	0.8
T2	0.05	0.2	0.2	0.7	0.8	0.7	0.75	0.8	0.53	± 0.316	0.05	0.8
T3	0.05	0.22	0.3	0.9	0	0.85	0.8	0.9	0.5	± 0.397	0	0.9
Visibility (cm)												
T1	90	65	75	50	45	35	30	28	52.2	-	28	90
T2	90	50	35	25	20	18	18	18	34.2	-	18	90
T3	90	44	15	8	5	5	5	5	22.1	-	5	90

TABLE 2. Multivariate analysis for physicochemical parameters of water in aquaponic crops.

Factor	Eigenvalor	Variation (%)
Dissolved oxygen (O ₂ mg/L)	3.11	44.43
Temperature (°C)	1.2	17.26
pH	0.91	13.01
Nitrate (NO ₃ ⁻ mg/L)	0.76	10.98
Nitrite (NO ₂ ⁻ mg/L)	0.43	6.18
Ammonia (NH ₃ -N ⁺ mg/L)	0.35	5.12
Visibility (cm)	0.2	10

B. Tilapia Culture

Fish growth comparison between systems shows that T1 (NFT) presents longer fish, while the other two systems (T2 and T3) show a lower fish length with results very similar to each other (Figure 1); also weight comparison shows that T1 was more productive than T2 and T3 (Figure 2).

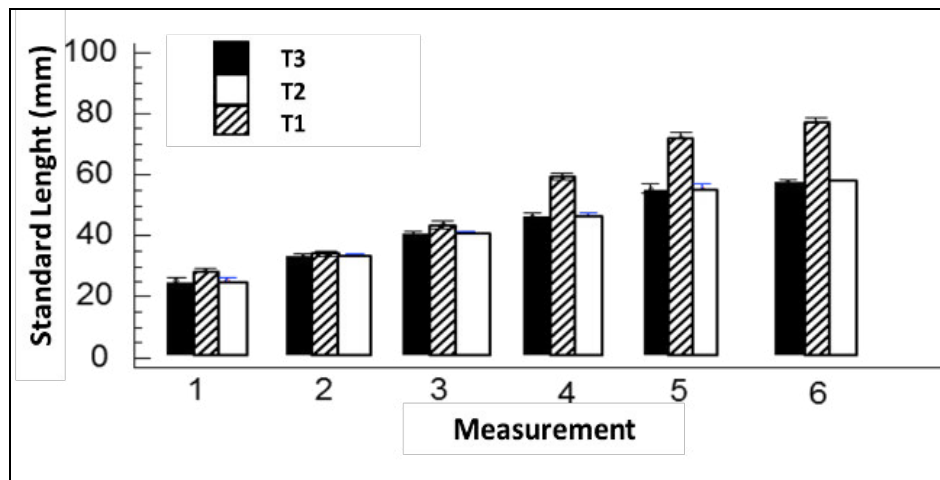


Figure 1. Fish standard length comparison between the three systems. Each point represents the average value \pm standard deviation.

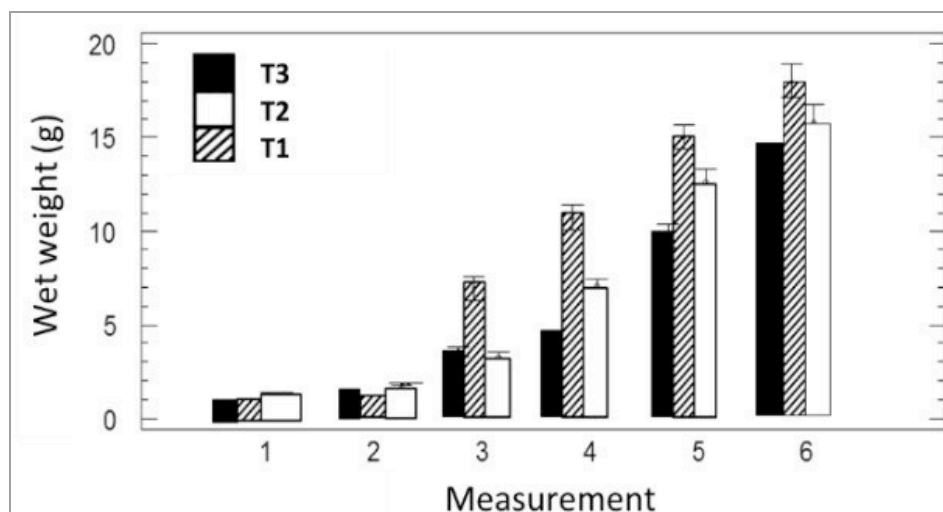


Figure 2. Fish wet weight comparison between the three systems. Each point represents the average value \pm standard deviation.

TABLE 3. Tilapia productive parameters.

	T1	T2	T3
Initial organisms (n)	1,080	1,080	1,080
Final organisms (n)	742	451	621
Initial Weight (g)	10,584	8,532	10,044
Final Weight (g)	25,228	12,177	18,443
Initial average weight (g)	9.8	7.9	9.3
Final average weight (g)	34.3	27.2	29.7
Weight gain (g)	14,644.00	3,645.00	8,399.70
Daily average weight gain (g)	162.71	40.5	93.33
Weight gain (%)	138.36	42.72	83.63
Weight gain (g/day)	0.22	0.09	0.15
Specific Growth Rate (SGR%/day)	2.07	2.05	1.94
Survival Rate (SR%)	68.7	41.76	57.5

Table 3 shows that T1 had higher mass gain than fish grown in T2 also had the lowest this crop was introduced which increased survival. The values of weight gain (g / day) were below what has been reported in other similar works like [7] where profits of 4g / day are mentioned individually.

C. Lettuce Culture

Lettuce growth comparison between systems shows that T3 was more productive than T1 and T2 (Figure 3); also leaf length comparison shows that T3 presented longer leaves

than T2 and T3 (Figure 4). However, those high values referred to a controlled filtration system and the organisms that were used had an average initial weight of 82.3g of wet biomass. Is a fact that using larger fish is a common practice because smaller fish have high mortalities [8].

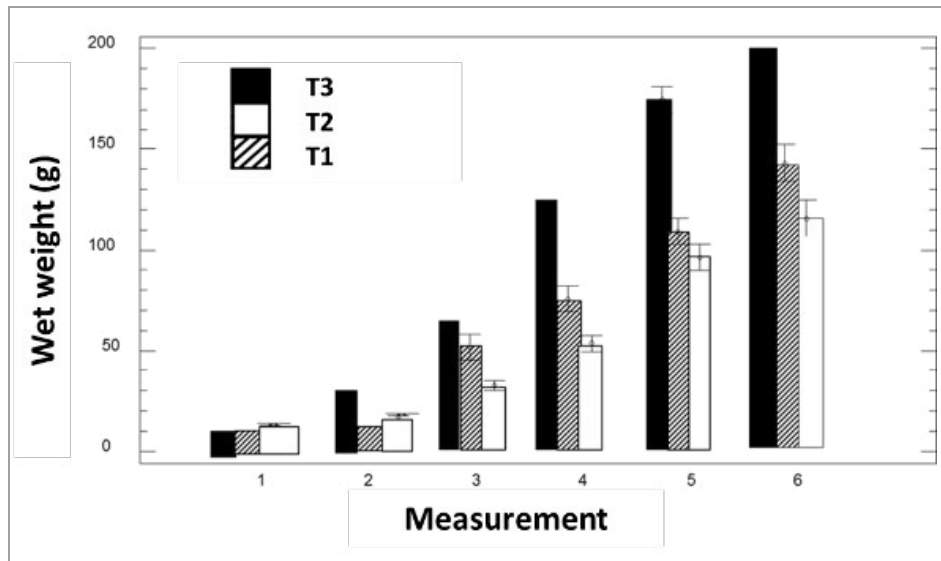


Figure 3. Lettuce wet weight comparison between the three systems. Each point represents the average value \pm standard deviation.

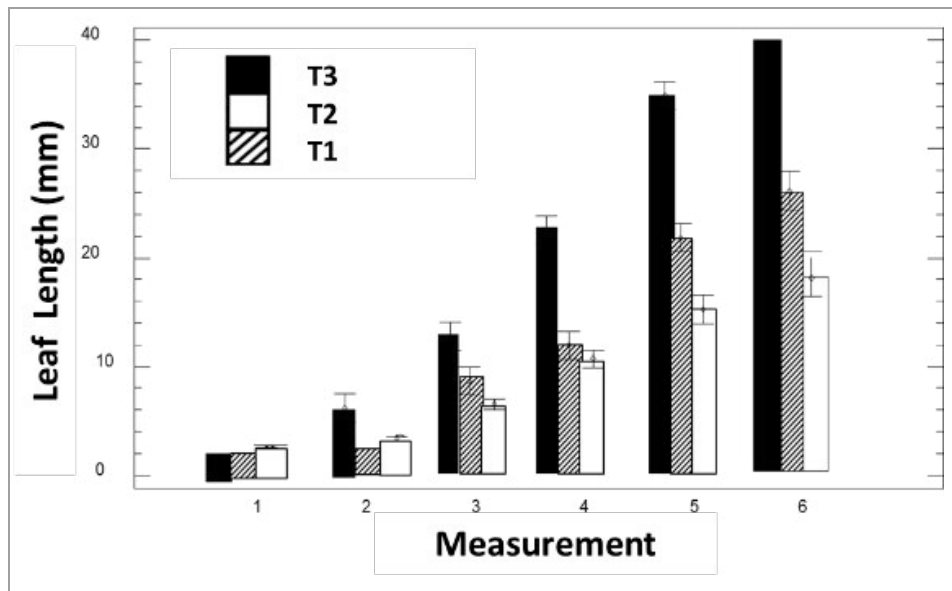


Figure 4. Lettuce leaf length comparison between the three systems. Each point represents the average value \pm standard deviation.

C. Nutrient deficiencies

A database using pictures was made to find out the behavior of the nutrients during the culture time. Some symptoms were observed and looked them in bibliography to determinate which of them were deficient or which of them not. According the symptoms observed can be determinate that calcium, potassium and iron were deficient. Iron deficiency causes yellowing between the veins on youngest leaves (Figure 5, A).

Calcium deficiency causes leaf tissue disorder tip burn, the tissue gets brown almost always affects leaves inside the heart of the plant. (Figure 5, B). Potassium deficiency causes gray develop on leave or areas near the margins. Oldest leaves are affected first with characteristic symptoms of scorching around the leaf margins (Figure 5, C).

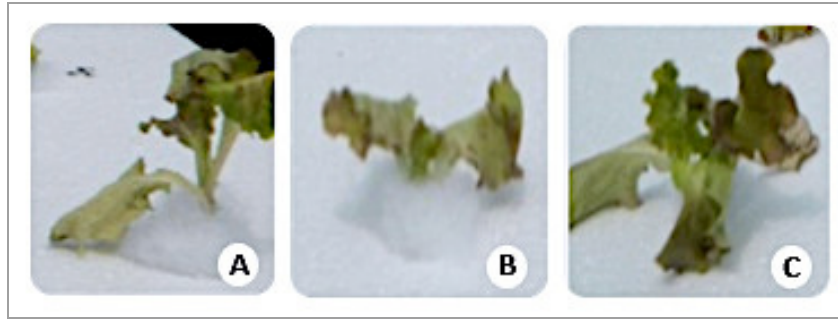


Figure 5. Deficiency symptoms observed on lettuce culture.

I. DISCUSSIONS

The monitoring of environmental temperature during the experimental period showed variations with minimum values of 3.6 °C at night and maximum values of 45 °C during the day. The water temperature was more stable with minimum values of 19 °C and maximum values of 30.5 °C reached during the day. Considering the case of the Nile Tilapia (*Oreochromis niloticus*) a range of 28 to 30 °C has been determined as the optimum for their development [9].

In the oxygen monitoring was observed that this parameter had an irregular behavior falls to 0 mg/L overnight and peaks of 8 mg/L during the day. References [6, 10] had reported ranges of 4.0 to 6.0 mg/L of O₂, for lettuce crops, basil and parsley, among others, while [11] remained higher than 5 mg/L O₂ concentrations.

The hydrogen potential values showed minimum values of 8 and maximum of 9.9. However, the recommended pH for the proper operation in the systems is between 7.5 and 9 units of value [12].

The statistical analysis showed that the factor that can explain most of the variation of the process is the dissolved oxygen, and after that the temperature, a better control of both of these parameters should be done in order to have avoid having experimental error. Temperature is a parameter hard to control under greenhouse conditions because it can take different ranges during each season and during the day, depends on the environment.

There were some differences between the three systems, according with the analysis of means and yield of fish culture, treatment 1, NFT system was more productive comparing wet weight and standard length than treatment 2, growing bed and treatment 3, soil irrigated with fish water. According with the analysis of means of lettuce culture, treatment 3, lettuce irrigated with fish water was more productive than the other treatments. To explain these results are analyzed in detail the requirements and nutritional deficiencies in plants, water quality parameters and nutrient dynamics presented in the systems.

II. CONCLUSIONS

By getting an average of 198.76 g wet weight in lettuce for soil culture system irrigated with water fish, 140.38 g for growing in NFT and 112.23 g for inert substrate system. Best results were obtained in the soil irrigated with fish water. Also the productivity in fish culture showed that the most productive system was T1 with an average wet weight of 25,228 g and the less productive was the inert substrate (T2).

According to the review that was made about the nutrients and its deficiency may be recommended supplement the systems because since the early days of culture was observed that the lettuce had deficits of some nutrients, some evident symptoms. After supplement them would be advisable to do further analysis to see if the system productivity is affected, or if supplementation does not cause any difference.

III. REFERENCES

- [1] J. Rakocy, The status of aquaponics, part 1. *Aquaculture Magazine* 25: 83-88, 1999.
- [2] R. Pillay, *Aquaculture and the Environment*. John Wiley and Sons, Inc, New York, NY, 1992.
- [3] S. Diver, Pond aquaponics: new pathways to sustainable integrate aquaculture and agriculture. *Aquanews*;34: :10-11, 2006.
- [4] M. Masser, *Hydroponics integration with aquaculture*. First Ed. Alabama: 23, 2002.
- [5] P.R. Adler, J. K. Harper, E. M. Wade , F. Takeda, and S. T. Summerfelt, Economic analysis of an aquaponic system for the integrated production of rainbow trout and plants. *International Journal of Recirculating Aquaculture*. 1: 10-13, 2000.
- [6] J.E. Rakocy, R. C. Shultz, D. S. Bailey, and E. S. Thoman, Aquaponic production of tilapia and basil: comparing a batch and staggered cropping system. *Acta Horticulturae (ISHS)* 648: 63-69, 2004.
- [7] J.E. Rakocy, M. Masser, and T. Losordo, Recirculating Aquaculture Tank Production Systems: Aquaponics—Integrating Fish and Plant Culture Revisión. Southern Regional Aquacultural Center: 24, 2006.
- [8] A.F.M. El-Sayed, Tilapia culture in salt water: Environmental requirements, nutritional implications and economic potentials. In: E. Cruz Suarez et al. (eds.) *Avances en nutrición acuícola VII*. Universidad Autónoma de Nuevo Leon, Nuevo Leon , Mexico, 2006.
- [9] M.B. Timmons, J. Ebeling, F. Wheaton , and S. Summerfel, *Recirculating Aquaculture Systems* Northeastern Regional Aquaculture Center, NY, USA, 2002.
- [10] J.E. Rakocy, J. A. Hargreaves, and D. S. Bailey, Nutrient accumulation in a recirculating aquaculture system integrated with vegetable hydroponic production *Techniques for Modern Aquaculture*. American Society of Agricultural Engineers. p 148-158. J. K. Wang, ed., Michigan, St. Joseph, USA, 1993.
- [11] D.E. Seawright, R. R, Stickney, and R. B, Walker, Nutrient dynamics in integrated aquaculture-hydroponics systems. *Aquaculture* 160: 215-237, 1998.
- [12] J.N. Hochheimer, and F. Wheaton, Biological filters: trickling and RBC design. In: *Second International Conference of Recirculating Aquaculture*, Roanoke, Virginia. p 291–318, 1998.

Implementation of High Resolution Unipolar PWM Inverter using Xilinx System Generator

Mendoza-Mondragón, F. ^{#1}, Espinosa-Calderón, A. ^{*2},

Martínez-Hernández, A. M. ^{#3}, Rodríguez-Reséndiz, J. ^{#4}

[#] *Mechatronics Department, Universidad Autónoma de Querétaro (UAQ)
Cerro de las Campanas S/N, Las Campanas, 76010, Querétaro, México*

¹ fmendoza@uaq.mx

³ moises.martinez@uaq.mx

⁴ juvenal@uaq.edu.mx

^{*} *Laboratorio de Investigación en Control Reconfigurable, LiCORE A.C
Constituyentes del Parque, Querétaro, Querétaro, México*

² a.espinosa@licore.org

Abstract— This paper presents an implementation technique of a high resolution Unipolar Pulse Width Modulator (UPWM) for power inverter applications. Unipolar switched inverter has the advantage of a higher efficiency and lower harmonic distortion. The technique was tested in a 2kW inverter with a typical LC filter and it was achieved a Total Harmonic Distortion below 2%. Simulations and experimental results were performed. The technique was developed with the Xilinx System Generator in MATLAB/Simulink and it was implemented on a System on Chip XC70Z020CLG484-1 Zynq device.

Keywords—Unipolar Pulse Width Modulation (UPWM); Power Inverters; Field Programmable Gate Array (FPGA), Total Harmonic Distortion (THD).

I. INTRODUCTION

Digital Pulse Width Modulation is the most common technique for the control of power converters. Several topologies for energy conversion performs a high frequency PWM signal used for modulate the desired voltage. The output of an ideal inverter (DC-AC converter), is a pure sinusoidal waveform. However, achieving such waveform with a real PWM inverter is difficult due to the high harmonic content of the nonlinear switching frequency. Typically a low pass filter is used to achieve desired THD, but the design of this filter can be quite challenging [1]. The THD depends on several factors, such as: the filter design, the nature of the inverter load, if it is linear or not, the switching strategy; and the modulation index.

II. SINGLE PHASE INVERTER

The energy conversion from DC to AC uses power switching devices such as Metal Oxide Semiconductor Field Effect Transistor (MOSFET), Insulated Gate Bipolar Transistor (IGBT), and

recently new high efficiency Silicon Carbide (SiC) devices [2]. To improve the efficiency and reliability of the traditional inverter (see Fig. 1) several new topologies and PWM schemes have been proposed [3-5]. In digitally controlled H-bridge Voltage Source Inverter (VSI) the Sinusoidal PWM (SPWM) is classified in two kinds, commonly known as Bipolar PWM (BPWM) and on the other hand as Unipolar PWM (UPWM). BPWM is widely used due its simplicity, that technique has an equivalent switching frequency with the carrier signal. However, the UPWM frequency of the output voltage is doubled using the same switching frequency [6]. Therefore, UPWM reduce the size of the filter elements but increase commutation losses due to higher switching frequency [7].

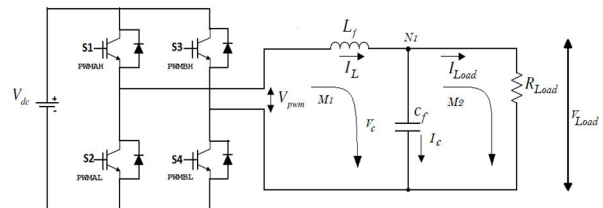


Fig. 1. Typical voltage source inverter with an LC filter.

It is a known fact that dedicated on-chip hardware like ASICs or FPGA devices are not easy to program, one of the main disadvantages is the long time development required due to hand written code and the time-consuming debugging. In [7] it is presented an implementation of a photovoltaic inverter using the Xilinx Systems Generator (XSG) with MATLAB/Simulink, the authors describe a bipolar and unipolar PWM counter based on the use of a rapid prototyping approach, an efficient power converter can be design in a shorter time.

This paper deals with an implementation of a UPWM using the XSG. The sinusoidal modulation signal and the UPWM have been implemented on a XC70Z020CLG484-1 Zynq device. A typical 2KW VSI is used for experimental testing. Theoretical LC filter design is validated through THD measurements, a discuss of the main practical aspect of the design of the UPWM inverter is carried out. Finally different resolutions for UPWM are compared in terms of using of FPGA resources and THD measurements.

III. DIGITAL PULSE WIDTH MODULATORS

Mainly two operating modes are used to achieve variable duty, edge aligned modes and center aligned mode, in the edge aligned the left edge of the signal is fixed and the trailing edge is modulated, as show in Fig. 2, on the edge aligned mode the PWM counter is an up-counter, and the frequency of the PWM (f_{pwm}) is given by the counter clock frequency (clk) and the maximum counter value (P_{max}).

$$f_{pwm} = \frac{clk}{(P_{max} - 1)} \quad (1)$$

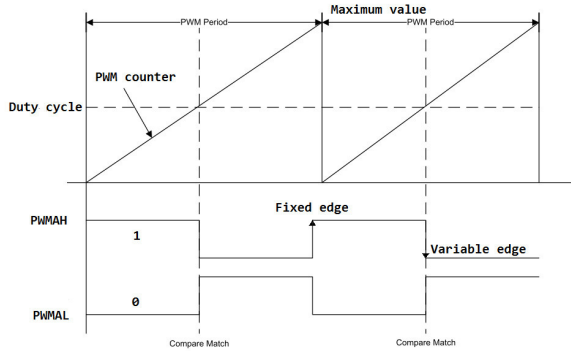


Fig. 2. Edge aligned digital PWM.

In the center aligned PWM mode, the center of the generated pulse are fixed and both edges are modulated by a variable duty cycle as shown in Fig. 3, commonly a single up-down counter unit and two comparators are used to implement a digital PWM. The disadvantage of the PWM counter strategy is that the nominal resolution depends directly on the maximum count value, it is worth notice that for the same PWM frequency when center aligned mode is used the counter value is the half of the edge aligned method, thus this method has lower resolution using the same clock frequency.

$$f_{pwm} = \frac{clk}{2 * (P_{max} - 1)} \quad (2)$$

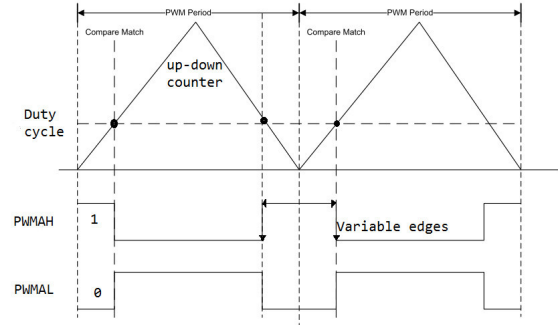


Fig. 3. Center aligned digital PWM.

So a higher PWM switching frequency gets a lower resolution. In order to keep the resolution constant for different PWM frequencies, advanced Phased Locked Loops (PLLs) components of the modern FPGA devices can be used to achieve the desired system clock frequency.

IV. UPWM MODULE DESCRIPTION

The proposed scheme (see Fig. 4) were implemented in MATLAB/Simulink through the XSG toolbox. Once the model is verified by simulation the automated VHDL or Verilog code generation can be done. This HDL code is synthesized in the Vivado Design Suite, then the resulting design is downloaded through JTAG interface.

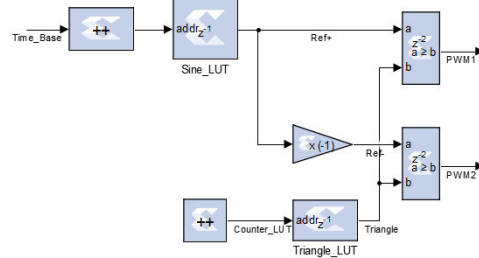


Fig. 4. UPWM gate signal generation.

The UPWM consist mainly in the generation of three signals, a discrete triangular carrier waveform, a modulated sinusoidal waveform and a complementary signal ($-\sin(\omega)$) as shown in the Fig. 5. Then this signal are compared in order to generate complementary PWM pulses ($S2 = \bar{S1}, S4 = \bar{S3}$).

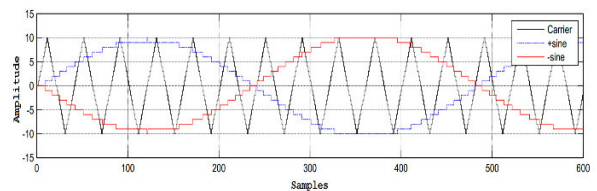


Fig. 5. Discrete modulated signals in the UPWM scheme.

The generation of the triangular and sinusoidal waveforms are implemented on a Look up Table (LUT), see Fig. 6, where the size of the LUT waveform is calculates as follows:

$$LUT_{size} = \frac{clk}{f_{pwm}} \quad (3)$$

Then the maximum and minimum values of the triangular waveform are given by:

$$Max = integer\left(\frac{LUT_{size}}{4}\right) \quad (4)$$

$$Min = -integer\left(\frac{LUT_{size}}{4}\right) \quad (5)$$

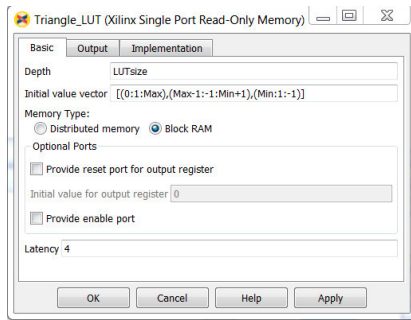


Fig. 6. Window properties of the triangle waveform block.

The generation of the modulated sinusoidal waveform depends on a Time Base (TB) pulse generation, which is used to enable the counter of the sine LUT and thus to generate desired modulated frequency (F_m). See Fig. 7. A free run counter is used to compare with the desired TB constant (TB_{const}).

$$TB_{const} = \frac{clk}{LUT_{size} * F_m} - 1 \quad (6)$$

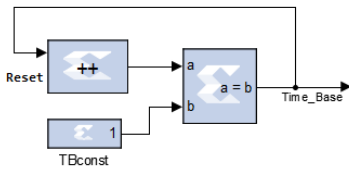


Fig. 7. Time base pulse generator.

V. DEAD TIME UNIT

In order to avoid damaging on the switching devices it is important to consider t_{on} and t_{off} of the power semiconductors, to prevent a short-circuit a dead-band is inserted, a small time in which, both

upper and lower switches in a bridge leg are turned off, see Fig. 8, however the dead-band in practice add current distortion and voltage loss [9-10]. The effect of dead-band becomes severe when the modulation index is small, near the zero crossing modulated signals.

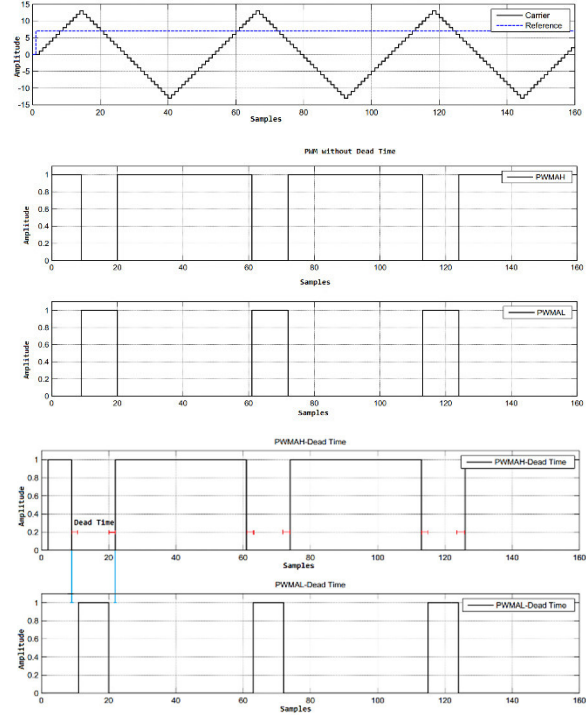


Fig. 8. PWM with dead time insertion.

Fig. 9 shows the subsystems for dead time insertion in both legs of the VSI. The dead time insertion is made from a circuit that detects rising and falling edges and integrates the duration of the pulse, and then its compared with a free running counter plus dead time constant as shown in Fig. 10, the dead time constant (DT_{const}) is calculate as follow to achieve the desired dead time (D_{time}).

$$DT_{const} = D_{time} * clk \quad (7)$$

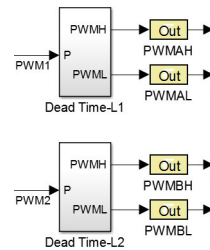


Fig. 9. Dead time insertion modules for complementary mode.

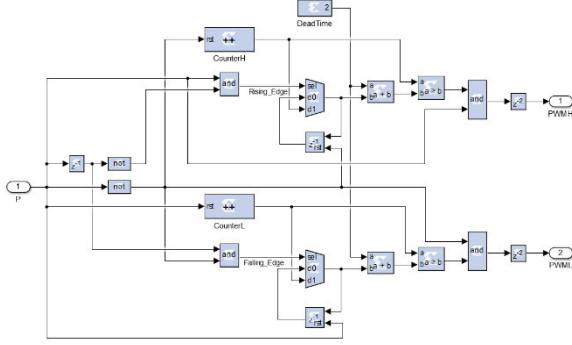


Fig. 10. Dead time generator subsystem.

VI. LC FILTER DESIGN

As it is shown in [11], the rms value of the output voltage and current harmonics (V_{oav} , I_{oav}) over one period of the fundamental is given by:

$$V_{oav} = \frac{V_{DC}}{C_f L_f f_{pwm}^2} K(m_a) \quad (8)$$

$$I_{oav} = \frac{V_{DC}}{L_f f_{pwm}} A(m_a) \quad (9)$$

$$K(m_a) = \sqrt{\frac{m_a^2 - \frac{15}{4}m_a^4 + \frac{64}{5\pi}m_a^5 - \frac{5}{4}m_a^6}{1440}} \quad (10)$$

$$A(m_a) = \sqrt{\frac{m_a^2 - \frac{16}{3}m_a^3 + \frac{3}{4}m_a^4}{24}} \quad (11)$$

Where V_{oav} and I_{oav} depends not only on the filter values, but also on factors $K(m_a)$ and $A(m_a)$. This gains are function of the modulation index (m_a).

For calculation of optimum value of the inductance of the filter, the nominal rms load current (I_{rms}) is needed, and it also proposes a value of the desired total harmonic distortion of the load voltage V_{oav} .

$$L_f = \frac{V_{rms}}{I_{rms} f_{pwm}} * Kf \quad (12)$$

$$Kf = \sqrt{\frac{4\pi f_o^2}{V_{oav}^2 f_{pwm}^2} K(m_a)^2 V_{DC}^2 + \frac{K(m_a)}{V_{oav}} V_{DC}} \quad (13)$$

$$C_f = \frac{V_{DC} I_{rms} K(m_a)}{V_{rms} V_{oav} f_{pwm} Qf} \quad (14)$$

$$Qf = \sqrt{\frac{4\pi f_o^2}{V_{oav}^2 f_{pwm}^2} K(m_a)^2 V_{DC}^2 + \frac{K(m_a)}{V_{oav}} V_{DC}} \quad (15)$$

VII. EXPERIMENTAL RESULTS

In order to verify the developed design and filter construction, a small 2KW single-phase full-bridge IGBT inverter was used, see experimental setup in Fig. 16. The experimental setup is shown in Table I.

TABLE I. EXPERIMENTAL CONDITIONS

Inverter characteristics	
DC bus voltage	400 V
Peak output voltage	179.6 V
Amplitude modulation index	0.449
Switching characteristics	
Modulated frequency	60 Hz
Frequency modulation index	166
PWM carrier frequency	9.96 KHz
Output voltage frequency	19.962 KHz
Desired harmonic distortion	
Desired V_{oav}	1.3%
LC filter and load	
Filter inductance	0.350 mH
Filter capacitance	16 μ F
Resistance load	50 Ω

Different PWM resolution design were tested, see Table II, the development tools used were MATLAB 2014a Student version, the XSG 2014.4 and, the Vivado Design Suite 2014.4. The settings for the HDL code generation used for the synthesis strategy were "Flow_PerfOptimized_High" and for the implementation strategy were "Performance_ExplorePostRoutePhysOpt". Synthesis results are shown in Table III.

TABLE II. SYSTEM PARAMETERS OF THE UPWM MODULES

	Module		
	UPWM_50	UPWM_100	UPWM_125
System Clock (MHz)	50	100	125
Resolution (Bits)	12	13	13
Peak values of the triangular carrier (+/-)	1255	2510	3138
Dead Time (μ s)	1	1	1
Minimum pulse width regulation (ns)	80	40	32

TABLE III. FPGA RESOURCE USAGE FOR DIFFERENT UPWM RESOLUTIONS

Resource	Utilization			Available
	UPWM_50	UPWM_100	UPWM_150	
FF	95	101	181	106400
LUT	140	151	186	53200
Memory LUT	11	11	11	17400
I/O	6	6	6	200
BRAM	6	13	13	140

DSP48	10	10	3	220
BUFG	2	2	2	32
PLL	1	1	1	4

Voltage and current waveform of the main signal of the system are measured to verify the successful implementation of the UPWM inverter. As can be seen in Fig. 11a the frequency of the output voltage (CH1) is doubled using the same switching frequency of the PWM signal (CH2), in Fig. 11b and Fig. 11c the output waveforms of the voltage before and after the filter stage.

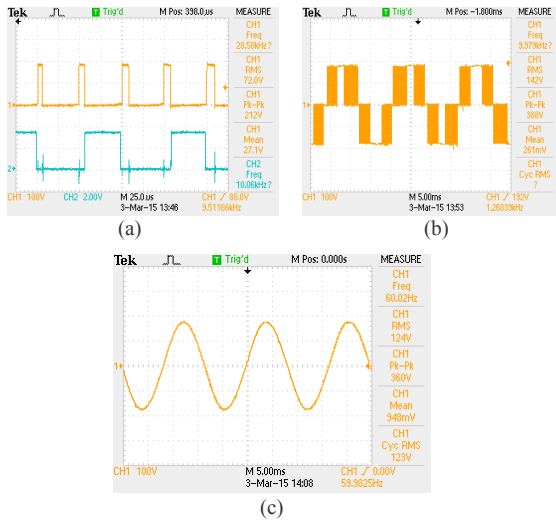


Fig. 11. a) The doubled frequency PWM output voltage and the PWM modulating signal. b) The bipolar output voltage of the full H-bridge. c) The output voltage of the load.

Fig 12a, b and c shows the waveforms of the current on the inductor, capacitor and resistive load respectively.

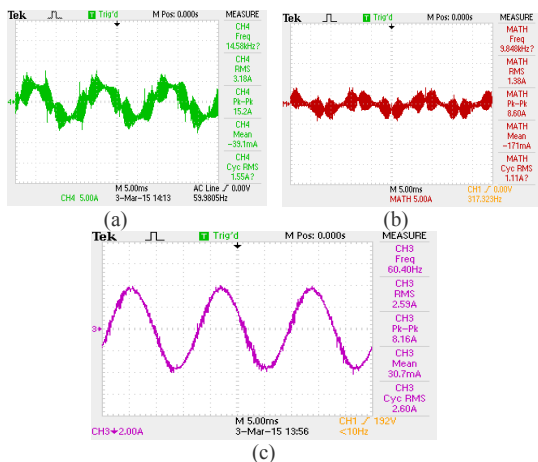


Fig. 12. a) Current waveform of the inductor. b) Current waveform of the capacitor. c) Output current waveform of the resistive load.

Fig. 13a and b shows the output voltage spectrum and the THD measurement respectively, as is expected, the first considerable harmonic is on the switching frequency of ~ 20 KHz, but also another group of harmonics appears on the ~ 10 KHz due to the dead time insertion. The THD measurement was carried out by a single phase power quality analyzer Fluke-43B.

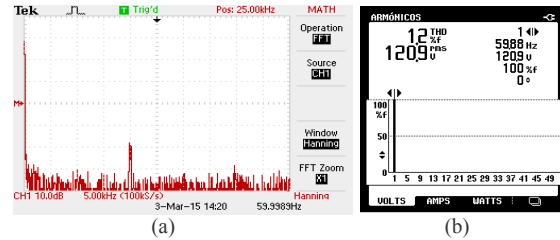


Fig. 13. a) Frequency spectrum of the output voltage. b) Power quality analyzer THD measurement.

For the different UPWM resolutions a recording of 30 minutes of the THD and rms output voltage was made, in order to compare and measure if there is a significant difference using a higher PWM resolution. The results are shown in Table IV, in Fig. 14 and Fig. 15 can be seen the trend of the recording data for the highest resolution synthesized module.

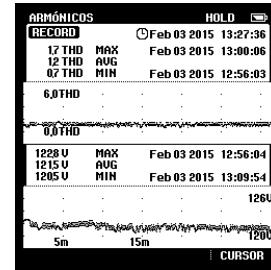


Fig. 14. Record over a period of 30 minutes of the THD and rms output voltage using the UPWM_125 module.

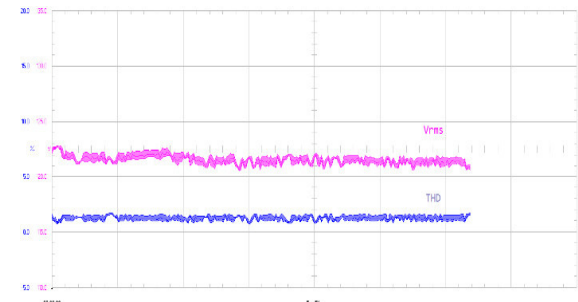


Fig. 15. Power quality analyzer trend measurement of the THD and rms output voltage using the UPWM_125 module.

TABLE IV. TRENDS OF THD AND VRMS MEAUREMENTS

	THD (%)		
	UPWM_50	UPWM_100	UPWM_125
Minimum	1.1	1.1	0.7
Average	1.3	1.3	1.2
Maximum	1.4	1.4	1.7
	Vrms (V)		
	UPWM_50	UPWM_100	UPWM_125
Minimum	121.3	121.8	120.5
Average	122.1	122.7	121.5
Maximum	122.6	123.9	122.8

CONCLUSIONS

A UPWM VSI has been implemented successfully on a Zynq FPGA using the XSG toolbox with MATLAB/Simulink. The LC filter design and THD requirement was validated through the measurements of a power quality analyzer Fluke 43B. Different resolutions of UPWM were tested. The measured average THD and RMS voltage over 30 minutes long shown a minimal deviation.

ACKNOWLEDGMENT

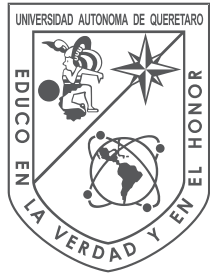
Authors thank to the *United States Agency for the International Development* (USAID) for its economic support through the Fixed Obligation Grant: *AID-523-F-14-00003*; and to the *Xilinx University Program* for its generous donation of development kits and software licensing. Authors also thank to the Fondo para el Fortalecimiento de la Vinculación 2013 from UAQ for its economic support for this research. FMM and MHMA would also thanks the *Consejo Nacional de Ciencia y Tecnología* (CONACYT) from Mexico for the grants 247771 and 370689 respectively.

REFERENCES

- [1] M. N. M. Isa, M. I. Ahmad, S. a Z. Murad, and M. K. M. Arshad, "FPGA based SPWM bridge inverter," *Am. J. Appl. Sci.*, vol. 4, no. 8, pp. 584–586, 2007.
- [2] V. Esteve, J. Jordán, E. Sanchis-Kilders, E. J. Dede, E. Maset, J. B. Ejea, and A. Ferreres, "Comparative Study of a Single Inverter Bridge for Dual-Frequency Induction Heating Using Si and SiC MOSFETs," *IEEE Trans. Ind. Electron.*, vol. 62, no. 3, pp. 1440–1450, 2015.
- [3] S. Guo and A. Q. Huang, "Control and Analysis of the High Efficiency Split Phase PWM Inverter," in *IEEE Applied Power Electronics Conference and Exposition (APEC)*, 2014, pp. 2415–2420.
- [4] M. I. Jahmeerbacus and M. Sunassee, "Evaluation of Selective Harmonic Elimination and sinusoidal PWM for single-phase DC to AC inverters under dead-time distortion," in *International Symposium on Industrial Electronics (ISIE)*, 2014, pp. 465–470.
- [5] L. U. Sudha, J. Baskaran, and S. Thamizharasan, "Hybrid PWM strategies for power balance in H bridge inverter," in *International Conference on Computation of Power, Energy, Information and Communication (ICCPEIC)*, 2014, vol. 2, pp. 536–539.
- [6] B. Lei, G.-C. Xiao, and X.-L. Wu, "Comparison of performance between bipolar and unipolar double-frequency sinusoidal pulse width modulation in a digitally controlled H-

bridge inverter system," *Chinese Phys. B*, vol. 22, no. 6, pp. 1–8, 2013.

- [7] R. Selvamuthukumar and R. Gupta, "Rapid prototyping of power electronics converters for photovoltaic system application using Xilinx System Generator," *IET Power Electron.*, vol. 7, no. 9, pp. 2269–2278, 2014.
- [8] S. Guo and A. Q. Huang, "Control and Analysis of the High Efficiency Split Phase PWM Inverter," in *IEEE Applied Power Electronics Conference and Exposition (APEC)*, 2014, pp. 2415–2420.
- [9] T. Sutikno and M. Facta, "An Efficient Strategy to Generate High Resolution Three-Phase Pulse Width Modulation Signal Based on Field Programmable Gate Array," *Int. J. Comput. Electr. Eng.*, vol. 2, no. 3, pp. 413–416, 2010.
- [10] L. Chen and F. Z. Peng, "Elimination of Dead-time in PWM Controlled Inverters," in *IEEE Applied Power Electronics Conference and Exposition (APEC)*, 2007, pp. 306–309.
- [11] P. A. Dahono, A. Purwadi, and Q. Qamaruzzaman, "An LC filter design method for single-phase PWM inverters," in *Proceedings of 1995 International Conference on Power Electronics and Drive Systems. PEDS 95*, 1995, no. 95, pp. 571–576.



UNIVERSIDAD
AUTÓNOMA DE
QUERÉTARO

